

Eugene M. Izhikevich  
The Neurosciences Institute

# Dynamical Systems in Neuroscience: The Geometry of Excitability and Bursting

December 19, 2005

The MIT Press



# Contents

Preface	ix
<b>1 Introduction</b>	<b>1</b>
1.1 Neurons . . . . .	1
1.1.1 What is a spike? . . . . .	2
1.1.2 Where is the threshold? . . . . .	3
1.1.3 Why are neurons different and why do we care? . . . . .	6
1.1.4 Building models . . . . .	6
1.2 Dynamical Systems . . . . .	7
1.2.1 Phase portraits . . . . .	8
1.2.2 Bifurcations . . . . .	10
1.2.3 Hodgkin classification . . . . .	14
1.2.4 Neuro-computational properties . . . . .	16
1.2.5 Building models (revisited) . . . . .	20
Summary and Bibliographical Notes . . . . .	20
<b>2 Electrophysiology of Neurons</b>	<b>25</b>
2.1 Ions . . . . .	25
2.1.1 Nernst potential . . . . .	26
2.1.2 Ionic currents and conductances . . . . .	27
2.1.3 Equivalent circuit . . . . .	28
2.1.4 Resting potential and input resistance . . . . .	29
2.1.5 Voltage-clamp and I-V relation . . . . .	30
2.2 Conductances . . . . .	32
2.2.1 Voltage-gated channels . . . . .	33
2.2.2 Activation of persistent currents . . . . .	34
2.2.3 Inactivation of transient currents . . . . .	36
2.2.4 Hyperpolarization-activated channels . . . . .	37
2.3 Hodgkin-Huxley Model . . . . .	38
2.3.1 Hodgkin-Huxley equations . . . . .	38
2.3.2 Action Potential . . . . .	40
2.3.3 Propagation of the action potentials . . . . .	42
2.3.4 Dendritic compartments . . . . .	43

2.3.5	Summary of voltage-gated currents . . . . .	45
	Summary and Bibliographical Notes . . . . .	49
	Exercises . . . . .	51
<b>3</b>	<b>One-Dimensional Systems</b>	<b>55</b>
3.1	Electrophysiological Examples . . . . .	55
3.1.1	I-V relations and dynamics . . . . .	56
3.1.2	Leak + instantaneous $I_{\text{Na},p}$ . . . . .	57
3.2	Dynamical Systems . . . . .	58
3.2.1	Geometrical analysis . . . . .	61
3.2.2	Equilibria . . . . .	62
3.2.3	Stability . . . . .	62
3.2.4	Eigenvalues . . . . .	63
3.2.5	Unstable equilibria . . . . .	63
3.2.6	Attraction domain . . . . .	64
3.2.7	Threshold and action potential . . . . .	65
3.2.8	Bistability and hysteresis . . . . .	66
3.3	Phase Portraits . . . . .	70
3.3.1	Topological equivalence . . . . .	71
3.3.2	Local equivalence and the Hartman-Grobman theorem . . . . .	71
3.3.3	Bifurcations . . . . .	72
3.3.4	Saddle-node (fold) bifurcation . . . . .	75
3.3.5	Slow transition . . . . .	79
3.3.6	Bifurcation diagram . . . . .	80
3.3.7	Bifurcations and I-V recordings . . . . .	81
3.3.8	Quadratic integrate-and-fire neuron . . . . .	82
	Summary and Bibliographical Notes . . . . .	86
	Exercises . . . . .	87
<b>4</b>	<b>Two-Dimensional Systems</b>	<b>93</b>
4.1	Planar Vector Fields . . . . .	93
4.1.1	Nullclines . . . . .	96
4.1.2	Trajectories . . . . .	98
4.1.3	Limit cycles . . . . .	101
4.1.4	Relaxation Oscillators . . . . .	101
4.2	Equilibria . . . . .	104
4.2.1	Stability . . . . .	104
4.2.2	Local linear analysis . . . . .	106
4.2.3	Eigenvalues and eigenvectors . . . . .	107
4.2.4	Local equivalence . . . . .	108
4.2.5	Classification of equilibria . . . . .	108
4.2.6	Example: FitzHugh-Nagumo model . . . . .	111
4.3	Phase Portraits . . . . .	113

4.3.1	Bistability and attraction domains . . . . .	113
4.3.2	Stable/unstable manifolds . . . . .	114
4.3.3	Homoclinic/heteroclinic trajectories . . . . .	116
4.3.4	Saddle-node bifurcation . . . . .	116
4.3.5	Andronov-Hopf bifurcation . . . . .	122
	Summary and Bibliographical Notes . . . . .	124
	Exercises . . . . .	127
<b>5</b>	<b>Conductance-Based Models and Their Reductions</b>	<b>133</b>
5.1	Minimal Models . . . . .	133
5.1.1	Amplifying and resonant gating variables . . . . .	135
5.1.2	$I_{Na,p}+I_K$ -model . . . . .	138
5.1.3	$I_{Na,t}$ -model . . . . .	139
5.1.4	$I_{Na,p}+I_h$ -model . . . . .	142
5.1.5	$I_h+I_{Kir}$ -model . . . . .	144
5.1.6	$I_K+I_{Kir}$ -model . . . . .	145
5.1.7	$I_A$ -model . . . . .	148
5.1.8	$Ca^{2+}$ -gated minimal models . . . . .	152
5.2	Reduction of multi-dimensional models . . . . .	155
5.2.1	Hodgkin-Huxley model . . . . .	155
5.2.2	Equivalent potentials . . . . .	158
5.2.3	Nullclines and I-V recordings . . . . .	158
5.2.4	Reduction to simple model . . . . .	161
	Summary and Bibliographical Notes . . . . .	163
	Exercises . . . . .	164
<b>6</b>	<b>Bifurcations</b>	<b>167</b>
6.1	Equilibrium (Rest State) . . . . .	167
6.1.1	Saddle-node (fold) . . . . .	170
6.1.2	Saddle-node on invariant circle . . . . .	173
6.1.3	Supercritical Andronov-Hopf . . . . .	177
6.1.4	Subcritical Andronov-Hopf . . . . .	181
6.2	Limit Cycle (Spiking State) . . . . .	186
6.2.1	Saddle-node on invariant circle . . . . .	188
6.2.2	Supercritical Andronov-Hopf . . . . .	189
6.2.3	Fold limit cycle . . . . .	190
6.2.4	Homoclinic . . . . .	194
6.3	Other Interesting Cases . . . . .	199
6.3.1	Three-dimensional phase space . . . . .	199
6.3.2	Cusp and pitchfork . . . . .	201
6.3.3	Bogdanov-Takens . . . . .	202
6.3.4	Relaxation oscillators and Canards . . . . .	207
6.3.5	Bautin . . . . .	209

6.3.6	Saddle-node homoclinic orbit . . . . .	210
6.3.7	Hard and soft loss of stability . . . . .	213
	Summary and Bibliographical Notes . . . . .	214
	Exercises . . . . .	220
<b>7</b>	<b>Neuronal Excitability</b>	<b>225</b>
7.1	Excitability . . . . .	225
7.1.1	Bifurcations . . . . .	226
7.1.2	Hodgkin's classification . . . . .	228
7.1.3	Classes 1 and 2 . . . . .	231
7.1.4	Class 3 . . . . .	232
7.1.5	Ramps, steps, and shocks . . . . .	234
7.1.6	Bistability . . . . .	236
7.1.7	Class 1 and 2 spiking . . . . .	238
7.2	Integrators vs. Resonators . . . . .	239
7.2.1	Fast subthreshold oscillations . . . . .	240
7.2.2	Frequency preference and resonance . . . . .	242
7.2.3	Frequency preference <i>in vivo</i> . . . . .	247
7.2.4	Thresholds and action potentials . . . . .	249
7.2.5	Threshold manifolds . . . . .	250
7.2.6	Rheobase . . . . .	252
7.2.7	Post-inhibitory spike . . . . .	253
7.2.8	Inhibition-induced spiking . . . . .	255
7.2.9	Spike latency . . . . .	257
7.2.10	Flipping from an integrator to a resonator . . . . .	259
7.2.11	Transition between integrators and resonators . . . . .	261
7.3	Slow Modulation . . . . .	264
7.3.1	Spike-frequency modulation . . . . .	265
7.3.2	I-V relation . . . . .	267
7.3.3	Slow Subthreshold oscillation . . . . .	270
7.3.4	Rebound response and voltage sag . . . . .	270
7.3.5	AHP and ADP . . . . .	272
	Summary and Bibliographical Notes . . . . .	274
	Exercises . . . . .	276
<b>8</b>	<b>Simple Models</b>	<b>279</b>
8.1	Simplest Models . . . . .	279
8.1.1	Integrate-and-fire . . . . .	280
8.1.2	Resonate-and-fire . . . . .	281
8.1.3	Quadratic integrate-and-fire . . . . .	282
8.1.4	Simple model of choice . . . . .	283
8.1.5	Canonical models . . . . .	289
8.2	Cortex . . . . .	292

8.2.1	Regular spiking (RS) neurons . . . . .	295
8.2.2	Intrinsically bursting (IB) neurons . . . . .	301
8.2.3	Multi-compartment dendritic tree . . . . .	305
8.2.4	Chattering (CH) neurons . . . . .	307
8.2.5	Low-threshold spiking (LTS) interneurons . . . . .	308
8.2.6	Fast spiking (FS) interneurons . . . . .	311
8.2.7	Late spiking (LS) interneurons . . . . .	313
8.2.8	Diversity of inhibitory interneurons . . . . .	314
8.3	Thalamus . . . . .	315
8.3.1	Thalamo-cortical (TC) relay neurons . . . . .	316
8.3.2	Reticular thalamic nucleus (RTN) neurons . . . . .	317
8.3.3	Thalamic interneurons . . . . .	317
8.4	Other interesting cases . . . . .	318
8.4.1	Hippocampal CA1 pyramidal neurons . . . . .	318
8.4.2	Spiny projection neurons of neostriatum and basal ganglia . . . . .	319
8.4.3	Mesencephalic V neurons of brainstem . . . . .	320
8.4.4	Stellate cells of entorhinal cortex . . . . .	320
8.4.5	Mitral neurons of olfactory bulb . . . . .	321
	Summary and Bibliographical Notes . . . . .	323
	Exercises . . . . .	326
<b>9</b>	<b>Bursting</b>	<b>341</b>
9.1	Electrophysiology . . . . .	341
9.1.1	Example: The $I_{Na,p}+I_K+I_{K(M)}$ -model . . . . .	343
9.1.2	Fast-Slow Dynamics . . . . .	345
9.1.3	Minimal models . . . . .	347
9.1.4	Central pattern generators and half-center oscillators . . . . .	351
9.2	Geometry . . . . .	351
9.2.1	Fast-slow bursters . . . . .	352
9.2.2	Phase portraits . . . . .	352
9.2.3	Averaging . . . . .	355
9.2.4	Equivalent voltage . . . . .	357
9.2.5	Hysteresis loops and slow waves . . . . .	358
9.2.6	Bifurcations “resting $\leftrightarrow$ bursting $\leftrightarrow$ spiking” . . . . .	360
9.3	Classification . . . . .	364
9.3.1	fold/homoclinic . . . . .	365
9.3.2	circle/circle . . . . .	371
9.3.3	subHopf/fold cycle . . . . .	374
9.3.4	fold/fold cycle . . . . .	381
9.3.5	fold/Hopf . . . . .	381
9.3.6	fold/circle . . . . .	381
9.4	Neuro-Computational Properties . . . . .	383
9.4.1	How to distinguish? . . . . .	383

9.4.2	Integrators vs. Resonators . . . . .	384
9.4.3	Bistability . . . . .	386
9.4.4	Bursts as a unit of neuronal information . . . . .	387
9.4.5	Synchronization . . . . .	389
	Summary and Bibliographical Notes . . . . .	392
	Exercises . . . . .	395
<b>10</b>	<b>Synchronization (see <a href="http://www.izhikevich.com">www.izhikevich.com</a>)</b>	<b>403</b>
	<b>Solutions to Exercises</b>	<b>407</b>
	<b>References</b>	<b>441</b>
<b>10</b>	<b>Synchronization (see <a href="http://www.izhikevich.com">www.izhikevich.com</a>)</b>	<b>457</b>
10.1	Pulsed Coupling . . . . .	457
10.1.1	Phase of oscillation . . . . .	458
10.1.2	Isochrons . . . . .	459
10.1.3	PRC . . . . .	460
10.1.4	Type 0 and 1 phase response . . . . .	463
10.1.5	Poincare phase map . . . . .	466
10.1.6	Fixed points . . . . .	467
10.1.7	Synchronization . . . . .	468
10.1.8	Phase locking . . . . .	469
10.1.9	Arnold tongues . . . . .	470
10.2	Weak Coupling . . . . .	471
10.2.1	Winfree's approach . . . . .	472
10.2.2	Kuramoto's approach . . . . .	474
10.2.3	Malkin's approach . . . . .	475
10.2.4	Measuring PRCs experimentally . . . . .	476
10.2.5	Phase model for coupled oscillators . . . . .	479
10.3	Synchronization . . . . .	481
10.3.1	Two oscillators . . . . .	483
10.3.2	Chains . . . . .	485
10.3.3	Networks . . . . .	487
10.3.4	Mean-field approximations . . . . .	488
10.4	Examples . . . . .	489
10.4.1	Phase oscillators . . . . .	489
10.4.2	SNIC oscillators . . . . .	490
10.4.3	Homoclinic oscillators . . . . .	496
10.4.4	Relaxation oscillators and FTM . . . . .	498
10.4.5	Bursting oscillators . . . . .	500
	Summary and Bibliographical Notes . . . . .	501
	Exercises . . . . .	506
	Solutions . . . . .	511

# Preface

Historically, much of theoretical neuroscience research concerned neuronal circuits and synaptic organization. The neurons were divided into excitatory and inhibitory types, but their electrophysiological properties were largely neglected or taken to be identical to those of Hodgkin-Huxley's squid axon. The present awareness of the importance of the electrophysiology of individual neurons is best summarized by David McCormick in the fifth edition of Gordon Shepherd's book "*The Synaptic Organization of the Brain*":

"Information processing depends not only on the *anatomical* substrates of synaptic circuits but also on the *electrophysiological* properties of neurons.... Even if two neurons in different regions of the nervous system possess identical morphological features, they may respond to the same synaptic input in very different manners because of each cell's intrinsic properties."

David A. McCormick (2004)

Much of present neuroscience research concerns voltage- and second-messenger-gated currents in individual cells with the goal to understand the cell's intrinsic neuro-computational properties. It is widely accepted that knowing the currents suffices to determine what the cell is doing and why. This, however, contradicts a half-century old observation that cells having similar currents can still exhibit quite different dynamics. Indeed, studying isolated axons having presumably similar electrophysiology (all are from crustacean *Carcinus maenas*), Hodgkin (1948) injected a dc-current of varying amplitude, and discovered that some preparations could exhibit repetitive spiking with arbitrarily low frequencies, while the others discharged in a narrow frequency band. This observation was largely ignored by the neuroscience community until the seminal paper by Rinzel and Ermentrout (1989), who showed that the difference in behavior is due to different *bifurcation* mechanisms of excitability.

Let us treat the amplitude of the injected current in Hodgkin's experiments as a bifurcation parameter: When the amplitude is small, the cell is quiescent; when the amplitude is large, the cell fires repetitive spikes. When we change the amplitude of the injected current, the cell undergoes a transition from quiescence to repetitive spiking. From the dynamical systems point of view the transition corresponds to a bifurcation from equilibrium to a limit cycle attractor. The type of bifurcation determines the most fundamental computational properties of neurons, such as the class of excitability, the existence or non-existence of threshold, all-or-none spikes, subthreshold oscillations, the ability to generate post-inhibitory rebound spikes, bistability of resting and spiking states, whether the neuron is an integrator or resonator, etc.

This book is devoted to a systematic study of the relationship between electrophysiology, bifurcations, and computational properties of neurons. The reader will learn why cells having nearly identical currents may undergo distinct bifurcations, and hence they will have fundamentally different neuro-computational properties. (Con-

versely, cells having quite different currents may undergo identical bifurcations, and hence they will have similar neuro-computational properties.) The major message of the book can be summarized as follows (compare with the McCormick statement above):

Information processing depends not only on the electrophysiological properties of neurons but also on their *dynamical properties*. Even if two neurons in the same region of the nervous system possess similar electrophysiological features, they may respond to the same synaptic input in very different manners because of each cell's bifurcation dynamics.

Non-linear dynamical system theory is a core of the computational neuroscience research, but it is not a standard part of the graduate neuroscience curriculum. Neither is it taught in most math/physics departments in a form suitable for a general biological audience. As a result, many neuroscientists fail to grasp such fundamental concepts as equilibrium, stability, limit cycle attractor, and bifurcations, even though neuroscientists encounter these non-linear phenomena constantly.

This book introduces dynamical systems starting with simple one- and two-dimensional spiking models and continuing all the way to bursting systems. Each chapter is organized “from simple to complex”, so everybody can start reading the book; the reader’s background would only determine where he or she stops. The book emphasizes the geometrical approach, so there are few equations but a lot of figures. Half of them are simulations of various neural models, so there are hundreds of possible exercises such as “Use MATLAB (GENESIS, NEURON, XPPAUT, etc.) and parameters in the caption of Fig. X to simulate the figure”. Additional homework problems are provided at the end of each chapter; the reader is encouraged to solve at least some of them and look at the solutions of the others at the end of the book. Problems marked [M.S.] or [Ph.D.] are suggested thesis topics.

**Acknowledgment.** The author thanks all scientists who reviewed the first draft of the book: Pablo Achard, Jose M. Amigo, Brent Doiron, George Bard Ermentrout, Richard FitzHugh, David Golomb, Andrei Iacob, Maciej Lazarewicz, Georgi Medvedev, John Rinzel, Anil K. Seth, Gautam C Sethia, Arthur Sherman, Klaus M. Stiefel, Takashi Tateno. The author thanks anonymous referees who peer-reviewed the book and made quite a few valuable suggestions instead of just rejecting it. Special thanks are to Niraj S. Desai who made most of the *in vitro* recordings used in the book (the data are available on the author’s webpage [www.izhikevich.com](http://www.izhikevich.com)) and to Bruno van Swinderen who drew the caricatures. The author has enjoyed the hospitality of The Neurosciences Institute — a monastery of interdisciplinary science, and he has benefited greatly from the expertise and support of its fellows.

Finally, the author thanks his wife Tatyana and wonderful daughters Elizabeth and Kate for their support and patience during the four-year gestation of this book.

# Chapter 1

## Introduction

This chapter highlights some of the most important concepts developed in the book. First, we discuss several common misconceptions regarding the spike-generation mechanism of neurons. Our goal is to motivate the reader into thinking of a neuron not only in terms of ions and channels, as many biologists do, and not only in terms of input/output relationship, as many theoreticians do, but also as a nonlinear dynamical system that looks at the input through the prism of its own intrinsic dynamics. We ask such questions as “what makes a neuron fire?” or “where is the threshold”, and then outline the answers using geometrical theory of dynamical systems.

From a dynamical systems point of view, neurons are excitable because they are near a transition, called bifurcation, from resting to sustained spiking activity. While there is a huge number of possible ionic mechanisms of excitability and spike-generation, there are only four different bifurcation mechanisms that can result in such a transition. Considering the geometry of phase portraits at these bifurcations, we can understand many computational properties of neurons, such as the nature of threshold and all-or-none spiking, the co-existence of resting and spiking states, the origin of spike latencies, post-inhibitory spikes, the mechanism of integration and resonance, etc. Moreover, we can understand how these properties are interrelated, why some are equivalent and some are mutually exclusive.

### 1.1 Neurons

If somebody were to put a gun to the head of the author of this book and ask him to name the single most important concept in brain science, he would say it is the concept of a *neuron*. There are only  $10^{11}$  or so neurons in the human brain, much fewer than the number of non-neural cells such as glia. Yet neurons are unique in the sense that only they can transmit electrical signals over long distances. From neuronal level we can go down to cell biophysics, to molecular biology of gene regulation, etc. From neuronal level we can go up to neuronal circuits, to cortical structures, to the whole brain, and finally to the behavior of the organism. So, let us see how much we understand of what is going on at the level of individual neurons.

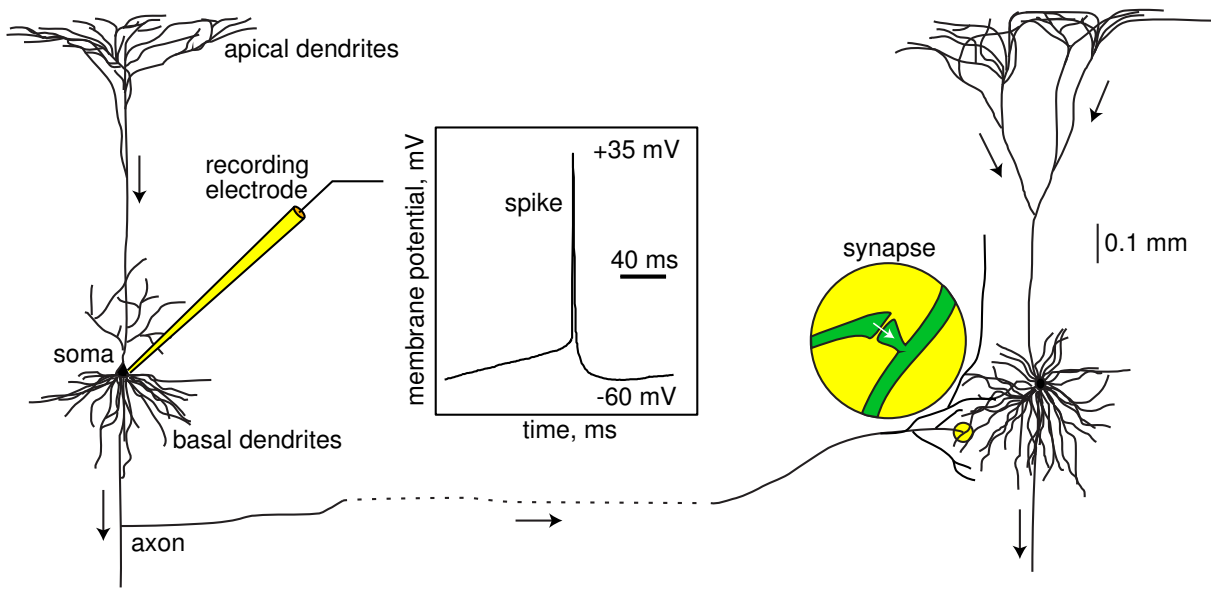


Figure 1.1: Two interconnected cortical pyramidal neurons (hand drawing) and *in vitro* recorded spike.

### 1.1.1 What is a spike?

A typical neuron receives inputs from more than 10,000 other neurons through the contacts on its dendritic tree called synapses; see Fig. 1.1. The inputs produce electrical transmembrane currents that change the membrane potential of the neuron. Synaptic currents produce changes, called post-synaptic potentials (PSPs). Small currents produce small PSPs; larger currents produce significant PSPs that could be amplified by the voltage-sensitive channels embedded in neuronal membrane and lead to the generation of an *action potential* or *spike* – an abrupt and transient change of membrane voltage that propagates to other neurons via a long protrusion called an axon.

Such spikes are the main means of communication between neurons. In general, neurons do not fire on their own, they do it as a result of the incoming spikes from other neurons. One of the most fundamental question of neuroscience is *what exactly makes neurons fire?* What is it in the incoming pulses that elicits a response in one neuron but not in another one? Why could two neurons have different responses to exactly the same input and identical responses to completely different inputs? To answer these questions, we need to understand the dynamics of spike-generation mechanisms of neurons.

Most introductory neuroscience books describe neurons as integrators with a threshold: Neurons sum up incoming PSPs and “compare” the integrated PSP with a certain voltage value, called firing threshold. If it is below the threshold, the neuron remains quiescent; when it is above the threshold, the neuron fires an all-or-none spike, as in Fig. 1.3, and resets its membrane potential. To add theoretical plausibility to this argument, the books refer to the Hodgkin-Huxley model of spike-generation in squid



Figure 1.2: What makes a neuron fire?

giant axons, which we study in the next chapter. The irony is that the Hodgkin-Huxley model does not have a well-defined threshold, it does not fire all-or-none spikes, and it is not an integrator, but a resonator, i.e., it prefers inputs having certain frequencies that resonate with the frequency of subthreshold oscillations of the neuron. We consider these and other properties in detail in this book.

### 1.1.2 Where is the threshold?

Much effort has been spent trying to determine experimentally the firing thresholds of neurons. Here, we challenge the classical view of a threshold. Let us consider two typical experiments, depicted in Fig. 1.4, that are designed to measure the threshold. On the left, we shock a cortical neuron, i.e., we inject brief but strong pulses of current of various amplitudes to depolarize the membrane potential to various values. Is there a clear-cut voltage value, as in Fig. 1.3, above which the neuron fires but below which no spikes occur? If you find one, let the author know! In Fig. 1.4b we inject long but weak pulses of current of various amplitudes, which result in slow depolarization and a spike. The firing threshold, if it exists, must be somewhere in the shaded region, but where? Where does the slow depolarization end and the spike start? Is it meaningful to talk about firing thresholds at all?

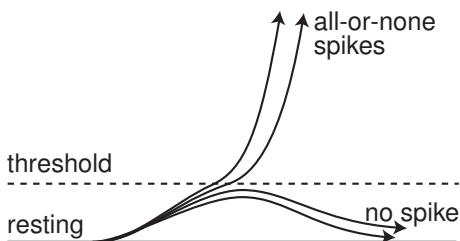


Figure 1.3: The concept of a firing threshold.

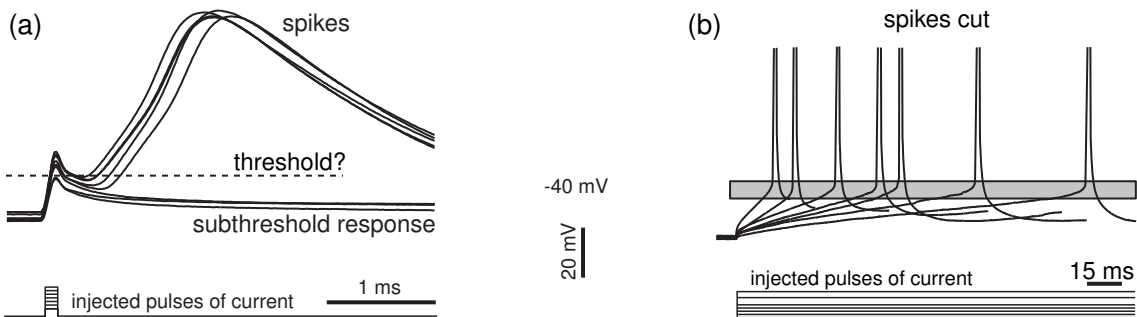


Figure 1.4: Where is the firing threshold? Shown are *in vitro* recordings of two layer 5 pyramidal neurons of rat. Notice the difference of voltage and time scales.

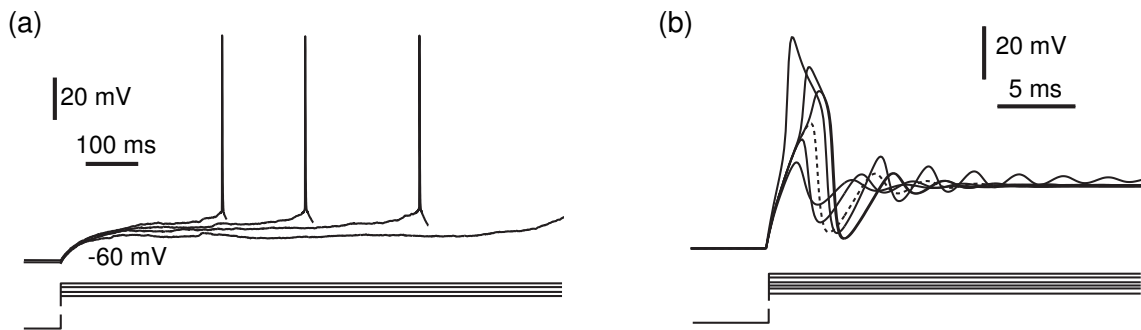


Figure 1.5: Where is the rheobase, i.e., the minimal current that fires the cell? (a) *in vitro* recordings of pyramidal neuron of layer 2/3 of rat's visual cortex show increasing latencies as the amplitude of the injected current decreases. (b) Simulation of the  $I_{Na,p} + I_K$ -model shows spikes of graded amplitude.

Perhaps, we should measure current thresholds instead of voltage thresholds? The current threshold, i.e., the minimal amplitude of injected current of infinite duration needed to fire a neuron, is called *rheobase*. In Fig. 1.5 we decrease the amplitudes of injected pulses of current to find the minimal one that still elicits a spike or the maximal one that does not. In Fig. 1.5a, progressively weaker pulses result in longer latencies to the first spike. Eventually the neuron does not fire because the latency is longer than the duration of the pulse, which is 1 second in the figure. Did we really measure the neuronal rheobase? What if we waited a bit longer? How long is long enough? In Fig. 1.5b the latencies do not grow but the spike amplitudes decrease until the spikes do not look like spikes at all. To determine the current threshold, we need to draw the line and separate spike responses from “subthreshold” ones. How can we do that if the spikes are not all-or-none? Is the response denoted by the dashed line a spike?

Risking adding more confusion to the notion of a threshold, consider the following: If excitatory inputs depolarize the membrane potential, i.e., bring it closer to the “firing threshold”, and inhibitory inputs hyperpolarize the potential and move it away from

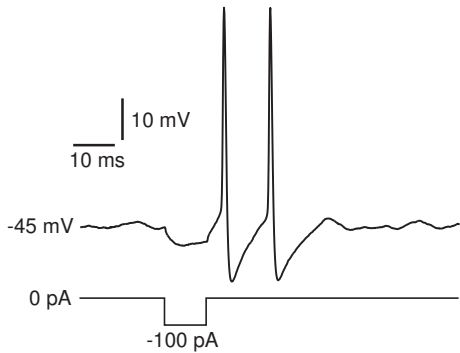


Figure 1.6: *In vitro* recording of rebound spikes of rats brainstem mesV neuron in response to a brief hyperpolarizing pulse of current.

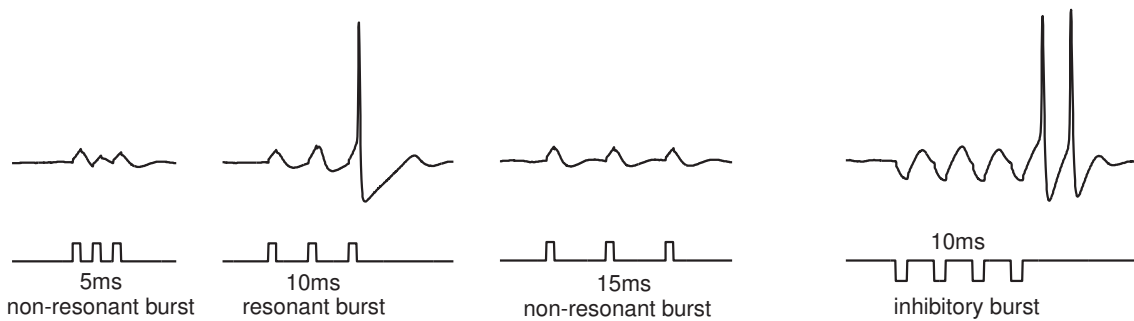


Figure 1.7: Resonant response of the mesencephalic V neuron of rat brainstem to pulses of injected current having 10 ms period (*in vitro*).

the threshold, then *how can the neuron in Fig. 1.6 fire in response to the inhibitory input?* This phenomenon is also observed in the Hodgkin-Huxley model, and it is called anodal break excitation, rebound spike, or post-inhibitory spike. Many biologists say that rebound responses are due to the activation and inactivation of certain slow currents, which bring the membrane potential over the threshold, or equivalently, lower the threshold upon release from the hyperpolarization – a phenomenon called a low-threshold spike in thalamocortical neurons. The problem with this explanation is that neither the Hodgkin-Huxley model nor the neuron in the figure have these currents, and even if they did, the hyperpolarization is too short and too weak to affect the currents.

Another interesting phenomenon is depicted in Fig. 1.7. The neuron is stimulated with brief pulses of current mimicking an incoming burst of three spikes. When the stimulation frequency is high (5 ms period), presumably reflecting a strong input, the neuron does not fire at all. However, stimulation with a lower frequency (10 ms period) that resonates with the frequency of subthreshold oscillation of the neuron evokes a spike response, regardless of whether the stimulation is excitatory or inhibitory. Stimulation with even lower frequency (15 ms period) cannot elicit spike response again. Thus, the neuron is sensitive only to the inputs having resonant frequency. The same pulses applied to a cortical pyramidal neuron evoke a response only in the first case (small period), but not in the other cases.

### 1.1.3 Why are neurons different and why do we care?

Why would two neurons respond completely differently to the same input? A biologist would say that the response of a neuron depends on many factors, such as the type of voltage- and  $\text{Ca}^{2+}$ -gated channels expressed by the neuron, the morphology of its dendritic tree, the location of the input, etc. These factors are indeed important, but they do not determine the neuronal response per se. They rather determine the rules that govern dynamics of the neuron. Different conductances and currents can result in the same rules and hence in the same responses, and conversely, similar currents can result in different rules and in different responses. The currents define what kind of a dynamical system the neuron is.

We study ionic transmembrane currents in the next chapter. In subsequent chapters we investigate how the type of currents determine neuronal dynamics. We divide all currents into two major classes: amplifying and resonant, with persistent  $\text{Na}^+$  current  $I_{\text{Na,p}}$  and persistent  $\text{K}^+$  current  $I_K$  being the typical examples of the former and the latter. Since there are tens of known currents, purely combinatorial argument implies that there are millions of different electrophysiological mechanisms of spike generation. We will show later that any such mechanism must have at least one amplifying and one resonant current. Some mechanisms, called minimal in this book, have precisely one resonant and one amplifying current. They provide an invaluable tool in classifying and understanding the electrophysiology of spike-generation.

Many illustrations in this book are based on simulations of the reduced  $I_{\text{Na,p}} + I_K$ -model, which consists of fast persistent  $\text{Na}^+$  (amplifying) current and slower persistent  $\text{K}^+$  (resonant) current. It is equivalent to the famous and widely used Morris-Lecar  $I_{\text{Ca}} + I_K$ -model (Morris and Lecar 1981). We show that the model exhibits quite different dynamics depending on the values of the parameters, e.g., the half-activation voltage of the  $\text{K}^+$  current: In one case, it can fire in a narrow frequency range, exhibit co-existence of resting and spiking states, damped subthreshold oscillations of membrane potential, etc. In another case, it can fire in a wide frequency range and show no co-existence of resting and spiking and no subthreshold oscillations. Thus, seemingly inessential differences in parameter values could result in drastically distinct behaviors.

### 1.1.4 Building models

To build a good model of a neuron, electrophysiologists apply different pharmacological blockers to tease out the currents that the neuron has. Then, they apply different stimulation protocols to measure the kinetic parameters of the currents, such as the Boltzmann activation function, time constants, maximal conductances, etc. We consider all these functions in the next chapter. Then, they create a Hodgkin-Huxley-type model and simulate it using NEURON, GENESIS, XPP environments or just plain MATLAB (the first two are invaluable tools for simulating realistic dendritic structures).

The problem is that the parameters are measured in different neurons and then put together into a single model. As an illustration, consider two neurons having the same

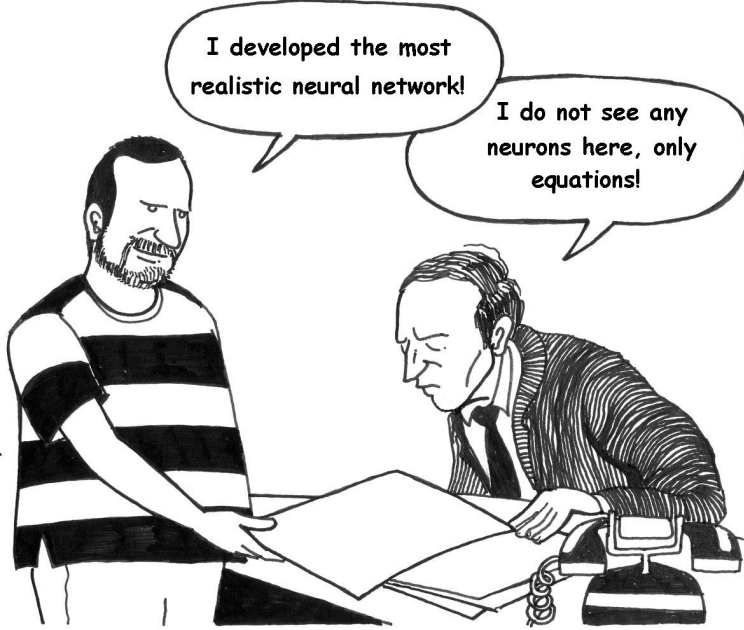


Figure 1.8: Neurons are dynamical systems.

currents, say  $I_{\text{Na,p}}$  and  $I_K$ , and exhibiting excitable behavior; that is, both neurons are quiescent but can fire a spike in response to a stimulation. Suppose the second neuron has stronger  $I_{\text{Na,p}}$ , which is balanced by stronger  $I_K$ . If we measure  $\text{Na}^+$  conductance using the first neuron and  $\text{K}^+$  conductance using the second neuron, the resulting  $I_{\text{Na,p}} + I_K$ -model would have an excess of  $\text{K}^+$  current and probably not be able to fire spikes at all. Conversely, if we measure  $\text{Na}^+$  and  $\text{K}^+$  conductances using the second and then the first neuron, respectively, the model would have too much  $\text{Na}^+$  current and probably exhibit sustained pacemaking activity. In any case, the model fails to reproduce the excitable behavior of the neurons whose parameters we measured.

Some of the parameters cannot be measured at all, so many arbitrary choices are made via a process called “fine-tuning”. Navigating in the dark, possibly with the help of some biological intuition, the researcher modifies parameters, compares simulations with experiment, and repeats this trial-and-error procedure until he or she is satisfied with the results. Since seemingly similar values of parameters can result in drastically different behaviors, and quite different parameters can result in seemingly similar behaviors, how do we know that the resulting model is correct? How do we know that its behavior is equivalent to that of the neuron we want to study? And what is *equivalent* in this case? Now, the reader is primed to consider dynamical systems.

## 1.2 Dynamical Systems

In the next chapter we introduce the Hodgkin-Huxley formalism to describe neuronal dynamics in terms of activation and inactivation of voltage-gated conductances. An important consequence of the Hodgkin-Huxley studies is that *neurons are dynamical systems*, so they should be studied as such. Below we mention some of the important

concepts of dynamical systems theory. The reader does not have to follow all the details of this section because the concepts are explained in a greater detail in subsequent chapters.

A dynamical system consists of a set of variables that describe its state and a law that describes the evolution of the state variables with time, i.e., how the state of the system in the next moment of time depends on the input and its state in the previous moment of time. The Hodgkin-Huxley model is a four-dimensional dynamical system because its state is determined uniquely by the membrane potential,  $V$ , and so called gating variables  $n, m$  and  $h$  for persistent  $K^+$  and transient  $Na^+$  currents. The evolution law is given by a four-dimensional system of ordinary differential equations.

Typically, all variables describing neuronal dynamics can be classified into four classes, according to their function and the time scale:

1. *Membrane potential.*
2. *Excitation variables*, such as activation of  $Na^+$  current. This variables are responsible for the upstroke of the spike.
3. *Recovery variables*, such as inactivation of  $Na^+$  current and activation of fast  $K^+$  current. This variables are responsible for the repolarization (downstroke) of the spike.
4. *Adaptation variables*, such as activation of slow voltage- or  $Ca^{2+}$ -dependent currents. This variables build up during prolonged spiking and can affect excitability on the long run.

The Hodgkin-Huxley model does not have variables of the fourth type, but many neuronal models do, especially those exhibiting bursting dynamics.

### 1.2.1 Phase portraits

The power of the dynamical systems approach to neuroscience, as well as to many other sciences, is that we can tell something, or many things, about a system without even knowing all the details that govern the system evolution. We do not even use equations to do that! Some may even wonder why we call it a mathematical theory.

As a start, let us consider a quiescent neuron whose membrane potential is resting. From the dynamical systems point of view, there are no changes of the state variables of such a neuron, hence it is at an equilibrium point. All the inward currents that depolarize the neuron are balanced, or equilibrated, by the outward currents that hyperpolarize it. If the neuron remains quiescent despite small disturbances and membrane noise, as in Fig. 1.9a, top, then we conclude that the equilibrium is stable. Isn't it amazing that we can make such a conclusion without knowing the equations that describe the neuron's dynamics? We do not even know the number of variables needed to describe the neuron; it could be infinite, for all we care.

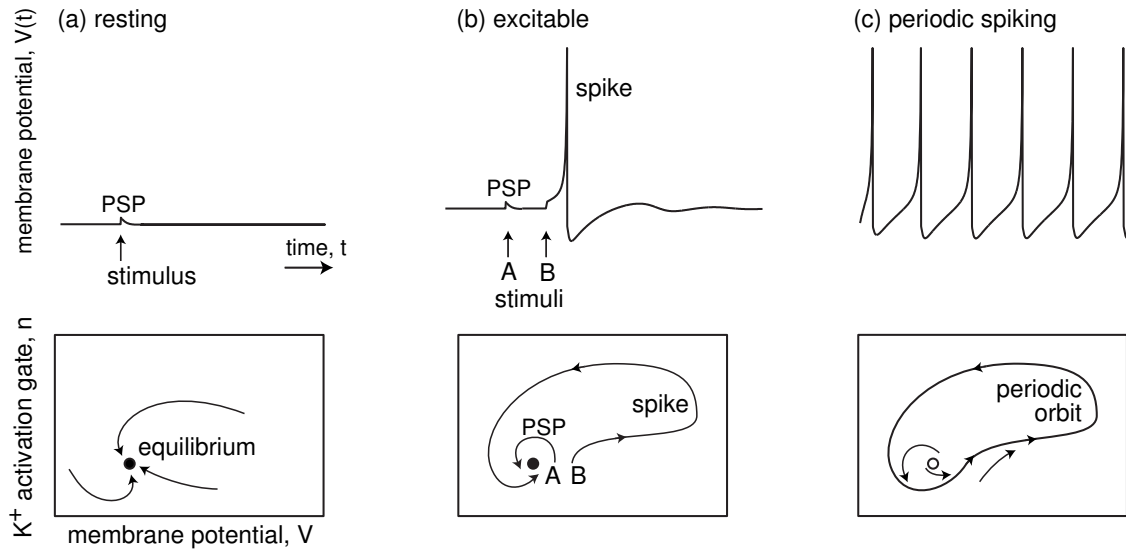


Figure 1.9: Resting, excitable, and periodic spiking activity correspond to a stable equilibrium (a and b) or limit cycle (c), respectively.

In this book we introduce the notions of equilibria, stability, threshold, and attraction domains using one- and two-dimensional dynamical systems, e.g., the  $I_{Na,p}+I_K$ -model with instantaneous  $Na^+$  kinetics. Its state is described by the membrane potential,  $V$ , and the activation variable,  $n$ , of the persistent  $K^+$  current, so it is a two-dimensional vector  $(V, n)$ . Instantaneous activation of  $Na^+$  current is a function of  $V$ , so it does not result in a separate variable of the model. The evolution of the model is a trajectory  $(V(t), n(t))$  on the  $V \times n$ -plane. Depending on the initial point, the system can have many trajectories, such as those depicted in Fig. 1.9a, bottom. Time is not present explicitly in the figure, but units of time may be thought of as plotted along each trajectory. All of the trajectories in the figure are attracted to the stable equilibrium denoted by the black dot, called an *attractor*. The overall qualitative description of dynamics can be obtained through the study of the *phase portrait* of the system, which depicts certain special trajectories (equilibria, separatrices, limit cycles) that determine the topological behavior of all the other trajectories in the phase space. Probably 50 % of illustrations in this book are phase portraits.

A fundamental property of neurons is *excitability*, illustrated in Fig. 1.9b. The neuron is resting, i.e., its phase portrait has a stable equilibrium. Small perturbations, such as A, result in small excursions from the equilibrium, denoted as PSP (post-synaptic potential). In contrast, larger perturbations, such as B, are amplified by the neuronal intrinsic dynamics and result in the spike response. To understand the dynamic mechanism of such amplification, we need to consider the geometry of the phase portrait near the equilibrium, i.e., in the region where the decision to fire or not to fire is made.

If we inject a sufficiently strong current into the neuron, we bring it to a pacemaking mode, so that it exhibits periodic spiking activity, as in Fig. 1.9c. From the dynamical

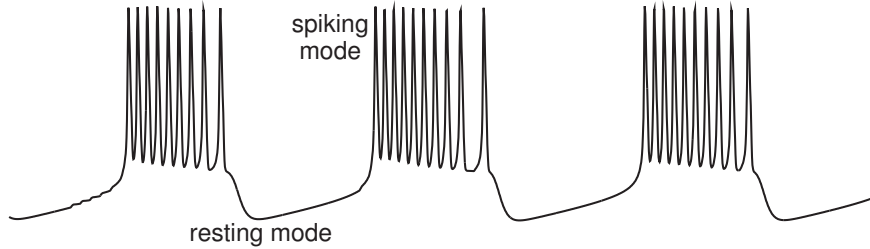


Figure 1.10: Rhythmic transitions between resting and spiking modes result in bursting behavior.

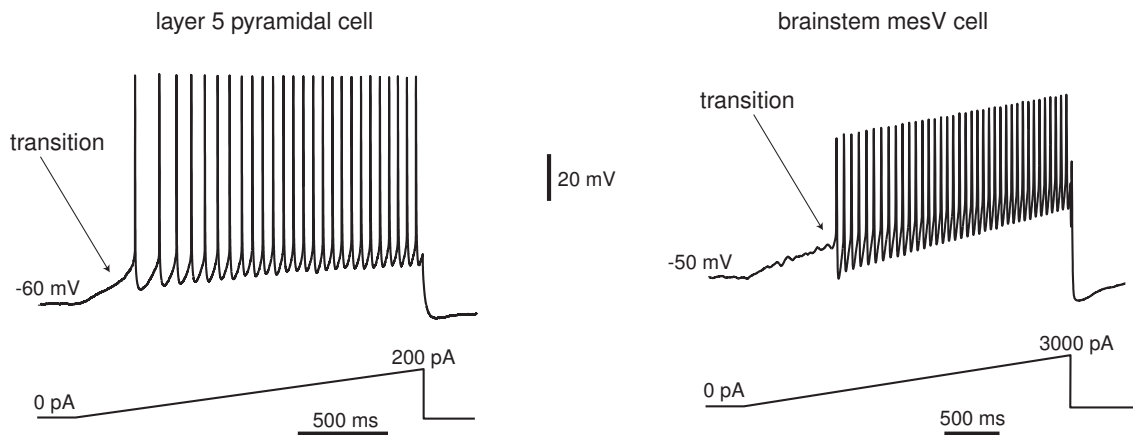


Figure 1.11: As the magnitude of the injected current slowly increases, the neurons bifurcate from resting (equilibrium) to tonic spiking (limit cycle) modes.

systems point of view, the state of such a neuron has a stable limit cycle, also known as a periodic orbit. The electrophysiological details of the neuron, i.e., the number and the type of currents it has, their kinetics, etc., determine only the location, the shape and the period of the limit cycle. As long as the limit cycle exists, the neuron can have periodic spiking activity. Of course, equilibria and limit cycles can co-exist, so a neuron can be switched from one mode to another one by a transient input. The famous example is the permanent extinguishing of ongoing spiking activity in the squid giant axon by a brief transient depolarizing pulse of current applied at a proper phase (Guttman et al. 1980) — a phenomenon predicted by John Rinzel (1978) purely on the basis of theoretical analysis of the Hodgkin-Huxley model. The transition between resting and spiking modes could be triggered by intrinsic slow conductances, resulting in the bursting behavior in Fig. 1.10.

### 1.2.2 Bifurcations

Now suppose that the magnitude of the injected current is a parameter that we can control, e.g., we can ramp it up as in Fig. 1.11. Each cell in the figure is quiescent at the beginning of the ramps, so its phase portrait has a stable equilibrium and it

may look like the one in Fig. 1.9a or b. Then it starts to fire tonic spikes, so its phase portrait has a limit cycle attractor and it may look like the one in Fig. 1.9c, with white circle denoting an unstable resting equilibrium. Apparently, there is some intermediate level of injected current that corresponds to the transition from resting to sustained spiking, i.e., from the phase portrait in Fig. 1.9b to Fig. 1.9c. What does the transition look like?

From dynamical systems point of view, the transition corresponds to a *bifurcation* of neuron dynamics, i.e., a qualitative change of phase portrait of the system. For example, there is no bifurcation going from phase portrait in Fig. 1.9a to that in Fig. 1.9b, since both have one globally stable equilibrium; the difference in behavior is quantitative but not qualitative. In contrast, there is a bifurcation going from Fig. 1.9b to Fig. 1.9c since the equilibrium is no longer stable and another attractor, limit cycle, appeared. The neuron is not excitable in Fig. 1.9a but it is in Fig. 1.9b simply because the former phase portrait is far away from the bifurcation and the latter is near.

In general, neurons are excitable *because* they are near bifurcations from resting to spiking activity, so the type of the bifurcation determines the excitable properties of the neuron. Of course, the type depends on the neuron's electrophysiology. An amazing observation is that there could be millions of different electrophysiological mechanisms of excitability and spiking, but there are only 4, yes *four*, different types of bifurcations of equilibrium that a system can undergo without any additional constraints, such as symmetry. Thus, considering these four bifurcations in a general setup we can understand excitable properties of many models, even those that have not been invented yet. What is even more amazing, we can understand excitable properties of neurons whose currents are not measured and whose models are not known, provided that we can identify experimentally which of the four bifurcations the resting state of the neuron undergoes.

The four bifurcations are summarized in Fig. 1.12, which plots the phase portrait before (left), at (center), and after (right) a particular bifurcation occurs. Mathematicians refer to these bifurcations as being of co-dimension-1 because we need to vary only one parameter, e.g., the magnitude of the injected dc-current  $I$ , to observe the bifurcations reliably in simulations or experiments. There are many more co-dimension-2, 3, etc., bifurcation, but they need special conditions to be observed. We discuss these later in Chap. 6.

Let us consider the four bifurcation and their phase portraits in the figure. The horizontal and vertical axes are the membrane potential with instantaneous activation variable and a recovery variable, respectively. At this stage, the reader is not required to fully understand the intricacies of the phase portraits in the figure, since they will be explained systematically in later chapters.

- *Saddle-node bifurcation.* As the magnitude of the injected current or any other bifurcation parameter changes, a stable equilibrium corresponding to the resting state (black circle marked “node” in Fig. 1.12a) is approached by an unstable equilibrium (white circle marked “saddle”), they coalesce and annihilate each other, as in Fig. 1.12a, middle. Since the resting state no longer exists, the

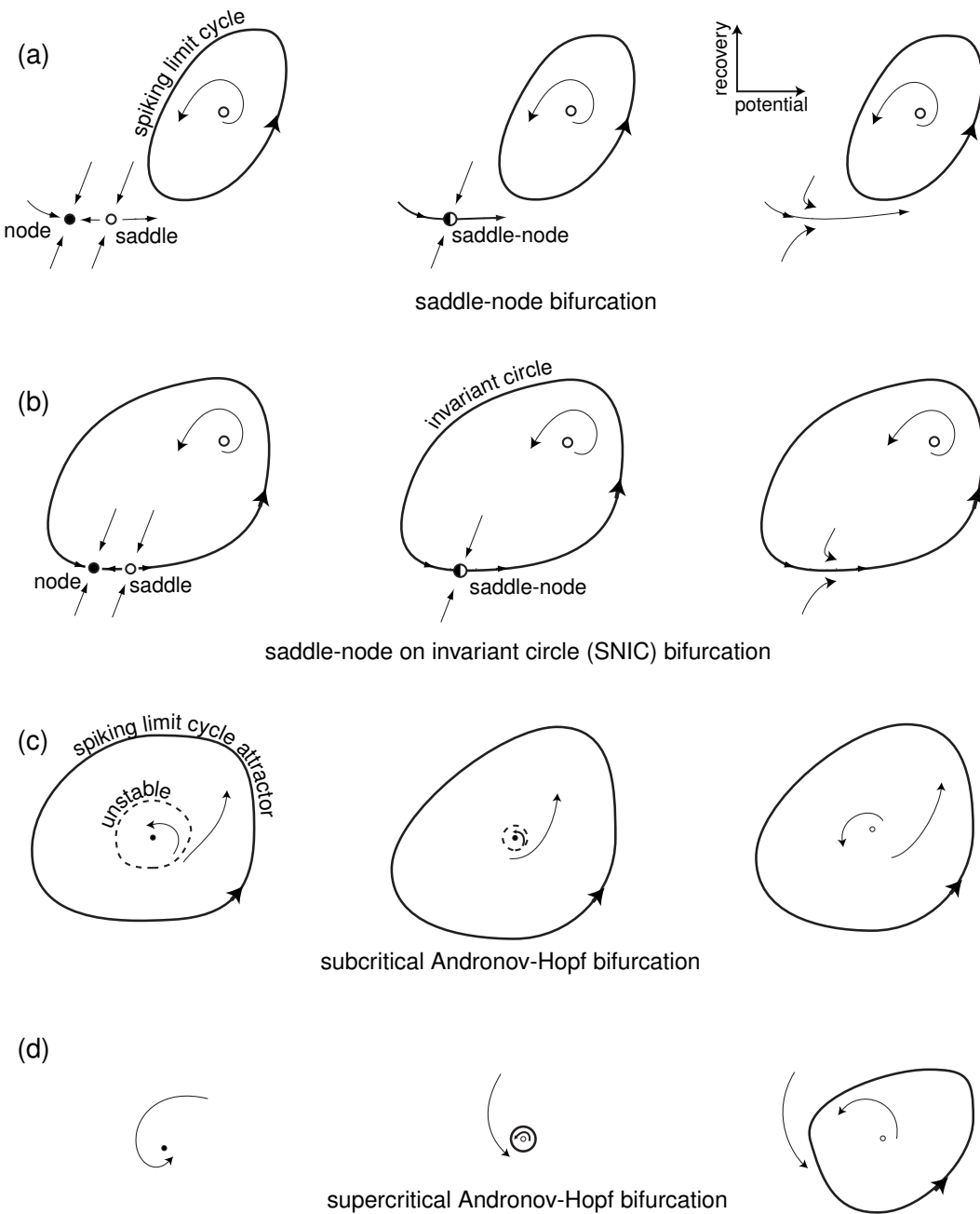


Figure 1.12: Four generic (co-dimension-1) bifurcations of an equilibrium state leading to the transition from resting to periodic spiking behavior in neurons.

trajectory describing the evolution of the system jumps to the limit cycle attractor indicating that the neuron starts to fire tonic spikes. Notice that the limit cycle, or some other attractor, must co-exist with the resting state in order for the transition resting → spiking to occur.

- *Saddle-node on invariant circle bifurcation* is similar to the saddle-node bifurcation above with the exception that there is an invariant circle at the moment of bifurcation, which then becomes a limit cycle attractor, as in Fig. 1.12b.
- *Subcritical Andronov-Hopf bifurcation*. A small unstable limit cycle shrinks to a stable equilibrium and makes it lose stability, as in Fig. 1.12c. Because of instabilities, the trajectory diverges from the equilibrium and approaches a large-amplitude spiking limit cycle or some other attractor.
- *Supercritical Andronov-Hopf bifurcation*. The stable equilibrium loses stability and gives birth to a small-amplitude limit cycle attractor, as in Fig. 1.12d. As the magnitude of the injected current increases, the amplitude of the limit cycle increases and it becomes full-size spiking limit cycle.

Notice that there is a co-existence of resting and spiking states in the case of saddle-node and subcritical Andronov-Hopf bifurcations, whereas there is not in the other two cases. Such a co-existence reveals itself via a hysteresis behavior when the injected current increases and then decreases past the bifurcation value, because the transitions “resting → spiking” and “spiking → resting” occur at different values of the current. In addition, brief stimuli applied at the appropriate times can switch the activity from spiking to resting and back. There are also spontaneous noise-induced transitions between the two modes resulting in the stuttering spiking, as e.g. exhibited by the so called fast spiking (FS) cortical interneurons when they are kept close to the bifurcation (Tateno et al. 2004). Some bistable neurons have a slow adaptation current that activates during the spiking mode and impedes spiking, often resulting in bursting activity.

Systems undergoing Andronov-Hopf bifurcations, whether subcritical or supercritical, exhibit damped oscillations of membrane potential, whereas systems near saddle-node bifurcations, whether on or off an invariant circle, do not. The existence of small amplitude oscillations creates the possibility of resonance to the frequency of the incoming pulses, as in Fig. 1.7, and other interesting features.

We refer to neurons with damped subthreshold oscillations as *resonators* and to those that do not have this property as *integrators*. We refer to the neurons that exhibit the co-existence of resting and spiking states, at least near the transition from resting to spiking, as *bistable*, and to those that do not exhibit the bistability as *monostable*. The four bifurcations in Fig. 1.12 are uniquely defined by these two features. For example, a bistable resonator is a neuron undergoing subcritical Andronov-Hopf bifurcation, and a monostable integrator is a neuron undergoing saddle-node on invariant circle bifurcation; see table in Fig. 1.13. Cortical fast spiking (FS) and regular spiking (RS) neurons, studied in Chap. 8, are typical examples of the former and the latter, respectively.

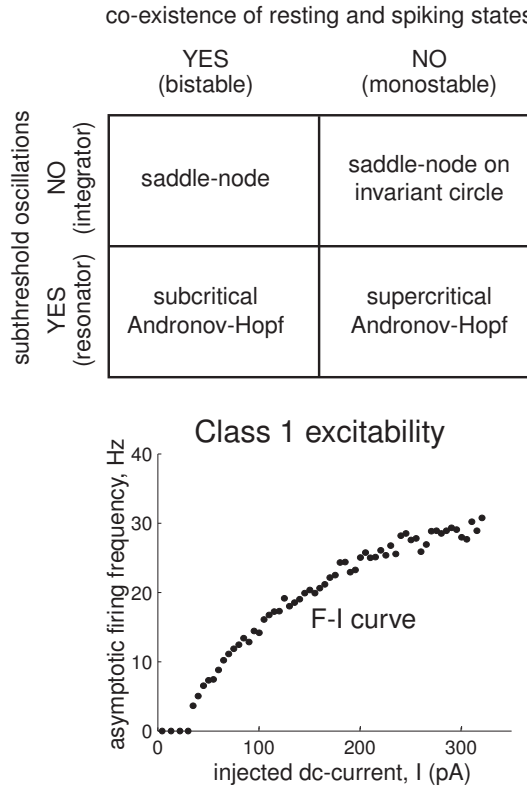


Figure 1.13: Classification of neurons into monostable/bistable integrators/resonators according to the bifurcation of the resting state in Fig. 1.12.

Figure 1.14: Frequency-current (F-I) curves of cortical pyramidal neuron and brainstem mesV neuron from Fig. 7.3. These are the same neurons used in the ramp experiment in Fig. 1.11.

### 1.2.3 Hodgkin classification

Hodgkin (1948) was the first to study bifurcations in neuronal dynamics, years before the mathematical theory of bifurcations was developed. He stimulated squid axons with pulses of various amplitudes and identified three classes of responses:

- **CLASS 1 NEURAL EXCITABILITY.** Action potentials can be generated with arbitrarily low frequency, depending on the strength of the applied current.
- **CLASS 2 NEURAL EXCITABILITY.** Action potentials are generated in a certain frequency band that is relatively insensitive to changes in the strength of the applied current.
- **CLASS 3 NEURAL EXCITABILITY.** A single action potential is generated in response to a pulse of current. Repetitive (tonic) spiking can be generated only for extremely strong injected currents or not at all.

The qualitative distinction between the classes is that the frequency-current relation (the F-I curve in Fig. 1.14) starts from zero and continuously increases for Class 1

neurons, is discontinuous for Class 2 neurons, and is not defined at all for Class 3 neurons.

Obviously, neurons belonging to different classes have different neuro-computational properties: Class 1 neurons, which include cortical excitatory pyramidal neurons, can smoothly encode the strength of the input into the output firing frequency, as in Fig. 1.11, left. In contrast, Class 2 neurons, such as fast-spiking (FS) cortical inhibitory interneurons, cannot do that; instead, they fire in a relatively narrow frequency band, as in Fig. 1.11, right. Class 3 neurons cannot exhibit sustained spiking activity, so Hodgkin regarded them as “sick” or “unhealthy”. There are other distinctions between the classes, which we discuss later.

Different classes of excitability occur because neurons have different bifurcations of resting and spiking states – a phenomenon first explained by Rinzel and Ermentrout (1989). If ramps of current are injected to measure the F-I curves, then Class 1 excitability occurs when the neuron undergoes the saddle-node bifurcation on invariant circle depicted in Fig. 1.12b. Indeed, the period of the limit cycle attractor is infinite at the bifurcation point, and then it decreases as the bifurcation parameter – say, the injected current – increases. The other three bifurcations result in Class 2 excitability. Indeed, the limit cycle attractor exists and has a finite period when the resting state in Fig. 1.12 undergoes a subcritical Andronov-Hopf bifurcation, so emerging spiking has a non-zero frequency. The period of the small limit cycle attractor appearing via supercritical Andronov-Hopf bifurcation is also finite, so the frequency of oscillations is non-zero, but their amplitudes are small. In contrast to the common and erroneous folklore, the saddle-node bifurcation (off limit cycle) also results in Class 2 excitability because the limit cycle has a finite period at the bifurcation. There is a considerable latency (delay) to the first spike in this case, but the subsequent spiking has non-zero frequency. Thus, the simple scheme “Class 1 = saddle-node, Class 2 = Hopf” that permeates many publications is incorrect.

When pulses of current are used to measure the F-I curve, as in Hodgkin’s experiments, the firing frequency depends on other factors, and not only the type of the bifurcation of the resting state. In particular, low-frequency firing can be observed in systems near Andronov-Hopf bifurcations, as we show in Chap. 7. To avoid possible confusion, we define the class of excitability based only on slow ramp experiments.

Hodgkin’s classification has an important historical value but it is of little use for the dynamic description of a neuron, since naming a class of excitability of a neuron does not tell much about the bifurcations of the resting state. Indeed, it only says that saddle-node on invariant circle bifurcation (Class 1) is different from the other three bifurcations (Class 2), and only when ramps are injected. Instead, dividing neurons into integrators and resonators with bistable or monostable activity is more informative, so we adopt the classification in Fig. 1.13 in this book. In this classification, Class 1 neuron is a monostable integrator, whereas Class 2 neuron could be a bistable integrator or a resonator.

### 1.2.4 Neuro-computational properties

Using the same arrangement as in Fig. 1.13, we depict typical geometry of phase portraits near the four bifurcations in Fig. 1.15. Let us use the portraits to explain what happens “near the threshold”, i.e., near the place where the decision to fire or not is made. To simplify our geometrical analysis we assume here that neurons receive shock inputs, i.e., brief but strong pulses of current that do not change the phase portraits but only push or reset the state of the neuron into various regions of the phase space. We consider these and other cases in detail in Chap. 7.

The horizontal axis in each plot in Fig. 1.15 corresponds to the membrane potential  $V$  with instantaneous  $\text{Na}^+$  current, and the vertical axis corresponds to a recovery variable, say activation of  $\text{K}^+$  current. Black circles denote stable equilibria corresponding to the neuronal resting state. Spiking limit cycle attractors correspond to sustained spiking states, which exist in the two cases depicted in the left half of the figure corresponding to the bistable dynamics. The limit cycles are surrounded by the shaded regions — their attraction domains. The white region is the attraction domain of the equilibrium. To initiate spiking, the external input should push the state of the system into the shaded region, and to extinguish spiking, the input should push the state back into the white region.

There are no limit cycles in the two cases depicted in the right half of the figure, so the entire phase space is the attraction domain of the stable equilibrium, and the dynamics are monostable. However, if the trajectory starts in the shaded region, it makes a large-amplitude rotation before returning to the equilibrium — a transient spike. Apparently, to elicit such a spike, the input should push the state of the system into the shaded region.

Now let us contrast the upper and lower halves of the figure corresponding to integrators and resonators, respectively. We distinguish these two modes of operation based on the existence of subthreshold oscillations near the equilibrium.

First, let us show that *inhibition impedes spiking in integrators, but can promote it in resonators*. In the integrator case, the shaded region is in the depolarized voltage range, i.e., to the right of the equilibrium. Excitatory inputs push the state of the system toward the shaded region, while inhibitory inputs push it away. In the case of resonators, both excitation and inhibition push the state toward the shaded region, because the region wraps around the equilibrium and can be reached along any direction. This explains the rebound spiking phenomenon depicted in Fig. 1.6.

*Integrators have all-or-none spikes while resonators may not.* Indeed, any trajectory starting in the shaded region in the upper half of the figure has to rotate around the white circle at the top corresponding to an unstable equilibrium. Moreover, the state of the system is quickly attracted to the spiking trajectory and moves along the trajectory thereby generating a stereotypical spike. A resonator neuron can also fire large-amplitude spikes when its state is pushed to or beyond the trajectory denoted “spike”. Such neurons generate subthreshold responses when the state slides along

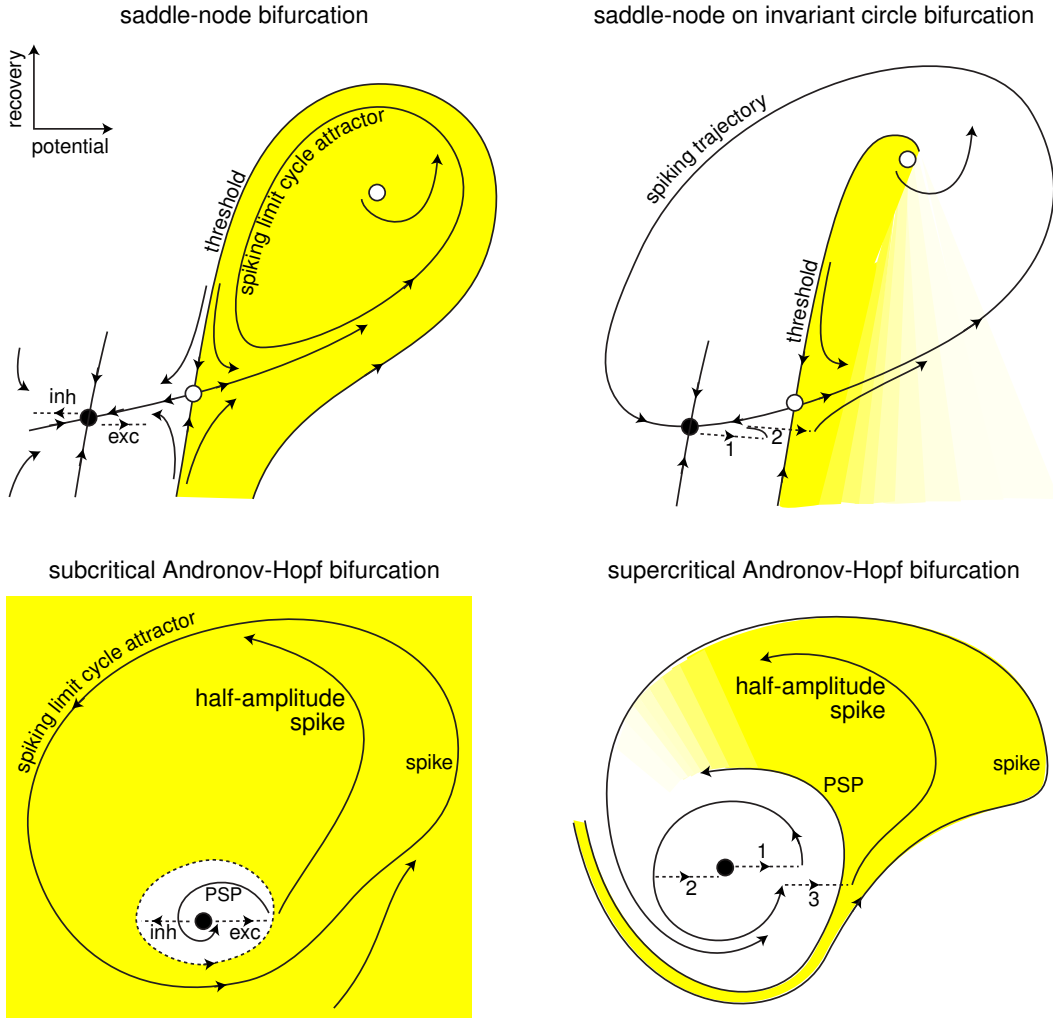


Figure 1.15: The geometry of phase portraits of excitable systems near 4 bifurcations can explain many neuro-computational properties (see Sect. 1.2.4 for detail).

the smaller trajectory denoted “PSP”; they can also generate spikes of an intermediate amplitude when the state is pushed between the “PSP” and “spike” trajectories, which explains the partial-amplitude spiking in Fig. 1.5 or in the squid axon in Fig. 7.26. The set of initial conditions corresponding to such spiking is quite small, so typical spikes have large amplitudes and partial spikes are rare.

*Integrators have well-defined thresholds while resonators may not.* The white circles near the resting states of integrators in Fig. 1.15 are called saddles. They are stable along the vertical direction and unstable along the horizontal direction. The two trajectories that lead to the saddle along the vertical direction are called separatrices because they separate the phase space into two regions, in this case into white and shaded. The separatrices play the role of thresholds since only those perturbations that push the state of the system beyond the separatrices result in a spike. The closer is the state of

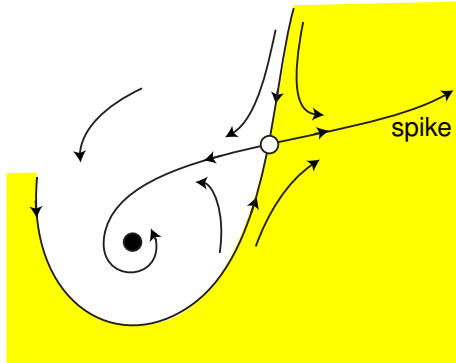


Figure 1.16: Phase portrait of a system near a Bogdanov-Takens bifurcation that corresponds to the transition from integrator to resonator mode.

the system to the separatrices, the longer it takes to converge and then diverge from the saddle, resulting in a long *latency to the spike*. Notice that the threshold is not a point but a tilted curve that spans a range of voltage values.

Resonators have a well-defined threshold in the case of subcritical Andronov-Hopf bifurcation: it is the small unstable limit cycle that separates the attraction domains of stable equilibrium and spiking limit cycle. Trajectories inside the small cycle spiral toward the stable equilibrium, while trajectories outside the cycle spiral away and eventually lead to sustained spiking activity. When a neuronal model is far from the subcritical Andronov-Hopf bifurcation, its phase portrait may look similar to the one corresponding to the supercritical Andronov-Hopf bifurcation. The narrow shaded band in the figure is not a threshold manifold but a fuzzy threshold set called “quasi-threshold” by FitzHugh (1955). Many resonators, including the Hodgkin-Huxley model have quasi-thresholds. The width of the quasi-threshold in the Hodgkin-Huxley model is so narrow, that it may be assumed to be just a curve for all practical reasons.

*Integrators integrate, resonators resonate.* Now consider inputs consisting of multiple pulses, e.g., a burst of spikes. Integrators prefer high-frequency inputs; the higher the frequency, the sooner they fire. Indeed, the first spike of such an input, marked “1” in the top-right phase portrait in Fig. 1.15, increases the membrane potential and shifts the state to the right toward the threshold. Since the state of the system is still in the white area, it slowly converges back to the stable equilibrium. To cross the threshold manifold, the second pulse must arrive shortly after the first one. The reaction of a resonator to a pair of pulses is quite different. The first pulse initiates a damped subthreshold oscillation of the membrane potential, which looks like a spiral in the bottom-right phase portrait in Fig. 1.15. The effect of the second pulse depends on its timing. If it arrives after the trajectory makes half a rotation, marked as “2” in the figure, it cancels the effect of the first pulse. If it arrives after the trajectory makes a full rotation, marked “3” in the figure, it adds to the first pulse and either increases the amplitude of subthreshold oscillation or evokes a spike response. Thus, the response of the resonator neuron depends on the frequency content of the input, as in Fig. 1.7.

Integrators and resonators constitute two major modes of activity of neurons. Most cortical pyramidal neurons, including the regular spiking (RS), intrinsically bursting

(IB), and chattering (CH) types considered in Chap. 8, are integrators. So are thalamocortical neurons in the relay mode of firing and neostriatal spiny projection neurons. Most cortical inhibitory interneurons, including the fast spiking type, are resonators. So are brainstem mesencephalic V neurons and stellate neurons of the entorhinal cortex. Some cortical pyramidal neurons and low-threshold spiking (LTS) interneurons can be at the border of transition between integrator and resonator modes. Such a transition corresponds to another bifurcation, which has co-dimension-2, and hence it is less likely to be encountered experimentally. We consider this and other uncommon bifurcations in detail later. The phase portrait near the bifurcation is depicted in Fig. 1.16 and it is a good exercise for the reader to explain why such a system has damped oscillations and post-inhibitory responses yet a well-defined threshold, all-or-none spikes with possibly long latencies.

Of course, figures 1.15 and 1.16 cannot encompass all the richness of neuronal behavior, otherwise this book would be only 19-pages long<sup>1</sup>. Many aspects of neuronal dynamics depend on other bifurcations, e.g., those corresponding to appearance and disappearance of spiking limit cycles. These bifurcations describe the transitions from spiking to resting, and they are especially important when we consider bursting activity. In addition, we need to take into account the relative geometry of equilibria, limit cycles, and other relevant trajectories, and how they depend on the parameters of the system, such as maximal conductances, activation time constants, etc. We explore all these issues systematically in subsequent chapters.

In Chap. 2 we review some of the most fundamental concepts of neuron electrophysiology, culminating with the Hodgkin-Huxley model. This chapter is aimed at mathematicians learning neuroscience. In Chapters 3 and 4 we use one- and two-dimensional neuronal models, respectively, to review some of the most fundamental concepts of dynamical systems, such as equilibria, limit cycles, stability, attraction domain, nullclines, phase portrait, bifurcation, etc. The material in these chapters, aimed at biologists learning the language of dynamical systems, is presented with the emphasis on geometrical rather than mathematical intuition. In fact, the spirit of the entire book is to explain concepts using pictures, not equations. Chap. 5 explores phase portraits of various conductance-based models and the relations between ionic currents and dynamic behavior. In Chap. 6 we use the  $I_{\text{Na,p}}+I_K$ -model to systematically introduce the geometric bifurcation theory. Chap. 7, probably the most important chapter of the book, applies the theory to explain many computational properties of neurons. In fact, all the material in the previous chapters is given so that the reader can understand this chapter. In Chap. 8 we use a simple phenomenological model to simulate many cortical and thalamic neurons. This chapter contains probably the most comprehensive up to date review of various firing patterns exhibited by mammalian neurons. In Chap. 9 we introduce the electrophysiological and topological classification of bursting dynamics, as well as some useful methods to study the bursters. Finally, the last and the most mathematically advanced chapter of the book, Chap. 10, deals

---

<sup>1</sup>This book is actually quite short; Most of the space is taken by figures, exercises, and solutions.

with coupled neurons. There we show how the details of spike-generation mechanism of neurons affect their collective properties, such as synchronization.

### 1.2.5 Building models (revisited)

To have a good model of a neuron, it is not enough to put the right kind of currents together and tune the parameters so that the model can fire spikes. It is not even enough to reproduce the right input resistance, rheobase, and firing frequencies. The model has to reproduce all the neuro-computational features of the neuron, starting with the co-existence of resting and spiking states, spike latencies, subthreshold oscillations, rebound spikes, etc.

A good way to start is to determine what kind of bifurcations the neuron under consideration undergoes and how the bifurcations depend on neuromodulators and pharmacological blockers. Instead of or in addition to measuring neuronal responses to get the kinetic parameters, we need to measure them to get the right bifurcation behavior. Only in this case we can be sure that the behavior of the model is *equivalent* to that of the neuron, even if we omitted a current or guessed some of the parameters incorrectly.

Implementation of this research program is still a pipe dream. The people who understand the mathematical aspects of neuron dynamics, those who see beyond conductances and currents, those people do not usually have the opportunity to do experiments. Conversely, those who study neurons *in vitro* or *in vivo* on a daily basis, those who see spiking, bursting, oscillations, those who can manipulate the experimental setup to test practically any aspect of neuronal activity, those people do not usually see the value of studying phase portraits, bifurcations, and nonlinear dynamics in general. One of the goals of this book is to change this state and bring these two groups of people closer together.

## Review of Important Concepts

- Neurons are dynamical systems.
- Resting state of neurons corresponds to a stable equilibrium, tonic spiking state corresponds to a limit cycle attractor.
- Neurons are excitable because the equilibrium is near a bifurcation.
- There are many ionic mechanisms of spike-generation, but only four generic bifurcations of equilibria.
- These bifurcations divide neurons into four categories: integrators or resonators, monostable or bistable.
- Analyses of phase portraits at bifurcations explain why some neurons have well-defined thresholds, all-or-none spikes, post-inhibitory spikes, frequency preference, hysteresis, etc., while others do not.
- These features, and not ionic currents per se, determine the neuronal responses, i.e., the kind of computations neurons do.
- A good neuronal model must reproduce not only electrophysiology but also the bifurcation dynamics of neurons.

## Bibliographical Notes

Richard FitzHugh at the National Institutes of Health (NIH) pioneered the phase plane analysis of neuronal models with the view to understand their neuro-computational properties. He was the first to analyze the Hodgkin-Huxley model (FitzHugh 1955; years before they received the Nobel prize) and to prove that it has neither threshold nor all-or-none spikes. FitzHugh (1961) introduced a simplified model of excitability and showed that one can get the right kind of neuronal dynamics in models lacking conductances and currents. Nagumo et al. (1962) designed a corresponding tunnel diode circuit, so the model is called the FitzHugh-Nagumo oscillator. Chapter 8 deals with such simplified models.

FitzHugh research program was further developed by John Rinzel and G. Bard Ermentrout. In their 1989 seminal paper, Rinzel and Ermentrout revived Hodgkin's classification of excitability and pointed out to the connection between the behavior of neuronal models and the bifurcations they exhibit. (They also refer to the excitability as "type I" and "type II"). Unfortunately, many people treat the connection in a simpleminded fashion and incorrectly identify "type I = saddle-node, type II = Hopf".



Figure 1.17: John Rinzel in 2004. Incidentally, his T-shirt shows the cover of the first issue of *Journal of Computational Neuroscience*, in which the Pinsky-Rinzel (1994) model appeared.



Figure 1.18: G. Bard Ermentrout (G. stands for George) with his parrot Junior in 1983.



Figure 1.19: Richard FitzHugh in 1984.

If only life was so simple!

The geometrical analysis of neuronal models was further developed, among others, by Izhikevich (2000), who stressed the integrator and resonator modes of operation and made connections to other neuro-computational properties.

The neuroscience and mathematics parts of this book are standard, though many connections are new. We point to the literature sources at the end of each chapter. Among many outstanding books on computational neuroscience, we especially recommend *Spikes, Decisions, and Actions* by Wilson (1999), *Biophysics of Computation* by Koch (1999), *Theoretical Neuroscience* by Dayan and Abbott (2001), and *Foundations of Cellular Neurophysiology* by Johnston and Wu (1995). The present monograph complements these excellent books in the sense that it is more ambitious, focused, and thorough in dealing with neurons as dynamical systems. Though the views in this monograph may be biased by the author's philosophy and taste, the payoffs in understanding neuronal dynamics are immense, provided that the reader has enough patience and perseverance to follow the author's line of thought.

NEURON simulation environment is described by Hines (1989) (<http://www.neuron.yale.edu>), GENESIS environment is described by Bower and Beeman (1995) (<http://www.genesis-sim.org>), XPP environment is described by Ermentrout (2002). The author of this book uses MATLAB (version 6.5 for Windows), which has become a standard computational tool in science and engineering (MATLAB is registered trademark of The MathWorks, Inc.; see <http://www.mathworks.com>).



# Chapter 2

## Electrophysiology of Neurons

In this chapter we remind the reader of some fundamental concepts of neuronal electrophysiology, which are necessary to understand the rest of the book. We start with ions and currents, and move quickly toward the dynamics of the Hodgkin-Huxley model. If the reader is already familiar with the Hodgkin-Huxley formalism, this chapter can be skipped. Our exposition is brief, and it cannot substitute a good introductory neuroscience course or reading of such excellent textbooks as *Theoretical Neuroscience* by Dayan and Abbott (2001), *Foundations of Cellular Neurophysiology* by Johnston and Wu (1995), *Biophysics of Computation* by Koch (1999) or *Ion Channels of Excitable Membranes* by Hille (2001).

### 2.1 Ions

Electrical activity in neurons is sustained and propagated via ionic currents through neuron membranes. Most of these transmembrane currents involve four ionic species: sodium ( $\text{Na}^+$ ), potassium ( $\text{K}^+$ ), calcium ( $\text{Ca}^{2+}$ ), and chloride ( $\text{Cl}^-$ ). The first three have a positive charge (cations) and the fourth has a negative charge (anion). The concentrations of these ions are different on the inside and outside of a cell, which creates electrochemical gradients — the major driving forces of neural activity. The extracellular medium has high concentration of  $\text{Na}^+$  and  $\text{Cl}^-$  (salty like seawater) and a relatively high concentration of  $\text{Ca}^{2+}$ . The intracellular medium has high concentration of  $\text{K}^+$  and negatively charged molecules (denoted by  $\text{A}^-$ ), as we illustrate in Fig. 2.1.

The cell membrane has large protein molecules forming channels through which ions (but not  $\text{A}^-$ ) can flow according to their electrochemical gradients. The flow of  $\text{Na}^+$  and  $\text{Ca}^{2+}$  ions is not significant, at least at rest, but the flow of  $\text{K}^+$  and  $\text{Cl}^-$  ions is. This, however, does not eliminate the concentration asymmetry due to the following two reasons.

- *Passive redistribution.* The impermeable anions  $\text{A}^-$  attract more  $\text{K}^+$  into the cell (opposites attract) and repel more  $\text{Cl}^-$  out of the cell, thereby creating concentration gradients.
- *Active transport.* Ions are pumped in and out of the cell via ionic pumps. For example, the  $\text{Na}^+-\text{K}^+$  pump depicted in Fig. 2.1 pumps out three  $\text{Na}^+$  ions for

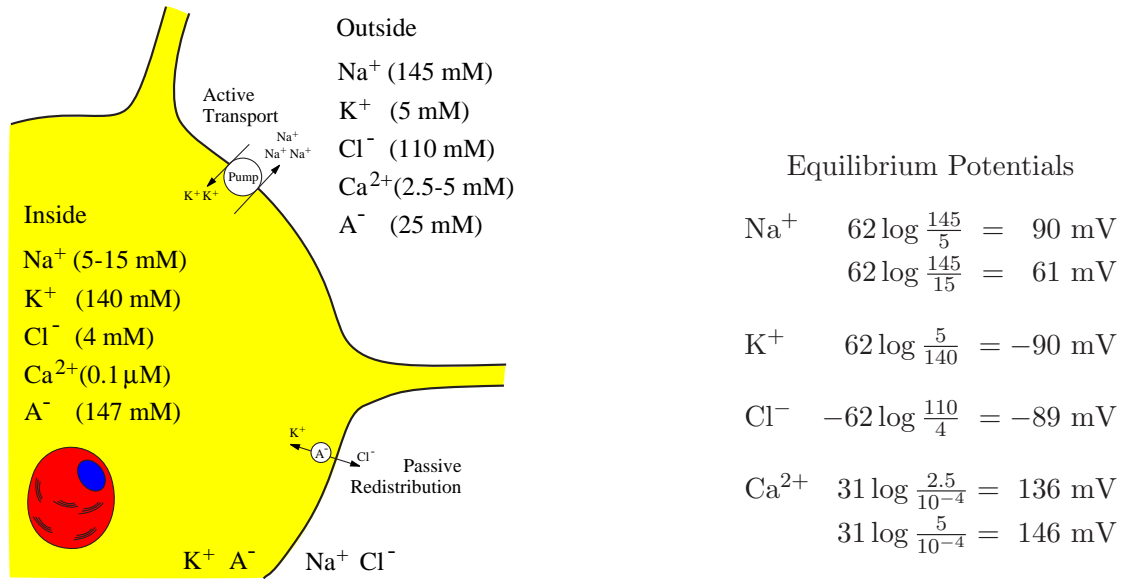


Figure 2.1: Ion concentrations and Nernst equilibrium potentials (2.1) in a typical mammalian neuron (modified from Johnston and Wu 1995).  $\text{A}^-$  are membrane-impermeant anions. Temperature  $T = 37^\circ\text{C}$  ( $310^\circ\text{K}$ ).

every two  $\text{K}^+$  ions pumped in, thereby maintaining concentration gradients.

### 2.1.1 Nernst potential

There are two forces that drive each ion species through the membrane channel: concentration and electric potential gradients. First, the ions diffuse down the concentration gradient. For example, the  $\text{K}^+$  ions depicted in Fig. 2.2a diffuse out of the cell because  $\text{K}^+$  concentration inside is higher than that outside. While exiting the cell,  $\text{K}^+$  ions carry positive charge with them and leave a net negative charge inside the cell (consisting mostly of impermeable anions  $\text{A}^-$ ), thereby producing the outward current. The positive and negative charges accumulate on the opposite sides of the membrane surface creating an electric potential gradient across the membrane – *transmembrane potential* or *membrane voltage*. This potential slows down the diffusion of  $\text{K}^+$ , since  $\text{K}^+$  ions are attracted to the negatively charged interior and repelled from the positively charged exterior of the membrane, as we illustrate in Fig. 2.2b. At some point an equilibrium is achieved: The concentration gradient and the electric potential gradient exert equal and opposite forces that counterbalance each other, and the net cross-membrane current is zero, as in Fig. 2.2c. The value of such an *equilibrium potential* depends on the ionic species, and it is given by the Nernst equation (Hille 2001)

$$E_{\text{ion}} = \frac{RT}{zF} \ln \frac{[\text{Ion}]_{\text{out}}}{[\text{Ion}]_{\text{in}}} , \quad (2.1)$$

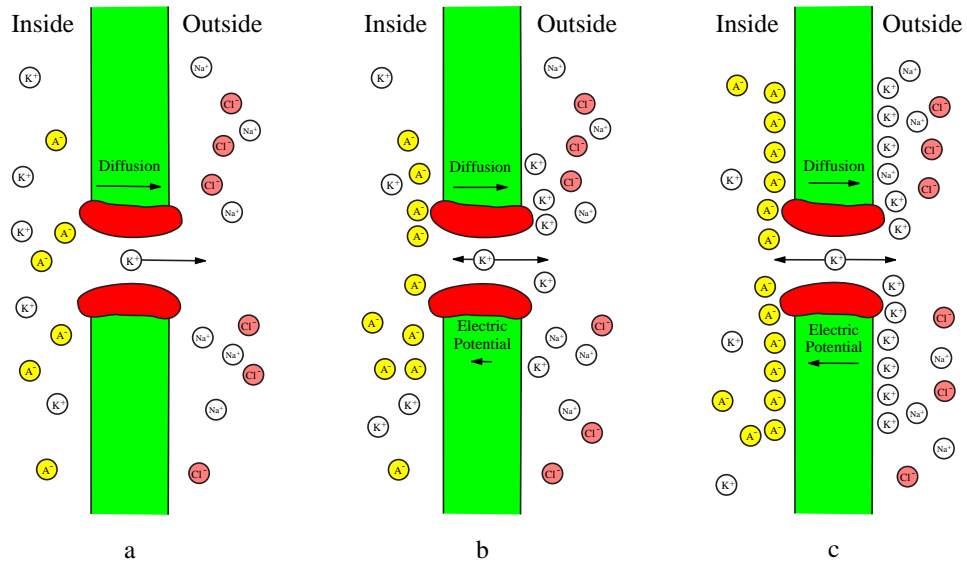


Figure 2.2: Diffusion of  $K^+$  ions down the concentration gradient though the membrane (a) creates an electric potential force pointing in the opposite direction (b) until the diffusion and electrical forces counter each other (c). The resulting transmembrane potential (2.1) is referred to as the Nernst equilibrium potential for  $K^+$ .

where  $[Ion]_{in}$  and  $[Ion]_{out}$  are concentrations of the ions inside and outside the cell, respectively,  $R$  is the universal gas constant ( $8,315 \text{ mJ/(K}^\circ\text{-Mol)}$ ),  $T$  is temperature in degrees Kelvin ( $K^\circ = 273.16 + C^\circ$ ),  $F$  is Faraday's constant ( $96,480 \text{ Coulombs/Mol}$ ),  $z$  is the valence of the ion ( $z = 1$  for  $Na^+$  and  $K^+$ ,  $z = -1$  for  $Cl^-$ , and  $z = 2$  for  $Ca^{2+}$ ). Substituting the numbers, taking  $\log_{10}$  instead of natural  $\ln$  and using body temperature  $T = 310^\circ\text{K}$  ( $37^\circ\text{C}$ ) results in

$$E_{ion} \approx 62 \log \frac{[Ion]_{out}}{[Ion]_{in}} \quad (\text{mV})$$

for monovalent ( $z = 1$ ) ions. Nernst equilibrium potentials in a typical mammalian neuron are summarized in Fig. 2.1.

### 2.1.2 Ionic currents and conductances

In the rest of the book  $V$  denotes the membrane potential and  $E_{Na}$ ,  $E_{Ca}$ ,  $E_K$ , and  $E_{Cl}$  denote the Nernst equilibrium potentials. When the membrane potential equals the equilibrium potential, say  $E_K$ , the net  $K^+$  current, denoted as  $I_K$  ( $\mu\text{A/cm}^2$ ), is zero (this is the definition of the Nernst equilibrium potential for  $K^+$ ). Otherwise, the net  $K^+$  current is proportional to the difference of potentials, i.e.

$$I_K = g_K (V - E_K) ,$$

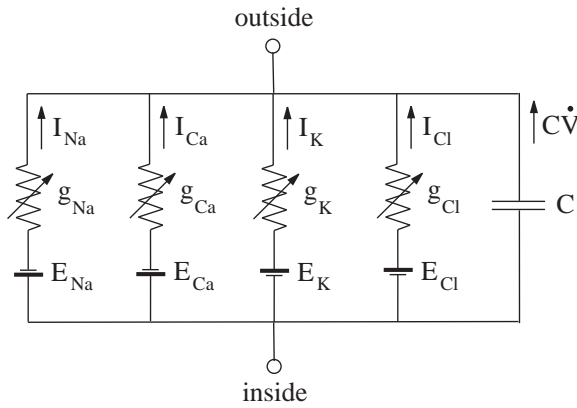


Figure 2.3: Equivalent circuit representation of a patch of cell membrane.

where the positive parameter  $g_K$  ( $\text{mS/cm}^2$ ) is the  $\text{K}^+$  conductance and  $(V - E_K)$  is the  $\text{K}^+$  driving force. The other major ionic currents

$$I_{\text{Na}} = g_{\text{Na}}(V - E_{\text{Na}}), \quad I_{\text{Ca}} = g_{\text{Ca}}(V - E_{\text{Ca}}), \quad I_{\text{Cl}} = g_{\text{Cl}}(V - E_{\text{Cl}})$$

could also be expressed as products of non-linear conductances and corresponding driving forces. A better description of membrane currents, especially  $\text{Ca}^{2+}$  current, is provided by the Goldman-Hodgkin-Katz equation (Hille 2001), which we do not use in this book.

When the conductance is constant, the current is said to be *Ohmic*. In general, ionic currents in neurons are not Ohmic, since the conductances may depend on time, membrane potential, and pharmacological agents, e.g., neurotransmitters, neuromodulators, second-messengers, etc. It is the time-dependent variation in conductances that allows a neuron to generate an action potential, or spike.

### 2.1.3 Equivalent circuit

It is traditional to represent electrical properties of membranes in terms of equivalent circuits similar to the one depicted in Fig. 2.3. According to Kirchhoff's law, the total current,  $I$ , flowing across a patch of a cell membrane is the sum of the membrane capacitive current  $C\dot{V}$  (the capacitance  $C \approx 1.0 \mu\text{F/cm}^2$  in the squid axon) and all the ionic currents

$$I = C\dot{V} + I_{\text{Na}} + I_{\text{Ca}} + I_K + I_{\text{Cl}},$$

where  $\dot{V} = dV/dt$  is the derivative of the voltage variable  $V$  with respect to time  $t$ . The derivative arises because it takes time to charge the membrane. This is the first *dynamic* term in the book! We write this equation in the standard “dynamical system” form

$$C\dot{V} = I - I_{\text{Na}} - I_{\text{Ca}} - I_K - I_{\text{Cl}} \tag{2.2}$$

or

$$C\dot{V} = I - g_{\text{Na}}(V - E_{\text{Na}}) - g_{\text{Ca}}(V - E_{\text{Ca}}) - g_K(V - E_K) - g_{\text{Cl}}(V - E_{\text{Cl}}). \tag{2.3}$$

If there are no additional current sources or sinks, such as synaptic current, axial current, tangential current along the membrane surface, or current injected via an electrode, then  $I = 0$ . In this case, the membrane potential is typically bounded by the equilibrium potentials in the following order (see Fig. 2.4):

$$E_K < E_{Cl} < V_{(\text{at rest})} < E_{Na} < E_{Ca},$$

so that  $I_{Na}, I_{Ca} < 0$  (inward currents) and  $I_K, I_{Cl} > 0$  (outward currents). From (2.2) it follows that inward currents increase the membrane potential, i.e., make it more positive (depolarization), whereas outward currents decrease it, i.e., make it more negative (hyperpolarization). Notice that  $I_{Cl}$  is called an outward current even though the flow of  $Cl^-$  ions is inward; the ions bring negative charge inside the membrane, which is equivalent to positively charged ions leaving the cell, as in  $I_K$ .

### 2.1.4 Resting potential and input resistance

If there were only  $K^+$  channels, as in Fig. 2.2, the membrane potential would quickly approach the  $K^+$  equilibrium potential,  $E_K$ , which is around  $-90$  mV. Indeed,

$$C \dot{V} = -I_K = -g_K(V - E_K)$$

in this case. However, most membranes contain a diversity of channels. For example,  $Na^+$  channels would produce an inward current and pull the membrane potential towards the  $Na^+$  equilibrium potential,  $E_{Na}$ , which could be as large as  $+90$  mV. The value of the membrane potential at which all inward and outward currents balance each other so that the net membrane current is zero corresponds to the *resting membrane potential*. It can be found from the equation (2.3,  $I = 0$ ) by setting  $\dot{V} = 0$ . The resulting expression

$$V_{\text{rest}} = \frac{g_{Na}E_{Na} + g_{Ca}E_{Ca} + g_KE_K + g_{Cl}E_{Cl}}{g_{Na} + g_{Ca} + g_K + g_{Cl}} \quad (2.4)$$

has a nice mechanistic interpretation:  $V_{\text{rest}}$  is the center of mass of the balance depicted in Fig. 2.4. Incidentally, the entire equation (2.3) can be written in the form

$$C \dot{V} = I - g_{\text{inp}}(V - V_{\text{rest}}), \quad (2.5)$$

where

$$g_{\text{inp}} = g_{Na} + g_{Ca} + g_K + g_{Cl}$$

is the total membrane conductance, called *input conductance*. The quantity  $R_{\text{inp}} = 1/g_{\text{inp}}$  is the *input resistance* of the membrane, and it measures the asymptotic sensitivity of the membrane potential to injected or intrinsic currents. Indeed, from (2.5) it follows that

$$V \rightarrow V_{\text{rest}} + IR_{\text{inp}}, \quad (2.6)$$

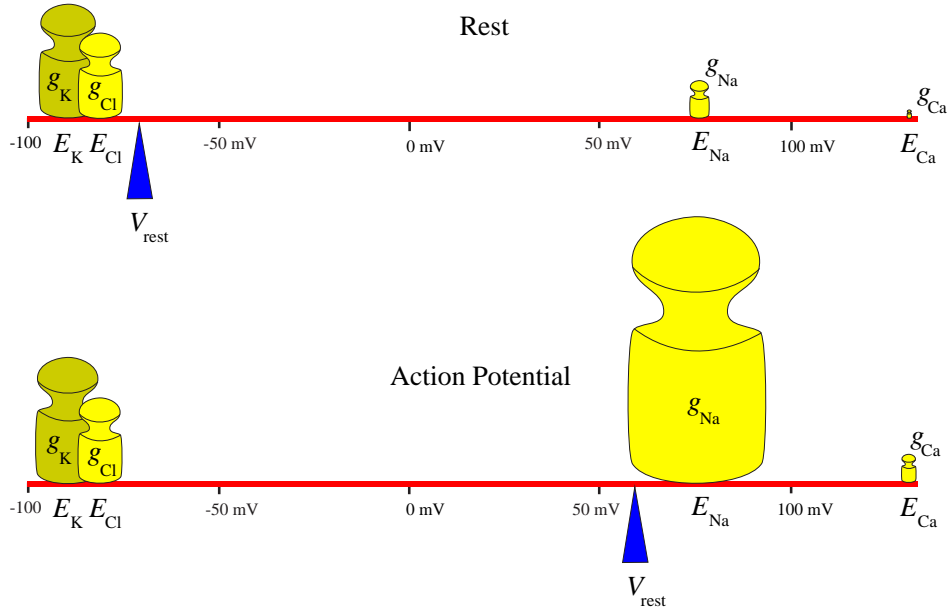


Figure 2.4: Mechanistic interpretation of the resting membrane potential (2.4) as the center of mass.  $\text{Na}^+$  conductance increases during the action potential.

so greater values of  $R_{\text{inp}}$  imply greater steady-state displacement of  $V$  due to the injection of dc current  $I$ .

A remarkable property of neuronal membranes is that ionic conductances, and hence the input resistance, are functions of  $V$  and time. We can use (2.6) to trace an action potential in a quasi-static fashion, i.e., assuming that time is frozen. When a neuron is quiescent,  $\text{Na}^+$  and  $\text{Ca}^{2+}$  conductances are relatively small,  $V_{\text{rest}}$  is near  $E_K$  and  $E_{\text{Cl}}$  as in Fig. 2.4,top, and so is  $V$ . During the upstroke of an action potential, the  $\text{Na}^+$  or  $\text{Ca}^{2+}$  conductance becomes very large,  $V_{\text{rest}}$  is near  $E_{\text{Na}}$ , as in Fig. 2.4,bottom, and  $V$  increases trying to catch  $V_{\text{rest}}$ . This event is however quite brief, due to the reasons explained in subsequent sections.

### 2.1.5 Voltage-clamp and I-V relation

In the next section we will study how the membrane potential affects ionic conductances and currents, assuming that the potential is fixed at certain value  $V_c$  controlled by an experimenter. To maintain the membrane potential constant (clamped), one inserts a metallic conductor to short-circuit currents along the membrane (space-clamp), and then injects a current proportional to the difference  $V_c - V$  (voltage-clamp), as in Fig. 2.5. From (2.2) and the clamp condition  $\dot{V} = 0$  it follows that the injected current  $I$  equals the net current generated by the membrane conductances.

In a typical voltage-clamp experiment the membrane potential is held at a certain resting value  $V_c$  and then reset to a new value  $V_s$ , as in Fig. 2.6a. The injected membrane

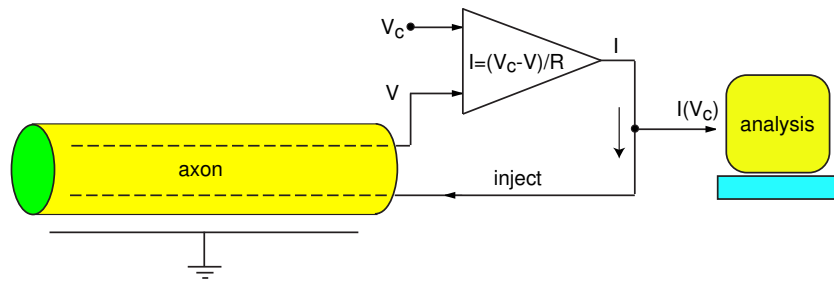


Figure 2.5: Two-wire voltage-clamp experiment on the axon: The top wire is used to monitor the membrane potential  $V$ . The bottom wire is used to inject the current  $I$  proportional to the difference  $V_c - V$  to keep the membrane potential at  $V_c$ .

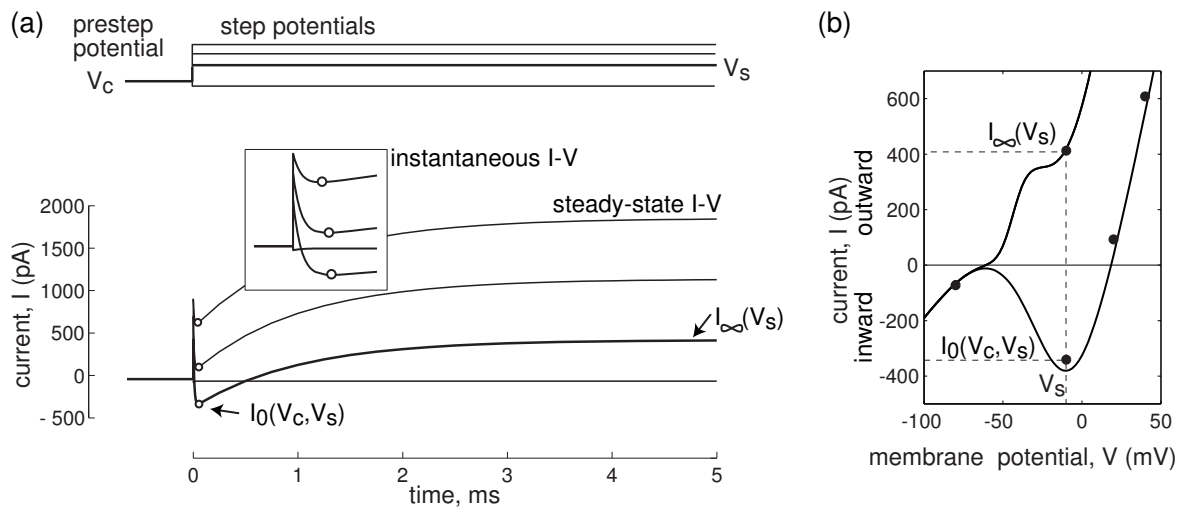


Figure 2.6: Voltage-clamp experiment to measure instantaneous and steady-state I-V relation. Shown are simulations of the  $I_{Na}+I_K$ -model (see Fig. 4.1b); the continuous curves are theoretically found I-V relations.



Figure 2.7: To tease out neuronal currents, biologists employ an arsenal of sophisticated “clamp” methods, such as current-, voltage-, conductance-, and dynamic-clamp.

current needed to stabilize the potential at the new value is a function of time, the pre-step holding potential  $V_c$ , and the step potential  $V_s$ . First, the current jumps to a new value to accommodate the instantaneous voltage change from  $V_c$  to  $V_s$ . From (2.5) we find that the amplitude of the jump is  $g_{\text{inp}}(V_s - V_c)$ . Then, time- and voltage-dependent processes start to occur and the current decreases and then increases. The value at the negative peak, marked by circle “o” in Fig. 2.6, depends only on  $V_c$  and  $V_s$  and it is called *the instantaneous current-voltage (I-V) relation*, or  $I_0(V_c, V_s)$ . The asymptotic ( $t \rightarrow \infty$ ) value depends only on  $V_s$  and it is called the *steady-state current-voltage (I-V) relation*, or  $I_\infty(V_s)$ .

Both relations, depicted in Fig. 2.6b, can be found experimentally (black dots) or theoretically (curves). The instantaneous I-V relation usually has a non-monotone N-shape reflecting non-linear auto-catalytic (positive feedback) transmembrane processes, which are fast enough on the time scale of the action potential so that they could be assumed to have instantaneous kinetics. The steady-state I-V relation measures the asymptotic values of all transmembrane processes, and it may be monotone, as in the figure, or not, depending on the properties of the membrane currents. Both I-V relations provide an invaluable quantitative information about the currents operating on fast and slow time scale, and both are useful in building mathematical models of neurons. Finally, when  $I_\infty(V) = 0$ , the net membrane current is zero, and the potential is at rest or equilibrium, which may still be unstable as we discuss in the next chapter.

## 2.2 Conductances

Ionic channels are large transmembrane proteins having aqueous pores through which ions can flow down their electrochemical gradients. The electrical conductance of indi-

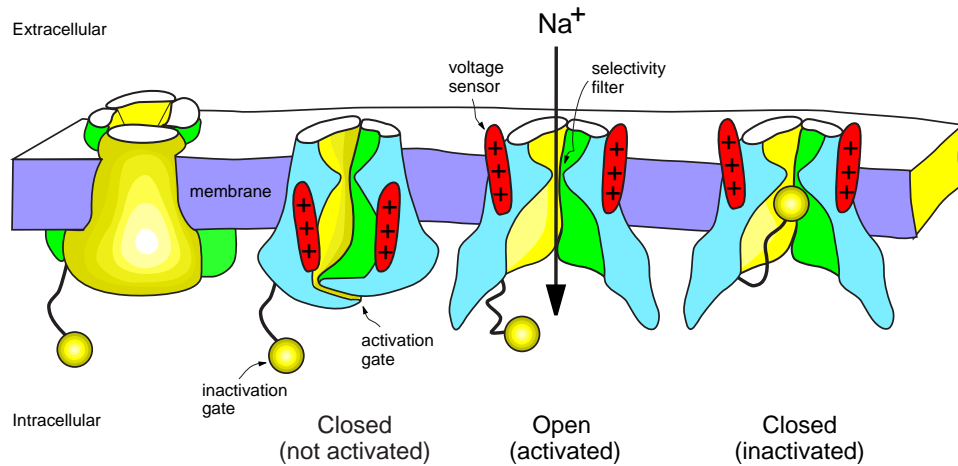


Figure 2.8: Structure of voltage-gated ion channels. Voltage sensors open activation gate and allow selected ions to flow through the channel according to their electrochemical gradients. The inactivation gate blocks the channel (modified from Armstrong and Hille 1998).

Individual channels may be controlled by gating particles (gates), which switch the channels between open and closed states. The gates are sensitive to one or more of the following factors:

- Membrane potential. Example: voltage-gated  $\text{Na}^+$  or  $\text{K}^+$  channels.
- Intracellular agents (second-messengers). Example:  $\text{Ca}^{2+}$ -gated  $\text{K}^+$  channels.
- Extracellular agents (neurotransmitters and neuromodulators). Example: AMPA, NMDA, or GABA receptors.

Despite the stochastic nature of transitions between open and closed states in individual channels, the net current generated by a large population or ensemble of identical channels can reasonably be described by the equation

$$I = \bar{g} p (V - E) \quad (2.7)$$

where  $p$  is the average proportion of channels in the open state,  $\bar{g}$  is the *maximal conductance* of the population, and  $E$  is the *reverse potential* of the current, i.e., the potential at which the current reverses its direction. If the channels are selective for a single ionic species, then the reverse potential  $E$  equals the Nernst equilibrium potential (2.1) for that ionic species, see Ex. 2.

### 2.2.1 Voltage-gated channels

When the gating particles are sensitive to the membrane potential, the channels are said to be *voltage-gated*. The gates are divided into two types: Those that *activate* or

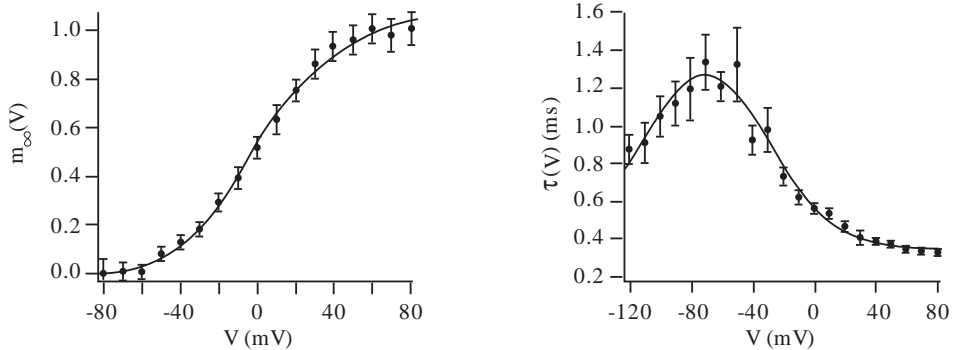


Figure 2.9: The activation function  $m_\infty(V)$  and the time constant  $\tau(V)$  of the fast transient  $K^+$  current in layer 5 neocortical pyramidal neurons (modified from Korngreen and Sakmann 2000).

open the channels, and those that *inactivate* or close them; see Fig. 2.8. According to the tradition initiated in the middle of 20th century by Hodgkin and Huxley, the probability of an activation gate to be in the open state is denoted by the variable  $m$  (sometimes the variable  $n$  is used for  $K^+$  and  $Cl^-$  channels). The probability of an inactivation gate to be in the open state is denoted by the variable  $h$ . The proportion of open channels in a large population is

$$p = m^a h^b , \quad (2.8)$$

where  $a$  is the number of activation gates and  $b$  is the number of inactivation gates per channel. The channels can be partially ( $0 < m < 1$ ) or completely *activated* ( $m = 1$ ); not activated or *deactivated* ( $m = 0$ ); *inactivated* ( $h = 0$ ); released from inactivation or *deinactivated* ( $h = 1$ ). Some channels do not have inactivation gates ( $b = 0$ ), hence  $p = m^a$ . Such channels do not inactivate, and they result in *persistent* currents. In contrast, channels that do inactivate result in *transient* currents.

Below we describe voltage- and time-dependent kinetics of gates. This description is often referred to as the *Hodgkin-Huxley gate model* of membrane channels.

### 2.2.2 Activation of persistent currents

The dynamics of the activation variable  $m$  is described by the first-order differential equation

$$\dot{m} = (m_\infty(V) - m)/\tau(V) \quad (2.9)$$

where the voltage-sensitive steady-state *activation function*  $m_\infty(V)$  and the *time constant*  $\tau(V)$  can be measured experimentally: They have sigmoid and unimodal shapes, respectively, as in Fig. 2.9; see also Fig. 2.20. The steady-state activation function  $m_\infty(V)$  gives the asymptotic value of  $m$  when the potential is fixed (voltage-clamp). Smaller values of  $\tau(V)$  result in faster dynamics of  $m$ .

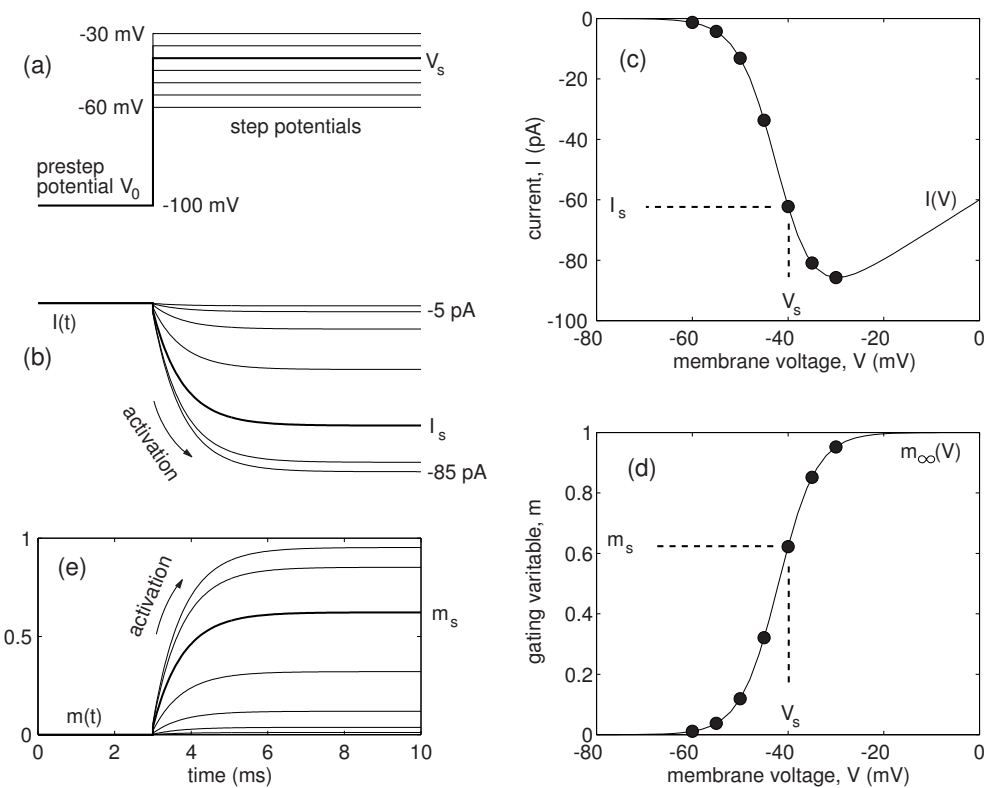


Figure 2.10: An experiment to determine  $m_\infty(V)$ . Shown are simulations of the persistent  $\text{Na}^+$  current in Purkinje cells (see Sect. 2.3.5).

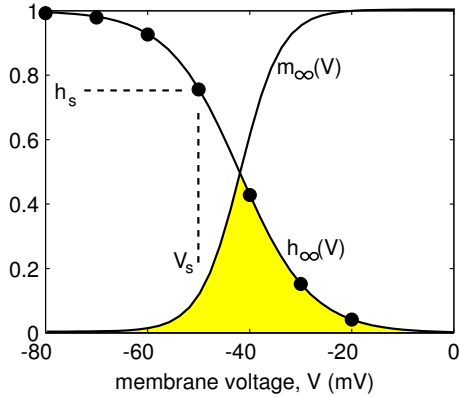


Figure 2.11: Steady-state activation function  $m_\infty(V)$  from Fig. 2.10, inactivation function  $h_\infty(V)$ , and values  $h_s$  from Fig. 2.12. Their overlap (shaded region) produces a noticeable persistent “window” current.

In Fig. 2.10 we depict a typical experiment to determine  $m_\infty(V)$  of a persistent current, i.e., a current having no inactivation variable. Initially we hold the membrane potential at a hyperpolarized value  $V_0$  so that all activation gates are closed and  $I \approx 0$ . Then we step-increase  $V$  to a greater value  $V_s$  ( $s = 1, \dots, 7$ ; see Fig. 2.10a) and hold it there until the current is essentially equal to its asymptotic value, which we denote here as  $I_s$  ( $s$  stands for “step”; see Fig. 2.10b). Repeating the experiment for various stepping potentials  $V_s$ , one can easily determine the corresponding  $I_s$ , and hence the entire steady-state I-V relation, which we depict in Fig. 2.10c. According to (2.7),  $I(V) = \bar{g}m_\infty(V)(V - E)$ , and the steady-state activation curve  $m_\infty(V)$  depicted in Fig. 2.10d is just  $I(V)$  divided by the driving force  $(V - E)$  and normalized so that  $\max m_\infty(V) = 1$ . To determine the time constant  $\tau(V)$ , one needs to analyze the convergence rates. In Ex. 6 we describe an efficient method to determine  $m_\infty(V)$  and  $\tau(V)$ .

### 2.2.3 Inactivation of transient currents

The dynamics of the inactivation variable  $h$  can also be described by the first-order differential equation

$$\dot{h} = (h_\infty(V) - h)/\tau(V) . \quad (2.10)$$

where  $h_\infty(V)$  is the voltage-sensitive steady-state *inactivation function* depicted in Fig. 2.11. In Fig. 2.12 we present a typical voltage-clamp experiment to determine  $h_\infty(V)$  in the presence of activation  $m_\infty(V)$ . It relies on the observation that inactivation kinetics is usually slower than activation kinetics. First, we hold the membrane potential at a certain pre-step potential  $V_s$  for a sufficiently long time so that the activation and inactivation variables are essentially equal to their steady-state values  $m_\infty(V_s)$  and  $h_\infty(V_s)$ , respectively, which have yet to be determined. Then we step-increase  $V$  to a sufficiently high value  $V_0$  chosen so that  $m_\infty(V_0) \approx 1$ . If activation is much faster than inactivation,  $m$  approaches 1 after a first few milliseconds while  $h$  continues to be near its asymptotic value  $h_s = h_\infty(V_s)$ , which can be found from the peak value of the current  $I_s \approx \bar{g} \cdot 1 \cdot h_s(V_s - E)$ . Repeating this experiment for various pre-step potentials, one can determine the steady-state inactivation curve  $h_\infty(V)$  in Fig. 2.11.

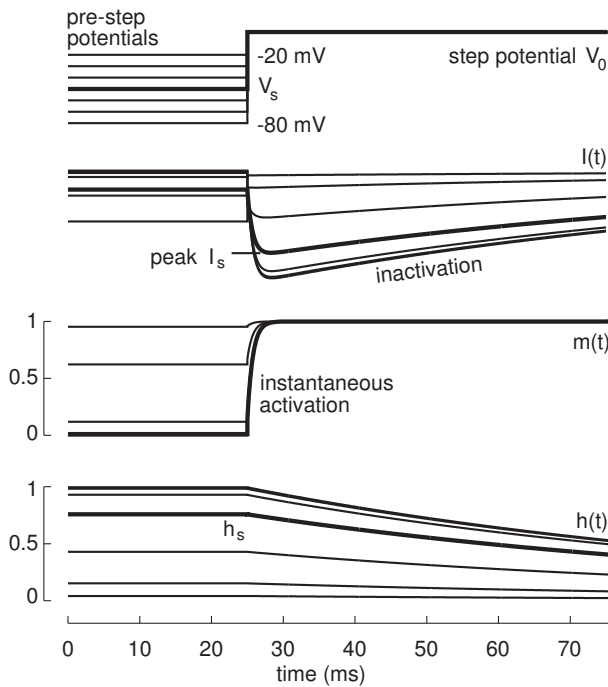


Figure 2.12: Dynamics of the current ( $I$ ), activation ( $m$ ) and inactivation ( $h$ ) variables in the voltage-clamp experiment aimed at measuring  $h_\infty(V)$  in Fig. 2.11.

In Ex. 6 we describe a better method to determine  $h_\infty(V)$  that does not rely on the difference between the activation and inactivation time scales.

The voltage-sensitive steady-state activation and inactivation functions overlap in a shaded window depicted in Fig. 2.11. Depending on the size of the shaded area in the figure, the overlap may result in a noticeable “window” current.

## 2.2.4 Hyperpolarization-activated channels

Many neurons in various parts of the brain have channels that are opened by hyperpolarization. These channels produce currents that are turned on by hyperpolarization and turned off by depolarization. Biologists refer to such currents as being “exceptional” or “weird”, and denoted them as  $I_Q$  (“queer”),  $I_f$  (“funny”),  $I_h$  (“hyperpolarization-activated”), or  $I_{Kir}$  ( $K^+$  inward rectifier). We will consider the last two currents in detail in the next chapter. Most neuroscience textbooks classify these currents in a special category — *hyperpolarization-activated currents*. However, from the theoretical point of view it is inconvenient to create special categories. In this book we treat these currents as “normal” transient currents with the understanding that they are always activated (either  $a = 0$  or variable  $m = 1$  in (2.8)), but can be inactivated by depolarization (variable  $h \rightarrow 0$ ) or deinactivated by hyperpolarization (variable  $h \rightarrow 1$ ). Moreover, there is biophysical evidence suggesting that closing/opening of  $I_{Kir}$  is indeed related to the inactivation/deinactivation process (Lopatin et al. 1994).

## 2.3 Hodgkin-Huxley Model

In Sect. 2.1 we have studied how the membrane potential depends on the membrane currents assuming that ionic conductances are fixed. In Sect. 2.2 we have used the Hodgkin-Huxley gate model to study how the conductances and currents depend on the membrane potential assuming that the potential is clamped at different values. In this section we put it all together and study how the potential  $\leftrightarrow$  current non-linear interactions lead to many interesting phenomena such as generation of action potentials.

### 2.3.1 Hodgkin-Huxley equations

One of the most important models in computational neuroscience is the Hodgkin-Huxley model of the squid giant axon. Using pioneering experimental techniques of that time, Hodgkin and Huxley (1952) determined that the squid axon carries three major currents: voltage-gated persistent  $K^+$  current with four activation gates (resulting in the term  $n^4$  in the equation below, where  $n$  is the activation variable for  $K^+$ ), voltage-gated transient  $Na^+$  current with three activation gates and one inactivation gate (term  $m^3h$  below), and Ohmic leak current,  $I_L$ , which is carried mostly by  $Cl^-$  ions. The complete set of space-clamped Hodgkin-Huxley equations is

$$\begin{aligned} C \dot{V} &= I - \overbrace{\bar{g}_K n^4 (V - E_K)}^{I_K} - \overbrace{\bar{g}_{Na} m^3 h (V - E_{Na})}^{I_{Na}} - \overbrace{g_L (V - E_L)}^{I_L} \\ \dot{n} &= \alpha_n(V)(1-n) - \beta_n(V)n \\ \dot{m} &= \alpha_m(V)(1-m) - \beta_m(V)m \\ \dot{h} &= \alpha_h(V)(1-h) - \beta_h(V)h , \end{aligned}$$

where

$$\begin{aligned} \alpha_n(V) &= 0.01 \frac{10 - V}{\exp(\frac{10-V}{10}) - 1} , \\ \beta_n(V) &= 0.125 \exp\left(\frac{-V}{80}\right) , \\ \alpha_m(V) &= 0.1 \frac{25 - V}{\exp(\frac{25-V}{10}) - 1} , \\ \beta_m(V) &= 4 \exp\left(\frac{-V}{18}\right) , \\ \alpha_h(V) &= 0.07 \exp\left(\frac{-V}{20}\right) , \\ \beta_h(V) &= \frac{1}{\exp(\frac{30-V}{10}) + 1} . \end{aligned}$$

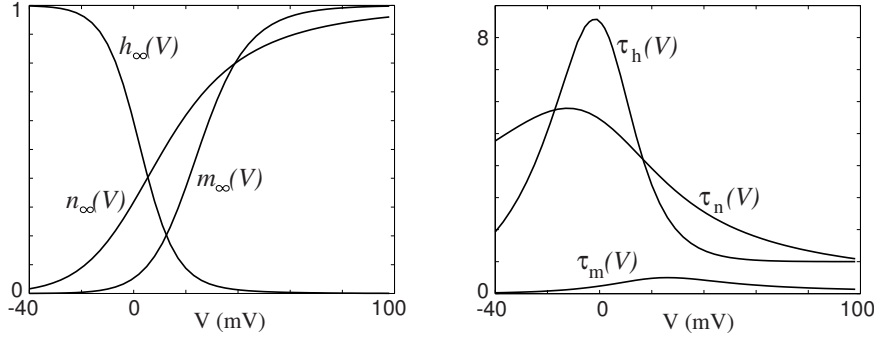


Figure 2.13: Steady-state (in)activation functions (left) and voltage-dependent time constants (right) in the Hodgkin-Huxley model.

These parameters, provided in the original Hodgkin and Huxley paper, correspond to the membrane potential shifted by approximately 65 mV so that the resting potential is at  $V \approx 0$ . Hodgkin and Huxley did that for the sake of convenience, but the shift has led to a lot of confusion over the years. The shifted Nernst equilibrium potentials are

$$E_K = -12 \text{ mV}, \quad E_{Na} = 120 \text{ mV}, \quad E_L = 10.6 \text{ mV};$$

see also Ex. 1. Typical values of maximal conductances are

$$\bar{g}_K = 36 \text{ mS/cm}^2, \quad \bar{g}_{Na} = 120 \text{ mS/cm}^2, \quad g_L = 0.3 \text{ mS/cm}^2.$$

$C = 1 \mu\text{F}/\text{cm}^2$  is the membrane capacitance and  $I = 0 \mu\text{A}/\text{cm}^2$  is the applied current. The functions  $\alpha(V)$  and  $\beta(V)$  describe the transition rates between open and closed states of the channels. We present this notation only for historical reasons. In the rest of the book, we use the standard form

$$\begin{aligned} \dot{n} &= (n_\infty(V) - n)/\tau_n(V), \\ \dot{m} &= (m_\infty(V) - m)/\tau_m(V), \\ \dot{h} &= (h_\infty(V) - h)/\tau_h(V), \end{aligned}$$

where

$$\begin{aligned} n_\infty &= \alpha_n/(\alpha_n + \beta_n), & \tau_n &= 1/(\alpha_n + \beta_n), \\ m_\infty &= \alpha_m/(\alpha_m + \beta_m), & \tau_m &= 1/(\alpha_m + \beta_m), \\ h_\infty &= \alpha_h/(\alpha_h + \beta_h), & \tau_h &= 1/(\alpha_h + \beta_h) \end{aligned}$$

are depicted in Fig. 2.13. These functions can be approximated by the Boltzmann and Gaussian functions; see Ex. 4. We also shift the membrane potential back to its true value, so that the resting state is near -65 mV.

The membrane of the squid giant axon carries only two major currents: transient  $\text{Na}^+$  and persistent  $\text{K}^+$ . Most neurons in the central nervous system have additional currents with diverse activation and inactivation dynamics, which we summarize in Sect. 2.3.5. The Hodgkin-Huxley formalism is the most accepted model to describe their kinetics.



Figure 2.14: Studies of spike-generation mechanism in “giant squid axons” won Alan Hodgkin and Andrew Huxley the 1963 Nobel prize for physiology or medicine (shared with Sir John Eccles); see also Fig. 4.1 in Keener and Sneyd (1998).

Since we are interested in geometrical and qualitative methods of analysis of neuronal models, we assume that all variables and parameters have appropriate scales and dimensions, but we do not explicitly state them. An exception is the membrane potential  $V$ , whose mV scale is stated in every figure.

### 2.3.2 Action Potential

Recall that when  $V = V_{\text{rest}}$ , which is 0 mV in the Hodgkin-Huxley model, all inward and outward currents balance each other so the net current is zero, as in Fig. 2.15. The rest state is stable: A small pulse of current applied via  $I(t)$  produces a small positive perturbation of the membrane potential (depolarization), which results in a small net current that drives  $V$  back to rest (repolarization). However, an intermediate size pulse of current produces a perturbation that is amplified significantly because membrane conductances depend on  $V$ . Such a non-linear amplification causes  $V$  to deviate considerably from  $V_{\text{rest}}$  — a phenomenon referred to as an *action potential* or *spike*.

In Fig. 2.15 we show a typical time course of an action potential in the Hodgkin-Huxley system. Strong depolarization increases activation variables  $m$  and  $n$  and decreases inactivation variable  $h$ . Since  $\tau_m(V)$  is relatively small, variable  $m$  is relatively fast. Fast activation of  $\text{Na}^+$  conductance drives  $V$  toward  $E_{\text{Na}}$ , resulting in further depolarization and further activation of  $g_{\text{Na}}$ . This positive feedback loop, depicted in Fig. 2.16 results in the *upstroke* of  $V$ . While  $V$  moves toward  $E_{\text{Na}}$ , the slower gating variables catch up. Variable  $h \rightarrow 0$ , causing inactivation of  $\text{Na}^+$  current, and variable  $n \rightarrow 1$ , causing slow activation of outward  $\text{K}^+$  current. The latter and the leak current

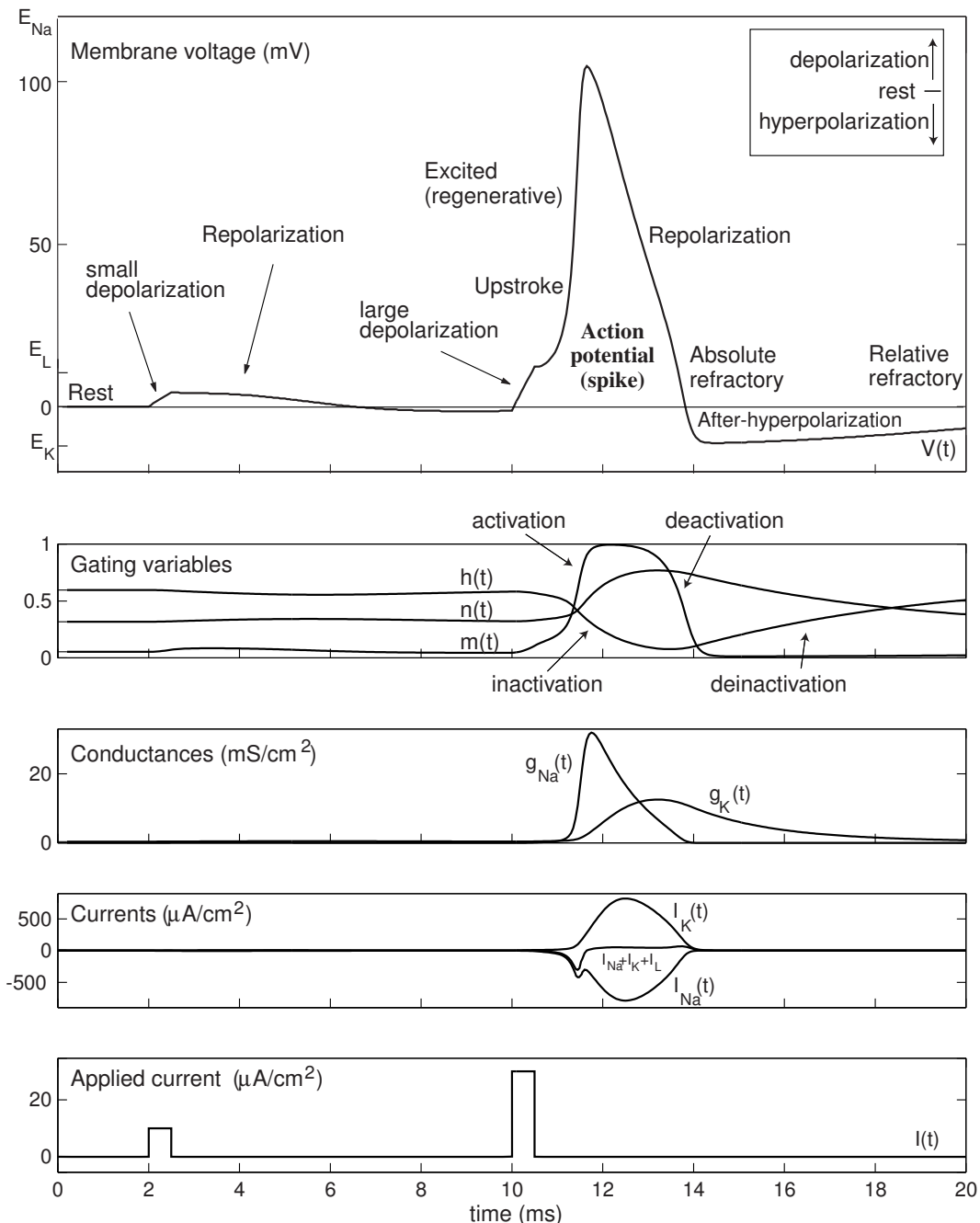


Figure 2.15: Action potential in the Hodgkin-Huxley model.

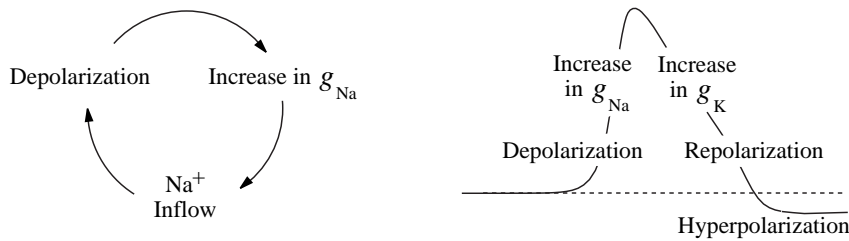


Figure 2.16: Positive and negative feedback loops resulting in excited (regenerative) behavior in neurons.

repolarize the membrane potential toward  $V_{\text{rest}}$ .

When  $V$  is near  $V_{\text{rest}}$ , the voltage-sensitive time constants  $\tau_n(V)$  and  $\tau_h(V)$  are relatively large, as one can see in Fig. 2.13. Therefore, recovery of variables  $n$  and  $h$  is slow. In particular, outward K<sup>+</sup> current continues to be activated ( $n$  is large) even after the action potential downstroke, thereby causing  $V$  to go below  $V_{\text{rest}}$  toward  $E_K$  — a phenomenon known as *afterhyperpolarization*.

In addition, Na<sup>+</sup> current continues to be inactivated ( $h$  is small) and not available for any regenerative function. The Hodgkin-Huxley system cannot generate another action potential during this *absolute refractory* period. While the current deinactivates, the system becomes able to generate an action potential provided that the stimulus is relatively strong (*relative refractory* period).

To study the relationship between these refractory periods, we stimulate the Hodgkin-Huxley model with 1-ms pulses of current having various amplitudes and latencies. The minimal amplitude of the stimulation needed to evoke a second spike in the model is depicted in Fig. 2.17, bottom. Notice that around 14 ms after the first spike, the model is hyper-excitable, that is, the stimulation amplitude is less than the baseline amplitude  $A_p \approx 6$  needed to evoke a spike from the resting state. This occurs because the Hodgkin-Huxley model exhibits damped oscillations of membrane potential, which we discuss in Chap. 7.

### 2.3.3 Propagation of the action potentials

The space-clamped Hodgkin-Huxley model of squid giant axon describes non-propagating action potentials since  $V(t)$  does not depend on the location,  $x$ , along the axon. To describe propagation of action potentials (pulses) along the axon having potential  $V(x, t)$ , radius  $a$  (cm) and intracellular resistivity  $R$  ( $\Omega \cdot \text{cm}$ ), the partial derivative  $V_{xx}$  is added to the voltage equation to account for axial currents along the membrane. The resulting non-linear parabolic partial differential equation

$$C V_t = \frac{a}{2R} V_{xx} + I - I_K - I_{\text{Na}} - I_L$$

is often referred to as the Hodgkin-Huxley cable or propagating equation. Its important type of solution, a traveling pulse, is depicted in Fig. 2.18. Studying this equation goes

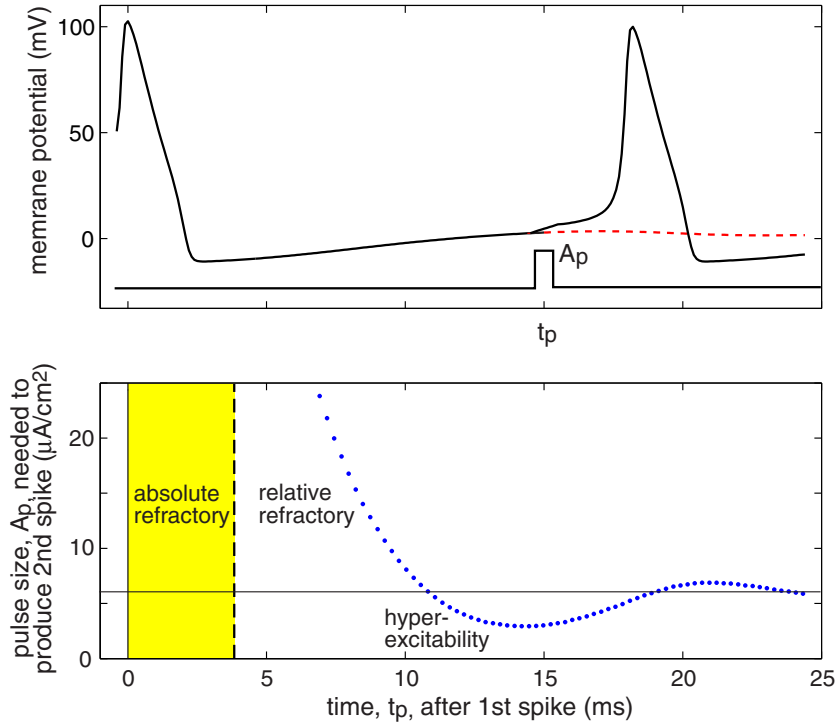


Figure 2.17: Refractory periods in the Hodgkin-Huxley model with  $I = 3$ .

beyond the scope of this book, and the reader can consult Keener and Sneyd (1998) and references therein.

### 2.3.4 Dendritic compartments

Modifications of the Hodgkin-Huxley model, often called Hodgkin-Huxley-type models, or conductance-based models, can describe the dynamics of spike-generation of many if not all neurons recorded in nature. However, there is more to the computational property of neurons than just the spike-generation mechanism. Many neurons have an extensive dendritic tree that can sample the synaptic input arriving at different locations and integrate it over space and time.

Many dendrites have voltage-gated currents, so the synaptic integration is non-linear, sometimes resulting in dendritic spikes that can propagate forward to the soma of the neuron or backwards to distant dendritic locations. Dendritic spikes are prominent in intrinsically bursting (IB) and chattering (CH) neocortical neurons considered in Chap. 8. In that chapter we also model regular spiking (RS) pyramidal neurons, the most numerous class of neurons in mammalian neocortex, and show that their spike-generation mechanism is one of the simplest. The computation complexity of RS neurons must be hidden then in the arbors of their dendritic trees.

It is not feasible at present to study analytically or geometrically the dynamics of membrane potential in dendritic trees, unless dendrites are assumed to be passive (lin-

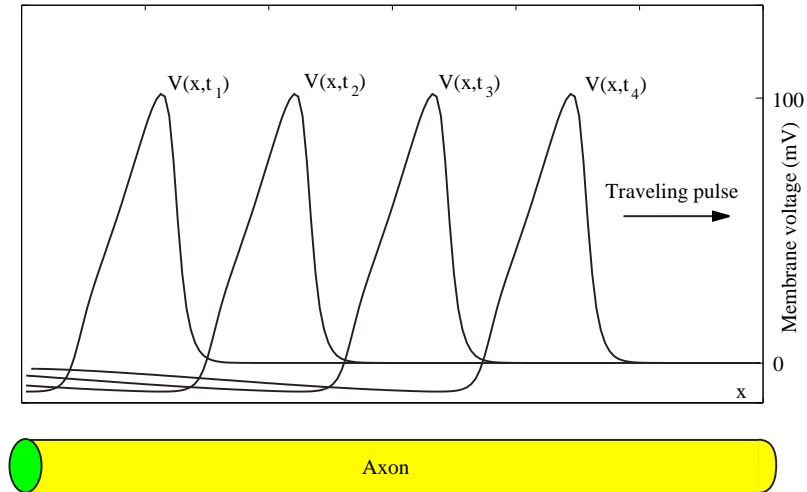


Figure 2.18: Traveling pulse solution of the Hodgkin-Huxley cable equation at four successive moments.

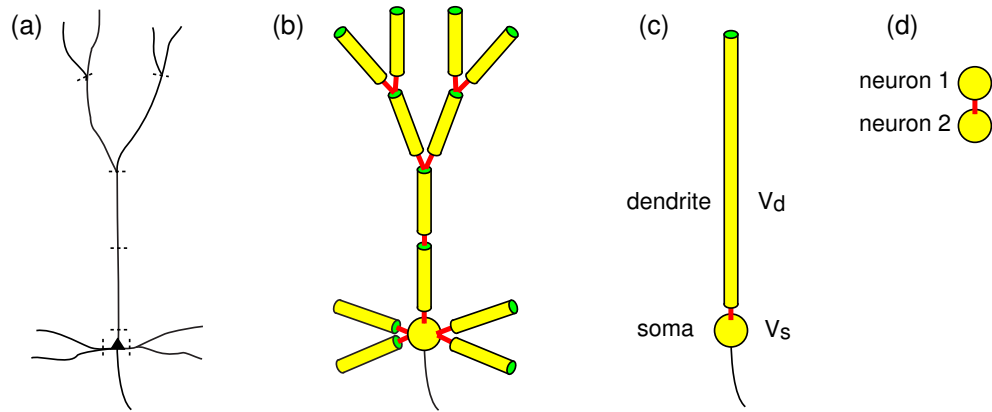


Figure 2.19: Dendritic tree of a neuron (a) is replaced by a network of compartments (b), each modeled by a Hodgkin-Huxley-type model. Two-compartment neuronal model (c) may be equivalent to two neurons coupled via gap junctions (electrical synapse).

ear), semi-infinite, and satisfy Rall's branching law (Rall 1959). Much of the insight can be obtained via simulations, which typically substitute the continuous dendritic structure in Fig. 2.19a by a network of discrete compartments in Fig. 2.19b. Dynamics of each compartment is simulated by a Hodgkin-Huxley-type model, and the compartments are coupled via conductances. For example, if  $V_s$  and  $V_d$  denote the membrane potential at the soma and in the dendritic tree, as in Fig. 2.19c, then

$$C_s \dot{V}_s = -I_s(V_s, t) + g_s(V_d - V_s) , \quad \text{and} \quad C_d \dot{V}_d = -I_d(V_d, t) + g_d(V_s - V_d) ,$$

where each  $I(V, t)$  represents the sum of all voltage-,  $\text{Ca}^{2+}$ -, and time-dependent currents in the compartment, and  $g_s$  and  $g_d$  are the coupling conductances that depend on the relative sizes of dendritic and somatic compartments. One can obtain many spiking and bursting patterns by changing the conductances and keeping all the other parameters fixed (Pinsky and Rinzel 1994, Mainen and Sejnowski 1996).

Once we understand how to couple two compartments, we can do it for hundreds or thousands of compartments. GENESIS and NEURON simulation environments could be useful here, especially since they contain databases of dendritic trees reconstructed from real neurons.

Interestingly, the somatic-dendritic pair in Fig. 2.19c is equivalent to a pair of neurons in Fig. 2.19d coupled via *gap-junctions*. These are electrical contacts that allow ions and small molecules to pass freely between the cells. Gap junctions are often called electrical synapses, because they allow potentials to be conducted directly from one neuron to another.

Computational study of multi-compartment dendritic processing is outside of the scope of this book. We consider multi-compartment models of cortical pyramidal neurons in Chap. 8 and gap-junction coupled neurons in Chap. 10.

### 2.3.5 Summary of voltage-gated currents

Throughout this book we model kinetics of various voltage-sensitive currents using the Hodgkin-Huxley gate model

$$I = \bar{g} m^a h^b (V - E)$$

where

$I$	$(\mu\text{A}/\text{cm}^2)$	current
$V$	(mV)	membrane voltage
$E$	(mV)	reverse potential
$\bar{g}$	$(\text{mS}/\text{cm}^2)$	maximal conductance
$m$		probability of activation gate to be open
$h$		probability of inactivation gate to be open
$a$		the number of activation gates per channel
$b$		the number of inactivation gates per channel

The gating variables  $m$  and  $n$  satisfy linear first order differential equations (2.9) and (2.10), respectively. We approximate the steady-state activation curve  $m_\infty(V)$  by the

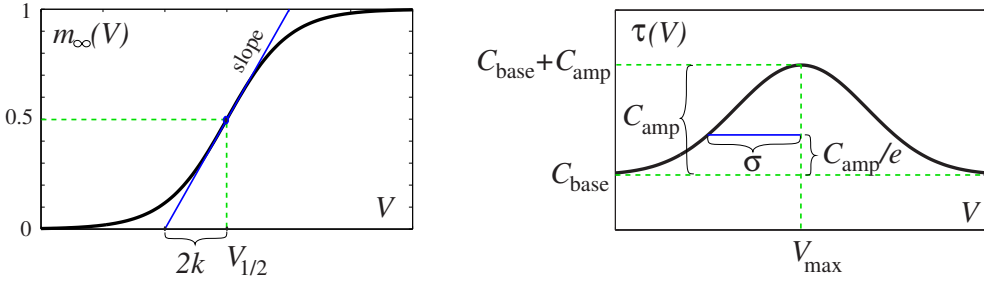


Figure 2.20: Boltzmann (2.11) and Gaussian (2.12) functions and geometrical interpretations of their parameters.

Boltzmann function depicted in Fig. 2.20,

$$m_\infty(V) = \frac{1}{1 + \exp \{(V_{1/2} - V)/k\}} \quad (2.11)$$

The parameter  $V_{1/2}$  satisfies  $m_\infty(V_{1/2}) = 0.5$ , and  $k$  is the slope factor (negative for inactivation curve  $h_\infty(V)$ ). Smaller values of  $|k|$  result in steeper  $m_\infty(V)$ .

The voltage-sensitive time constant  $\tau(V)$  can be approximated by the Gaussian function

$$\tau(V) = C_{\text{base}} + C_{\text{amp}} \exp \frac{-(V_{\max} - V)^2}{\sigma^2}, \quad (2.12)$$

see Fig. 2.20. The graph of the function is above  $C_{\text{base}}$  with amplitude  $C_{\text{amp}}$ . The maximal value is achieved at  $V_{\max}$ . The parameter  $\sigma$  measures the characteristic width of the graph, i.e.,  $\tau(V_{\max} \pm \sigma) = C_{\text{base}} + C_{\text{amp}}/e$ . The Gaussian description is often not adequate, so we substitute it by other functions whenever appropriate.

Below is the summary of voltage-gated currents whose kinetics were measured experimentally. The division into persistent and transient is somewhat artificial since most “persistent” currents can still inactivate after seconds of prolonged depolarization. Hyperpolarization-activated currents, such as the h-current or  $K^+$  inwardly rectifying current, are mathematically equivalent to currents that are always activated, but can be inactivated by depolarization. To avoid possible confusion we mark these currents as “opened by hyperpolarization”.

<b>Na<sup>+</sup> currents</b>	Parameters (Fig. 2.20)					
	Eq. 2.11		Eq. 2.12			
$V_{1/2}$	$k$	$V_{\max}$	$\sigma$	$C_{\text{amp}}$	$C_{\text{base}}$	
Fast transient <sup>1</sup>	$I_{\text{Na,t}} = \bar{g} m^3 h(V - E_{\text{Na}})$					
activation	-40	15	-38	30	0.46	0.04
inactivation	-62	-7	-67	20	7.4	1.2
Fast transient <sup>2</sup>	$I_{\text{Na,t}} = \bar{g} m_\infty(V)h(V - E_{\text{Na}})$					
activation	-30	5.5	-	-	-	-
inactivation	-70	-5.8	$\tau_h(V) = 3 \exp((-40 - V)/33)$			
Fast transient <sup>3</sup>	$I_{\text{Na,t}} = \bar{g} m_\infty(V)h(V - E_{\text{Na}})$					
activation	-28	6.7	-	-	-	-
inactivation	-66	-6	$\tau_h(V) = 4 \exp((-30 - V)/29)$			
Fast persistent <sup>4,a</sup>	$I_{\text{Na,p}} = \bar{g} m_\infty(V)h(V - E_{\text{Na}})$					
activation	-50	4	-	-	-	-
inactivation	-49	-10	-66	35	4.5 sec	2 sec
Fast persistent <sup>5,a</sup>	$I_{\text{Na,p}} = \bar{g} m_\infty(V)(0.14 + 0.86h)(V - E_{\text{Na}})$					
activation	-50	6	-	-	-	-
inactivation	-56	-7	$\tau_h(V) = 63.2 + 25 \exp(-V/25.5)$			
Fast persistent <sup>2</sup>	$I_{\text{Na,p}} = \bar{g} m(V - E_{\text{Na}})$					
activation	-54	9	-	-	-	0.8
Fast persistent <sup>6</sup>	$I_{\text{Na,p}} = \bar{g} m(V - E_{\text{Na}})$					
activation	-42	4	-	-	-	0.8

1. Squid giant axon (Hodgkin and Huxley 1954); see Ex. 4.
2. Thalamocortical neurons in rats (Parri and Crunelli 1999).
3. Thalamocortical neurons in cats (Parri and Crunelli 1999).
4. Layer-II principal neurons in entorhinal cortex (Magistretti and Alonso 1999).
5. Large dorsal root ganglion neurons in rats (Baker and Bostock 1997, 1998).
6. Purkinje cells (Kay et al. 1998).

a Very slow inactivation.

<b>K<sup>+</sup> currents</b>	Parameters (Fig. 2.20)					
	Eq. 2.11 V <sub>1/2</sub>	k	Eq. 2.12 V <sub>max</sub>	σ	C <sub>amp</sub>	C <sub>base</sub>
Delayed rectifier <sup>1</sup>	$I_K = \bar{g} n^4(V - E_K)$					
activation	-53	15	-79	50	4.7	1.1
Delayed rectifier <sup>2,4</sup>	$I_K = \bar{g} mh(V - E_K)$					
activation	-3	10	-50	30	47	5
inactivation	-51	-12	-50	50	1000	360
M current <sup>3</sup>	$I_{K(M)} = \bar{g} m(V - E_K)$					
activation	-44	8	-50	25	320	20
Transient <sup>4</sup>	$I_A = \bar{g} mh(V - E_K)$					
activation	-3	20	-71	60	0.92	0.34
inactivation	-66	-10	-73	23	50	8
Transient <sup>5</sup>	$I_A = \bar{g} mh(V - E_K)$					
activation	-26	20	-	-	-	-
inactivation	-72	-9.6	-	-	-	15.5
Transient <sup>6</sup>	$I_A = \bar{g} m^4 h(V - E_K)$					
Fast component (60% of total conductance)						
activation	-60	8.5	-58	25	2	0.37
inactivation	-78	-6	-78	25	45	19
Slow component (40% of total conductance)						
activation	-36	20	-58	25	2	0.37
inactivation	-78	-6	-78	25	45	19
	$\tau_h(V) = 60 \text{ when } V > -73$					
Inward rectifier <sup>7</sup>	$I_{Kir} = \bar{g} h_\infty(V)(V - E_K)$					
(opened by hyperpolarization)						
inactivation	-80	-12	-	-	-	< 1

1. Squid giant axon (Hodgkin and Huxley 1954); see Ex. 4.
2. Neocortical pyramidal neurons (Bekkers 2000).
3. Rodent neuroblastoma-glioma hybrid cells (Robbins et al. 1992).
4. Neocortical pyramidal neurons (Korngreen and Sakmann 2000).
5. Hippocampal mossy fiber boutons (Geiger and Jonas 2000).
6. Thalamic relay neurons (Huguenard and McCormick 1992).
7. Horizontal cells in catfish retina (Dong and Werblin 1995); AP cell of leech (Wessel et al. 1999); rat locus coeruleus neurons (Williams et al. 1988,  $V_{1/2} = E_K$ ).

Cation currents	Parameters (Fig. 2.20)						
	Eq. 2.11		Eq. 2.12				
	$V_{1/2}$	$k$	$V_{max}$	$\sigma$	$C_{amp}$	$C_{base}$	
$I_h$ current <sup>1</sup> (opened by hyperpolarization)				$E_h = -43$ mV			
inactivation	-75	-5.5	-75	15	1000	100	
$I_h$ current <sup>2</sup>				$E_h = -1$ mV			
inact. (soma)	-82	-9	-75	20	50	10	
inact. (dendrite)	-90	-8.5	-75	20	40	10	
$I_h$ current <sup>3</sup>				$E_h = -21$ mV			
fast inact. (65%)	-67	-12	-75	30	50	20	
slow inact. (35%)	-58	-9	-65	30	300	100	

1. Thalamic relay neurons (McCormick and Pape 1990; Huguenard and McCormick 1992).
2. Hippocampal pyramidal neurons in CA1 (Magee 1998).
3. Entorhinal cortex Layer II neurons (Dickson et al. 2000).

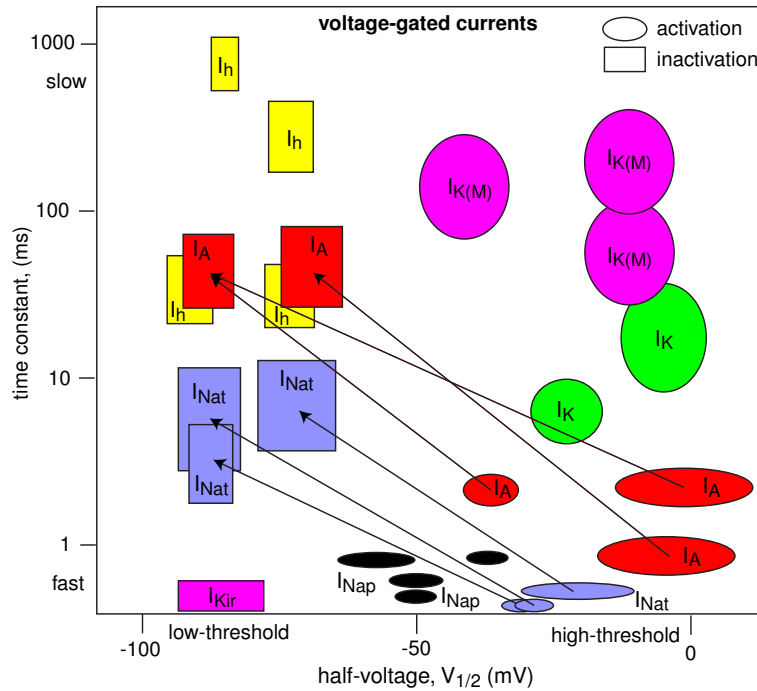


Figure 2.21: Summary of current kinetics. Each oval (rectangle) denotes the voltage and temporal scale of activation (inactivation) of a current. Transient currents are represented by arrows connecting ovals and rectangles.



Figure 2.22: Alan Hodgkin (right) and Andrew Huxley (left) in their Plymouth Marine Lab in 1949 (photo was kindly provided by National Marine Biological Library, Plymouth, UK).

## Review of Important Concepts

- Electrical signals in neurons are carried by  $\text{Na}^+$ ,  $\text{Ca}^{2+}$ ,  $\text{K}^+$ , and  $\text{Cl}^-$  ions, which move through membrane channels according to their electrochemical gradients.
- The membrane potential  $V$  is determined by the membrane conductances  $g_i$  and corresponding reversal potentials  $E_i$ :

$$C \dot{V} = I - \sum_i g_i \cdot (V - E_i) .$$

- Neurons are excitable because the conductances depend on the membrane potential and time.
- The most accepted description of kinetics of voltage-sensitive conductances is the Hodgkin-Huxley gate model.
- Voltage-gated activation of inward  $\text{Na}^+$  or  $\text{Ca}^{2+}$  current depolarizes (increases) the membrane potential.
- Voltage-gated activation of outward  $\text{K}^+$  or  $\text{Cl}^-$  current hyperpolarizes (decreases) the membrane potential.
- An action potential or spike is a brief regenerative depolarization of the membrane potential followed by its repolarization and possibly hyperpolarization, as in Fig. 2.16.

## Bibliographical Notes

Our summary of the membrane electrophysiology is limited: We present only those concepts that are necessary to understand the Hodgkin-Huxley description of generation of action potentials. We have omitted such important topics as Goldman-Hodgkin-Katz equation, cable theory, dendritic and synaptic function, etc., although some of those will be introduced later in the book.

The standard textbook on membrane electrophysiology is the second edition of *Ion Channels of Excitable Membranes* by B. Hille (2001). An excellent introductory textbook with an emphasis on the quantitative approach is *Foundations of Cellular Neurophysiology* by D. Johnston and S. Wu (1995). A detailed introduction into mathematical aspects of cellular biophysics can be found in *Mathematical Physiology* by J. Keener and J. Sneyd (1998). The latter two books complement rather than repeat each other. *Biophysics of Computation* by Koch (1999) and Chapters 5 and 6 of *Theoretical Neuroscience* by Dayan and Abbott (2001) provide a good introduction into biophysics of excitable membranes.

The first book devoted exclusively to dendrites is *Dendrites* by Stuart et al. (1999). It emphasizes the active nature of dendritic dynamics. Arshavsky et al. (1971; Russian language edition - 1969) make the first and probably still the best theoretical attempt to understand the neuro-computational properties of branching dendritic trees endowed with voltage-gated channels and capable of generating action potentials. Had they published their results in the 90s, they would have been considered classics in the field; Unfortunately, the computational neuroscience community of the 70s was not ready to accept the “heretic” idea that dendrites can fire spikes, that spikes can propagate back and forward along the dendritic tree, that EPSPs can be scaled-up with distance, that individual dendritic branches can perform coincidence detection and branching points can perform non-linear summation, and that different and independent computations can be carried out at different parts of the neuronal dendritic tree. We touch some of these issues in Chap. 8.

## Exercises

1. Determine Nernst equilibrium potentials for the membrane of the squid giant axon using the following data

	Inside (mM)	Outside (mM)
K <sup>+</sup>	430	20
Na <sup>+</sup>	50	440
Cl <sup>-</sup>	65	560

and  $T = 20^\circ\text{C}$ .

2. Show that a non-selective cation current

$$I = \bar{g}_{\text{Na}} p (V - E_{\text{Na}}) + \bar{g}_{\text{K}} p (V - E_{\text{K}})$$

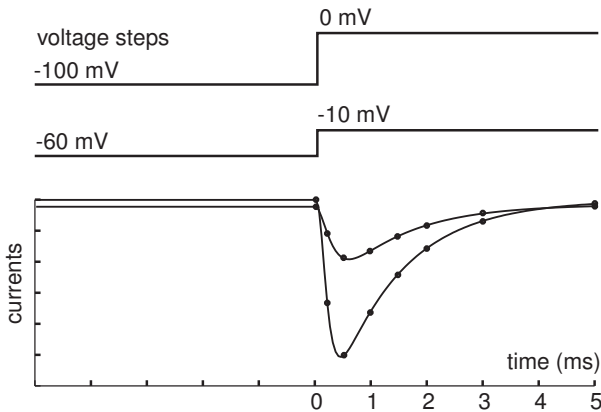


Figure 2.23: Current traces corresponding to voltage steps of various amplitudes; see Ex. 6.

can be written in the form (2.7) with

$$\bar{g} = \bar{g}_{\text{Na}} + \bar{g}_{\text{K}} \quad \text{and} \quad E = \frac{\bar{g}_{\text{Na}}E_{\text{Na}} + \bar{g}_{\text{K}}E_{\text{K}}}{\bar{g}_{\text{Na}} + \bar{g}_{\text{K}}}.$$

3. Show that applying a dc-current  $I$  in the neuronal model

$$C\dot{V} = I - g_{\text{L}}(V - E_{\text{L}}) - I_{\text{other}}(V)$$

is equivalent to changing the leak reverse potential  $E_{\text{L}}$ .

4. Steady-state (in)activation curves and voltage-sensitive time constants can be approximated by the Boltzmann (2.11) and Gaussian (2.12) functions, respectively, depicted in Fig. 2.20. Explain the meaning of the parameters  $V_{1/2}$ ,  $k$ ,  $C_{\text{base}}$ ,  $C_{\text{amp}}$ ,  $V_{\text{max}}$  and  $\sigma$  and find their values that provide satisfactory fit near the rest state  $V = 0$  to the Hodgkin-Huxley functions depicted in Fig. 2.13.
5. (Willms et al. 1999) Consider the curve  $m_{\infty}^p(V)$ , where  $m_{\infty}(V)$  is the Boltzmann function with parameters  $V_{1/2}$  and  $k$ , and  $p > 1$ . This curve can be approximated by another Boltzmann function with some parameters  $\tilde{V}_{1/2}$  and  $\tilde{k}$  (and  $p = 1$ ). Find the formulae that relate  $\tilde{V}_{1/2}$  and  $\tilde{k}$  to  $V_{1/2}$ ,  $k$ , and  $p$ .
6. (Willms et al. 1999) Write a MATLAB program that determines activation and inactivation parameters via a simultaneous fitting of current traces from a voltage-clamp experiment similar to the one in Fig. 2.23. Assume that the values of the voltage pairs, e.g.,  $-60, -10; -100, 0$  (mV); are in the file `v.dat`. The values of the current (circles in Fig. 2.23) are in the file `current.dat`, and the sampling times, e.g.,  $0, 0.25, 0.5, 1, 1.5, 2, 3, 5$  (ms), are in the file `times.dat`.
7. Modify the MATLAB program from the previous exercise to handle multi-step (Fig. 2.24) and ramp protocols.
8. [M.S.] Find the best sequence of step potentials that can determine activation and inactivation parameters (a) in the shortest time, (b) with the highest precision.

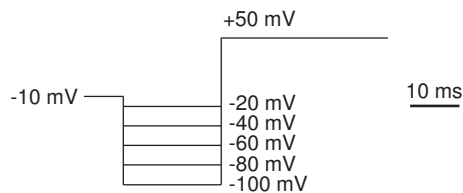


Figure 2.24: Multiple voltage steps are often needed to determine time constants of inactivation; see Ex. 7.

9. [M.S.] Modify the MATLAB program from Ex. 6 to handle multiple currents.
10. [M.S.] Add a PDE solver to the MATLAB program from exercise 6 to simulate poor space and voltage clamp conditions.
11. [Ph.D.] Introduce numerical optimization into the dynamic clamp protocol to analyze experimentally in real time the (in)activation parameters of membrane currents.
12. [Ph.D.] Use new classification of families of channels (Kv3,1, Na<sub>v</sub>1.2, etc. see Hille 2001), determine the kinetics of each subgroup, and provide a complete table similar to those in Sect. 2.3.5.



# Chapter 3

## One-Dimensional Systems

In this chapter we describe geometrical methods of analysis of one-dimensional dynamical systems, i.e., systems having only one variable. An example of such a system is the space-clamped membrane having Ohmic leak current  $I_L$

$$C \dot{V} = -g_L(V - E_L) . \quad (3.1)$$

Here the membrane voltage  $V$  is a time-dependent variable, and the capacitance  $C$ , leak conductance  $g_L$  and leak reverse potential  $E_L$  are constant parameters described in the previous chapter. We use this and other one-dimensional neural models to introduce and illustrate the most important concepts of dynamical system theory: equilibrium, stability, attractor, phase portrait, and bifurcation.

### 3.1 Electrophysiological Examples

The Hodgkin-Huxley description of dynamics of membrane potential and voltage-gated conductances can be reduced to a one-dimensional system when all transmembrane conductances have fast kinetics. For the sake of illustration, let us consider a space-clamped membrane having leak current and a fast voltage-gated current  $I_{\text{fast}}$  having only one gating variable  $p$ ,

$$C \dot{V} = -\overbrace{g_L(V - E_L)}^{\text{Leak } I_L} - \overbrace{g p(V - E)}^{I_{\text{fast}}} \quad (3.2)$$

$$\dot{p} = (p_\infty(V) - p)/\tau(V) \quad (3.3)$$

with dimensionless parameters  $C = 1$ ,  $g_L = 1$ , and  $g = 1$ . Suppose that the gating kinetics (3.3) is much faster than the voltage kinetics (3.2), which means that the voltage-sensitive time constant  $\tau(V)$  is very small, i.e.  $\tau(V) \ll 1$ , in the entire biophysical voltage range. Then, the gating process may be treated as being instantaneous, and the asymptotic value  $p = p_\infty(V)$  may be used in the voltage equation (3.2) to

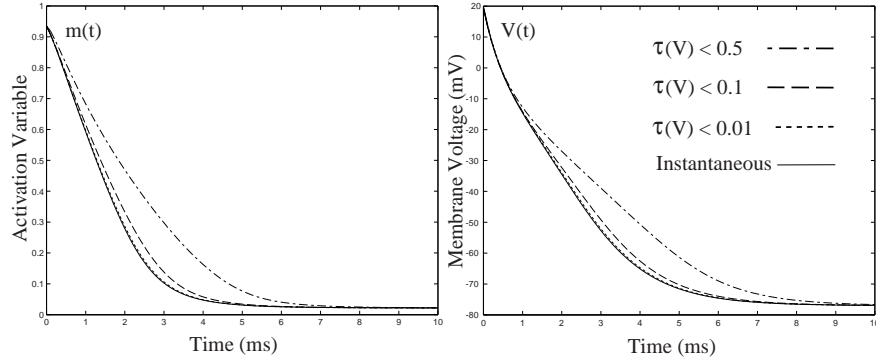


Figure 3.1: Solution of the full system (3.2, 3.3) converges to that of the reduced one-dimensional system (3.4) as  $\tau(V) \rightarrow 0$

reduce the two-dimensional system (3.2, 3.3) to a one-dimensional equation

$$C \dot{V} = -g_L(V - E_L) - \overbrace{g p_\infty(V) (V - E)}^{\text{instantaneous } I_{\text{fast}}} . \quad (3.4)$$

This reduction introduces a small error of the order  $\tau(V) \ll 1$ , as one can see in Fig. 3.1.

Since the hypothetical current  $I_{\text{fast}}$  can be either inward ( $E > E_L$ ) or outward ( $E < E_L$ ), and the gating process can be either activation ( $p$  is  $m$ , as in the Hodgkin-Huxley model) or inactivation ( $p$  is  $h$ ), there are four fundamentally different choices for  $I_{\text{fast}}(V)$ , which we summarize in Fig. 3.2 and elaborate on below.

		Current	
		inward	outward
Gating	activation	$I_{\text{Na},p}$	$I_K$
	inactivation	$I_h$	$I_{\text{Kir}}$

Figure 3.2: Four fundamental examples of voltage-gated currents with one gating variable. In this book we treat “hyperpolarization-activated” currents  $I_h$  and  $I_{\text{Kir}}$  as being inactivating currents, which are turned off (inactivated via  $h$ ) by depolarization and turned on (deinactivated) by hyperpolarization; see discussion in Sect. 2.2.4.

### 3.1.1 I-V relations and dynamics

The four choices in Fig. 3.2 result in four simple one-dimensional models of the form (3.4):

$$I_{\text{Na},p}\text{-model}, \quad I_K\text{-model}, \quad I_h\text{-model}, \quad \text{and} \quad I_{\text{Kir}}\text{-model}.$$

These models might seem too simple to biologists, who can easily understand their behavior just by looking at the I-V relations of the currents depicted in Fig. 3.3 without

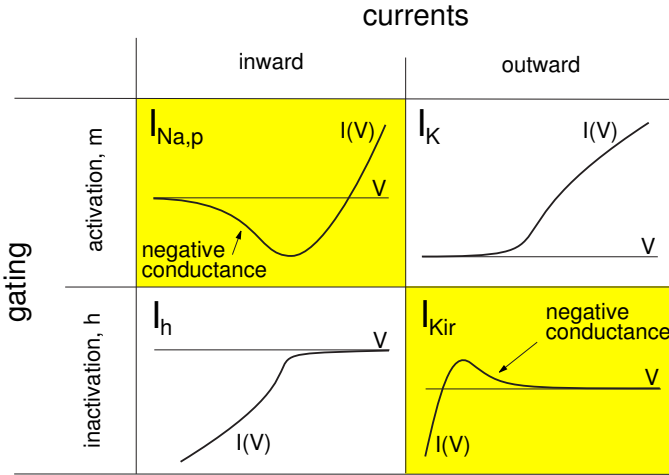


Figure 3.3: Typical current-voltage (I-V) relations of the four currents considered in this chapter. Shaded boxes correspond to non-monotonic I-V relations having a region of negative conductance ( $I'(V) < 0$ ) in the biophysically relevant voltage range.

using any dynamical systems theory. The models might also appear too simple to mathematicians, who can easily understand their dynamics just by looking at the graphs of the right-hand side of (3.4) without using any electrophysiological intuition. In fact, the models provide an invaluable learning tool, since they establish a bridge between electrophysiology and dynamical systems.

In Fig. 3.3 we plot typical steady-state current-voltage (I-V) relations of the four currents considered above. Notice that the I-V curve is non-monotonic for  $I_{Na,p}$  and  $I_{Kir}$  but monotonic for  $I_K$  and  $I_h$ , at least in the biophysically relevant voltage range. This subtle difference is an indication of the fundamentally different roles these currents play in neuron dynamics: The I-V relation in the first group has a region of “negative conductance”, i.e.,  $I'(V) < 0$ , which creates positive feedback between the voltage and the gating variable (Fig. 3.4), and plays an amplifying role in neuron dynamics. We refer to such currents as *amplifying currents*. In contrast, the currents in the second group have negative feedback between voltage and gating variable, and they often result in damped oscillation of the membrane potential, as we show in the next chapter. We refer to such currents as *resonant currents*. Most neural models involve a combination of at least one amplifying and one resonant current, as we discuss in Chap. 5. The way these currents are combined determines whether the neuron is an *integrator* or a *resonator*.

### 3.1.2 Leak + instantaneous $I_{Na,p}$

To ease our introduction into dynamical systems, we will use the  $I_{Na,p}$ -model

$$C \dot{V} = I - g_L(V - E_L) - \overbrace{g_{Na} m_\infty(V) (V - E_{Na})}^{\text{instantaneous } I_{Na,p}} \quad (3.5)$$

with

$$m_\infty(V) = 1/(1 + \exp \{(V_{1/2} - V)/k\})$$

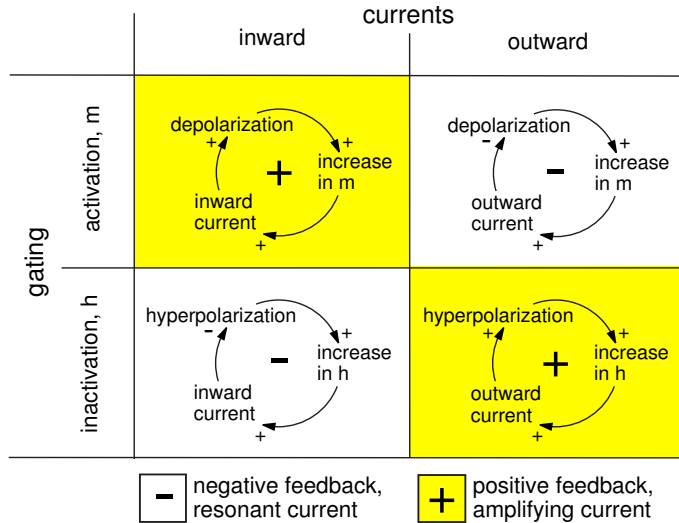


Figure 3.4: Feedback loops between voltage and gating variables in the four models presented above; see also Fig. 5.2.

throughout the rest of this chapter. (Some biologists refer to transient  $\text{Na}^+$  currents with very slow inactivation as being persistent, since the current does not change much on the time scale of 1 sec.) We obtain the experimental parameter values

$$C = 10 \mu\text{F}, \quad I = 0 \text{ pA}, \quad g_L = 19 \text{ mS}, \quad E_L = -67 \text{ mV}, \\ g_{\text{Na}} = 74 \text{ mS}, \quad V_{1/2} = 1.5 \text{ mV}, \quad k = 16 \text{ mV}, \quad E_{\text{Na}} = 60 \text{ mV}$$

using whole-cell patch clamp recordings of a layer 5 pyramidal neuron in the visual cortex of a rat at room temperature. We prove in Ex. 3.3.8 and illustrate in Fig. 3.15 that the model approximates the action potential upstroke dynamics of this neuron.

The model's I-V relation,  $I(V)$ , is depicted in Fig. 3.5a. Due to the negative conductance region in the I-V curve, this one-dimensional model can exhibit a number of interesting non-linear phenomena, such as bistability, i.e. co-existence of resting and excited states. From a mathematical point of view, bistability occurs because the right-hand side function in the differential equation (3.5), depicted in Fig. 3.5b, is not monotonic. In Fig. 3.6 we depict typical voltage time courses of the model (3.5) with two values of injected dc-current  $I$  and 16 different initial conditions. The qualitative behavior in Fig. 3.6a is clearly bistable: depending on the initial condition, the trajectory of the membrane potential goes either up to the excited state or down to the resting state. In contrast, the behavior in Fig. 3.6b is monostable, since the resting state does not exist. The goal of the dynamical system theory reviewed in this chapter is to understand why and how the behavior depends on the initial conditions and the parameters of the system.

## 3.2 Dynamical Systems

In general, dynamical systems can be continuous or discrete, depending on whether they are described by differential or difference equations. Continuous one-dimensional

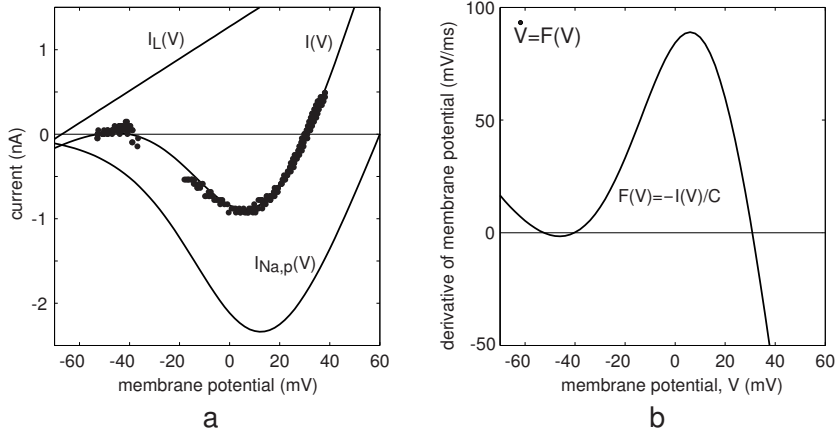


Figure 3.5: *a.* I-V relations of the leak current,  $I_L$ , fast  $\text{Na}^+$  current,  $I_{\text{Na}}$ , and combined current  $I(V) = I_L(V) + I_{\text{Na}}(V)$  in the  $I_{\text{Na},p}$ -model (3.5). Dots denote  $I_0(V)$  data from layer 5 pyramidal cell in rat visual cortex. *b.* The right-hand side of the  $I_{\text{Na},p}$ -model (3.5).

dynamical systems are usually written in the form

$$\dot{V} = F(V), \quad V(0) = V_0 \in \mathbb{R}, \quad (3.6)$$

for example,

$$\dot{V} = -80 - V, \quad V(0) = -20,$$

where  $V$  is a scalar time-dependent variable denoting the current state of the system,  $\dot{V} = V_t = dV/dt$  is its derivative with respect to time  $t$ ,  $F$  is a scalar function (its output is one-dimensional) that determines the evolution of the system, e.g., the right-hand side of (3.5) divided by  $C$ ; see Fig. 3.5b.  $V_0 \in \mathbb{R}$  is an initial condition, and  $\mathbb{R}$  is the real line, i.e., a line of real numbers ( $\mathbb{R}^n$  would be the  $n$ -dimensional real space).

In the context of dynamical systems, the real line  $\mathbb{R}$  is called *phase line* or *state line* (phase space or state space for  $\mathbb{R}^n$ ) to stress the fact that each point in  $\mathbb{R}$  corresponds to a certain, possibly inadmissible state of the system, and each state of the system corresponds to a certain point in  $\mathbb{R}$ . For example, the state of the Ohmic membrane (3.1) is just its membrane potential  $V \in \mathbb{R}$ . The state of the Hodgkin-Huxley model (see Sect. 2.3) is the four-dimensional vector  $(V, m, n, h) \in \mathbb{R}^4$ . The state of the  $I_{\text{Na},p}$ -model (3.5) is again its membrane potential  $V \in \mathbb{R}$ , because the value  $m = m_\infty(V)$  is unequivocally defined by  $V$ .

When all parameters are constant, the dynamical system is called *autonomous*. When at least one of the parameters is time-dependent, the system is non-autonomous, denoted as  $\dot{V} = F(V, t)$ .

To solve (3.6) means to find a function  $V(t)$  whose initial value is  $V(0) = V_0$  and whose derivative is  $F(V(t))$  at each moment  $t \geq 0$ . For example, the function  $V(t) = V_0 + at$  is an explicit analytical solution to the dynamical system  $\dot{V} = a$ . The exponentially decaying function  $V(t) = E_L + (V_0 - E_L)e^{-g_L t/C}$  depicted in Fig. 3.7,

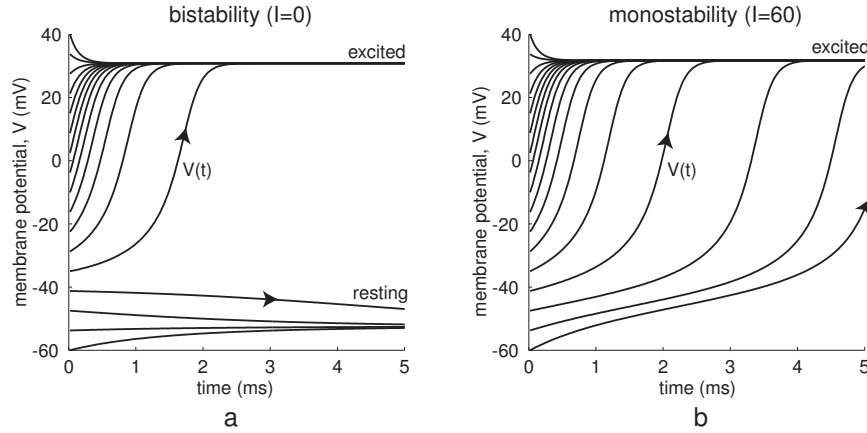


Figure 3.6: Typical voltage trajectories of the  $I_{Na,p}$ -model (3.5) having different values of  $I$ .

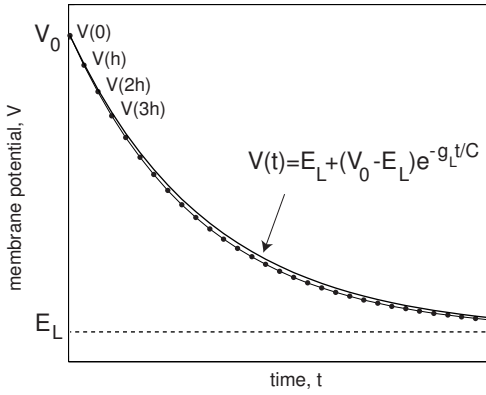


Figure 3.7: Explicit analytical solution ( $V(t) = E_L + (V_0 - E_L)e^{-g_L t/C}$ ) of the linear equation (3.1) and corresponding numerical approximation (dots) using Euler's method (3.7).

solid curve, is an explicit analytical solution to the linear equation (3.1) (check by differentiating).

Finding explicit solutions is often impossible even for such simple systems as (3.5), so quantitative analysis is carried out mostly via numerical simulations. The simplest procedure to solve (3.6) numerically, known as first-order *Euler method*, replaces (3.6) by the discretized system

$$[V(t+h) - V(t)]/h = F(V(t))$$

where  $t = 0, h, 2h, 3h, \dots$ , is the discrete time and  $h$  is a small time step. Knowing the current state  $V(t)$ , we can find the next state point via

$$V(t+h) = V(t) + hF(V(t)) . \quad (3.7)$$

Iterating this *difference* equation starting with  $V(0) = V_0$ , we can approximate the

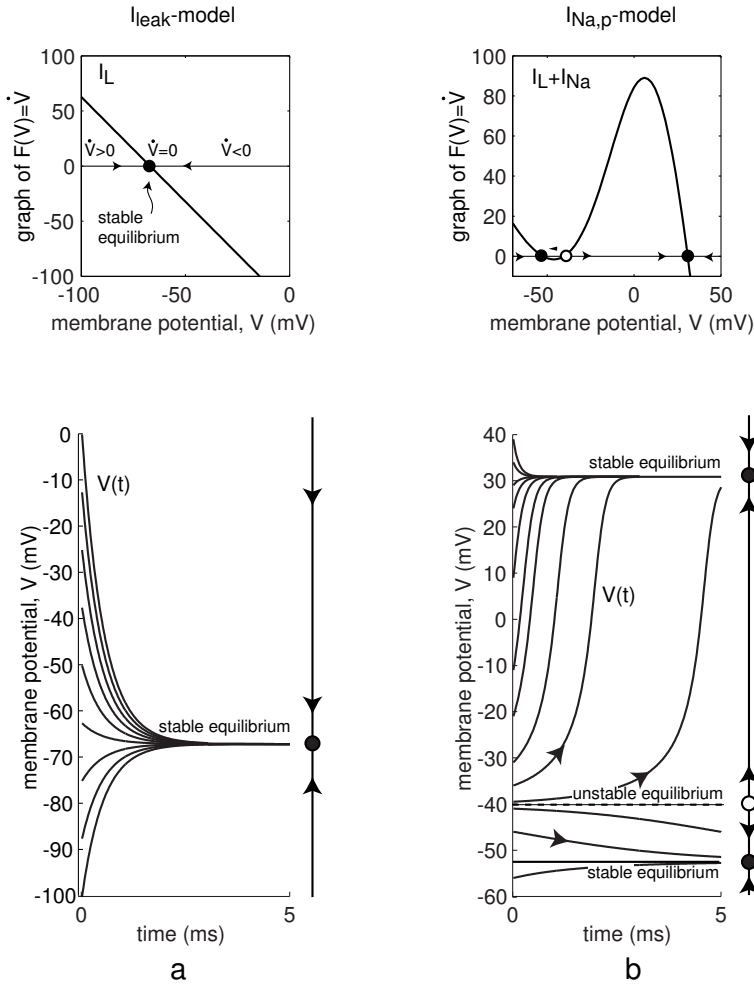


Figure 3.8: Graphs of the right-hand side functions of equations (3.1) and (3.5) and corresponding numerical solutions starting from various initial conditions.

analytical solution of (3.6), see the dots in Fig. 3.7. The approximation has a noticeable error of order  $h$ , so scientific software packages, such as MATLAB, use more sophisticated high-precision numerical methods.

In many cases, however, we do not need exact solutions, but rather qualitative understanding of the behavior of (3.6) and how it depends on parameters and the initial state  $V_0$ . For example, we might be interested in the number of equilibria (rest) points the system could have, whether the equilibria are stable, their attraction domains, etc.

### 3.2.1 Geometrical analysis

The first step in the qualitative geometrical analysis of any one-dimensional dynamical system is to plot the graph of the function  $F$ , as we do in Fig. 3.8,top. Since  $F(V) = \dot{V}$ ,

at every point  $V$  where  $F(V)$  is negative, the derivative  $\dot{V}$  is negative, and hence the state variable  $V$  decreases. In contrast, at every point where  $F(V)$  is positive,  $\dot{V}$  is positive, and the state variable  $V$  increases; the greater the value of  $F(V)$ , the faster  $V$  increases. Thus, the direction of movement of the state variable  $V$ , and hence the evolution of the dynamical system, is determined by the sign of the function  $F(V)$ .

The right-hand side of the  $I_{\text{leak}}$ -model (3.1) or the  $I_{\text{Na,p}}$ -model (3.5) in Fig. 3.8 is the steady-state current-voltage (I-V) relation,  $I_L(V)$  or  $I_L(V) + I_{\text{Na,p}}(V)$  respectively, taken with the minus sign, see Fig. 3.5. Positive values of the right-hand side  $F(V)$  mean negative I-V, corresponding to a net inward current that depolarizes the membrane. Conversely, negative values mean positive I-V, corresponding to a net outward current that hyperpolarizes the membrane.

### 3.2.2 Equilibria

The next step in the qualitative analysis of any dynamical system is to find its *equilibria* or *rest points*, i.e., the values of the state variable where

$$F(V) = 0 \quad (V \text{ is an equilibrium}).$$

At each such point  $\dot{V} = 0$ , the state variable  $V$  does not change. In the context of membrane potential dynamics, equilibria correspond to the points where the steady-state I-V curve passes zero. At each such point there is a balance of the inward and outward currents so that the net transmembrane current is zero, and the membrane voltage does not change. (Incidentally, the part *libra* in the Latin word *aequilibrium* means balance).

The  $I_K$ - and  $I_h$ -models mentioned in Sect. 3.1 can have only one equilibrium because their I-V relations  $I(V)$  are monotonic increasing functions. The corresponding functions  $F(V)$  are monotonic decreasing and can have only one zero.

In contrast, the  $I_{\text{Na,p}}$ - and  $I_{\text{Kir}}$ -models can have many equilibria because their I-V curves are not monotonic, and hence there is a possibility for multiple intersections with the  $V$ -axis. For example, there are three equilibria in Fig. 3.8b corresponding to the rest state (around  $-53$  mV), threshold state (around  $-40$  mV) and the excited state (around  $30$  mV). Each equilibrium corresponds to the balance of the outward leak current and partially (rest), moderately (threshold) or fully (excited) activated persistent  $\text{Na}^+$  inward current. Throughout this book we denote equilibria as small open or filled circles depending on their stability, as in Fig. 3.8.

### 3.2.3 Stability

If the initial value of the state variable is exactly at equilibrium, then  $\dot{V} = 0$  and the variable will stay there forever. If the initial value is near the equilibrium, the state variable may approach the equilibrium or diverge from it. Both cases are depicted in Fig. 3.8. We say that an equilibrium is *asymptotically stable* if all solutions starting sufficiently near the equilibrium will approach it as  $t \rightarrow \infty$ .

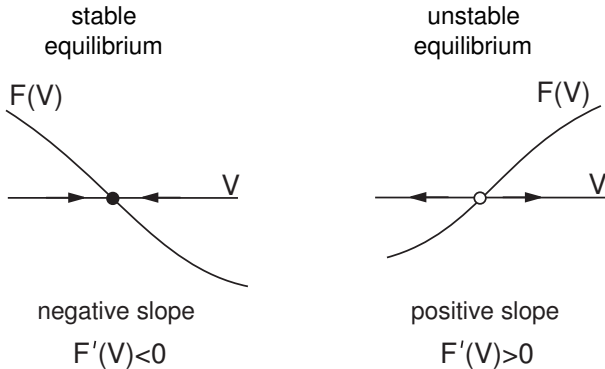


Figure 3.9: The sign of the slope,  $\lambda = F'(V)$ , determines the stability of the equilibrium.

Stability of an equilibrium is determined by the signs of the function  $F$  around it. The equilibrium is stable when  $F(V)$  changes the sign from “+” to “-” as  $V$  increases, as in Fig. 3.8a. Obviously, all solutions starting near such an equilibrium converge to it. Such an equilibrium “attracts” all nearby solutions, and it is called an *attractor*. A stable equilibrium point is the only type of attractor that can exist in one-dimensional continuous dynamical systems defined on a state line  $\mathbb{R}$ . Multidimensional systems can have other attractors, e.g., limit cycles.

The differences between stable, asymptotically stable, and exponentially stable equilibria are discussed in Ex. 18 in the end of the chapter. The reader is also encouraged to solve Ex. 4 (piece-wise continuous  $F(V)$ ).

### 3.2.4 Eigenvalues

A sufficient condition for an equilibrium to be stable is that the derivative of the function  $F$  with respect to  $V$  at the equilibrium is negative, provided that the function is differentiable. We denote this derivative here by the Greek letter

$$\lambda = F'(V), \quad (V \text{ is an equilibrium; that is, } F(V) = 0)$$

and note that it is just the slope of graph of  $F$  at the point  $V$ ; see Fig. 3.9. Obviously, when the slope,  $\lambda$ , is negative, the function changes the sign from “+” to “-”, and the equilibrium is stable. Positive slope  $\lambda$  implies instability. The parameter  $\lambda$  defined above is the simplest example of an *eigenvalue* of an equilibrium. We introduce eigenvalues formally in the next chapter and show that eigenvalues play an important role in defining the types of equilibria of multi-dimensional systems.

### 3.2.5 Unstable equilibria

If a one-dimensional system has two stable equilibrium points, then they must be separated by at least one unstable equilibrium point, as we illustrate in Fig. 3.10. (This may not be true in multidimensional systems.) Indeed, a continuous function  $F$  has to change the sign from “-” to “+” somewhere in between those equilibria; that is, it has to cross the  $V$  axis in some point, as in Fig. 3.8b. This point would be

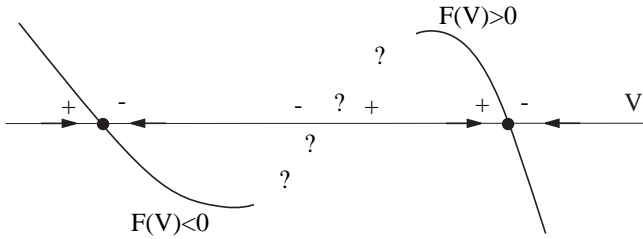


Figure 3.10: Two stable equilibrium points must be separated by at least one unstable equilibrium point because  $F(V)$  has to change the sign from “ $-$ ” to “ $+$ ”.

an unstable equilibrium, since all nearby solutions diverge from it. In the context of neuronal models, unstable equilibria correspond to the region of the steady-state I-V curve with negative conductance. (Please, check that this is in accordance with the fact that  $F(V) = -I(V)/C$ ; see Fig. 3.5.) An unstable equilibrium is sometimes called a *repeller*. Attractors and repellers have a simple mechanistic interpretation depicted in Fig. 3.11.

If the initial condition  $V_0$  is set to an unstable equilibrium point, then the solution will stay at this unstable equilibrium; i.e.,  $V(t) = V_0$  for all  $t$ , at least in theory. In practice, the location of an equilibrium point is known only approximately. In addition, small noisy perturbations that are always present in biological systems can make  $V(t)$  deviate slightly from the equilibrium point. Because of instability, such deviations will grow, and the state variable  $V(t)$  will eventually diverge from the repelling equilibrium the same way as the ball set at the top of the hill in Fig. 3.11 will eventually roll downhill. If the level of noise is low, it could take a long time to diverge from the repeller.

### 3.2.6 Attraction domain

Even though unstable equilibria are hard to see experimentally, they still play an important role in dynamics, since they separate attraction domains. Indeed, the ball in Fig. 3.11 could go left or right depending on what side of the hilltop it is on initially. Similarly, the state variable of a one-dimensional system decreases or increases depending on what side of the unstable equilibrium the initial condition is, as one can clearly see in Fig. 3.8b.

In general, the *basin of attraction* or *attraction domain* of an attractor is the set of all initial conditions that lead to the attractor. For example, the attraction domain of the equilibrium in Fig. 3.8a is the entire voltage range. Such an attractor is called *global*. In Fig. 3.12 we plot attraction domains of two stable equilibria. The middle unstable equilibrium is always the boundary of the attraction domains.

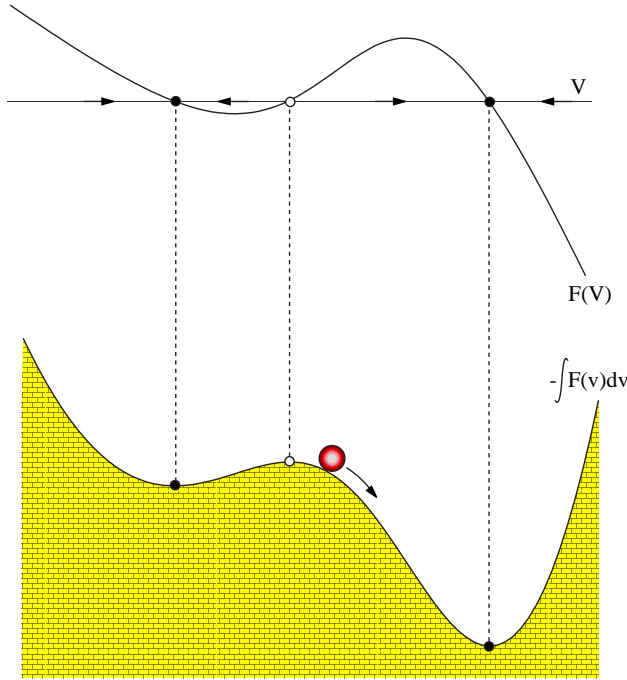


Figure 3.11: Mechanistic interpretation of stable and unstable equilibria. A massless (inertia free) ball moves toward energy minima with the speed proportional to the slope. A one-dimensional system  $\dot{V} = F(V)$  has the energy landscape  $E(V) = - \int_{-\infty}^V F(v) dv$ ; see Ex. 17. Zeros of  $F(V)$  with negative (positive) slope correspond to minima (maxima) of  $E(V)$ .

### 3.2.7 Threshold and action potential

Unstable equilibria play the role of thresholds in one-dimensional bistable systems, i.e., in systems having two attractors. We illustrate this in Fig. 3.13, which is believed to describe the essence of the mechanism of bistability in many neurons. Suppose the state variable is initially at the stable equilibrium point marked as “state A” in the figure, and suppose that perturbations can kick it around the equilibrium. Small perturbations may not kick it over the unstable equilibrium so that the state variable continues to be in the attraction domain of “state A”. We refer to such perturbations as being *subthreshold*. In contrast, we refer to perturbations as being *superthreshold* (also known as *suprathreshold*) if they are large enough to push the state variable over the unstable equilibrium so that it becomes attracted to the “state B”. We see that the unstable equilibrium acts as a threshold that separates two states.

The transition between two stable states separated by a threshold is relevant to the mechanism of excitability and generation of action potentials in many neurons, which we illustrate in Fig. 3.14. In the  $I_{\text{Na,p}}$ -model (3.5) with the I-V relation in Fig. 3.5 the existence of the rest state is largely due to the leak current  $I_L$ , while the existence of the excited state is largely due to the persistent inward  $\text{Na}^+$  current  $I_{\text{Na,p}}$ . Small

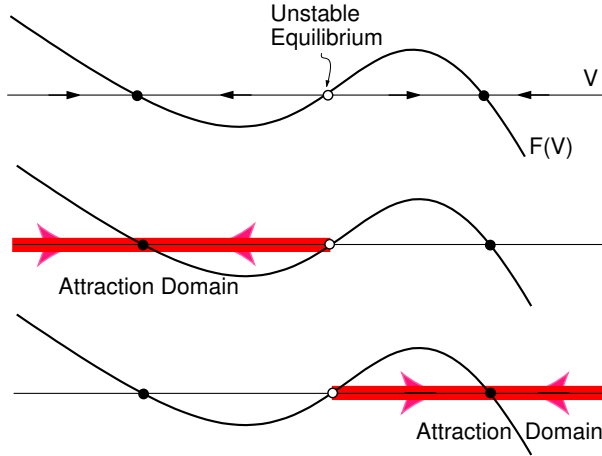


Figure 3.12: Two attraction domains in a one-dimensional system are separated by the unstable equilibrium.

(subthreshold) perturbations leave the state variable in the attraction domain of the rest state, while large (superthreshold) perturbations initiate the regenerative process — the upstroke of an action potential, and the voltage variable becomes attracted to the excited state. Generation of the action potential must be completed via repolarization, which moves  $V$  back to the rest state. Typically, repolarization occurs because of a relatively slow inactivation of  $\text{Na}^+$  current and/or slow activation of an outward  $\text{K}^+$  current, which are not taken into account in the one-dimensional system (3.5). To account for such processes, we consider two-dimensional systems in the next chapter.

Recall that the parameters of the  $I_{\text{Na},p}$ -model (3.5) were obtained from a cortical pyramidal neuron. In Fig. 3.15, left, we stimulate (*in vitro*) the cortical neuron by short (0.1 ms) strong pulses of current to reset its membrane potential to various initial values and interpret the results using the  $I_{\text{Na},p}$ -model. Since activation of  $\text{Na}^+$  current is not instantaneous in real neurons, we allow variable  $m$  to converge to  $m_\infty(V)$ , and ignore the 0.3-ms transient activity that follows each pulse. We also ignore the initial segment of the downstroke of the action potential, and plot the magnification of the voltage traces in Fig. 3.15, right. Comparing this figure with Fig. 3.8b, we see that the  $I_{\text{Na},p}$ -model is a reasonable one-dimensional approximation of the action potential upstroke dynamics; It predicts the value of the resting ( $-53$  mV), instantaneous threshold ( $-40$  mV), and the excited ( $+30$  mV) states of the cortical neuron.

### 3.2.8 Bistability and hysteresis

Systems having two (many) co-existing attractors are called *bistable* (*multi-stable*). Many neurons and neuronal models, such as the Hodgkin-Huxley model, exhibit bistability between resting (equilibrium) and spiking (limit cycle) attractors. Some neurons can exhibit bistability of two stable resting states in the subthreshold voltage range, e.g.,  $-59$  mV and  $-75$  mV in the thalamocortical neurons (Hughes et al. 1999) depicted

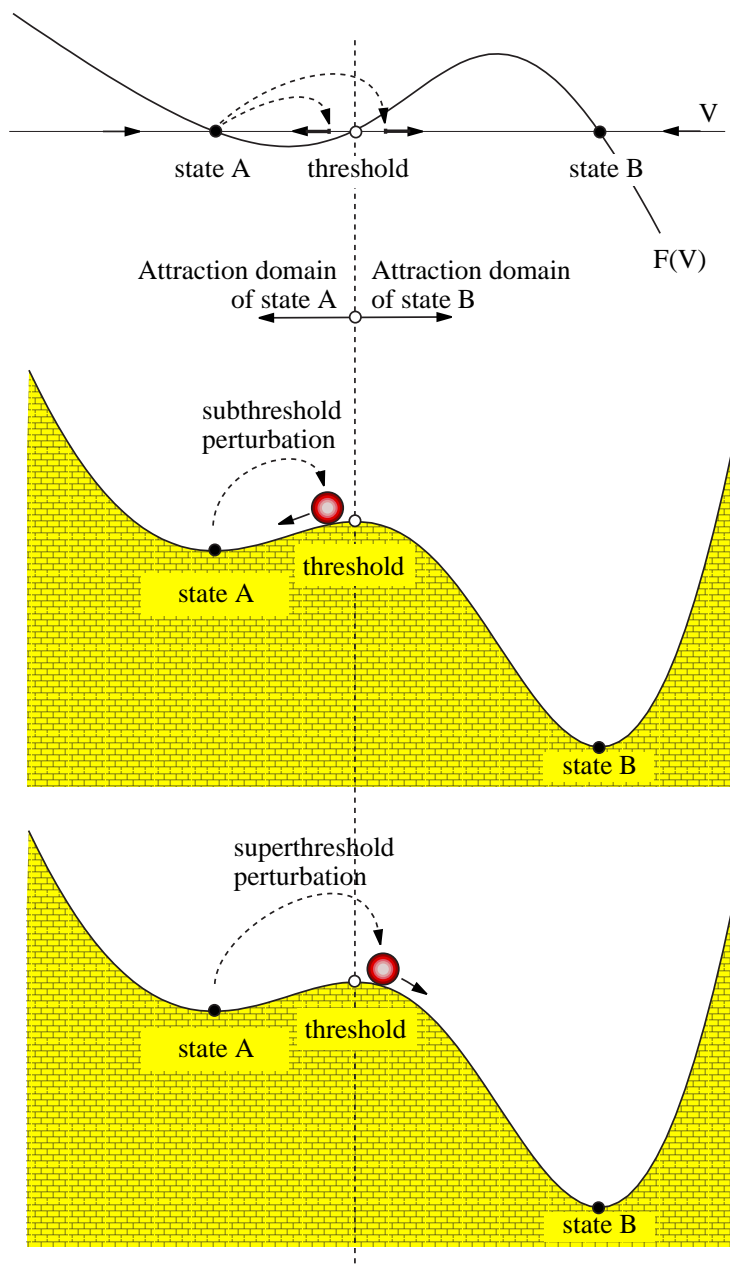


Figure 3.13: Unstable equilibrium plays the role of a threshold that separates two attraction domains.

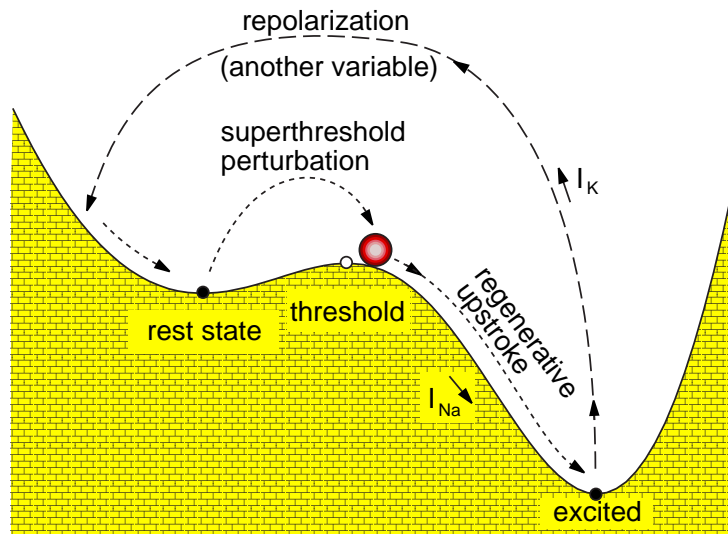


Figure 3.14: Mechanistic illustration of the mechanism of generation of an action potential.

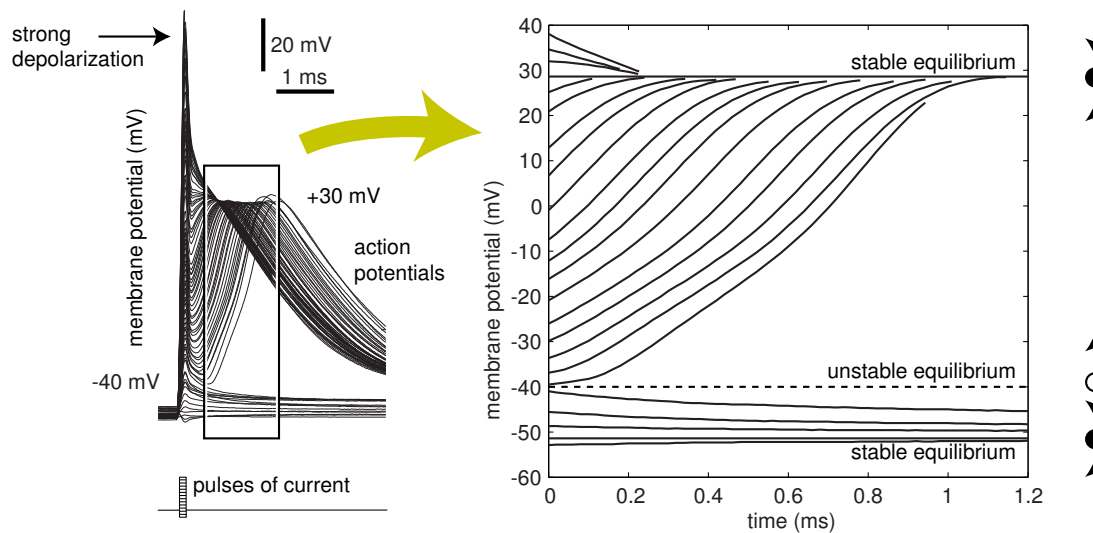


Figure 3.15: Upstroke dynamics of layer 5 pyramidal neuron *in vitro* (compare with the  $I_{Na,p}$ -model (3.5) in Fig. 3.8b).

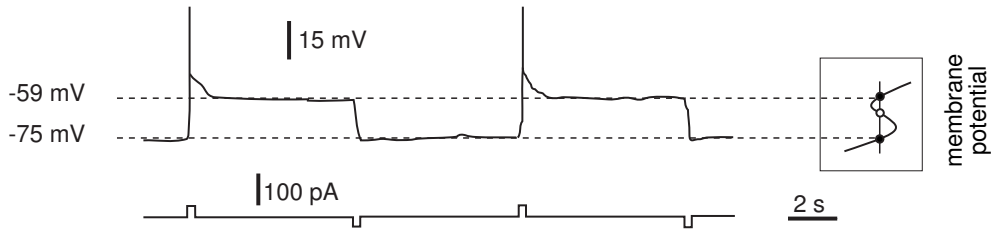


Figure 3.16: Membrane potential bistability in a cat TC neuron in the presence of ZD7288 (pharmacological blocker of  $I_h$ ; modified from Fig. 6B of Hughes et al. 1999).

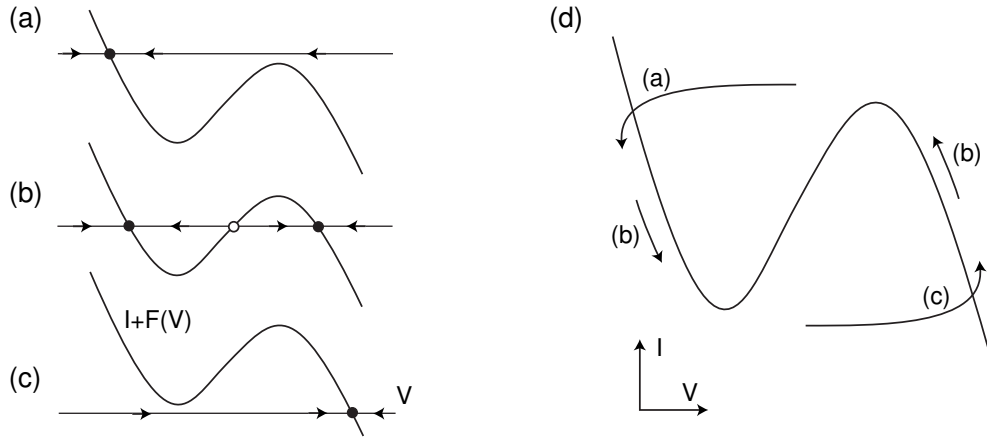


Figure 3.17: Bistability and hysteresis loop as  $I$  changes.

in Fig. 3.16, or  $-50$  mV and  $-60$  mV in mitral cells of the olfactory bulb (Heyward et al. 2001), or  $-45$  mV and  $-60$  mV in Purkinje neurons. Brief inputs can switch such neurons from one state to the other, as in Fig. 3.16. Though the ionic mechanisms of bistability are different in the three neurons, the mathematical mechanism is the same.

Consider a one-dimensional system  $\dot{V} = I + F(V)$  with function  $F(V)$  having a cubic N-shape. Injection of a dc-current  $I$  shifts the function  $I + F(V)$  up or down. When  $I$  is negative, the system has only one equilibrium, depicted in Fig. 3.17a. As we remove the injected current  $I$ , the system becomes bistable, as in Fig. 3.17b, but its state is still at the left equilibrium. As we inject positive current, the left stable equilibrium disappears via another saddle-node bifurcation, and the state of the system jumps to the right equilibrium, as in Fig. 3.17c. But as we slowly remove the injected current that caused the jump and go back to Fig. 3.17b, the jump to the left equilibrium does not occur until a much lower value corresponding to Fig. 3.17a is reached. The failure of the system to return to the original value when the injected current is removed is called *hysteresis*. If  $I$  were a slow  $V$ -depended variable, then the system could exhibit relaxation oscillations depicted in Fig. 3.17d and described in the next chapter.

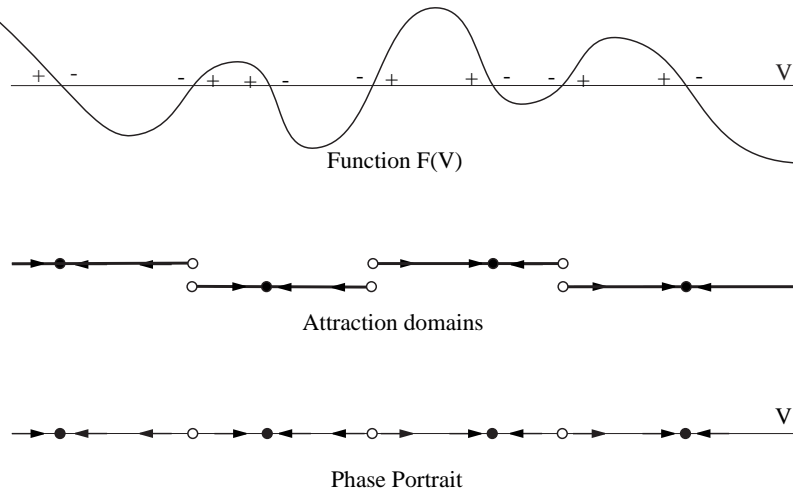


Figure 3.18: Phase portrait of a one-dimensional system  $\dot{V} = F(V)$ .

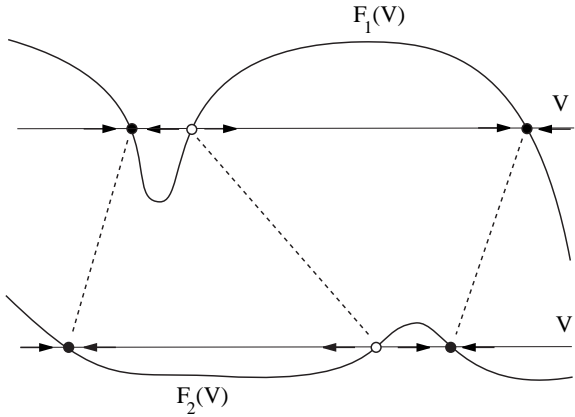


Figure 3.19: Two “seemingly different” dynamical systems  $\dot{V} = F_1(V)$  and  $\dot{V} = F_2(V)$  are topologically equivalent, hence they have qualitatively similar dynamics.

### 3.3 Phase Portraits

An important component in the qualitative analysis of any dynamical system is reconstruction of its *phase portrait*. For this one depicts all stable and unstable equilibria (as black and white circles respectively), representative trajectories, and corresponding attraction domains in the system’s state/phase space, as we illustrate in Fig. 3.18. The phase portrait is a geometrical representation of system dynamics. It depicts all possible evolutions of the state variable and how they depend on the initial state. Looking at the phase portrait, one immediately gets all important information about the system’s qualitative behavior without even knowing the equation for  $F$ .

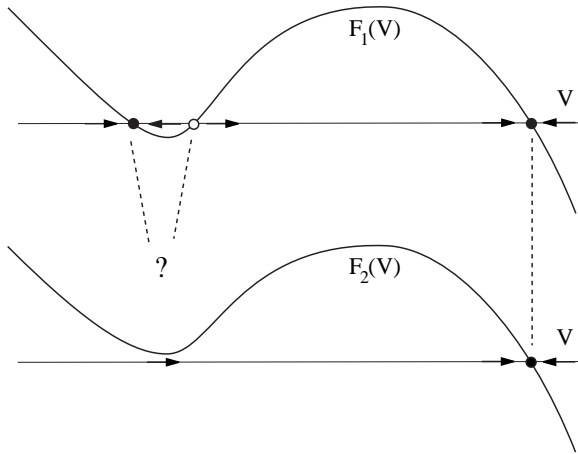


Figure 3.20: Two “seemingly alike” dynamical systems  $\dot{V} = F_1(V)$  and  $\dot{V} = F_2(V)$  are not topologically equivalent, hence they do not have qualitatively similar dynamics. (The first system has three equilibria, while the second system has only one.)

### 3.3.1 Topological equivalence

Phase portraits can be used to determine qualitative similarity of dynamical systems. In particular, two one-dimensional systems are said to be *topologically equivalent* when the phase portrait of one of them treated as a piece of rubber can be stretched or shrunk to fit the other one, as in Fig. 3.19. Topological equivalence is a mathematical concept that clarifies the imprecise notion of “qualitative similarity”, and its rigorous definition is provided, e.g., by Guckenheimer and Holmes (1983).

The stretching and shrinking of the “rubber” phase space are topological transformations that do not change the number of equilibria or their stability. Thus, two systems having different number of equilibria cannot be topologically equivalent, hence they have qualitatively different dynamics, as we illustrate in Fig. 3.20. Indeed, the top system is bistable because it has two stable equilibria separated by an unstable one. The evolution of the state variable depends on which attraction domain the initial condition is in initially. Such a system has “memory” of the initial condition. Moreover, sufficiently strong perturbations can switch it from one equilibrium state to another. In contrast, the bottom system in Fig. 3.20 has only one equilibrium, which is a global attractor, and the state variable converges to it regardless of the initial condition. Such a system has quite primitive dynamics, and it is topologically equivalent to the linear system (3.1).

### 3.3.2 Local equivalence and the Hartman-Grobman theorem

In computational neuroscience, we usually face quite complicated systems describing neuronal dynamics. A useful strategy is to substitute such systems by simpler ones having topologically equivalent phase portraits. For example, both systems in Fig. 3.19 are topologically equivalent to  $\dot{V} = V - V^3$  (please, check this), which is easier to deal with analytically.

Quite often we cannot find a simpler system that is topologically equivalent to our neuronal model on the entire state line  $\mathbb{R}$ . In this case, we make a sacrifice: we restrict

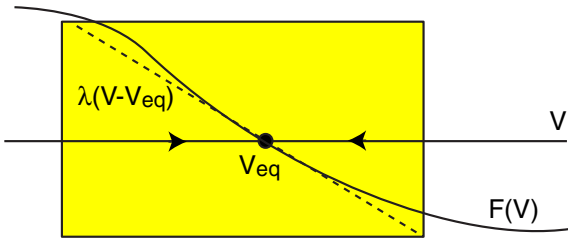


Figure 3.21: Hartman-Grobman theorem: The non-linear system  $\dot{V} = F(V)$  is topologically equivalent to the linear one  $\dot{V} = \lambda(V - V_{\text{eq}})$  in the local (shaded) neighborhood of the hyperbolic equilibrium  $V_{\text{eq}}$ .

our analysis to a small neighborhood of the line  $\mathbb{R}$ , e.g., a neighborhood of the resting state or of the threshold, and study behavior locally in this neighborhood.

An important tool in the local analysis of dynamical systems is the Hartman-Grobman theorem, which says that a non-linear one-dimensional system

$$\dot{V} = F(V)$$

sufficiently near an equilibrium  $V = V_{\text{eq}}$  is locally topologically equivalent to the linear one

$$\dot{V} = \lambda(V - V_{\text{eq}}) \quad (3.8)$$

provided that the eigenvalue

$$\lambda = F'(V_{\text{eq}})$$

at the equilibrium is non-zero, i.e., the slope of  $F(V)$  is non-zero. Such an equilibrium is called *hyperbolic*. Thus, nonlinear systems near hyperbolic equilibria behave as if there were linear, as in Fig. 3.21.

It is easy to find the exact solution of the linearized system (3.8) with an initial condition  $V(0) = V_0$ . It is  $V(t) = V_{\text{eq}} + e^{\lambda t}(V_0 - V_{\text{eq}})$  (check by differentiating). If the eigenvalue  $\lambda < 0$ , then  $e^{\lambda t} \rightarrow 0$  and  $V(t) \rightarrow V_{\text{eq}}$  as  $t \rightarrow \infty$ , so that the equilibrium is stable. Conversely, if  $\lambda > 0$ , then  $e^{\lambda t} \rightarrow \infty$  meaning that the initial displacement,  $V_0 - V_{\text{eq}}$ , grows with the time, and the equilibrium is unstable. Thus, the linearization predicts qualitative dynamics at the equilibrium and quantitative rate of convergence/divergence to/from the equilibrium.

If the eigenvalue  $\lambda = 0$ , then the equilibrium is non-hyperbolic, and analysis of the linearized system  $\dot{V} = 0$  cannot describe the behavior of the nonlinear system. Typically, non-hyperbolic equilibria arise when the system undergoes a bifurcation, i.e., a qualitative change of behavior, which we consider next. To study stability, we need to consider higher-order terms of the Taylor series of  $F(V)$  at  $V_{\text{eq}}$ .

### 3.3.3 Bifurcations

The final and the most advanced step in the qualitative analysis of any dynamical system is the bifurcation analysis. In general, a system is said to undergo a bifurcation when its phase portrait changes qualitatively. For example, the energy landscape in Fig. 3.22 changes so that the system is no longer bistable. The precise mathematical definition of a bifurcation will be given later.

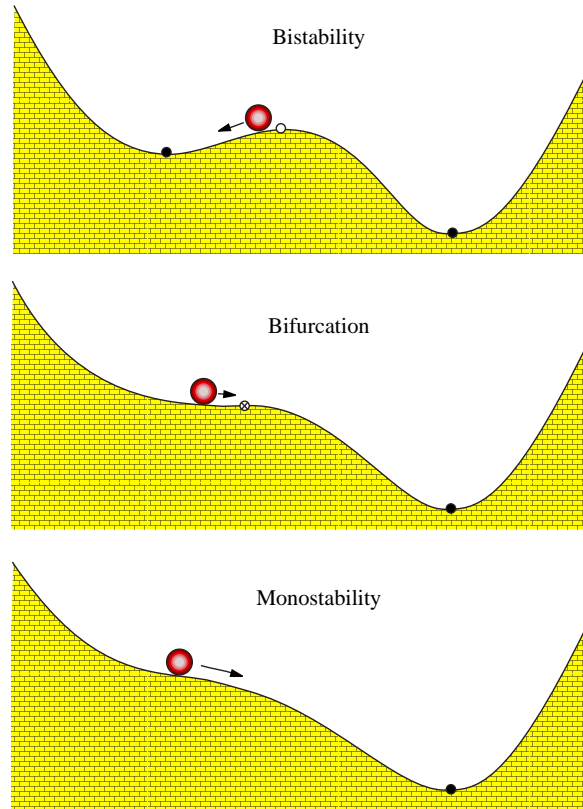


Figure 3.22: Mechanistic illustration of a bifurcation as a change of the landscape.

Qualitative change of the phase portrait may or may not necessarily reveal itself in a qualitative change of behavior, depending on the initial conditions. For example, there is a bifurcation in Fig. 3.23, left, but no change of behavior because the ball remains in the attraction domain of the right equilibrium. To see the change, we need to drop the ball at different initial conditions and observe the disappearance of the left equilibrium. In the same vain, there is no bifurcation Fig. 3.23, middle and right, (the phase portraits in each column are topologically equivalent) but the apparent change of behavior is caused by the expansion of the attraction domain of the left equilibrium or by the external input. Dropping the ball at different locations would result in the same qualitative picture — two stable equilibria whose attraction domains are separated by the unstable equilibrium. When mathematicians talk about bifurcations, they assume that all initial conditions could be sampled, in which case bifurcations do result in a qualitative change of behavior of the system as a whole.

To illustrate the importance of sampling all initial conditions, let us consider the *in vitro* recordings of a pyramidal neuron in Fig. 3.24. We inject 0.1-ms strong pulses of current of various amplitude to set the membrane potential to different initial values. Right after each pulse, we inject a 4 ms step of dc-current of amplitude  $I = 0$ ,  $I = 16$  or  $I = 60$  pA. The case  $I = 0$  pA is the same as in Fig. 3.15, so some initial conditions

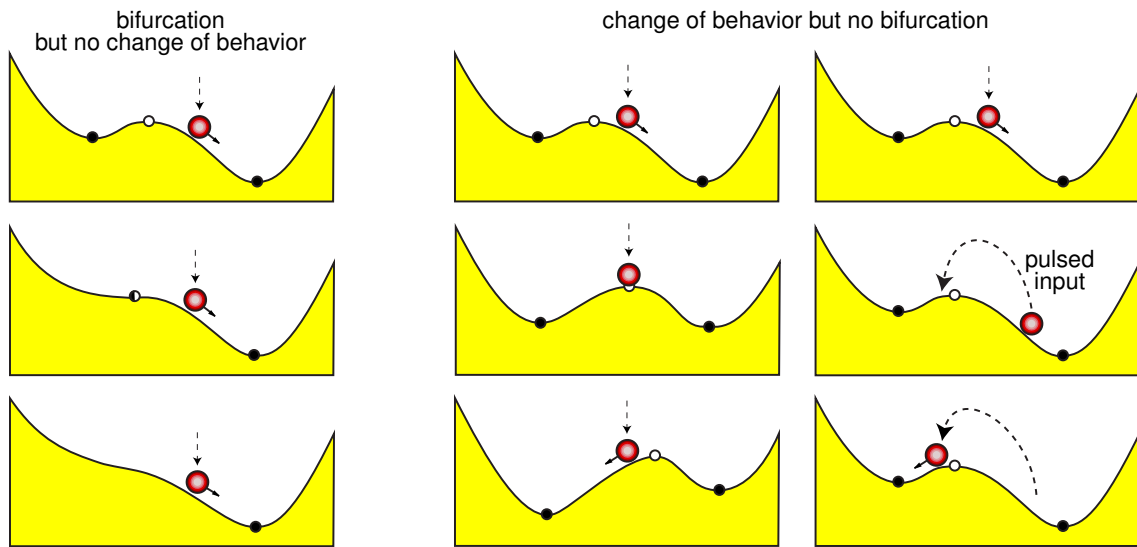


Figure 3.23: Bifurcations are not equivalent to qualitative change of behavior if the system is started with the same initial condition or subject to external input.

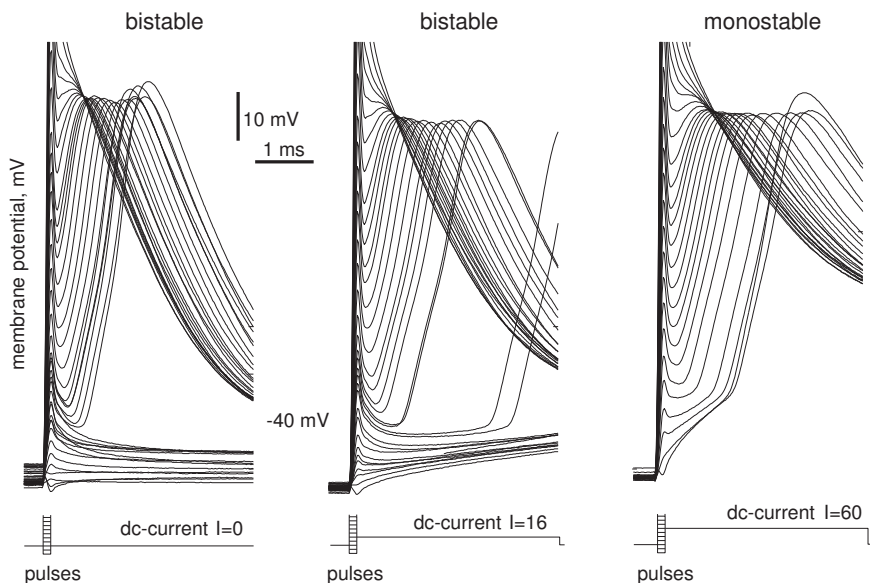


Figure 3.24: Qualitative change of the up-stroke dynamics of a layer 5 pyramidal neuron from rat visual cortex (the same neuron as in Fig. 3.15).

result in upstroke of the action potential, while others do not. When  $I = 60$  pA, all initial conditions result in the generation of an action potential. Clearly, a change of qualitative behavior occurs for some  $I$  between 0 and 60.

To understand the qualitative dynamics in Fig. 3.24, we consider the one-dimensional  $I_{\text{Na},p}$ -model (3.5) having different values of the parameter  $I$  and depict its trajectories in Fig. 3.25. One can clearly see that the qualitative behavior of the model depends on whether  $I$  is greater or less than 16. When  $I = 0$  (top of Fig. 3.25), the system is bistable. The rest and the excited states coexist. When  $I$  is large (bottom of Fig. 3.25) the rest state no longer exists because the leak outward current cannot balance the large injected dc-current  $I$  and the inward  $\text{Na}^+$  current.

What happens when we change  $I$  past 16? The answer lies in the details of the geometry of the right-hand side function  $F(V)$  of (3.5) and how it depends on the parameter  $I$ . Increasing  $I$  elevates the graph of  $F(V)$ . The higher the graph of  $F(V)$  is, the closer its intersections with the  $V$ -axis are, as we illustrate in Fig. 3.26 depicting only the low-voltage range of the system. When  $I$  approaches 16, the distance between the stable and unstable equilibria vanishes; the equilibria coalesce and annihilate each other. The value  $I = 16$  at which the equilibria coalesce is called the *bifurcation value*. This value separates two qualitatively different regimes: When  $I$  is near but less than 16, the system has three equilibria and bistable dynamics. The quantitative features, such as the exact locations of the equilibria, depend on the particular values of  $I$ , but the qualitative behavior remains unchanged no matter how close  $I$  to the bifurcation value is. In contrast, when  $I$  is near but greater than 16 the system has only one equilibrium and monostable dynamics.

In general, a dynamical system may depend on a vector of parameters, say  $p$ . A point in the parameter space, say  $p = a$ , is said to be a *regular* or non-bifurcation point, if the system's phase portrait at  $p = a$  is topologically equivalent to the phase portrait at  $p = c$  for any  $c$  sufficiently close to  $a$ . For example, the value  $I = 13$  in Fig. 3.26 is regular, since the system has topologically equivalent phase portraits for all  $I$  near 13. Similarly, the value  $I = 18$  is also regular. Any point in the parameter space that is not regular is called a bifurcation point. Namely, a point  $p = b$  is a bifurcation point, if the system's phase portrait at  $p = b$  is not topologically equivalent to the phase portrait at a point  $p = c$  no matter how close  $c$  to  $b$  is. The value  $I = 16$  in Fig. 3.26 is a bifurcation point. It corresponds to the *saddle-node* (also known as *fold* or *tangent*) bifurcation for reasons described later. It is one of the simplest bifurcations considered in this book.

### 3.3.4 Saddle-node (fold) bifurcation

In general, a one-dimensional system

$$\dot{V} = F(V, I)$$

having an equilibrium point  $V = V_{\text{sn}}$  for some value of the parameter  $I = I_{\text{sn}}$  (i.e.,  $F(V_{\text{sn}}, I_{\text{sn}}) = 0$ ) is said to be at a *saddle-node* bifurcation (sometimes called a *fold*

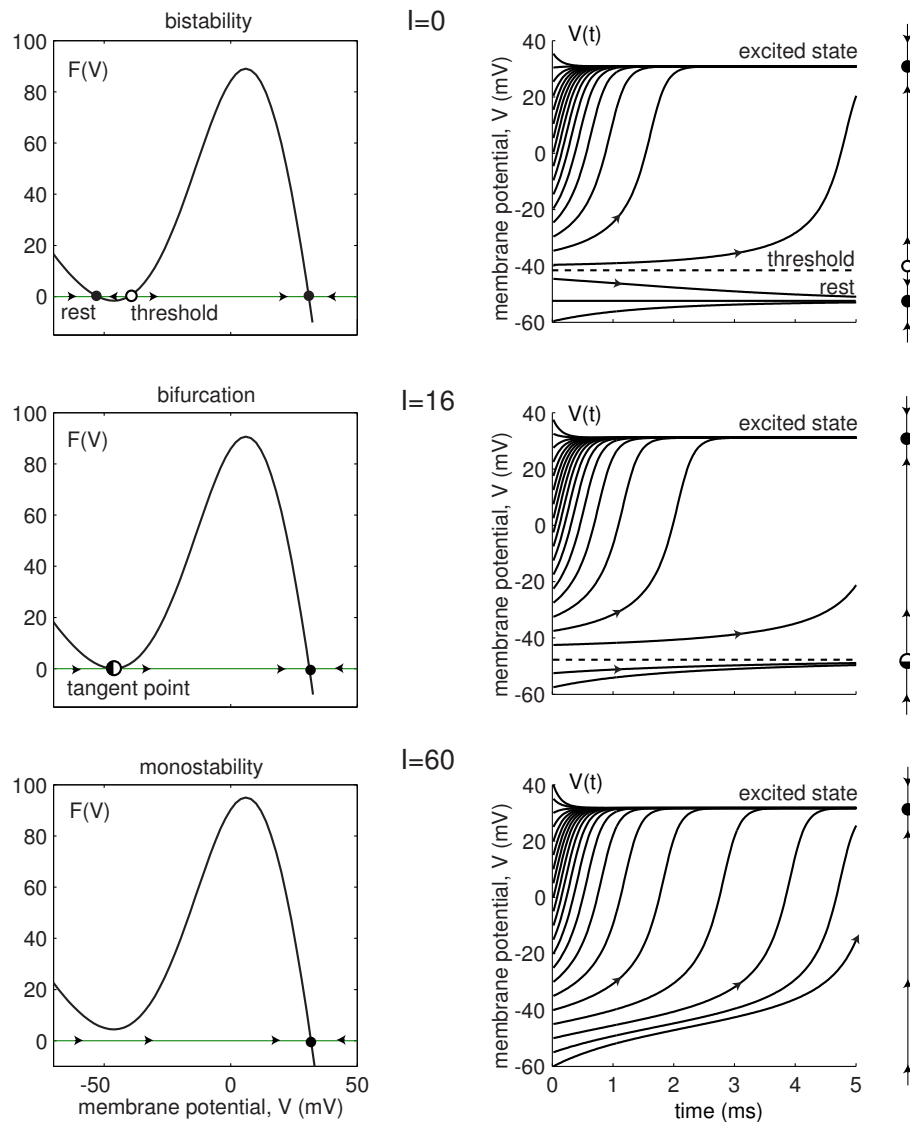


Figure 3.25: Bifurcation in the  $I_{Na,p}$ -model (3.5): The rest state and the threshold state coalesce and disappear when the parameter  $I$  increases.

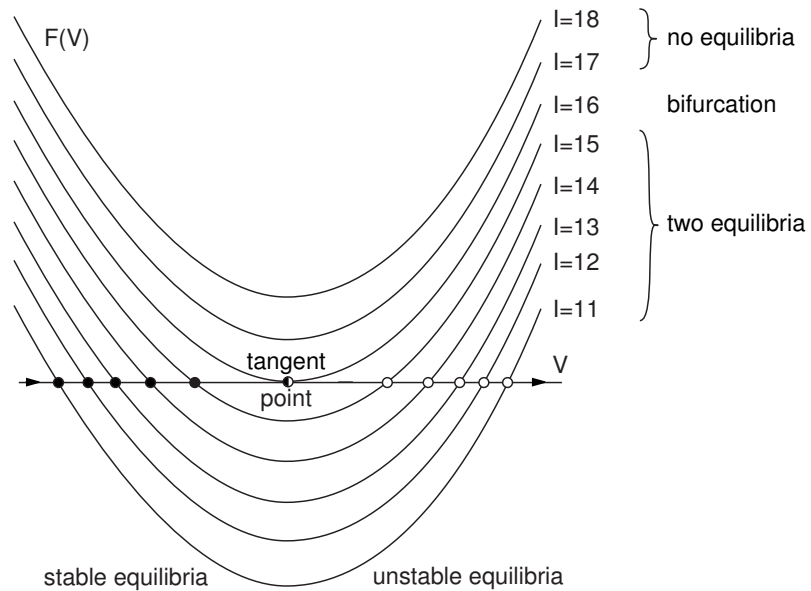


Figure 3.26: Saddle-node bifurcation: As the graph of the function  $F(V)$  is lifted up, the stable and unstable equilibria approach each other, coalesce at the tangent point, and then disappear.

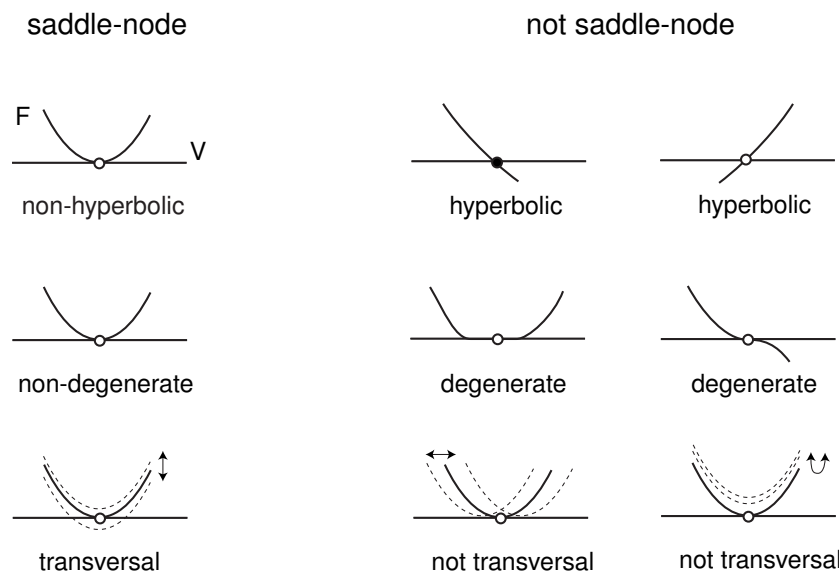


Figure 3.27: Geometrical illustration of the three conditions defining saddle-node bifurcations. Arrows denote the direction of displacement of the function  $F(V, I)$  as the bifurcation parameter  $I$  changes.

bifurcation) if the following mathematical conditions, illustrated in Fig. 3.27, are satisfied:

- (Non-hyperbolicity) The eigenvalue  $\lambda$  at  $V_{\text{sn}}$  is zero; that is,

$$\lambda = F_V(V, I_{\text{sn}}) = 0 \quad (\text{at } V = V_{\text{sn}}),$$

where  $F_V$  denotes the derivative of  $F$  with respect to  $V$ , that is,  $F_V = \partial F / \partial V$ . Equilibria with zero or pure imaginary eigenvalues are called non-hyperbolic. Geometrically, this condition implies that the graph of  $F$  has horizontal slope at the equilibrium.

- (Non-degeneracy) The second order derivative with respect to  $V$  at  $V_{\text{sn}}$  is non-zero; that is,

$$F_{VV}(V, I_{\text{sn}}) \neq 0 \quad (\text{at } V = V_{\text{sn}}).$$

Geometrically, this means that the graph of  $F$  looks like the square parabola  $V^2$  in Fig. 3.27.

- (Transversality) The function  $F(V, I)$  is non-degenerate with respect to the bifurcation parameter  $I$ ; that is,

$$F_I(V_{\text{sn}}, I) \neq 0 \quad (\text{at } I = I_{\text{sn}}),$$

where  $F_I$  denotes the derivative of  $F$  with respect to  $I$ . Geometrically, this means that as  $I$  changes past  $I_{\text{sn}}$ , the graph of  $F$  approaches, touches, and then intersects the  $V$  axis.

Saddle-node bifurcation results in appearance or disappearance of a pair of equilibria, as in Fig. 3.26. None of the six examples on the right-hand side of Fig. 3.27 can undergo a saddle-node bifurcation because at least one of the conditions above is violated.

The number of conditions involving strict equality (“ $=$ ”) is called the *co-dimension* of a bifurcation. The saddle-node bifurcation has *co-dimension-1* because there is only one condition involving “ $=$ ”, and the other two conditions involve inequalities (“ $\neq$ ”). Co-dimension-1 bifurcations can be reliably observed in systems with one parameter.

It is an easy exercise to check that the one-dimensional system

$$\dot{V} = I + V^2 \tag{3.9}$$

is at saddle-node bifurcation when  $V = 0$  and  $I = 0$  (please, check all three conditions). This system is called the *topological normal form* for saddle-node bifurcation. The phase portraits of this system are topologically equivalent to those depicted in Fig. 3.26, except that the bifurcation occurs at  $I = 0$ , and not at  $I = 16$ .

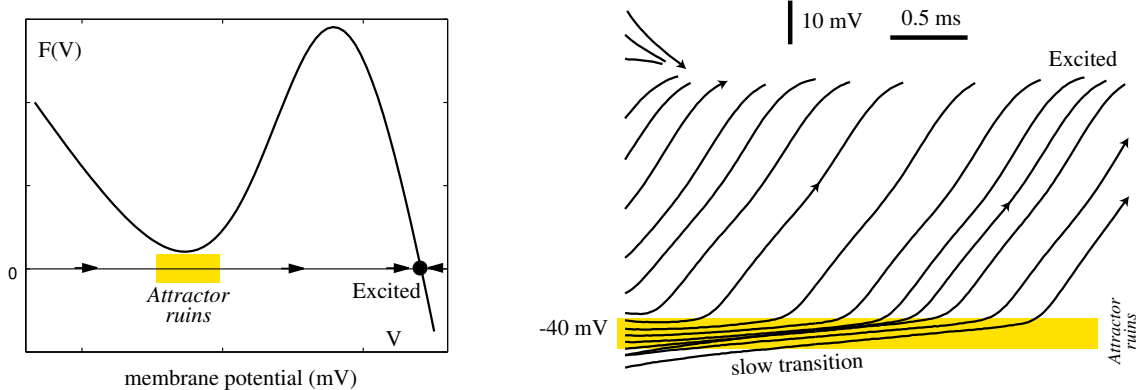


Figure 3.28: Slow transition through the ghost of the resting state attractor in a cortical pyramidal neuron with  $I = 30$  pA (the same neuron as in Fig. 3.15). Even though the resting state has already disappeared, the function  $F(V)$ , and hence the rate of change,  $\dot{V}$ , is still small when  $V \approx -46$  mV.

### 3.3.5 Slow transition

All physical, chemical, and biological systems near saddle-node bifurcations possess certain universal features that do not depend on particulars of the systems. Consequently, all neural systems near such a bifurcation share common neuro-computational properties, which we will discuss in detail in Chapter 7. Here we take a look at one such property — slow transition through the ruins (or ghost) of the rest state attractor, which is relevant to the dynamics of many neocortical neurons.

In Fig. 3.28 we show the function  $F(V)$  of the system (3.5) with  $I = 30$  pA, which is greater than the bifurcation value 16 pA, and the corresponding behavior of a cortical neuron; compare with Fig. 3.15. The system has only one attractor — the excited state, and any solution starting from an arbitrary initial condition should quickly approach this attractor. However, the solutions starting from the initial conditions around  $-50$  mV do not seem to hurry. Instead, they slow down near  $-46$  mV and spend a considerable amount of time in the voltage range corresponding to the resting state, as if the state were still present. The closer is  $I$  to the bifurcation value, the more time the membrane potential spends in the neighborhood of the resting state. Obviously, such a slow transition cannot be explained by a slow activation of the inward  $\text{Na}^+$  current, since  $\text{Na}^+$  activation in a cortical neuron is practically instantaneous.

The slow transition occurs because the neuron or the system (3.5) in Fig. 3.28 is near a saddle-node bifurcation. Even though  $I$  is greater than the bifurcation value, and the rest state attractor is already annihilated, the function  $F(V)$  is barely above the  $V$ -axis at the “annihilation site”. In other words, the rest state attractor has already been ruined, but its “ruins” (or its “ghost”) can still be felt because

$$\dot{V} = F(V) \approx 0 \quad (\text{at attractor ruins, } V \approx -46 \text{ mV}),$$

as one can see in Fig. 3.28. In Chapter 7 we will show how this property explains the

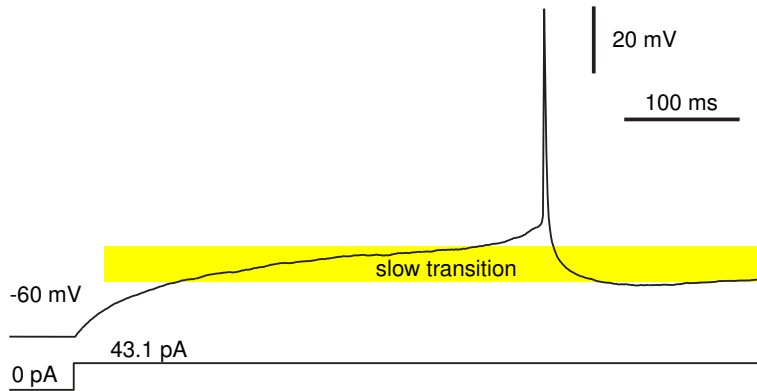


Figure 3.29: A 400-ms latency in a layer 5 pyramidal neuron of rat visual cortex.

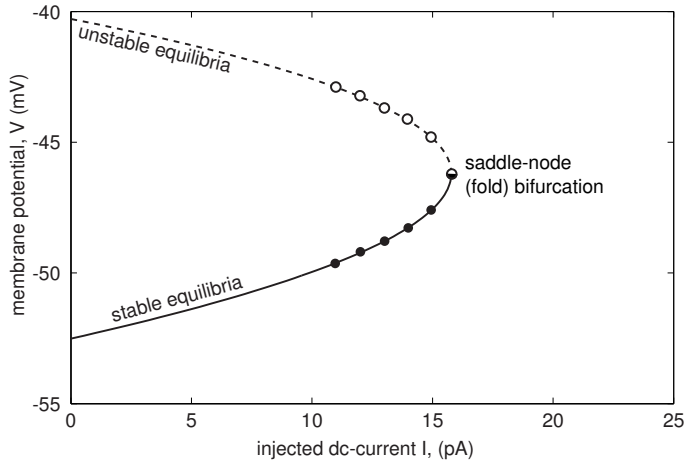


Figure 3.30: Bifurcation diagram of the system in Fig. 3.26.

ability of many neocortical neurons, such as the one in Fig. 3.29, to generate repetitive action potentials with small frequency, and how it predicts that all such neurons, considered as dynamical systems, reside near saddle-node bifurcations.

### 3.3.6 Bifurcation diagram

The final step in the geometrical bifurcation analysis of one-dimensional systems is the analysis of bifurcation diagrams, which we do in Fig. 3.30 for the saddle-node bifurcation shown in Fig. 3.26. To draw the bifurcation diagram, we determine the locations of the stable and unstable equilibria for each value of the parameter  $I$  and plot them as white or black circles in the  $(I, V)$  plane in Fig. 3.30. The equilibria form two branches that join at the fold point corresponding to the saddle-node bifurcation (hence the alternative name of *fold* bifurcation). The branch corresponding to the unstable equilibria is dashed to stress its instability. As the bifurcation parameter  $I$  varies from left to right passing through the bifurcation point, the stable and unstable

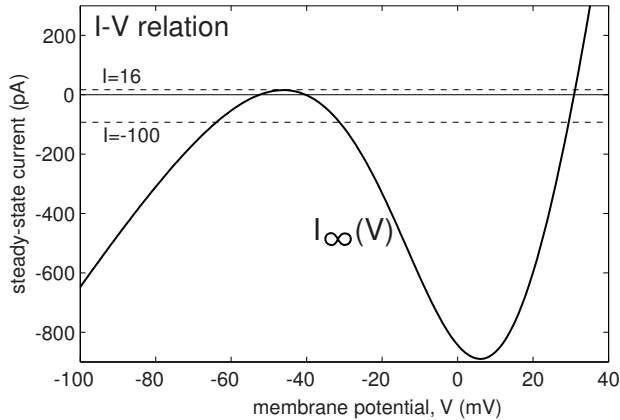


Figure 3.31: Equilibria are intersections of the steady-state I-V curve  $I_\infty(V)$  and a horizontal line  $I = \text{const.}$

equilibria coalesce and annihilate each other. As the parameter varies from right to left, two equilibria — one stable and one unstable — appear from a single point. Thus, depending on the direction of movement of the bifurcation parameter, the saddle-node bifurcation explains disappearance or appearance of a new stable state. In any case, the qualitative behavior of the systems changes exactly at the bifurcation point.

### 3.3.7 Bifurcations and I-V recordings

In general, determining saddle-node bifurcation diagrams of neurons may be a daunting mathematical task. However, it is a trivial exercise when the bifurcation parameter is the injected dc-current  $I$ . In this case, the bifurcation diagram, such as the one in Fig. 3.30, is just the steady-state I-V relation  $I_\infty(V)$  plotted on the  $(I, V)$ -plane. Indeed, the equation

$$C\dot{V} = I - I_\infty(V) = 0$$

states that  $V$  is an equilibrium if and only if the net membrane current,  $I - I_\infty(V)$ , is zero. For example, equilibria of the  $I_{\text{Na},p}$ -model are solutions of the equation

$$0 = I - \overbrace{(g_L(V - E_L) + g_{\text{Na}}m_\infty(V)(V - E_{\text{Na}}))}^{I_\infty(V)},$$

which follows directly from (3.5). In Fig. 3.31 we illustrate how to find the equilibria geometrically: We plot the steady-state I-V curve  $I_\infty(V)$  and draw a horizontal line with altitude  $I$ . Any intersection satisfies the equation  $I = I_\infty(V)$ , and hence is an equilibrium (stable or unstable). Obviously, when  $I$  increases past 16, the saddle-node bifurcation occurs.

Notice that the equilibria are points on the curve  $I_\infty(V)$ , so flipping and rotating the curve by  $90^\circ$ , as we do in Fig. 3.32, left, results in a complete saddle-node bifurcation diagram. The diagram conveys in a very condensed manner all important information about the qualitative behavior of the  $I_{\text{Na},p}$ -model. The three branches of the S-shaped curve, which is the  $90^\circ$ -rotated and flipped copy of the N-shaped I-V curve, correspond to the rest, threshold, and excited states of the model. Each slice  $I = \text{const}$  represents

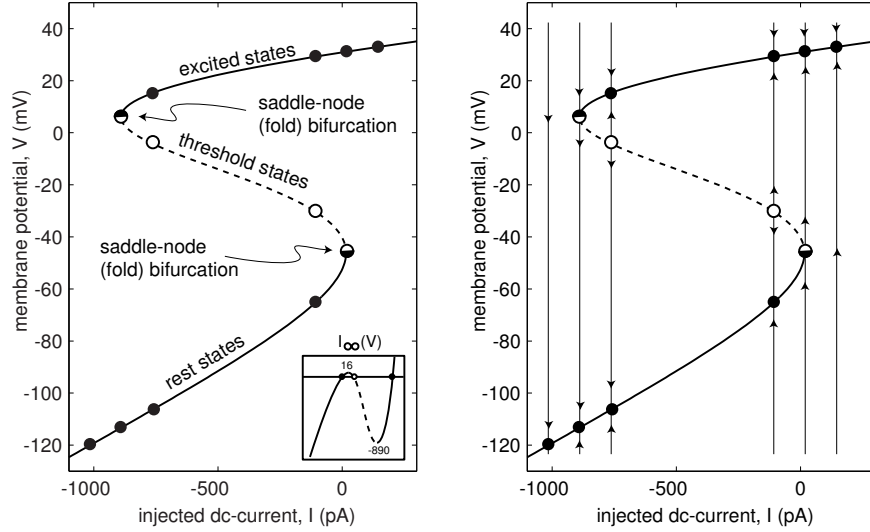


Figure 3.32: Bifurcation diagram of the  $I_{\text{Na},p}$ -model (3.5).

the phase portrait of the system, as we illustrate in Fig. 3.32, right. Each point where the branches fold (max or min of  $I_\infty(V)$ ) corresponds to a saddle-node bifurcation. Since there are two such folds, at  $I = 16 \text{ pA}$  and at  $I = -890 \text{ pA}$ , there are two saddle-node bifurcations in the system. The first one, studied in Fig. 3.25, corresponds to the disappearance of the rest state. The other one, illustrated in Fig. 3.33, corresponds to the disappearance of the excited state. It occurs because  $I$  becomes so negative that the  $\text{Na}^+$  inward current is no longer strong enough to balance the leak outward current and the negative injected dc-current to keep the membrane in the depolarized (excited) state.

Below the reader can find more examples of bifurcation analysis of the  $I_{\text{Na},p}$ - and  $I_{\text{Kir}}$ -models, which have non-monotonic I-V relations and can exhibit multi-stability of states. The  $I_K$ - and  $I_h$ -models have monotonic I-V relations and hence only one equilibrium state. These models cannot have saddle-node bifurcations, as the reader is asked to prove in Ex. 13 and 14.

### 3.3.8 Quadratic integrate-and-fire neuron

Let us consider the topological normal form for the saddle-node bifurcation (3.9). From  $0 = I + V^2$  we find that there are two equilibria,  $V_{\text{rest}} = -\sqrt{|I|}$  and  $V_{\text{thresh}} = +\sqrt{|I|}$  when  $I < 0$ . The equilibria approach and annihilate each other via saddle-node bifurcation when  $I = 0$ , so there are no equilibria when  $I > 0$ . In this case,  $\dot{V} \geq I$  and  $V(t)$  increases to infinity. Because of the quadratic term, the rate of increase also increases, resulting in a positive feedback loop corresponding to the regenerative activation of  $\text{Na}^+$  current. In Ex. 15 we show that  $V(t)$  escapes to infinity in a finite time, which corresponds to the up-stroke of the action potential. The same up-stroke is generated when  $I < 0$ , if the voltage variable is pushed beyond the threshold value  $V_{\text{thresh}}$ .

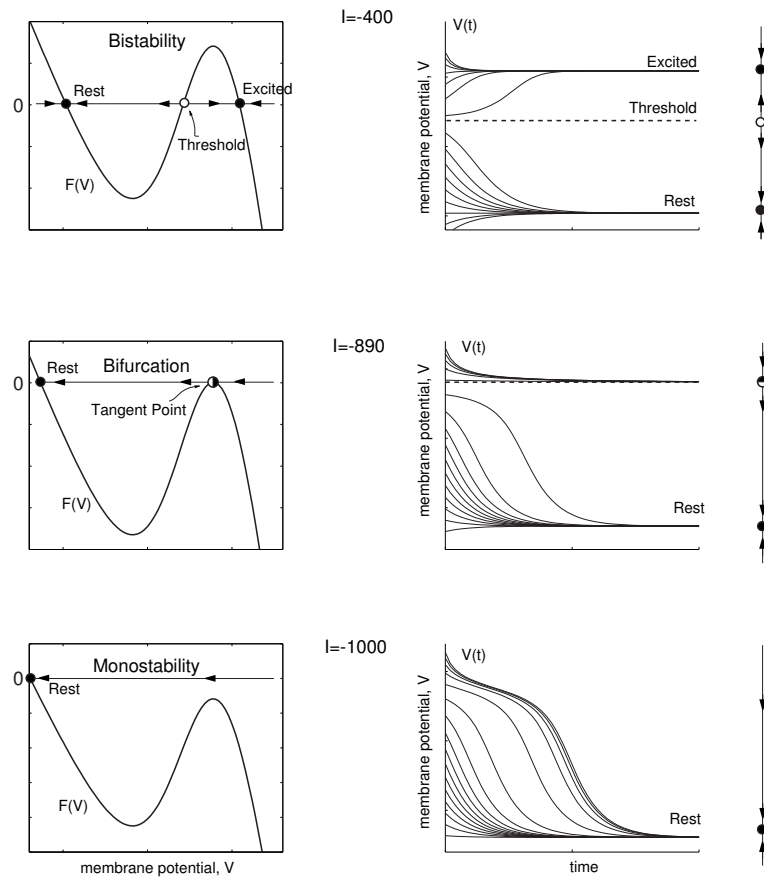


Figure 3.33: Bifurcation in the  $I_{Na,p}$ -model (3.5): The excited state and the threshold state coalesce and disappear when the parameter  $I$  is sufficiently small.

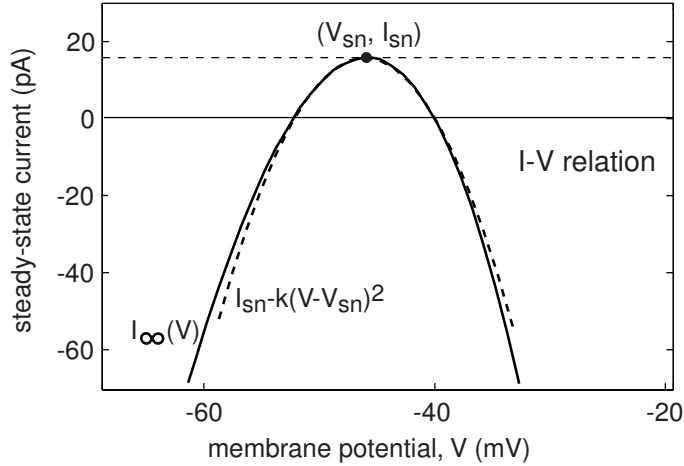


Figure 3.34: Magnification of the I-V curve in Fig. 3.31 at the left knee shows that it can be approximated by a square parabola.

Considering infinite values of the membrane potential may be convenient from a purely mathematical point of view, but this has no physical meaning and no way to simulate it on a digital computer. Instead, we fix a sufficiently large constant  $V_{\text{peak}}$  and say that (3.9) generated a spike when  $V(t)$  reached  $V_{\text{peak}}$ . After the peak of the spike is reached, we reset  $V(t)$  to a new value  $V_{\text{reset}}$ . The topological normal form for the saddle-node bifurcation with the after-spike resetting

$$\dot{V} = I + V^2, \quad \text{if } V \geq V_{\text{peak}}, \quad \text{then } V \leftarrow V_{\text{reset}} \quad (3.10)$$

is called the *quadratic integrate-and-fire neuron*. It is the simplest model of a spiking neuron. The name stems from its resemblance to the *leaky* integrate-and-fire neuron  $\dot{V} = I - V$  considered in Chap. 8. In contrast to the common folklore, the leaky neuron is not a *spiking model* because it does not have a spike-generation mechanism, i.e., a regenerative up-stroke of the membrane potential, whereas the quadratic neuron does. We discuss this and other issues in detail in Chap. 8.

In general, quadratic integrate-and-fire model could be derived directly from the equation  $C\dot{V} = I - I_\infty(V)$  by approximating the steady-state I-V curve near the resting state by the square parabola  $I_\infty(V) \approx I_{\text{sn}} - k(V - V_{\text{sn}})^2$ , where  $k > 0$  and the peak of the curve  $(V_{\text{sn}}, I_{\text{sn}})$  could be easily found experimentally; see Fig. 3.34. Approximating the I-V curve by other functions, for example  $I_\infty(V) = g_{\text{leak}}(V - V_{\text{rest}}) - ke^{pV}$ , results in other forms of the model, e.g., the exponential integrate-and-fire model (Fourcaud-Trocme et al. 2003), which has certain advantages over the quadratic form. Unfortunately, the model is not solvable analytically, and it is expensive to simulate. The form  $I_\infty(V) = g_{\text{leak}}(V - V_{\text{leak}}) - k(V - V_{\text{th}})_+^2$ , where  $x_+ = x$  when  $x > 0$  and  $x_+ = 0$  otherwise, combines the advantages of both models. The parameters  $V_{\text{peak}}$  and  $V_{\text{reset}}$  are derived from the shape of the spike. Normalization of variables and parameters results in the form (3.10) with  $V_{\text{peak}} = 1$ .

In Fig. 3.35 we simulated the quadratic integrate-and-fire neuron to illustrate a

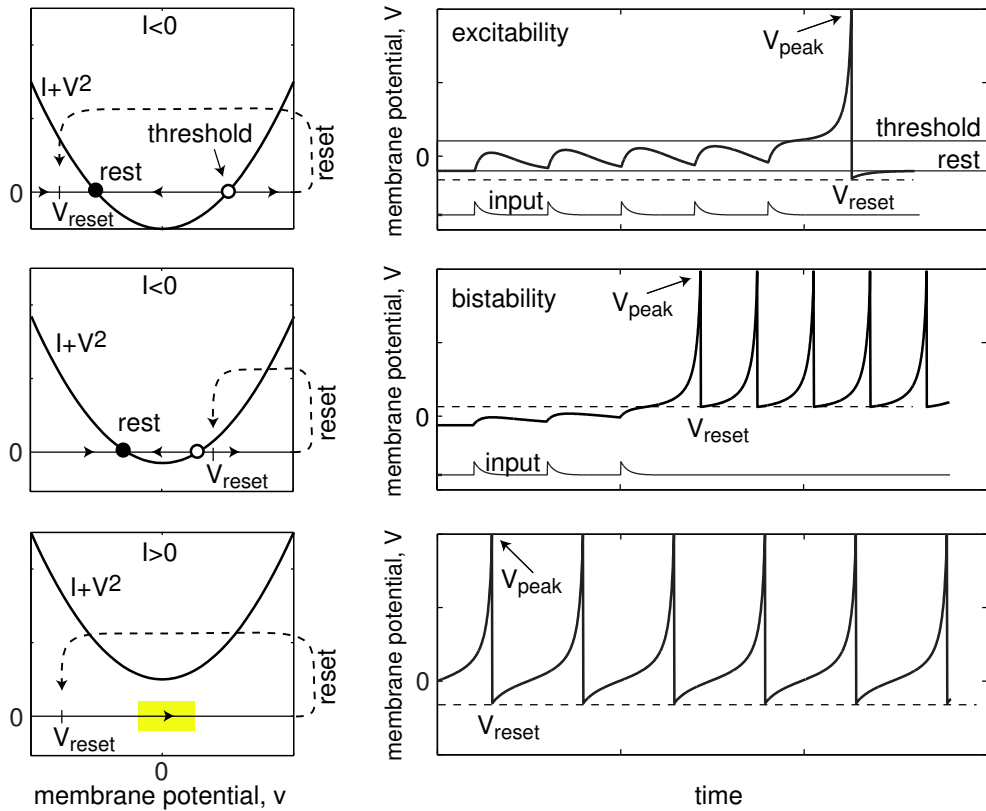


Figure 3.35: Quadratic integrate-and-fire neuron (3.10) with time-dependent input.

number of its features, which will be described in detail in subsequent chapters using conductance-based models. First, the neuron is an integrator; each input pulse in Fig. 3.35, top, pushes  $V$  closer to the threshold value; the higher the frequency of the input, the sooner  $V$  reaches the threshold and starts the up-stroke of a spike. The neuron is monostable when  $V_{\text{reset}} \leq 0$  and could be bistable otherwise. Indeed, the first spike in Fig. 3.35, middle, is evoked by the input, but the subsequent spikes occur because the reset value is superthreshold.

The neuron could be Class 1 or Class 2 excitable depending on the sign of  $V_{\text{reset}}$ . Suppose the injected current  $I$  slowly ramps up from a negative to a positive value. The membrane potential follows the resting state  $-\sqrt{|I|}$  in a quasi-static fashion until the bifurcation point  $I = 0$  is reached. At this moment, the neuron starts to fire tonic spikes. In the monostable case  $V_{\text{reset}} < 0$  in Fig. 3.35, bottom, the membrane potential is reset to the left of the ghost of the saddle-node point (see Sect. 3.3.5), thereby producing spiking with an arbitrary small frequency and hence Class 1 excitability. Because of the recurrence, such a bifurcation is called saddle-node on invariant circle. Many pyramidal neurons in mammalian neocortex exhibit such a bifurcation. In contrast, in the bistable case  $V_{\text{reset}} > 0$ , not shown in the figure, the membrane potential is reset to the right of the ghost, no slow transition is involved, and the tonic spiking starts with a non-zero frequency. As an exercise, explain why there is a noticeable latency (delay) to the first

spike right after the bifurcation. This type of behavior is typical in spiny projection neurons of neostriatum and basal ganglia, as we show in Chap. 8.

## Review of Important Concepts

- The one-dimensional dynamical system  $\dot{V} = F(V)$  describes how the rate of change of  $V$  depends on  $V$ . Positive  $F(V)$  means  $V$  increases, negative  $F(V)$  means  $V$  decreases.
- In the context of neuronal dynamics,  $V$  is often the membrane potential, and  $F(V)$  is the steady-state I-V curve taken with the minus sign.
- A zero of  $F(V)$  corresponds to an equilibrium of the system. (Indeed, if  $F(V) = 0$ , then the state of the system,  $V$ , neither increases nor decreases.)
- An equilibrium is stable when  $F(V)$  changes the sign from “+” to “−”. A sufficient condition for stability is that the eigenvalue  $\lambda = F'(V)$  at the equilibrium be negative.
- A phase portrait is a geometrical representation of the system’s dynamics. It depicts all equilibria, their stability, representative trajectories, and attraction domains.
- A bifurcation is a qualitative change of the system’s phase portrait.
- The saddle-node (fold) is a typical bifurcation in one-dimensional systems: As a parameter changes, a stable and an unstable equilibrium approach, coalesce, and then annihilate each other.

## Bibliographical Notes

There is no standard textbook on dynamical systems theory. The classical book *Non-linear Oscillations, Dynamical Systems, and Bifurcations of Vector Fields* by Guckenheimer and Holmes (1983) plays the same role in the dynamical systems community as the book *Ion Channels of Excitable Membranes* by Hille (2001) in the neuroscience community. A common feature of these books is that they are not suitable as a first reading on the subject.

Most textbooks on differential equations, such as *Differential Equations and Dynamical Systems* by Perko (1996), develop the theory starting with a comprehensive analysis of linear systems, then applying it to local analysis of non-linear systems, and then discussing global behavior. By the time the reader gets to bifurcations, he has to go through a lot of daunting math, which is fun only for mathematicians. Here we

follow approach similar to that in *Nonlinear Dynamics and Chaos* by Strogatz (1994): Instead of going from linear to non-linear systems, we go from one-dimensional non-linear systems (this chapter) to two-dimensional non-linear systems (next chapter). Rather than burdening the theory with a lot of mathematics, we use the geometrical approach to stimulate the reader's intuition. (There is plenty of fun math in exercises and in the later chapters.)

## Exercises

1. Consider a neuron having  $\text{Na}^+$  current with fast activation kinetics. Assume that inactivation of this current, as well as (in)activations of the other currents in the neuron are much slower. Prove that the initial segment of action potential upstroke of this neuron can be approximated by the  $I_{\text{Na},p}$ -model (3.5). Use Fig. 3.15 to discuss the applicability of this approximation.
2. Draw phase portraits of the systems in Fig. 3.36. Clearly mark all equilibria, their stability, attraction domains, and direction of trajectories. Determine the signs of eigenvalues at each equilibrium.

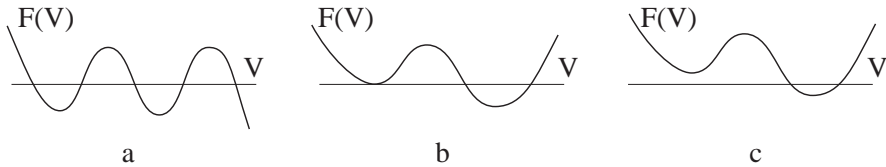


Figure 3.36: Draw phase portrait of the system  $\dot{V} = F(V)$  with shown  $F(V)$ .

3. Draw phase portraits of the following systems

$$\begin{aligned} \text{(a)} \quad & \dot{x} = -1 + x^2, \\ \text{(b)} \quad & \dot{x} = x - x^3. \end{aligned}$$

Determine the eigenvalues at each equilibrium.

4. Determine stability of the equilibrium  $x = 0$  and draw phase portraits of the following piece-wise continuous systems

$$\begin{aligned} \text{(a)} \quad & \dot{x} = \begin{cases} 2x, & \text{if } x < 0 \\ x, & \text{if } x \geq 0 \end{cases} \\ \text{(b)} \quad & \dot{x} = \begin{cases} -1, & \text{if } x < 0 \\ 0, & \text{if } x = 0 \\ 1, & \text{if } x > 0 \end{cases} \\ \text{(c)} \quad & \dot{x} = \begin{cases} -2/x, & \text{if } x \neq 0 \\ 0, & \text{if } x = 0 \end{cases} \end{aligned}$$

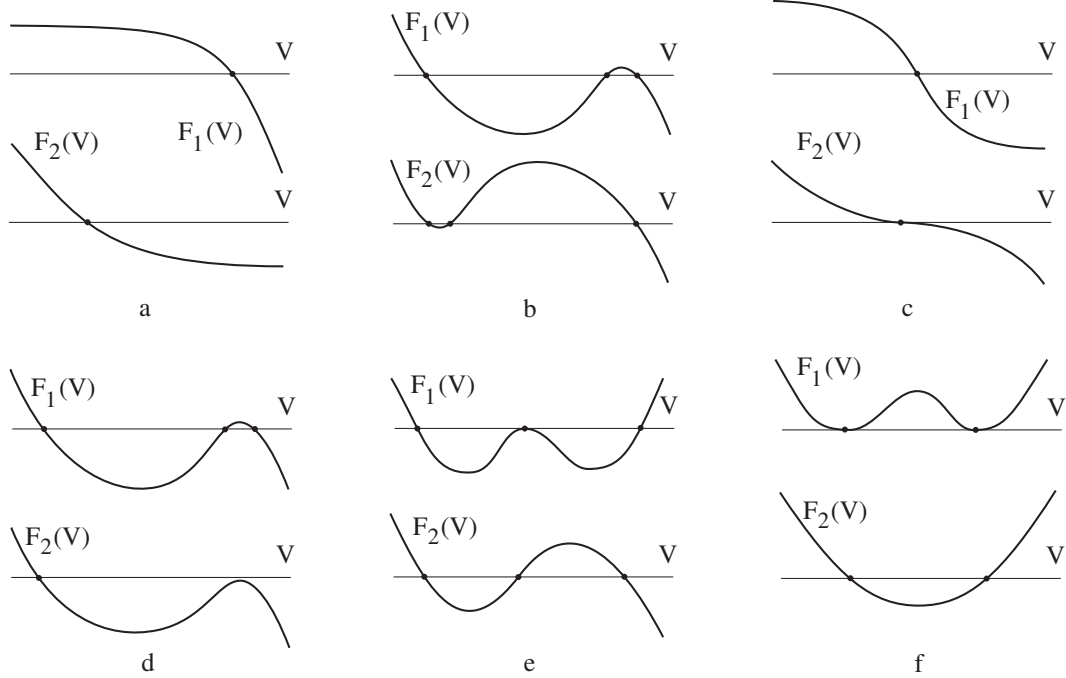


Figure 3.37: Which of the pairs correspond to topologically equivalent dynamical systems? (All intersections with the  $V$  axis are marked as dots.)

5. Draw phase portraits of the systems in Fig. 3.37. Which of the pairs in the figure correspond to topologically equivalent dynamical systems?
6. (Saddle-node bifurcation) Draw the bifurcation diagram and representative phase portraits of the system  $\dot{x} = a + x^2$ , where  $a$  is a bifurcation parameter. Find the eigenvalues at each equilibrium.
7. (Saddle-node bifurcation) Use definition in Sect. 3.3.4 to find saddle-node bifurcation points in the following systems:
  - (a)  $\dot{x} = a + 2x + x^2$ ,
  - (b)  $\dot{x} = a + x + x^2$ ,
  - (c)  $\dot{x} = a - x + x^2$ ,
  - (d)  $\dot{x} = a - x + x^3$  (Hint: verify the non-hyperbolicity condition first),
  - (e)  $\dot{x} = 1 + ax + x^2$ ,
  - (f)  $\dot{x} = 1 + 2x + ax^2$ ,

where  $a$  is the bifurcation parameter.

8. (Pitchfork bifurcation) Draw the bifurcation diagram and representative phase portraits of the system  $\dot{x} = bx - x^3$ , where  $b$  is a bifurcation parameter. Find the eigenvalues at each equilibrium.

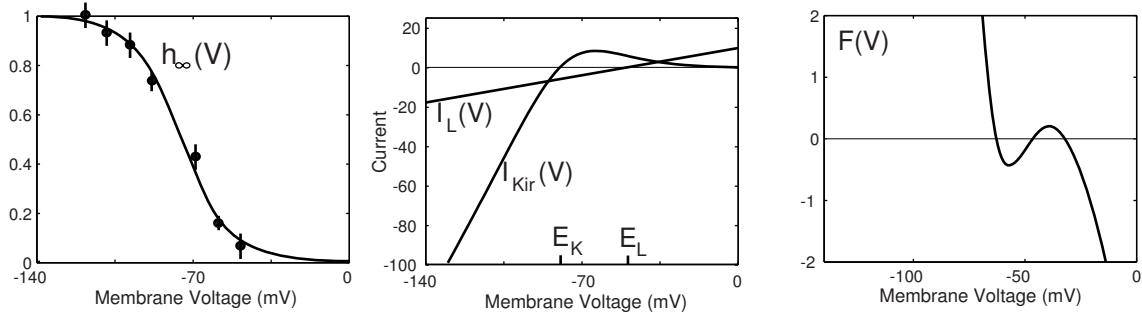


Figure 3.38: The  $I_{Kir}$ -model having injected current ( $I$ ), leak current ( $I_L$ ), and instantaneous K<sup>+</sup> inward rectifier current ( $I_{Kir}$ ) and described by (3.11). Inactivation curve  $h_\infty(V)$  is modified from Wessel et. al (1999). Parameters:  $C = 1$ ,  $I = 6$ ,  $g_L = 0.2$ ,  $E_L = -50$ ,  $g_{Kir} = 2$ ,  $E_K = -80$ ,  $V_{1/2} = -76$ ,  $k = -12$  (see Fig. 2.20).

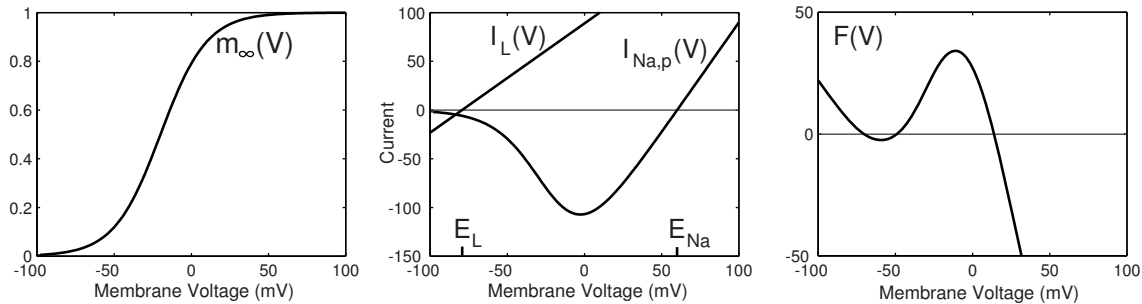


Figure 3.39: The  $I_{Na,p}$ -model with leak current ( $I_L$ ) and persistent Na<sup>+</sup> current ( $I_{Na,p}$ ), described by (3.5) with the right-hand side function  $F(V)$ . Parameters:  $C = 1$ ,  $I = 0$ ,  $g_L = 1$ ,  $E_L = -80$ ,  $g_{Na} = 2.25$ ,  $E_{Na} = 60$ ,  $V_{1/2} = -20$ ,  $k = 15$  (see Fig. 2.20).

9. Draw the bifurcation diagram of the  $I_{Kir}$ -model

$$C \dot{V} = I - g_L(V - E_L) - \overbrace{g_{Kir} h_\infty(V)(V - E_K)}^{\text{instantaneous } I_{Kir}}, \quad (3.11)$$

using parameters from Fig. 3.38 and treating  $I$  as a bifurcation parameter.

10. Derive an explicit formula that relates the position of the equilibrium in the Hodgkin-Huxley model to the magnitude of the injected dc-current  $I$ . Are there any saddle-node bifurcations?
11. Draw the bifurcation diagram of the  $I_{Na,p}$ -model (3.5) using parameters from Fig. 3.39 and treating
  - (a)  $g_L$  as a bifurcation parameter,
  - (b)  $E_L$  as a bifurcation parameter.

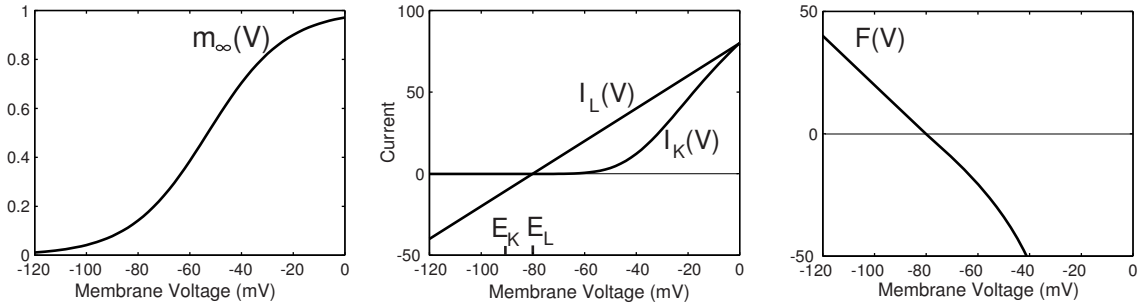


Figure 3.40: The  $I_K$ -model with leak current ( $I_L$ ) and persistent K<sup>+</sup> current ( $I_K$ ), described by (3.12). Parameters:  $C = 1$ ,  $g_L = 1$ ,  $E_L = -80$ ,  $g_K = 1$ ,  $E_K = -90$ ,  $V_{1/2} = -53$ ,  $k = 15$  (see Fig. 2.20).

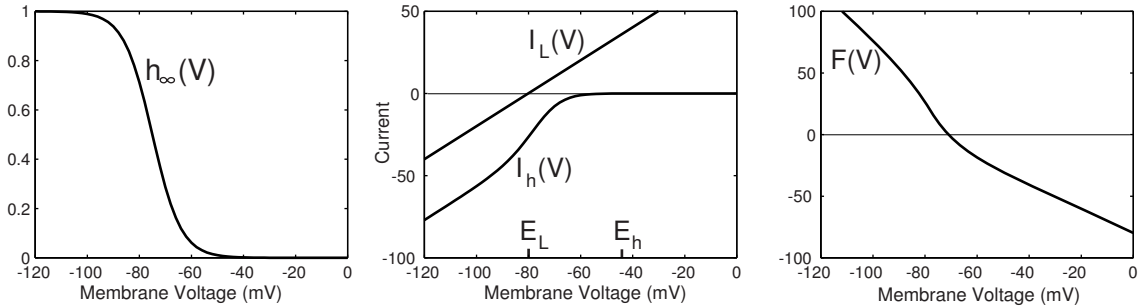


Figure 3.41: The  $I_h$ -model with leak current ( $I_L$ ) and “hyperpolarization-activated” inward current  $I_h$ , described by (3.13). Parameters:  $C = 1$ ,  $g_L = 1$ ,  $E_L = -80$ ,  $g_h = 1$ ,  $E_h = -43$ ,  $V_{1/2} = -75$ ,  $k = -5.5$  (Huguenard and McCormick 1992).

12. Draw the bifurcation diagram of the  $I_{\text{Kir}}$ -model (3.11) using parameters from Fig. 3.38 and treating
  - (a)  $g_L$  as a bifurcation parameter,
  - (b)  $g_{\text{Kir}}$  as a bifurcation parameter.

13. Show that the  $I_K$ -model in Fig. 3.40

$$C \dot{V} = -g_L(V - E_L) - \overbrace{g_K m_\infty^4(V)(V - E_K)}^{\text{instantaneous } I_K}. \quad (3.12)$$

cannot exhibit saddle-node bifurcation for  $V > E_K$ . (Hint: show that  $F'(V) \neq 0$  for all  $V > E_K$ .)

14. Show that the  $I_h$ -model in Fig. 3.41

$$C \dot{V} = -g_L(V - E_L) - \overbrace{g_h h_\infty(V)(V - E_h)}^{\text{instantaneous } I_h} \quad (3.13)$$

cannot exhibit saddle-node bifurcation for any  $V < E_h$ .

15. Prove that the upstroke of the spike in the quadratic integrate-and-fire neuron (3.9) has the asymptote  $1/(c - t)$  for some  $c > 0$ .
16. (Cusp bifurcation) Draw the bifurcation diagram and representative phase portraits of the system  $\dot{x} = a + bx - x^3$ , where  $a$  and  $b$  are bifurcation parameters. Plot the bifurcation diagram in the  $(a, b, x)$ -space and on the  $(a, b)$ -plane.
17. (Gradient systems) An  $n$ -dimensional dynamical system  $\dot{x} = f(x)$ , with  $x = (x_1, \dots, x_n) \in \mathbb{R}^n$  is said to be *gradient* when there is a potential (energy) function  $E(x)$  such that

$$\dot{x} = -\operatorname{grad} E(x),$$

where

$$\operatorname{grad} E(x) = (E_{x_1}, \dots, E_{x_n})$$

is the gradient of  $E(x)$ . Show that all one-dimensional systems are gradient (Hint: see Fig. 3.11). Find potential (energy) functions for the following one-dimensional systems

a. $\dot{V} = 0$ ,	b. $\dot{V} = 1$ ,	c. $\dot{V} = -V$ ,
d. $\dot{V} = -1 + V^2$ ,	e. $\dot{V} = V - V^3$ ,	f. $\dot{V} = -\sin V$ .

18. Consider a dynamical system  $\dot{x} = f(x)$ ,  $x(0) = x_0$ .

- (a) (Stability) An equilibrium  $y$  is *stable* if any solution  $x(t)$  with  $x_0$  sufficiently close to  $y$  remains near  $y$  for all time. That is, for all  $\varepsilon > 0$  there exists  $\delta > 0$  such that if  $|x_0 - y| < \delta$  then  $|x(t) - y| < \varepsilon$  for all  $t \geq 0$ .
- (b) (Asymptotic stability) A stable equilibrium  $y$  is *asymptotically stable* if all solutions starting sufficiently close to  $y$  approach it as  $t \rightarrow \infty$ . That is, if  $\delta > 0$  from the definition above can be chosen so that  $\lim_{t \rightarrow \infty} x(t) = y$ .
- (c) (Exponential stability) A stable equilibrium  $y$  is said to be *exponentially stable* when there is a constant  $a > 0$  such that  $|x(t) - y| < \exp(-at)$  for all  $x_0$  near  $y$  and all  $t \geq 0$ .

Prove that (c) implies (b), and (b) implies (a). Show that (a) does not imply (b) and (b) does not imply (c); That is, present a system having stable but not asymptotically stable equilibrium, and a system having asymptotically but not exponentially stable equilibrium.

19. ( $I_{\text{NMDA}}$ -model) Show that voltage-depended activation of NMDA synaptic receptors in a passive dendritic tree with a constant concentration of glutamate is mathematically equivalent to the  $I_{\text{Na,p}}$ -model.



# Chapter 4

## Two-Dimensional Systems

In this chapter we introduce methods of phase plane analysis of two-dimensional systems. Most concepts will be illustrated using the  $I_{\text{Na,p}}+I_K$ -model in Fig. 4.1:

$$C \dot{V} = I - \underbrace{g_L(V-E_L)}_{\text{leak } I_L} - \underbrace{g_{\text{Na}} m_\infty(V) (V-E_{\text{Na}})}_{\text{instantaneous } I_{\text{Na,p}}} - \underbrace{g_K n (V-E_K)}_{I_K}, \quad (4.1)$$

$$\dot{n} = (n_\infty(V) - n)/\tau(V), \quad (4.2)$$

having leak current  $I_L$ , persistent  $\text{Na}^+$  current  $I_{\text{Na,p}}$  with instantaneous activation kinetic and a relatively slower persistent  $\text{K}^+$  current  $I_K$  with either high (Fig. 4.1a) or low (Fig. 4.1b) threshold (the two choices result in fundamentally different dynamics). The state of the  $I_{\text{Na,p}}+I_K$ -model is a two-dimensional vector  $(V, n) \in \mathbb{R}^2$  on the *phase plane*  $\mathbb{R}^2$ . New types of equilibria, orbits, and bifurcations can exist on the phase plane that cannot exist on the phase line  $\mathbb{R}$ . Many interesting features of single neuron dynamics can be illustrated or explained using two-dimensional systems. Even neuronal bursting, which occurs in multi-dimensional systems, can be understood via bifurcation analysis of two-dimensional systems.

This model is equivalent in many respects to the well-known and widely used  $I_{\text{Ca}}+I_K$ -model proposed by Morris and Lecar (1981) to describe voltage oscillations in the barnacle giant muscle fiber.

### 4.1 Planar Vector Fields

Two-dimensional dynamical systems, also called *planar* systems, are often written in the form

$$\begin{aligned} \dot{x} &= f(x, y), \\ \dot{y} &= g(x, y), \end{aligned}$$

where the functions  $f$  and  $g$  describe the evolution of the two-dimensional state variable  $(x(t), y(t))$ . For any point  $(x_0, y_0)$  on the phase plane the vector  $(f(x_0, y_0), g(x_0, y_0))$

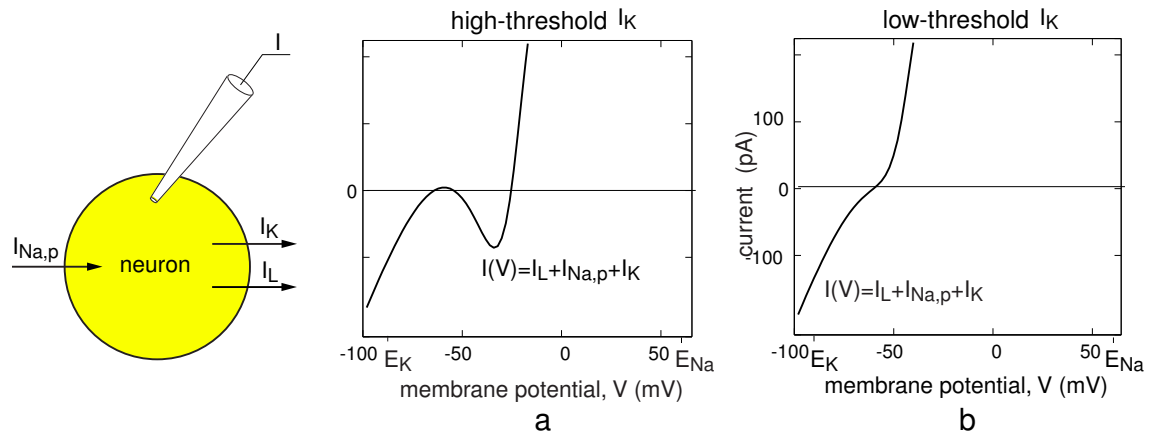


Figure 4.1: The  $I_{\text{Na},p} + I_K$ -model (4.1, 4.2). Parameters in (a):  $C = 1$ ,  $I = 0$ ,  $E_L = -80$  mV,  $g_L = 8$ ,  $g_{\text{Na}} = 20$ ,  $g_K = 10$ ,  $m_\infty(V)$  has  $V_{1/2} = -20$  and  $k = 15$ ,  $n_\infty(V)$  has  $V_{1/2} = -25$  and  $k = 5$ , and  $\tau(V) = 1$ ,  $E_{\text{Na}} = 60$  mV and  $E_K = -90$  mV. Parameters in (b) as in (a) except  $E_L = -78$  mV and  $n_\infty(V)$  has  $V_{1/2} = -45$ ; see Sect. 2.3.5.

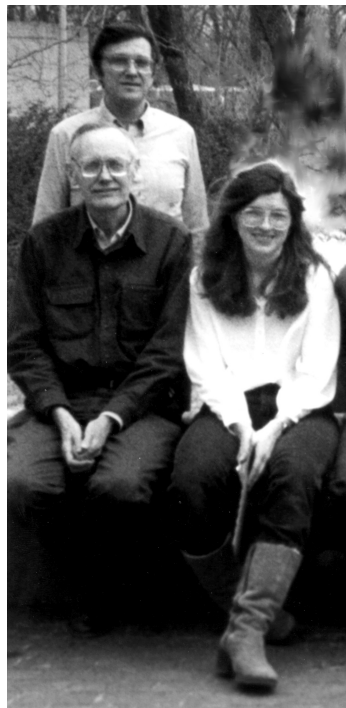


Figure 4.2: Harold Lecar (back), Richard FitzHugh (front), and Cathy Morris at NIH Biophysics Lab, summer of 1983.

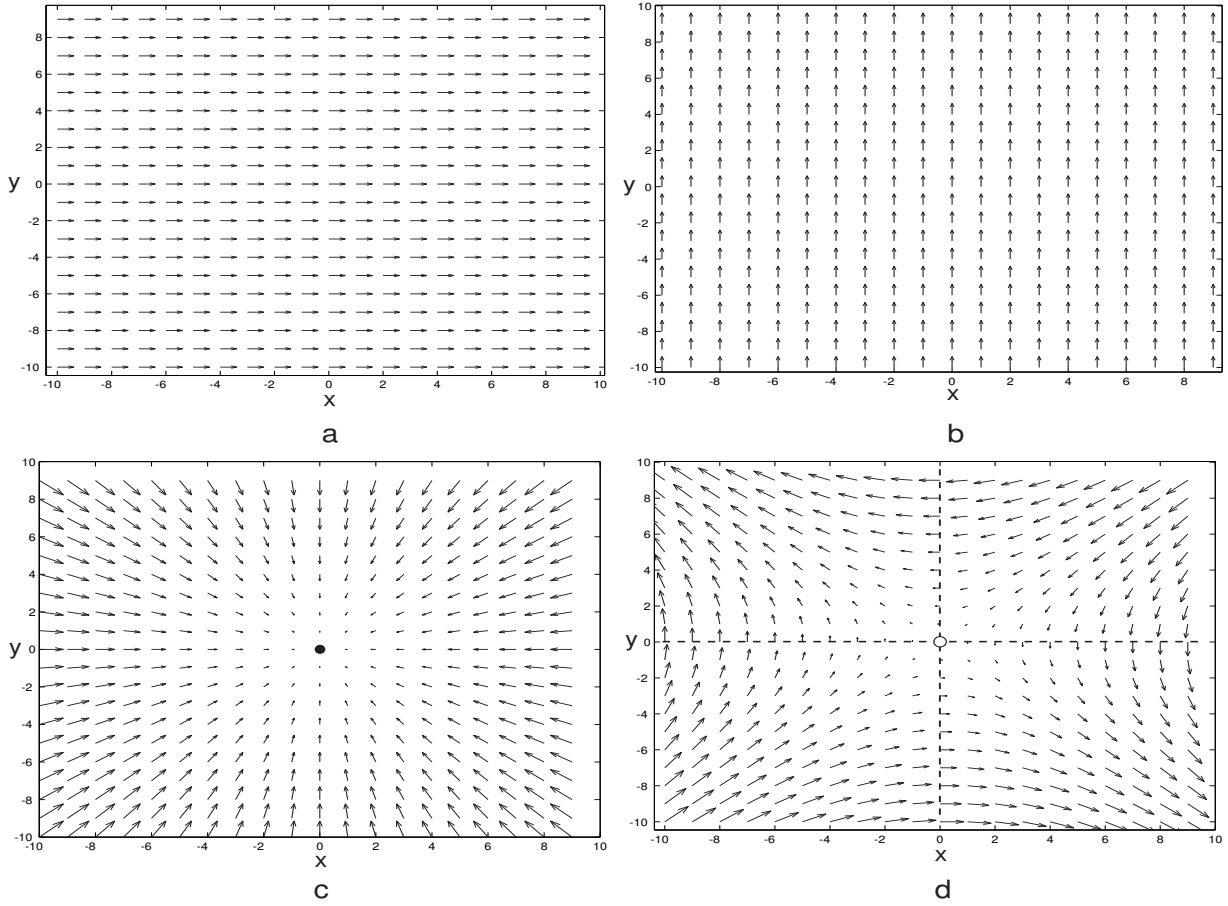


Figure 4.3: Examples of vector fields.

indicates the direction of change of the state variable. For example, negative  $f(x_0, y_0)$  and positive  $g(x_0, y_0)$  imply that  $x(t)$  decreases and  $y(t)$  increases at this particular point. Since each point on the phase plane  $(x, y)$  has its own vector  $(f, g)$ , the system above is said to define a *vector field* on the plane, also known as direction field or velocity field, see Fig. 4.3. Thus, the vector field defines the direction of motion; depending on where you are, it tells you *where you are going*.

Let us consider a few examples. The two-dimensional system

$$\begin{aligned}\dot{x} &= 1, \\ \dot{y} &= 0\end{aligned}$$

defines a constant horizontal vector field in Fig. 4.3a since each point has a horizontal vector  $(1, 0)$  attached to it. (Of course, we depict only a small sample of vectors.) Similarly, the system

$$\begin{aligned}\dot{x} &= 0, \\ \dot{y} &= 1\end{aligned}$$

defines a constant vertical vector field depicted in Fig. 4.3b. The system

$$\begin{aligned}\dot{x} &= -x, \\ \dot{y} &= -y\end{aligned}$$

defines a vector field that points to the origin  $(0, 0)$ , as in Fig. 4.3c, and the system

$$\dot{x} = -y, \tag{4.3}$$

$$\dot{y} = -x \tag{4.4}$$

defines a saddle vector field, as in Fig. 4.3d. Vector fields provide geometrical information about the joint evolution of state variables. For example, the vector field in Fig. 4.3d is directed rightward in the lower half-plane and leftward in the upper half-plane. Therefore the variable  $x(t)$  increases when  $y < 0$  and decreases otherwise, which obviously follows from the equation (4.3). Quite often however geometrical analysis of vector fields can provide information about the behavior of the system that may not be obvious from the form of the functions  $f$  and  $g$ .

### 4.1.1 Nullclines

The vector field in Fig. 4.3d is directed rightward ( $x$  increases) or leftward ( $x$  decreases) in different regions of the phase plane. The set of points where the vector field changes its horizontal direction is called *x-nullcline*, and it is defined by the equation  $f(x, y) = 0$ . Indeed, at any such point  $x$  neither increases nor decreases because  $\dot{x} = 0$ . The *x*-nullcline partitions the phase plane into two regions where  $x$  moves in opposite directions. Similarly, the *y-nullcline* is defined by the equation  $g(x, y) = 0$ , and it denotes the set of points where the vector field changes its vertical direction. This nullcline partitions the phase plane into two regions where  $y$  either increases or decreases. The *x*- and *y*-nullclines partition the phase plane into 4 different regions: (a)  $x$  and  $y$  increase, (b)  $x$  decreases,  $y$  increases, (c)  $x$  and  $y$  decrease, and (d)  $x$  increases,  $y$  decreases, as we illustrate in Fig. 4.4.

Each point of intersection of the nullclines is an *equilibrium point*, since  $f(x, y) = g(x, y) = 0$  and hence  $\dot{x} = \dot{y} = 0$ . Conversely, every equilibrium of a two-dimensional system is the point of intersection of its nullclines. Because nullclines are so important, we consider two examples in detail below (the reader is urged to solve Ex. 1 at the end of this chapter).

Let us determine nullclines of the system (4.3, 4.4) with the vector field shown in Fig. 4.3d. From (4.3) it follows that *x*-nullcline is the horizontal line  $y = 0$ , and from (4.4) it follows that *y*-nullcline is the vertical line  $x = 0$ . These nullclines (dashed lines in Fig. 4.3d) partition the phase plane into 4 quadrants, in each of which the vector field has a different direction. The intersection of the nullclines is the equilibrium  $(0, 0)$ . Later in this chapter we will study how to determine stability of equilibria in two-dimensional systems, though in this particular case one can easily guess that the equilibrium is not stable.

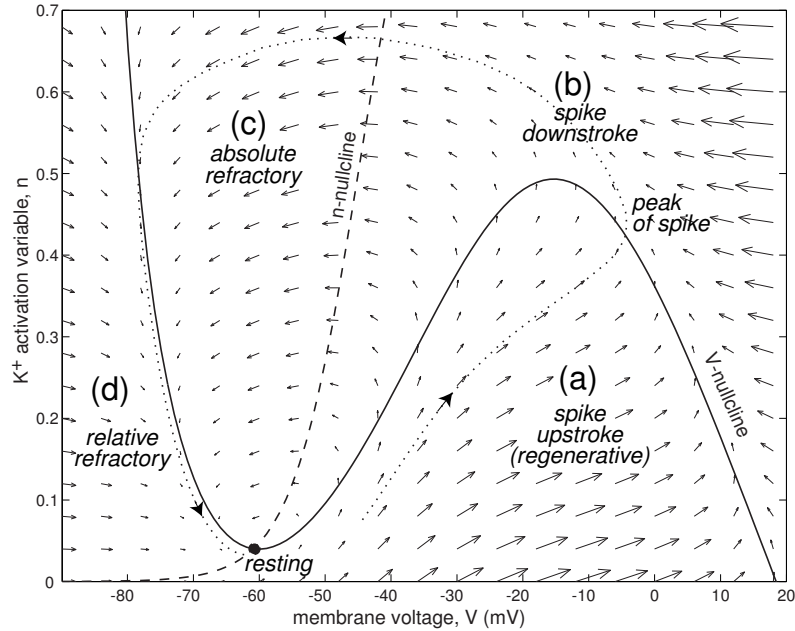


Figure 4.4: Nullclines of the  $I_{\text{Na},p} + I_K$ -model (4.1, 4.2) with low-threshold  $K^+$  current in Fig. 4.1b. (The vector field is slightly distorted for the sake of clarity of illustration).

As another example, let us determine the nullclines of the  $I_{\text{Na},p} + I_K$ -model (4.1, 4.2). The  $V$ -nullcline is given by the equation

$$I - g_L(V - E_L) - g_{\text{Na}} m_\infty(V) (V - E_{\text{Na}}) - g_K n (V - E_K) = 0,$$

which has the solution

$$n = \frac{I - g_L(V - E_L) - g_{\text{Na}} m_\infty(V) (V - E_{\text{Na}})}{g_K (V - E_K)} \quad (\text{V-nullcline})$$

depicted in Fig. 4.4. It typically has the form of a cubic parabola. The equation

$$n_\infty(V) - n = 0$$

defines the  $n$ -nullcline

$$n = n_\infty(V) \quad (\text{n-nullcline}),$$

which coincides with the  $K^+$  steady-state activation function  $n_\infty(V)$ , though only an initial segment of this curve fits in Fig. 4.4. It is easy to see how the  $V$ - and  $n$ -nullclines partition the phase plane into four regions, in each of which the vector field has a different direction:

- (a) Both  $V$  and  $n$  increase: Both  $\text{Na}^+$  and  $K^+$  currents activate and lead to the upstroke of the action potential.
- (b)  $V$  decreases but  $n$  still increases:  $\text{Na}^+$  current deactivates but the slower  $K^+$  current still activates and leads to the downstroke of the action potential.

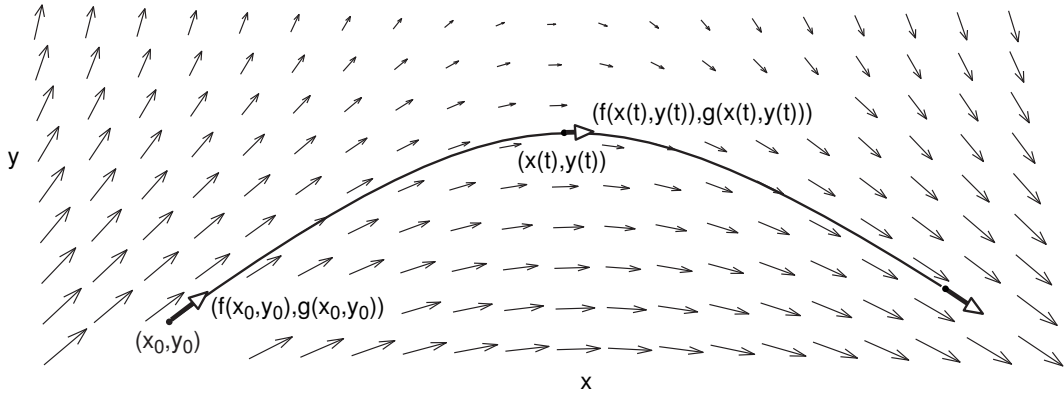


Figure 4.5: Solutions are trajectories tangent to the vector field.

- (c) Both  $V$  and  $n$  decrease: Both  $\text{Na}^+$  and  $\text{K}^+$  currents deactivate while  $V$  is small, leading to a refractory period.
- (d)  $V$  increases but  $n$  still decreases: Partial activation of  $\text{Na}^+$  current combined with further deactivation of the residual  $\text{K}^+$  current lead to a relative refractory period, then to an excitable period, and possibly to another action potential.

The intersection of the  $V$ - and  $n$ -nullclines in Fig. 4.4 is an equilibrium corresponding to the rest state. The number and location of equilibria might be difficult to infer via analysis of equations (4.1, 4.2), but it is a trivial geometrical exercise once the nullclines are determined. Because nullclines are so useful and important in geometrical analysis of dynamical systems, few scientists bother to plot vector fields. Following this tradition, we will not show vector fields in the rest of the book (except for this chapter). Instead, we plot nullclines and representative trajectories, which we discuss next.

### 4.1.2 Trajectories

A vector-function  $(x(t), y(t))$  is a solution of the two-dimensional system

$$\begin{aligned}\dot{x} &= f(x, y), \\ \dot{y} &= g(x, y),\end{aligned}$$

starting with an initial condition  $(x(0), y(0)) = (x_0, y_0)$  when  $dx(t)/dt = f(x(t), y(t))$  and  $dy(t)/dt = g(x(t), y(t))$  at each  $t \geq 0$ . This requirement has a simple geometrical interpretation: A solution is a curve  $(x(t), y(t))$  on the phase plane  $\mathbb{R}^2$  which is tangent to the vector field, as we illustrate in Fig 4.5. Such a curve is often called a *trajectory* or an *orbit*.

One can think of the vector field as a stationary flow of a fluid. Then a solution is just a trajectory of a small particle dropped at a certain (initial) point and carried by the flow. To study the flow, it is useful to drop a few particles and see where they are

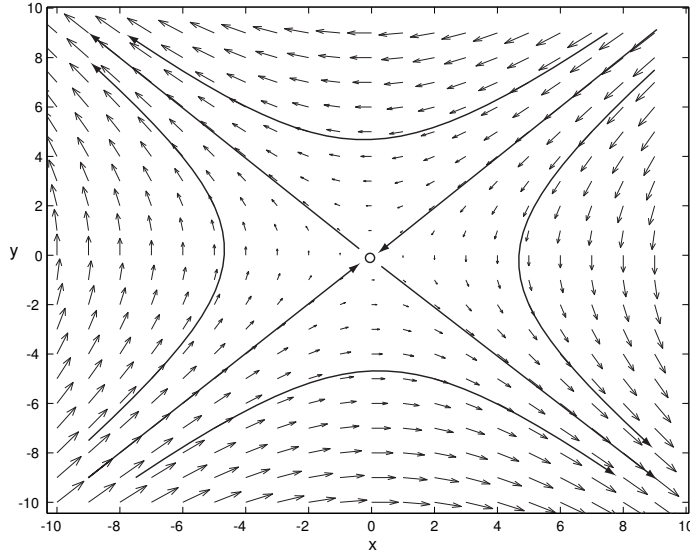


Figure 4.6: Representative trajectories of the two-dimensional system (4.3,4.4).

going. Thus, to understand the geometry of a vector field, it is always useful to plot a few representative trajectories starting from various initial points, as we do in Fig. 4.6. Due to the uniqueness of the solutions, the trajectories cannot cross, so they partition the phase space into various regions. This is an important step toward determining the phase portrait of a two-dimensional system.

Let us return to the  $I_{\text{Na,p}}+I_{\text{K}}$ -model (4.1, 4.2) with low-threshold  $\text{K}^+$  current and explain two odd phenomena discussed in the first chapter: Failure to generate all-or-none action potentials (Fig. 1.5b) and inability to have a fixed value of the threshold voltage. Brief and strong current pulses in Fig. 4.7 reset the value of the voltage variable  $V$  but do not change the value of the  $\text{K}^+$  activation variable  $n$ . Thus, each voltage trace after the pulse corresponds to a trajectory starting with different values of  $V_0$  but the same value  $n_0$ . We see that each trajectory makes a counter-clockwise excursion and returns to the rest state. However, the size of the excursion depends on the initial value of the voltage variable and can be small (subthreshold response), intermediate, or large (action potential). This phenomenon was considered theoretically by FitzHugh in early sixties (see bibliography) and demonstrated experimentally by Cole et al. (1970) using squid giant axon at higher than normal temperatures.

In Fig. 4.8 we apply a long pre-pulse current of various amplitudes to reset the  $\text{K}^+$  activation variable  $n$  to various values, and then a brief strong pulse to reset  $V$  to exactly  $-48$  mV. Each voltage trace after the pulse corresponds to a trajectory starting with the same  $V_0 = -48$  mV, but different values of  $n_0$ . We see that some trajectories return immediately to the rest state while others do so after generating an action potential. Therefore,  $V = -48$  mV is a subthreshold value when  $n_0$  is large, and a superthreshold one otherwise.

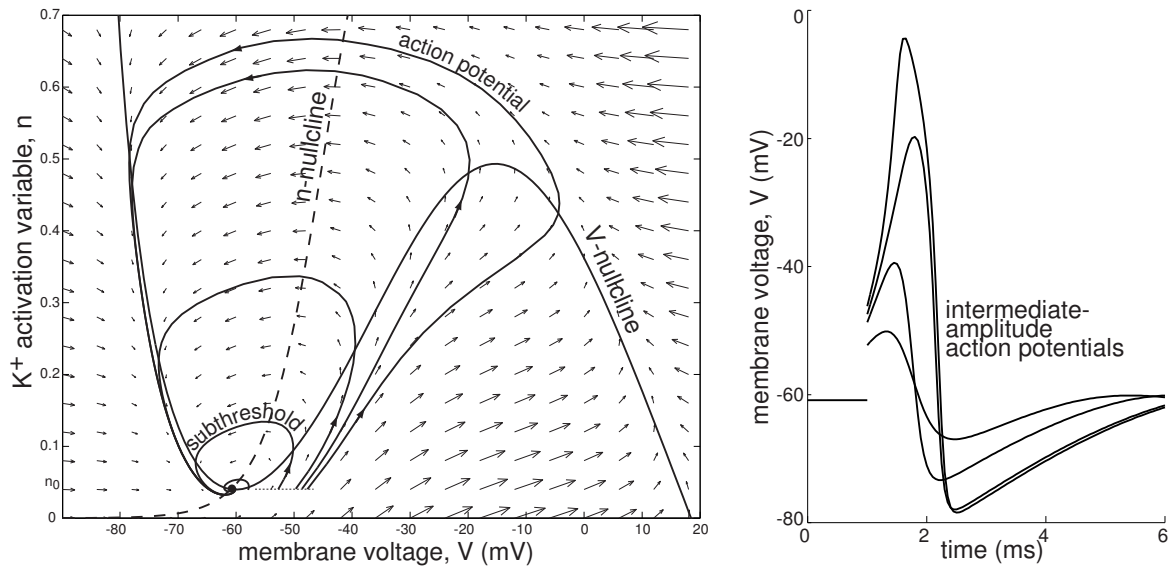


Figure 4.7: Failure to generate all-or-none action potentials in the  $I_{Na,p} + I_K$ -model (4.1, 4.2)

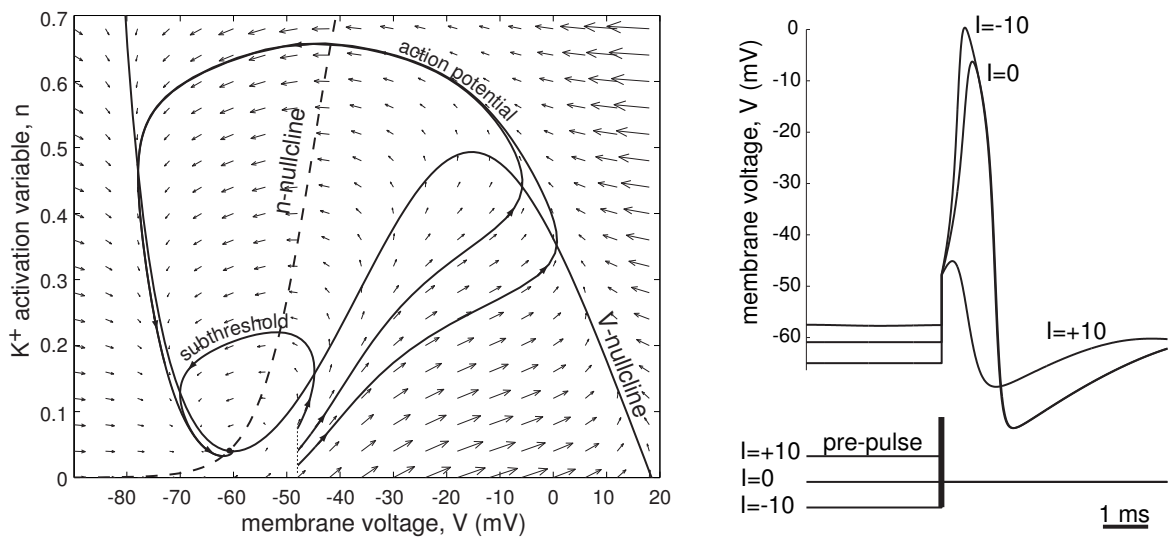


Figure 4.8: Failure to have a fixed value of threshold voltage in the  $I_{Na,p} + I_K$ -model (4.1, 4.2).

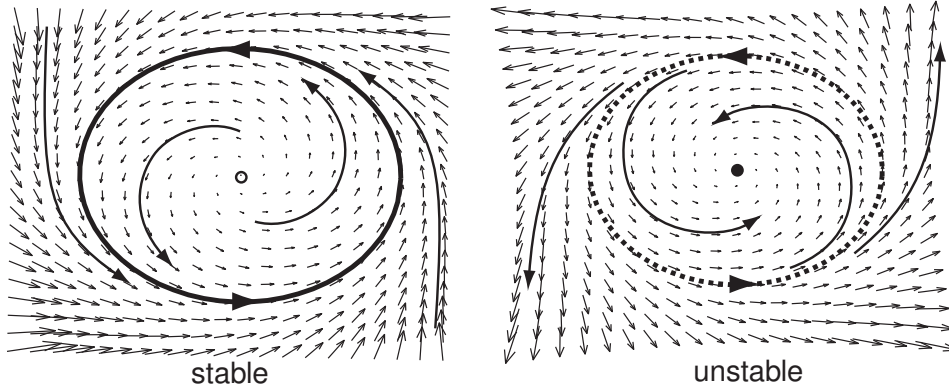


Figure 4.9: Limit cycles (periodic orbits).

### 4.1.3 Limit cycles

A trajectory that forms a closed loop is called a *periodic trajectory* or a *periodic orbit* (the latter is usually reserved for mappings, which we do not consider here). Sometimes periodic trajectories are isolated, as in Fig. 4.9, sometimes they are part of a continuum, as in Fig. 4.13, left. An isolated periodic trajectory is called a *limit cycle*. The existence of limit cycles is a major feature of two-dimensional systems that cannot exist in  $\mathbb{R}^1$ . If the initial point is on a limit cycle, then the solution  $(x(t), y(t))$  stays on the cycle forever, and the system exhibits periodic behavior; i.e.,

$$x(t) = x(t + T) \quad \text{and} \quad y(t) = y(t + T) \quad (\text{for all } t)$$

for some  $T > 0$ . The minimal  $T$  for which this equality holds is called the *period* of the limit cycle. A limit cycle is said to be *asymptotically stable* if any trajectory with the initial point sufficiently near the cycle approaches the cycle as  $t \rightarrow \infty$ . Such asymptotically stable limit cycles are often called *limit cycle attractors*, since they “attract” all nearby trajectories. The stable limit cycle in Fig. 4.9 is an attractor. The limit cycle in Fig. 4.10 is also an attractor; It corresponds to the periodic (tonic) spiking of the  $I_{\text{Na,p}}+I_{\text{K}}$ -model (4.1, 4.2). The unstable limit cycle in Fig. 4.9 is often called a repeller, since it repels all nearby trajectories. Notice that there is always at least one equilibrium inside any limit cycle on a plane.

In Fig. 4.11 we depict limit cycles of three types of neurons recorded *in vitro*. Since we do not know the state of the internal variables, such as the magnitude of the activation and inactivation of  $\text{Na}^+$  and  $\text{K}^+$  currents, we plot the cycles on the  $(V, V')$ -plane, where  $V'$  is the time derivative of  $V$ . The cycles look jerky because of the poor data sampling rate during each spike.

### 4.1.4 Relaxation Oscillators

Many models in science and engineering can be reduced to two-dimensional fast/slow systems of the form

$$\dot{x} = f(x, y) \quad (\text{fast variable})$$

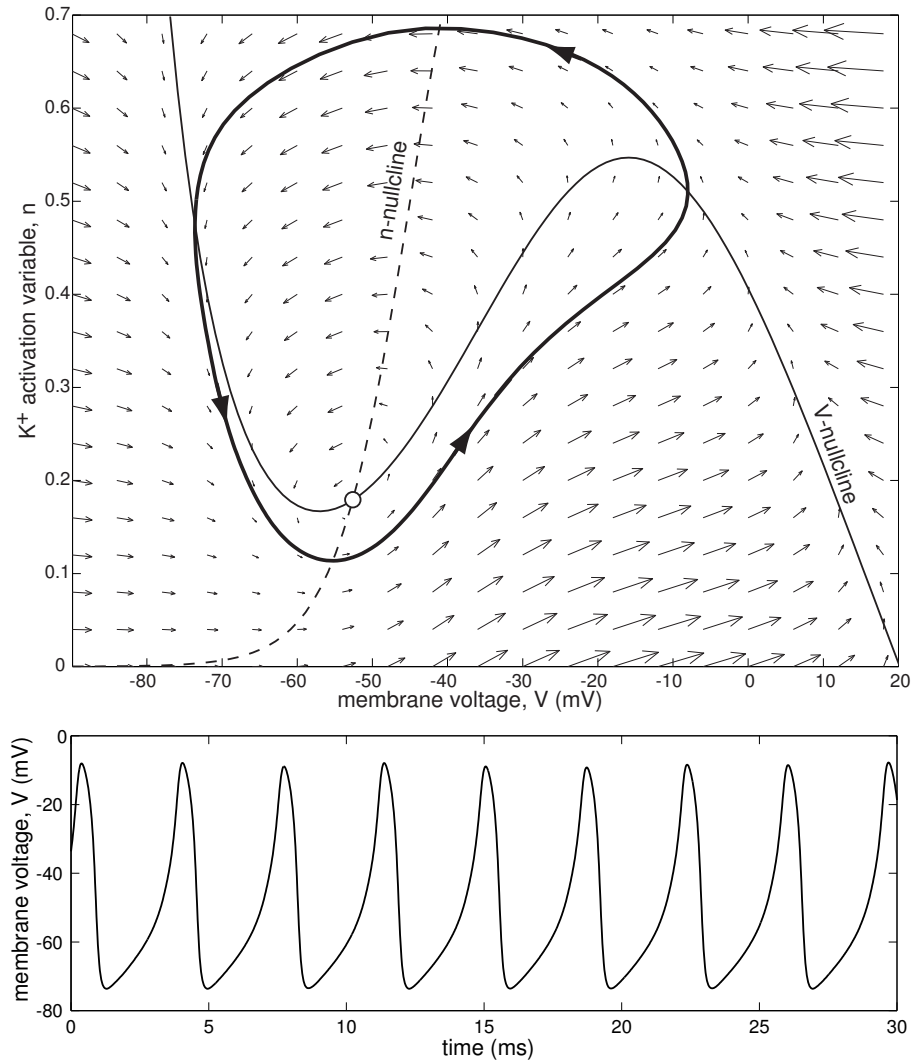


Figure 4.10: Stable limit cycle in the  $I_{Na,p} + I_K$ -model (4.1, 4.2) with low-threshold  $K^+$  current and  $I = 40$ .

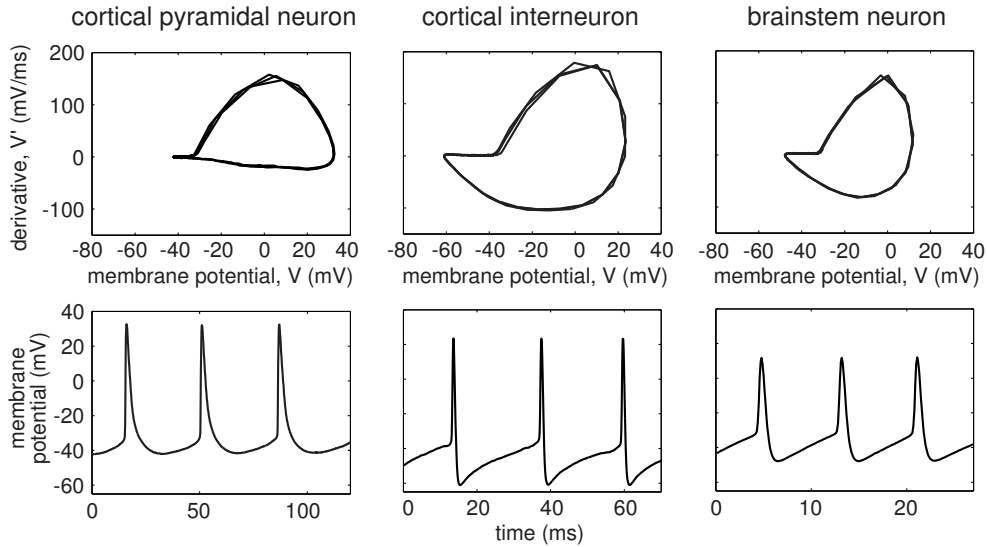


Figure 4.11: Limit cycles corresponding to tonic spiking of three types of neurons recorded *in vitro*.

$$\dot{y} = \mu g(x, y) \quad (\text{slow variable})$$

where small parameter  $\mu$  describes the ratio of time scales of variables  $x$  and  $y$ . Typically, fast variable  $x$  has a cubic-like nullcline that intersects the  $y$ -nullcline somewhere in the middle branch, as in Fig. 4.12a, resulting in *relaxation oscillations*. The periodic trajectory of the system slides down along the left (stable) branch of the cubic nullcline until it reaches the left knee A. At this moment, it quickly jumps to the point B and then slowly slides up along the right (also stable) branch of the cubic nullcline. Upon reaching the right knee C, the system jumps to the left branch and starts to slide down again, thereby completing one oscillation. Relaxation oscillations are easy to grasp conceptually, but some of their features are quite difficult to study mathematically. We consider relaxation oscillations in detail in Sect. 6.3.4.

Notice that the jumps in Fig. 4.12a are nearly horizontal — a distinctive signature of relaxation oscillations that is due to the disparately different time scales in the system. Although many neuronal models have fast and slow time scales and could be reduced to the fast/slow form above, they do not exhibit relaxation oscillations because the parameter  $\mu$  is not small enough. Anybody who records from neurons would probably notice the weird square shape of “spikes” in Fig. 4.12b, something that most biological neurons do not exhibit. Nevertheless, relaxation oscillations in fast/slow systems are important when we consider neuronal bursting in Chap. 9, though the fast variable  $x$  is two-dimensional there.

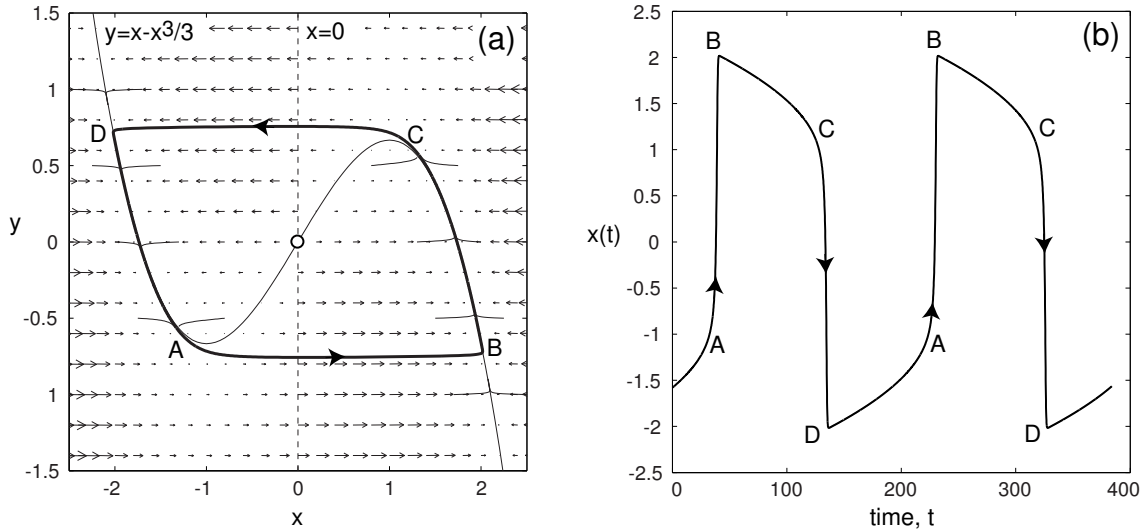


Figure 4.12: Relaxation oscillations in the van der Pol model  $\dot{x} = x - x^3/3 - y$ ,  $\dot{y} = \mu x$  with  $\mu = 0.01$ .

## 4.2 Equilibria

An important step in the analysis of any dynamical system is to find its equilibria, i.e., points where

$$\begin{aligned} f(x, y) &= 0, & (\text{point } (x, y) \text{ is an equilibrium}). \\ g(x, y) &= 0 \end{aligned}$$

As we mentioned before, equilibria are intersections of nullclines. If the initial point  $(x_0, y_0)$  is an equilibrium, then  $\dot{x} = 0$  and  $\dot{y} = 0$ , and the trajectory stays at equilibrium; that is,  $x(t) = x_0$  and  $y(t) = y_0$  for all  $t \geq 0$ . If the initial point is near the equilibrium, then the trajectory may converge to or diverge from the equilibrium depending on its stability.

From the electrophysiological point of view, any equilibrium of a neuronal model is the zero crossing of its steady-state I-V relation  $I_\infty(V)$ . For example, the  $I_{\text{Na,p}} + I_{\text{K}}$ -model (4.1, 4.2) with high-threshold K<sup>+</sup> current has an I-V curve with three zeroes (Fig. 4.1a), hence it has three equilibria: around -66 mV, -56 mV, and -28 mV. In contrast, the same model with low-threshold K<sup>+</sup> current has a monotonic I-V curve with only one zero (Fig. 4.1b), hence it has a unique equilibrium, which is around -61 mV.

### 4.2.1 Stability

In Chap. 3, Exercise 18 we provide rigorous definitions of stability of equilibria in one-dimensional systems. The same definitions apply to higher-dimensional systems.

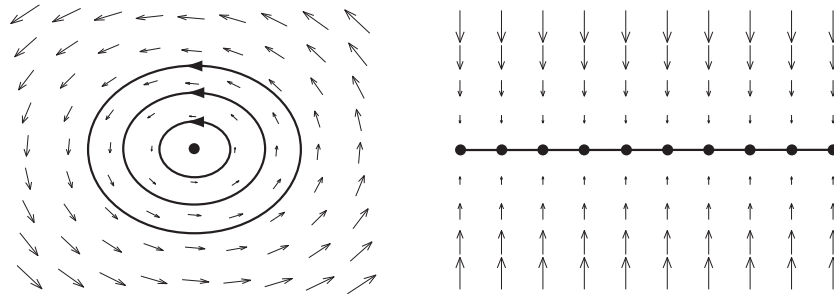


Figure 4.13: Neutrally stable equilibria. Some trajectories neither converge to nor diverge from the equilibria.

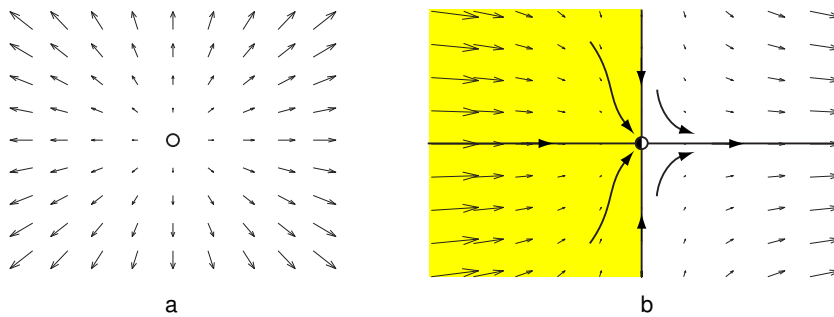


Figure 4.14: Unstable equilibria.

Briefly, an equilibrium is *stable* if any trajectory starting sufficiently close to the equilibrium remains near it for all  $t \geq 0$ . If, in addition, all such trajectories converge to the equilibrium as  $t \rightarrow \infty$ , the equilibrium is *asymptotically stable*, as in Fig. 4.3c. When the convergence rate is exponential or faster, then the equilibrium is said to be *exponentially stable*. Notice that stability does not imply asymptotic stability. For example, all equilibria in Fig. 4.13 are stable but not asymptotically stable. They are often referred to as being *neutrally stable*.

An equilibrium is called *unstable*, if it is not stable. Obviously, if all nearby trajectories diverge from the equilibrium, as in Fig. 4.14a, then it is unstable. This, however, is an exceptional case. For instability it suffices to have at least one trajectory that diverges from the equilibrium no matter how close the initial condition to the equilibrium is, as in Fig. 4.14b. Indeed, any trajectory starting in the shaded area (attraction domain) converges to the equilibrium, but any trajectory starting in the white area diverges from it regardless of how close the initial point to the equilibrium is.

In contrast to the one-dimensional case, the stability of a two-dimensional equilibrium cannot be inferred from the slope of the steady-state I-V curve. For example, the equilibrium around  $-28$  mV in Fig. 4.1a is unstable even though the I-V curve has positive slope.

To determine the stability of an equilibrium, we need to look at the behavior of the two-dimensional vector field in a small neighborhood of the equilibrium. Quite often visual inspection of the vector field does not give conclusive information about stability.

For example, is the equilibrium in Fig. 4.4 stable? What about the equilibrium in Fig. 4.10? The vector fields in the neighborhoods of the two equilibria exhibit subtle differences that are difficult to spot without the help of analytical tools, which we discuss next.

### 4.2.2 Local linear analysis

Below we remind the reader some basic concepts of linear algebra, assuming that the reader has some familiarity with matrices, eigenvectors and eigenvalues. Consider a two-dimensional dynamical system

$$\dot{x} = f(x, y) \quad (4.5)$$

$$\dot{y} = g(x, y) \quad (4.6)$$

having an equilibrium point  $(x_0, y_0)$ . The nonlinear functions  $f$  and  $g$  can be linearized near the equilibrium; i.e., written in the form

$$\begin{aligned} f(x, y) &= a(x - x_0) + b(y - y_0) + \text{higher-order terms}, \\ g(x, y) &= c(x - x_0) + d(y - y_0) + \text{higher-order terms}, \end{aligned}$$

where higher-order terms include  $(x - x_0)^2$ ,  $(x - x_0)(y - y_0)$ ,  $(x - x_0)^3$ , etc., and

$$\begin{aligned} a &= \frac{\partial f}{\partial x}(x_0, y_0), & b &= \frac{\partial f}{\partial y}(x_0, y_0), \\ c &= \frac{\partial g}{\partial x}(x_0, y_0), & d &= \frac{\partial g}{\partial y}(x_0, y_0), \end{aligned}$$

are the partial derivatives of  $f$  and  $g$  with respect of the state variables  $x$  and  $y$  evaluated at the equilibrium  $(x_0, y_0)$  (first, evaluate the derivatives, then substitute  $x = x_0$  and  $y = y_0$ ). Many questions regarding the stability of the equilibrium can be answered by considering the corresponding linear system

$$\dot{u} = au + bw, \quad (4.7)$$

$$\dot{w} = cu + dw, \quad (4.8)$$

where  $u = x - x_0$  and  $w = y - y_0$  are the deviations from the equilibrium, and the higher-order terms,  $u^2$ ,  $uw$ ,  $w^3$ , etc., are neglected. We can write this system in the vector form

$$\begin{pmatrix} \dot{u} \\ \dot{w} \end{pmatrix} = \begin{pmatrix} a & b \\ c & d \end{pmatrix} \begin{pmatrix} u \\ w \end{pmatrix}.$$

The linearization matrix

$$L = \begin{pmatrix} a & b \\ c & d \end{pmatrix}$$

is called the *Jacobian matrix* of the system (4.5, 4.6) at the equilibrium  $(x_0, y_0)$ . For example, the Jacobian matrix of the system (4.3, 4.4) at the origin is

$$\begin{pmatrix} 0 & -1 \\ -1 & 0 \end{pmatrix}. \quad (4.9)$$

It is important to remember that Jacobian matrices are defined for equilibria, and that a nonlinear system can have many equilibria and hence many different Jacobian matrices.

### 4.2.3 Eigenvalues and eigenvectors

A non-zero vector  $v \in \mathbb{R}^2$  is said to be an *eigenvector* of the matrix  $L$  corresponding to the *eigenvalue*  $\lambda$  if

$$Lv = \lambda v \quad (\text{matrix notation}).$$

For example, the matrix (4.9) has two eigenvectors

$$v_1 = \begin{pmatrix} 1 \\ 1 \end{pmatrix} \quad \text{and} \quad v_2 = \begin{pmatrix} 1 \\ -1 \end{pmatrix}$$

corresponding to the eigenvalues  $\lambda_1 = -1$  and  $\lambda_2 = 1$ , respectively. Any textbook on linear algebra explains how to find eigenvectors and eigenvalues of an arbitrary matrix. It is important for the reader to get comfortable with these notions, since they are used extensively in the rest of the book.

Eigenvalues play important role in analysis of stability of equilibria. To find the eigenvalues of a  $2 \times 2$ -matrix  $L$ , one solves the *characteristic equation*

$$\det \begin{pmatrix} a - \lambda & b \\ c & d - \lambda \end{pmatrix} = 0.$$

This equation can be written in the polynomial form  $(a - \lambda)(d - \lambda) - bc = 0$  or

$$\lambda^2 - \tau\lambda + \Delta = 0,$$

where

$$\tau = \text{tr } L = a + d \quad \text{and} \quad \Delta = \det L = ad - bc$$

are the *trace* and the *determinant* of the matrix  $L$ , respectively. Such a quadratic polynomial has two solutions of the form

$$\lambda_1 = \frac{\tau + \sqrt{\tau^2 - 4\Delta}}{2} \quad \text{and} \quad \lambda_2 = \frac{\tau - \sqrt{\tau^2 - 4\Delta}}{2} \quad (4.10)$$

and they are either real (when  $\tau^2 - 4\Delta \geq 0$ ) or complex-conjugate (when  $\tau^2 - 4\Delta < 0$ ). What can you say about the case  $\tau^2 = 4\Delta$ ?

In general,  $2 \times 2$ -matrices have two eigenvalues with distinct (independent) eigenvectors. In this case a general solution of the linear system has the form

$$\begin{pmatrix} u(t) \\ w(t) \end{pmatrix} = c_1 e^{\lambda_1 t} v_1 + c_2 e^{\lambda_2 t} v_2 ,$$

where  $c_1$  and  $c_2$  are constants that depend on the initial condition. This formula is valid for real and complex-conjugate eigenvalues. When both eigenvalues are negative (or have negative real parts),  $u(t) \rightarrow 0$  and  $w(t) \rightarrow 0$ , meaning  $x(t) \rightarrow x_0$  and  $y(t) \rightarrow y_0$ , so that the equilibrium  $(x_0, y_0)$  is exponentially (and hence asymptotically) stable. It is unstable when at least one eigenvalue is positive or has a positive real part. We denote stable equilibria as filled circles  $\bullet$  and unstable equilibria as open circles  $\circ$  throughout the book.

#### 4.2.4 Local equivalence

An equilibrium whose Jacobian matrix does not have zero eigenvalues or eigenvalues with zero real part is called *hyperbolic*. Such an equilibrium can be stable or unstable. The Hartman-Grobman theorem states that the vector-field and hence the dynamics of a nonlinear system, e.g., (4.5, 4.6) near such a hyperbolic equilibrium is topologically equivalent to that of its linearization (4.7, 4.8). That is, the higher-order terms that are neglected when (4.5, 4.6) is substituted by (4.7, 4.8) do not play any qualitative role. Thus, understanding and classifying the geometry of vector-fields of linear systems provides an exhaustive description of all possible behaviors of nonlinear systems near hyperbolic equilibria.

A zero eigenvalue (or eigenvalues with zero real parts) arise when the equilibrium undergoes a bifurcation, e.g., as in Fig. 4.14b, and such equilibria are called non-hyperbolic. Linear analysis cannot answer the question of stability of a nonlinear system in this case, since small nonlinear (high-order) terms play a crucial role here. We denote equilibria undergoing a bifurcation as half-filled circles, e.g.,  $\bullet\circ$ .

#### 4.2.5 Classification of equilibria

Besides defining the stability of an equilibrium, the eigenvalues also define the geometry of the vector field near the equilibrium, as we illustrate in Fig. 4.15 and ask the reader to prove in Ex. 4. (The proof is a straightforward consequence of (4.10)). There are three major types of equilibria:

**Node (Fig. 4.16):** The eigenvalues are real and of the same sign. The node is stable when the eigenvalues are negative, and unstable when they are positive. The trajectories tend to converge to or diverge from the node along the eigenvector corresponding to the eigenvalue having the smallest absolute value.

**Saddle (Fig. 4.17):** The eigenvalues are real and of opposite signs. Saddles are always unstable, since one of the eigenvalues is always positive. Most trajectories

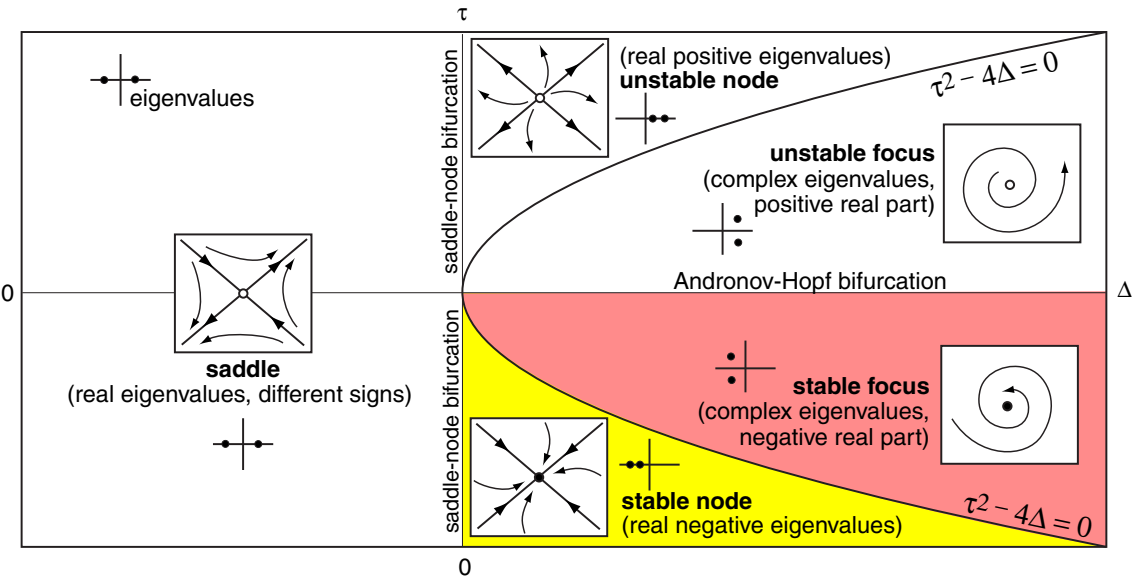


Figure 4.15: Classification of equilibria according to the trace ( $\tau$ ) and the determinant ( $\Delta$ ) of the Jacobian matrix  $L$ . The shaded region corresponds to stable equilibria.

approach the saddle equilibrium along the eigenvector corresponding to the negative (stable) eigenvalue and then diverge from it along the eigenvector corresponding to the positive (unstable) eigenvalue.

**Focus (Fig. 4.18):** The eigenvalues are complex-conjugate. Foci are stable when the eigenvalues have negative real parts, and unstable when the eigenvalues have positive real parts. The imaginary part of the eigenvalues determines the frequency of rotation of trajectories around the focus equilibrium.

When the system undergoes a saddle-node bifurcation, one of the eigenvalues becomes zero and a mixed type of equilibrium occurs — saddle-node equilibrium, illustrated in Fig. 4.14b. There could be other types of mixed equilibria, such as saddle-focus, focus-node, etc., in dynamical systems having dimension three and higher.

Depending upon the value of the injected current  $I$ , the  $I_{\text{Na,p}} + I_K$ -model (4.1, 4.2) with a low-threshold  $K^+$  current has a stable focus (Fig. 4.8) or an unstable focus (Fig. 4.10) surrounded by a stable limit cycle. In Fig. 4.19 we depict the vector field and nullclines of the same model with a high-threshold  $K^+$  current. As one expects from the shape of the steady-state I-V curve in Fig. 4.1a, the model has three equilibria: a stable node, a saddle, and an unstable focus. Notice that the third equilibrium is unstable even though the I-V relation has a positive slope around it.

Also notice that the  $y$ -axis starts at the negative value -0.1. However, the gating variable  $n$  represents the proportion (probability) of the  $K^+$  channels in the open state, hence a value less than zero has no physical meaning. So while we can happily calculate the nullclines for the negative  $n$ , and even start the trajectory with initial condition

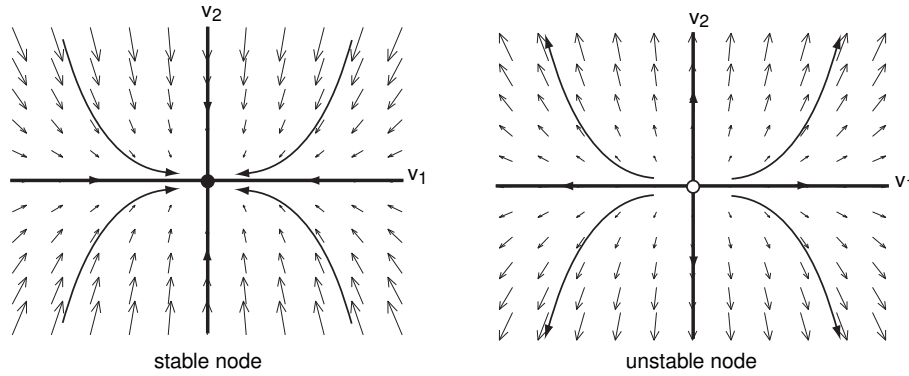


Figure 4.16: Node equilibrium occurs when both eigenvalues are real and have the same sign, e.g.,  $\lambda_1 = -1$  and  $\lambda_2 = -3$  (stable) or  $\lambda_1 = +1$  and  $\lambda_2 = +3$  (unstable). Most trajectories converge to or diverge from the node along the eigenvector  $v_1$  corresponding to the eigenvalue having the smallest absolute value.

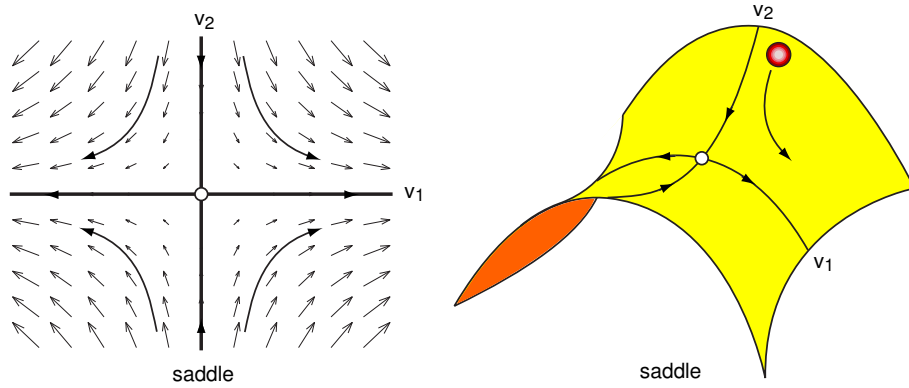


Figure 4.17: Saddle equilibrium occurs when two real eigenvalues have opposite signs, e.g.,  $\lambda_1 = +1$  and  $\lambda_2 = -1$ . Most trajectories diverge from the equilibrium along the eigenvector corresponding to the positive eigenvalue (in this case  $v_1$ ).

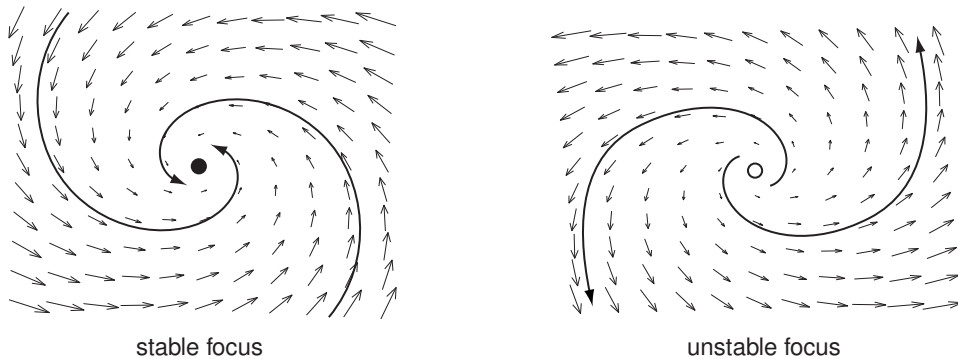


Figure 4.18: Focus equilibrium occurs when the eigenvalues are complex-conjugate, e.g.,  $\lambda = -3 \pm i$  (stable) or  $\lambda = +3 \pm i$  (unstable). The imaginary part (here 1) determines the frequency of rotation around the focus.

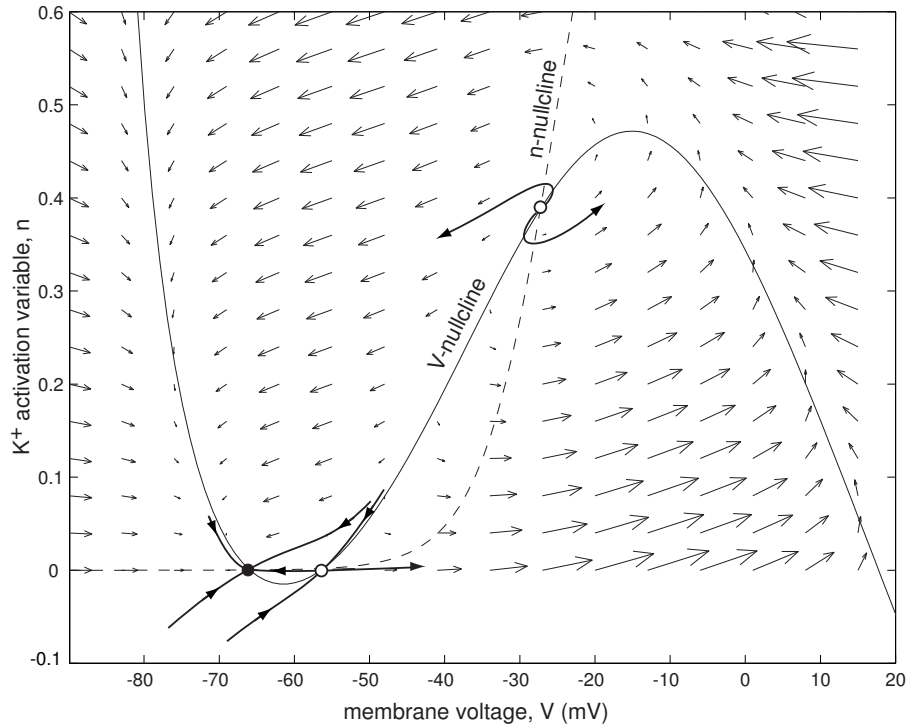


Figure 4.19: Phase portrait of the  $I_{\text{Na},p} + I_K$ -model having high-threshold  $K^+$  current.

$n < 0$ , we cannot interpret the result. As an exercise, prove that if all gating variables of a model are initially in the range  $[0, 1]$ , then they stay in the range for all  $t \geq 0$ .

#### 4.2.6 Example: FitzHugh-Nagumo model

The FitzHugh-Nagumo model (FitzHugh 1961, Nagumo et al. 1962)

$$\dot{V} = V(a - V)(V - 1) - w + I, \quad (4.11)$$

$$\dot{w} = bV - cw, \quad (4.12)$$

imitates generation of action potentials by Hodgkin-Huxley-type models having cubic (N-shaped) nullclines as in Fig. 4.4. Here  $V$  mimics the membrane voltage and the “recovery” variable  $w$  mimics activation of an outward current. Parameter  $I$  mimics the injected current, and for the sake of simplicity we set  $I = 0$  in our analysis below. Parameter  $a$  describes the shape of the cubic parabola  $V(a - V)(V - 1)$ , and parameters  $b > 0$  and  $c \geq 0$  describe the kinetics of the recovery variable  $w$ . When  $b$  and  $c$  are small, the model may exhibit relaxation oscillations.

The nullclines of the FitzHugh-Nagumo model have the cubic and linear form

$$\begin{aligned} w &= V(a - V)(V - 1) + I && (V\text{-nullcline}), \\ w &= b/c V && (w\text{-nullcline}), \end{aligned}$$

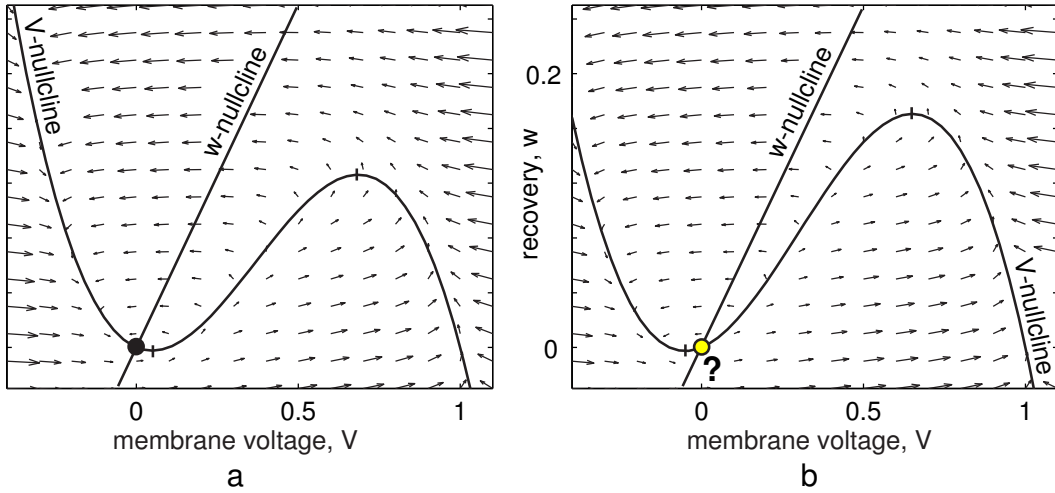


Figure 4.20: Nullclines in the FitzHugh-Nagumo model (4.11, 4.12). Parameters:  $I = 0, b = 0.01, c = 0.02, a = 0.1$  (left) and  $a = -0.1$  (right).

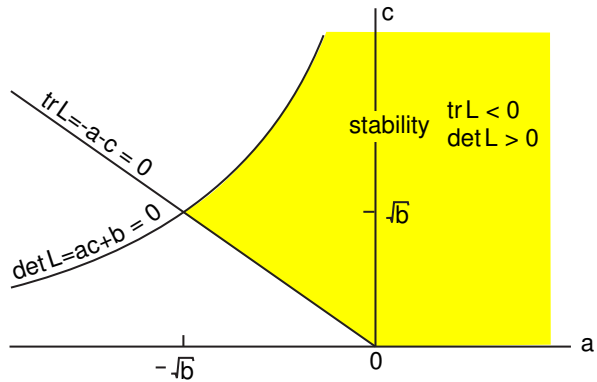


Figure 4.21: Stability diagram of the equilibrium  $(0,0)$  in the FitzHugh-Nagumo model (4.11,4.12).

and they can intersect in one, two, or three points resulting in one, two, or three equilibria, all of which may be unstable. Below we consider the simple case  $I = 0$ , so that the origin,  $(0,0)$ , is an equilibrium. Indeed, the nullclines of the model, depicted in Fig. 4.20, always intersect at  $(0,0)$  in this case. The intersection may occur on the left (Fig. 4.20a) or middle (Fig. 4.20b) branch of the cubic  $V$ -nullcline depending on the sign of the parameter  $a$ . Let us determine how the stability of the equilibrium  $(0,0)$  depends on the parameters  $a$ ,  $b$ , and  $c$ .

There is a common dogma that the equilibrium in Fig. 4.20a corresponding to  $a > 0$  is always stable, the equilibrium in Fig. 4.20b corresponding to  $a < 0$  is always unstable, and the loss of stability occurs “exactly” at  $a = 0$ , i.e., at the bottom of the left knee. Let us check that this is not necessarily true, at least when  $c \neq 0$ . The Jacobian matrix of the FitzHugh-Nagumo model (4.11,4.12) at the equilibrium  $(0,0)$  has the form

$$L = \begin{pmatrix} -a & -1 \\ b & -c \end{pmatrix}.$$

It is easy to check that

$$\tau = \text{tr } L = -a - c \quad \text{and} \quad \Delta = \det L = ac + b.$$

Using Fig. 4.15 we conclude that the equilibrium is stable when  $\text{tr } L < 0$  and  $\det L > 0$ , which corresponds to the shaded region in Fig. 4.21. Both conditions are always satisfied when  $a > 0$ , hence the equilibrium in Fig. 4.20a is indeed stable. However, both conditions may also be satisfied for negative  $a$ , therefore, the equilibrium in Fig. 4.20b may also be stable. Thus, the equilibrium loses stability not at the left knee, but slightly to the right of it, so that a part of the “unstable branch” of the cubic nullcline is actually stable. The part is small when  $b$  and  $c$  are small, i.e., when (4.11,4.12) is in a relaxation regime.

## 4.3 Phase Portraits

An important step in geometrical analysis of dynamical systems is sketching of their phase portraits. The *phase portrait* of a two-dimensional system is a partitioning of the phase plane into orbits or trajectories. Instead of depicting all possible trajectories, it usually suffices to depict some representative trajectories. The phase portrait contains all important information about qualitative behavior of the dynamical system, such as relative location and stability of equilibria, their attraction domains, separatrices, limit cycles, and other special trajectories that are discussed in this section.

### 4.3.1 Bistability and attraction domains

Non-linear two-dimensional systems can have many co-existing attractors. For example, the FitzHugh-Nagumo model (4.11,4.12) with nullclines depicted in Fig. 4.22 has two stable equilibria separated by an unstable equilibrium. Such a system is called *bistable* (*multi-stable* when there are more than two attractors). Depending on the initial conditions, the trajectory may approach the left or right equilibrium. The shaded area denotes the *attraction domain* of the right equilibrium; that is, the set of all initial conditions that lead to this equilibrium. Since there are only two attractors, the complementary white area denotes the attraction domain of the other equilibrium. The domains are separated not by equilibria as in one-dimensional case, but by special trajectories called *separatrices*, which we discuss in Sect. 4.3.2.

Many neural models are bistable or can be made bistable when the parameters have appropriate values. Often bistability results from the co-existence of an equilibrium attractor corresponding to the rest state and a limit cycle attractor corresponding to the repetitive firing state. Fig. 4.23 depicts one of many possible cases. Here we use the  $I_{\text{Na,p}}+I_K$ -model with a high-threshold fast  $K^+$  current. The rest state exists due to the balance of partially activated  $\text{Na}^+$  and leak currents. The repetitive spiking state persists because the  $K^+$  current deactivates too fast and cannot bring the membrane potential into the subthreshold voltage range. If the initial state is in the shaded area,

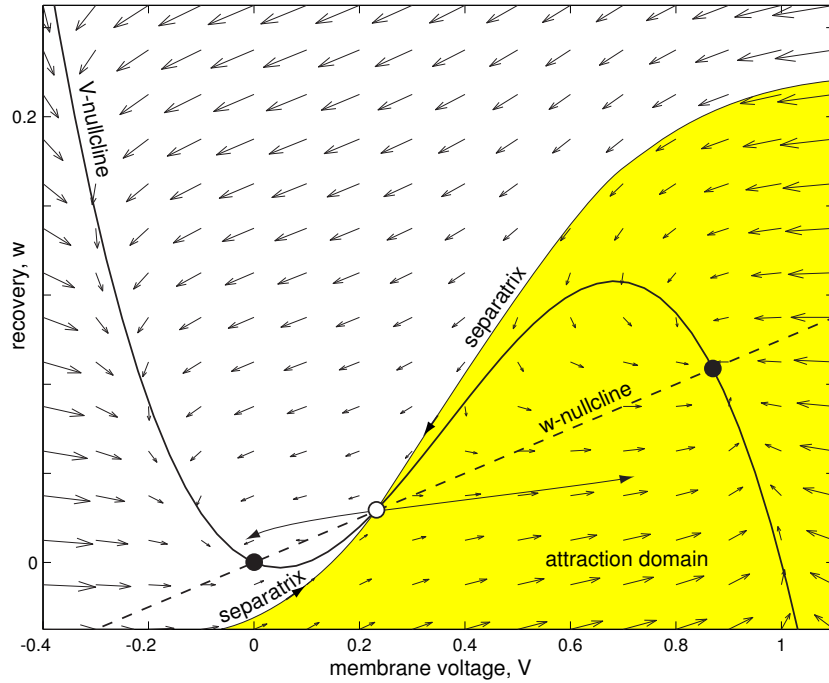


Figure 4.22: Bistability of two equilibrium attractors (black circles) in the FitzHugh-Nagumo model (4.11,4.12). The shaded area — attraction domain of the right equilibrium. Parameters:  $I = 0$ ,  $b = 0.01$ ,  $a = c = 0.1$ .

which is the attraction domain of the limit cycle attractor, the trajectory approaches the limit cycle attractor and the neuron fires an infinite train of action potentials.

### 4.3.2 Stable/unstable manifolds

In contrast to one-dimensional systems, in two-dimensional systems unstable equilibria do not necessarily separate attraction domains. Nevertheless, they play an important role in defining the boundary of attraction domains, as in Fig. 4.22 and Fig. 4.23. In both cases the attraction domains are separated by a pair of trajectories, called *separatrices*, which converge to the saddle equilibrium. Such trajectories form the *stable manifold* of a saddle point. Locally, the manifold is parallel to the eigenvector corresponding to the negative (stable) eigenvalue; see Fig. 4.24. Similarly, the *unstable manifold* of a saddle is formed by the two trajectories that originate exactly from the saddle (or approach the saddle if the time is reversed). Locally, the unstable manifold is parallel to the eigenvector corresponding to the positive (unstable) eigenvalue.

The stable manifold of the saddle in Fig. 4.23 plays the role of a threshold, since it separates rest and spiking states. We illustrate this concept in Fig. 4.24: If the initial state of the system, denoted as A, is in the shaded area, the trajectory will converge to the spiking attractor (right) no matter how close the initial condition to the stable manifold is. In contrast, if the initial condition, denoted as B, is in the white area, the

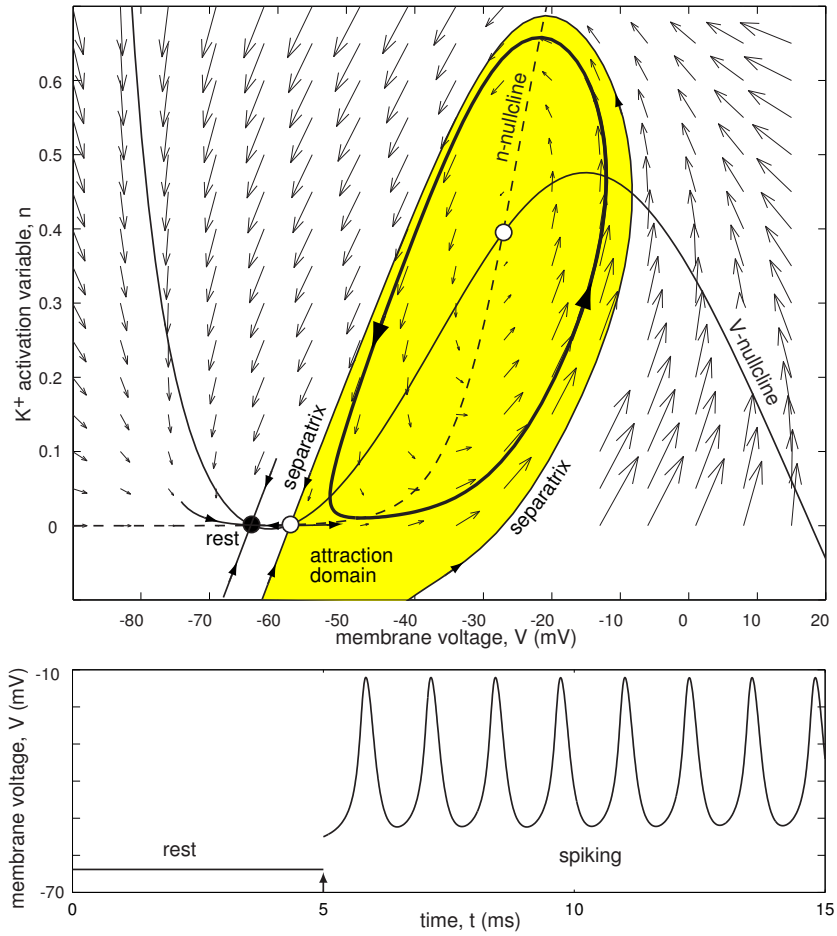


Figure 4.23: Bistability of rest and spiking states in the  $I_{Na,p} + I_K$ -model (4.1, 4.2) with high-threshold fast ( $\tau(V) = 0.152$ )  $K^+$  current and  $I = 3$ . A brief strong pulse of current (arrow) brings the state vector of the system into the attraction domain of the stable limit cycle.

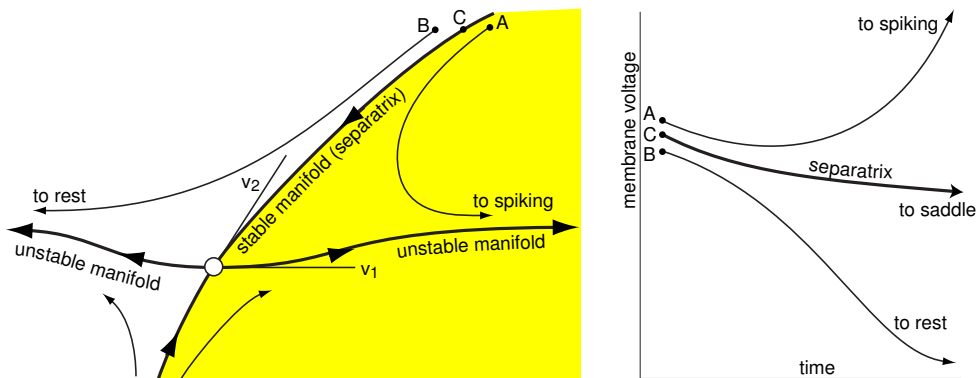


Figure 4.24: Stable and unstable manifolds to a saddle. The eigenvectors  $v_1$  and  $v_2$  correspond to positive and negative eigenvalues, respectively.

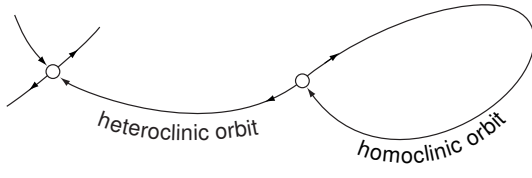


Figure 4.25: A heteroclinic orbit starts and ends at different equilibria. A homoclinic orbit starts and ends at the same equilibrium.

trajectory will converge to the rest attractor (left). If the initial condition is precisely on the stable manifold (point C), the trajectory converges neither to rest nor to spiking state, but to the saddle equilibrium. Of course, this case is highly unstable and small perturbations will certainly push the trajectory to one or the other side. The important message in Fig. 4.24 is that a threshold is not a point, i.e., a single voltage value, but a trajectory on the phase plane. (Find an exceptional case when the threshold looks like a single voltage value. Hint: see Fig. 4.17.)

### 4.3.3 Homoclinic/heteroclinic trajectories

Fig. 4.24 shows that trajectories forming the unstable manifold originate from the saddle. Where do they go? Similarly, the trajectories forming the stable manifold terminate at the saddle. Where do they come from? We say that a trajectory is *heteroclinic* if it originates at one equilibrium and terminates at another equilibrium, as in Fig. 4.25. A trajectory is *homoclinic* if it originates and terminates at the same equilibrium. These types of trajectories play an important role in geometrical analysis of dynamical systems.

Heteroclinic trajectories connect unstable and stable equilibria, as in Fig. 4.26, and they are ubiquitous in dynamical systems having two or more equilibrium points. In fact, there are infinitely many heteroclinic trajectories in Fig. 4.26, since all trajectories inside the bold loop originate at the unstable focus and terminate at the stable node. (Find the exceptional trajectory that ends elsewhere.)

In contrast, homoclinic trajectories are rare. First, a homoclinic trajectory diverges from an equilibrium, therefore the equilibrium must be unstable. Next, the trajectory makes a loop and returns to the same equilibrium, as in Fig. 4.27. It needs to hit the unstable equilibrium precisely, since a small error would make it deviate from the unstable equilibrium. Though uncommon, homoclinic trajectories indicate that the system undergoes a bifurcation — appearance or disappearance of a limit cycle. The homoclinic trajectory in Fig. 4.27 indicates that the limit cycle in Fig. 4.23 is about to (dis)appear via *saddle homoclinic orbit* bifurcation. The homoclinic trajectory in Fig. 4.28 indicates that a limit cycle is about to (dis)appear via *saddle-node on invariant circle* bifurcation. We study these bifurcations in detail in Chap. 6.

### 4.3.4 Saddle-node bifurcation

In Fig. 4.29 we simulate the injection of a ramp current  $I$  into the  $I_{\text{Na,p}}+I_{\text{K}}$ -model having high-threshold  $\text{K}^+$  current. Our goal is to understand the transition from the

rest state to repetitive spiking. When  $I$  is small, the phase portrait of the model is similar to the one depicted in Fig. 4.26 for  $I = 0$ . There are two equilibria in the low-voltage range — a stable node corresponding to the rest state and a saddle. The equilibria are the intersections of the cubic  $V$ -nullcline and the  $n$ -nullcline. Increasing the parameter  $I$  changes the shape of the cubic nullcline and shifts it upward, but does not change the  $n$ -nullcline. As a result, the distance between the equilibria decreases, until they coalesce as in Fig. 4.28 so that the nullclines only touch each other in the low-voltage range. Further increase of  $I$  results in the disappearance of the saddle and node equilibrium, and hence in the disappearance of the rest state. The new phase portrait is depicted in Fig. 4.30; it has only a limit cycle attractor corresponding to repetitive firing. We see that increasing  $I$  past the value  $I = 4.51$  results in transition from rest to periodic spiking dynamics. What kind of a bifurcation occurs when  $I = 4.51$ ?

Those readers who did not skip Sect. 3.3.3 in the previous chapter will immediately recognize the saddle-node bifurcation, whose major stages are summarized in Fig. 4.31. As a bifurcation parameter changes, the saddle and the node equilibrium approach each other, coalesce, and then annihilate each other so there are no equilibria left. When coalescent, the joint equilibrium is neither a saddle nor a node, but a *saddle-node*. Its major feature is that it has precisely one zero eigenvalue, and it is stable on one side of the neighborhood and unstable on the other side. In Chap. 6 we will provide an exact definition of a saddle-node bifurcation in a multi-dimensional system, and we will show that there are two important subtypes of this bifurcation, resulting in slightly different

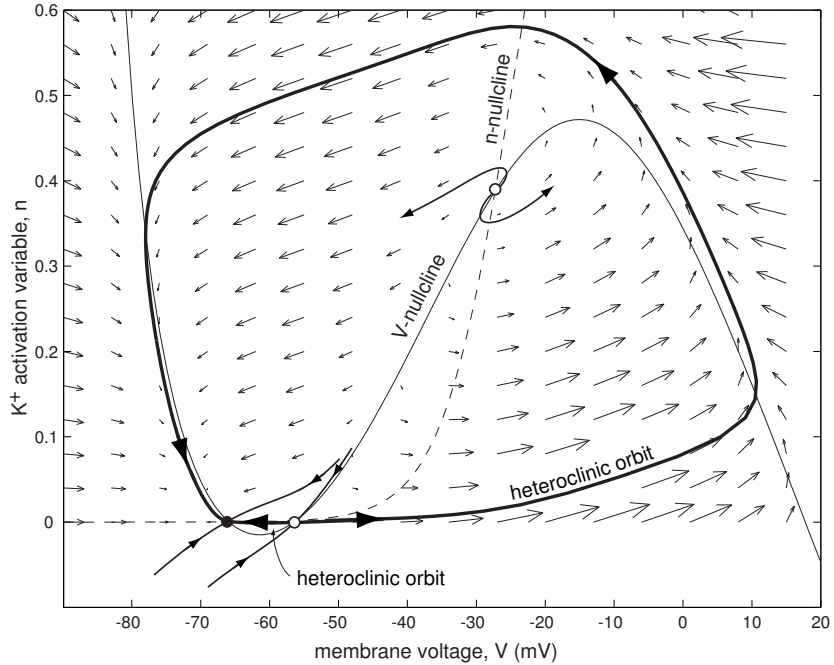


Figure 4.26: Two heteroclinic orbits (bold curves connecting stable and unstable equilibria) in the  $I_{Na,p} + I_K$ -model with high-threshold  $K^+$  current.

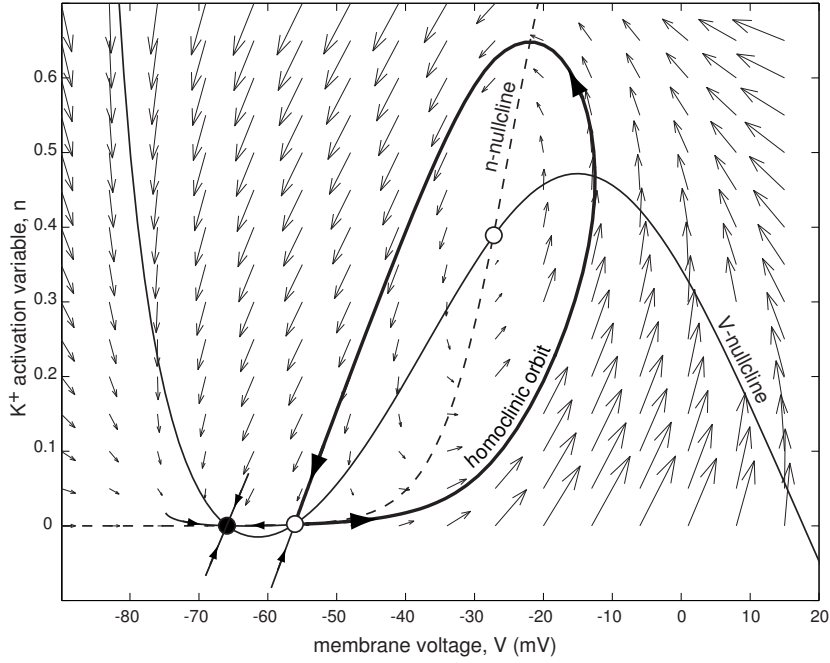


Figure 4.27: Homoclinic orbit (bold) in the  $I_{\text{Na},p} + I_K$ -model with high-threshold fast ( $\tau(V) = 0.152$ )  $K^+$  current.

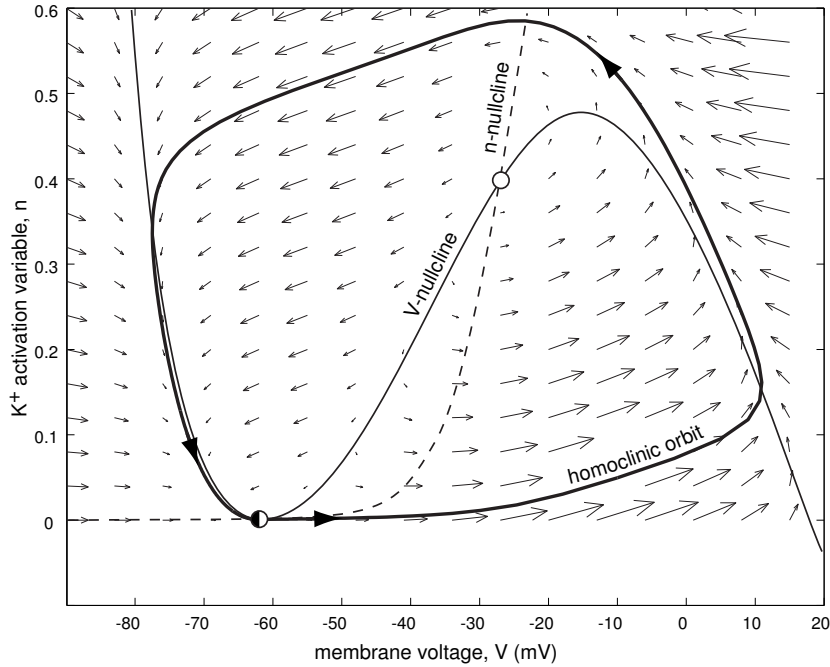


Figure 4.28: Homoclinic orbit (bold) to saddle-node equilibrium in the  $I_{\text{Na},p} + I_K$ -model with high-threshold  $K^+$  current and  $I = 4.51$ .

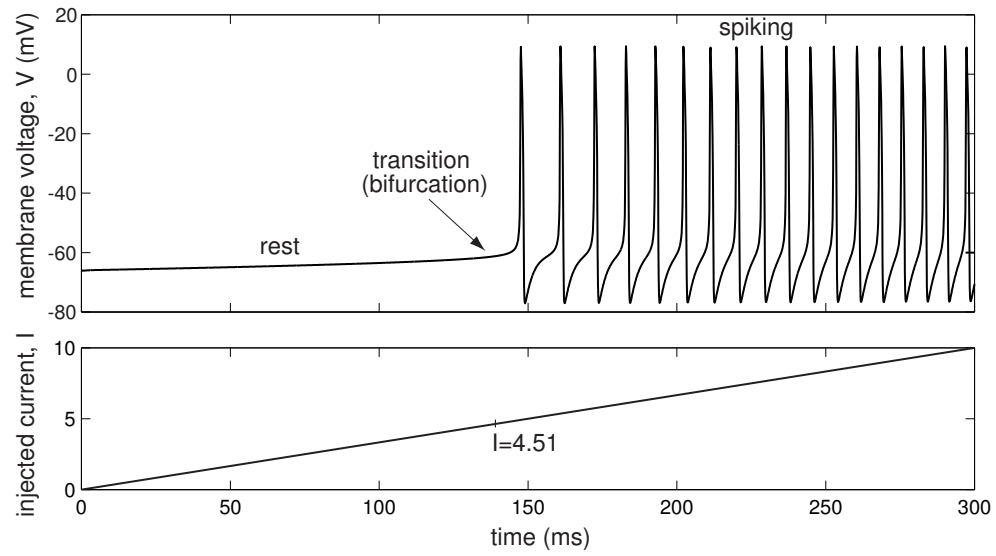


Figure 4.29: Transition from rest state to repetitive spiking in the  $I_{\text{Na,p}}+I_K$ -model with injected ramp current  $I$ ; see also Fig. 4.26, Fig. 4.28, and Fig. 4.30. Notice that the frequency of spiking is initially small, and then it increases as the amplitude of the injected current increases.

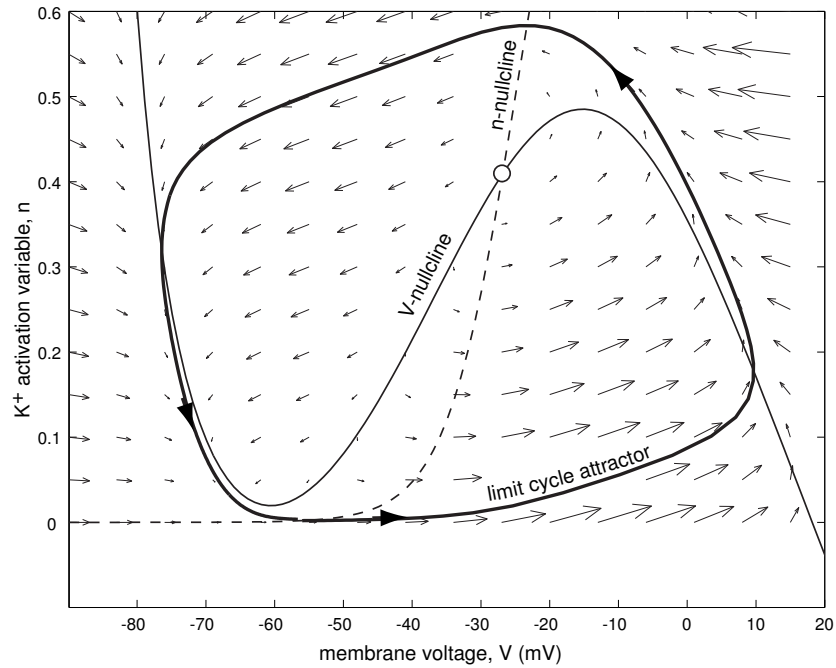


Figure 4.30: Limit cycle attractor (bold) in the  $I_{\text{Na,p}}+I_K$ -model when  $I = 10$  (compare with Fig. 4.26 and Fig. 4.28).

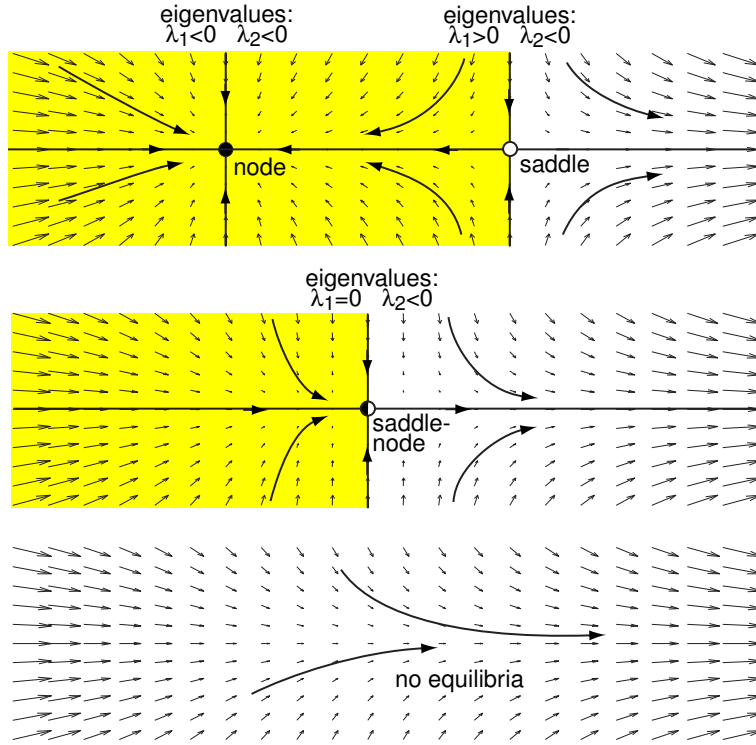


Figure 4.31: Saddle-node bifurcation: The saddle and node equilibria approach each other, coalesce, and annihilate each other (shaded area is the basin of attraction of the stable node).

neuro-computational properties.

It is a relatively simple exercise to determine bifurcation diagrams for saddle-node bifurcations in neuronal models. For this, we just need to determine all equilibria of the model and how they depend on the injected current  $I$ . Any equilibrium of the  $I_{\text{Na,p}} + I_{\text{K}}$ -model satisfies the one-dimensional equation

$$0 = I - g_L(V - E_L) - g_{\text{Na}} m_\infty(V)(V - E_{\text{Na}}) - g_K n_\infty(V)(V - E_K),$$

where  $n = n_\infty(V)$ . Instead of solving this equation for  $V$ , we use  $V$  as a free parameter and solve it for  $I$ ,

$$I = \overbrace{g_L(V - E_L) + g_{\text{Na}} m_\infty(V)(V - E_{\text{Na}}) + g_K n_\infty(V)(V - E_K)}^{\text{steady-state } I_\infty(V)}, \quad (4.13)$$

and then depict the solution as a curve in the  $(I, V)$  plane in Fig. 4.32. In the magnification (Fig. 4.32, right) one can clearly see how two branches of equilibria approach and annihilate each other as  $I$  approaches the bifurcation value 4.51. Is there any other saddle-node bifurcation in the figure?

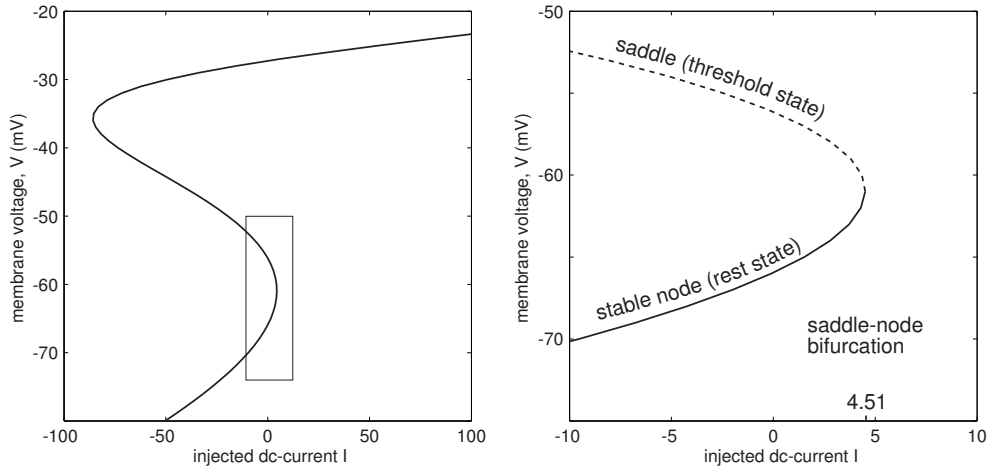


Figure 4.32: Saddle-node bifurcation diagram of the  $I_{\text{Na},p} + I_K$ -model. The curve is given by the equation (4.13).

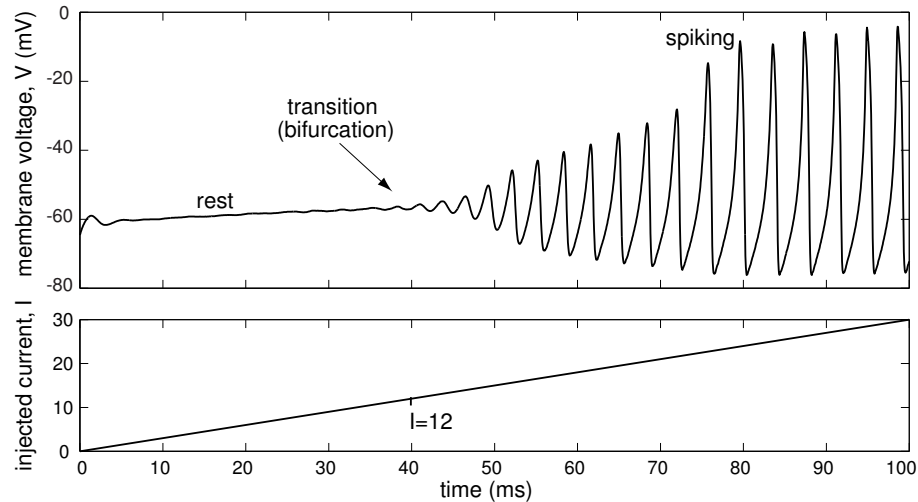


Figure 4.33: Transition from rest state to repetitive spiking in the  $I_{\text{Na},p} + I_K$ -model with ramp injected current  $I$ ; see also Fig. 4.34 (small-amplitude noise is added to the model to mask the slow passage effect). Notice that the frequency of spiking is relatively constant for a wide range of injected current.

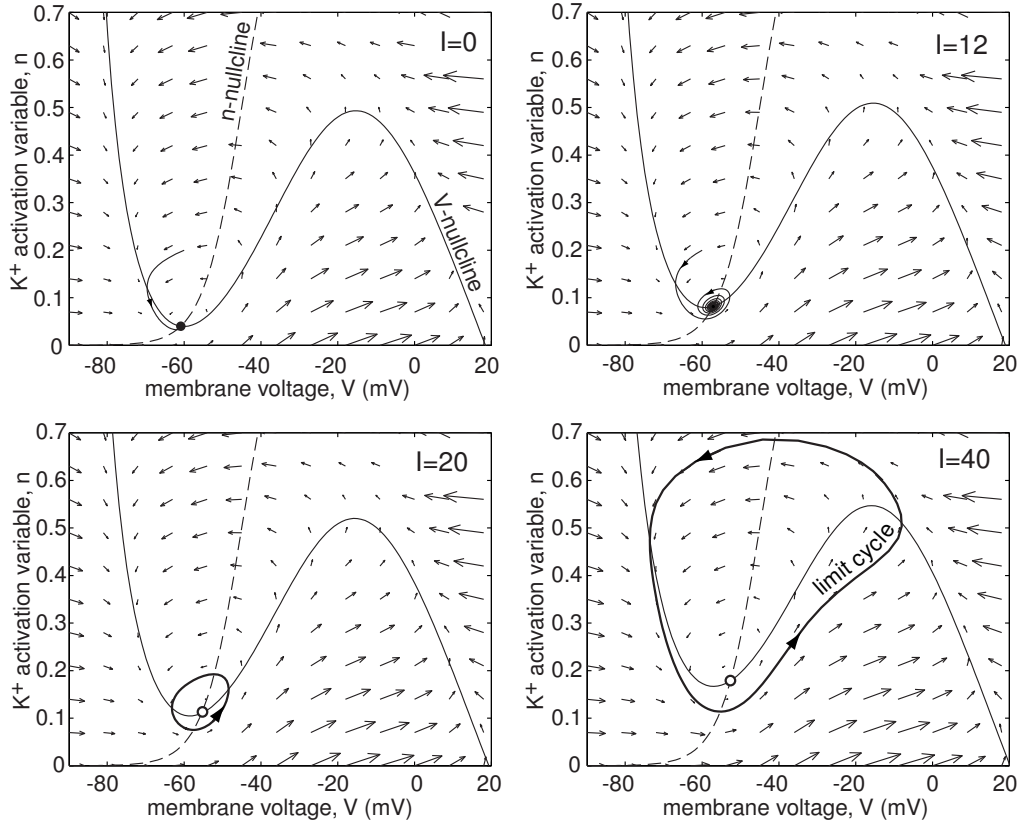


Figure 4.34: Supercritical Andronov-Hopf bifurcation in the  $I_{\text{Na},p} + I_K$ -model (4.1, 4.2) with low-threshold  $K^+$  current when  $I = 12$ ; see also Fig. 4.33.

### 4.3.5 Andronov-Hopf bifurcation

In Fig. 4.33 we repeat the current ramp experiment using the  $I_{\text{Na},p} + I_K$ -model with low-threshold  $K^+$  current. The phase portrait of such a model is simple — it has a unique equilibrium, as we illustrate in Fig. 4.34. When  $I$  is small, the equilibrium is a stable focus corresponding to the rest state. When  $I$  increases past  $I = 12$ , the focus loses stability and gives birth to a small-amplitude limit cycle attractor. The amplitude of the limit cycle grows as  $I$  increases. We see that increasing  $I$  beyond  $I = 12$  results in the transition from rest to spiking behavior. What kind of a bifurcation occurs there?

Recall that stable foci have a pair of complex-conjugate eigenvalues with negative real part. When  $I$  increases, the real part of the eigenvalues also increases until it becomes zero (at  $I = 12$ ) and then positive (when  $I > 12$ ) meaning that the focus is no longer stable. The transition from stable to unstable focus described above is called *Andronov-Hopf* bifurcation. It occurs when the eigenvalues become purely imaginary, as it happens when  $I = 12$ . We will study Andronov-Hopf bifurcations in detail in Chap. 6, where we will show that they can be *supercritical* or *subcritical*. The former correspond to birth of a small-amplitude limit cycle attractor, as in Fig. 4.34. The latter correspond to a death of an unstable limit cycle.

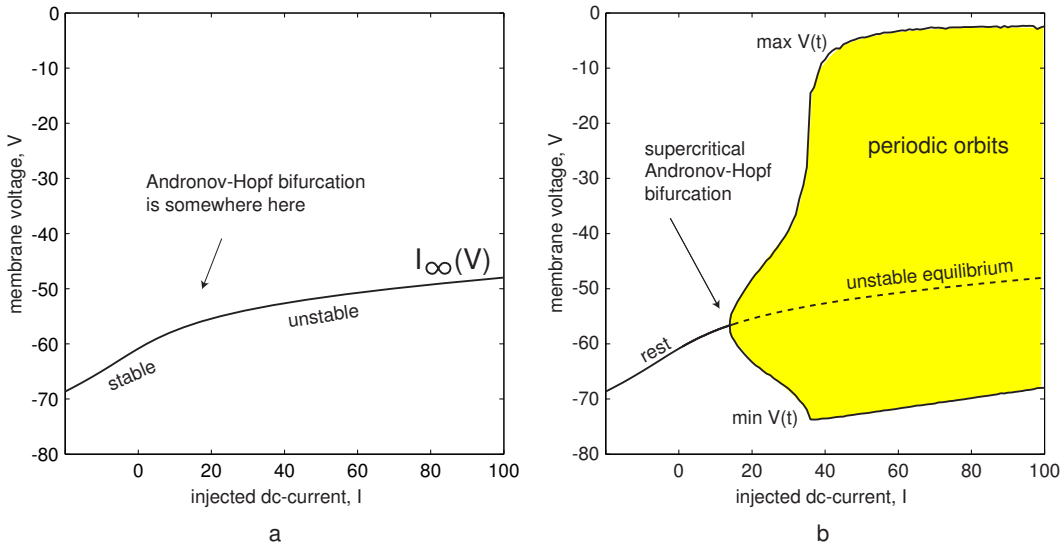


Figure 4.35: Andronov-Hopf bifurcation diagram in the  $I_{\text{Na},p}+I_{\text{K}}$ -model with low-threshold  $\text{K}^+$  current. a. Equilibria of the model (solution of (4.13)). b. Equilibria and limit cycles of the model.

In Fig. 4.35a we plot the solution of (4.13) as an attempt to determine the bifurcation diagram for the Andronov-Hopf bifurcation in the  $I_{\text{Na},p}+I_{\text{K}}$ -model. However, all we can see is that the equilibrium persists as  $I$  increases, but there is no information on its stability or on the existence of a limit cycle attractor. To study the limit cycle attractor, we need to simulate the model with various values of parameter  $I$ . For each  $I$ , we disregard the transient period and plot  $\min V(t)$  and  $\max V(t)$  on the  $(I, V)$ -plane, as in Fig. 4.35b. When  $I$  is small, the solutions converge to the stable equilibrium, and both  $\min V(t)$  and  $\max V(t)$  are equal to the resting voltage. When  $I$  increases past  $I = 12$ , the  $\min V(t)$  and  $\max V(t)$  values start to diverge, meaning that there is a limit cycle attractor whose amplitude increases as  $I$  does. This method is appropriate for analysis of supercritical Andronov-Hopf bifurcations but it fails for subcritical Andronov-Hopf bifurcations. Why?

Figure 4.36 depicts an interesting phenomenon observed in many biological neurons — *excitation block*. Spiking activity of the layer 5 pyramidal neuron of rat's visual cortex is blocked by strong excitation, i.e., injection of strong depolarizing current. The geometry of this phenomenon is illustrated in Fig. 4.37, bottom. As the magnitude of the injected current increases, the unstable equilibrium, which is the intersection point of the nullclines, moves to right branch of the cubic  $V$ -nullcline and becomes stable. The limit cycle shrinks and the spiking activity disappears, typically but not necessarily via supercritical Andronov-Hopf type. Thus, the  $I_{\text{Na},p}+I_{\text{K}}$ -model with low-threshold  $\text{K}^+$  current can exhibit two such bifurcations in response to ramping up of the injected current, one leading to the appearance of periodic spiking activity (Fig. 4.34), and then one leading to its disappearance (Fig. 4.37).

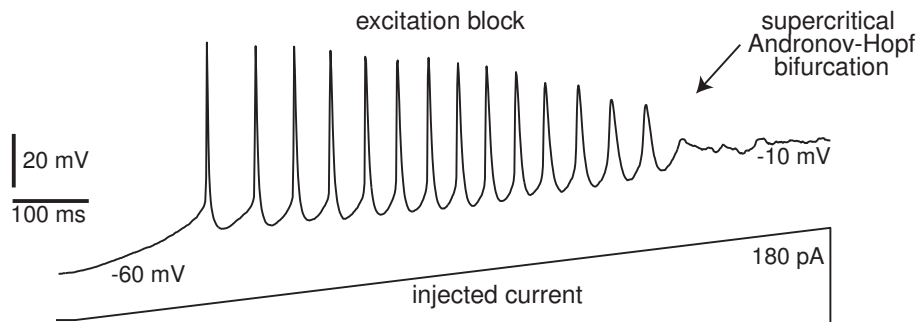


Figure 4.36: Excitation block in layer 5 pyramidal neuron of rat's visual cortex as the amplitude of the injected current ramps up.

Supercritical and subcritical Andronov-Hopf bifurcations in neurons result in slightly different neuro-computational properties. In contrast, the saddle-node and Andronov-Hopf bifurcations result in *dramatically* different neuro-computational properties. In particular, neurons near saddle-node bifurcation act as *integrators* — they prefer high-frequency input: The higher the frequency of the input, the sooner they fire. In contrast, neural systems near Andronov-Hopf bifurcation have damped oscillatory potentials and they act as *resonators* — they prefer oscillatory input with the same frequency as that of damped oscillations. Increasing the frequency may delay or even terminate their response. We discuss this and other neuro-computational properties in Chap. 7.

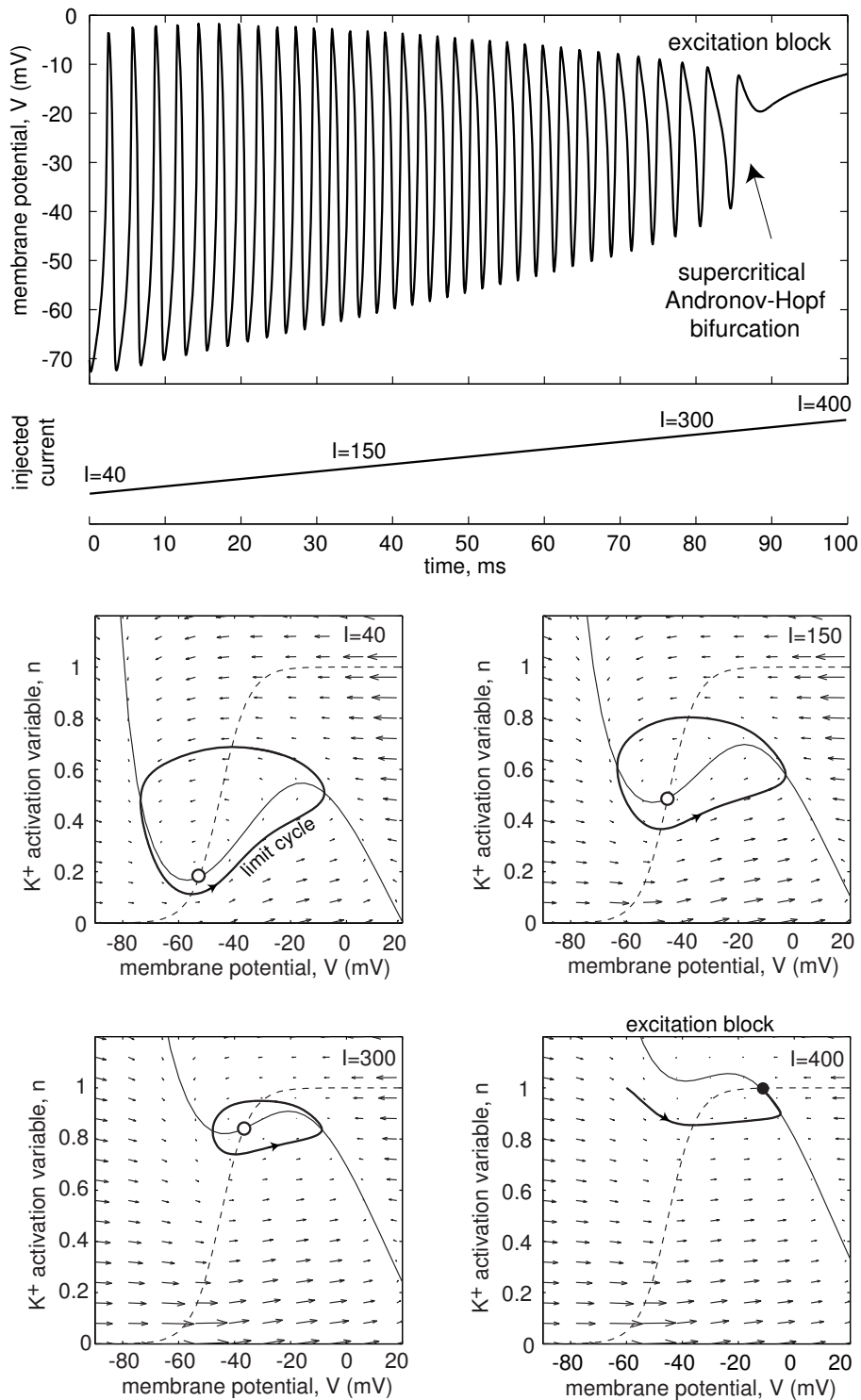


Figure 4.37: Excitation block in the  $I_{Na,p} + I_K$ -model: As the magnitude of the injected current  $I$  ramps up, the spiking stops.

## Review of Important Concepts

- A two-dimensional system of differential equations

$$\begin{aligned}\dot{x} &= f(x, y) \\ \dot{y} &= g(x, y),\end{aligned}$$

describes joint evolution of state variables  $x$  and  $y$ , which often are the membrane voltage and a “recovery” variable.

- Solutions of the system are trajectories on the phase plane  $\mathbb{R}^2$  that are tangent to the vector field  $(f, g)$ .
- The sets given by the equations  $f(x, y) = 0$  and  $g(x, y) = 0$  are the  $x$ - and  $y$ -nullclines, respectively, where trajectories change their  $x$  and  $y$  directions.
- Intersections of the nullclines are equilibria of the system.
- Periodic dynamics correspond to closed loop trajectories.
- Some special trajectories, e.g., separatrices, define thresholds and separate attraction domains.
- An equilibrium or a periodic trajectory is stable if all nearby trajectories are attracted to it.
- To determine the stability of an equilibrium, one needs to consider the Jacobian matrix of partial derivatives

$$L = \begin{pmatrix} f_x & f_y \\ g_x & g_y \end{pmatrix}.$$

- The equilibrium is stable when both eigenvalues of  $L$  are negative or have negative real parts.
- The equilibrium is a saddle, a node, or a focus, when  $L$  has real eigenvalues of opposite signs, of the same signs, or complex-conjugate eigenvalues, respectively.
- When the equilibrium undergoes a saddle-node bifurcation, one of the eigenvalues becomes zero.
- When the equilibrium undergoes an Andronov-Hopf bifurcation (birth or death of a small periodic trajectory) the complex-conjugate eigenvalues become purely imaginary.
- The saddle-node and Andronov-Hopf bifurcations are ubiquitous in neural models, and they result in different neuro-computational properties.

## Bibliographical Notes

Among many textbooks on the mathematical theory of dynamical systems we recommend the following three:

- *Nonlinear Dynamics and Chaos* by Strogatz (1994) is suitable as an introductory book for undergraduate math or physics majors or graduate students in life sciences. It contains many exercises and worked out examples.
- *Differential Equations and Dynamical Systems* by Perko (1996, Third edition in 2000) is suitable for math and physics graduate students, but may be too technical for life scientists. Nevertheless, it should be a standard textbook for computational neuroscientists.
- *Elements of Applied Bifurcation Theory* by Kuznetsov (1995, Third edition in 2004) is suitable for advanced graduate students in mathematics or physics and for computational neuroscientists who want to pursue bifurcation analysis of neural models.

The second edition of *The Geometry of Biological Time* by Winfree (2001) is a good introductory book into oscillations, limit cycles, and synchronization in biology. It requires little background in mathematics and can be suitable even for undergraduate life science majors. *Mathematical Biology* by Murray (1993, Third edition in 2003) is an excellent example how dynamical system theory can solve many problems in population biology and shed light on pattern formation in biological systems. Most of this book is suitable for advance undergraduate or graduate students in mathematics and physics. *Mathematical Physiology* by Keener and Sneyd (1998) is similar to Murray's book, but is more focused on neural systems. *Spikes, Decisions, and Actions* by Wilson (1999) is a short introduction to dynamical systems with many neuroscience examples.

## Exercises

1. Use pencil (as in Fig. 4.39) to sketch the nullclines of the vector fields depicted in figures 4.40 through 4.44.
2. Assume that the continuous curve is the  $x$ -nullcline and the dashed curve is the  $y$ -nullcline in Fig. 4.38, and that  $\dot{x}$  or  $\dot{y}$  changes sign when  $(x, y)$  passes through the corresponding nullcline. The arrow indicates the direction of the vector field in one region. Determine the approximate directions of the vector field in the other regions of the phase plane.
3. Use pencil (as in Fig. 4.39) to sketch phase portraits of the vector fields depicted in figures 4.40 through 4.44. Clearly mark all equilibria, their stability, and attraction domains. Show directions of all homoclinic, heteroclinic and periodic

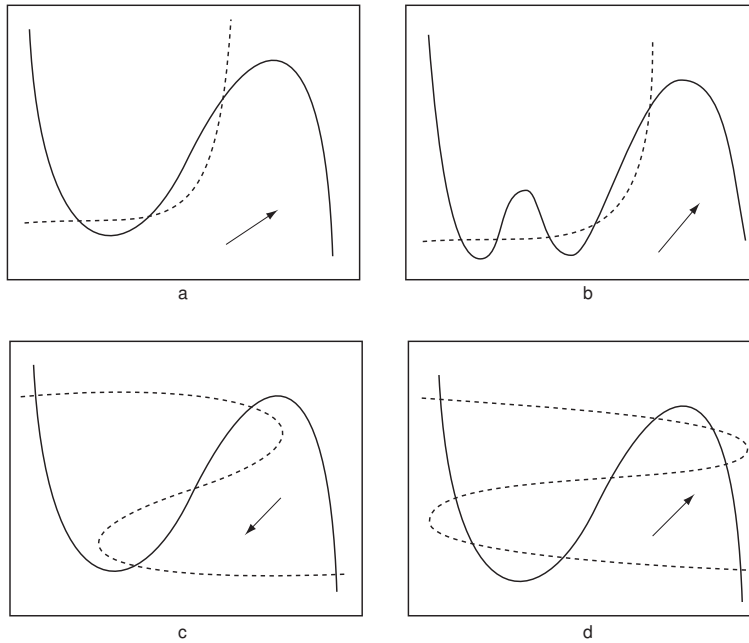


Figure 4.38: Determine the approximate direction of the vector field in each region between the nullclines. Continuous (dashed) curve is the  $x$ -nullcline ( $y$ -nullcline), and the direction of vector field in one region is indicated by the arrow.

trajectories, as well as other representative trajectories. Estimate the signs of eigenvalues at each equilibrium.

4. Prove the classification diagram in Fig. 4.15.
5. (van der Pol oscillator) Determine nullclines and draw phase portrait of the van der Pol oscillator (given in the Liénard (1928) form)

$$\begin{aligned}\dot{x} &= x - x^3/3 - y, \\ \dot{y} &= bx,\end{aligned}$$

where  $b > 0$  is a parameter.

6. (Bonhoeffer–van der Pol oscillator) Determine the nullclines and sketch representative phase portraits of the Bonhoeffer–van der Pol oscillator

$$\begin{aligned}\dot{x} &= x - x^3/3 - y, \\ \dot{y} &= b(x - a) - cy,\end{aligned}$$

in the case of  $c = 0$ . Treat  $a$  and  $b > 0$  as parameters.

7. (Hindmarsh-Rose spiking neuron) The following system is a generalization of the FitzHugh-Nagumo model (Hindmarsh and Rose 1982)

$$\begin{aligned}\dot{x} &= f(x) - y + I, \\ \dot{y} &= g(x) - y,\end{aligned}$$

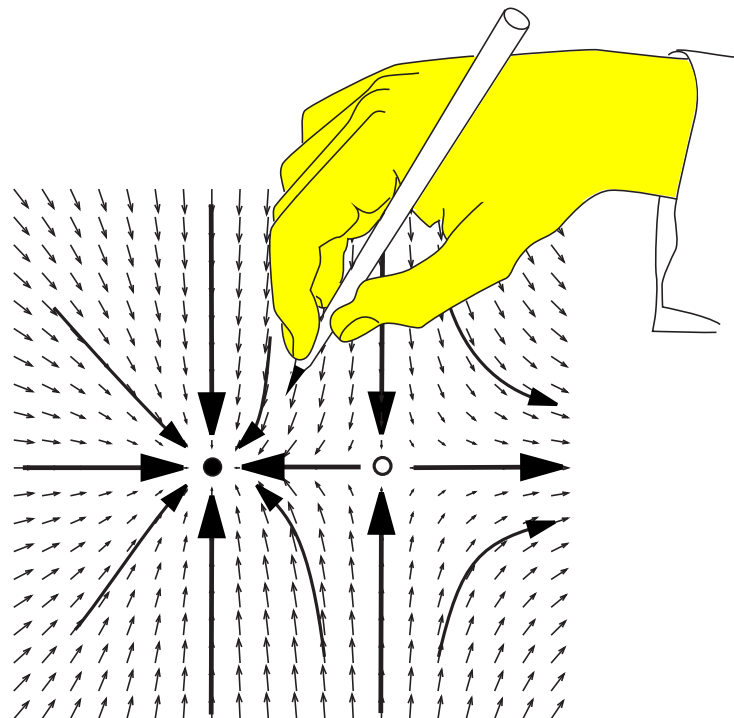


Figure 4.39: Phase portrait of a vector field. Use pencil to draw phase portraits in figures 4.40 through 4.44.

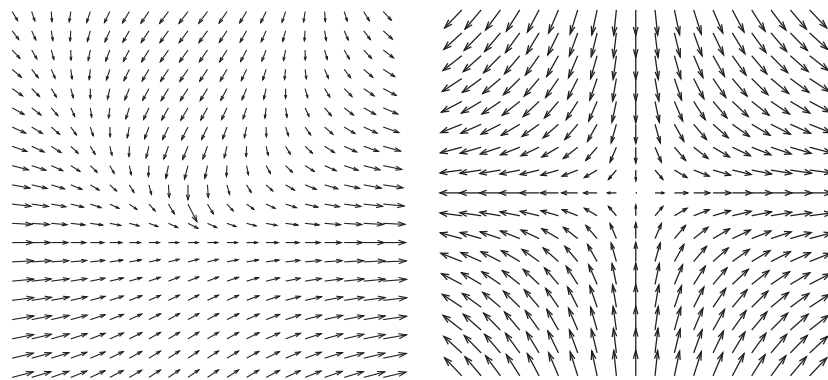


Figure 4.40: Use pencil to draw a phase portrait as in Fig. 4.39.

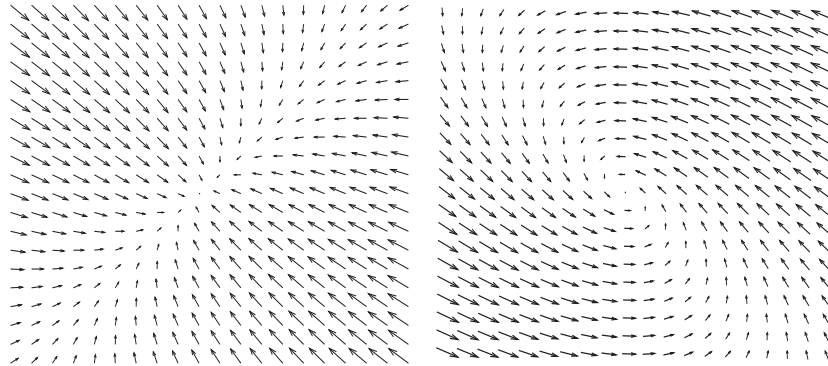


Figure 4.41: Use pencil to draw a phase portrait as in Fig. 4.39.

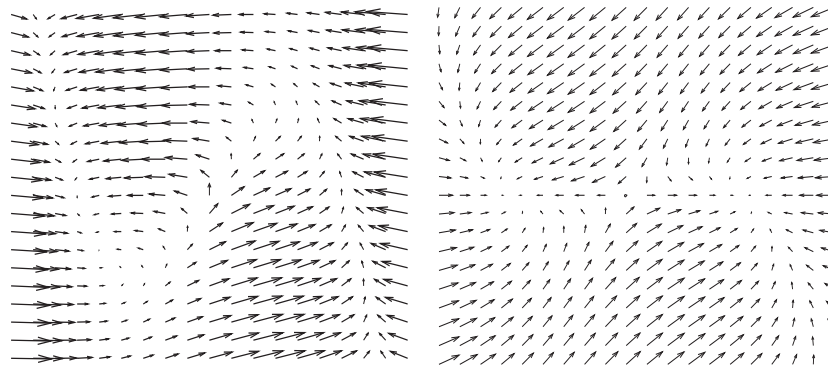


Figure 4.42: Use pencil to draw a phase portrait as in Fig. 4.39.

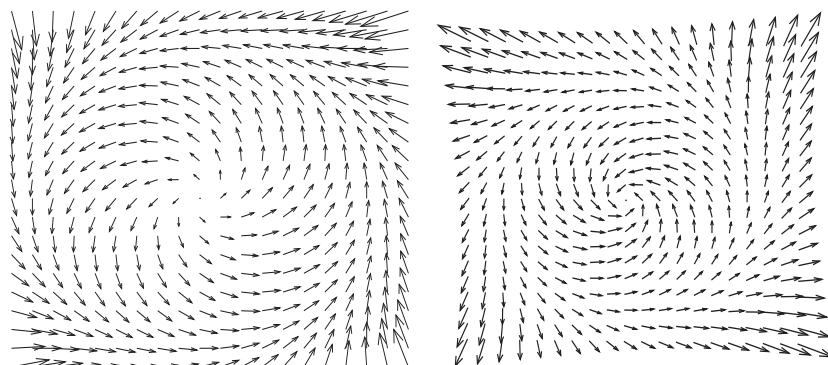


Figure 4.43: Use pencil to draw a phase portrait as in Fig. 4.39.

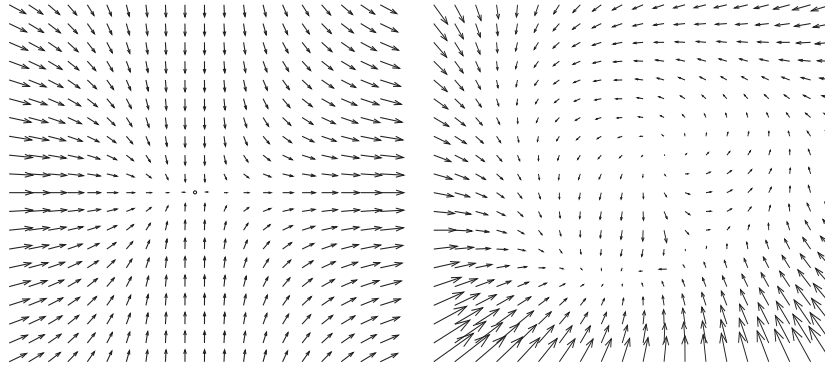


Figure 4.44: Use pencil to draw a phase portrait as in Fig. 4.39.

where  $f(x) = -ax^3 + bx^2$ ,  $g(x) = -c + dx^2$ , and  $a, b, c, d$ , and  $I$  are parameters. Suppose  $(\bar{x}, \bar{y})$  is an equilibrium. Determine its type and stability as a function of  $f' = f'(\bar{x})$  and  $g' = g'(\bar{x})$ ; that is, plot a diagram similar to the one in Fig. 4.15 with  $f'$  and  $g'$  as coordinates.

8. ( $I_K$ -model) Show that the unique equilibrium in the  $I_K$ -model

$$C \dot{V} = -g_L(V - E_L) - g_K m^4(V - E_K), \quad (4.14)$$

$$\dot{m} = (m_\infty(V) - m)/\tau(V). \quad (4.15)$$

discussed in the previous chapter (see Fig. 3.40) is always stable, at least when  $E_L > E_K$ . (Hint: look at the signs of the trace and determinant of the Jacobian matrix).

9. ( $I_h$ -model) Show that the unique equilibrium in the full  $I_h$ -model

$$\begin{aligned} C \dot{V} &= -g_L(V - E_L) - g_h h(V - E_h), \\ \dot{h} &= (h_\infty(V) - h)/\tau(V), \end{aligned}$$

discussed in the previous chapter is always stable.

10. (Bendixson's criterion) If the divergence of the vector field

$$\frac{\partial f(x, y)}{\partial x} + \frac{\partial g(x, y)}{\partial y}$$

of a two-dimensional dynamical system is not identically zero and does not change sign on the plane, then the dynamical system cannot have limit cycles. Use this criterion to show that the  $I_K$ -model and the  $I_h$ -model cannot oscillate.

11. Determine stability of equilibria in the model

$$\begin{aligned} \dot{x} &= a + x^2 - y, \\ \dot{y} &= bx - cy, \end{aligned}$$

where  $a \in \mathbb{R}$ ,  $b \geq 0$  and  $c > 0$  are some parameters.



# Chapter 5

## Conductance-Based Models and Their Reductions

In this chapter we present examples of geometrical phase plane analysis of various two-dimensional neural models. In particular, we consider minimal models, i.e., those having minimal sets of currents that enable the models to generate action potentials. The remarkable fact is that all these models can be reduced to planar systems having N-shaped  $V$ -nullclines. We will see that the behavior of the models depends not so much on the ionic currents as on the relationship between (in)activation curves and the time constants. That is, models involving completely different currents can have identical dynamics, and conversely, models involving similar currents can have completely different dynamics.

### 5.1 Minimal Models

There are a few dozens of known voltage- and  $\text{Ca}^{2+}$ -gated currents having diverse activation and inactivation dynamics, and this number grows every year. Some of them are summarized in Sect. 2.3.5. Almost any combination of the currents would result in interesting non-linear behavior, such as excitability. Therefore, there are billions (more than  $2^{30}$ ) of different electrophysiological models of neurons. Here we say that two models are “different” if for example one has the h-current  $I_h$  and the other does not, without even considering how much of the  $I_h$  is there. How can we classify all such models?

Let us do the following thought experiment: Consider a conductance-based model capable of exhibiting periodic spiking, i.e., having a limit cycle attractor. Let us remove completely a current or one of its gating variables, and ask the question “Does the reduced model have a limit cycle attractor, at least for some values of parameters?” If it does, we remove one more gating variable or current, and proceed until we arrive at a model that satisfies the following two properties:

- It has a limit cycle attractor, at least for some values of parameters.

- If one removes any current or gating variable, the model has only equilibrium attractors for any values of parameters.

We refer to such a model as being *minimal* or *irreducible* for spiking. Thus, minimal models can exhibit periodic activity, even if of small amplitude, but their reductions cannot. According to this definition, any space-clamped conductance-based model is either a minimal model, or could be reduced to a minimal model or models by removing gating variables. This will be the basis for our classification of electrophysiological mechanisms in neurons.

For example, the Hodgkin-Huxley model considered in Sect. 2.3 is not minimal for spiking. Recall that the model consists of three currents: leakage  $I_L$ , transient sodium  $I_{Na,t}$  (gating variables  $m$  and  $h$ ) and persistent potassium  $I_K$  (gating variable  $n$ ); see Fig. 5.1. Which of these currents are responsible for excitability and spiking?

We can remove the leakage current and the gating variable,  $h$ , for the inactivation of the sodium current: The resulting  $I_{Na,p}+I_K$ -model

$$\begin{aligned} C \dot{V} &= I - \overbrace{g_K n^4 (V - E_K)}^{I_K} - \overbrace{g_{Na} m^3 (V - E_{Na})}^{I_{Na,p}}, \\ \dot{n} &= (n_\infty(V) - n)/\tau_n(V), \\ \dot{m} &= (m_\infty(V) - m)/\tau_m(V), \end{aligned}$$

was considered in the previous chapter where we have shown that it could oscillate due to the interplay between the activation of persistent sodium and potassium currents. Alternatively, we can remove the  $K^+$  current from the Hodgkin-Huxley model, yet the new  $I_{Na,t}$ -model

$$\begin{aligned} C \dot{V} &= I - \overbrace{g_{Na} m^3 h (V - E_{Na})}^{I_{Na,t}} - \overbrace{g_L (V - E_L)}^{I_L}, \\ \dot{m} &= (m_\infty(V) - m)/\tau_m(V), \\ \dot{h} &= (h_\infty(V) - h)/\tau_h(V), \end{aligned}$$

can still oscillate via the interplay between activation and inactivation of the  $Na^+$  current, as we will see later in this chapter. Both models are minimal, because removal of any other gating variable results in either the  $I_{Na,p}$ -,  $I_K$ -, or  $I_h$ -models, neither of which can have a limit cycle attractor, as the reader is asked to prove at the end of the previous chapter.

We see that the Hodgkin-Huxley model is not minimal, but it is a combination of two minimal models. Minimal models are appealing because they are relatively simple; each individual variable has an established electrophysiological meaning, and its role in dynamics can be easily identified. As we show below, many minimal models can

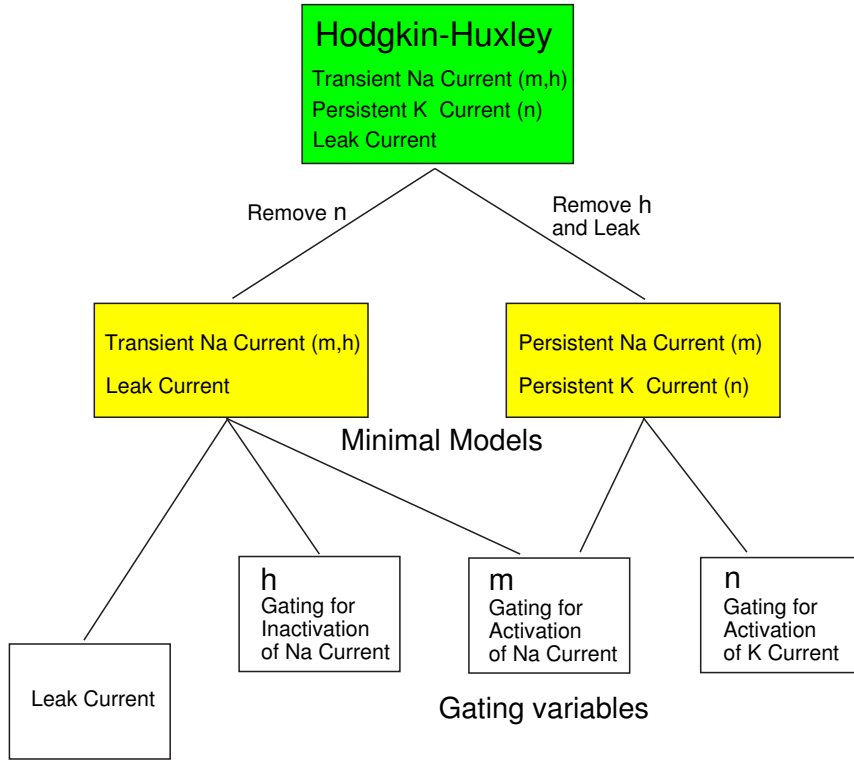


Figure 5.1: The Hodgkin-Huxley model (top box) is a combination of minimal models (shaded boxes on second level). Each minimal model can oscillate at least for some values of its parameters.

be reduced to planar systems, which are amenable to analysis using geometrical phase plane methods. In Sect. 5.2 we discuss other methods of reduction of multi-dimensional models, e.g., the Hodgkin-Huxley model, to planar systems.

There are only few minimal models, and understanding their dynamics can shed light on dynamics of more complicated electrophysiological models. However, the reader should be aware of limitations of such an approach: Understanding minimal models cannot provide exhaustive information about all electrophysiological models (the same way as understanding the zeros of the equations  $y = x$ , and  $y = x^2$  does not provide complete information about the zeros of the equation  $y = x + x^2$ ).

### 5.1.1 Amplifying and resonant gating variables

The definition of the minimal models involves a top-down approach: Take a complicated model and strip it down to minimal ones. It is unlikely that this could be done for all 2<sup>30</sup> or so electrophysiological models. Instead, we employ here a bottom-up approach, which is based on the following rule of thumb: A mixture of one amplifying and one resonant (recovery) gating variable (plus an Ohmic leak current) results in a minimal model. Indeed, neither of the variables alone can produce oscillation, but together they

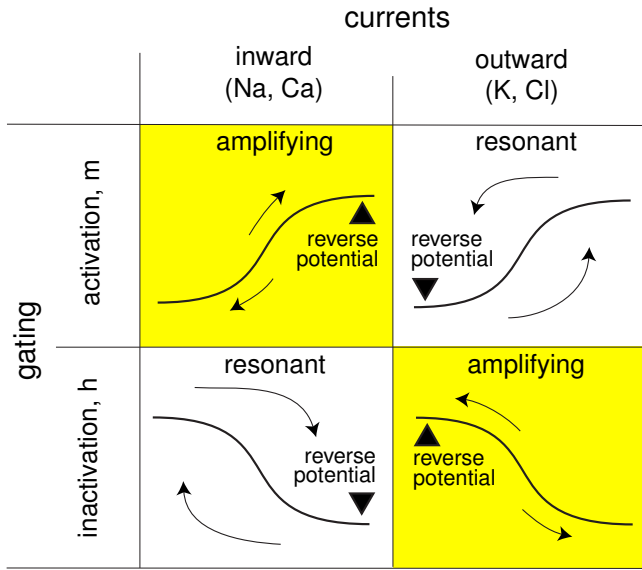


Figure 5.2: Gating variables may be amplifying or resonant depending on whether they represent activation/inactivation of inward/outward currents (see also Fig. 3.3 and Fig. 3.4).

can, as we will see below.

The *amplifying* gating variable is the activation variable  $m$  for voltage-gated inward current or inactivation variable  $h$  for voltage-gated outward current, as in Fig. 5.2. These variables amplify voltage changes via a positive feedback loop. Indeed, a small depolarization increases  $m$  and decreases  $h$ , which in turn increase inward and decrease outward currents and increase depolarization. Similarly, a small hyperpolarization decreases  $m$  and increases  $h$ , resulting in less inward and more outward current, and hence in more hyperpolarization.

The *resonant* gating variable is the inactivation variable  $h$  for an inward current or activation variable  $n$  for an outward current. These variables resist voltage changes via a negative feedback loop. A small depolarization decreases  $h$  and increases  $n$ , which in turn decrease inward and increase outward currents and produce a net outward current that resists the depolarization. Similarly, a small hyperpolarization produces inward current and possibly rebound depolarization.

Currents with amplifying gating variables can result in bistability, and they behave essentially like the  $I_{Na,p}$ -model or  $I_{Kir}$ -model considered in Chap. 3. Currents with resonant gating variables have one stable equilibrium with possibly damped oscillation, and they behave essentially like the  $I_K$ -model or  $I_h$  model (compare Fig. 5.2 with Fig. 3.3). A typical neuronal model consists of at least one amplifying and at least one resonant gating variable. Amplifying and resonant gating variables for  $\text{Ca}^{2+}$ -sensitive currents are discussed at the end of this chapter.

To get spikes in a minimal model, we need a fast positive feedback and a slower negative feedback. Indeed, if an amplifying gating variable has a long time constant, it would act more as a low-pass filter, hardly affecting fast fluctuations, and only amplifying slow fluctuations. If a resonant gating variable has a fast time constant, it would act to damp input fluctuations (faster than they could be amplified by the amplifying variable), resulting in stability of the resting state. Instead, the resonant

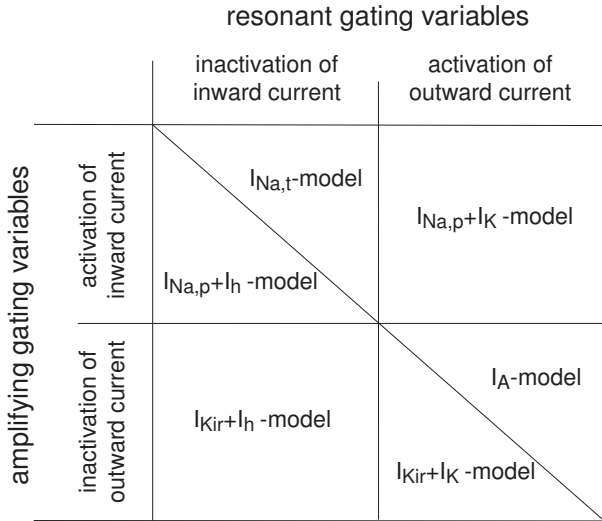


Figure 5.3: Any combination of one amplifying and one resonant gating variables results in a spiking model.

variable acts as a band-pass filter; It has no effect on oscillations with a period much smaller than its time constant. It damps oscillations having period much larger than its time constant, because the variable oscillates in phase with the voltage fluctuations; It amplifies oscillations with a period that is about the same as its time constant because the variable lags the voltage fluctuations.

Since the amplifying gating variable, say  $m$ , has relatively fast kinetics, it can be replaced by its equilibrium (steady-state) value  $m_\infty(V)$ . This allows to reduce the dimension of the minimal models from three (say  $V, m, n$ ) to two ( $V$  and  $n$ ).

Two amplifying and two resonant gating variables produce four different combinations, depicted in Fig. 5.3. However, the number of minimal models is not four, but six. The additional models arise due to the fact that a pair of gating variables may describe activation/inactivation properties of the same current or of two different currents. For example, the activation and inactivation gating variables  $m$  and  $h$  may describe the dynamics of a transient inward current, such as  $I_{Na,t}$ , or the dynamics of a combination of one persistent inward current, such as  $I_{Na,p}$ , and one “hyperpolarization-activated” inward current, such as  $I_h$ . Hence this pair results in two models,  $I_{Na,t}$ - and  $I_{Na,p} + I_h$ -model. Similarly, the pair of activation and inactivation variables of an outward current may describe the dynamics of the same transient current, such as  $I_A$ , or the dynamics of two different outward currents, hence the two models,  $I_A$ - and  $I_{Kir} + I_K$ -model.

Below we present the geometrical analysis of the six minimal voltage-gated models shown in Fig. 5.3. Though based on different ionic currents, the models have many similarities from the dynamical systems point of view. In particular, all can exhibit saddle-node and Andronov-Hopf bifurcations. For each model we first provide a word description of the mechanism of generation of sustained oscillations, and then use phase plane analysis to provide a geometrical description. The first two,  $I_{Na,p} + I_K$ - and  $I_{Na,t}$ -models are common; they describe the mechanism of generation of action potentials or subthreshold oscillations by many cells. The other four models are rare; they even might be classified as weird or bizarre by biologists, since these models reveal

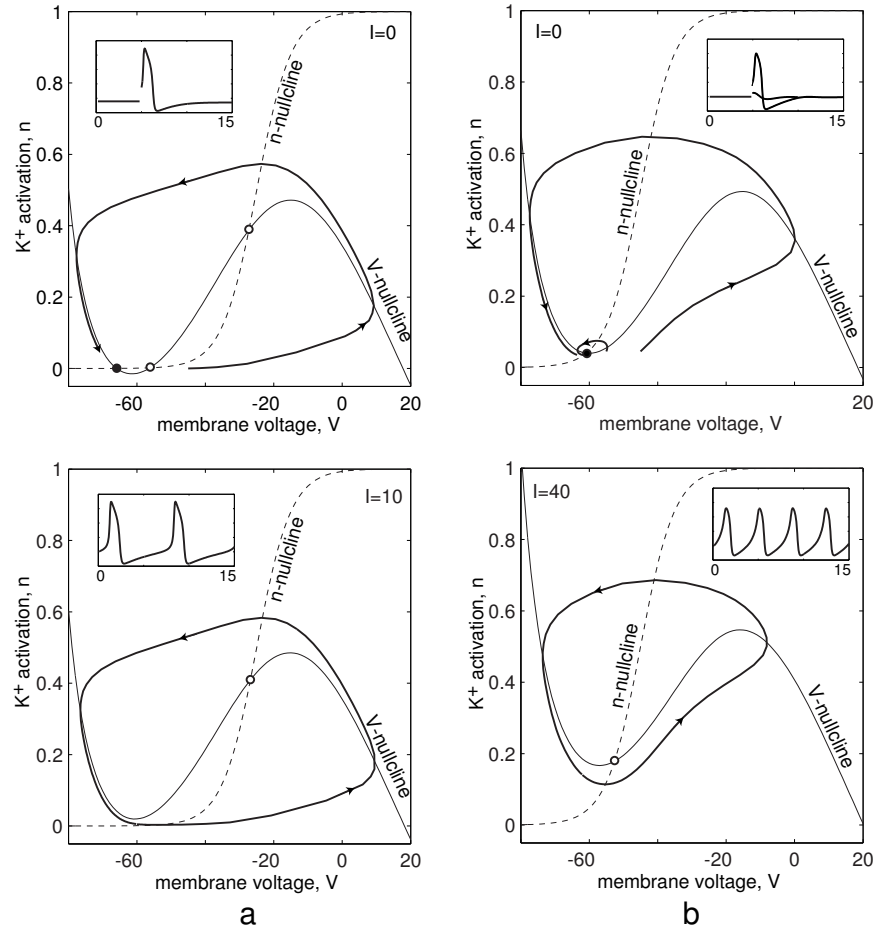


Figure 5.4: Possible forms of nullclines in the  $I_{\text{Na},p}+I_K$ -model. Parameters as in the previous chapter (see caption to Fig. 4.1).

rather unexpected mechanisms for voltage oscillations. Nevertheless, it is educational to consider all 6 models to see how the theory of dynamical systems works where intuition and common sense fail.

### 5.1.2 $I_{\text{Na},p}+I_K$ -model

One of the most fundamental models in computational neuroscience is the  $I_{\text{Na},p}+I_K$ -model consisting of a fast  $\text{Na}^+$  current and a relatively slower  $\text{K}^+$  current:

$$\begin{aligned} C \dot{V} &= I - \underbrace{g_L(V - E_L)}_{\text{leak } I_L} - \underbrace{g_{\text{Na}}m(V - E_{\text{Na}})}_{I_{\text{Na},p}} - \underbrace{g_Kn(V - E_K)}_{I_K}, \\ \dot{m} &= (m_\infty(V) - m)/\tau_m(V), \\ \dot{n} &= (n_\infty(V) - n)/\tau_n(V). \end{aligned}$$

This model is in many respects equivalent to the  $I_{\text{Ca}}+I_{\text{K}}$ -model proposed by Morris and Lecar (1981) to describe voltage oscillations in the barnacle giant muscle fiber. A reasonable assumption based on experimental observations is that the  $\text{Na}^+$  gating variable  $m(t)$  is much faster than the voltage variable  $V(t)$ , so that  $m$  approaches the asymptotic value  $m_\infty(V)$  practically instantaneously. In this case we can substitute  $m = m_\infty(V)$  in the voltage equation and reduce the three-dimensional system above to a planar system

$$C \dot{V} = I - \underbrace{g_L(V - E_L)}_{\text{leak } I_L} - \underbrace{g_{\text{Na}} m_\infty(V) (V - E_{\text{Na}})}_{\text{instantaneous } I_{\text{Na,p}}} - \underbrace{g_K n (V - E_K)}_{I_K} \quad (5.1)$$

$$\dot{n} = (n_\infty(V) - n)/\tau(V), \quad (5.2)$$

which was considered in detail in the previous chapter. In Fig. 5.4 we summarize its dynamic repertoire. A striking observation is that the other minimal models can have similar nullclines and similar dynamic repertoire, even though they consist of quite different ionic currents.

### 5.1.3 $I_{\text{Na,t}}$ -model

An interesting example of a spiking mechanism, implicitly present in practically every biological neuron, is given by the  $I_{\text{Na,t}}$ -model

$$C \dot{V} = I - \underbrace{g_L(V - E_L)}_{\text{leak } I_L} - \underbrace{g_{\text{Na}} m^3 h (V - E_{\text{Na}})}_{I_{\text{Na,t}}},$$

$$\dot{m} = (m_\infty(V) - m)/\tau_m(V),$$

$$\dot{h} = (h_\infty(V) - h)/\tau_h(V),$$

consisting only of an Ohmic leak current and a transient voltage-gated inward  $\text{Na}^+$  current. How could such a model generate action potentials? The upstroke of an action potential is generated because of the regenerative process involving the activation gate  $m$ . This mechanism is similar to the one in the Hodgkin-Huxley model or in the  $I_{\text{Na,p}}+I_{\text{K}}$ -model: Increase of  $m$  results in increase of the inward current, hence more depolarization and further increase of  $m$  until the excited state is achieved. At the excited state there is a balance of the  $\text{Na}^+$  inward current and the leak outward current.

Since there is no  $I_{\text{K}}$ , the downstroke from the excited state occurs via a different mechanism: While in the excited state, the  $\text{Na}^+$  current inactivates (turns off) and the Ohmic leak current slowly repolarizes the membrane potential toward the leak reverse potential  $E_L$ , which determines the resting state. While at rest, the  $\text{Na}^+$  current deinactivates; i.e., becomes available, and the neuron is ready to generate another action potential. This mechanism is summarized in Fig. 5.5.

To study the dynamics of the  $I_{\text{Na,t}}$ -model, we first reduce it to a planar system. Assuming that activation dynamics is instantaneous, we use  $m = m_\infty(V)$  in the voltage

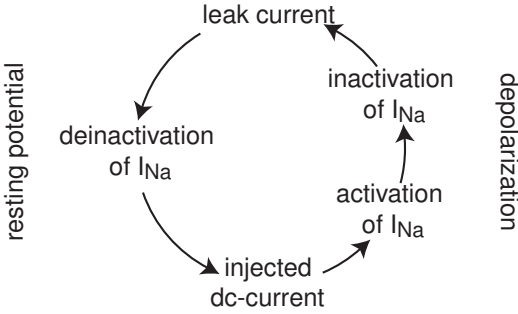


Figure 5.5: Mechanism of generation of sustained oscillations in the  $I_{Na,t}$ -model.

equation and obtain

$$\begin{aligned} C \dot{V} &= I - \underbrace{g_L(V - E_L)}_{\text{leak } I_L} - \underbrace{g_{Na}m_\infty^3(V)h(V - E_{Na})}_{I_{Na,t}, \text{ inst. activation}}, \\ \dot{h} &= (h_\infty(V) - h)/\tau_h(V). \end{aligned}$$

One can easily find the nullclines

$$h = \frac{I - g_L(V - E_L)}{g_{Na}m_\infty^3(V)(V - E_{Na})} \quad (V\text{-nullcline})$$

and

$$h = h_\infty(V) \quad (h\text{-nullcline}).$$

The  $V$ -nullcline looks like a cubic parabola (flipped N shape), and the  $h$ -nullcline has a sigmoid shape. In Fig. 5.6 we depict two typical cases (we invert the  $h$ -axis so that the vector field is directed counterclockwise and this phase portrait is consistent with the other phase portraits in this book).

When the inactivation curve  $h_\infty(V)$  has a high threshold (i.e.,  $I_{Na,t}$  is a window current), there are three intersections of the nullclines, hence three equilibria, as in Fig. 5.6a. A stable node (filled circle) corresponds to the rest state, and a nearby saddle corresponds to the threshold state. Another equilibrium, an unstable focus denoted by white circle at the top of the figure, determines the shape of the action potential since all “spiking” trajectories have to go around it. Because of the high threshold of inactivation, the  $I_{Na,t}$  current is deinactivated at rest. Moreover, small fluctuations of  $V$  do not produce significant changes of the inactivation variable  $h$  because the  $h$ -nullcline is nearly horizontal at rest. Such a system does not perform damped oscillations, and the nonlinear dynamics of  $V$  near rest state can be described by the one-dimensional system (where  $h = h_\infty(V)$ )

$$C \dot{V} = I - g_L(V - E_L) - g_{Na}m_\infty^3(V)h_\infty(V)(V - E_{Na})$$

studied in Chap. 3. When  $I$  increases, the stable node and the saddle approach, coalesce, and annihilate each other via saddle-node bifurcation. When  $I = 0.5$ , there is

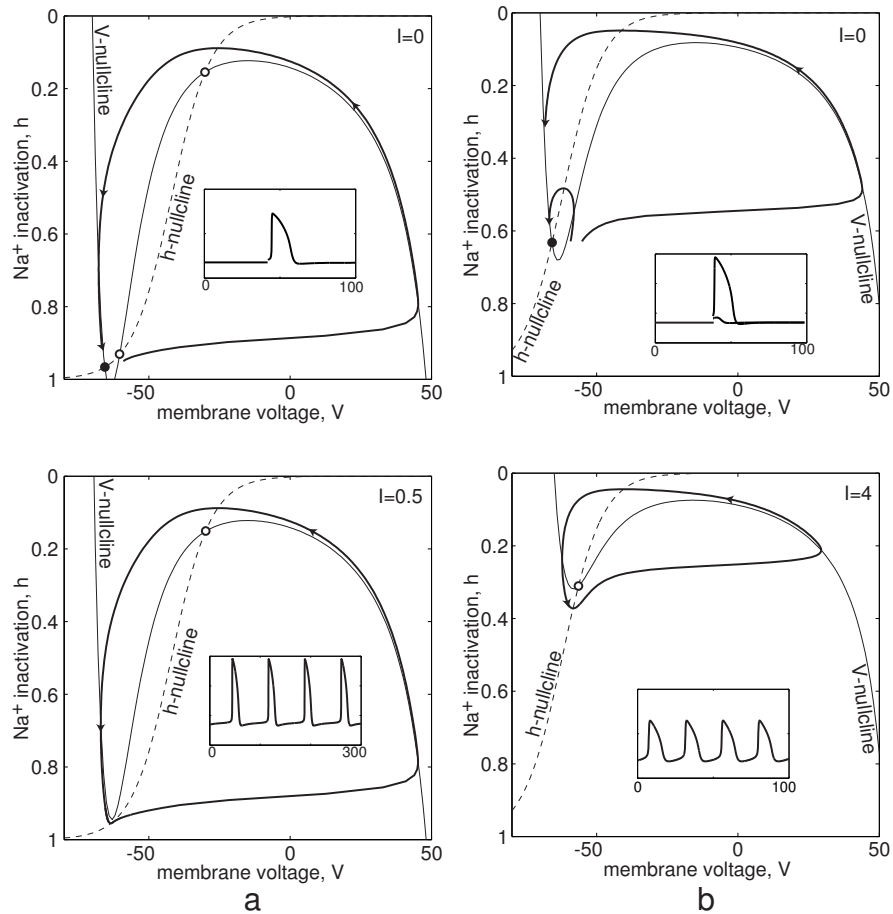


Figure 5.6: Possible forms of nullclines in the  $I_{\text{Na},t}$ -model. Notice that the  $h$ -axis is inverted. Parameters for  $I_{\text{Na},t}$  are as in Hodgkin-Huxley model except  $\tau_h(V) = 5 \text{ ms}$ .  $E_{\text{Na}} = 60 \text{ mV}$ ,  $E_L = -70 \text{ mV}$ ,  $g_L = 1$ ,  $g_{\text{Na}} = 15$  (in b) and  $g_{\text{Na}} = 10$  and  $V_{1/2} = -42 \text{ mV}$  (in a).

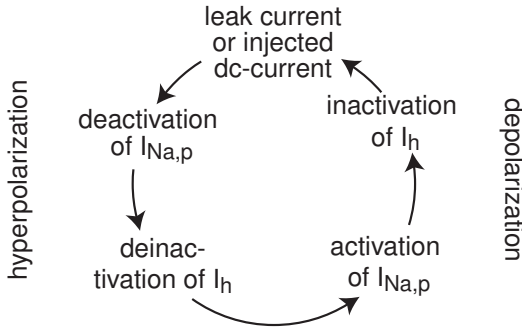


Figure 5.7: Mechanism of generation of sustained voltage oscillations in the  $I_{Na,p}+I_h$ -model.

a periodic trajectory with a long period (compare the time scales in the bottom insets in Fig. 5.6a and b).

When the  $\text{Na}^+$  inactivation curve  $h_\infty(V)$  has a low threshold, the nullclines have only one intersection, hence there is only one equilibrium, as in Fig. 5.6b. When  $I = 0$ , the equilibrium (filled circle) is stable and all trajectories converge to it. There are damped oscillations near the equilibrium, though they can hardly be seen in the figure. The oscillations occur because the  $I_{Na,t}$  current is partially inactivated at rest. An increase of  $V$  leads to more inactivation, less inward current, and hence rebound decrease of  $V$ , which in turn leads to partial deinactivation, more inward current, and rebound increase of  $V$ . When the applied dc-current  $I$  increases, the equilibrium loses stability via Andronov-Hopf bifurcation. When  $I = 4$ , the equilibrium is an unstable focus (white circle in the figure), and there is a stable limit cycle attractor around it corresponding to periodic spiking.

We see that the  $I_{Na,t}$ -model exhibits essentially the same dynamic repertoire as the  $I_{Na,p}+I_h$ -model, even though the models are quite different from the electrophysiological point of view.

### 5.1.4 $I_{Na,p}+I_h$ -model

The system

$$\begin{aligned} C \dot{V} &= I - \overbrace{g_L(V-E_L)}^{\text{leak } I_L} - \overbrace{g_{Na}m(V-E_{Na})}^{I_{Na,p}} - \overbrace{g_hh(V-E_h)}^{I_h}, \\ \dot{m} &= (m_\infty(V) - m)/\tau_m(V), \\ \dot{h} &= (h_\infty(V) - h)/\tau_h(V), \end{aligned}$$

is believed to describe the essence of the mechanism of slow subthreshold voltage oscillations in some cortical, thalamic, and hippocampal neurons, which we summarize in Fig. 5.7. As any other minimal model in this section, it consists of one amplifying ( $I_{Na,p}$ ) and one resonant ( $I_h$ ) current. Both currents may be partially active at resting voltage. Recall that we treat the  $h$ -current as being an inward current that is always activated (its activation variable  $m = 1$  all the time), but can be inactivated (turned

off) by depolarization and deinactivated (turned on) by hyperpolarization. At resting voltage this current is usually inactivated (turned off). A sufficient hyperpolarization of  $V$  deinactivates (turns on) the h-current resulting in rebound depolarization. While depolarized, the h-current inactivates (turns off), and the leak current repolarizes the membrane potential toward resting state. Without the persistent  $\text{Na}^+$  current, or some other amplifying current, these oscillations always subside, as the reader was asked to prove in Chap. 4, Ex. 10. However, they may become sustained when  $I_{\text{Na,p}}$  is involved.

To study dynamics of the  $I_{\text{Na,p}}+I_h$ -model we assume that the activation kinetics of the  $\text{Na}^+$  current is instantaneous, and use  $m = m_\infty(V)$  in the voltage equation to obtain a two-dimensional system

$$\begin{aligned} C \dot{V} &= I - \underbrace{g_L(V - E_L)}_{\text{leak } I_L} - \underbrace{g_{\text{Na}}m_\infty(V)(V - E_{\text{Na}})}_{\text{instantaneous } I_{\text{Na,p}}} - \underbrace{g_h h(V - E_h)}_{I_h}, \\ \dot{h} &= (h_\infty(V) - h)/\tau_h(V). \end{aligned}$$

The nullclines of this system

$$h = \frac{I - g_L(V - E_L) - g_{\text{Na}}m_\infty(V)(V - E_{\text{Na}})}{g_h(V - E_h)} \quad (\text{V-nullcline})$$

and

$$h = h_\infty(V) \quad (\text{h-nullcline})$$

have the familiar N and sigmoid shapes depicted in Fig. 5.8. We take the parameters for both currents from the experimental studies of thalamic relay neurons (see Sect. 2.3.5). This choice results in one intersection of the nullclines in the relevant voltage range, which corresponds to only one equilibrium. This equilibrium is a stable resting state when no current is injected, i.e., when  $I = 0$ . In Fig. 5.8, top, one can clearly see that  $h \approx 0$ ; that is, the h-current is inactivated (turned off). The rest state is due to the balance of inward persistent  $\text{Na}^+$  current and the Ohmic leak current. A small hyperpolarization deactivates the fast  $\text{Na}^+$  current and shifts the balance toward the leak current, which brings  $V$  closer to  $E_{\text{leak}}$ . This, in turn, results in slow deinactivation (turning on) of the h-current, which produces strong inward current and brings the membrane voltage back to the resting state.

Negative injected current (case  $I = -1$  in Fig. 5.8) destroys the balance of inward ( $I_{\text{Na,p}}$ ) and outward ( $I_{\text{leak}}$ ) currents at rest, and makes the resting state unstable. As a result, the model exhibits sustained subthreshold oscillations of membrane potential. Indeed, prolonged hyperpolarization turns on strong h-current and produces prolonged depolarization. Such a depolarization turns off the h-current, and the negative injected current hyperpolarizes the membrane potential again. As a result, the model exhibits sustained oscillations in the voltage range of  $-55$  mV to  $-65$  mV. The frequency of such oscillations depends on the parameters of the voltage equation and the time constant  $\tau(V)$  of the h-current, and it is near 4 Hz in Fig. 5.8.

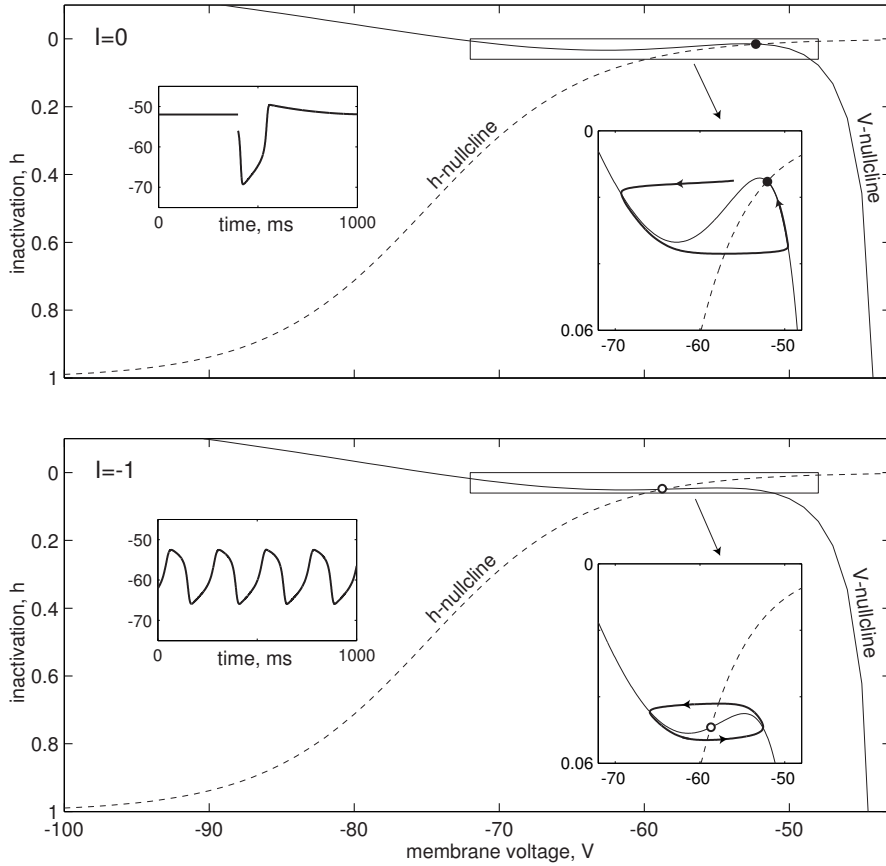


Figure 5.8: Rest and sustained subthreshold oscillations in the  $I_{\text{Na},p}+I_h$ -model. Parameters for currents as in thalamocortical neurons,  $E_{\text{Na}} = 20$  mV,  $E_h = -43$  mV,  $E_L = -80$  mV,  $g_L = 1.3$ ,  $g_{\text{Na}} = 0.9$ , and  $g_h = 3$ .

### 5.1.5 $I_h+I_{\text{Kir}}$ -model

The persistent  $\text{Na}^+$  current, which amplifies the damped oscillations in the  $I_{\text{Na},p}+I_h$ -model, can be substituted by the  $\text{K}^+$  inwardly rectifying current  $I_{\text{Kir}}$  to achieve the same amplifying effect. The resulting  $I_h+I_{\text{Kir}}$ -model

$$\begin{aligned} C \dot{V} &= I - \overbrace{g_L(V-E_L)}^{\text{leak } I_L} - \overbrace{g_{\text{Kir}}h_{\text{Kir}}(V-E_K)}^{I_{\text{Kir}}} - \overbrace{g_hh(V-E_h)}^{I_h}, \\ \dot{h}_{\text{Kir}} &= (h_{\text{Kir},\infty}(V) - h_{\text{Kir}})/\tau_{\text{Kir}}(V), \\ \dot{h} &= (h_\infty(V) - h)/\tau_h(V), \end{aligned}$$

can exhibit sustained subthreshold oscillations of membrane voltage via a rather weird mechanism illustrated in Fig. 5.9. The inwardly rectifying  $\text{K}^+$  current  $I_{\text{Kir}}$  behaves similarly to  $I_h$ , except that it is an outward current. A brief hyperpolarization deinactivates (turns on) the fast outward current  $I_{\text{Kir}}$  and produces more hyperpolarization

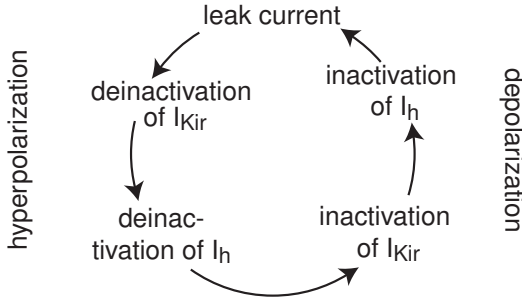


Figure 5.9: Mechanism of generation of sustained voltage oscillations in the  $I_h + I_{K\text{ir}}$ -model.

via a positive feedback loop. Such a regenerative process results in a prolonged hyperpolarization that deinactivates (turns on) the slower inward current  $I_h$  and produces a rebound depolarization. This depolarization is enhanced by inactivation (turning off) of the fast  $I_{K\text{ir}}$ . However, the membrane potential cannot hold long in the depolarized state because of the slow inactivation of  $I_h$ , and the leak current repolarizes the membrane potential. The repolarization is enhanced by the deinactivation of  $I_{K\text{ir}}$  and becomes a hyperpolarization again, leading to the oscillations summarized in Fig. 5.9.

Since the kinetics of  $I_{K\text{ir}}$  is practically instantaneous, we can use  $h_{K\text{ir}} = h_{K\text{ir},\infty}(V)$  in the voltage equation above and consider the two-dimensional system

$$\begin{aligned} C \dot{V} &= I - \underbrace{g_L(V-E_L)}_{\text{leak } I_L} - \underbrace{g_{K\text{ir}}h_{K\text{ir},\infty}(V)(V-E_K)}_{\text{instantaneous } I_{K\text{ir}}} - \underbrace{g_hh(V-E_h)}_{I_h}, \\ \dot{h} &= (h_\infty(V) - h)/\tau_h(V). \end{aligned}$$

One can easily find the nullclines of this system

$$h = \frac{I - g_L(V-E_L) - g_{K\text{ir}}h_{K\text{ir},\infty}(V)(V-E_K)}{g_h(V-E_h)} \quad (\text{V-nullcline})$$

and

$$h = h_\infty(V) \quad (\text{h-nullcline}),$$

which have the familiar form depicted in Fig. 5.10. Most values of the parameters result in a phase portrait similar to the one depicted in Fig. 5.10, left. The  $V$ -nullcline is a monotonic curve that intersects the  $h$ -nullcline in one point corresponding to a stable resting state. An injected dc-current  $I$  shifts the resting state, but does not change its stability: Voltage perturbations always subside, resulting only in damped oscillations. There is, however, a narrow region in parameter space (it took the author a few hours to find that region) that produces just the right relationship between inactivation curves and conductances so that the  $V$ -nullcline becomes N-shaped, and the subthreshold oscillations become sustained, as in Fig. 5.10, right.

### 5.1.6 $I_K + I_{K\text{ir}}$ -model

The last two minimal models consist exclusively of outward  $K^+$  currents, yet they can exhibit sustained oscillations of membrane voltage. The models defy imagination of

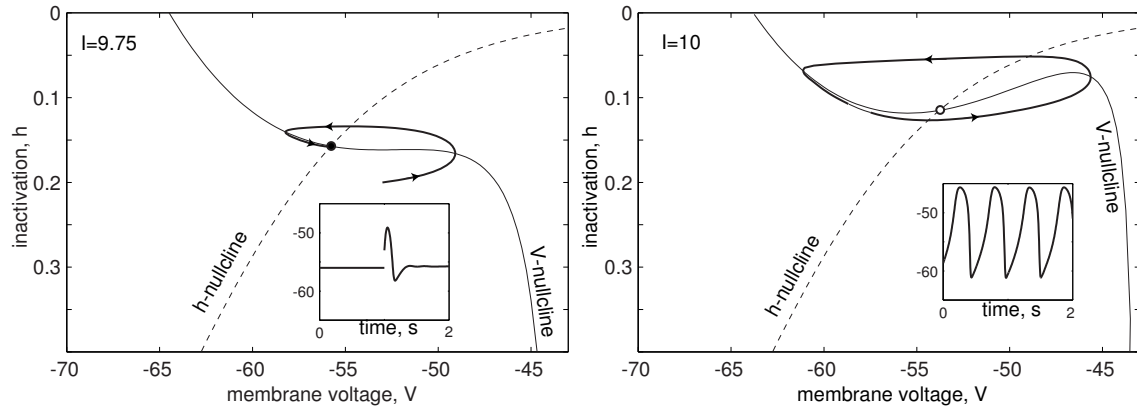


Figure 5.10: Rest and sustained subthreshold oscillations in the  $I_h + I_{\text{Kir}}$ -model. Parameters:  $E_K = -80 \text{ mV}$ ,  $E_h = -43 \text{ mV}$ ,  $E_L = -50 \text{ mV}$ ,  $g_{\text{Kir}} = 4$ ,  $g_h = 0.5$ ,  $g_L = 0.44$ .  $h$ -current is the same as in the previous section, except  $V_{1/2} = -65 \text{ mV}$ . Instantaneous  $I_{\text{Kir}}$  has  $V_{1/2} = -76 \text{ mV}$  and  $k = -11$ .

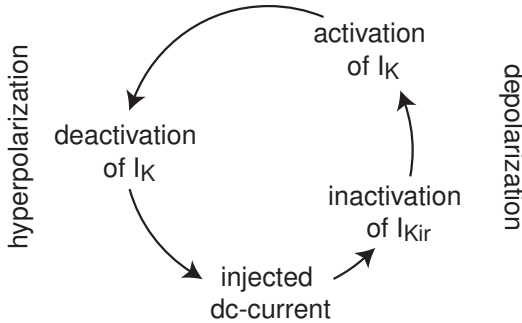


Figure 5.11: Mechanism of generation of sustained voltage oscillations in the  $I_K + I_{\text{Kir}}$ -model.

many biologists: How can a neuron with only outward  $K^+$  currents and no inward  $Na^+$  or  $Ca^{2+}$  currents fire action potentials?

In the  $I_K + I_{\text{Kir}}$ -model

$$\begin{aligned} C \dot{V} &= I - \overbrace{g_{\text{Kir}} h(V - E_K)}^{I_{\text{Kir}}} - \overbrace{g_K n(V - E_K)}^{I_K}, \\ \dot{n} &= (n_\infty(V) - n)/\tau_n(V), \\ \dot{h} &= (h_\infty(V) - h)/\tau_h(V), \end{aligned}$$

the amplifying current is  $I_{\text{Kir}}$  with inactivation gating variable  $h$ , and the resonant current is  $I_K$  with activation variable  $n$ . The mechanism of generation of action potentials is summarized in Fig. 5.11. A strong injected current depolarizes the membrane potential and inactivates (turns off)  $I_{\text{Kir}}$ , which amplifies the depolarization. While depolarized, the slower  $K^+$  current  $I_K$  activates and brings the potential down with possible hyperpolarization, which is amplified by the deinactivation of  $I_{\text{Kir}}$ . While the membrane potential is hyperpolarized,  $I_K$  deactivates and the strong injected current

brings the potential up again. Thus, the upstroke of the action potential is due exclusively to the injected dc-current  $I$ , while the downstroke is due to the persistent outward  $K^+$  current.

To perform the geometrical phase plane analysis of the model we take advantage of the same observation as before: The kinetics of the amplifying current  $I_{Kir}$  is relatively fast, so that  $h = h_\infty(V)$  can be used in the voltage equation to reduce the three-dimensional system above to the two-dimensional system

$$\begin{aligned} C \dot{V} &= I - \overbrace{g_{Kir} h_\infty(V)(V - E_K)}^{\text{instantaneous } I_{Kir}} - \overbrace{g_K n(V - E_K)}^{I_K}, \\ \dot{n} &= (n_\infty(V) - n)/\tau_n(V). \end{aligned}$$

It is an easy exercise to find the nullclines

$$n = I/\{g_K(V - E_K)\} - g_{Kir} h_\infty(V)/g_K \quad (V\text{-nullcline})$$

and

$$n = n_\infty(V) \quad (n\text{-nullcline}),$$

which we depict in Fig. 5.12. There are two interesting cases corresponding to high-threshold (Fig. 5.12a) and low-threshold (Fig. 5.12b)  $K^+$  current  $I_K$ .

When the  $I_K$  has low threshold, it is partially activated at resting potential. In this case, rest state corresponds to the balance of partially activated  $I_K$ , partially inactivated  $I_{Kir}$ , and a strong injected dc-current  $I$  (without the dc-current the membrane voltage would converge to  $E_K = -80$  mV and stay there forever). A small depolarization partially inactivates fast  $I_{Kir}$  but leaves slower  $I_K$  relatively unchanged. This results in an imbalance of the inward dc-current  $I$  and all outward currents, and the net inward current further depolarizes the membrane voltage. Depending on the size of the depolarization, the model may generate a subthreshold response or an action potential, as one can see in Fig. 5.12b, top. During the generation of the action potential, the persistent  $K^+$  current activates and causes after-hyperpolarization. During the after-hyperpolarization, the persistent  $K^+$  current deactivates below the resting level. This lets the injected dc-current  $I$  depolarize the membrane potential again, provided that  $I$  is strong enough, as in Fig. 5.12b, bottom.

In Fig. 5.12a we leave all parameters unchanged except that we increase the half-voltage activation  $V_{1/2}$  of  $I_K$  by 15 mV and decrease  $I$  to compensate for the deficit of outward current. Now, the resting state corresponds to the balance of the  $I_{Kir}$  and  $I$ , because the high-threshold persistent  $K^+$  current is completely deactivated in this voltage range. The behavior near the rest state is determined by the interplay between instantaneous  $I_{Kir}$  and  $I$ , and it was studied in Chap. 3 (see  $I_{Kir}$ -model). There are two equilibria: a stable node corresponding to the resting state, and a saddle corresponding to the threshold state. A sufficiently strong perturbation can push  $V$  beyond the saddle equilibrium, as in Fig. 5.12a, top, and can cause the minimal model to fire an action

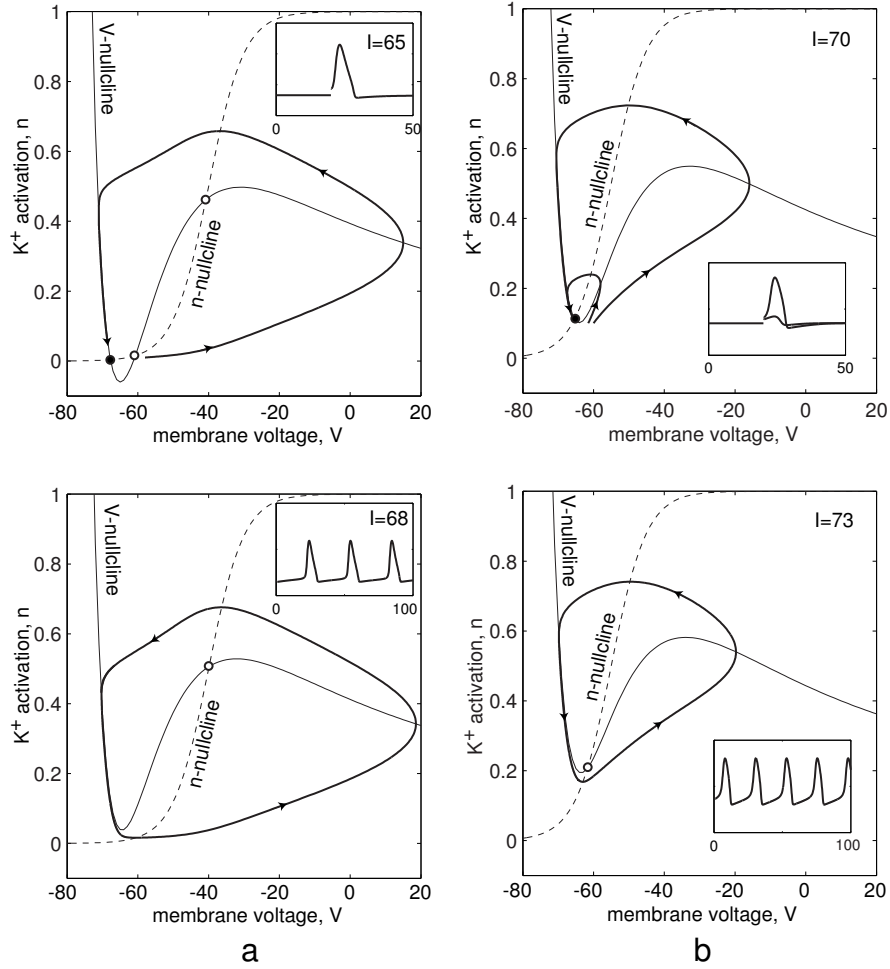


Figure 5.12: Possible intersections of nullclines in the  $I_K + I_{\text{Kir}}$ -model. Parameters:  $E_K = -80$  mV,  $g_{\text{Kir}} = 20$ ,  $g_K = 2$ . Instantaneous  $I_{\text{Kir}}$  with  $V_{1/2} = -80$  mV and  $k = -12$ . Slower  $I_K$  with  $k = 5$ ,  $\tau(V) = 5$  ms, and  $V_{1/2} = -40$  mV (in a) or  $V_{1/2} = -55$  mV (in b).

potential. If we increase  $I$ , the node and the saddle approach, coalesce, and annihilate each other via a saddle-node bifurcation, and the model start to fire action potentials periodically.

We see that  $I_K + I_{\text{Kir}}$ -model has essentially the same dynamic repertoire as the more conventional  $I_{\text{Na,p}} + I_K$ -model or  $I_{\text{Na,t}}$ -model, despite the fact that it is based on a rather bizarre ionic mechanism for excitability and spiking.

### 5.1.7 $I_A$ -model

The last minimal voltage-gated model has only one transient  $K^+$  current, often referred to as being A-current  $I_A$ , yet it can also generate sustained oscillations. In some sense, the model is similar to the  $I_{\text{Na,t}}$ -model. Indeed, each consists of only one transient

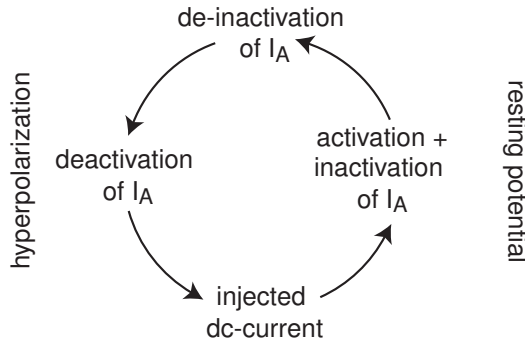


Figure 5.13: Mechanism of generation of sustained voltage oscillations in the  $I_A$ -model.

current and an Ohmic leak current. The only difference is that A-current is outward, and as a result, the action potentials are fired downward; see Fig. 5.14 and Fig. 5.15 below.

The A-current has activation and inactivation variables  $m$  and  $h$ , respectively, and the model has the form

$$\begin{aligned} C \dot{V} &= I - \overbrace{g_L(V - E_L)}^{\text{leak } I_L} - \overbrace{g_A m h (V - E_K)}^{I_A} \\ \dot{m} &= (m_\infty(V) - m)/\tau_m(V) \\ \dot{h} &= (h_\infty(V) - h)/\tau_h(V). \end{aligned}$$

The mechanism of generation of downward action potentials is summarized in Fig. 5.13. Due to a strong injected dc-current, the rest state is in the depolarizing voltage range, and it corresponds to the balance of the partially activated, partially inactivated A-current, leak outward current, and the injected dc-current. A small hyperpolarization can simultaneously deactivate and deinactivate the A-current, i.e., decrease variable  $m$  and increase variable  $h$ . Depending on the relationship between the activation and inactivation time constants, this may result in an increase of the A-current conductance, which is proportional to the product  $mh$ . More outward current produces more hyperpolarization and even more outward current. As a result of this regenerative process, the membrane voltage produces a sudden downstroke. While hyperpolarized, the A-current deactivates (variable  $m \rightarrow 0$ ), and the injected dc-current slowly brings the membrane potential toward the resting state, resulting in a slow upstroke. Fast downstroke and a slower upstroke from a depolarized resting state look like an action potential pointing downwards.

If activation kinetics is much faster than the inactivation kinetics, we can substitute  $m = m_\infty(V)$  into the voltage equation above and reduce the  $I_A$ -model to a two-dimensional system, which hopefully would have the right kind of nullclines and a limit cycle attractor. After all, this is what we have done with previous minimal models and it always worked. As the reader is asked to prove in Ex. 1, the  $I_A$ -model cannot have a limit cycle attractor when the A-current activation kinetics is instantaneous. Oscillations are possible only when the activation and inactivation kinetics

have comparable time constants or inactivation is much faster than activation.

Even though none of the experimentally measured A-currents show fast inactivation and a relatively slower activation, this case is still interesting from the pure theoretical point of view, since it shows how a single  $K^+$  current can give rise to oscillations. Assuming instantaneous inactivation and using  $h = h_\infty(V)$  in the voltage equation, we obtain a two-dimensional system

$$\begin{aligned} C \dot{V} &= I - \underbrace{g_L(V - E_L)}_{\text{leak } I_L} - \underbrace{g_A m h_\infty(V)(V - E_K)}_{I_A, \text{ inst. inactivation}}, \\ \dot{m} &= (m_\infty(V) - m)/\tau_m(V), \end{aligned}$$

whose nullclines can easily be found:

$$m = \frac{I - g_L(V - E_L)}{g_A h_\infty(V)(V - E_K)} \quad (V\text{-nullcline})$$

and

$$m = m_\infty(V) \quad (m\text{-nullcline}).$$

Two typical cases are depicted in Fig. 5.14a and b. We start with the simpler case in Fig. 5.14b.

Figure 5.14b depicts nullclines when the A-current has low activation threshold. There is only one intersection of the nullclines, hence there is only one equilibrium, which is a stable focus when the injected dc-current  $I$  is not strong enough (Fig. 5.14b, top). Increasing  $I$  makes the equilibrium lose stability via a supercritical Andronov-Hopf bifurcation that gives birth to a small amplitude limit cycle attractor (not shown in the figure). A further increase of  $I$  increases the amplitude of oscillations, and e.g., when  $I = 10$  (middle of Fig. 5.14b), the attractor corresponds to periodic firing of action potentials. When  $I = 10.5$ , the attractor disappears and the equilibrium becomes stable (via Andronov-Hopf bifurcation) again. The model, however, becomes excitable. A small hyperpolarization does not change significantly the A-current, and the voltage returns back to rest resulting in a “subthreshold response”. A sufficiently large hyperpolarization deactivates enough  $I_A$  to open the  $K^+$  current and hyperpolarize the membrane even further. This regenerative process produces the downstroke and brings  $V$  close to  $E_K$ . During the state of hyperpolarization, the A-current deactivates ( $m \rightarrow 0$ ), and the dc-current  $I$  brings  $V$  back to rest. Notice that the action potential is directed downward.

In Fig. 5.14a we consider the  $I_A$ -model with exactly the same parameters except that we shift the half-voltage activation  $V_{1/2}$  of  $I_A$  by 10 mV so that the A-current has higher activation threshold. This does not affect much the behavior of the system when  $I$  is small. However, when  $I \approx 10.7$  the spiking limit cycle attractor undergoes a new kind of bifurcation — saddle-node bifurcation — resulting in the appearance of two new equilibria: a stable node and a saddle. If the reader looks at Fig. 5.14a upside-down, he will notice that this figure resembles figures 5.4a, 5.6a, or 5.12a, with all the

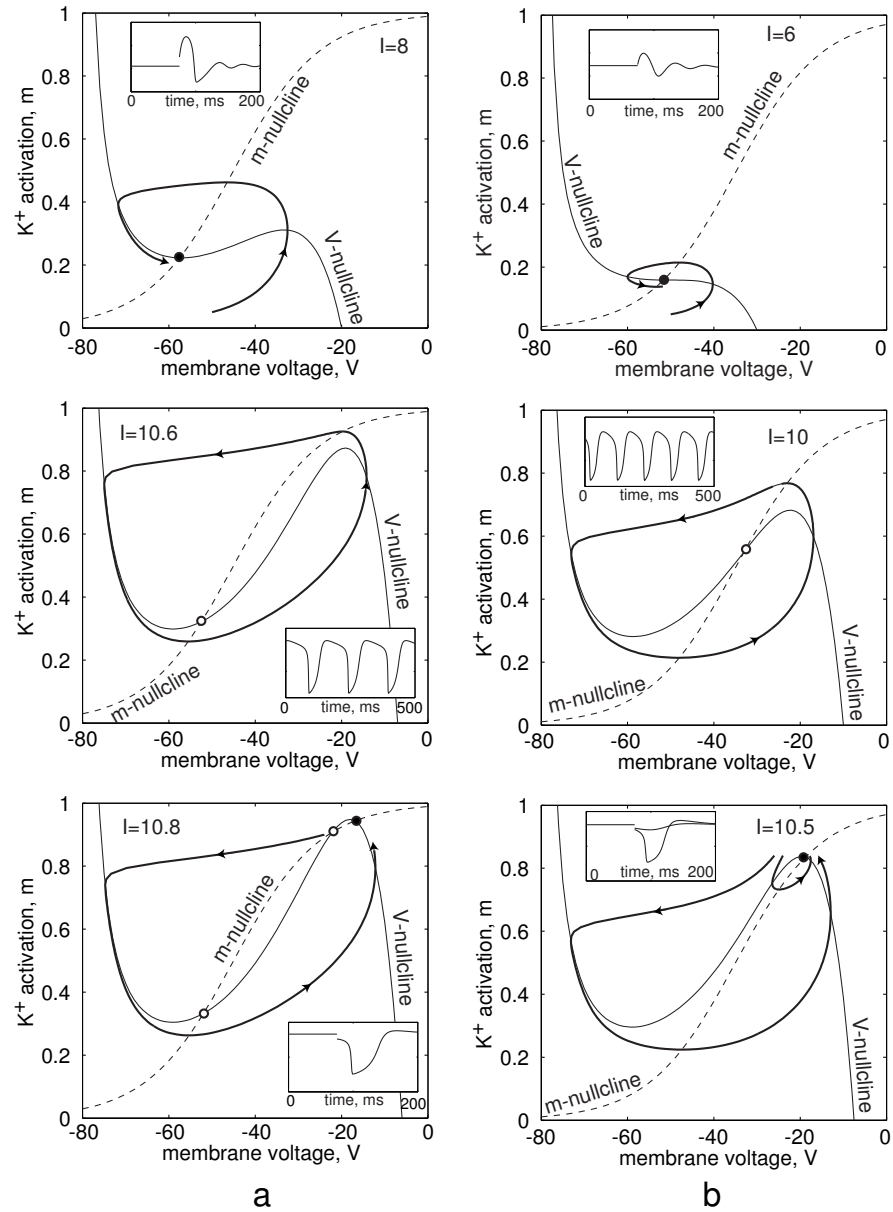


Figure 5.14: Possible intersections of nullclines in the  $I_A$ -model. Parameters:  $E_K = -80$  mV,  $E_L = -60$  mV,  $g_A = 5$ ,  $g_L = 0.2$ . Instantaneous inactivation kinetics with  $V_{1/2} = -66$  mV and  $k = -10$ . Activation of the A-current with  $k = 10$ ,  $\tau(V) = 20$  ms, and  $V_{1/2} = -45$  mV (in a) or  $V_{1/2} = -35$  mV (in b).

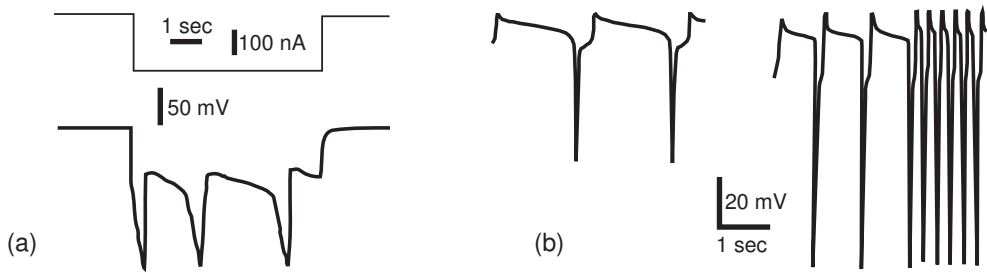


Figure 5.15: Anomalous (upside-down) spikes in (a) lobster muscle fibers (modified from Fig.2 of Reuben et al. 1961) and in (b) *Ascaris* Esophageal cells (modified from Fig.16 of del Castillo and Morales 1967; the cell is depolarized by injected dc-current). The voltage axis is not inverted.

consequences: The node corresponds to a resting state, and the saddle corresponds to the threshold state. The large-amplitude trajectory that starts at the saddle and terminates at the node corresponds to an action potential, though to a weird one. Thus, the behavior of this model is similar to the behavior of other models with the exception that the  $V$ -axis is reversed.

The existence of “upside-down”  $K^+$  spikes may (or better say *does*) look bizarre to many researchers, even though “inverted”  $K^+$  and  $Cl^-$  spikes were reported in many preparations, including frog and toad axons, squid axons, lobster muscle fibers, dog cardiac muscle, etc., as reviewed by Reuben et al. (1961) and Grundfest (1971). Two such cases are depicted in Fig. 5.15. Interestingly, Reuben et al. (1961) postulated, albeit reluctantly, that the inverted spikes are caused by the inactivation of  $K^+$  current. The reluctance was due to the fact that transient  $K^+$   $I_A$  was not known at that time.

By now the reader must have convinced himself that quite different models can have practically identical dynamics. Conversely, the same model could have quite different behavior if only one parameter, e.g.,  $V_{1/2}$ , is changed by as little as 10 mV. Such dramatic conclusions emphasize the importance of geometrical phase plane analysis of neuronal models, since the conclusions can hardly be drawn from mere word descriptions of the spiking mechanisms.

### 5.1.8 $Ca^{2+}$ -gated minimal models

So far, we considered minimal models consisting of voltage-gated currents only. However, there are many ionic currents that depend not only on the membrane potential, but also on the concentration of intracellular ions, mostly  $Ca^{2+}$ . Such currents are referred to as being  $Ca^{2+}$ -gated, and they are summarized in Fig. 5.16. In addition, there are  $Cl^-$ -gated,  $K^+$ -gated, and  $Na^+$ -gated currents, such as SLO gene family of  $Cl^-$ -gated  $K^+$  currents discovered in *C. elegans*, and related “slack and slick” family of  $Na^+$ -gated  $K^+$  currents (Yuan et al. 2000, 2003). Considering minimal models involving these currents goes outside the scope of this book, but it could be a good

Currents	Voltage-Gated		Ca <sup>2+</sup> -Gated	
	Activation	Inactivation	Activation	Inactivation
$I_{\text{leak}}$				
Inward				
$I_{\text{Na,p}}$	fast			
$I_{\text{Na,t}}$	fast	fast		
$I_{\text{Ca(P)}}$	fast	slow		
$I_{\text{Ca(L)}}$	fast			slow
$I_{\text{Ca(N)}}$	fast	medium		medium
$I_h$		medium		
$I_{\text{CAN}}$			slow	
Outward				
$I_K$	fast			
$I_{K(M)}$	slow			
$I_A$	fast	fast		
$I_{K(D)}$	medium	slow		
$I_{K(Ca)}$	fast		fast	
$I_{\text{AHP}}$			slow	
$I_{\text{Kir}}$		fast		

Figure 5.16: Some representative voltage- and Ca<sup>2+</sup>-gated ionic currents (Johnston and Wu 1995, Hille 2001, Shepherd 2004).

intellectual exercise for an expert reader (see also Ex. 7 and 8).

Ca<sup>2+</sup>-gated currents can also be divided into amplifying and resonant. Ca<sup>2+</sup>-activated inward currents, such as the cation non-selective  $I_{\text{CAN}}$ , act as amplifying currents. Indeed, activation of such a current leads to an influx of Ca<sup>2+</sup> ions and to more activation. Similarly, a hypothetical outward current inactivated by Ca<sup>2+</sup>, not present in the figure, might also act as an amplifying current. Indeed, a depolarization due to the Ca<sup>2+</sup> influx inactivates such a hypothetical outward current, thereby producing a net shift toward inward currents and leading to more depolarization.

In contrast, Ca<sup>2+</sup>-inactivating inward currents and Ca<sup>2+</sup>-activating outward currents, such as  $I_{\text{Ca(L)}}$  and  $I_{\text{AHP}}$ , respectively, act as resonant currents. Indeed, a depolarization due to the Ca<sup>2+</sup> influx inactivates the inward current and activates the outward current, and resists further depolarization.

		resonant gate			
		voltage-gated		Ca <sup>2+</sup> -gated	
		inactivation of inward current	activation of outward current	inactivation of inward current	activation of outward current
amplifying gate	voltage-gated	$I_{Na,p}+I_h$ $I_{Na,t}$	$I_{Na,p}+I_K$	$I_{Ca}+I_2$ $I_{Ca(L)}$	$I_{Ca}+I_K(Ca)$
	voltage-gated	$I_{Kir}+I_h$	$I_{Kir}+I_K$ $I_A$	$I_{Kir}+I_2$	
	Ca <sup>2+</sup> -gated	$I_{CAN}+I_h$ $I_1$	$I_{CAN}+I_K$	$I_{CAN}+I_2$ $I_{CAN,t}$	$I_{CAN}+I_K(Ca)$
	Ca <sup>2+</sup> -gated	$I_4+I_3$		$I_4+I_2$	

Figure 5.17: Voltage- and Ca<sup>2+</sup>-gated minimal models.  $I_1, \dots, I_4$  are four hypothetical currents that could exist theoretically, but has never been recorded experimentally; see text.

Any combination of one voltage- or Ca<sup>2+</sup>-gated amplifying current and one voltage- or Ca<sup>2+</sup>-gated resonant current leads to a minimal model for spiking. All such combinations are depicted in Fig. 5.17. Here,  $I_1$  denotes a hypothetical Ca<sup>2+</sup>-activated voltage-inactivated transient inward current. Though such a current is not currently known, one can easily write a conductance-gated model for it. A biologist would treat such a current as hyperpolarization- and Ca<sup>2+</sup>-activated.  $I_2$  is a hypothetical Ca<sup>2+</sup> current that is inactivated by Ca<sup>2+</sup>.  $I_3$  is a hypothetical voltage-inactivated Ca<sup>2+</sup> current.  $I_4$  is an outward Ca<sup>2+</sup>-inactivated current.

We see that there are many minimal models in Fig. 5.17. Six of them are purely voltage-gated, and they have been investigated above. The others are mixed-mode or purely Ca<sup>2+</sup>-gated models. An interested reader can work out the details of their phase portraits.

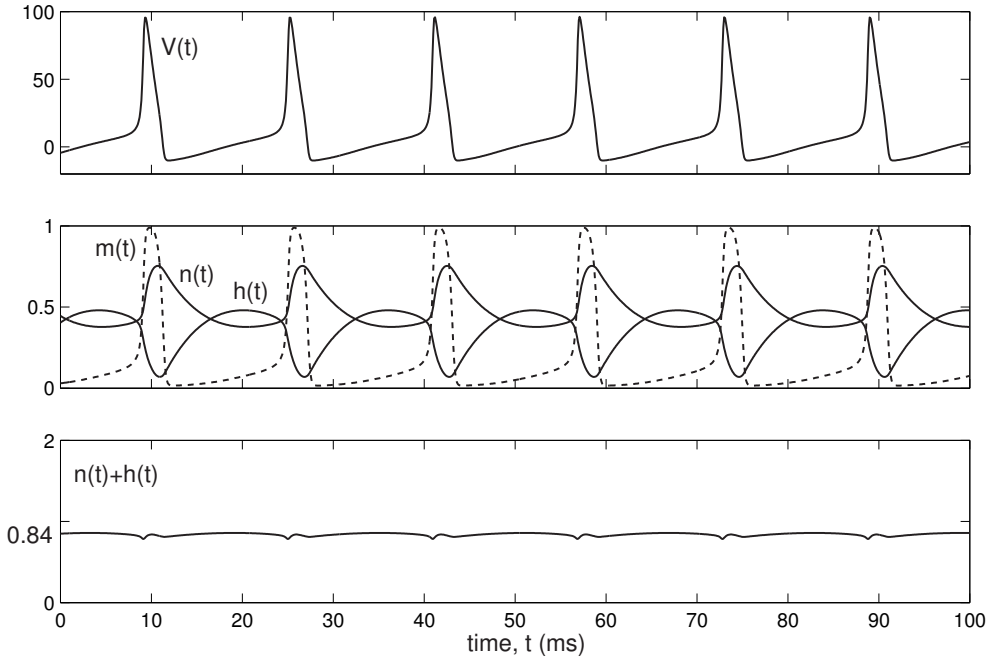


Figure 5.18: The sum  $n(t) + h(t) \approx 0.84$  in the Hodgkin-Huxley model. Parameters as in Chap. 2 and  $I = 8$ .

## 5.2 Reduction of multi-dimensional models

### 5.2.1 Hodgkin-Huxley model

Let us consider again the Hodgkin-Huxley model

$$\begin{aligned} C \dot{V} &= I - \overbrace{g_K n^4 (V - E_K)}^{I_K} - \overbrace{g_{Na} m^3 h (V - E_{Na})}^{I_{Na}} - \overbrace{g_L (V - E_L)}^{I_L}, \\ \dot{n} &= (n_\infty(V) - n)/\tau_n(V), \\ \dot{m} &= (m_\infty(V) - m)/\tau_m(V), \\ \dot{h} &= (h_\infty(V) - h)/\tau_h(V), \end{aligned}$$

with the original values of parameters presented in Chap. 2. How can we understand the qualitative dynamics of this model? One way, discussed above, is to throw away variable  $h$  or  $n$  and to reduce this model to the  $I_{Na,p} + I_K$ -model or  $I_{Na,t}$ -model, respectively. Although the reduced minimal models can tell a lot about the behavior of the original model, they are not equivalent to the Hodgkin-Huxley model from the electrophysiological or the dynamical systems point of view. Below we discuss another method of reduction of multidimensional electrophysiological models to planar systems.

The Hodgkin-Huxley model has four independent variables. Early computer simulations by Krinskii and Kokoz (1973) have shown that there is a relationship between

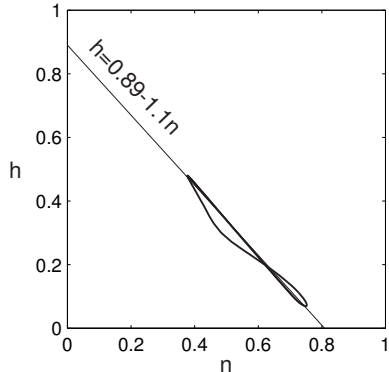


Figure 5.19: The relationship between  $n(t)$  and  $h(t)$  in the Hodgkin-Huxley model can better be described by  $h = 0.89 - 1.1n$ .

the gating variables  $n(t)$  and  $h(t)$ , namely,

$$n(t) + h(t) \approx 0.84 ,$$

as shown in Fig. 5.18. In fact, plotting the variables on the  $(n, h)$  plane, as we do in Fig. 5.19, reveals that the orbit is near the straight line

$$h = 0.89 - 1.1n .$$

We can use this relationship in the voltage equation to reduce the Hodgkin-Huxley model to a three-dimensional system. If, in addition, we assume that the activation kinetics of the  $\text{Na}^+$  current is instantaneous, i.e.,  $m = m_\infty(V)$ , then the Hodgkin-Huxley model can be reduced to the two-dimensional system

$$\begin{aligned} C \dot{V} &= I - \overbrace{g_K n^4 (V - E_K)}^{I_K} - \overbrace{g_{\text{Na}} m_\infty^3 (V) (0.89 - 1.1n) (V - E_{\text{Na}})}^{\text{instantaneous } I_{\text{Na}}} - \overbrace{g_L (V - E_L)}^{I_L} , \\ \dot{n} &= (n_\infty(V) - n) / \tau_n(V) , \end{aligned}$$

whose solutions retain qualitative and some quantitative agreement with the original four-dimensional Hodgkin-Huxley system; see Fig. 5.20.

The first step in the analysis of any two-dimensional system is to find its nullclines. The  $V$ -nullcline can be found by solving numerically the equation

$$I - g_K n^4 (V - E_K) - g_{\text{Na}} m_\infty^3 (V) (0.89 - 1.1n) (V - E_{\text{Na}}) - g_L (V - E_L) = 0$$

for  $n$ . The nullcline has the familiar N-shape depicted in Fig. 5.21. Notice that it has only one intersection with the  $n$ -nullcline  $n = n_\infty(V)$ , hence there is only one equilibrium, which is stable when  $I = 0$ . When the parameter  $I$  increases, the equilibrium loses stability via subcritical Andronov-Hopf bifurcation, as discussed in the next chapter. When  $I$  is sufficiently large (e.g.  $I = 12$  in Fig. 5.21), there is a limit cycle attractor corresponding to periodic spiking. In Ex. 2 we discuss what happens when  $I$  becomes very large.

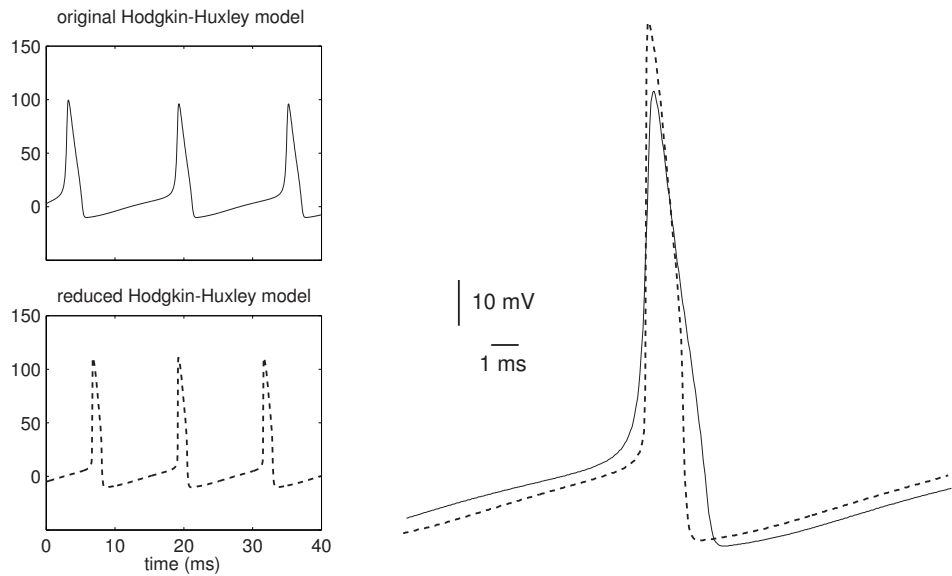


Figure 5.20: Action potentials in the original (top) and reduced (bottom) Hodgkin-Huxley model ( $I = 8$ ).

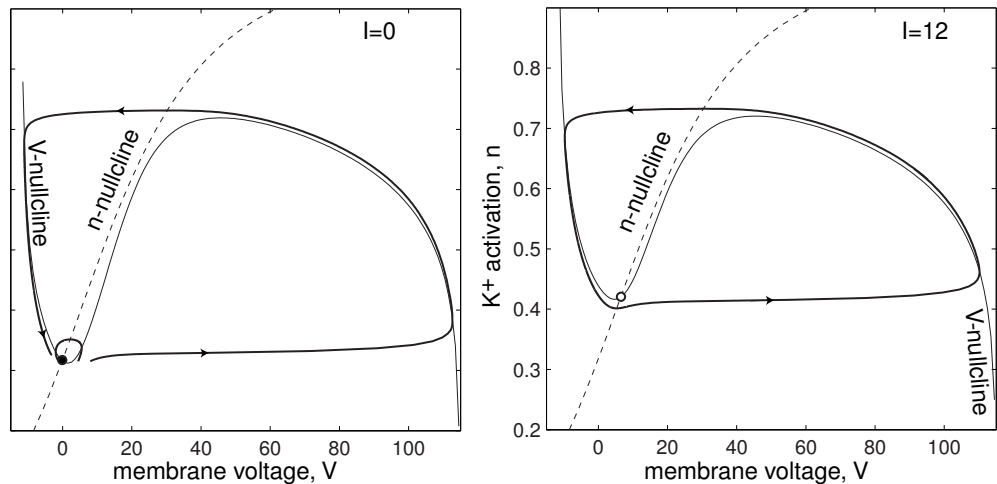


Figure 5.21: Reduction of the Hodgkin-Huxley model to the  $(V, n)$ -phase plane.

### 5.2.2 Equivalent potentials

Inspired by the reduction idea of Krinskii and Kokoz (1973), Kepler et al. (1992) suggested a systematic method of reducing the complexity of conductance-based Hodgkin-Huxley-type models

$$\begin{aligned} C\dot{V} &= I - I(V, x_1, \dots, x_n) \\ \dot{x}_i &= (m_{i,\infty}(V) - x_i)/\tau_i(V), \quad i = 1, \dots, n, \end{aligned}$$

where  $x_1, \dots, x_n$  is a set of gating variables. The goal is to find certain patterns or combinations of the gating variables that can be lumped to reduce the dimension of the system. For example, we want to combine all resonant variables operating on a similar time scale into a “master” recovery variable, then do the same for amplifying variables.

Let us convert each variable  $x_i(t)$  to the *equivalent potential*  $v_i(t)$  that satisfies

$$x_i = m_{i,\infty}(v_i).$$

In other words, the equivalent potential is the voltage which, in a voltage clamp, would give the value  $x_i$  when the model is at an equilibrium. Applying the chain rule to  $v_i = m_{i,\infty}^{-1}(x_i)$ , we express the model above in terms of equivalent potentials:

$$\begin{aligned} C\dot{V} &= I - I(V, m_{1,\infty}(v_1), \dots, m_{n,\infty}(v_n)), \\ \dot{v}_i &= (m_{i,\infty}(V) - m_{i,\infty}(v_i))/(\tau_i(V) m'_{i,\infty}(v_i)). \end{aligned}$$

Since the Boltzmann functions  $m_{i,\infty}(V)$  are invertible, the denominators do not vanish. No approximations have been made yet; the new model is entirely equivalent to the original one, it is just expressed in a different coordinate system. The new coordinates, however, expose many patterns among the equivalent voltage variables that were not obvious in the original, gating coordinate system.

Kepler et al. (1992) developed an algorithm that substitutes resonant and amplifying variables by their weighted averages. The weights are found using Lagrange multipliers and strictly local criteria aimed at preserving the bifurcation structure of the model. There is also a set of tests that informs the user when the method is likely to fail. The method results in a lower-dimensional system that is easier to simulate, visualize, and understand.

### 5.2.3 Nullclines and I-V recordings

We saw that the form and the position of nullclines provided important information about the neuron dynamics, i.e., the number of equilibria, their stability, the existence of limit cycle attractors, etc. The same information, in principle, can also be obtained from the analysis of the neuronal current-voltage (I-V) relations. This is not a coincidence, since there is a profound relationship between nullclines and experimentally measured I-V curves.

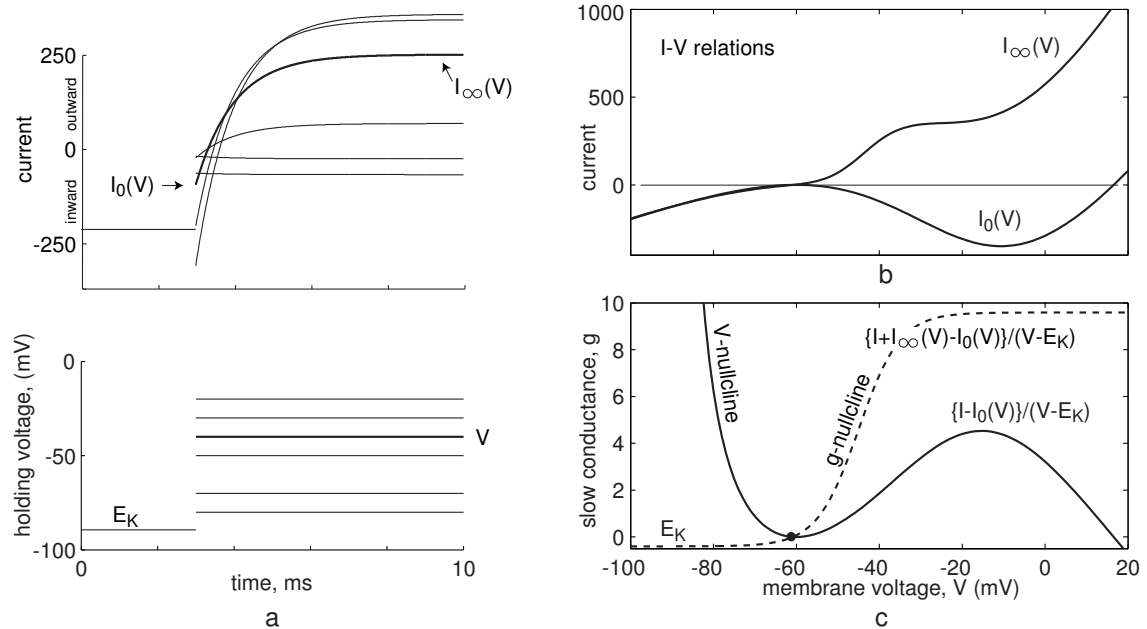


Figure 5.22: Voltage-clamp protocol to measure instantaneous (peak) and steady state current-voltage (I-V) relations. (Shown simulations of the  $I_{\text{Na,p}}+I_K$ -model from Fig. 5.4b.)

Let us illustrate the relationship using the  $I_{\text{Na,p}}+I_K$ -model, which we write in the form

$$C \dot{V} = I - I_0(V) - g(V - E_K), \quad (5.3)$$

$$\dot{g} = f(V, g), \quad (5.4)$$

where

$$I_0(V) = g_L(V - E_L) + g_{\text{Na}}m_\infty(V)(V - E_{\text{Na}})$$

is the instantaneous (peak) current, and  $g = g_Kn$  is the slow conductance. The function  $f(V, g)$  describes the dynamics of  $g$ , and its form is not important here. The method described below is quite general, and it can be used in many circumstances when little is known about the neuron's electrophysiology.

In Fig. 5.22 we describe a typical voltage-clamp experiment to measure the instantaneous (peak) and the steady-state I-V relations, denoted here as  $I_0(V)$  and  $I_\infty(V)$ , respectively. The holding voltage (Fig. 5.22a, bottom) is kept at  $E_K$  and then stepped to various values  $V$ . The recorded current (Fig. 5.22a, top) typically consists of a fast (peak) component  $I_0(V)$  that is due to the instantaneous activation of  $\text{Na}^+$  currents, leak current, and other fast currents, and then it relaxes to the asymptotic steady state value  $I_\infty(V)$ . Repeating this experiment for various  $V$ , one can measure the I-V functions  $I_0(V)$  and  $I_\infty(V)$  depicted in Fig. 5.22b. Notice that  $I_0(V)$  has the N-shape with a large region of negative slope. This region corresponds to the regenerative activation

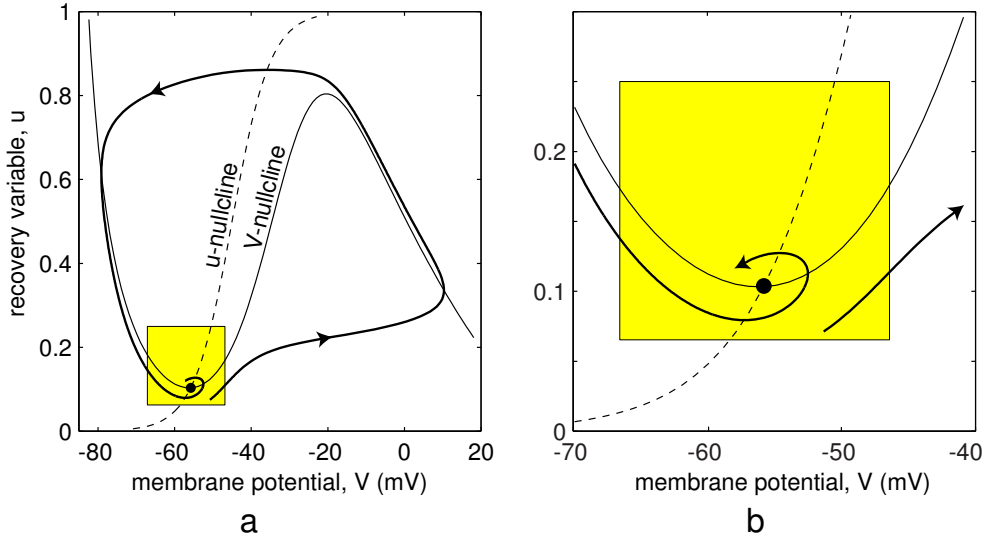


Figure 5.23: Phase portrait (a) and its magnification (b) of a typical neuronal model having voltage variable  $V$  and a recovery variable  $u$ .

of the  $\text{Na}^+$  current, and it is responsible for the excitability property of the neuron. It is also responsible for the N-shape of the  $V$ -nullcline, as we see next.

Once the I-V relations are found, we can find the nullclines of the system (5.3, 5.4). From the equation

$$I - I_0(V) - g(V - E_K) = 0$$

we can easily find the  $V$ -nullcline

$$g = \{I - I_0(V)\}/(V - E_K) \quad (\text{V-nullcline}) ,$$

which has the inverted N-shape depicted in Fig. 5.22c because  $I_0(V)$  does. While measuring  $I_\infty(V)$ , we hold  $V$  long enough so that all conductances reach their steady-state values. The steady-state value  $g = g_\infty(V)$  can be obtained from the equation

$$I - I_0(V) - g(V - E_K) = -I_\infty(V) ,$$

which says that the asymptotic steady-state current is the sum of the steady-state fast current and steady-state slow current. Therefore

$$g = \{I + I_\infty(V) - I_0(V)\}/(V - E_K) \quad (g\text{-nullcline})$$

depicted in Fig. 5.22c. Since we used the  $I_{\text{Na,p}}+I_K$ -model with parameters as in Fig. 5.4b, top, we are not surprised that the  $V$ - and  $g$ -nullclines found here have the same shape and relative position as those in Fig. 5.4b, top. In Ex. 5 we further explore the relationship between the I-V curves and neuronal dynamics.

### 5.2.4 Reduction to simple model

All models discussed in this chapter can be reduced to two-dimensional systems having a fast voltage variable,  $V$ , and a slower “recovery” variable,  $u$ , with N-shaped and sigmoidal nullclines, respectively. The decision to fire or not to fire is made at the resting state, which is the intersection of the nullclines near the left knee, as we illustrate in Fig. 5.23a. To model the subthreshold behavior of such neurons and the initial segment of the up-stroke of an action potential, we need to consider only a small neighborhood of the left knee confined to the shaded square in Fig. 5.23. The rest of the phase space is needed only to model the peak and the down-stroke of the action potential. If the shape of the action potential is less important than the subthreshold dynamics leading to this action potential, then we can retain detailed information about the left knee and its neighborhood and simplify the vector field outside the neighborhood. This approach results in a simple model capable to exhibit quite realistic dynamics, as we see in Chap. 8.

#### Derivation via nullclines

The fast nullcline in Fig. 5.23b can be approximated by the quadratic parabola

$$u = u_{\min} + p(V - V_{\min})^2 ,$$

where  $(V_{\min}, u_{\min})$  is the location of the minimum on the left knee, and  $p \geq 0$  is a scaling coefficient. Similarly, the slow nullcline can be approximated by the straight line

$$u = s(V - V_0) ,$$

where  $s$  is the slope and  $V_0$  is the  $V$ -intercept. All these parameters can easily be determined geometrically or analytically.

Using these nullclines, we approximate the dynamics in the shaded region in Fig. 5.23 by the system

$$\begin{aligned}\dot{V} &= \tau_f \{p(V - V_{\min})^2 - (u - u_{\min})\} , \\ \dot{u} &= \tau_s \{s(V - V_0) - u\} ,\end{aligned}$$

where the parameters  $\tau_f$  and  $\tau_s$  describe the fast and slow time scales. Because of the term  $(V - V_{\min})^2$ , the variable  $V$  can escape to infinity in a finite time. This corresponds to the firing of an action potential, more precisely, to its upstroke. To model the downstroke, we assume that  $V_{\max}$  is the peak value of the action potential, and we reset the state of the system

$$(V, u) \leftarrow (V_{\text{reset}}, u + u_{\text{reset}}) , \quad \text{when } V = V_{\max} ,$$

as if the spiking trajectory disappears at the right edge and appears at the left edge in Fig. 5.23b. Here  $V_{\text{reset}}$  and  $u_{\text{reset}}$  are parameters. Appropriate re-scaling of variables

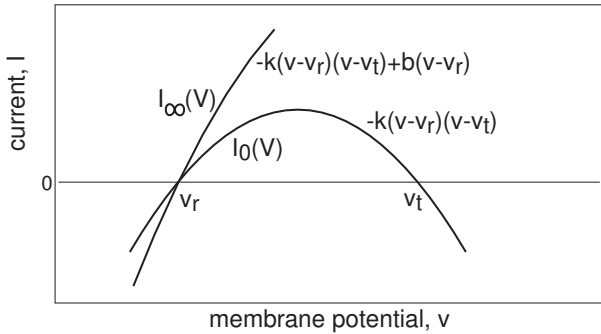


Figure 5.24: The relationship between the parameters of the simple model (5.7, 5.8) and the instantaneous and steady-state I-V relations,  $I_0(V)$  and  $I_\infty(V)$ , respectively.

transforms the simple model into the equivalent form

$$\dot{v} = I + v^2 - u \quad \text{if } v \geq 1, \text{ then} \quad (5.5)$$

$$\dot{u} = a(bv - u) \quad v \leftarrow c, u \leftarrow u + d \quad (5.6)$$

having only four dimensionless parameters.

### Derivation via I-V relations

The parameters of the simple model can be derived using instantaneous (peak) and steady-state I-V relations. Let us represent the model in the following equivalent form

$$C\dot{v} = k(v - v_r)(v - v_t) - u + I \quad \text{if } v \geq v_{\text{peak}}, \text{ then} \quad (5.7)$$

$$u = a\{b(v - v_r) - u\} \quad v \leftarrow c, u \leftarrow u + d \quad (5.8)$$

where  $v$  is the membrane potential,  $u$  is the recovery current, and  $C$  is the membrane capacitance. The quadratic polynomial  $-k(v - v_r)(v - v_t)$  approximates the subthreshold part of the instantaneous I-V relation  $I_0(V)$ . Here,  $v_r$  is the resting membrane potential, and  $v_t$  is the instantaneous threshold potential, as in Fig. 5.24. That is, instantaneous depolarizations above  $v_t$  result in spike response. The polynomial  $-k(v - v_r)(v - v_t) + b(v - v_r)$  approximates the subthreshold part of the steady-state I-V relation  $I_\infty(V)$ . When  $b < 0$ , its maximum approximates the rheobase current of the neuron, i.e., the minimal amplitude of a dc-current needed to fire a cell. Its derivative with respect to  $v$  at  $v = v_r$ , i.e.,  $b - k(v_r - v_t)$ , corresponds to the resting input conductance, which is the inverse of the input resistance. Knowing both the rheobase and the input resistance of a neuron, one could determine the parameters  $k$  and  $b$ , as we do in Chap. 8. This method does not work when  $b > 0$ .

The sum of all slow currents that modulate the spike-generation mechanism are combined in the phenomenological variable  $u$  with outward currents taken with the plus sign. The form of (5.8) ensures that  $u = 0$  at rest, i.e., when  $I = 0$  and  $v = v_r$ . The sign of  $b$  determines whether  $u$  is an amplifying ( $b < 0$ ) or a resonant ( $b > 0$ ) variable. In the latter case, the neuron sags in response to hyperpolarized pulses of current, peaks in response to depolarized subthreshold pulses, and produces rebound (post-inhibitory) responses. The recovery time constant is  $a$ . The spike cut-off value is

$v_{\text{peak}}$ , and the voltage reset value is  $c$ . The parameter  $d$  describes the total amount of outward minus inward currents activated during the spike and affecting the after-spike behavior. All these parameters can be easily fit to any particular neuron type, as we show in Chap. 8.

## Review of Important Concepts

- Amplifying gating variables describe activation of an inward current or inactivation of an outward current. They amplify voltage changes.
- Resonant gating variables describe inactivation of an inward current or activation of an outward current. They resist voltage changes.
- To exhibit excitability, it is enough to have one amplifying and one resonant gating variable in a neuronal model.
- Many models can be reduced to two-dimensional systems with one equation for voltage and instantaneous amplifying currents, and one equation for resonant gating variable.
- The behavior of a two-dimensional model depends on the position of its nullclines. Many models have an N-shaped  $V$ -nullcline and a sigmoid shaped nullcline for the gating variable.
- There is a relationship between nullclines and I-V curves.
- Quite different electrophysiological models can have similar nullclines, and hence essentially the same dynamics.
- The spike-generation mechanism of detailed electrophysiological models depends on the dynamics near the left knee of the fast  $V$ -nullcline, and it can be captured by a simple model (5.5, 5.6).

## Bibliographical Notes

Richard FitzHugh pioneered the usage of phase planes and nullclines to study the Hodgkin-Huxley model (FitzHugh 1955). Later, he suggested a simple model with N-shaped cubic  $V$ -nullcline and a straight-line slow nullcline, known as the FitzHugh-Nagumo model, to illustrate the mechanism of excitability of the Hodgkin-Huxley system. However, it was Krinskii and Kokoz (1973) who first discovered the relationship  $n(t) + h(t) \approx \text{const}$  and were thus able to reduce the four-dimensional Hodgkin-Huxley model to a two-dimensional system. Since then, the phase plane analysis of neuronal models became standard, at least in Russian language literature.

Current awareness of the geometrical methods of phase plane analysis of neuronal

models is mostly due to the seminal paper by John Rinzel and Bard Ermentrout “Analysis of Neural Excitability and Oscillations”, published as a chapter in Koch and Segev’s book *Methods in Neuronal Modeling* (1989, second edition in 1999). Not only did they introduced the geometrical methods to a wide computational neuroscience audience, but also were able to explain a number of outstanding problems, such as the origin of Class 1 and 2 excitability observed by Hodgkin in 1949.

Rinzel and Ermentrout illustrated most of the concepts using the Morris-Lecar (1981) model, which is a  $I_{\text{Ca}} + I_K$ -minimal voltage-gated model equivalent to the  $I_{\text{Na,p}} + I_K$ -model considered above. Due to its simplicity, the Morris-Lecar model is widely used in computational neuroscience research. This is the reason we use its analogue, the  $I_{\text{Na,p}} + I_K$ -model, throughout the book.

Hutcheon and Yarom (2000) suggested to classify all currents into amplifying and resonant. There have been no attempts to classify various electrophysiological mechanisms of excitability in neurons, though minimal models, such as the  $I_{\text{Na,t}}$ -model or the  $I_{\text{Ca}}+I_{K(C)}$ -model, would not surprise most researchers. The other models would probably look bizarre for classical electrophysiologists, though they provide a good opportunity to practice geometrical phase plane analysis and support FitzHugh’s observation that N-shaped  $V$ -nullcline is the key characteristic of neuronal dynamics. Izhikevich (2003) took advantage of this observation and suggested the simple model (5.5, 5.6) that captures the spike-generation mechanism of many known neuronal types, see Chap. 8.

## Exercises

1. Show that the  $I_A$ -model cannot have a limit cycle attractor when  $I_A$  has instantaneous activation kinetics. (Hint: Use Bendixson criterion.)
2. When the injected dc-current  $I$  or the  $\text{Na}^+$  maximal conductance  $g_{\text{Na}}$  in the  $I_{\text{Na,p}}+I_K$ -model have large values, the excited state ( $V \approx -20$  mV) becomes stable. Sketch possible intersections of nullclines of the model.
3. Using  $I$  as a bifurcation parameter, determine the saddle-node bifurcation diagram of
  - the  $I_{\text{Na,t}}$ -model with parameters as in Fig. 5.6a,
  - the  $I_A$ -model with parameters as in Fig. 5.14a.
4. Why is  $g$  in Fig. 5.22c negative when  $V$  is hyperpolarized?
5. In Fig. 5.25 we plot the currents that constitute the right-hand side of the voltage equation (5.3),

$$I - I_{\text{fast}}(V) \quad \text{and} \quad I_{\text{slow}}(V) = g(V - E_K) ,$$

on the  $(V, I)$ -plane. The curves define fast and slow movements of the state of the system. Interpret the figure. (Hint: treat the curves as “sort-of-nullclines”).

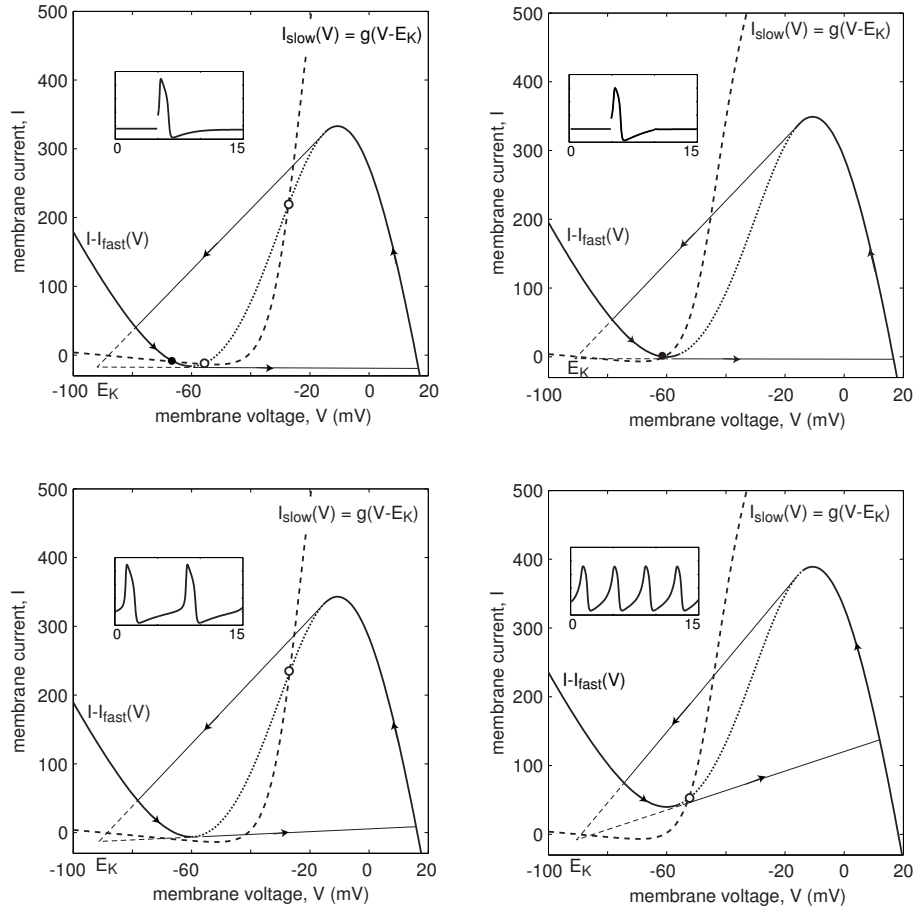


Figure 5.25: Ex. 5: The  $(V, I)$ -phase plane of the  $I_{\text{Na},p} + I_K$ -model (compare with Fig. 5.4).

6. Show that  $I_{\text{Cl}} + I_K$ -model can have oscillations. (Hint: inject negative dc-current so that the voltage-gated  $\text{Cl}^-$  current becomes inward/amplifying).
7. (NMDA +  $I_K$ -model) Show that a neuronal model consisting of an NMDA current and a resonant current, say  $I_K$ , can exhibit excitability and periodic spiking.
8. The Nernst potential of an ion is a function of its concentration inside/outside the cell membrane, which may change. Consider the  $I_{\text{Na},p} + E_{\text{Na}}([{\text{Na}}^+]_{\text{in/out}})$ -model and show that it can exhibit excitability and oscillations on a slow time scale.
9. Determine when the  $I_A$ -model has a limit cycle attractor without assuming  $\tau_h(V) \ll \tau_m(V)$ .
10. [Ph.D.] There are  $\text{Na}^+$ -gated and  $\text{Cl}^-$ -gated currents besides the  $\text{Ca}^{2+}$ -gated currents considered in this book. In addition, the Nernst potentials may change as concentrations of ions inside/outside the cell membrane change. This may lead to new minimal models. Classify and study all these models.



# Chapter 6

## Bifurcations

Neuronal models can be excitable for some values of parameters, and fire spikes periodically for other values. These two types of dynamics correspond to a stable equilibrium and a limit cycle attractor, respectively. When the parameters change, e.g., the injected dc-current in Fig. 6.1 ramps up, the models can exhibit a bifurcation — a transition from one qualitative type of dynamics to another. We consider transitions away from equilibrium point in Sect. 6.1 and transitions away from a limit cycle in Sect. 6.2. All these transitions can be reliably observed when only one parameter, in our case  $I$ , changes. Mathematicians refer to such as being bifurcations of *codimension-1*. In this chapter we provide definitions and examples of all codimension-1 bifurcations of an equilibrium and a limit cycle that can occur in two-dimensional systems. In Sect. 6.3 we mention some codimension-1 bifurcations in high-dimensional systems, as well as some codimension-2 bifurcations. In the next chapter we discuss how the type of bifurcation determines a cell’s neuro-computational properties.

### 6.1 Equilibrium (Rest State)

A neuron is excitable because its resting state is near a bifurcation, i.e., near a transition from quiescence to periodic spiking. Typically, such a bifurcation can be revealed by injecting a ramp current, as we do in Fig. 6.1. The four bifurcations in the figure have qualitatively different properties, summarized in Fig. 6.2. In this section we use analytical and geometrical tools to understand what the differences among the bifurcations are.

Recall (see Chap. 4) that an equilibrium of a dynamical system is stable if all the eigenvalues of the Jacobian matrix at the equilibrium have negative real parts. When a parameter, say  $I$ , changes, two events can happen:

1. A negative eigenvalue increases and becomes 0. This happens at the saddle-node bifurcation: the equilibrium disappears.
2. Two complex-conjugate eigenvalues with negative real part approach the imaginary axis and become purely imaginary. This happens at the Andronov-Hopf

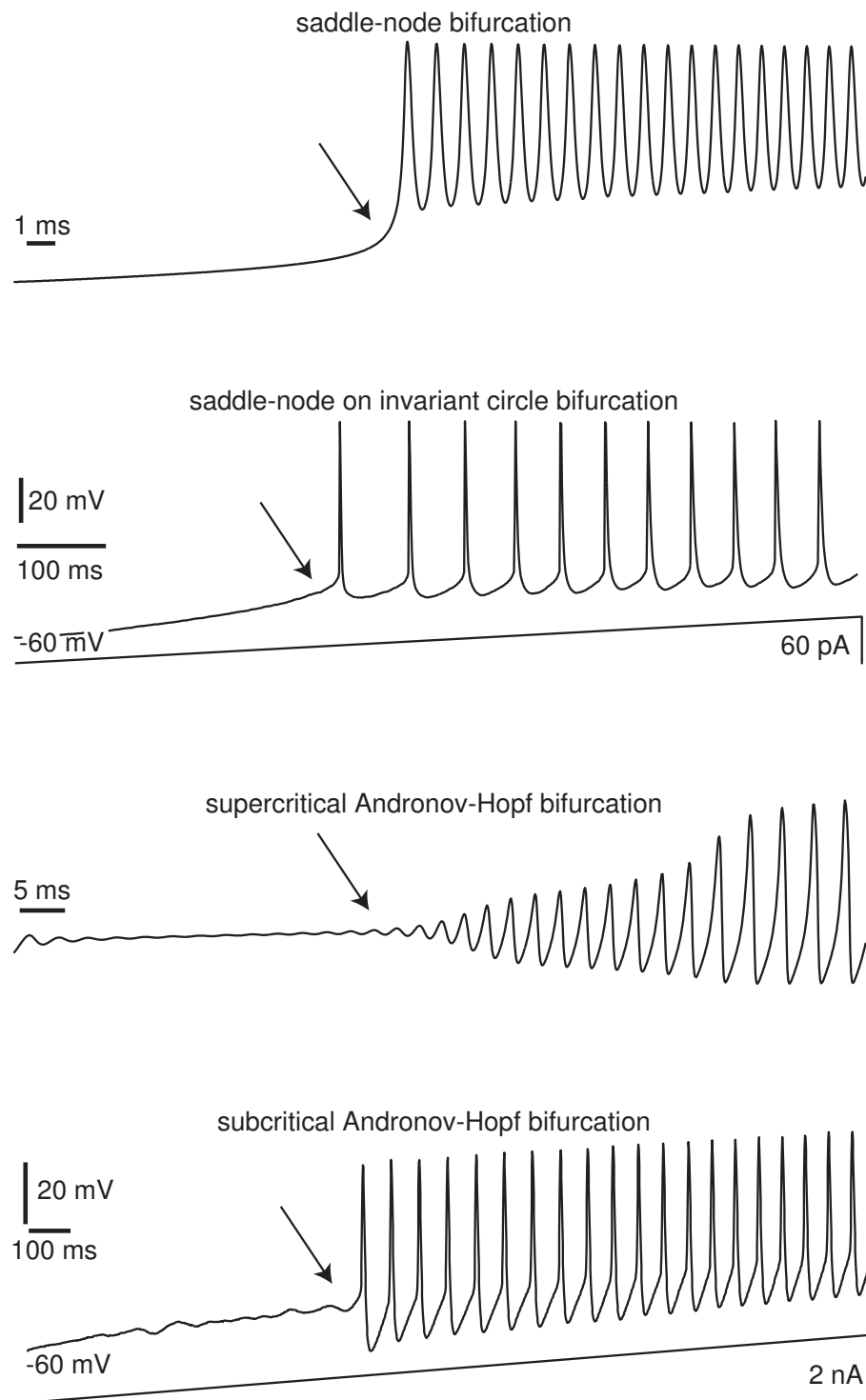


Figure 6.1: Transitions from resting to tonic (periodic) spiking occur via bifurcations of equilibrium (marked by arrows). Saddle-node on invariant circle bifurcation: *in vitro* recording of pyramidal neuron of rat's primary visual cortex. Subcritical Andronov-Hopf bifurcation: *in vitro* recording of brainstem mesencephalic V neuron. The other two traces are simulations of the  $I_{Na,p} + I_K$ -model.

Bifurcation of an equilibrium	fast subthreshold oscillations	amplitude of spikes	frequency of spikes
saddle-node	no	non-zero	non-zero
saddle-node on invariant circle	no	non-zero	$A\sqrt{I-I_b} \rightarrow 0$
supercritical Andronov-Hopf	yes	$A\sqrt{I-I_b} \rightarrow 0$	non-zero
subcritical Andronov-Hopf	yes	non-zero	non-zero

Figure 6.2: Summary of codimension-1 bifurcations of an equilibrium. Here,  $I$  denotes the amplitude of the injected current,  $I_b$  is the bifurcation value,  $A$  is a parameter that depends on the biophysical details.

bifurcation: the equilibrium loses stability, but does not disappear.

Thus, there are only two qualitative events that can happen with a stable equilibrium in a dynamical system of arbitrary dimension: It can either disappear or lose stability. Of course, there could be a third event: All eigenvalues continue to have negative real parts, in which case the equilibrium remains stable.

Since any equilibrium of a neuronal model is the zero of the steady-state I-V curve  $I_\infty(V)$  (the net current at the equilibrium must be zero), analysis of the shape of the I-V curve can provide an invaluable information about possible bifurcations of the rest state.

Two typical steady-state I-V curves are depicted in Fig. 6.3. The I-V curve in Fig. 6.3a has a region with a negative slope so that it may have 3 equilibria: the left equilibrium is probably<sup>1</sup> stable, the middle is unstable, and the right equilibrium could be stable or unstable depending on the kinetics of the gating variables (it is stable in the one-dimensional case, i.e., when gating variables have instantaneous kinetics). The I-V curve in Fig. 6.3b is monotone. A positive (inward) injected dc-current  $I$  shifts the I-V curves down. This leads to the disappearance of the equilibrium in Fig. 6.3a, but not in Fig. 6.3b. Therefore, Fig. 6.3a corresponds to the saddle-node bifurcation and Fig. 6.3b to Andronov-Hopf bifurcation. When exactly the equilibrium loses stability in Fig. 6.3b cannot be inferred from the I-V relations (for this, we need to consider the full neuronal model). But what we can infer is that the bifurcation *cannot be* of the saddle-node type. Surprisingly, non-monotonic I-V curves result in saddle-node bifurcations but do not exclude Andronov-Hopf bifurcations, as the reader is asked to demonstrate in Ex. 8. This phenomenon is relevant to the cortical pyramidal neurons

---

<sup>1</sup>It may be unstable; see Ex. 8

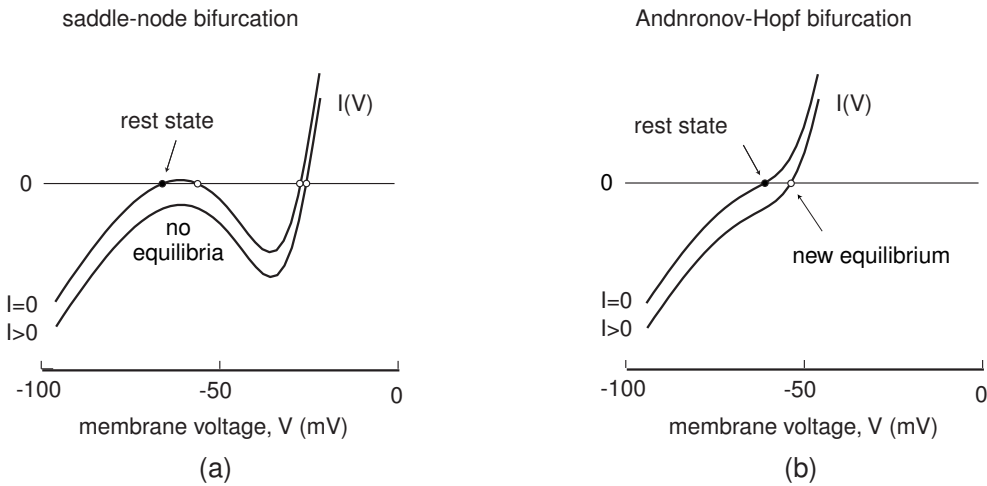


Figure 6.3: Steady-state I-V curves of the  $I_{Na,p} + I_K$ -model with high-threshold (left) or low-threshold (right)  $K^+$  current (parameters as in Fig. 4.1).

considered in the last chapter.

### 6.1.1 Saddle-node (fold)

We provided the definition of a saddle-node bifurcation in one-dimensional systems in Sect. 3.3.4, and the reader is encouraged to look at that section and Fig. 4.31 before proceeding further.

A  $k$ -dimensional dynamical system

$$\dot{x} = f(x, b), \quad x \in \mathbb{R}^k$$

having an equilibrium point  $x_{\text{sn}}$  for some value of the bifurcation parameter  $b_{\text{sn}}$  (i.e.,  $f(x_{\text{sn}}, b_{\text{sn}}) = 0$ ) exhibits *saddle-node* (also known as *fold*) bifurcation, if the equilibrium is non-hyperbolic with a simple zero eigenvalue, the function  $f$  is non-degenerate, and it is transversal with respect to  $b$ . The first condition is easy to check:

- (Non-hyperbolicity) The Jacobian  $k \times k$  matrix of partial derivatives at the equilibrium (see Sect. 4.2.2) has exactly one zero eigenvalue, and the other eigenvalues have non-zero real parts.

In general, the remaining two conditions have complicated forms, since they involve projections of the vector field on the *center manifold*, which is tangent to the eigenvector corresponding to the zero eigenvalue of the Jacobian matrix. However, there is a shortcut for conductance-based neuronal models.

Let  $\mathbf{I}(V, b)$  denote the steady-state I-V relation, which can be measured experimentally, divided by the membrane capacitance  $C$ . For example,  $\mathbf{I}(V, I) = \{I - I_\infty(V)\}/C$  when the injected dc-current  $I$  is used as a bifurcation parameter. We substitute the multi-dimensional neuronal model by the one-dimensional system  $\dot{V} = \mathbf{I}(V, b)$ . From

$\mathbf{I}(V, b) = 0$  (equilibrium condition) we find  $b = I_\infty(V)$ . Non-hyperbolicity condition implies  $\mathbf{I}_V(V, b) = 0$ , so that the bifurcation occur at the local maxima and minima of  $I_\infty(V)$ . We considered all these properties in Chap. 3.

- (Non-degeneracy) The second-order derivative of  $\mathbf{I}(V, b_{\text{sn}})$  with respect to  $V$  is non-zero, that is,

$$a = \frac{1}{2} \frac{\partial^2 \mathbf{I}(V, b_{\text{sn}})}{\partial V^2} \neq 0 \quad (\text{at } V = V_{\text{sn}}). \quad (6.1)$$

That is, the piece of the I-V curve,  $I_\infty(V)$ , at the bifurcation point,  $V_{\text{sn}}$ , looks like the square parabola.

- (Transversality) Function  $\mathbf{I}(V, b)$  is non-degenerate with respect to the bifurcation parameter  $b$ ; that is,

$$c = \frac{\partial \mathbf{I}(V_{\text{sn}}, b)}{\partial b} \neq 0 \quad (\text{at } b = b_{\text{sn}}).$$

This condition is always satisfied when the injected dc-current  $I$  is the bifurcation parameter, because  $\partial \mathbf{I} / \partial b = \partial \mathbf{I} / \partial I = 1/C$ .

The saddle-node bifurcation has codimension 1 because only one condition (non-hyperbolicity) involves strict equality (“=”), and the other two involve inequalities (“≠”). The dynamics of multi-dimensional neuronal systems near a saddle-node bifurcation can be reduced to that of the topological normal form

$$\dot{V} = c(b - b_{\text{sn}}) + a(V - V_{\text{sn}})^2, \quad (6.2)$$

where  $V$  is the membrane voltage, and  $a$  and  $c$  are defined above. In the context of neuronal models, this equation with an after-spike resetting is called the quadratic integrate-and-fire neuron, which we discuss in Chapters 3 and 8.

### Example: The $I_{\text{Na,p}}+I_{\text{K}}$ -model

Let us use the  $I_{\text{Na,p}}+I_{\text{K}}$ -model (4.1, 4.2) with high-threshold  $\text{K}^+$  current to illustrate these conditions. The saddle-node bifurcation occurs when the  $V$ -nullcline touches the  $n$ -nullcline, as in Fig. 6.4. Solving the equations numerically, we find that this occurs when  $I_{\text{sn}} = 4.51$  and  $(V_{\text{sn}}, n_{\text{sn}}) = (-61, 0.0007)$ . The Jacobian matrix at the equilibrium,

$$L = \begin{pmatrix} 0.0435 & -290 \\ 0.00015 & -1 \end{pmatrix},$$

has two eigenvalues  $\lambda_1 = 0$  and  $\lambda_2 = -0.9565$ , with corresponding eigenvectors

$$v_1 = \begin{pmatrix} 1 \\ 0.00015 \end{pmatrix} \quad \text{and} \quad v_2 = \begin{pmatrix} 1 \\ 0.0034 \end{pmatrix},$$

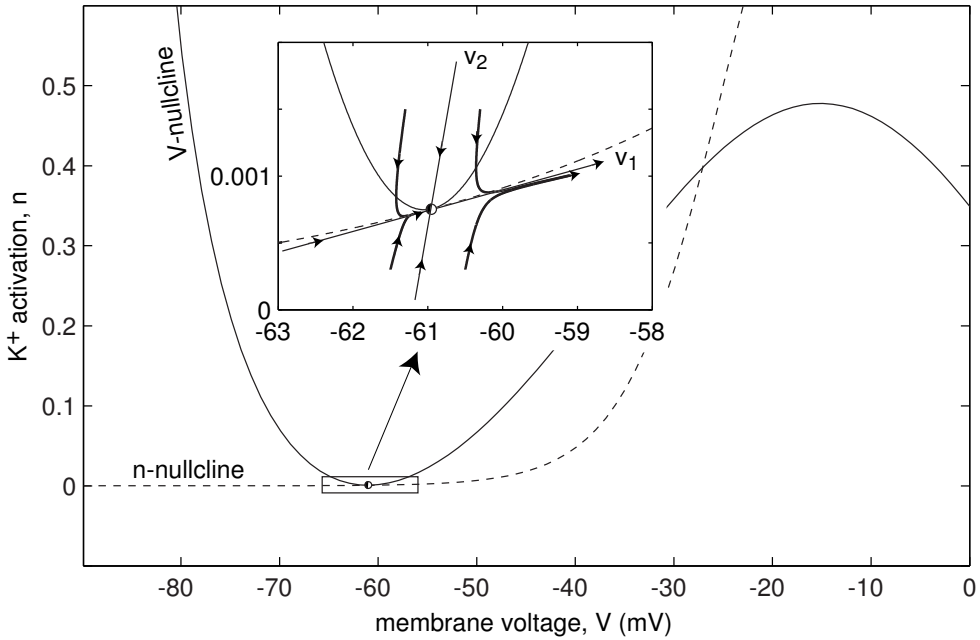


Figure 6.4: Saddle-node bifurcation in the  $I_{Na,p} + I_K$ -model (4.1, 4.2) with high-threshold  $K^+$  current (parameters as in Fig. 4.1a) and  $I = 4.51$ .

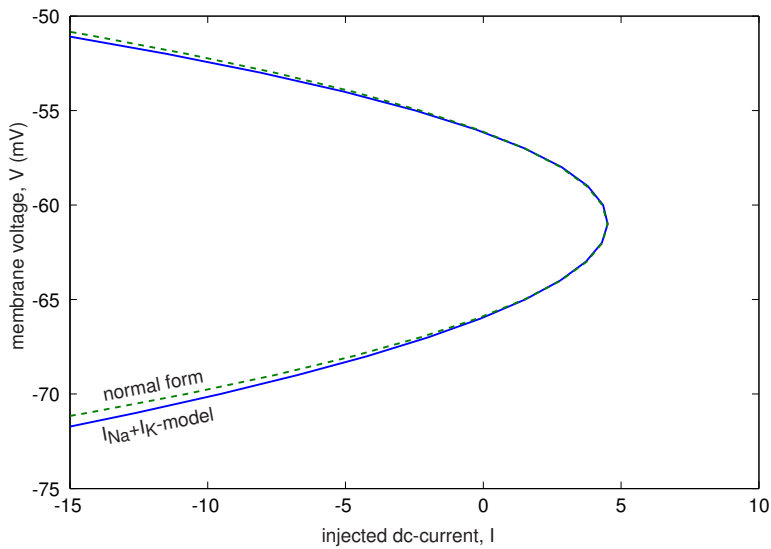


Figure 6.5: Bifurcation diagrams of the topological normal form (6.3) and the  $I_{Na,p} + I_K$ -model (4.1, 4.2).

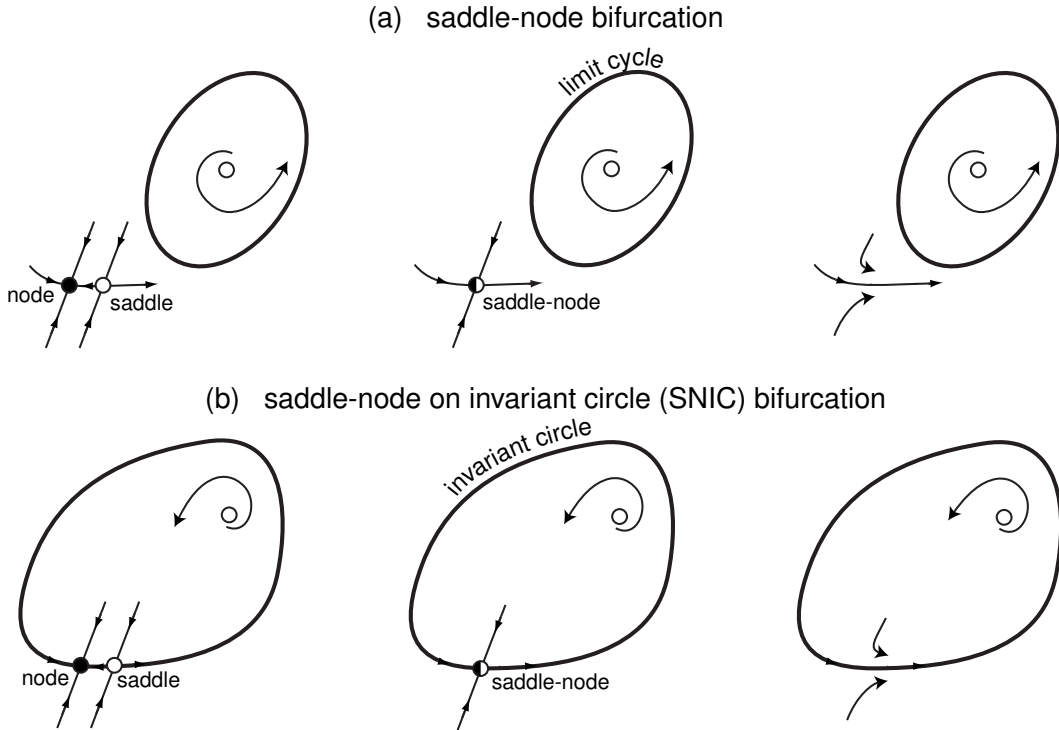


Figure 6.6: Two types of saddle-node bifurcation.

depicted in the inset in Fig. 6.4. (It is easy to check that  $Lv_1 = 0$  and  $Lv_2 = -0.9565v_2$ .) The non-degeneracy and transversality conditions yields  $a = 0.1887$  and  $c = 1$ , so that the topological normal form for the  $I_{Na,p} + I_K$ -model is

$$\dot{V} = (I - 4.51) + 0.1887(V + 61)^2, \quad (6.3)$$

which can be solved analytically. The corresponding bifurcation diagrams are depicted in Fig. 6.5. There is no surprise that there is a fairly good match when  $I$  is near the bifurcation value.

### 6.1.2 Saddle-node on invariant circle

As its name stands, saddle-node on invariant circle bifurcation (also known as SNIC or SNLC bifurcation) is a standard *saddle-node* bifurcation described above with an additional caveat: it occurs on an *invariant circle*, compare Fig. 6.6a and b. Here, the invariant circle consists of two trajectories connecting the node and the saddle, called heteroclinic trajectories. It is called invariant because any solution starting on the circle remains on the circle. As the saddle and node coalesce, the small trajectory shrinks and the large heteroclinic trajectory becomes a homoclinic invariant circle, i.e., originating and terminating at the same point. When the point disappears, the circle becomes a limit cycle.

Both types of the bifurcation can occur in the  $I_{\text{Na,p}} + I_K$ -model as we show in Fig. 6.7. The difference between top and bottom of the figure is the time constant  $\tau(V)$  of the  $K^+$  current. Since the  $K^+$  current has high threshold, the time constant does not affect dynamics at rest, but it makes a huge difference when action potential is generated. If the current is fast (top), it activates during the upstroke thereby decreasing the amplitude of action potential, and deactivates during the downstroke thereby resulting in overshoot and another action potential. In contrast, slower  $K^+$  current (bottom) does not have time to deactivate during the downstroke, thereby resulting in undershoot (short after-hyperpolarization), with  $V$  going below the resting state.

From the geometrical point of view, the phase portraits in Fig. 6.6b and in Fig. 6.7, bottom, have the same topological structure: there is a homoclinic trajectory (an invariant circle) that originates at the saddle-node point, leaves its small neighborhood (to fire an action potential), then reenters the neighborhood again, and terminates at the saddle-node point. This homoclinic trajectory is a limit cycle attractor with infinite period, which corresponds to firing with zero frequency. This and other neurocomputational features of saddle-node bifurcations are discussed in the next chapter. Below we only explore how the frequency of oscillation depends on the bifurcation parameter, e.g., on the injected dc-current  $I$ .

A remarkable fact is that we can estimate the frequency of the large-amplitude limit cycle attractor by considering a small neighborhood of the saddle-node point. Indeed, a trajectory on the limit cycle generates a fast spike from point B to A in Fig. 6.8 and then slowly moves from A to B (shaded region in the figure) because the vector field (the velocity) in the neighborhood between A and B is very small. The duration of the stereotypical action potentials, denoted here as  $T_1$ , is relatively constant and does not depend much on the injected current  $I$ . In contrast, the time spent in the neighborhood (A, B) depends significantly on  $I$ . Since the behavior in the neighborhood is described by the topological normal form (6.2), we can estimate the time the trajectory spends there in terms of the parameters  $a$ ,  $b$  and  $c$  (see Ex. 3). This yields

$$T_2 = \frac{\pi}{\sqrt{ac(b - b_{\text{sn}})}} ,$$

where the parameters  $a$ ,  $b$ , and  $c$  are those defined in the previous section. So the period of one oscillation is  $T = T_1 + T_2$ .

In Fig. 6.8, top, we illustrate the accuracy of this estimation using the  $I_{\text{Na,p}} + I_K$ -model, whose topological normal form (6.3) was derived earlier. The duration of the action potential is  $T_1 = 4.7$  ms, and the duration of time the voltage variable spends in the shaded neighborhood (A,B) (here  $-61 \pm 11$  mV) is approximated by

$$T_2 = \frac{\pi}{\sqrt{0.1887(I - 4.51)}} \quad (\text{ms})$$

The analytical curve

$$\omega = \frac{1000}{T_1 + T_2} \quad (\text{Hz})$$

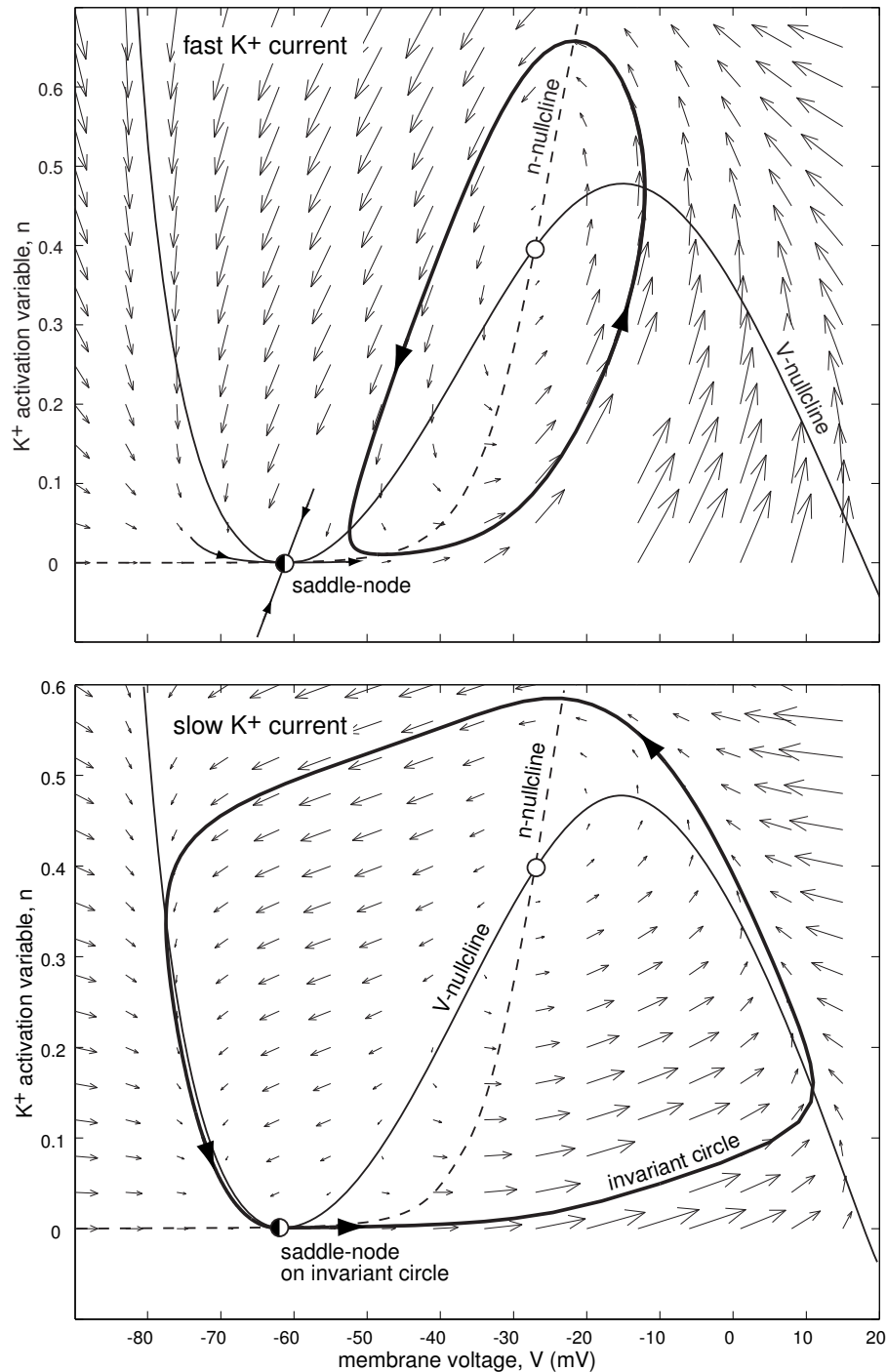


Figure 6.7: Saddle-node bifurcation in the  $I_{Na,p} + I_K$ -model with high-threshold  $K^+$  current can be off the limit cycle (top) or on the invariant circle (bottom). Parameters as in Fig. 4.1a with  $\tau(V) = 0.152$  (top) or  $\tau(V) = 1$  (bottom).

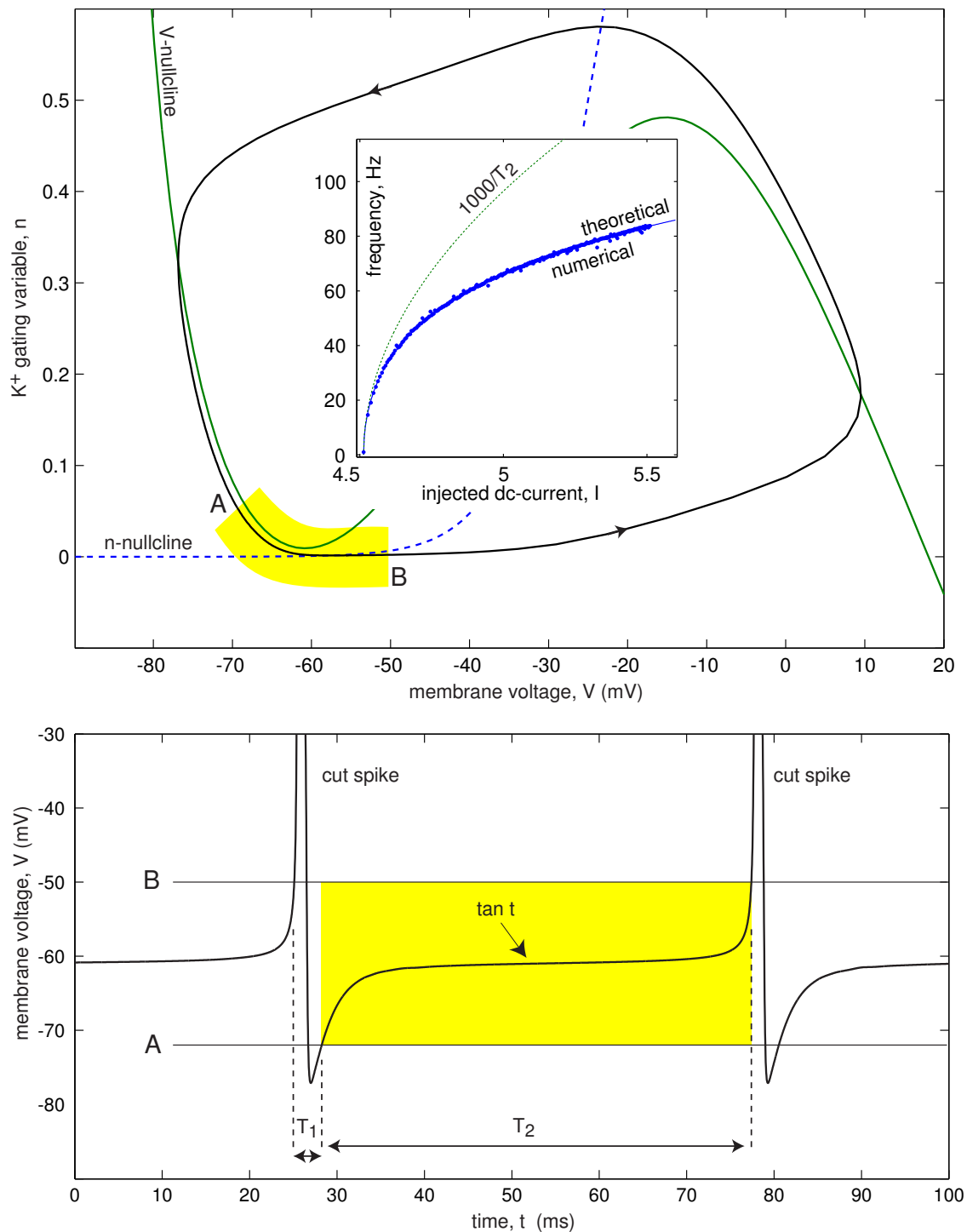


Figure 6.8: The  $I_{Na,p} + I_K$ -model can fire periodic train of action potentials with arbitrary small frequency when it is near a saddle-node on invariant circle bifurcation. The trajectory moves fast from point B to A (a spike) and slowly in the shaded region from point A to B.

matches numerically the found frequency of oscillation (Fig. 6.8, top) in a fairly broad frequency range. For comparison, we plot the curve  $1000/T_2$  to show that neglecting the duration of the spike,  $T_1$ , can be justified only when  $I$  is very close to the bifurcation point.

### 6.1.3 Supercritical Andronov-Hopf

If a neuronal model has a monotonic steady-state I-V relation, a saddle-node bifurcation cannot occur. The resting state in such a model does not disappear, but it loses stability, typically via an Andronov-Hopf (sometimes called Hopf) bifurcation. The loss of stability is accompanied either by an appearance of a stable limit cycle (super-critical Andronov-Hopf) or by a disappearance of an unstable limit cycle (subcritical Andronov-Hopf).

Let us consider a two-dimensional system

$$\begin{aligned}\dot{v} &= F(v, u, b) \\ \dot{u} &= G(v, u, b)\end{aligned}\tag{6.4}$$

and suppose that  $(v, u) = (0, 0)$  is an equilibrium when the bifurcation parameter  $b = 0$ , that is,  $F(0, 0, 0) = G(0, 0, 0) = 0$ . This system undergoes an *Andronov-Hopf bifurcation* at the equilibrium if the following three conditions are satisfied:

- (Non-hyperbolicity) The Jacobian  $2 \times 2$  matrix of partial derivatives at the equilibrium (see Sect. 4.2.2),

$$L = \begin{pmatrix} F_v & F_u \\ G_v & G_u \end{pmatrix},$$

has a pair of purely imaginary eigenvalues,  $\pm i\omega \in \mathbb{C}$  with  $\omega \neq 0$ . That is,  $\text{tr } L = F_v + G_u = 0$  and  $\omega^2 = \det L = F_v G_u - F_u G_v > 0$  at  $v = u = b = 0$ .

The linear change of variables

$$v = x \quad \text{and} \quad F_u u = -F_v x - \omega y \tag{6.5}$$

converts (6.4) into the form

$$\begin{aligned}\dot{x} &= -\omega y + f(x, y) \\ \dot{y} &= \omega x + g(x, y),\end{aligned}\tag{6.6}$$

where functions

$$f(x, y) = F(v, u) + \omega y \quad \text{and} \quad g(x, y) = -(F_v F(v, u) + F_u G(v, u))/\omega - \omega x$$

have no linear terms in  $x$  and  $y$ . Now we are ready to state the other two conditions:

- (Non-degeneracy) The parameter

$$a = \frac{1}{16} \{f_{xxx} + f_{xyy} + g_{xxy} + g_{yyy}\} + \frac{1}{16\omega} \{f_{xy}(f_{xx} + f_{yy}) - g_{xy}(g_{xx} + g_{yy}) - f_{xx}g_{xx} + f_{yy}g_{yy}\} \tag{6.7}$$

is non-zero.

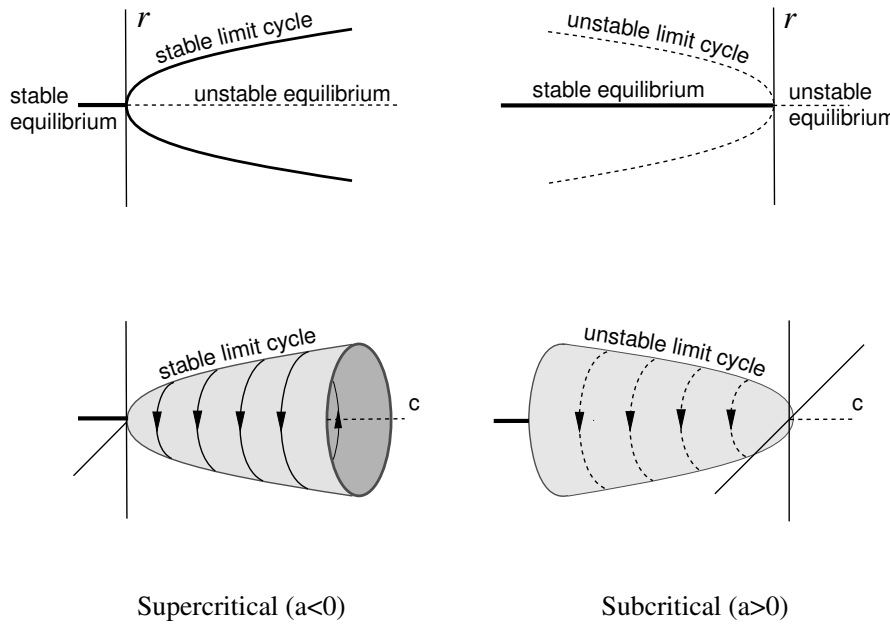


Figure 6.9: Andronov-Hopf bifurcation: A stable equilibrium becomes unstable in system (6.8, 6.9).

- (Transversality) Let  $c(b) \pm i\omega(b)$  denote the complex-conjugate eigenvalues of the Jacobian matrix of (6.4) for  $b$  near 0, with  $c(0) = 0$  and  $\omega(0) = \omega$ . The real part,  $c(b)$ , must be non-degenerate with respect to  $b$ , that is,  $c'(0) \neq 0$ .

The Andronov-Hopf bifurcation has codimension *one*, since only one condition involves strict equality ( $\text{tr } L = 0$ ), and the other two involve inequalities (“ $\neq$ ”).

The sign of  $a$  determines the type of the Andronov-Hopf bifurcation, depicted in Fig. 6.9:

- *Supercritical* Andronov-Hopf bifurcation occurs when  $a < 0$ . It corresponds to a stable limit cycle appearing from a stable equilibrium.
- *Subcritical* Andronov-Hopf bifurcation occurs when  $a > 0$ . It corresponds to an unstable limit cycle shrinking to a stable equilibrium.

Finding  $a$  in applications could be challenging. A few useful examples are considered in Exercises 14-18.

Any system undergoing an Andronov-Hopf bifurcation can be reduced by a change of variables to the topological normal form (see also Ex. 4)

$$\dot{r} = c(b)r + ar^3, \quad (6.8)$$

$$\dot{\varphi} = \omega(b) + dr^2, \quad (6.9)$$

where  $r \geq 0$  is the amplitude (radius), and  $\varphi$  is the phase (angle) of oscillation, as in Fig. 6.10, and  $a, b, c(b)$ , and  $\omega(b)$  as above.

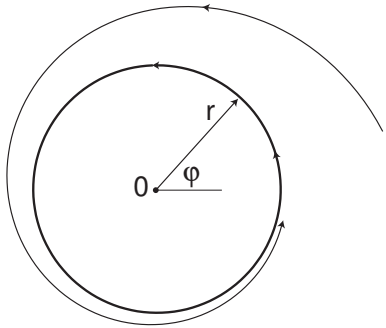


Figure 6.10: Polar coordinates:  $r$  is the amplitude (radius) and  $\varphi$  is the phase (angle) of oscillation.

The function  $c(b)$  in the normal form (6.8,6.9) determines the stability of the equilibrium  $r = 0$  corresponding to a non-oscillatory state. (Stable for  $c < 0$  and unstable for  $c > 0$ , regardless of the value of  $a$ ). The function  $\omega(b)$  determines the frequency of damped or sustained oscillations around this state. The parameter  $d$  describes how the frequency of oscillation depends on its amplitude. A state-dependent change of time can remove the term  $dr^2$  from (6.9) (Kuznetsov 1995), so many assume that  $d = 0$  to start with.

### Example: The $I_{\text{Na,p}} + I_K$ -model

Let us use the  $I_{\text{Na,p}} + I_K$ -model with low-threshold  $K^+$  current in Fig. 6.11 to illustrate the three conditions above. As the magnitude of the injected dc-current  $I$  increases, the equilibrium loses stability and gives birth to a stable limit cycle with growing amplitude. Using simulations we find that the bifurcation occurs when  $I_{\text{ah}} = 14.66$  and  $(V_{\text{ah}}, n_{\text{ah}}) = (-56.5, 0.09)$ . The Jacobian matrix at the equilibrium,

$$L = \begin{pmatrix} 1 & -335 \\ 0.0166 & -1 \end{pmatrix},$$

has a pair of complex conjugate eigenvalues  $\pm 2.14i$ , so the non-hyperbolicity condition is satisfied. Next, we find numerically (in Fig. 6.12 or analytically in Ex. 9) that the eigenvalues at the equilibrium can be approximated by

$$c(I) + \omega(I)i \approx 0.03\{I - 14.66\} \pm (2.14 + 0.04\{I - 14.66\})i$$

in a neighborhood of the bifurcation point  $I = 14.66$ . Since the slope of  $c(I)$  is non-zero, the transversality condition is also satisfied. Using Ex. 17 we find that  $a = -0.0026$  and  $d = -0.0029$ , so that the non-degeneracy condition is also satisfied, and the bifurcation is of the supercritical type. The corresponding topological normal form is

$$\begin{aligned} \dot{r} &= 0.03\{I - 14.66\}r - 0.0026r^3, \\ \dot{\varphi} &= (2.14 + 0.04\{I - 14.66\}) - 0.0029r^2. \end{aligned}$$

To analyze the normal form we consider the  $r$ -equation and neglect the phase variable  $\varphi$ . From

$$r(c(b) + ar^2) = 0$$

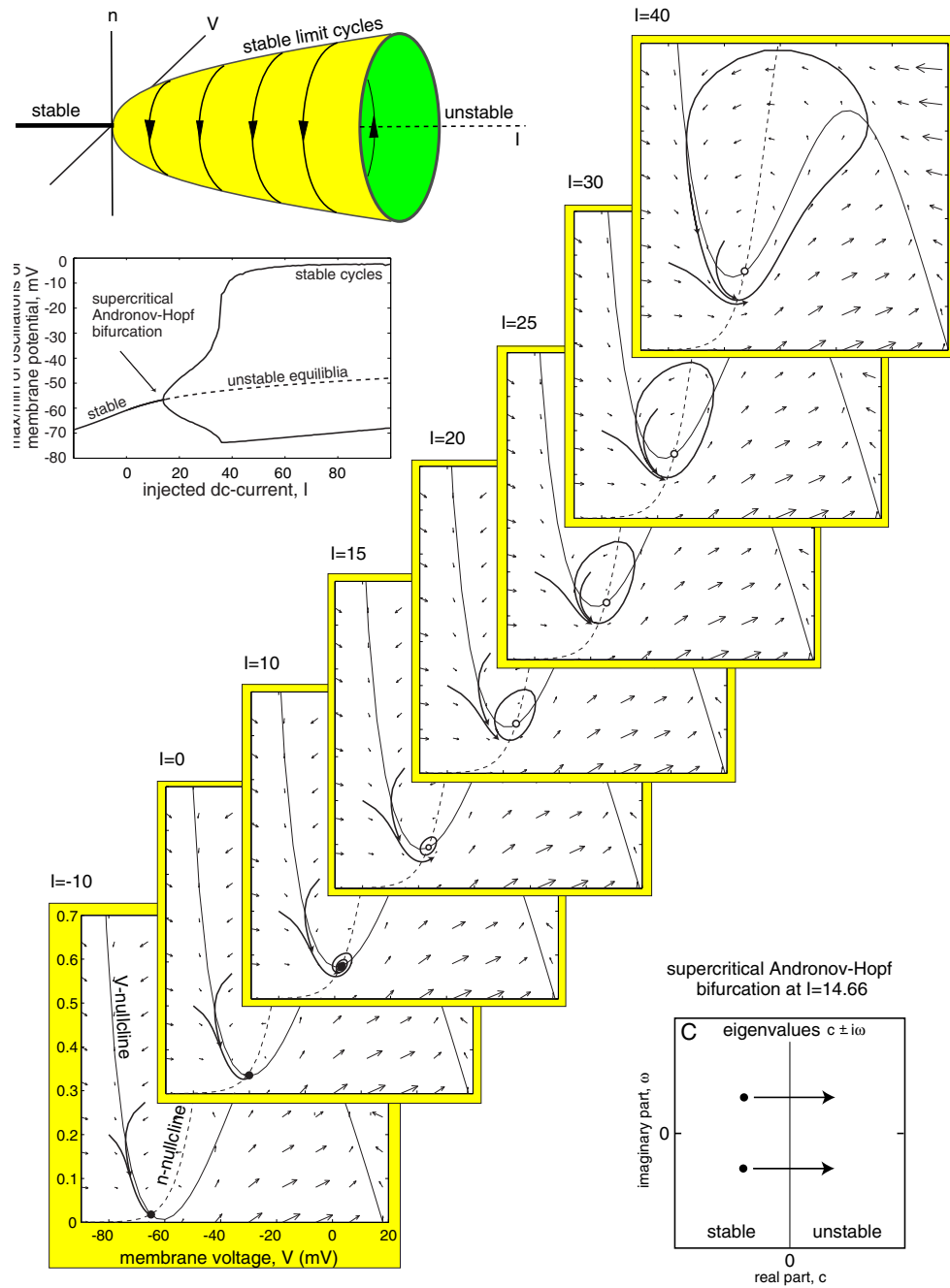


Figure 6.11: Supercritical Andronov-Hopf bifurcation in the  $I_{Na,p} + I_K$ -model with low-threshold  $K^+$  current: As a bifurcation parameter  $I$  increases, an equilibrium loses stability and gives birth to a stable limit cycle with growing amplitude. Parameters as in Fig. 4.1b.

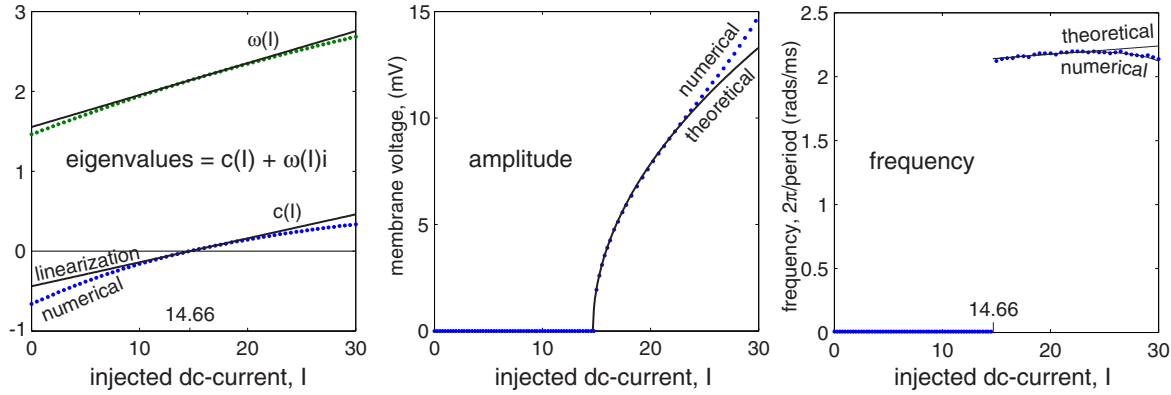


Figure 6.12: Supercritical Andronov-Hopf bifurcation in the  $I_{\text{Na,p}}+I_K$ -model with low-threshold  $\text{K}^+$  current (see Fig. 6.11). Dots — numerical simulation of the full model, continuous curves — analytical results using the topological normal form (6.8, 6.9).

we conclude that  $r = 0$  is an equilibrium for any value of  $c(b)$ . Since

$$(c(b)r + ar^3)_r = c(b) \quad \text{at } r = 0,$$

the equilibrium is stable for  $c(b) < 0$  and unstable for  $c(b) > 0$ , as we illustrate in Fig. 6.13. Indeed, the rest state in the  $I_{\text{Na,p}}+I_K$ -model is stable when  $I < 14.66$  and unstable when  $I > 14.66$ .

When  $c(b) > 0$ , the normal form has a family of stable periodic solutions with amplitude

$$r = \sqrt{c(b)/|a|} \quad \text{and} \quad (\text{frequency}) = \omega(b) + d c(b)/|a| .$$

Hence, the  $I_{\text{Na,p}}+I_K$ -model has a family of periodic attractors with

$$r = \sqrt{0.03\{I - 14.66\}/0.0026}$$

and

$$(\text{frequency}) = (2.14 + 0.04\{I - 14.66\}) - 0.0029 \cdot 0.03\{I - 14.66\}/0.0026 ,$$

depicted in Fig. 6.12. We see that the topological normal form describes not only qualitatively but also quantitatively the full  $I_{\text{Na,p}}+I_K$ -model near the Andronov-Hopf bifurcation.

#### 6.1.4 Subcritical Andronov-Hopf

Neuronal models with monotonic steady-state I-V relations can also exhibit subcritical Andronov-Hopf bifurcations, as we illustrate in Fig. 6.16 using the  $I_{\text{Na,p}}+I_K$ -model having low-threshold  $\text{K}^+$  current and a steep activation curve for  $\text{Na}^+$  current. The

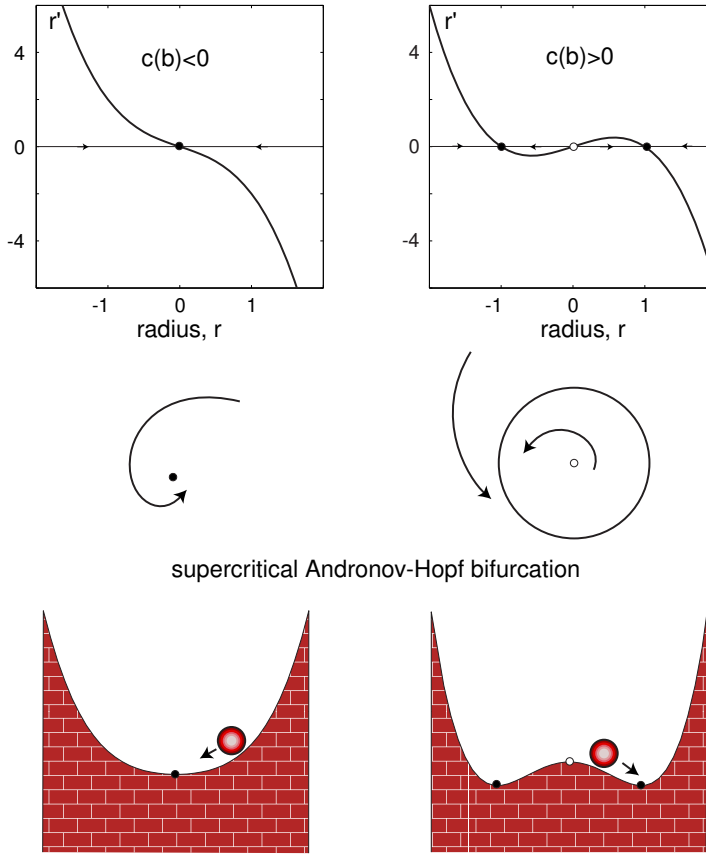


Figure 6.13: Supercritical Andronov-Hopf bifurcation in (6.8, 6.9) with  $c = \pm 1$  and  $a = -1$ .

stable equilibrium in such a system is surrounded by an unstable limit cycle (dashed circle), which is often surrounded by another stable cycle, as in Fig. 6.14 (not depicted in Fig. 6.16 for clarity). As the magnitude of the injected dc-current  $I$  increases, the unstable cycle shrinks to the stable equilibrium and makes it lose stability. Systems undergoing such a bifurcation satisfy the same three conditions, non-hyperbolicity, non-degeneracy, and transversality, presented in the previous section, and they can be reduced to the topological normal form (6.8, 6.9) with positive  $a$ .

Analysis of the normal form shows that the stability of the non-oscillatory equilibrium  $r = 0$  depends on the sign of  $c(b)$ :

- When  $c(b) < 0$  (see Fig. 6.15, left), there is a pair of equilibria,  $r = \pm\sqrt{|c(b)|/a}$  corresponding to an unstable periodic solution that shrinks to  $r = 0$  as  $c(b) \rightarrow 0$  and makes the stable equilibrium  $r = 0$  lose its stability.
- When  $c(b) > 0$  (see Fig. 6.15, right), the non-oscillatory state  $r = 0$  is unstable, and all trajectories diverge from it.

This behavior can be clearly seen in Fig. 6.16.

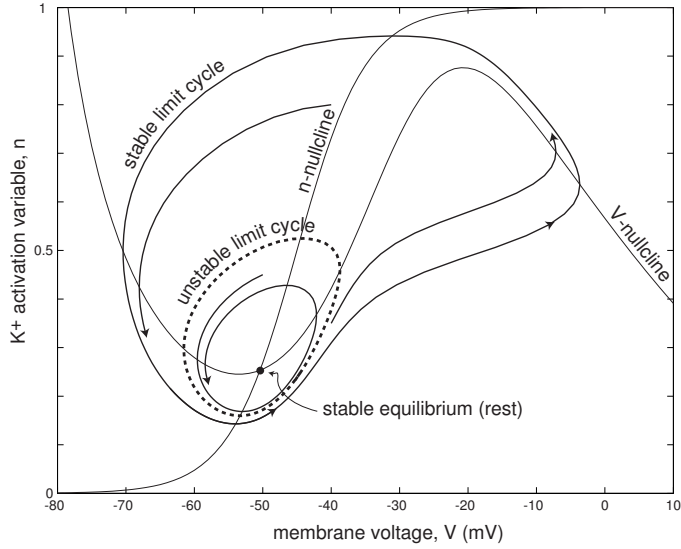


Figure 6.14: Phase portrait of the  $I_{\text{Na},p} + I_K$ -model: Unstable limit cycle (dashed circle) is often surrounded by a stable one (solid circle) in two-dimensional neuronal models.

Finally, notice that there is always a bistability, i.e., co-existence, of the resting attractor and some other attractor near a subcritical Andronov-Hopf bifurcation in 2-dimensional conductance-based models, as in Fig. 6.14 (in non-neural models, the trajectories could go to infinity and there need not be bistability). The bistability must also be present at the saddle-node bifurcation of an equilibrium, but may or may not be present at the saddle-node on invariant circle or at a supercritical Andronov-Hopf bifurcation.

### Delayed loss of stability

In Fig. 6.17a we inject a ramp of current into the  $I_{\text{Na},p} + I_K$ -model to drive it slowly through the subcritical Andronov-Hopf bifurcation point  $I \approx 48.75$  (see Fig. 6.16). We choose the ramp so that the bifurcation occurs exactly at  $t = 100$ . Even though the focus equilibrium is unstable for  $t > 100$ , the membrane potential remains near -50 mV as if the equilibrium were still stable. This phenomenon, discovered by Shishkova (1973), is called *delayed loss of stability*. It is ubiquitous in simulations of smooth dynamical systems near subcritical or supercritical Andronov-Hopf bifurcations.

The mechanism of delayed loss of stability is quite simple. The state of the system is attracted to the stable focus while  $t < 100$ . Even though the focus loses stability at  $t = 100$ , the state of the system is infinitesimally close to the equilibrium, so it takes a long time to diverge from it. The longer the convergence to the equilibrium, the longer the divergence from it, hence the noticeable delay. The delay has an upper bound that depends on the smoothness of the dynamical system (Nejshtadt 1985). It can be shortened or even reversed (advanced loss of stability) by weak noise that is always present in neurons. This may explain why the delay has never been seen

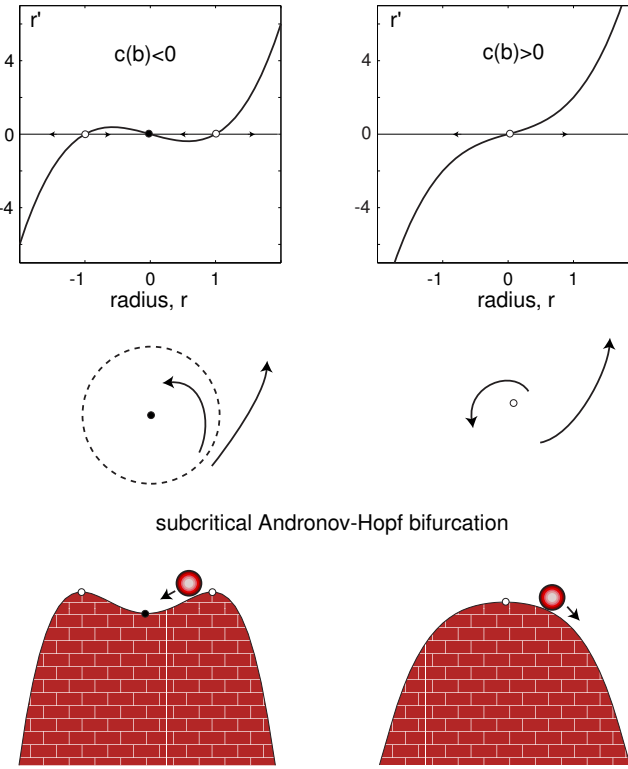


Figure 6.15: Subcritical Andronov-Hopf bifurcation in (6.8, 6.9) with  $c = \pm 1$  and  $a = 1$ .

experimentally despite the fact that it is practically unavoidable in simulations.

### Unmasking of oscillations by noise

In Fig. 6.17b we repeat the same simulation as in Fig. 6.17a, except we add a weak conductance noise to the  $I_{\text{Na,p}} + I_K$ -model. Starting with the same initial conditions, the system converges to the stable focus equilibrium, as expected, exhibiting damped oscillations of membrane potential. After a while, however, it diverges from the equilibrium and exhibits sustained waxing and waning oscillations as if there were a small amplitude limit cycle attractor with a variable amplitude. The oscillations persist until the state of the system escapes from the attraction domain of the stable focus, which is bounded by the unstable limit cycle, to the attraction domain of the large-amplitude stable limit cycle.

Let us explain how weak noise unmasks damped oscillations and makes them sustained. It is convenient to treat noise as a series of perturbations that push the membrane potential in random directions, often away from the resting state. Each such perturbation evokes a damped oscillation toward the resting state. Superposition of many such damped oscillations occurring at different times results in the waxing and

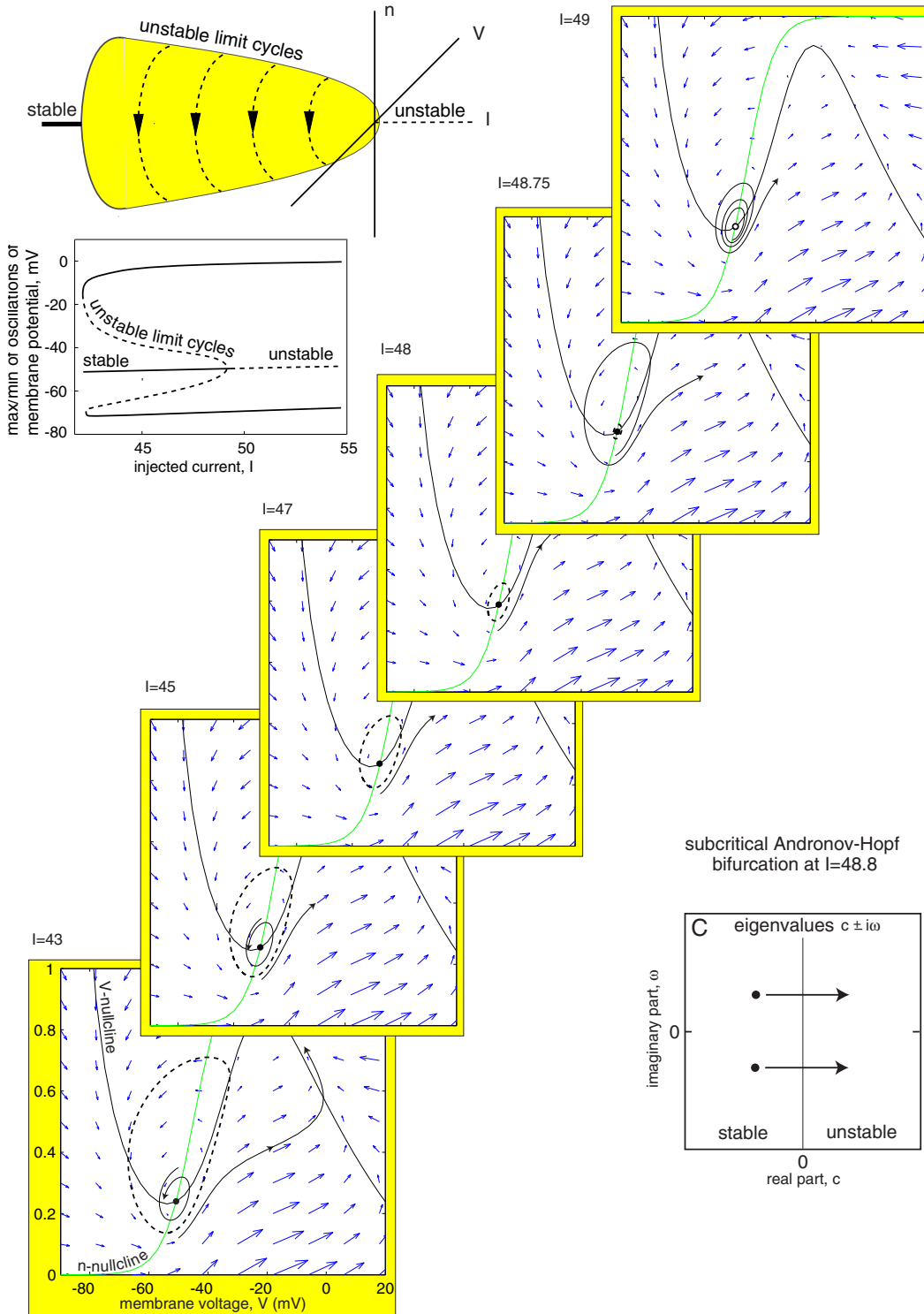


Figure 6.16: Subcritical Andronov-Hopf bifurcation in the  $I_{\text{Na,p}}+I_K$ -model: As the bifurcation parameter  $I$  increases, an unstable limit cycle (dashed circle; see also Fig. 6.14) shrinks to an equilibrium and makes it lose stability. Parameters as in Fig. 4.1b except  $g_L = 1$ ,  $g_{\text{Na}} = g_K = 4$ , and the  $\text{Na}^+$  activation function has  $V_{1/2} = -30$  mV and  $k = 7$ .

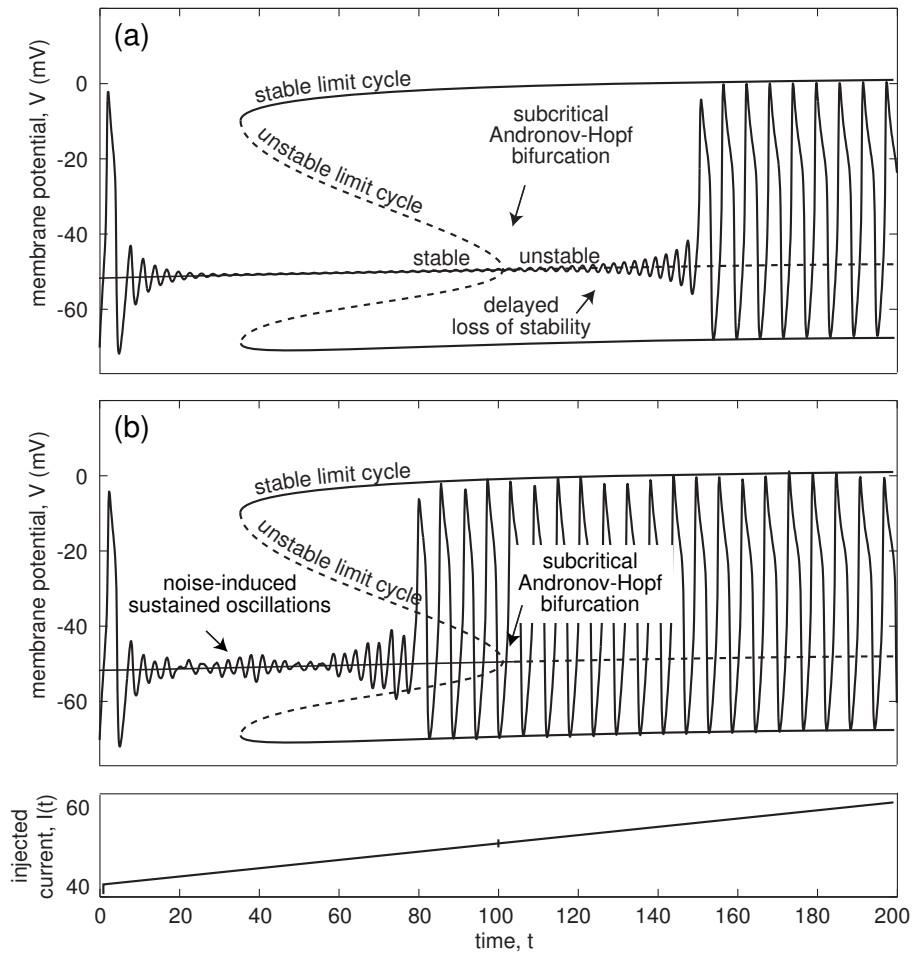


Figure 6.17: Delayed loss of stability (a) and noise-induced sustained oscillations (b) near subcritical Andronov-Hopf bifurcation. Shown are simulations of the  $I_{Na,p}+I_{K^-}$  model with parameters as in Fig. 6.16 and the same initial conditions. Small conductance noise is added in (b) to unmask oscillations.

waning rhythmic activity seen in the figure (see also Ex. 3 in Chap. 7). In Chapters 8 and 9 we present many examples of noise-induced sustained oscillations in biological neurons, and in Chap. 7 we study their neuro-computational properties.

## 6.2 Limit Cycle (Spiking State)

In the previous section we considered all codimension-1 bifurcations of equilibria, which typically correspond to transitions from resting to spiking states in neuronal models. Below we consider all codimension-1 bifurcations of limit cycle attractors on a phase plane. These bifurcations typically correspond to transitions from repetitive spiking to resting behavior, as we illustrate in Fig. 6.18, and they will be important in Chap. 9 where we consider bursting dynamics.

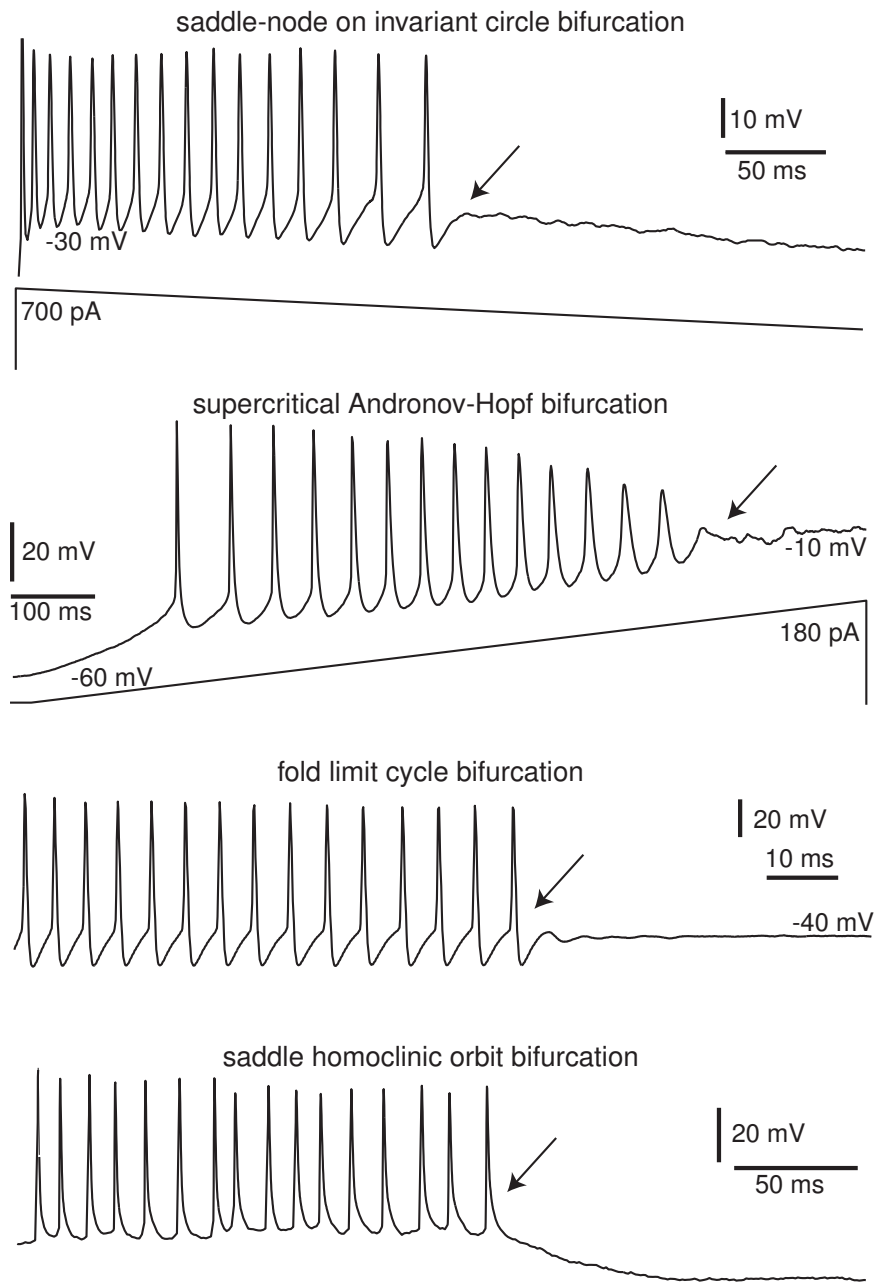


Figure 6.18: Transitions from tonic (periodic) spiking to resting occurs via bifurcations of a limit cycle attractors (marked by arrows). Saddle-node on invariant circle bifurcation: recording of layer 5 pyramidal neuron in rat's visual cortex. Supercritical Andronov-Hopf bifurcation: excitation block in pyramidal neuron of rat's visual cortex. Fold limit cycle bifurcation: brainstem mesencephalic V neuron of rat. Saddle homoclinic orbit bifurcation: neuron in pre-Botzinger complex of rat brainstem (data provided by C.A. Del Negro and J.L. Feldman).

Bifurcation of a limit cycle attractor	amplitude	frequency
saddle-node on invariant circle	non-zero	$A\sqrt{I-I_b} \rightarrow 0$
supercritical Andronov-Hopf	$A\sqrt{I-I_b} \rightarrow 0$	non-zero
fold limit cycle	non-zero	non-zero
saddle homoclinic orbit	non-zero	$\frac{-A}{\ln I-I_b } \rightarrow 0$

Figure 6.19: Summary of codimension-1 bifurcations of a limit cycle attractor on a plane. Here,  $I$  denotes the amplitude of the injected current,  $I_b$  is the bifurcation value,  $A$  is a parameter that depends on the biophysical details.

In Fig. 6.19 we summarize how the bifurcations affect a periodic attractor. Saddle-node on invariant circle and saddle homoclinic orbit bifurcations involve homoclinic trajectories having infinite period (zero frequency). They result in oscillations with drastically increasing interspike intervals as the system approaches the bifurcation state (see Fig. 6.18).

In contrast, supercritical Andronov-Hopf bifurcation results in oscillations with vanishing amplitude, as one can clearly see in Fig. 6.18. If neither the frequency nor the amplitude vanishes, then the bifurcation is of the fold limit cycle type. Indeed, the amplitude and the interspike period are constant before the arrow in Fig. 6.18 corresponding to the fold limit cycle bifurcation. Damped small-amplitude oscillation after the arrow occurs because of oscillatory convergence to the equilibrium.

We start with a brief review of the saddle-node on invariant circle and the supercritical Andronov-Hopf bifurcations, which we considered in detail in Sect. 6.1. These bifurcations can explain not only transitions from rest to spiking but also transitions from spiking to rest states. Then, we consider fold limit cycle and saddle homoclinic orbit bifurcations.

### 6.2.1 Saddle-node on invariant circle

A stable limit cycle can disappear via a saddle-node on invariant circle bifurcation as depicted in Fig. 6.20. The necessary condition for such a bifurcation is that the steady-state I-V relation is not monotonic.

We considered this bifurcation in Sect. 6.1.2 as a bifurcation from an equilibrium to a limit cycle; that is from left to right in Fig. 6.20. Now consider it from right to left: As a bifurcation parameter changes, e.g., the injected dc-current  $I$  decreases, a stable limit cycle (circle in Fig. 6.20, right) disappears because there is a saddle-

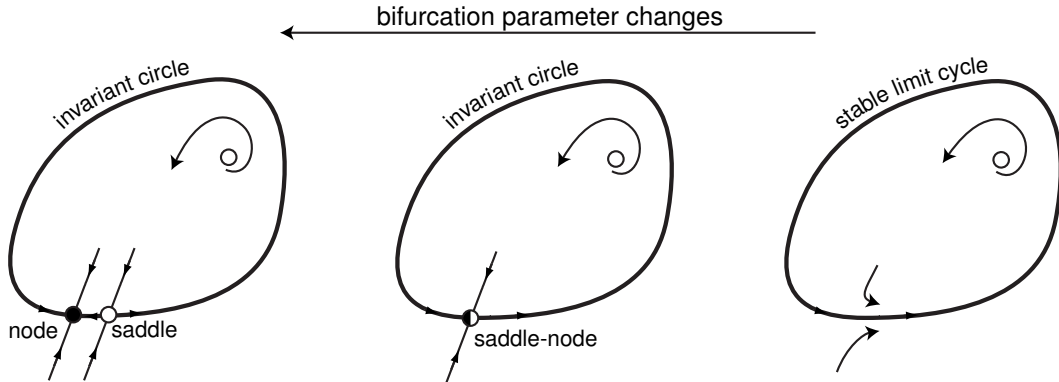


Figure 6.20: Saddle-node on invariant circle (SNIC) bifurcation of a limit cycle attractor.

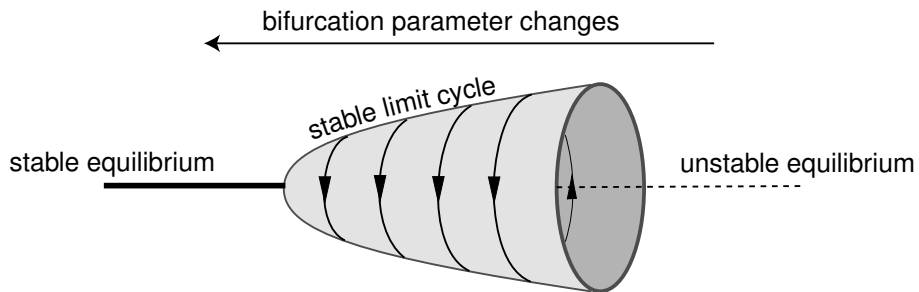


Figure 6.21: Supercritical Andronov-Hopf bifurcation of a limit cycle attractor.

node bifurcation (Fig. 6.20, center) that breaks the cycle and gives birth to a pair of equilibria—stable node and unstable saddle (Fig. 6.20, left). After the bifurcation, the limit cycle becomes an invariant circle consisting of a union of two heteroclinic trajectories.

Depending on the direction of change of a bifurcation parameter, the saddle-node on invariant circle bifurcation can explain either appearance or disappearance of a limit cycle attractor. In either case, the amplitude of the limit cycle remains relatively constant but its period becomes infinite at the bifurcation point because the cycle becomes a homoclinic trajectory to the saddle-node equilibrium (Fig. 6.20, center). As we showed in Sect. 6.1.2 (see Fig. 6.8), the frequency of oscillation scales as  $\sqrt{I - I_b}$  when the bifurcation parameter approaches the bifurcation value  $I_b$ .

## 6.2.2 Supercritical Andronov-Hopf

A stable limit cycle can shrink to a point via supercritical Andronov-Hopf bifurcation in Fig. 6.21, which we considered in Sect. 6.1.3. Indeed, as the bifurcation parameter changes, e.g., the injected dc-current  $I$  in Fig. 6.11 decreases, the amplitude of the limit cycle attractor vanishes, and the cycle becomes just a stable equilibrium. As we showed in Sect. 6.1.3 (see Fig. 6.12), the amplitude scales as  $\sqrt{I - I_b}$  when the

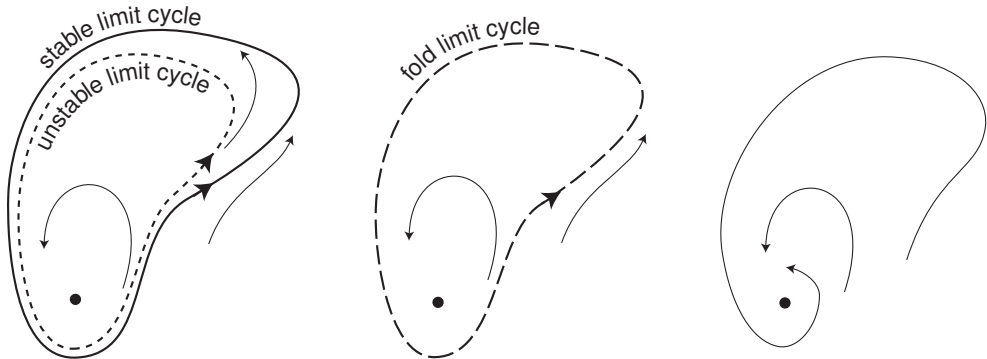


Figure 6.22: Fold limit cycle bifurcation: A stable and an unstable limit cycle approach and annihilate each other.

bifurcation parameter approaches the bifurcation value  $I_b$ .

### 6.2.3 Fold limit cycle

A stable limit cycle can appear (or disappear) via the *fold limit cycle* bifurcation depicted in Fig. 6.22. Let us consider the figure from left to right, which corresponds to the disappearance of the limit cycle, and hence to the disappearance of periodic spiking activity. As the bifurcation parameter changes, the stable limit cycle is approached by an unstable one, they coalesce and annihilate each other. At the point of annihilation, there is a periodic orbit, but it is neither stable nor unstable. More precisely, it is stable from the side corresponding to the stable cycle (outside in Fig. 6.22), and unstable from the other side (inside in Fig. 6.22). This periodic orbit is referred to as being a fold (also known as a saddle-node) limit cycle, and it is analogous to the fold (saddle-node) equilibrium studied in Sect. 6.1. Considering Fig. 6.22 from right to left explains how a stable limit cycle can appear seemingly out of nowhere: As a bifurcation parameter changes, a fold limit cycle appears, which then bifurcates into a stable limit cycle and an unstable one.

Fold limit cycle bifurcation can occur in the  $I_{\text{Na,p}} + I_K$ -model having low-threshold  $K^+$  current, as we demonstrate in Fig. 6.23. The top phase portrait corresponding to  $I = 43$  is the same as the one in Fig. 6.16. In that figure we studied how the equilibrium loses stability via subcritical Andronov-Hopf bifurcation, which occurs when an unstable limit cycle shrinks to a point. We never questioned where the unstable limit cycle came from. Neither were we concerned with the existence of a large-amplitude stable limit cycle corresponding to the periodic spiking state. In Fig. 6.23 we study this problem. We decrease the bifurcation parameter  $I$  to see what happens with the limit cycles. As  $I$  approaches the bifurcation value 42.18, the unstable and stable limit cycles approach and annihilate each other. When  $I$  is less than the bifurcation value, there are no periodic orbits, only one stable equilibrium corresponding to the resting state.

Notice that the fold limit cycle bifurcation explains how (un)stable limit cycles

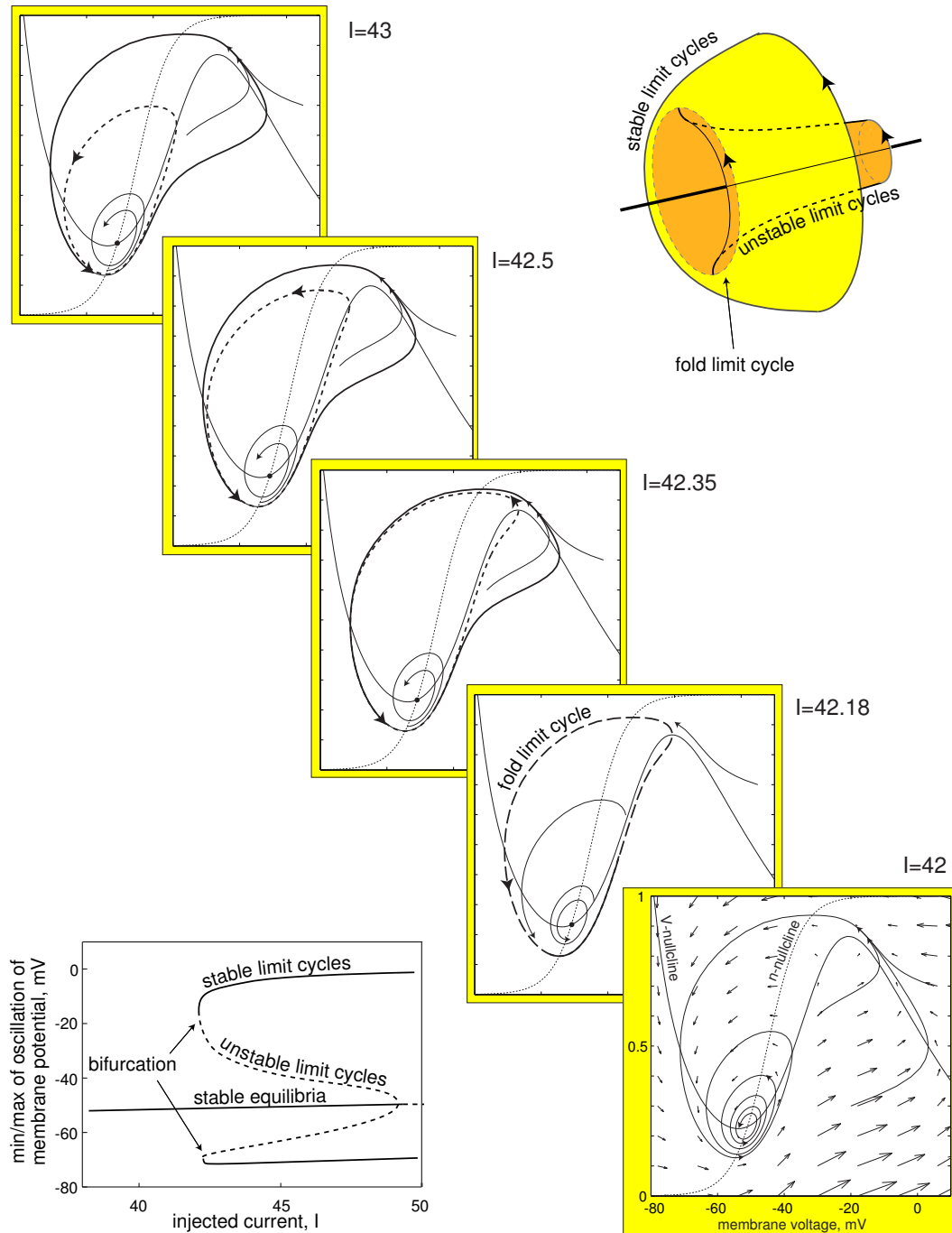


Figure 6.23: Fold limit cycle bifurcation in the  $I_{Na,p} + I_K$ -model. As the bifurcation parameter  $I$  decreases, the stable and unstable limit cycles approach and annihilate each other. Parameters as in Fig. 6.16.

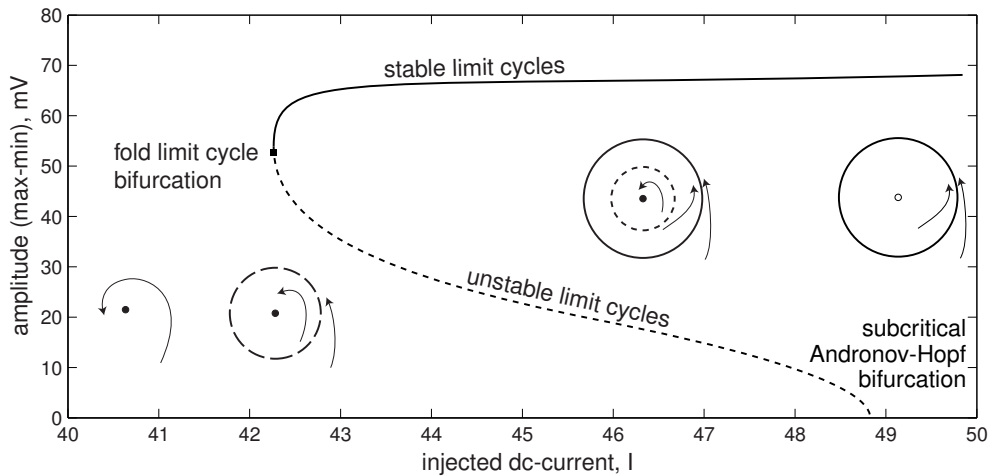


Figure 6.24: Bifurcation diagram of the  $I_{\text{Na},p} + I_K$ -model. Parameters as in Fig. 6.16.

appear or disappear, but it *does not* explain how stable periodic spiking behavior appears. Indeed, let us start with  $I = 42$  in Fig. 6.23 and slowly increase the parameter. The state of the  $I_{\text{Na},p} + I_K$ -model is at the stable equilibrium. When  $I$  passes the bifurcation value, a large-amplitude stable limit cycle corresponding to periodic spiking appears, yet the model is still quiescent, because it is still at the stable equilibrium. Thus, the limit cycle is just a geometrical object in the phase space that corresponds to spiking behavior. However, to actually exhibit spiking, the state of the system must be somehow pushed into the attraction domain of the cycle, say by external stimulation. This issue is related to the computational properties of neurons, and it is discussed in detail in the next chapter.

In Fig. 6.24 we depict the bifurcation diagram of the  $I_{\text{Na},p} + I_K$ -model. For each value of  $I$ , we simulate the model forward ( $t \rightarrow \infty$ ) to find the stable limit cycle and backward ( $t \rightarrow -\infty$ ) to find the unstable limit cycle. Then we plot their amplitudes (maximal voltage minus minimal voltage along the limit cycle) on the  $(I, V)$ -plane. One can clearly see that there is a fold limit cycle bifurcation (left) and a subcritical Andronov-Hopf bifurcation (right). The left part of the bifurcation diagram looks exactly like the one for saddle-node bifurcation, which explains why the fold limit cycle bifurcation is often referred to as *fold* or *saddle-node of periodics*.

The similarity of the fold limit cycle bifurcation and the saddle-node bifurcation is not a coincidence. Stability of limit cycles can be studied using Floquet theory, Poincaré cross-section maps (Kuznetsov 1995), or by brute force, e.g., by reducing the model to an appropriate polar coordinate system. When a limit cycle attractor undergoes fold limit cycle bifurcation, its radius undergoes saddle-node bifurcation (this is a hint to Ex. 10).

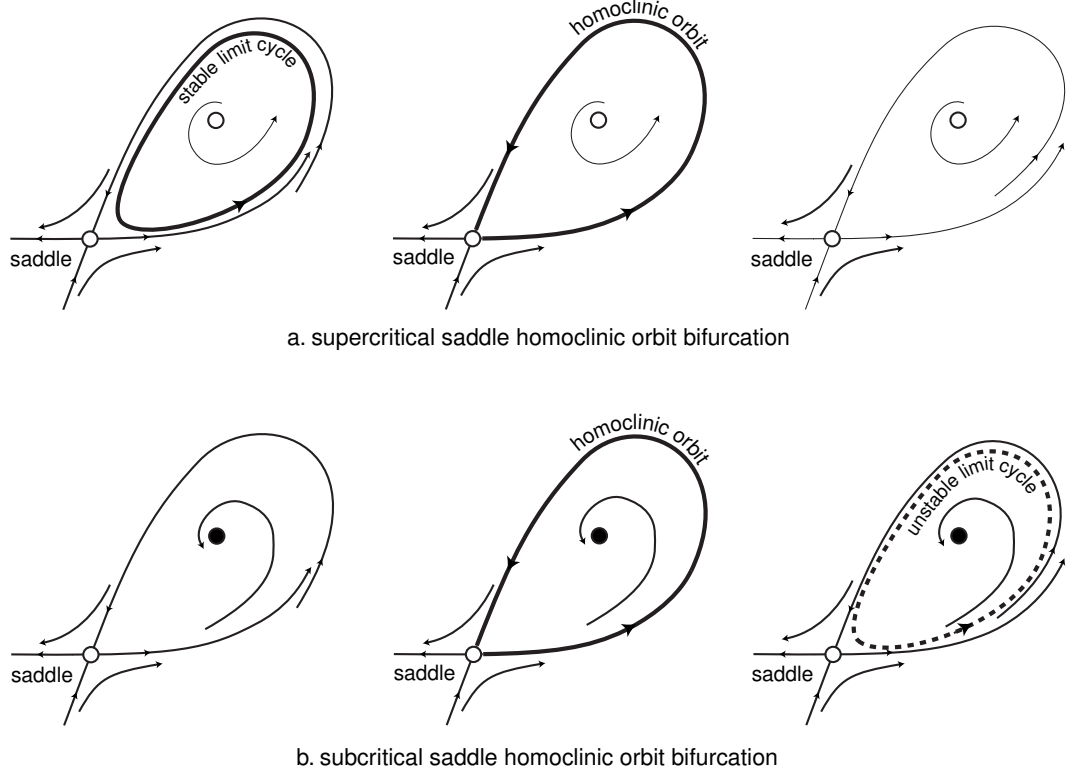


Figure 6.25: Saddle homoclinic orbit bifurcation.

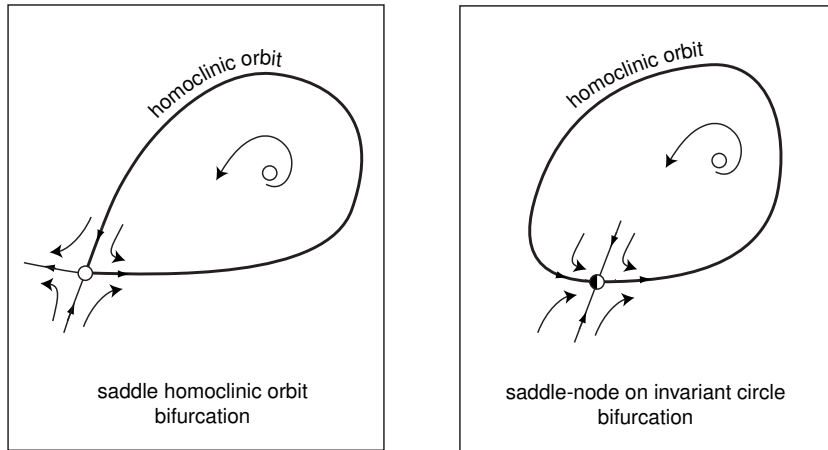


Figure 6.26: Two bifurcations involving homoclinic trajectories to an equilibrium.

#### 6.2.4 Homoclinic

A limit cycle can appear or disappear via a saddle homoclinic orbit bifurcation, as depicted in Fig. 6.25. As the bifurcation parameter changes, the cycle becomes a homoclinic orbit to the saddle equilibrium, and its period becomes infinite. After the bifurcation, the cycle no longer exists. A necessary condition for such a bifurcation is that the steady-state I-V relation is not monotonic.

One should be careful to distinguish the saddle homoclinic orbit bifurcation from the saddle-node on invariant circle bifurcation depicted in Fig. 6.26. Indeed, it might be easy to confuse these bifurcations, since both involve an equilibrium and a large-amplitude homoclinic trajectory that becomes a limit cycle. The key difference is that the equilibrium is a saddle in the former and a saddle-node in the latter. The saddle equilibrium persists as the bifurcation parameter changes, whereas the saddle-node equilibrium disappears or bifurcates into two points, depending on the direction of change of the bifurcation parameter.

Recall that a saddle on a plane has two real eigenvalues of opposite signs. Their sum,  $\lambda_1 + \lambda_2$ , is called the *saddle quantity*.

- If  $\lambda_1 + \lambda_2 < 0$ , then the saddle homoclinic orbit bifurcation is *supercritical*, which corresponds to the (dis)appearance of a *stable* limit cycle.
- If  $\lambda_1 + \lambda_2 > 0$ , then the saddle homoclinic orbit bifurcation is *subcritical*, which corresponds to the (dis)appearance of an *unstable* limit cycle.

Thus, the saddle quantity plays the same role as the parameter  $a$  in the Andronov-Hopf bifurcation. The supercritical saddle homoclinic orbit bifurcation is more common in neuronal models than the subcritical one due to the reason explained in Sect. 6.3.6. Hence, we consider only the supercritical case below, and we drop the word “supercritical” for the sake of brevity.

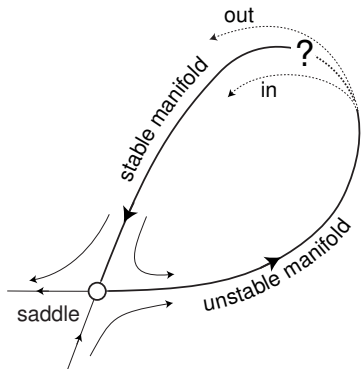


Figure 6.27: Saddle homoclinic orbit bifurcation occurs when the stable and unstable submanifolds of the saddle make a loop.

A useful way to look at the bifurcation is to note that the saddle has one stable and one unstable direction on a phase plane. There are two orbits associated with these directions, called the stable and unstable submanifolds, depicted in Fig. 6.27. Typically, the submanifolds miss each other, that is, the unstable submanifold goes either inside or outside the stable one. This could happen for two different values of the bifurcation parameter. One can image that as the bifurcation parameter changes continuously from one value to the other, the submanifolds join at some point and form a single homoclinic trajectory that starts and ends at the saddle.

The saddle homoclinic orbit bifurcation is ubiquitous in neuronal models, and it can easily be observed in the  $I_{\text{Na,p}} + I_K$ -model with fast  $K^+$  conductance, as we illustrate in Fig. 6.28. Let us start with  $I = 7$  (top of Fig. 6.28) and decrease the bifurcation parameter  $I$ . First, there is only a stable limit cycle corresponding to periodic spiking activity. When  $I$  decreases, a stable and an unstable equilibrium appear via saddle-node bifurcation (not shown in the figure), but the state of the model is still on the limit cycle attractor. Further decrease of  $I$  moves the saddle equilibrium closer to the limit cycle (case  $I = 4$  in the figure), until the cycle becomes an infinite period homoclinic orbit to the saddle (case  $I \approx 3.08$ ), and then disappears (case  $I = 1$ ). At this moment, the state of the system approaches the stable equilibrium, and the tonic spiking stops.

Similarly to the fold limit cycle bifurcation, the saddle homoclinic orbit bifurcation explains how the limit cycle attractor corresponding to periodic spiking behavior appears and disappears. However, it does not explain the transition to periodic spiking behavior. Indeed, when  $I = 4$  in Fig. 6.28, the limit cycle attractor exists, yet the neuron may still be quiescent because its state may be at the stable node. The periodic spiking behavior appears only after external perturbations push the state of the system into the attraction domain of the limit cycle attractor, or  $I$  increases further and the stable node disappears via a saddle-node bifurcation.

We can use linear theory to estimate the frequency of the limit cycle attractor near saddle homoclinic orbit bifurcation. Because the vector field is small near the equilibrium, the periodic trajectory slowly passes through a small neighborhood of the equilibrium, then quickly makes a rotation and returns to the neighborhood, as we illustrate in Fig. 6.29. Let  $T_1$  denote the time required to make one rotation (dashed

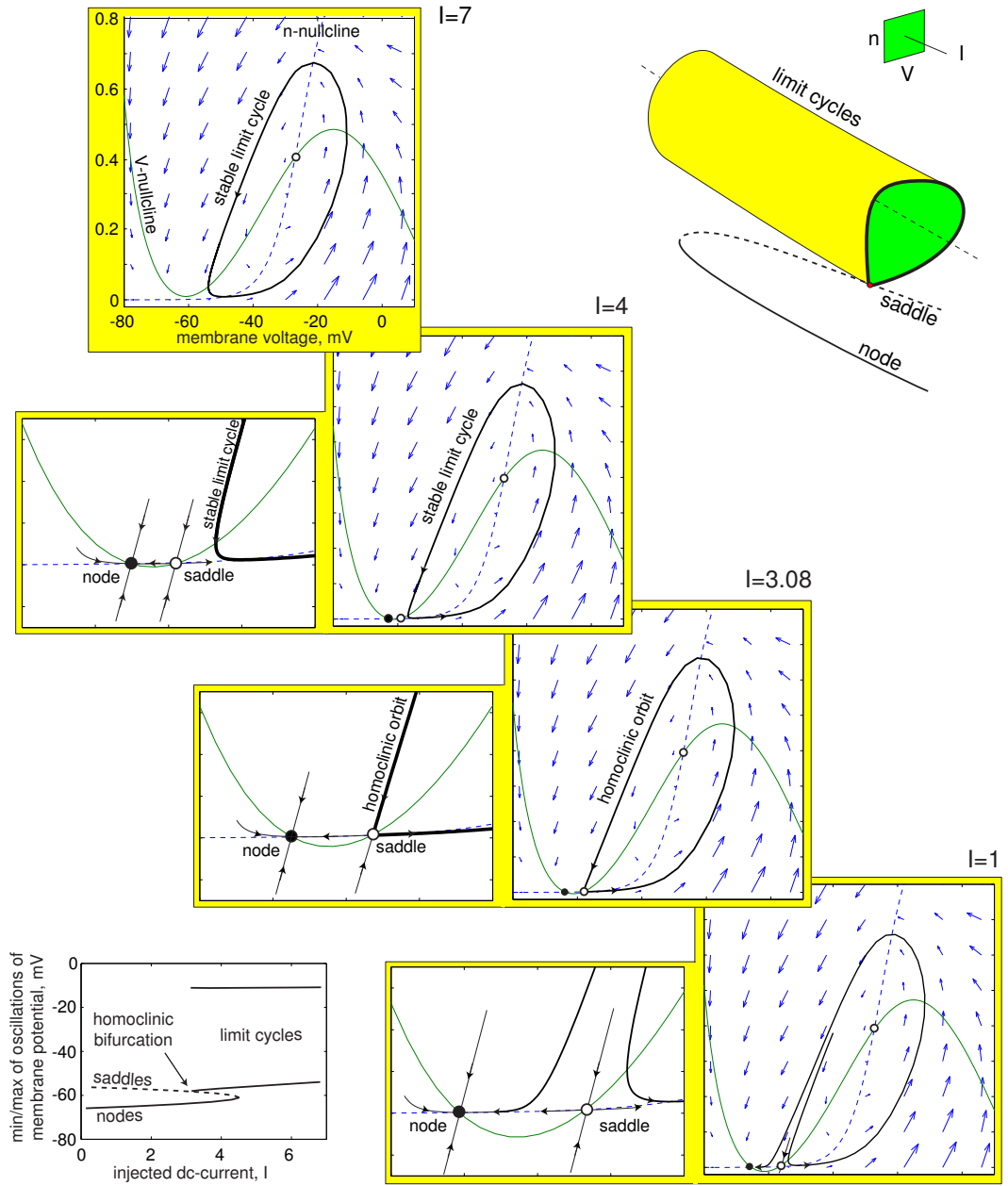


Figure 6.28: Saddle homoclinic orbit bifurcation in the  $I_{\text{Na},p} + I_K$ -model with parameters as in Fig. 4.1a and fast  $K^+$  current ( $\tau(V) = 0.16$ ). As the bifurcation parameter  $I$  decreases, the stable limit cycle becomes a homoclinic orbit to a saddle.

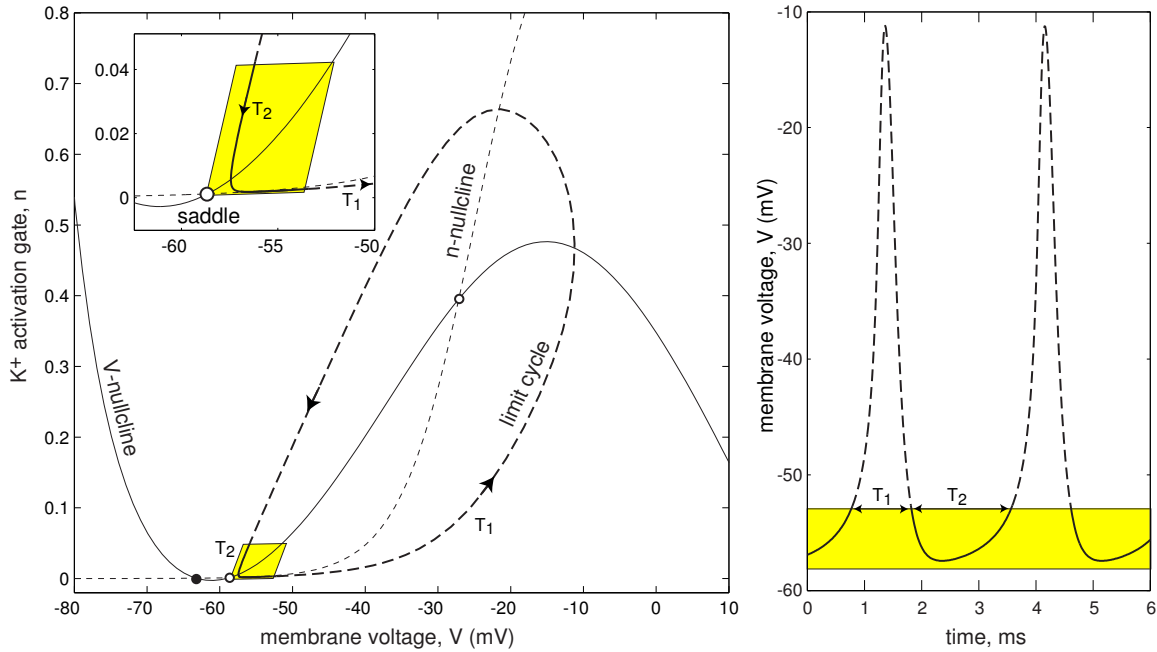


Figure 6.29: The period of the limit cycle is  $T = T_1 + T_2$  with  $T_2 \rightarrow \infty$  as the cycle approaches the saddle equilibrium. Shown is the  $I_{\text{Na},p} + I_K$ -model with  $I = 3.5$ .

part of the limit cycle in the figure) and  $T_2$  denote the time spent in the small neighborhood of the saddle equilibrium (continuous part of the limit cycle in the shadowed region), so that the period of limit cycle is  $T = T_1 + T_2$ . While  $T_1$  is relatively constant,  $T_2 \rightarrow \infty$  as  $I$  approaches the bifurcation value  $I_b = 3.08$ , and the limit cycle approaches the saddle. In Ex. 11 we show that

$$T_2 = -\frac{1}{\lambda_1} \ln\{\tau(I - I_b)\} ,$$

where  $\lambda_1$  is the positive (unstable) eigenvalue of the saddle, and  $\tau$  is a parameter that depends on the size of the neighborhood, global features of the vector field, etc. We can represent the period,  $T$ , in the form

$$T(I) = -\frac{1}{\lambda_1} \ln\{\tau_1(I - I_b)\} ,$$

where a single parameter  $\tau_1 = \tau e^{-\lambda_1 T_1}$  accounts for all global features of the model, including the width of the action potential, the shape of the limit cycle, etc. One can easily determine  $\tau_1$  if the eigenvalue  $\lambda_1$  and the period of the limit cycle is known for at least one value of  $I$ . The  $I_{\text{Na},p} + I_K$ -model has  $\tau_1 = 0.2$ , as we show in Fig. 6.30. Notice that the theoretical frequency  $1000/T(I)$  matches the numerically found frequency in a broad range. Also, notice how imprecise the numerical results are (see inset in the figure).

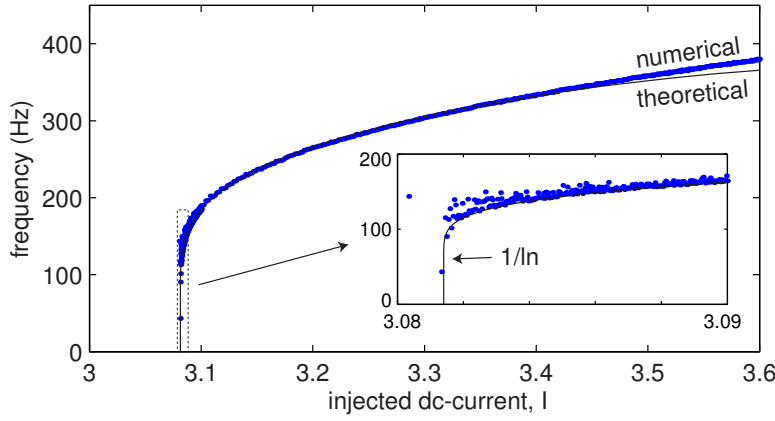


Figure 6.30: Frequency of spiking in the  $I_{\text{Na,p}}+I_K$ -model with parameters as in Fig. 6.28 near a saddle homoclinic orbit bifurcation. Dots are numerical results; the continuous curve is  $\omega(I) = 1000\lambda(I)/\{-\ln(0.2(I - 3.0814))\}$ , where the eigenvalue  $\lambda(I) = 0.87\sqrt{4.51 - I}$  was obtained from the normal form (6.3). The inset shows a magnified region near the bifurcation value  $I = 3.0814$ .

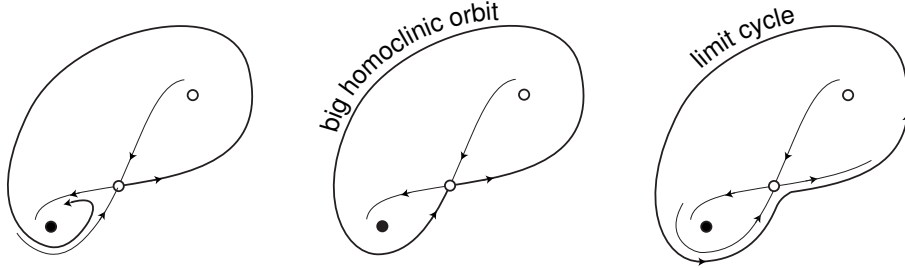


Figure 6.31: Big saddle homoclinic orbit bifurcation.

Both, the saddle-node on invariant circle bifurcation and the saddle homoclinic orbit bifurcation result in spiking with decreasing frequency so that their frequency-current (F-I) curves go continuously to zero. The key difference is that the former asymptotes as  $\sqrt{I - I_b}$ , whereas the latter as  $1/\ln(I - I_b)$ . The striking feature of the logarithmic decay in Fig. 6.30 is that the frequency is greater than 100 Hz and the theoretical curve does not seem to go to zero for all  $I$  except those in an infinitesimal neighborhood of the bifurcation value  $I_b$ . Such a neighborhood is almost impossible to catch numerically, let alone experimentally in real neurons.

Many neuronal models, and even some cortical pyramidal neurons (see Fig. 7.42) exhibit a saddle homoclinic orbit bifurcation depicted in Fig. 6.31. Here, the unstable manifold of a saddle returns to the saddle along the opposite side, thereby making a big loop, hence the name *big saddle homoclinic orbit* bifurcation. This kind of bifurcation often occurs when an excitable system is near a codimension-2 Bogdanov-Takens bifurcation considered in Sect. 6.3.3, and it has the same properties as the “small” homoclinic orbit bifurcation considered above: it could be subcritical or supercritical,

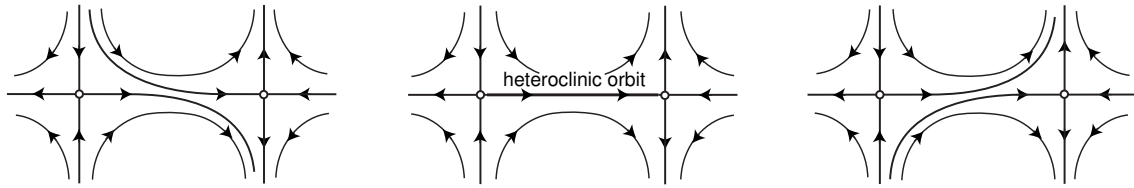


Figure 6.32: Heteroclinic orbit bifurcation does not change the existence of stability of any equilibrium or periodic orbit.

depending on the saddle quantity, it results in a logarithmic F-I curve, and it implies the co-existence of attractors. All methods of analysis of excitable systems near “small” saddle homoclinic orbit bifurcations can also be applied to the case in Fig. 6.31.

## 6.3 Other Interesting Cases

Saddle-node and Andronov-Hopf bifurcations of equilibria combined with fold limit cycle, homoclinic orbit bifurcation, and heteroclinic orbit bifurcation (see Fig. 6.32) exhaust all possible bifurcations of codimension-1 on a plane. These bifurcations can also occur in higher-dimensional systems. Below we discuss additional codimension-1 bifurcations in three-dimensional phase space, and then we consider some codimension-2 bifurcations that play an important role in neuronal dynamics. The first-time reader may read only Sect. 6.3.6 and skip the rest.

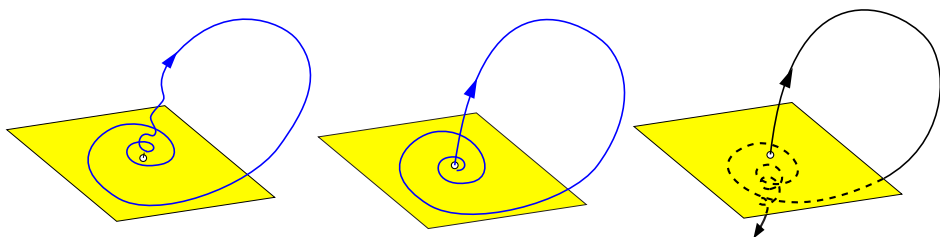
### 6.3.1 Three-dimensional phase space

So far we considered four bifurcations of equilibria and four bifurcations of limit cycles on a phase plane. The same eight bifurcations can appear in multi-dimensional systems. Below we briefly discuss the new kinds of bifurcations that are possible in a three-dimensional phase space but cannot occur on a plane.

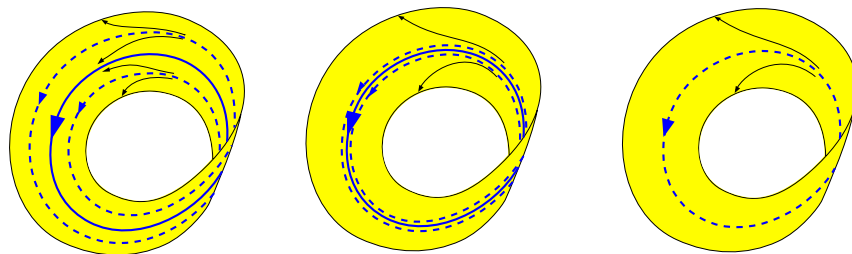
First, there are no new bifurcations of *equilibria* in multi-dimensional phase space. Indeed, what could possibly happen with the Jacobian matrix of an equilibrium of a multi-dimensional dynamical system? A simple zero eigenvalue would result in a saddle-node bifurcation, and a simple pair of purely imaginary complex-conjugate eigenvalues would result in an Andronov-Hopf bifurcation. Both are exactly the same as in the lower-dimensional systems considered before. Thus, adding dimensions to a dynamical system does not create new possibilities for bifurcations of equilibria.

In contrast, adding the third dimension to a planar dynamical system creates new possibilities for bifurcations of *limit cycles*, some of which are depicted in Fig. 6.33. Below we briefly describe these bifurcations.

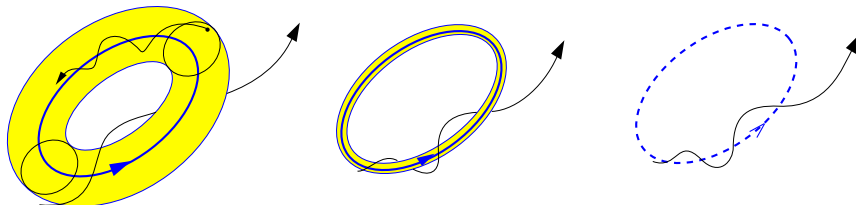
The *saddle-focus homoclinic orbit* bifurcation in Fig. 6.33 is similar to the saddle homoclinic orbit bifurcation considered in Sect. 6.2.4 except that the equilibrium has a pair of complex-conjugate eigenvalues and a non-zero real eigenvalue. The homoclinic orbit originates in the subspace spanned by the eigenvector corresponding to



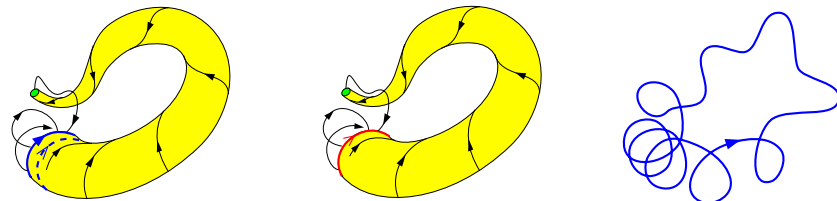
Saddle-Focus Homoclinic Orbit Bifurcation



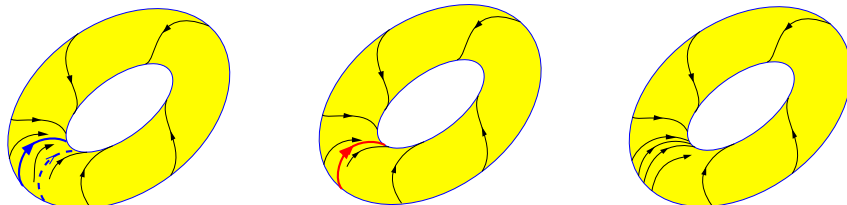
Subcritical Flip Bifurcation



Subcritical Neimark-Sacker Bifurcation



Blue-Sky Catastrophe



Fold Limit Cycle on Homoclinic Torus Bifurcation

Figure 6.33: Some codimension-1 bifurcations of limit cycles in three-dimensional phase space (modified from Izhikevich 2000).

the real eigenvalue (as in Fig. 6.33) and terminates along the subspace spanned by the eigenvectors corresponding to the complex-conjugate pair. The reverse direction is also possible. Depending on the direction and the relative magnitude of the eigenvalues, this bifurcation can result in the (dis)appearance or a stable (supercritical) or unstable (subcritical) twisted large-period orbit.

The *subcritical flip* bifurcation in Fig. 6.33 occurs when a stable periodic orbit is surrounded by an unstable orbit of twice the period. The unstable periodic orbit shrinks to the stable one and makes it lose stability. This bifurcation is similar to the pitchfork bifurcation studied below, except it has codimension 1 (pitchfork bifurcation has infinite codimension unless one considers dynamical systems with symmetry). A supercritical flip bifurcation is similar, except that an unstable cycle is surrounded by a stable double-period cycle.

The *subcritical Neimark-Sacker* bifurcation in Fig. 6.33 occurs when a stable periodic orbit is surrounded by an unstable invariant torus. The latter shrinks and makes the periodic orbit lose its stability. In some sense, which we will not elaborate on here, this bifurcation is similar to the supercritical Andronov-Hopf bifurcation of an equilibrium. The supercritical Neimark-Sacker bifurcation occurs when an unstable orbit is surrounded by a stable invariant torus.

The *blue-sky catastrophe* in Fig. 6.33 occurs when a small amplitude stable limit cycle disappears and a large-amplitude large-period stable orbit appears out of nowhere (from the blue sky): The orbit has an infinite period at the bifurcation, yet it is not homoclinic to any equilibrium. A careful analysis shows that the large orbit is homoclinic to the small limit cycle at the moment the cycle disappears. In some sense, which we elaborate on later, this bifurcation is similar to the saddle-node on invariant circle bifurcation (see Ex. 20). In particular, both bifurcations share the same asymptotics.

The *fold limit cycle on homoclinic torus* bifurcation in Fig. 6.33 is similar to the blue-sky catastrophe except that the disappearance of the small periodic orbit results in a large-amplitude torus (quasi-periodic) attractor.

### 6.3.2 Cusp and pitchfork

Recall that an equilibrium  $x_b$  of a one-dimensional system  $\dot{x} = f(x, b)$  is at a saddle-node bifurcation when  $f_x = 0$  (first derivative of  $f$ ) but  $f_{xx} \neq 0$  (second derivative of  $f$ ) at the equilibrium. The latter is called the non-degeneracy condition, and it guarantees that the system dynamics is equivalent to that of  $\dot{x} = c(b) + x^2$ .

If  $f_x = 0$  and  $f_{xx} = 0$ , but  $f_{xxx} \neq 0$ , then the equilibrium is at the codimension-2 *cusp* bifurcation, and the behavior of the system near the equilibrium can be described by the topological normal form

$$\dot{x} = c_1(b) + c_2(b)x + ax^3 ,$$

where

$$c_1(b) = f(x_b, b) , \quad c_2(b) = f_x(x_b, b) , \quad a = f_{xxx}/6 \neq 0 ,$$

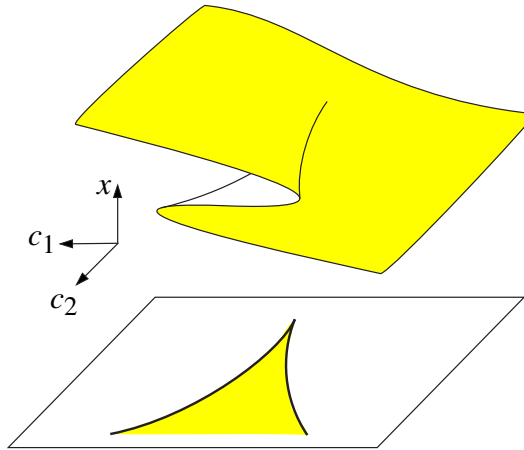


Figure 6.34: Cusp surface.

in particular,  $c_1 = c_2 = 0$  at the cusp point. The cusp bifurcation is supercritical when  $a < 0$  and subcritical otherwise. It is explained by the shape of the surface

$$c_1 + c_2 x + ax^3 = 0$$

depicted in Fig. 6.34.

Let us treat  $c_1$  and  $c_2$  as two independent parameters, and check that there are saddle-node bifurcations in any neighborhood of the cusp point. The bifurcation sets of the topological normal form can easily be found. Differentiating  $c_1 + c_2 x + ax^3$  with respect to  $x$  gives  $c_2 + 3ax^2$ . Equating both of these expressions to zero and eliminating  $x$  gives the saddle-node bifurcation curves

$$c_1 = \pm \frac{2}{\sqrt{a}} \left( \frac{c_2}{3} \right)^{3/2},$$

depicted at the bottom of Fig. 6.34.

Since  $c_1 = c_1(b)$  and  $c_2 = c_2(b)$ , varying the bifurcation parameter  $b$  results in a path on the  $(c_1, c_2)$ -plane. Depending on the shape and location of this path, one can get many 1-dimensional bifurcation diagrams. A summary of some special cases is depicted in Fig. 6.35 showing that there can be many interesting dynamical regimes in the vicinity of a cusp bifurcation point.

An important special case is when  $c_1 = 0$  and  $c_2(b) = b$ , so that the topological normal form is

$$\dot{x} = bx + ax^3.$$

This form corresponds to a *pitchfork* bifurcation, whose diagram is depicted in Fig. 6.36 (see also the bottom bifurcation diagram in Fig. 6.35). This bifurcation has an infinite codimension unless one considers dynamical systems with symmetry, e.g.,  $\dot{x} = f(x, b)$  with  $f(-x, b) = -f(x, b)$  for all  $x$  and  $b$ .

### 6.3.3 Bogdanov-Takens

Can an equilibrium undergo Andronov-Hopf and saddle-node bifurcations simultaneously? There are two possibilities, illustrated in Fig. 6.37:

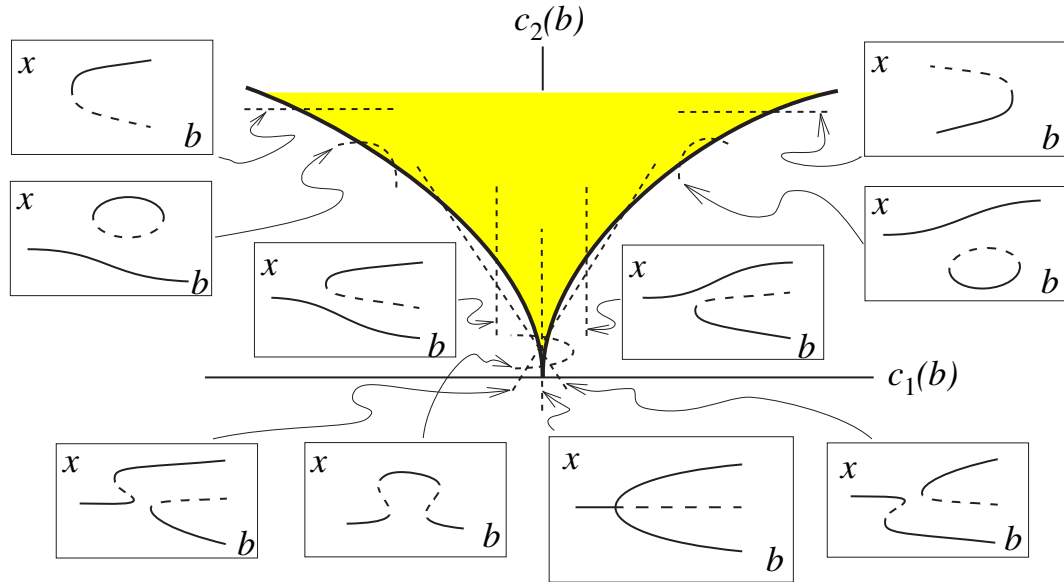


Figure 6.35: Summary of special cases for the supercritical cusp bifurcation. Dotted segments are paths  $c_1 = c_1(b)$ ,  $c_2 = c_2(b)$ , where  $b$  is a one-dimensional bifurcation parameter. The corresponding bifurcation diagrams are depicted in boxes. Continuous curves represent stable solutions, dashed curves represent unstable solutions (modified from Hoppensteadt and Izhikevich 1997).

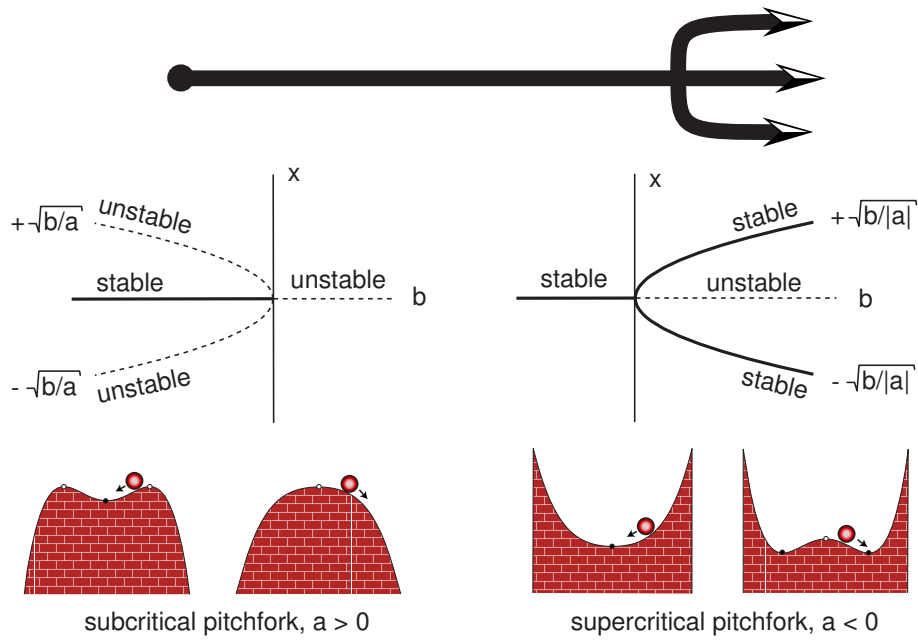


Figure 6.36: Pitchfork bifurcation diagrams.

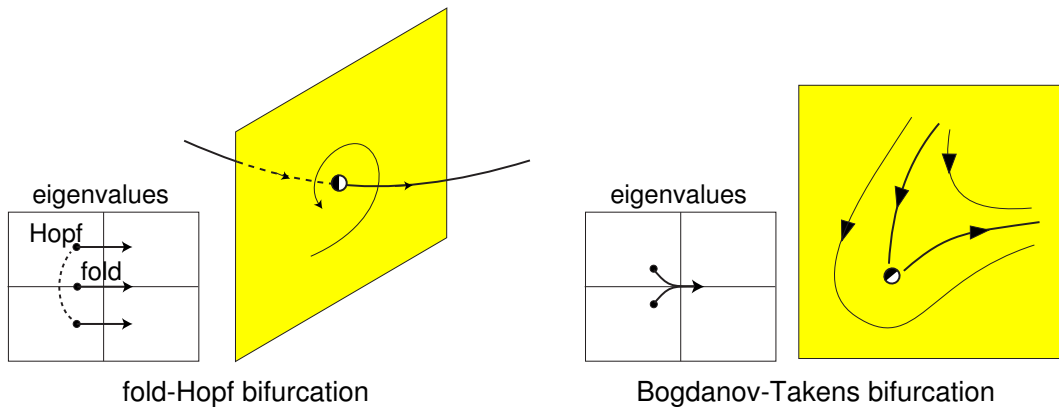


Figure 6.37: Two ways an equilibrium can undergo a saddle-node (fold) and an Andronov-Hopf bifurcations simultaneously.

- **(Fold-Hopf)** The Jacobian matrix at the equilibrium has a pair of pure imaginary complex-conjugate eigenvalues (Andronov-Hopf bifurcation) and one zero eigenvalue (saddle-node bifurcation). In this case the two bifurcations occur in different subspaces.
- **(Bogdanov-Takens)** The Jacobian matrix has two zero eigenvalues. In this case the two bifurcations occur in the same subspace.

The fold-Hopf bifurcations occurs in systems having dimension 3 and up, while the Bogdanov-Takens bifurcation can occur in two-dimensional systems. Both bifurcations have codimension-2; that is, they require 2 bifurcation parameters. Notice that fold-Hopf bifurcation has 3 eigenvalues with zero real part, whereas Bogdanov-Takens bifurcation has only 2 zero eigenvalues. This bifurcation can on the one hand be viewed as a saddle-node bifurcation in which another (negative) eigenvalue gets arbitrary close to zero, and on the other hand as an Andronov-Hopf bifurcation in which imaginary part of the complex-conjugate eigenvalues goes to zero.

The Jacobian matrix of an equilibrium at the Bogdanov-Takens bifurcation satisfies two conditions:  $\det L = 0$  (saddle-node bifurcation) and  $\text{tr } L = 0$  (Andronov-Hopf bifurcation). For example, it can have the form

$$L = \begin{pmatrix} 0 & 1 \\ 0 & 0 \end{pmatrix}. \quad (6.10)$$

Because of these two conditions, the codimension of this bifurcation is 2. There are also certain non-degeneracy and transversality conditions (see Kuznetsov 1995). The corresponding topological normal form,

$$\begin{aligned} \dot{u} &= v, \\ \dot{v} &= a + bu + u^2 + \sigma uv, \end{aligned} \quad (6.11)$$

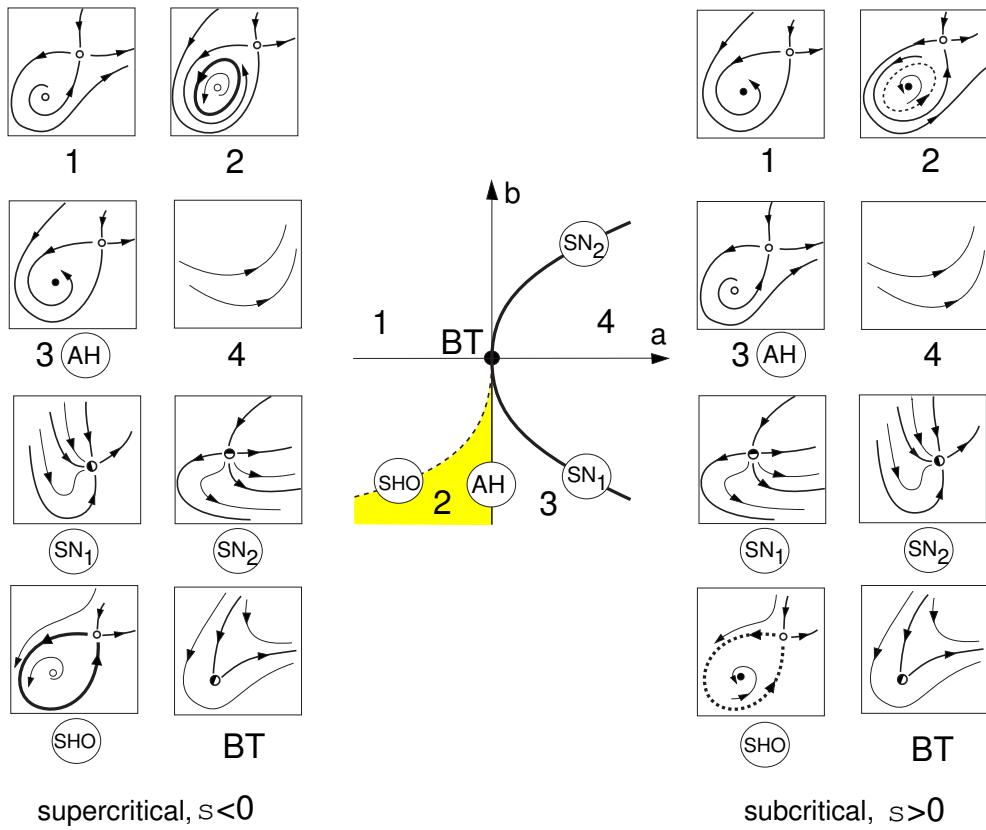


Figure 6.38: Bogdanov-Takens (BT) bifurcation diagram of the topological normal form (6.11). Abbreviations: AH - Andronov-Hopf bifurcation, SN - saddle-node bifurcation, SHO - saddle homoclinic orbit bifurcation.

has two bifurcation parameters,  $a$  and  $b$ , and the parameter  $\sigma = \pm 1$  determines whether the bifurcation is subcritical or supercritical. This parameter depends on the combination of the second-order partial derivatives with respect to the first variable, and it is non-zero because of the non-degeneracy conditions (Kuznetsov 1995). Bifurcation diagram and representative phase portraits for various  $a$ ,  $b$  and  $\sigma$  are depicted in Fig. 6.38 (the case  $\sigma > 0$  can be reduced to  $\sigma < 0$  by the substitution  $t \rightarrow -t$  and  $v \rightarrow -v$ ). A remarkable fact is that the saddle-node and the Andronov-Hopf bifurcations do not occur alone. There is also a saddle homoclinic orbit bifurcation appearing near the Bogdanov-Takens point.

Bogdanov-Takens bifurcation occurs often in neuronal models with nullclines intersecting as in Fig. 6.39a. We show in the next chapter that this bifurcation separates integrators from resonators, and it could occur in some layer 5 pyramidal neurons of rat visual cortex, as we discuss in Sect. 7.2.11 and Sect. 8.2.1. The two equilibria in the lower (left) knee of the fast nullcline in Fig. 6.39b are not necessarily a saddle and a stable node, but could be a saddle and an (un)stable focus, as in the phase portraits in Fig. 6.38.

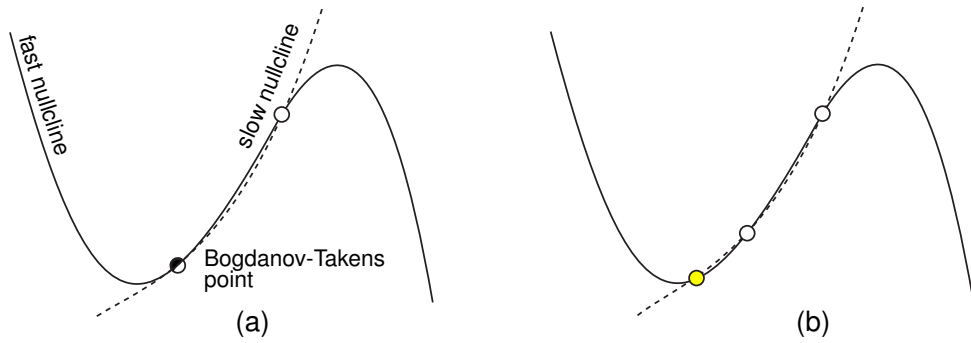


Figure 6.39: Intersection of nullclines of a two-dimensional system resulting in Bogdanov-Takens bifurcation.

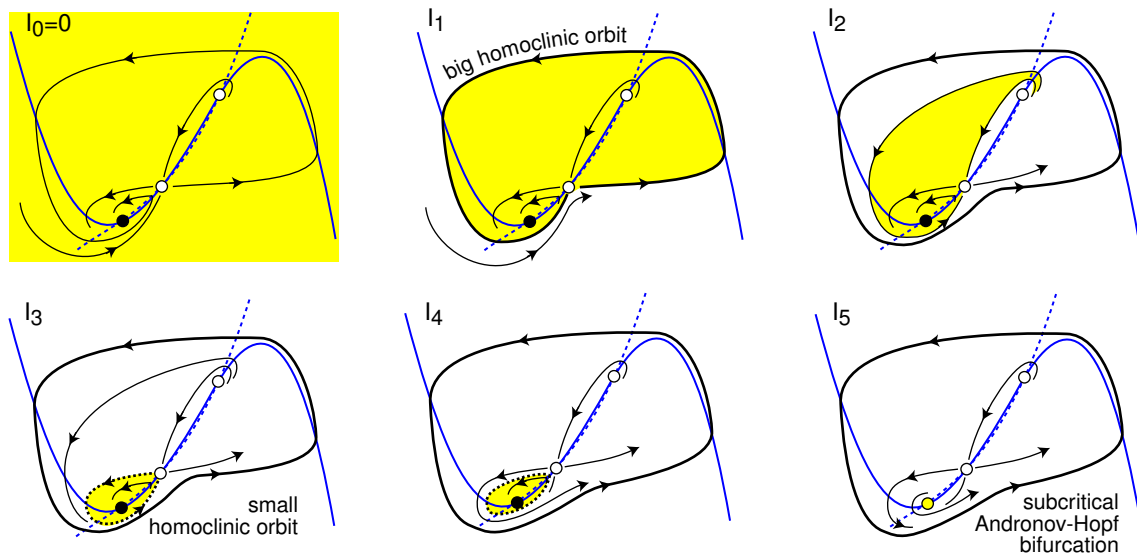


Figure 6.40: Transformations of phase portraits of a neuronal model near subcritical Bogdanov-Takens bifurcation point as the magnitude of the injected current  $I$  increases (here  $I_{k+1} > I_k$ ). Shaded regions are the attraction domains of the equilibrium corresponding to the resting state.

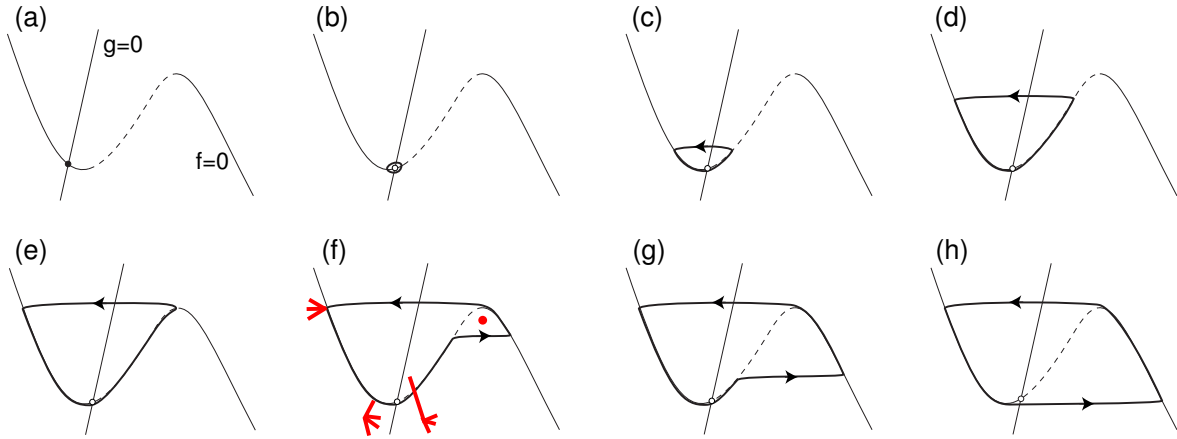


Figure 6.41: Canard (French duck) limit cycles in a relaxation oscillator (hand drawing).

Interestingly, the global vector field structure of neuronal models with nullclines as in Fig. 6.39a results in the birth of a spiking limit cycle attractor via a big saddle homoclinic orbit bifurcation, so the neuronal model undergoes a cascade of bifurcations depicted in Fig. 6.40 as the amplitude of the injected current  $I$  increases. The local phase portraits corresponding to  $I_0$ ,  $I_1$ , and  $I_2$  are topologically equivalent to the phase portrait “1” in Fig. 6.38, right. (The equivalence is only local near the left knee; there is no global equivalence because of the extra equilibrium in Fig. 6.40 and because of the big homoclinic or periodic orbit.) As  $I$  increases, a stable large-amplitude spiking limit cycle appears via a big supercritical homoclinic orbit bifurcation at some  $I_1$ . It coexists with the stable resting state for all  $I_1 < I < I_5$ . At some point  $I_2$ , the saddle quantity, i.e., the sum of its eigenvalues, changes from negative to positive (it is zero at the Bogdanov-Takens bifurcation), so another saddle homoclinic orbit bifurcation (at some  $I_3$ ) occurs, which is subcritical, giving birth to an unstable limit cycle. The phase portrait at  $I_3$  is locally topologically equivalent to the one marked SHO in Fig. 6.38. Similarly, the phase portrait at  $I_4$  is locally equivalent to the one marked “2” in Fig. 6.38. The unstable cycle shrinks to the equilibrium and makes it lose stability via a subcritical Andronov-Hopf bifurcation at some  $I_5$ , which corresponds to case AH in Fig. 6.38. Further increase of  $I$  converts the unstable focus into an unstable node, which approaches the saddle and disappears via the saddle-node bifurcation  $SN_1$  in Fig. 6.38 (not shown in Fig. 6.40).

### 6.3.4 Relaxation oscillators and Canards

Let us consider a relaxation oscillator

$$\begin{aligned}\dot{x} &= f(x, y, b) && \text{(fast variable)} \\ \dot{y} &= \mu g(x, y, b) && \text{(slow variable)}\end{aligned}$$

with fast and slow nullclines as in Fig. 6.41a and  $\mu \ll 1$ . Suppose that there is a stable equilibrium, as in Fig. 6.41a, for some values of the bifurcation parameter  $b < 0$ , and a stable limit cycle, as in Fig. 6.41h, for some other values  $b > 0$ . What kind of a bifurcation of the equilibrium occurs when  $b$  increases from negative to positive, and the slow nullcline passes the left knee of the fast N-shaped nullcline?

The Jacobian matrix at the equilibrium has the form

$$L = \begin{pmatrix} f_x & f_y \\ \mu g_x & \mu g_y \end{pmatrix}$$

Since  $f_x = 0$  at the knee (prove this), but  $f_y$  is typically not, the Jacobian matrix resembles the one for the Bogdanov-Takens bifurcation (6.10) in the limit  $\mu = 0$ . However, the resemblance is only superficial, since the relaxation oscillator does not satisfy the non-degeneracy conditions. In particular, second-order partial derivatives of  $\mu g(x, y, b)$  vanish in the limit  $\mu \rightarrow 0$ , resulting in  $\sigma = 0$  and in the disappearance of the term  $u^2$  in the topological normal form (6.11).

A purely geometrical consideration confirms that the transition from Fig. 6.41a to Fig. 6.41h cannot be of the Bogdanov-Takens type, since there is a unique equilibrium and no possibility for a saddle-node bifurcation, which always accompanies the Bogdanov-Takens bifurcation. Actually, the equilibrium loses stability via Andronov-Hopf bifurcation that occurs when

$$\text{tr } L = f_x + \mu g_y = 0 \quad \text{and} \quad \det L = \mu(f_x g_y - f_y g_x) > 0.$$

The loss of stability typically happens not at the left knee, where  $f_x = 0$ , but a little bit to the right of the knee, where  $f_x = -\mu g_y > 0$  (because  $g_y < 0$  in neuronal models). We already saw this phenomenon in Sect. 4.2.6 when we considered FitzHugh-Nagumo model.

An interesting observation is that the period of damped or sustained oscillations near the Andronov-Hopf bifurcation point in Fig. 6.41b is of the order  $1/\sqrt{\mu}$ , because the frequency  $\omega = \sqrt{\det L} \approx \sqrt{\mu}$ , whereas the period of large-amplitude relaxation oscillation is of the order  $1/\mu$ , because it takes  $1/\mu$  units of time to slide up and down along the branches of the fast nullcline in Fig. 6.41h. Thus, the period of small subthreshold oscillations of a neural model may have no relation to the period of spiking, if the model is a relaxation oscillator.

The Andronov-Hopf bifurcation could be supercritical or subcritical, depending on the functions  $f$  and  $g$ ; see Ex. 14 and Ex. 18. Figure 6.41 depicts the supercritical case. In the subcritical case, stable and unstable limit cycles are typically born via fold limit cycle bifurcation, then the unstable limit cycle goes through the shapes as in Fig. 6.41g,f,e,d,c, and b, and then shrinks to a point.

## Canards

The distinctive feature of limit cycles in Fig. 6.41c-g is that they follow the unstable branch (dashed curve) of the fast nullcline before jumping to the left or to the right

(stable) branches. Due to the relaxation nature of the system, the vector field is horizontal outside the N-shape fast nullcline, so any transition from Fig. 6.41b to Fig. 6.41h must gradually go through the stages in Fig. 6.41c-g. Because the cycle in Fig. 6.41f resembles a *French duck*, at least in the eyes of the French mathematicians E. Benoit, J.-L. Callot, F. Diener, and M. Diener, who discovered this phenomenon in 1977, it is often called a *canard cycle*.

In general, any trajectory that follows the unstable branch is called a *canard trajectory*. Canard trajectories play an important role in defining thresholds for resonator neurons, as we discuss in Sect. 7.2.5. It takes of the order of  $1/\mu$  units of time to slide along the unstable branch of the fast nullcline. A small perturbation to the left or to the right could result in an immediate jump to the corresponding stable branch of the nullcline. Hence, the initial conditions should be specified with an unrealistic precision of the order of  $e^{-1/\mu}$  to follow the branch, which explains why the canard trajectories are difficult to catch numerically, let alone experimentally. Consequently, the canard cycles, though stable, also exits in an exponentially small region of values of the parameter  $b$ . A typical simulation shows an explosion of a stable limit cycle from small (Fig. 6.41b) to large (Fig. 6.41h) as the parameter  $b$  is slowly varied. In summary, canard cycles in two-dimensional relaxation oscillators play an important role of thresholds, but they are fragile and rather exceptional.

In contrast, canard trajectories in three-dimensional relaxation oscillators (one fast and two slow variables) are generic in the sense that they exits in a wide range of parameter values. A simple way to see this is to treat  $b$  as the second slow variable. Then, there is a set of initial conditions corresponding to the canard trajectories. Studying canards in  $\mathbb{R}^3$  goes beyond the scope of this book (see bibliography at the end of this chapter).

### 6.3.5 Bautin

What happens when a subcritical Andronov-Hopf bifurcation becomes supercritical, that is, when the parameter  $a$  in the topological normal form for Andronov-Hopf bifurcation (6.8,6.9) changes sign? The bifurcation becomes degenerate when  $a = 0$ , and the behavior of the system is described by the topological normal form for *Bautin bifurcation*, which we write here in the complex form

$$\dot{z} = (c + i\omega)z + az|z|^2 + a_2z|z|^4, \quad (6.12)$$

where  $z \in \mathbb{C}$  is a complex variable, and  $c, a$  and  $a_2$  are real parameters. The parameters  $a$  and  $a_2$  are called the first and second *Liapunov coefficients* (often spelled *Lyapunov coefficients*). The Bautin bifurcation occurs when  $a = c = 0$  and  $a_2 \neq 0$ , and hence it has codimension 2. It is subcritical when  $a_2 > 0$  and supercritical otherwise. If  $a_2 = 0$ , then one needs to consider the next term  $a_3z|z|^6$  in the normal form to get a bifurcation of codimension-3, etc.

We can easily determine bifurcations of the topological normal form. First of all, (6.12) undergoes Andronov-Hopf bifurcation when  $c = 0$ , which is supercritical for

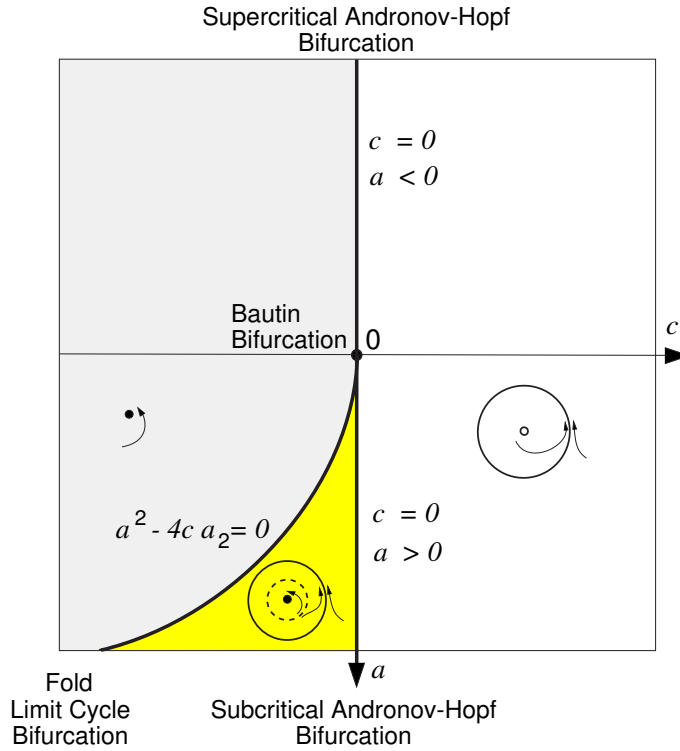


Figure 6.42: Supercritical Bautin bifurcation in (6.12); see also Fig. 9.42, left.

$a < 0$  and subcritical otherwise. Moreover, if  $a$  and  $a_2$  have different signs, then (6.12) undergoes fold limit cycle bifurcation when

$$a^2 - 4ca_2 = 0 ,$$

as we illustrate in Fig. 6.42. Thus, both Andronov-Hopf and fold limit cycle bifurcations occur simultaneously at the Bautin point  $a = c = 0$ . Many two-dimensional neuronal models, such as the  $I_{\text{Na,p}} + I_K$ -model with low-threshold  $K^+$  current, are relatively near this bifurcation, which explains why the unstable limit cycle involved in the subcritical Andronov-Hopf bifurcation is usually born via fold limit cycle bifurcation. There is some evidence that rodent trigeminal interneurons, dorsal root ganglion neurons, and mes V neuron in brainstem are also near this bifurcation; see Sect. 9.3.3.

### 6.3.6 Saddle-node homoclinic orbit

Let us compare the saddle-node on invariant circle bifurcation and the saddle homoclinic orbit bifurcation depicted in Fig. 6.43, top. In both cases there is a homoclinic orbit, i.e., a trajectory that originates and terminates at the same equilibrium. However, the equilibria are of different types, and the orbit returns to them along different directions. Now suppose a system undergoes both bifurcations simultaneously, as we illustrate in Fig. 6.43, bottom. Such a bifurcation, called *saddle-node homoclinic orbit*

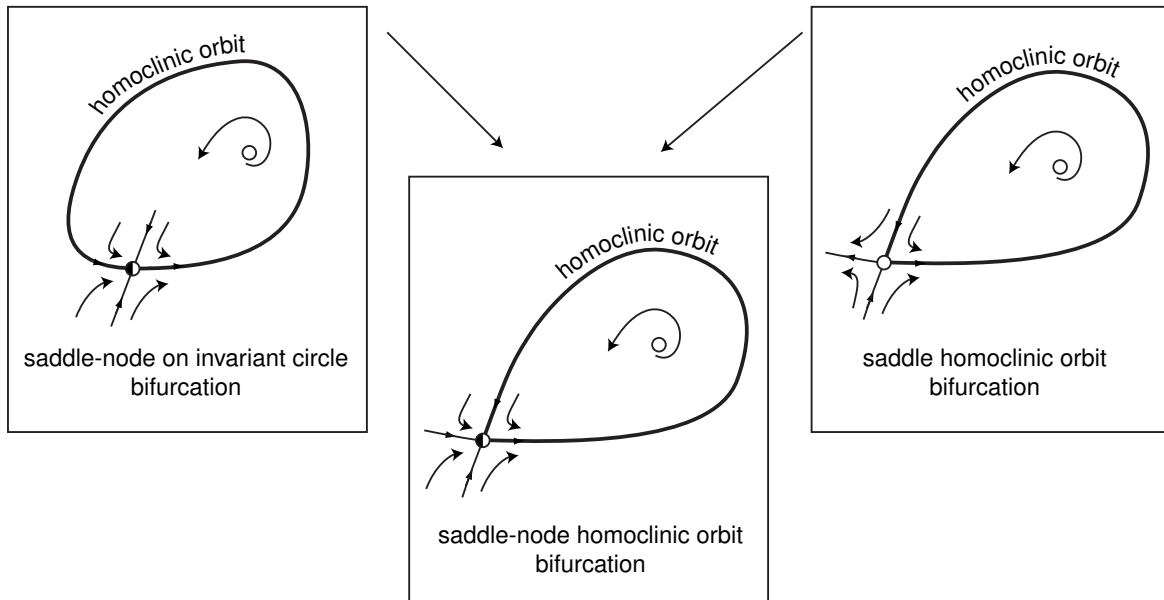


Figure 6.43: Saddle-node homoclinic orbit bifurcation occurs when a system undergoes a saddle-node on invariant circle and saddle homoclinic orbit bifurcations simultaneously.

bifurcation, has codimension 2, since two strict conditions must be satisfied: First, the equilibrium must be at the saddle-node bifurcation point, i.e., must have eigenvalue  $\lambda_1 = 0$ . Second, the homoclinic trajectory must return to the equilibrium along the non-central direction, i.e., along the stable direction corresponding to the negative eigenvalue  $\lambda_2$ . Since the saddle-node quantity,  $\lambda_1 + \lambda_2$ , is always negative, this bifurcation always results in the (dis)appearance of a *stable* limit cycle.

In Fig. 6.44 we illustrate the saddle-node homoclinic orbit bifurcation using the  $I_{Na,p}+I_K$ -model with two bifurcation parameters: the injected dc-current  $I$  and the  $K^+$  time constant  $\tau$ . The bifurcation occurs at the point  $(I, \tau) = (4.51, 0.17)$ . Notice that there are three other codimension-1 bifurcation curves converging to this codimension-2 point, as we illustrate in Fig. 6.45. Since the model undergoes a saddle-node bifurcation at  $I = 4.51$  and any  $\tau$ , the straight vertical line  $I = 4.51$  is the saddle-node bifurcation curve. The point  $\tau = 0.17$  on this line separates two cases: When  $\tau > 0.17$ , the activation and deactivation of  $K^+$  current is sufficiently slow so that the membrane potential  $V$  undershoots the equilibrium, resulting in the saddle-node *on* invariant circle bifurcation. When  $\tau < 0.17$ , deactivation of  $K^+$  current is fast, and  $V$  overshoots the saddle-node equilibrium, resulting in the saddle-node *off* limit cycle bifurcation.

Shaded triangular areas in the figures denote the parameter region corresponding to the bistability of stable equilibrium and a limit cycle attractor (resting and spiking states). Let us decrease the parameter  $I$  and cross such a region from right to left. When  $I = 4.51$ , a saddle and a node equilibria appear. Decreasing  $I$  further moves the saddle equilibrium rightward and the limit cycle leftward, until they merge. This occurs

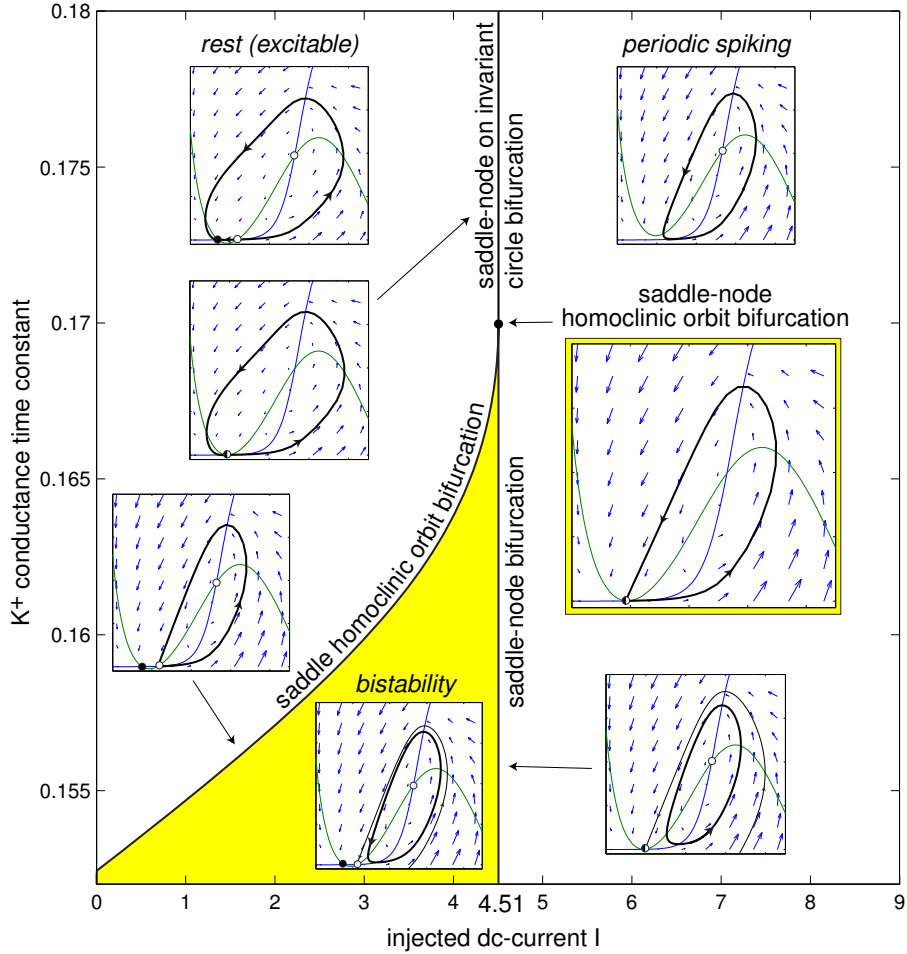


Figure 6.44: Unfolding of saddle-node homoclinic orbit bifurcation in the  $I_{\text{Na},p} + I_K$ -model with parameters as in Fig. 6.28.

on the saddle homoclinic orbit bifurcation curve, which is determined numerically in Fig. 6.44.

Neuronal models exhibiting saddle-node homoclinic bifurcations can be reduced to a topological normal form

$$\dot{V} = c(b - b_{\text{sn}}) + a(V - V_{\text{sn}})^2, \quad \text{if } V(t) = V_{\max}, \text{ then } V(t) \leftarrow V_{\text{reset}} \quad (6.13)$$

which is similar to that for saddle-node bifurcation (6.2) except that there is a reset  $V \leftarrow V_{\text{reset}}$  when the membrane voltage reaches certain large value  $V_{\max}$ . Any sufficiently large  $V_{\max}$  would work equally well, even  $V_{\max} = +\infty$ , because  $V$  reaches  $+\infty$  in a finite time; see Ex. 3. Using  $V_{\max} = 30$  and results of Sect. 6.1.1, we find that the topological normal form for the  $I_{\text{Na},p} + I_K$ -model is

$$\dot{V} = (I - 4.51) + 0.1887(V + 61)^2, \quad \text{if } V(t) = 30, \text{ then } V(t) \leftarrow V_{\text{reset}}.$$

The saddle-node homoclinic bifurcation occurs when  $I = 4.51$  and  $V_{\text{reset}} = -61$ . This normal form is called quadratic integrate-and-fire neuron; see Chapters 3 and 8.

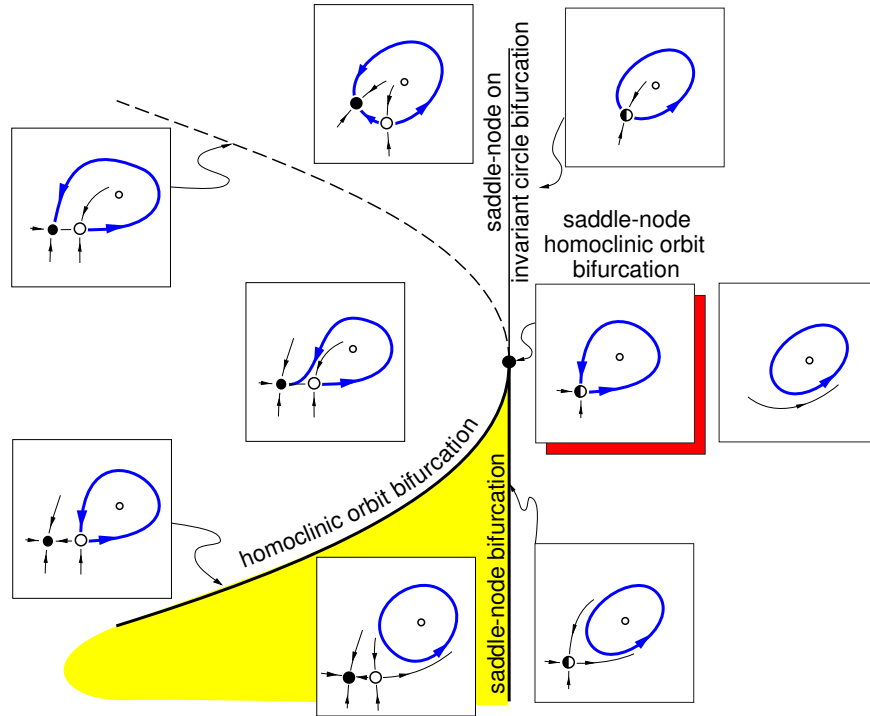


Figure 6.45: Unfolding of saddle-node homoclinic orbit bifurcation.

The topological normal form (6.13) is a useful equation, as we will see in the rest of the book. It describes quantitative and qualitative features of neuronal dynamics remarkably well, yet it has only one non-linear term. This makes it suitable for real-time simulations of huge numbers of neurons. Its bifurcation structure is studied in Ex. 12 (see also Fig. 8.3), and the reader should at least look at the solution at the end of the book.

### 6.3.7 Hard and soft loss of stability

Bifurcation is a qualitative change of the phase portrait of a system. Not all changes however are equally dramatic. Some are even hardly noticeable. For example, consider an equilibrium undergoing supercritical Andronov-Hopf bifurcation: As a bifurcation parameter changes, the equilibrium loses stability and a small-amplitude stable limit cycle appears, as in Fig. 6.11. The state of the system remains near the equilibrium; it just exhibits small-amplitude oscillations around it. We can change the parameter in the opposite direction, and then the limit cycle shrinks to a point and the system returns to the equilibrium. In neurons, such a bifurcation does not lead to an immediate spike. The neuron remains quiescent; it just exhibits subthreshold small-amplitude sustained oscillations. Such a loss of stability is called *soft*: the equilibrium is no longer stable, but its small neighborhood remains attractive. Supercritical pitchfork, cusp and flip bifurcations correspond to soft loss of stability.

In contrast, if the equilibrium loses stability via subcritical Andronov-Hopf bifurcation, the state of the system diverges from it, which results in an immediate spike or some kind of a large-amplitude jump. Such a loss of stability is called *hard*: neither the equilibrium nor its neighborhood are attractive. The hard loss of stability usually leads to noticeable or catastrophic changes in systems behavior, and the stability boundary is called *dangerous* (Bautin 1949). Changing the bifurcation parameter in the opposite direction will make the equilibrium stable again, but may not bring the state of the system back to it. Saddle-node bifurcation is hard unless it is on an invariant circle. In this case, the loss of stability is catastrophic, i.e., leading to noticeable spikes, but reversible. Saddle homoclinic orbit bifurcation is hard, regardless of whether it is subcritical or supercritical. In general, most bifurcations in neurons or at least in neuronal models are hard.

## Review of Important Concepts

- Stable equilibrium (resting state) in a typical neuronal model can either
  - disappear via saddle-node bifurcation, which can be *off* or *on* invariant circle, or
  - lose stability via Andronov-Hopf bifurcation, which can be supercritical or subcritical.

These four cases are summarized in Fig. 6.46.

- Stable limit cycle (periodic spiking state) in a typical two-dimensional neuronal model can either
  - be cut by saddle-node on invariant circle bifurcation,
  - shrink to a point via supercritical Andronov-Hopf bifurcation,
  - disappear via fold limit cycle bifurcation, or
  - disappear via saddle homoclinic orbit bifurcation.

These four cases are summarized in Fig. 6.47.

- Some atypical (codimension-2) bifurcations may play important roles in neuronal dynamics.
- Bogdanov-Takens bifurcation separates integrators from resonators.

## Bibliographical Notes

Though bifurcation theory can be traced back to Poincare and Andronov, it is a relatively new branch of mathematics. The first attempt to apply it to neuroscience was as

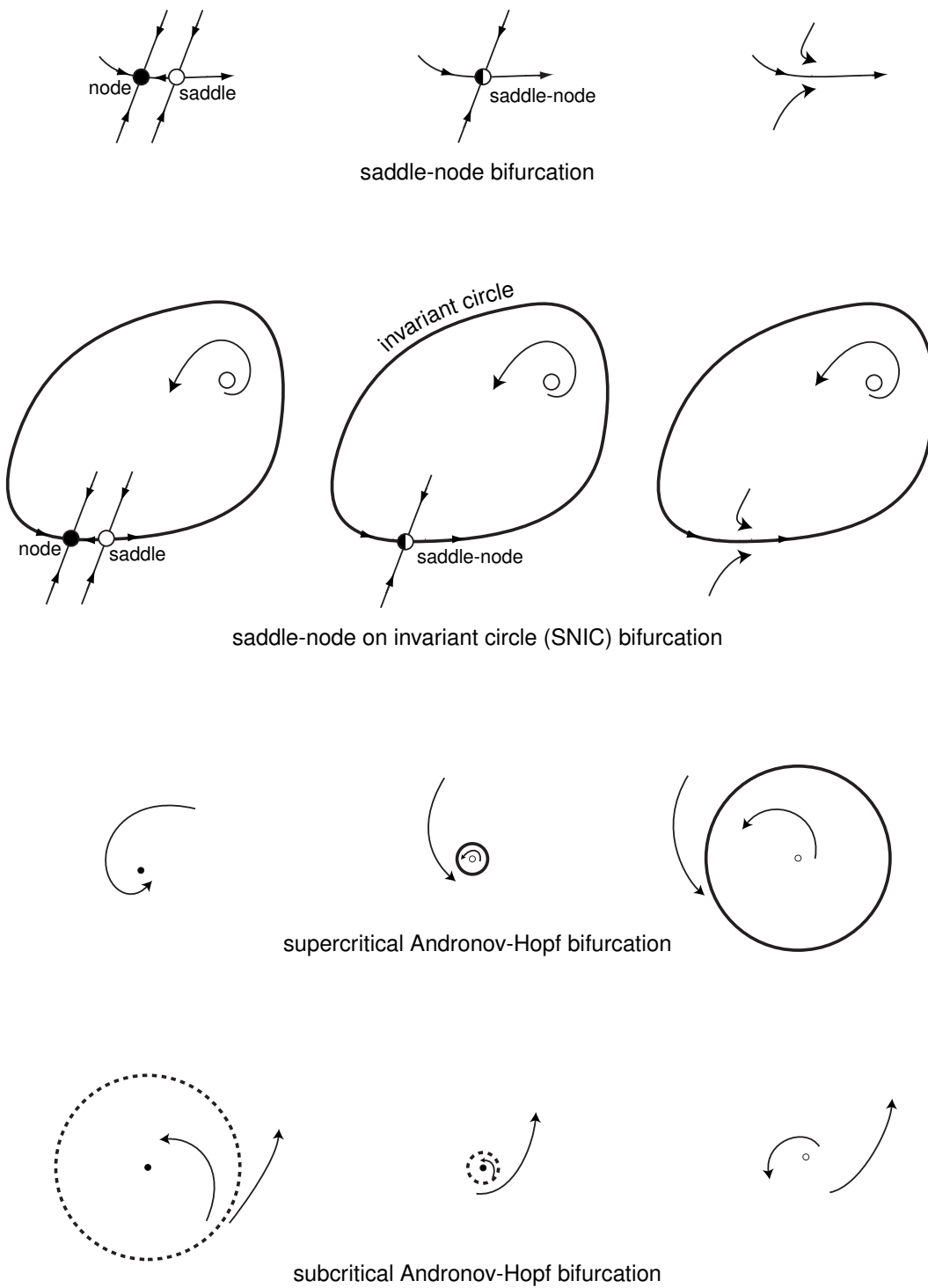
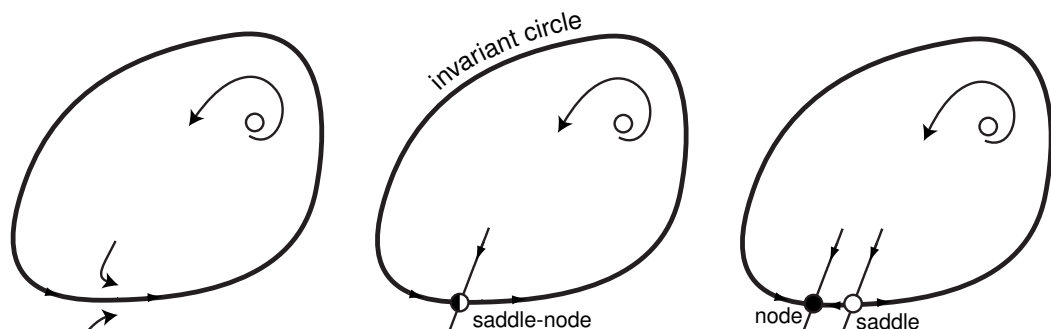
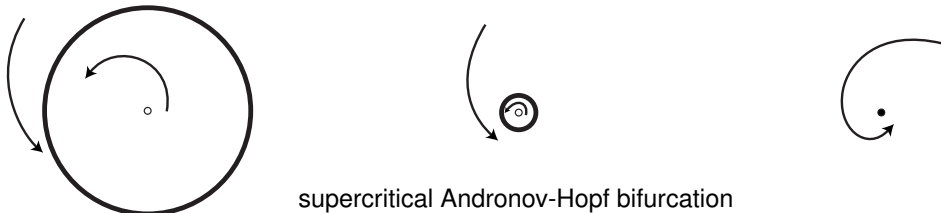


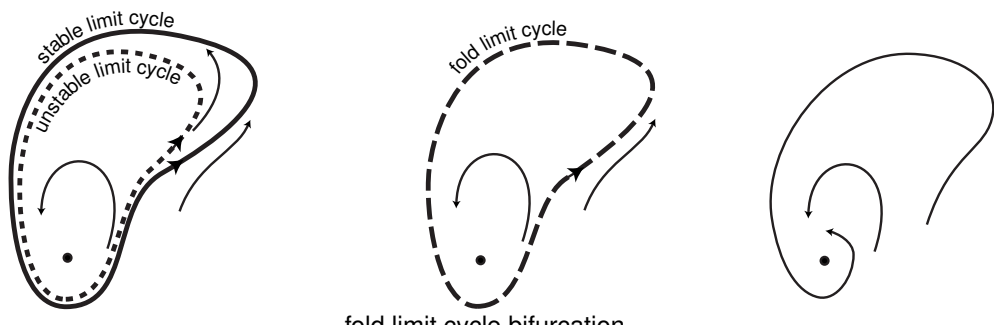
Figure 6.46: Summary of all codimension-1 bifurcations of a stable equilibrium (resting state).



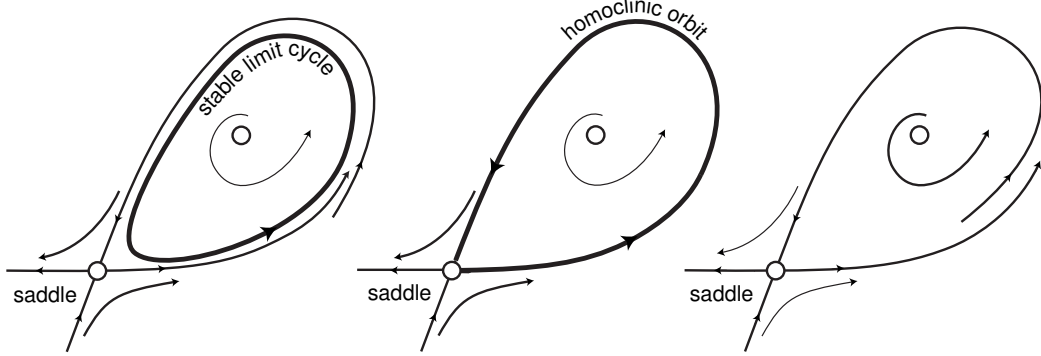
saddle-node on invariant circle (SNIC) bifurcation



supercritical Andronov-Hopf bifurcation



fold limit cycle bifurcation



saddle homoclinic orbit bifurcation

Figure 6.47: Summary of all codimension-1 bifurcations of a stable limit cycle (tonic spiking state) on a plane.

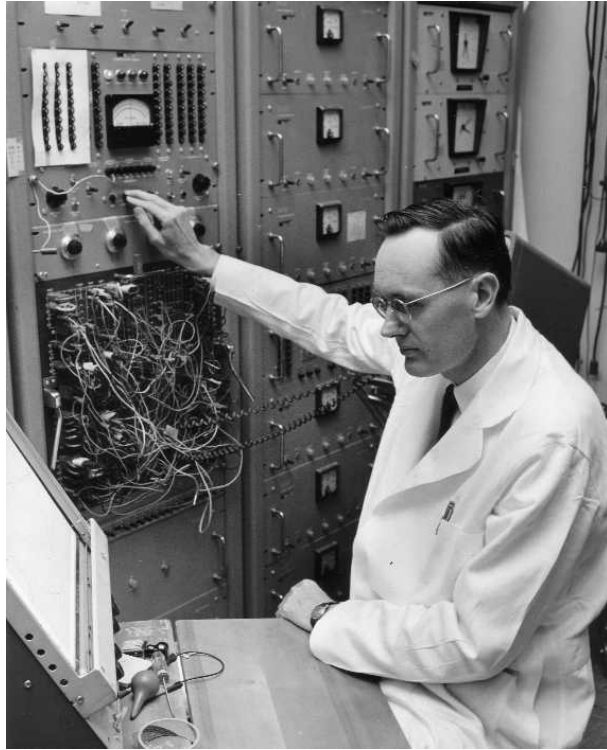


Figure 6.48: Richard FitzHugh with analog computer, National Institute of Health, Bethesda, Maryland, ca. 1960 (photograph provided by R. FitzHugh in 2005).

early as 1955, when Richard FitzHugh concluded his paper on mathematical modeling of threshold phenomena saying that many neuronal properties

“... are invariant under continuous, one-to-one transformations of the coordinates of phase space and fall within the domain of topology, a branch of mathematics which may be intrinsically better fitted for the preliminary description and classification of biological systems than analysis, which includes differential equations. This suggestion is of little practical value at present, since too little is known of the topology of vector fields in many-dimensional spaces, at least to those interested in theoretical biology. Nevertheless, the most logical procedure in the description of a complex biological system might be to characterize the topology of its phase space, then to establish a set of physically identifiable coordinates in the space, and finally to fit differential equations to the trajectories, instead of trying to reach this final goal at one leap.”

It is remarkable that FitzHugh was explicitly talking about topological equivalence and bifurcations, though never called them such, years before these mathematical notions were firmly established. This book continues the line of research initiated by FitzHugh and further developed by Rinzel and Ermentrout (1989).

In this chapter we provided a fairly detailed exposition of bifurcation theory. What we covered should be sufficient not only for understanding the rest of the book, but also for navigating through bifurcation papers concerned with computational neuro-

bifurcations	alternative names
saddle-node	fold, limit point, saddle-node off limit cycle
saddle-node on invariant circle	SNIC, saddle-node on limit cycle (SNLC), circle, saddle-node homoclinic, saddle-node central homoclinic, saddle-node infinite period (SNIPer), homoclinic
Andronov-Hopf	Hopf, Poincare-Andronov-Hopf
saddle homoclinic orbit	homoclinic, saddle-loop, saddle separatrix loop, Andronov-Leontovich
fold limit cycle	saddle-node of limit cycles, double limit cycle, fold cycle, saddle-node (fold) of periodics
saddle-node homoclinic orbit	saddle-node noncentral homoclinic, saddle-node separatrix-loop
Bogdanov-Takens	Takens-Bogdanov, double-zero
Bautin	degenerate Hopf, generalized Hopf
flip	period doubling

Figure 6.49: Popular alternative names to some of the bifurcations considered in this chapter.

science. More bifurcation theory, including bifurcations in mappings  $x_{n+1} = f(x_n, b)$ , can be found in the excellent book “*Elements of Applied Bifurcation Theory*” by Yuri Kuznetsov (1995, new edition 2004), which, however, might be a bit technical for a non-mathematician. Some of the bifurcations considered in this chapter, such as the blue-sky catastrophe, are classified as “exotic” by Kuznetsov (1995), though the catastrophe was recently found in a model of a leech heart interneuron (Shilnikov and Cymbalyuk 2005).

There is no unified naming scheme for the bifurcations, mostly because they were discovered and rediscovered independently in many fields and in many countries. For example, the Andronov-Hopf bifurcation was known to Poincare, so some scientists refer to it as Poincare-Andronov-Hopf bifurcation. Many refer to it as just Hopf bifurcation due to the fault of no lesser men than the famous Russian mathematician Vladimir Igorevich Arnold and famous French mathematician Rene Thom. According to Arnold’s own accounts, he was visited by Thom in the 1960s. While discussing various bifurcations, Arnold put too much emphasis on the “recent” Hopf (1942) paper. As a result of Arnold’s misattribution, Thom popularized the bifurcation as being Hopf bifurcation. In Fig. 6.49 we provide some common alternative names to the bifurcations considered in this chapter. The complete list of names of known bifurcations is too long, and it resembles the list of faculty members of the department of RadioPhysics (Gorky State University, now Nizhnii Novgorod, Russia) founded by A.A. Andronov in 1945.

The division of bifurcations into subcritical and supercritical ones may be confusing for a novice. For example, some scientists erroneously think that supercritical bifurcations result in appearance of attractors (stable equilibria, limit cycles, etc.) and subcritical bifurcations result in their disappearance. Let us emphasize here that the appearance or disappearance of an equilibrium or a limit cycle depends on the direction of change of the bifurcation parameter. For example, the subcritical pitchfork



Figure 6.50: The founder of Russian school of nonlinear dynamics, Alexander Aleksandovich Andronov (1901–1952) in 1950 (picture provided by M.I. Rabinovich).

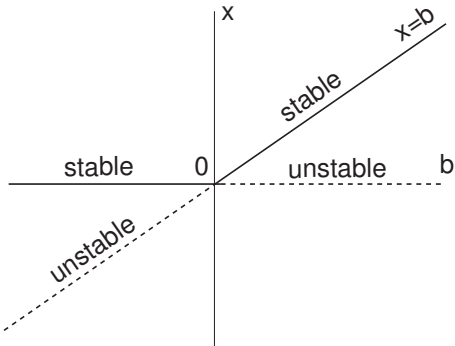


Figure 6.51: Transcritical bifurcation in  $\dot{x} = x(b - x)$ .

bifurcation in Fig. 6.36 could result in the appearance of a stable equilibrium  $x = 0$  if  $b$  decreases past 0. Our classification of bifurcations into subcritical and supercritical is consistent with the following widely accepted rule: Let the bifurcation parameter change in the direction leading to the increase in a number of objects (equilibria, limit cycles). The bifurcation is supercritical if stable objects appear, subcritical if unstable objects appear, and *transcritical*, such as in Fig. 6.51, if equal numbers of stable and unstable objects appear or disappear. The condition for supercritical (subcritical) Andronov-Hopf bifurcation, Eq. (6.7), is taken from Guckenheimer and Holmes (1983).

Delayed loss of stability was first described by Shishkova (1973), and then studied in detail by Nejshtadt (1985), though many find his paper difficult to read. An alternative description is given by Arnold et al. (1994) and Baer et al. (1989).

Canard (French duck) solutions were reported by Benoit et al. (1981). Due to the recent political climate in the USA, some refer to “French ducks” as “freedom ducks”, probably to emphasize that “French = freedom”. Canards in  $\mathbb{R}^3$  were studied by Benoit (1984), Samborskij (1985, in  $\mathbb{R}^n$ ), and recently by Szmolyan and Wechselberger (2001, 2004) and Wechselberger (2005).

## Exercises

1. (Transcritical bifurcation) Justify the bifurcation diagram shown in Fig. 6.51.
2. Show that the non-degeneracy and transversality conditions are necessary for the saddle-node bifurcation. That is, present a system that does not exhibit saddle-node bifurcation, but satisfies
  - (a) the non-hyperbolicity and non-degeneracy conditions, or
  - (b) the non-hyperbolicity and transversality conditions.
3. Consider the model

$$\dot{V} = c(b - b_{\text{sn}}) + a(V - V_{\text{sn}})^2,$$

with positive  $a$  and  $c$ , and  $b > b_{\text{sn}}$ . Show that the sojourn time in a bounded neighborhood of the point  $V = V_{\text{sn}}$  scales as

$$T = \frac{\pi}{\sqrt{ac(b - b_{\text{sn}})}}$$

when  $b$  is near  $b_{\text{sn}}$ . (Hint: Find the solution that starts at  $-\infty$  and terminates at  $+\infty$ .)

4. Show that the two-dimensional system

$$\dot{u} = c(b)u - \omega(b)v + (au - dv)(u^2 + v^2), \quad (6.14)$$

$$\dot{v} = \omega(b)u + c(b)v + (du + av)(u^2 + v^2), \quad (6.15)$$

the complex-valued system

$$\dot{z} = (c(b) + i\omega(b))z + (a + id)z|z|^2,$$

and the polar-coordinate system

$$\dot{r} = c(b)r + ar^3$$

$$\dot{\phi} = \omega(b) + dr^2,$$

are equivalent.

5. Show that the non-degeneracy and transversality conditions are necessary for the Andronov-Hopf bifurcation. That is, present a system that does not exhibit Andronov-Hopf bifurcation, but satisfies
  - (a) the non-hyperbolicity and non-degeneracy conditions, or
  - (b) the non-hyperbolicity and transversality conditions.
6. Show that the system (6.14, 6.15) with  $c(b) = b$ ,  $\omega(b) = 1$ ,  $a \neq 0$  and  $d = 0$  exhibits Andronov-Hopf bifurcation. Check all three conditions.

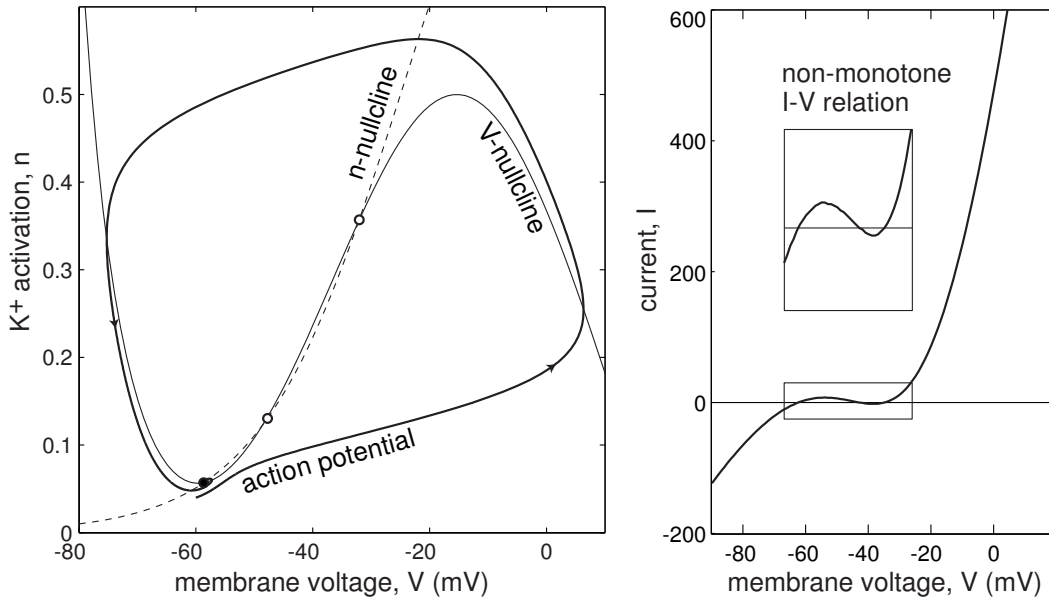


Figure 6.52: Ex. 8: This  $I_{Na,p} + I_K$ -model has a non-monotonic I-V relation, yet the resting state becomes unstable via Andronov-Hopf bifurcation before disappearing via saddle-node bifurcation. Parameters as in Fig. 4.1a (Chapter 4) except that  $E_{\text{leak}} = -78$  mV and  $n_\infty(V)$  has  $k = 12$  mV.

7. Determine the stability of the limit cycle near an Andronov-Hopf bifurcation.  
(Hint: consider the equilibrium  $r = \sqrt{|c/a|}$  in the topological normal form (6.8)).
8. The model in Fig. 6.52 has a non-monotonic I-V relation. Nevertheless, the rest state *loses stability* via Andronov-Hopf bifurcation before disappearing via saddle-node bifurcation. Draw representative phase portraits of the model. Is the system near Bogdanov-Takens bifurcation?
9. Consider a generic two-dimensional conductance-based model

$$\dot{V} = I - I(V, x), \quad (6.16)$$

$$\dot{x} = (x_\infty(V) - x)/\tau(V), \quad (6.17)$$

where  $V$  and  $x$  are the membrane voltage and a gating variable, respectively,  $I$  is the injected dc-current, and  $I(V, x)$  is the instantaneous I-V relation, which of course depends on the gating variable  $x$ . Here the membrane capacitance  $C = 1$  for the sake of simplicity. Show that the eigenvalues at an equilibrium  $c \pm \omega$  are given by

$$c = (I_V(V, x) + 1/\tau(V))/2$$

and

$$\omega = \sqrt{c^2 - I'_\infty(V)/\tau(V)}$$

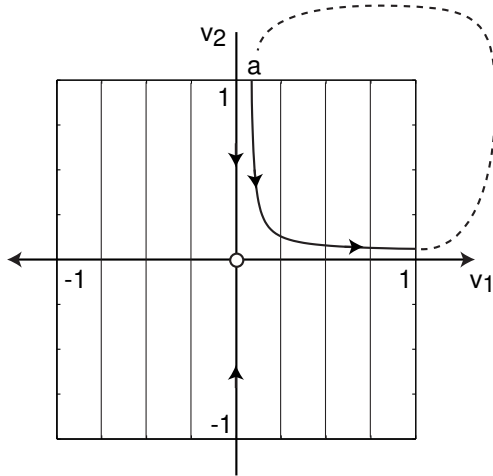


Figure 6.53: See Ex. 11.

where  $I_\infty(V) = I(V, x_\infty(V))$  is the steady-state I-V relation of the model. In particular, the frequency at the Andronov-Hopf bifurcation is

$$(\text{frequency}) = \sqrt{I'_\infty(V)/(C\tau(V))} ,$$

where  $C$  is the membrane capacitance.

10. Determine when the system

$$z' = (a + \omega i)z + z|z|^2 - z|z|^4 , \quad z \in \mathbb{C} ,$$

undergoes fold limit cycle bifurcation.

11. Consider a square neighborhood of a saddle equilibrium in Fig. 6.53 (compare with the inset in Fig. 6.29). Here  $v_1$  and  $v_2$  are eigenvectors with eigenvalues  $\lambda_2 < 0 < \lambda_1$ . Suppose the limit cycle enters the square at the point  $a = \tau(I - I_b)$ , where  $\tau > 0$  is some parameter. Determine the amount of time the trajectory spends in the square as a function of  $I$ .
12. Determine the bifurcation diagram of the topological normal form (6.13) for saddle-node homoclinic bifurcation.
13. Prove that the system

$$\begin{aligned} \dot{v} &= I + v^2 - u , \\ \dot{u} &= a(bv - u) \end{aligned}$$

with  $a > 0$  undergoes

- saddle-node bifurcation when  $b^2 = 4I$ ,

- Andronov-Hopf bifurcation when  $a < b$  and  $a^2 - 2ab + 4I = 0$ ,
- Bogdanov-Takens bifurcation when  $a = b = 2\sqrt{I}$ .

Use results of Ex. 15 to prove that the Andronov-Hopf bifurcation in the model above is always subcritical.

14. Use (6.7) to prove that the relaxation oscillator

$$\begin{aligned}\dot{v} &= f(v) - u \\ \dot{u} &= \mu(v - b)\end{aligned}$$

with an N-shaped fast nullcline  $u = f(v)$  undergoes Andronov-Hopf bifurcation when  $f'(b) = 0$ , i.e., at the knee. The bifurcation is supercritical when  $f'''(b) < 0$  and subcritical when  $f'''(b) > 0$ .

15. Prove that the Andronov-Hopf bifurcation point in

$$\begin{aligned}\dot{v} &= F(v) - u \\ \dot{u} &= \mu(bv - u)\end{aligned}$$

satisfies  $F' = \mu$  and  $b > \mu$ . Use (6.7) to show that

$$a = \{F''' + (F'')^2/(b - \mu)\}/16 .$$

16. Prove that the Andronov-Hopf bifurcation point in

$$\begin{aligned}\dot{v} &= F(v) - u \\ \dot{u} &= \mu(G(v) - u)\end{aligned}$$

satisfies  $F' = \mu$  and  $G' > \mu$ . Use (6.7) to show that

$$a = \{F''' + F''(F'' - G'')/(G' - \mu)\}/16 .$$

17. Prove that the Andronov-Hopf bifurcation point in

$$\begin{aligned}\dot{v} &= F(v) - (v + 1)u \\ \dot{u} &= \mu(G(v) - u)\end{aligned}$$

satisfies  $F' = \mu$  and  $G' > \mu$ . Use (6.7) to show that

$$a = \{F''' + \mu - (F'' - \mu)(1 + \mu[G'' - F'' + 2\mu]/\omega^2)\}/16 .$$

18. Use (6.7) to show that a two-dimensional relaxation oscillator

$$\begin{aligned}\dot{v} &= F(v, u) \\ \dot{u} &= \mu G(v, u)\end{aligned}$$

at an Andronov-Hopf bifurcation point has

$$a = \frac{1}{16} \left\{ F_{vvv} + F_{vv} \left[ \frac{F_{vv}G_u - F_uG_{vv}}{F_uG_v} - \frac{F_{vu}}{F_u} \right] \right\} + \mathcal{O}(\sqrt{\mu}) .$$

19. [M.S.] A leaky integrate-and-fire model has the same asymptotic firing rate ( $1/\ln$ ) as a system near saddle homoclinic orbit bifurcation. Explore the possibility that integrate-and-fire models describe neurons near such a bifurcation.
20. [M.S.] (blue-sky catastrophe) Prove that

$$\dot{\varphi} = \omega, \quad \dot{x} = a + x^2, \quad \text{if } x = +\infty, \quad \text{then } x \leftarrow -\infty, \quad \text{and} \quad \varphi \leftarrow 0,$$

is the canonical model (see Sect. 8.1.5) for blue-sky catastrophe. This model without the reset of  $\varphi$  is canonical for the fold limit cycle on homoclinic torus bifurcation. The model with the reset  $x \leftarrow b + \sin \varphi$  is canonical for the Lukyanov-Shilnikov bifurcation of a fold limit cycle with non-central homoclinics (Shilnikov and Cymbalyuk 2004, Shilnikov et al. 2005). Here,  $\varphi$  is the phase variable on the unit circle and  $a$  and  $b$  are bifurcation parameters.

21. [M.S.] Define topological equivalence and the notion of a bifurcation for piecewise continuous flows.
22. [Ph.D.] Use the definition above to classify codimension-1 bifurcations in piecewise continuous flows.
23. [M.S.] The bifurcation sequence in Fig. 6.40 seems to be typical in 2-dimensional neuronal models. Develop the theory of Bogdanov-Takens bifurcation with a global reentrant orbit.
24. [Ph.D.] Develop an automated dynamic clamp protocol (Sharp et al. 1993) that analyzes bifurcations in neurons *in vitro*, similar to what AUTO, XPPAUT, or MATCONT do in models.

# Chapter 7

## Neuronal Excitability

Neurons are excitable in the sense that they are typically at rest but can fire spikes in response to certain forms of stimulation. What kind of stimulation is needed to fire a given neuron? What is the evoked firing pattern? These are the questions concerning the neuron's computational properties, e.g., whether they are integrators or resonators, their firing frequency range, the spike latencies (delays), the co-existence of resting and spiking states, etc. From the dynamical systems point of view, neurons are excitable because they are near a bifurcation from rest to spiking activity. The type of bifurcation, and not the ionic currents per se, determines the computational properties of neurons. In this chapter we continue our effort to understand the relationship between bifurcations of the resting state and the neuro-computational properties of excitable systems.

### 7.1 Excitability

A textbook definition of neuronal excitability is that a “subthreshold” synaptic input evokes a small graded post-synaptic potential (PSP), while a “superthreshold” input evokes a large all-or-none action potential, which is an order of magnitude larger than the amplitude of the subthreshold response. Unfortunately, we cannot adopt this definition to define excitability of dynamical systems because many systems, including some neuronal models discussed in Chap. 4, have neither all-or-none action potentials nor firing thresholds. Instead, we employ a purely geometrical definition.

From the geometrical point of view, a dynamical system with a stable equilibrium is *excitable* if there is a large-amplitude piece of trajectory that starts in a small neighborhood of the equilibrium, leaves the neighborhood, and then returns to the equilibrium, as we illustrate in Fig. 7.1, left.

In the context of neurons, the equilibrium corresponds to the resting state. Because it is stable, all trajectories starting in a sufficiently small region of the equilibrium, much smaller than the shaded neighborhood in the figure, converge back to the equilibrium. Such trajectories correspond to subthreshold PSPs. In contrast, the large trajectory in the figure corresponds to firing a spike. Therefore, superthreshold PSPs are those

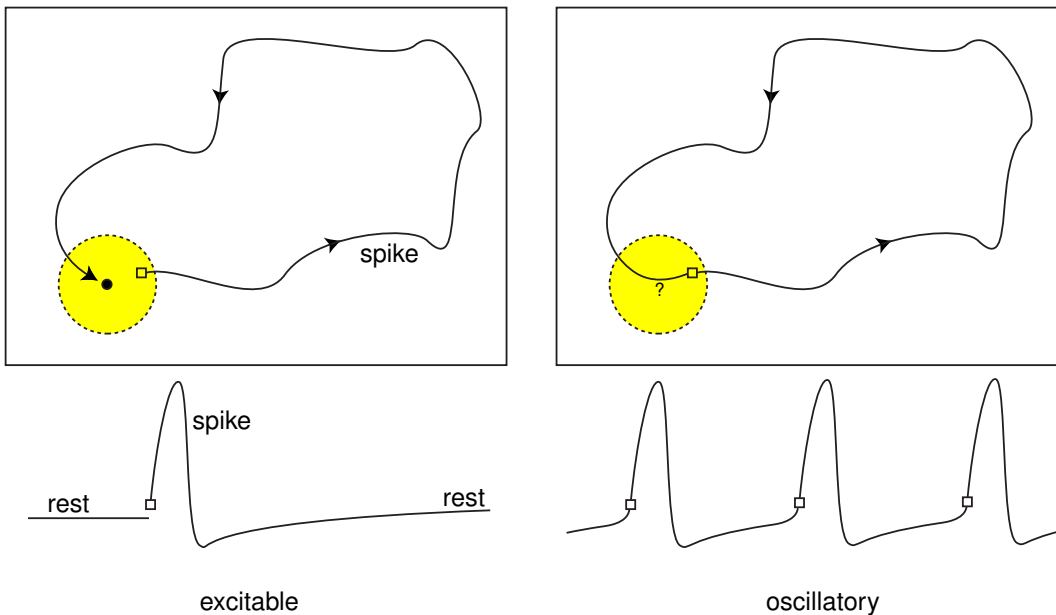


Figure 7.1: *Left:* An abstract definition of excitability. There is a spike trajectory that starts near a stable equilibrium and returns to it. *Right:* Excitable systems are near bifurcations. A modification of the vector field in the small shaded region can result in a periodic trajectory.

that push the state of the neuron to or near the beginning of the large trajectory (small square in Fig. 7.1), thereby initiating the spike. These inputs can be injected by experimenter via an attached electrode, or they can represent the total synaptic input from the other neurons in the network, or both.

### 7.1.1 Bifurcations

The definition in Fig. 7.1 is quite general, and it does not make any assumptions regarding the details of the vector field inside or outside of the small shaded neighborhood. Using the theory presented in the previous chapter, we can show that such an excitable system is near a bifurcation from resting to oscillatory dynamics.

- *Bifurcation of a limit cycle.* The vector field in the small shaded neighborhood of the equilibrium can be modified slightly so that the spike trajectory enters the square and becomes periodic, as in Fig. 7.1, right. That is, the dynamical system goes through a bifurcation resulting in the appearance of a limit cycle.

What happens to the stable equilibrium, denoted as “?” in the figure? Depending on the type of the bifurcation of the limit cycle, the equilibrium may disappear or may lose stability. This happens when the limit cycle appears via saddle-node on invariant circle or supercritical Andronov-Hopf bifurcations, respectively. Both cases are depicted in Fig. 7.2.

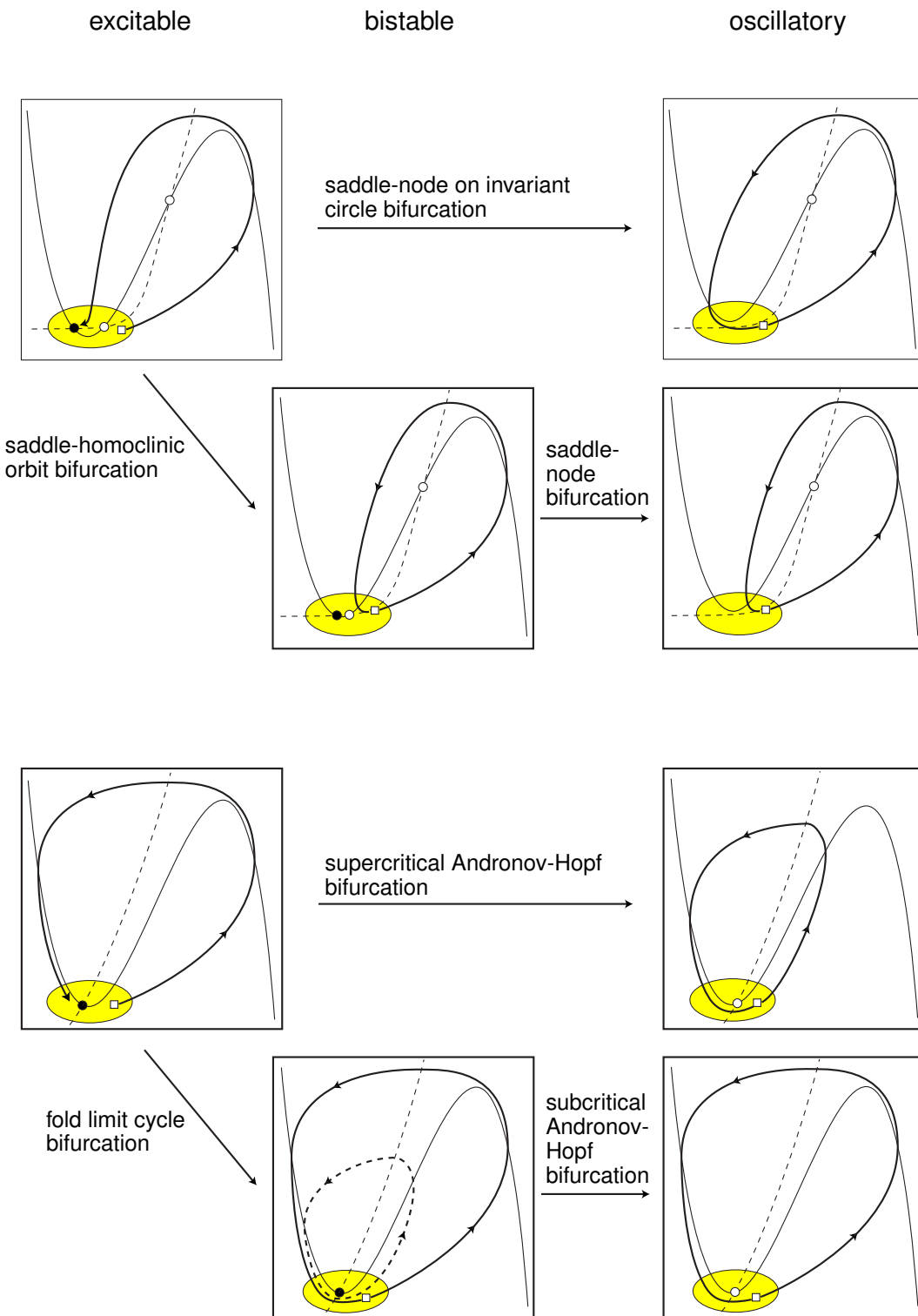


Figure 7.2: Excitable dynamical systems bifurcate into oscillatory ones either directly or indirectly, via bistable systems.

Alternatively, the equilibrium may remain stable and co-exist with the newly born limit cycle, as it happens during saddle homoclinic orbit or fold limit cycle bifurcations in Fig. 7.2. The dynamical system is no longer excitable, but *bistable*, though many scientists still treat bistable systems as excitable. An appropriate synaptic input can switch the behavior from resting to spiking and back. Notice that we considered only bifurcations of a limit cycle so far.

- *Bifurcation of the equilibrium.* Suppose the system is bistable, as in Fig. 7.2. Since the equilibrium is near the cycle, a small modification of the vector field in the shaded neighborhood can make it disappear via saddle-node bifurcation, or lose stability via subcritical Andronov-Hopf bifurcation.

In any case, excitable dynamical systems can bifurcate into oscillatory systems either directly or indirectly through bistable systems. All these cases are summarized in Fig. 7.2.

### 7.1.2 Hodgkin's classification

As we mentioned in the introduction chapter, the first one to study bifurcation mechanisms of excitability (years before mathematicians discovered such bifurcations) was Hodgkin (1948), who injected steps of currents of various amplitudes into excitable membranes and looked at the resulting spiking behavior. We illustrate his experiments in Fig. 7.3 using recordings of rat neocortical and brainstem neurons. When the current strength is small, the neurons are quiescent. When the current is strong, the neurons fire trains of action potentials. Depending on the average frequency of such firing, Hodgkin identified two major classes of excitability:

- **CLASS 1 NEURAL EXCITABILITY.** Action potentials can be generated with arbitrarily low frequency, depending on the strength of the applied current.
- **CLASS 2 NEURAL EXCITABILITY.** Action potentials are generated in a certain frequency band that is relatively insensitive to changes in the strength of the applied current.

Class 1 neurons, sometimes called type I neurons, fire with a frequency that may vary smoothly over a broad range of about 2 to 100 Hz or even higher. The important observation here is that the frequency can be changed tenfold. In contrast, the frequency band of Class 2 neurons is quite limited, e.g., 150–200 Hz, but it can vary from neuron to neuron. The exact numbers are not important to us here. The qualitative distinction between the classes noticed by Hodgkin is that the frequency-current relation (the F-I curve in Fig. 7.3, bottom) starts from zero and continuously increases for Class 1 neurons, but is discontinuous for Class 2 neurons.

Obviously, the two classes of excitability have different neuro-computational properties. Class 1 excitable neurons can smoothly encode the strength of an input, e.g.,

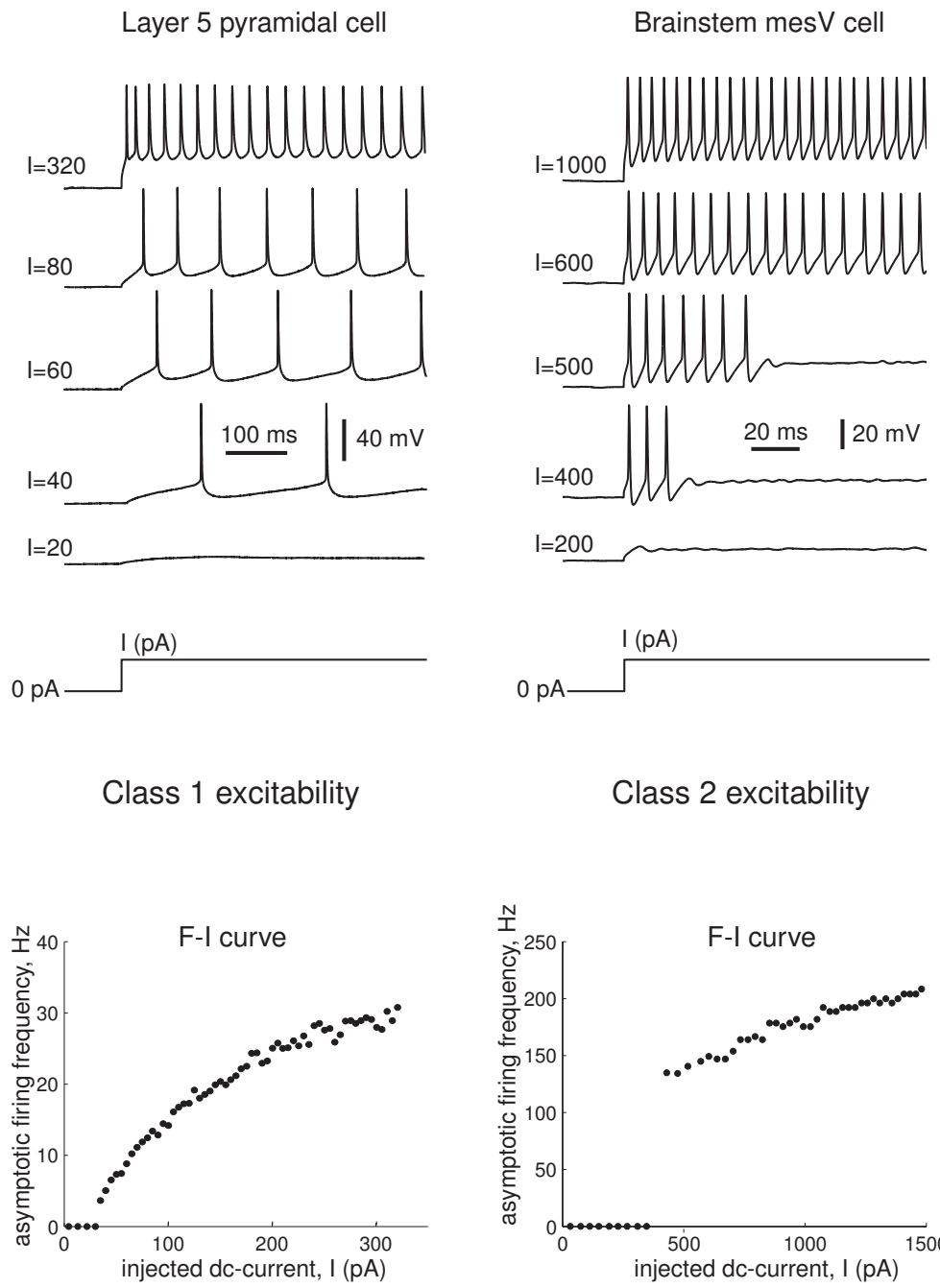


Figure 7.3: *Top:* Typical responses of membrane potentials of two neurons to steps of dc-current of various magnitudes  $I$ . *Bottom:* Corresponding frequency-current (F-I) relations are qualitatively different. Shown are recordings of layer 5 pyramidal neurons from rat primary visual cortex (left) and mesV neuron from rat brainstem (right). The asymptotic frequency is  $1000/T_\infty$ , where  $T_\infty$  is taken to be the interval between the last two spikes in a long spike train.

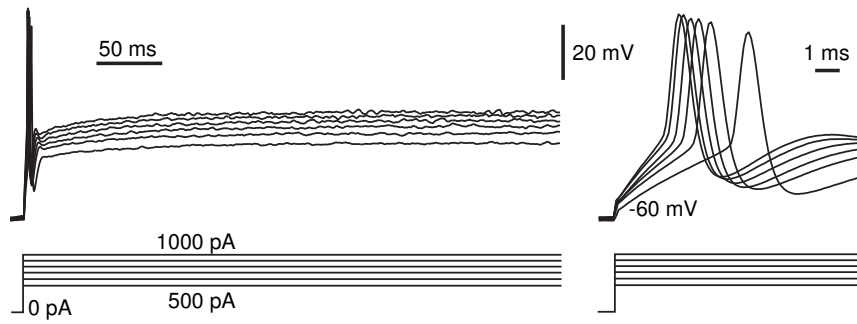


Figure 7.4: Class 3 excitability of a mesV neuron of rat brainstem (contrast with Fig. 7.3).

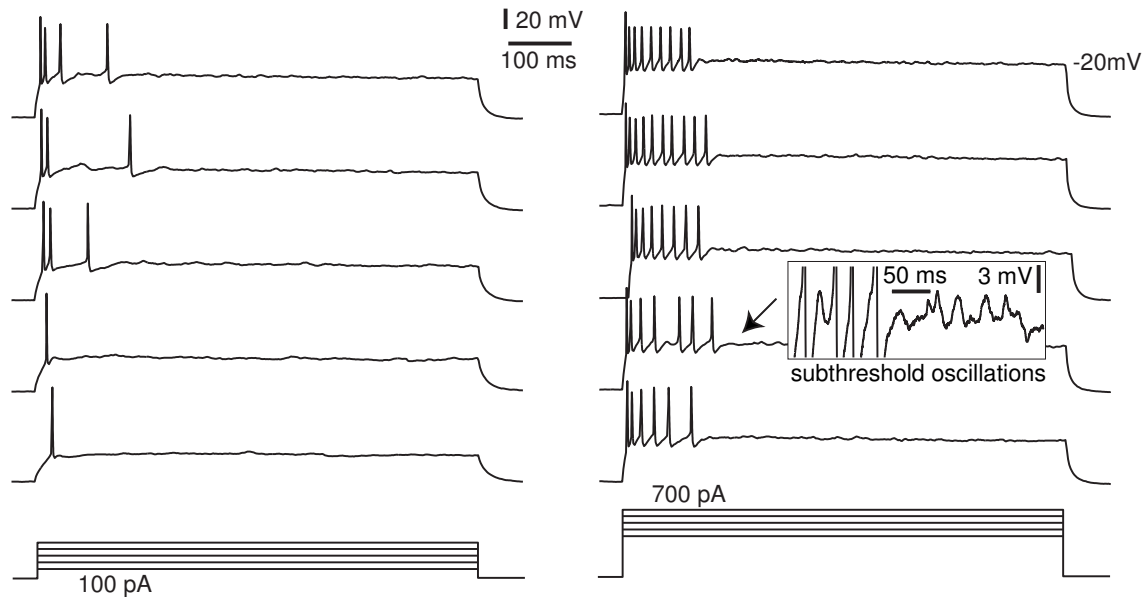


Figure 7.5: Class 3 excitability of a layer 5 pyramidal neuron of rat visual cortex. The inset shows subthreshold oscillations of membrane potential.

the strength of the applied dc-current or the strength of the incoming synaptic bombardment, into the frequency of their spiking output. Class 2 neurons cannot do that. Instead, they can act as threshold elements reporting when the strength of input is above a certain value. Both properties are important in neural computations.

Hodgkin also observed that axons left in oil or sea water for long periods exhibited

- **CLASS 3 NEURAL EXCITABILITY.** A single action potential is generated in response to a pulse of current. Repetitive (tonic) spiking can be generated only for extremely strong injected currents or not at all.

Two examples of Class 3 excitable systems are depicted in Fig. 7.4 and Fig. 7.5. The mesV neuron in the figure fires a phasic spike at the onset of the pulse of current, and then remains quiescent. Even injecting pulses as high as 1000 pA, which result in spike

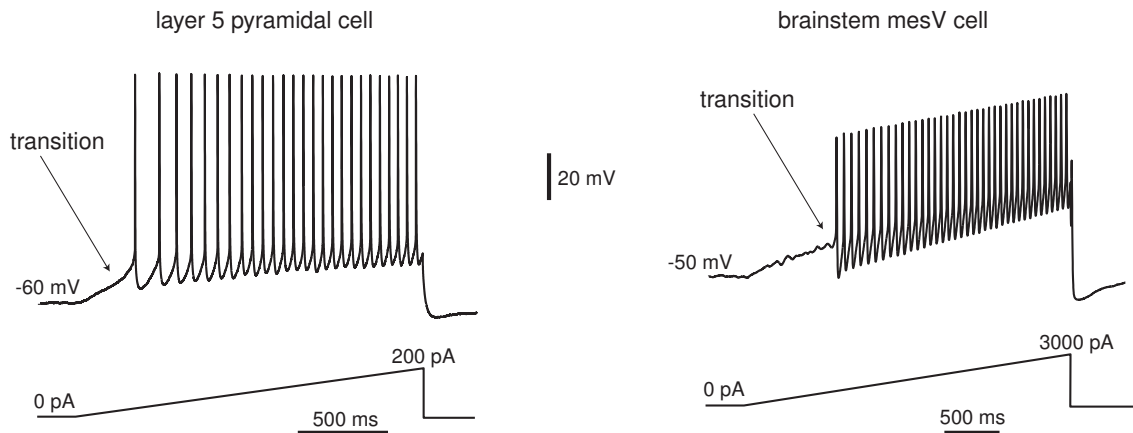


Figure 7.6: As the magnitude of injected dc-current increases, the neurons bifurcates from resting to repetitive spiking behavior. Shown are recordings of the same neurons as in Fig. 7.3. Notice that the ratio of the first and last interspike intervals of the pyramidal cell is much greater than that in mes V neuron.

trains in another mesV neuron in Fig. 7.3, cannot evoke multiple spikes in this neuron. Similarly, the pyramidal neuron in Fig. 7.5 cannot sustain tonic spiking even when the injected current is ten times stronger than the neuron's rheobase. Ironically, neurons exhibiting such a behavior would most likely be discarded as “sick” or “unhealthy”, though the neurons analyzed in the figures looked normal from any other point of view. We will study the dynamic mechanism of this class of excitability and show that it may have nothing to do with sickness.

It will be clear shortly that this classification is of limited value except that it points to the fact that neurons should be distinguished according not only to ionic mechanisms of excitability, but also to dynamic mechanisms, in particular, to the type of bifurcation of the rest state.

### 7.1.3 Classes 1 and 2

Let us consider the strength of the applied current in Hodgkin's experiments as being a bifurcation parameter. Instead of changing the parameter abruptly, as in Fig. 7.3, we change it slowly in Fig. 7.6 using recordings of the same neurons as in the previous figure. In Sect. 7.1.5 we explain the fundamental difference between these two protocols.

When the current ramps up, the rest potential increases until a bifurcation occurs, resulting in loss of stability or disappearance of the equilibrium corresponding to the rest state, and the neuron activity becomes oscillatory. Notice that the pyramidal neuron in Fig. 7.6 starts to fire with a small frequency, which then increases according to the F-I curve in Fig. 7.3 (a slower current ramp is needed to span the entire frequency range of the F-I curve). In contrast, the brainstem neuron starts to fire with a high frequency that remains relatively constant even though the magnitude of the injected current increases.

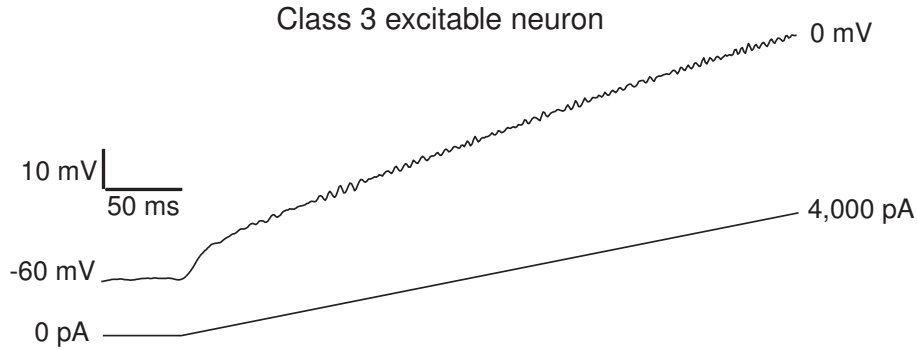


Figure 7.7: A Class 3 excitable brainstem mesV neuron does not fire in response to a ramp current, even though the injected current is stronger than the one in Fig. 7.4.

Among all four codimension-1 bifurcations of equilibrium, discussed in the previous chapter and mentioned in Fig. 7.2, only saddle-node on invariant circle bifurcation results in a limit cycle attractor with arbitrary small frequency and continuous F-I curve. The other three bifurcations result in limit cycle attractors with relatively large frequencies and discontinuous F-I curves. Therefore,

- CLASS 1 NEURAL EXCITABILITY corresponds to the rest state disappearing via saddle-node on invariant circle bifurcation.
- CLASS 2 NEURAL EXCITABILITY corresponds to the rest state disappearing via saddle-node (*off* invariant circle) bifurcation or losing stability via subcritical or supercritical Andronov-Hopf bifurcations.

Of course, the rest state can lose stability or disappear via other bifurcations having higher codimension, sometimes leading to counter-intuitive results (e.g., Class 1 excitability near Andronov-Hopf bifurcation; see Ex. 6 and Sect. 7.2.11). In this chapter we concentrate on the four bifurcations above because they have the lowest codimension and hence are the most likely to be seen experimentally.

### 7.1.4 Class 3

In Fig. 7.7 we inject a slow ramp current into the Class 3 excitable system. In contrast to Fig. 7.6, no spiking and no bifurcation occurs in this experiment despite the fact that the membrane potential goes all the way to 0 mV. Therefore,

- CLASS 3 NEURAL EXCITABILITY occurs when the resting state remains stable for any fixed  $I$  in a biophysically relevant range.

Then, why are there single spikes in Fig. 7.4? Their existence in the figure and their absence in the ramp experiment is related to the phenomenon of *accommodation* that we show now describe.

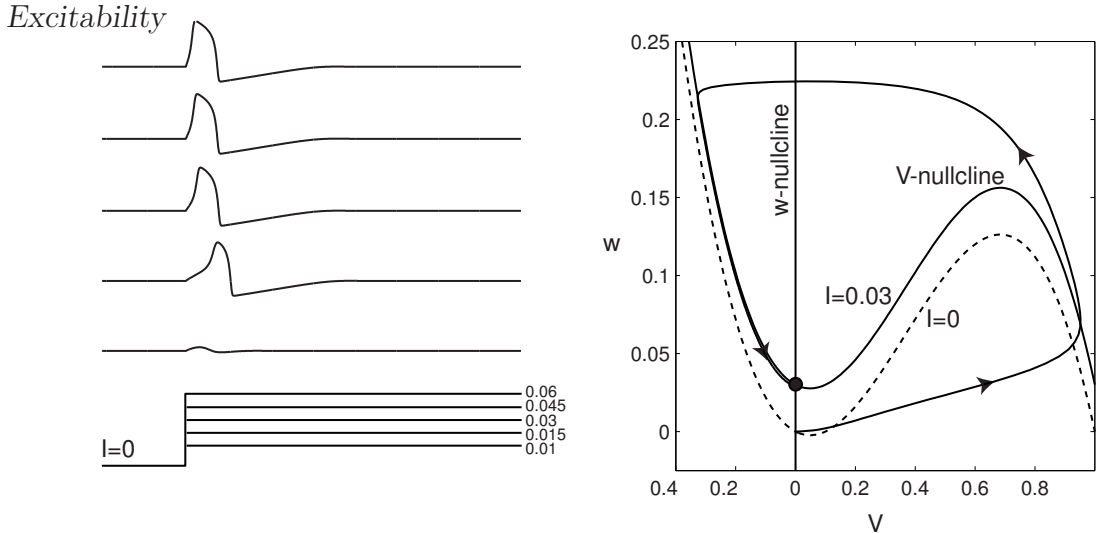


Figure 7.8: Class 3 excitability in FitzHugh-Nagumo model (4.11, 4.12) with  $a = 0.1$ ,  $b = 0.01$ ,  $c = 0$ . The model fires a single spike for any pulse of current.

Let us consider a neuron having a transient  $\text{Na}^+$  current with relatively fast inactivation. If a sufficiently slow ramp of current is injected, the current has enough time to inactivate and no action potentials could be generated. Such a neuron accommodates to the slow ramp. In contrast, a quick membrane depolarization due to a strong step of current does not give enough time for  $\text{Na}^+$  inactivation, thereby resulting in a spike. During the spike, the current inactivates quickly and precludes any further action potentials. Instead of inactivating  $\text{Na}^+$  current, we could have used low-threshold persistent  $\text{K}^+$  current, or any other resonant current, to illustrate the phenomenon of accommodation.

From the dynamical systems point of view, slow ramp results in quasi-static dynamics so that all gating variables follow their steady-state values,  $x = x_\infty(V)$ , and the membrane potential follows its I-V curve. As long as the equilibrium corresponding to the resting state is stable, the neuron is at rest. Even global bifurcations resulting in the appearance of stable limit cycles do not change that. Only when the equilibrium bifurcates (loses stability or disappears), the neuron changes its behavior, e.g., jumps to a limit cycle attractor and starts to fire spikes. Class 3 excitable systems do not fire in response to slow ramps because the resting state does not bifurcate.

In contrast, a pulse of current changes the phase portrait in a rather abrupt manner, as we illustrate in Fig. 7.8 using the FitzHugh-Nagumo model with vertical slow nullcline. Though no bifurcation can occur in the model, and the resting state is stable for any value of  $I$ , its location suddenly shifts when  $I$  jumps. The trajectory from the old equilibrium,  $(0, 0)$ , to the new one goes through the right branch of the cubic  $V$ -nullcline thereby resulting in a single spike. Since the new equilibrium  $(0, 0.03)$  is a global attractor and no limit cycles exist, periodic spiking cannot be generated. In Ex. 7 we explore the relationship between Class 3 excitability and Andronov-Hopf bifurcation (notice the subthreshold oscillations of membrane potential of the pyramidal neuron in Fig. 7.5). We see that injecting ramps of current is not equivalent to inject-

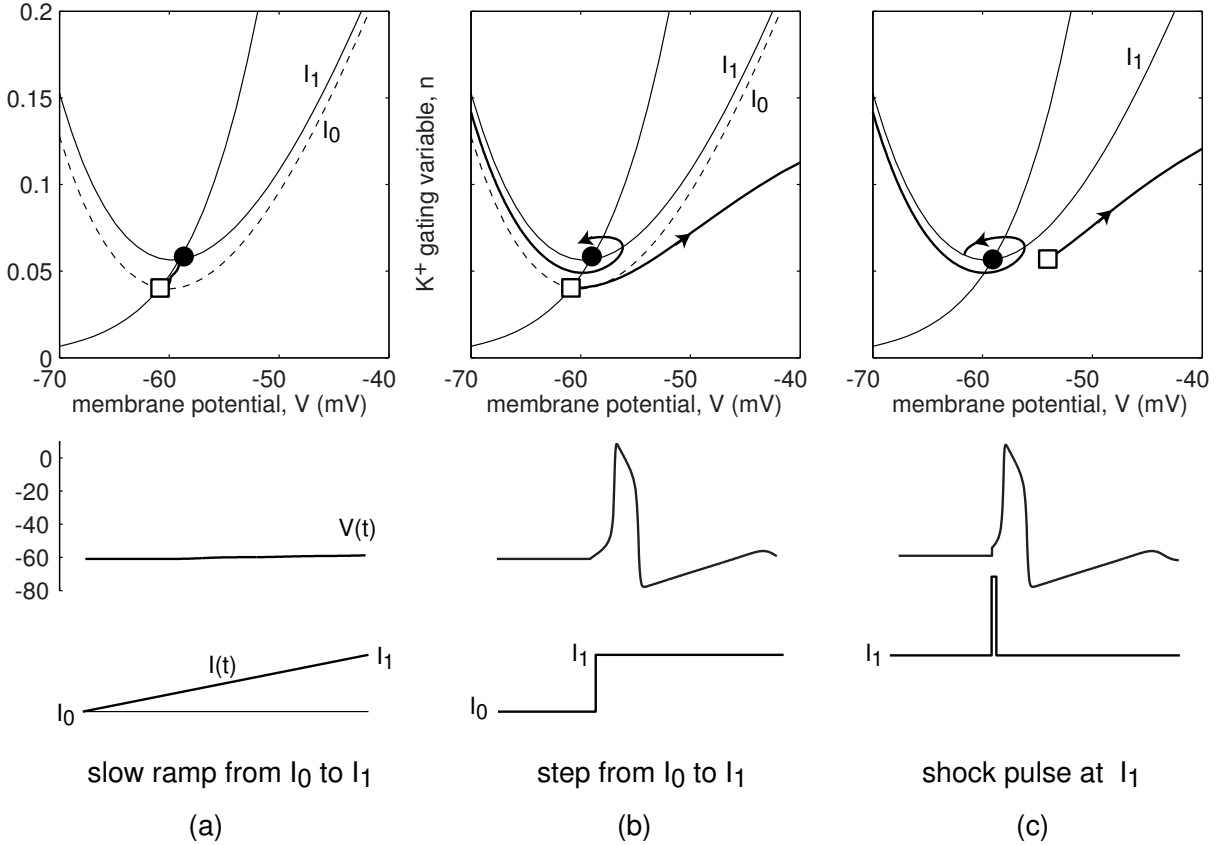


Figure 7.9: The difference between ramp, step, and shock stimulation is in the resetting of initial condition.

ing pulses of current. The system goes through a bifurcation of the equilibrium in the former, but may bypass it and jump somewhere else in the latter.

### 7.1.5 Ramps, steps, and shocks

In Fig. 7.9 we elaborate the difference between injecting slow ramps, steps, and shocks (i.e., brief pulses) of current. In the first two cases the magnitude of the injected current changes from  $I_0$  to  $I_1$ , while in the third case the current is  $I_1$  except the infinitesimally brief moment when it has an infinitely large strength. In all three cases the dynamics of the model can be understood via analysis of its phase portrait at  $I = I_1$ . The key difference among the stimulation protocols is how they reset the initial condition.

At the beginning of the slow ramp in Fig. 7.9a, the state of the neuron is at the stable equilibrium. As the current slowly increases, the equilibrium slowly moves, and the trajectory follows it. When the current reaches  $I = I_1$ , the trajectory is at the new equilibrium, so no response is evoked because the equilibrium is stable. In contrast, when the current is stepped from  $I_0$  to  $I_1$  in Fig. 7.9b, the location of the equilibrium changes instantaneously, but the membrane potential and the gating variables do not have the time to catch up. To understand the response of the model to the step, we

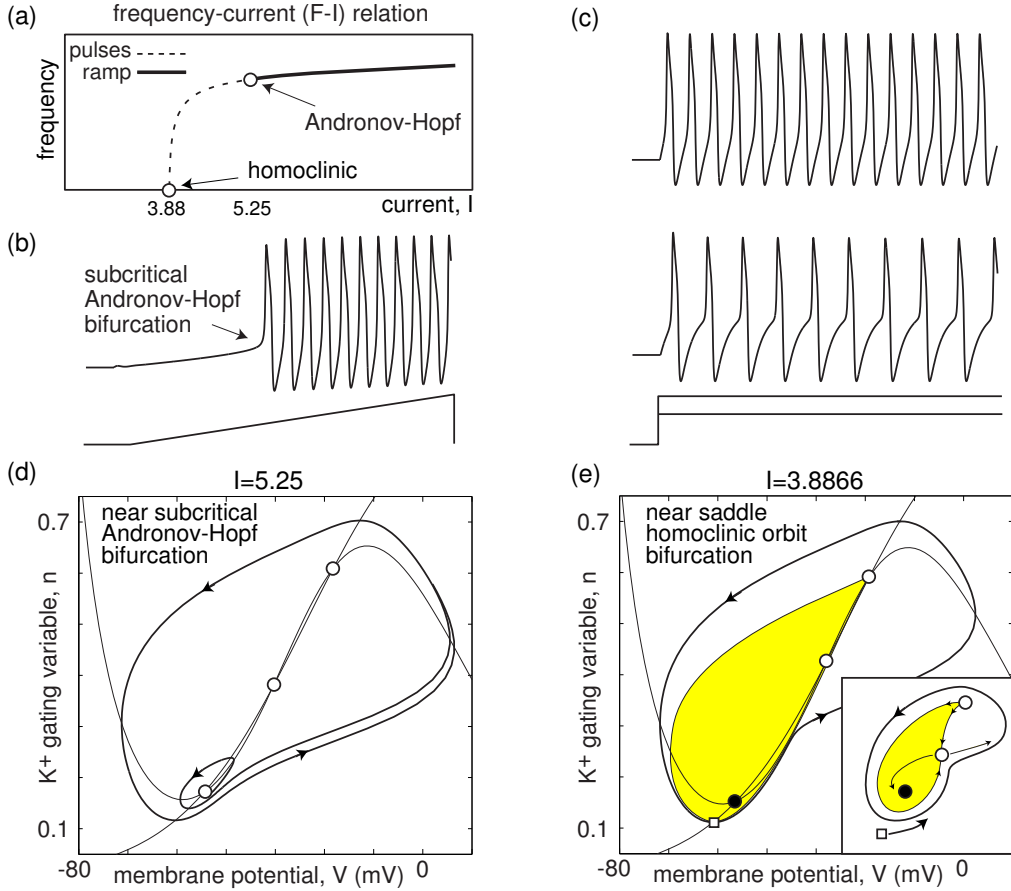


Figure 7.10: The  $I_{\text{Na},p} + I_K$ -model undergoes subcritical Andronov-Hopf bifurcation yet can exhibit low-frequency firing when pulses (but not ramps) of current are injected. Parameters:  $C = 1$ ,  $I = 0$ ,  $E_L = -66.2$ ,  $g_L = 2$ ,  $g_{\text{Na}} = 5$ ,  $g_K = 4.5$ ,  $m_\infty(V)$  has  $V_{1/2} = -30$  and  $k = 10$ ,  $n_\infty(V)$  has  $V_{1/2} = -34$  and  $k = 13$ , and  $\tau(V) = 1$ ,  $E_{\text{Na}} = 60$  mV and  $E_K = -90$  mV. The shaded region denotes the attraction domain of the resting state. The inset shows a distorted drawing of the phase portrait.

need to consider its dynamics at  $I = I_1$  with the initial condition set to the location of the old equilibrium marked by the white square in the figure. Such a step evokes a spike response even though the new equilibrium is stable. Finally, shocking the neuron results in an instantaneous increase of its membrane potential to a new value. As an exercise, prove that the magnitude of the increase equals the product of pulse width and pulse height divided by the membrane capacitance. This shifts the initial condition horizontally to a new point, marked by the white square in Fig. 7.9c, and results in a spike response.

Now, let us revisit the Hodgkin experiments and demonstrate the fundamental difference between the stimulation protocols. In Fig. 7.10a,b,c we simulate the  $I_{\text{Na},p} + I_K$ -model and show that it is Class 2 excitable in response to ramps of current but Class 1 excitable in response to steps of current. The apparent contradiction is resolved in

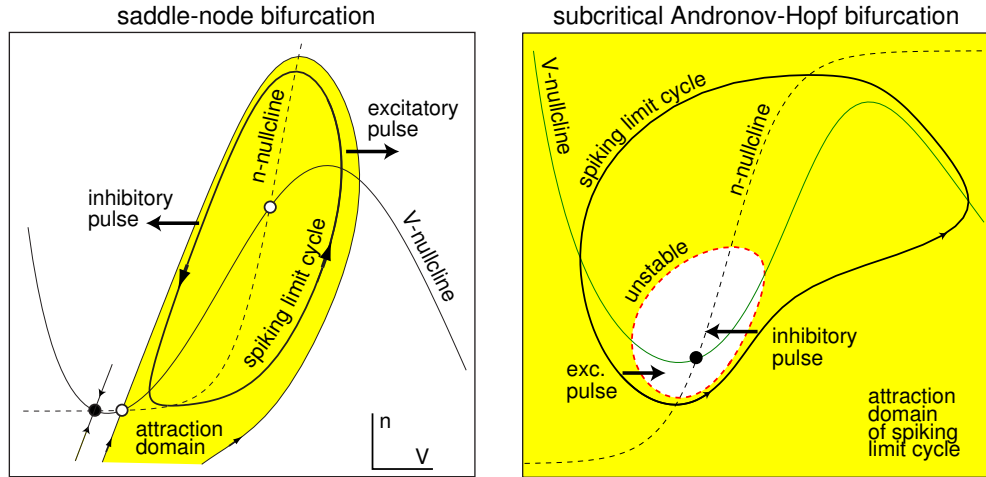


Figure 7.11: Co-existence of stable equilibrium and spiking limit cycle attractor in the  $I_{Na,p} + I_K$ -model. *Left:* The rest state is about to disappear via saddle-node bifurcation. *Right:* The rest state is about to lose stability via subcritical Andronov-Hopf bifurcation. Right (left) arrows denote the location and the direction of an excitatory (inhibitory) pulse that switches spiking behavior to resting.

Fig. 7.10d and e, where we consider the model's phase portraits. Notice the co-existence of the resting state and a limit cycle attractor. The resting state loses stability via subcritical Andronov-Hopf bifurcation at  $I = 5.25$ , so the emerging spiking has non-zero frequency at  $I \approx 5.25$ . However, injecting steps of current results in transitions to the limit cycle even before the resting state loses its stability. The limit cycle in the model appears via saddle homoclinic orbit bifurcation at  $I \approx 3.8866$ , its period is quite large resulting in the Class 1 response to steps of current. The F-I curves for homoclinic bifurcations have logarithmic scaling, so small frequency oscillations are difficult to catch numerically let alone experimentally.

The surprising discrepancy in Fig. 7.10a occurs because the resting state of the  $I_{Na,p} + I_K$ -model is near the Bogdanov-Takens bifurcation, i.e., the model is near a transition from resonator to integrator. Such a bifurcation was recorded, though indirectly, in some neocortical pyramidal neurons, as we will show later in this chapter and in Chap. 8. Another surprising example of Andronov-Hopf bifurcation with Class 1 excitability is presented in Ex. 6. To avoid such surprises, we adopt the ramp definition of excitability throughout the book.

### 7.1.6 Bistability

When transition from resting to spiking states occurs via saddle-node (off invariant circle) or subcritical Andronov-Hopf bifurcation, there is a co-existence of a stable equilibrium and a stable limit cycle attractor just before the bifurcation, as we illustrate in Fig. 7.11. We refer to such systems as bistable. They have a remarkable

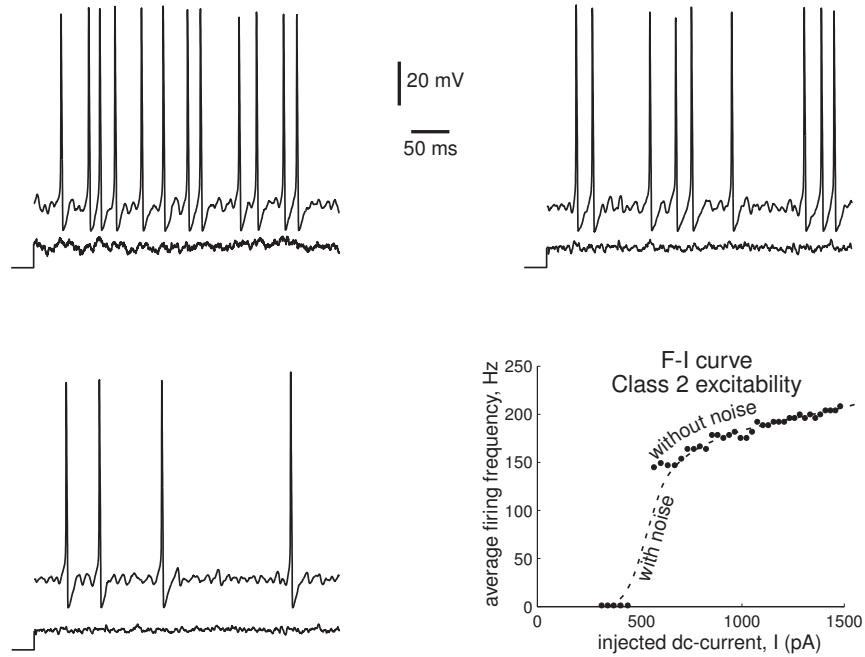


Figure 7.12: Examples of noise-induced low-frequency firings of Class 2 excitable system. The F-I curve may look like the one for Class 1 excitability. Shown are recordings of brainstem mesV neuron.

neuro-computational property: Bistable systems can be switched from one state to the other by an appropriately timed brief stimulus. Rinzel (1978) predicted such a behavior in the Hodgkin-Huxley model, and then bistability and hysteresis were found experimentally in the squid axon (Guttman et al. 1980). What was really surprising for many neuroscientists is that neurons can be switched from repetitive spiking to resting by brief *depolarizing* shock-stimuli.

This phenomenon is illustrated in Fig. 7.11. Each shaded area in the figure denotes the attraction domain of a spiking limit cycle attractor. Obviously, the state of the resting neuron must be pushed into the shaded area to initiate periodic spiking. Similarly, the state of the periodically spiking neuron must be pushed out of the shaded area to stop the spiking. As the arrows in the figure indicate, both excitatory and inhibitory stimuli can do that, depending on their timing relative to the phase of spiking oscillation. This protocol can be used to test bistability experimentally.

Bistable behavior reveals itself indirectly when a neuron is kept close to the bifurcation, e.g., when the injected dc-current is just below the rheobase. Noisy perturbations can switch the neuron from resting to spiking states thereby creating an irregular spike train consisting of short bursts of spikes. Such *stuttering* spiking have been observed in many neurons, including some regular spiking (RS) and fast spiking (FS) neocortical neurons, as we discuss in Chap. 8. The mean firing frequency during stuttering is proportional to the amplitude of the injected current and it can be quite low even for Class 2 excitable system, as we illustrate in Fig. 7.12. Thus, caution should be

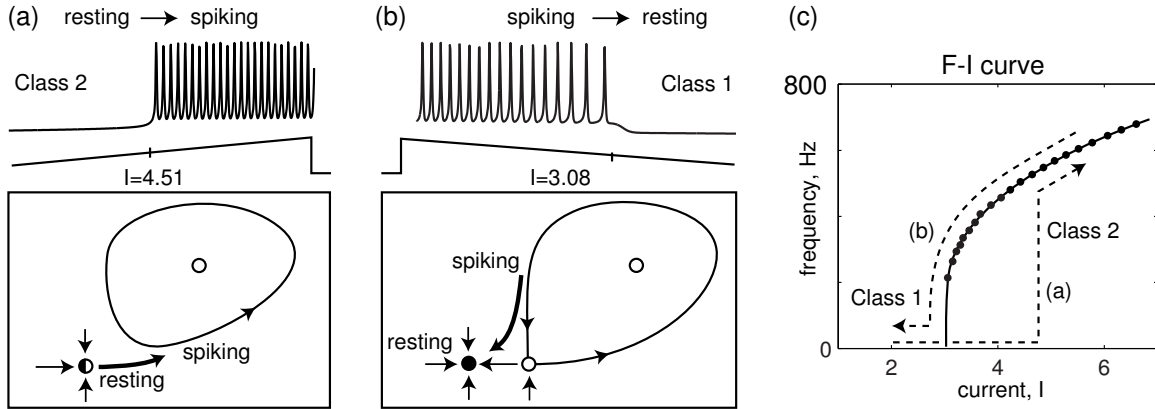


Figure 7.13: (a) The frequency of emerging oscillations at the transition “resting → spiking” defines the class of excitability. (b) The frequency of disappearing oscillations at the transition “spiking → resting” defines the class of spiking. (c) The  $I_{\text{Na,p}}+I_{\text{K}}$ -model with high-threshold  $\text{K}^+$  current exhibits class 2 excitability but class 1 spiking. Its F-I curve has a hysteresis.

used when determining experimentally the class of excitability; only spike trains with regular interspike periods should be accepted to measure the F-I relations.

### 7.1.7 Class 1 and 2 spiking

The class of excitability is determined by the frequency of emerging oscillations at the transition “resting → spiking”, as in Fig. 7.13a. Let us look at the frequency of disappearing oscillations at the transition “spiking → resting”. To induce such a transition, we inject a strong pulse of dc-current of slowly decreasing amplitude, as in Fig. 7.13b. Similarly to the Hodgkin’s classification of excitability, we say that a neuron has *Class 1 spiking* if the frequency-current (F-I) curve at the transition “spiking → resting” decreases to zero, as in Fig. 7.13c, and *Class 2 spiking* if it stops at a certain non-zero value.

The class of excitability coincides with the class of spiking when the transitions “resting ↔ spiking” occur via saddle-node on invariant circle bifurcation or supercritical Andronov-Hopf bifurcation. Indeed, if the current ramps are sufficiently slow, the neuron as a dynamical system goes through the same bifurcation, just in the opposite directions. The classes may differ when the bifurcation is of the saddle-node (off invariant circle) type or subcritical Andronov-Hopf type because of the bistability of the resting and spiking states. Such a bistability results in the hysteresis behavior of the system when the injected current  $I$  increases and decreases slowly, which may result in the hysteresis of the F-I curve. For example, the transition “resting → spiking” in Fig. 7.13a occurs via saddle-node bifurcation at  $I = 4.51$ , and the frequency of spiking equals the frequency of the limit cycle attractor, which is non-zero at this value of  $I$ . Decreasing  $I$  results in the transition “spiking → resting” via the saddle homoclinic

		co-existence of resting and spiking states	
		YES (bistable)	NO (monostable)
subthreshold oscillations	NO (integrator)	saddle-node	saddle-node on invariant circle
	YES (resonator)	subcritical Andronov-Hopf	supercritical Andronov-Hopf

Figure 7.14: Classification of neurons into monostable/bistable integrators/resonators according to the bifurcation of the resting state.

orbit bifurcation in Fig. 7.13b, and in the oscillations with zero frequency at  $I = 3.08$ . Thus, the F-I behavior of the model in this figure (and in Fig. 7.10) exhibits Class 2 excitability but Class 1 spiking. Because of the logarithmic scaling of the F-I curve at the saddle homoclinic bifurcation (see Sect. 6.2.4), estimating experimentally the zero value of the F-I curves is challenging.

Interestingly, steps of injected dc-current, as in Fig. 7.10c, induce the transition “resting  $\rightarrow$  spiking”. But because the model in the figure is near codimension-2 Bogdanov-Takens bifurcation, the steps test the frequency of the limit cycle attractor at the bifurcation “spiking  $\rightarrow$  resting”, as in Fig. 7.10e; that is, they test the class of spiking! The F-I curve in response to steps in the figure is the same as the F-I curve in response to a slowly decreasing current ramp. As an exercise, explain why this is true for Fig. 7.10 but not for Fig. 7.13.

To summarize, we define the class of excitability according to the frequency of emerging spiking of a neuron in response to a slowly increasing current ramp. The class of excitability corresponds to a bifurcation of the resting state (equilibrium) resulting in the transition “resting  $\rightarrow$  spiking”. We define the class of spiking according to the frequency of disappearing spiking of a neuron in response to a slowly decreasing current ramp. The class of spiking corresponds to the bifurcation of the limit cycle resulting in the transition “spiking  $\rightarrow$  resting”. Stimulating a neuron with the ramps (and pulses) is the first step in exploring the bifurcations in the neuron dynamics. Combined with the test for the existence of subthreshold oscillations of the membrane potential, it tells whether the neuron is an integrator or a resonator, and whether it is monostable or bistable, as we discuss next.

## 7.2 Integrators vs. Resonators

In this book we classify excitable systems based on two features: the co-existence of resting and spiking states and the existence of subthreshold oscillations. The former feature divides all systems into *monostable* and *bistable*. The latter feature divides all systems into *integrators* (no oscillations) and *resonators*. These features determine

properties	integrators		resonators	
bifurcation	saddle-node on invariant circle	saddle-node	subcritical Andronov-Hopf	supercritical Andronov-Hopf
excitability	class 1	class 2	class 2	class 2
oscillatory potentials		no		yes
frequency preference		no		yes
I-V relation at rest		non-monotone		monotone
spike latency		large		small
threshold and rheobase		well-defined		may not be defined
all-or-none action potentials		yes		no
co-existence of resting and spiking	no	yes	yes	no
post-inhibitory spike or facilitation (brief stimuli)		no		yes
inhibition-induced spiking		no		possible

Figure 7.15: Summary of neuro-computational properties.

uniquely the type of bifurcation of the resting state, as we summarize in Fig. 7.14. For example, a bistable integrator corresponds to a saddle-node bifurcation whereas monostable resonator corresponds to a supercritical Andronov-Hopf bifurcation. Integrators and resonators have drastically different neuro-computational properties, summarized in Fig. 7.15 and discussed next (the I-V curves are discussed in the previous chapter).

### 7.2.1 Fast subthreshold oscillations

According to the definition, resonators have oscillatory potentials whereas integrators do not. This feature is so important that many of the other neuronal properties discussed later are just mere consequences of the existence or absence of such oscillations.

Fast subthreshold oscillations, as in Fig. 7.16, are typically due to a fast low-threshold persistent  $K^+$  current. At rest, there is a balance of all inward currents and this partially activated  $K^+$  current. A brief depolarization further activates  $K^+$  current and results in fast after-hyperpolarization. While the cell is hyperpolarized, the current de-activates below its steady state level, the balance is shifted toward the inward currents, and the membrane potential depolarizes again, and so on.

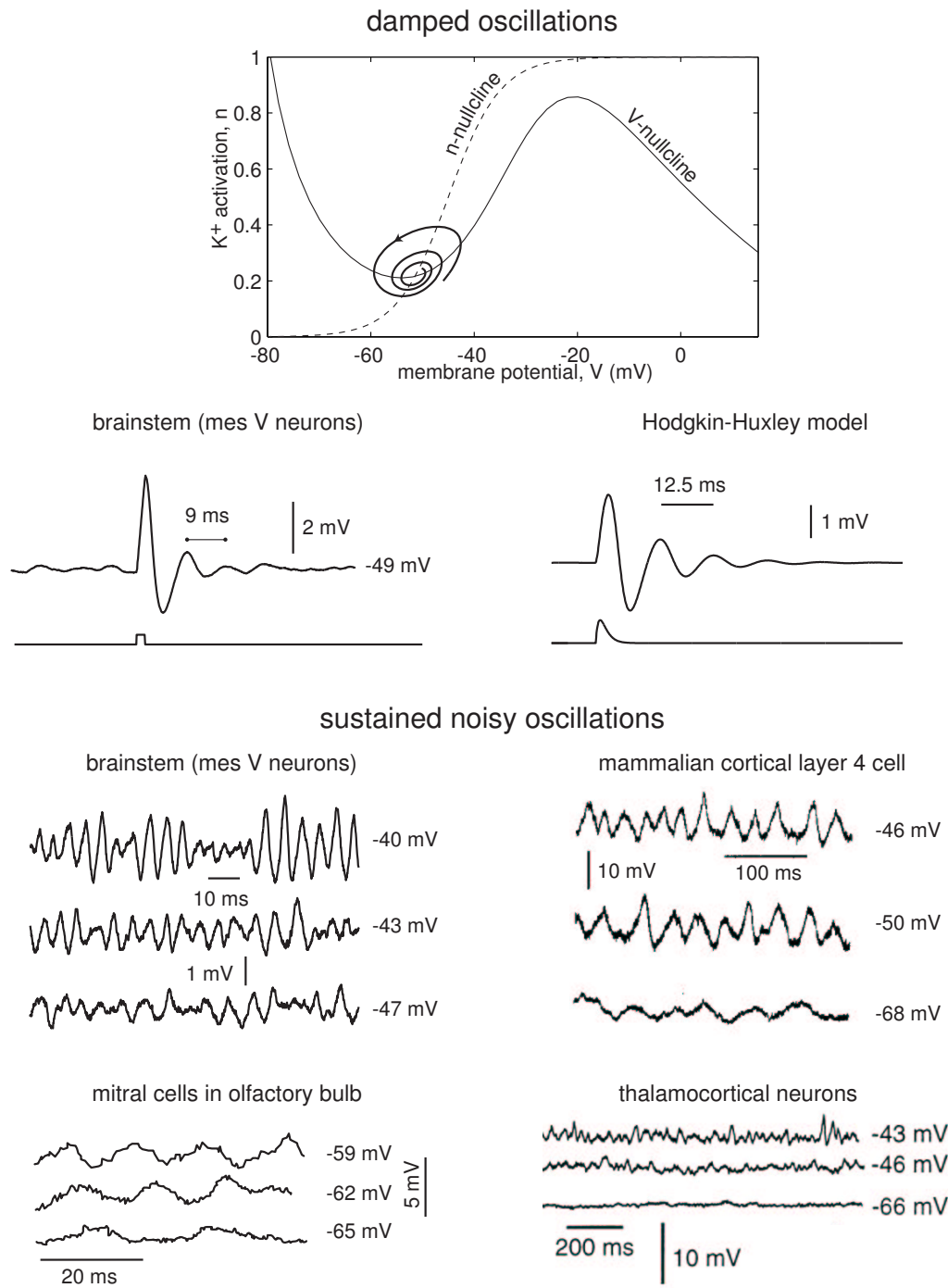


Figure 7.16: Examples of fast damped (top) or sustained (bottom) subthreshold oscillations of membrane potential in neurons and their voltage dependence. Modified from Izhikevich et al. (2003).

The existence of fast subthreshold oscillatory potentials is a distinguishable feature of neurons near Andronov-Hopf bifurcation. Indeed, the resting state of such a neuron is a stable focus. When stimulated by a brief synaptic input or an injected pulse of current, the state of the system deviates from the focus equilibrium, and then returns to the equilibrium along a spiral trajectory, as depicted in Fig. 7.16, top, thereby producing a damped oscillation. The frequency of such an oscillation is the imaginary part of the complex-conjugate eigenvalues at the equilibrium (see Sect. 6.1.3), and it can be as large as 200 Hz in mammalian neurons.

In Ex. 3 we prove that noise can make such oscillations sustained. While the state of the system is perturbed and returns to the focus equilibrium, another strong random perturbation may push it away from the equilibrium, thereby starting a new damped oscillation. As a result, persistent noisy perturbations create a random sequence of damped oscillations and do not let the neuron rest. The membrane potential of such a neuron exhibits noisy sustained oscillations of small amplitude depicted in Fig. 7.16 and discussed in Sect. 6.1.4.

Injected dc-current or background synaptic noise increase the rest potential, change its eigenvalues and, hence change the frequency and amplitude of noisy oscillations. Fig. 7.16 depicts typical cases when the frequency and the amplitude increase as the resting state becomes more depolarized.

One should be careful to distinguish *fast* and *slow* subthreshold oscillations of membrane potential. Fast oscillations, as in Fig. 7.16, are those having period comparable with the membrane time constant or with the period of repetitive spiking. In contrast, some neurons found in entorhinal cortex, inferior olive, hippocampus, thalamus, and many other brain regions can exhibit slow subthreshold oscillations with the period of 100 ms and more. These oscillations reflect the interplay between fast and slow membrane currents, e.g.,  $I_h$  or  $I_T$ , and may be irrelevant to the bifurcation mechanism of excitability. We will discuss this issue in detail in Sect. 7.3.3 and in Chap. 9. Amazingly, such neurons still possess many neuro-computational properties of resonators, such as frequency preference and rebound spiking, but exhibit these properties on a slower time scale.

## 7.2.2 Frequency preference and resonance

A standard experimental procedure to test the propensity of a neuron to subthreshold oscillations is to stimulate it with a sinusoidal current having slowly increasing frequency, called a *zap current*, as in Fig. 7.17. The amplitude of the evoked oscillations of the membrane potential, normalized by the amplitude of stimulating oscillatory current, is called the neuronal *impedance* — a frequency-domain extension of the concept of resistance. The impedance profile of integrators is decreasing while that of resonators has a peak corresponding to the frequency of subthreshold oscillations, around 140 Hz in the mesV neuron in the figure. Thus, integrators act as low-pass filters while resonators act as band-pass filters to periodic signals.

Instead of sinusoidal stimulation, consider more biological stimulation with pulses

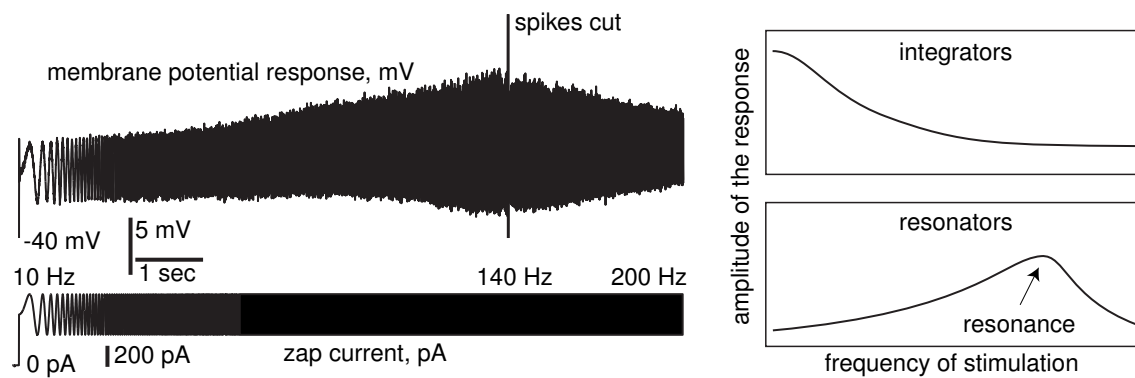


Figure 7.17: Response of the mesV neuron to injected zap current sweeping through a range of frequencies. Integrators and resonators have different responses.

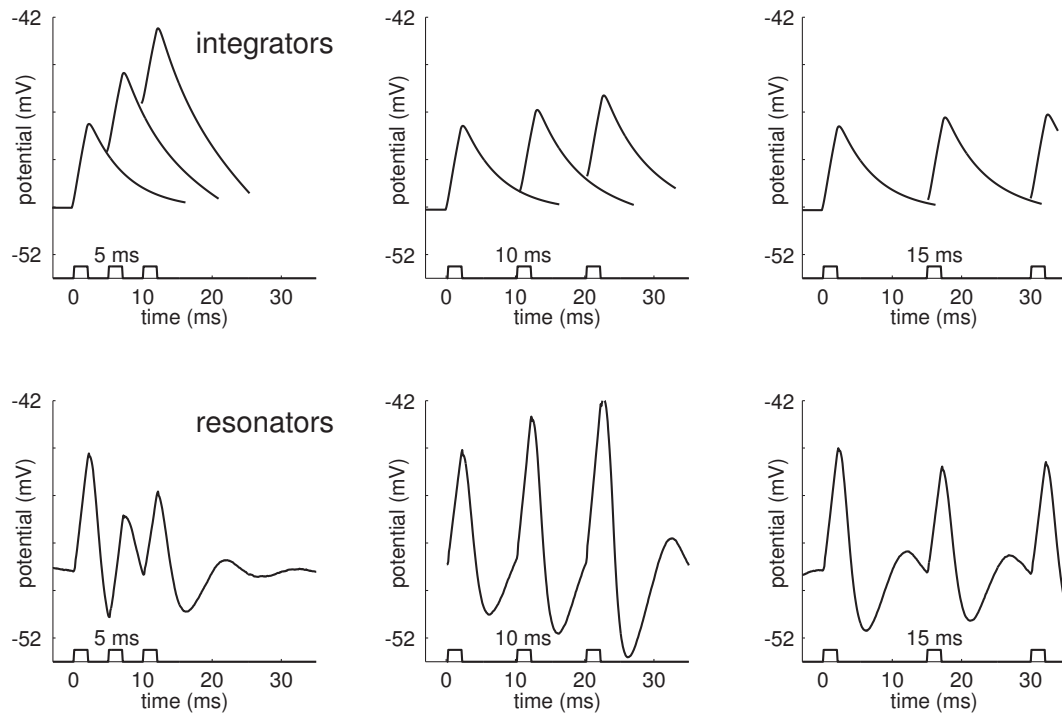


Figure 7.18: Responses of integrators (*top*) and resonators (*bottom*) to input pulses having various inter-pulse periods.

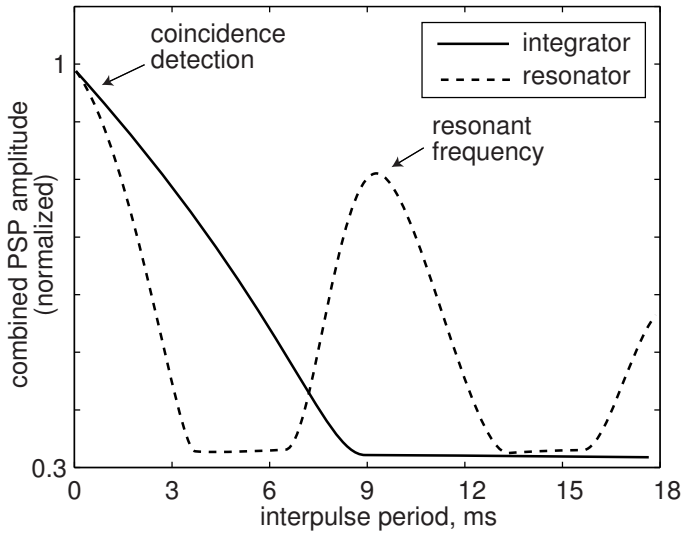


Figure 7.19: Dependence of combined PSP amplitude on the inter-pulse period; see Fig. 7.18.

of current simulating synaptic bombardment. The response of any neuron to input pulses depends on the frequency content of these pulses. In Fig. 7.18 we use triplets with various inter-pulse periods to illustrate the issue. The pulses may arrive from three different presynaptic neurons or from a single presynaptic neuron firing short bursts.

In Fig. 7.18, top, we show that integrators prefer high-frequency inputs. The first pulse in each triplet evokes a post-synaptic potential (PSP) that decays exponentially. The PSP evoked by the second pulse adds to the first one, and so on. The dependence of the combined PSP amplitude on the inter-pulse period is shown in Fig. 7.19. Apparently, the integrator acts as a coincidence detector because it is most sensitive to the pulses arriving simultaneously.

Resonators can also detect coincidences, as one can see in Fig. 7.19. In addition, they can detect resonant inputs. Indeed, the first pulse in each triplet in Fig. 7.18, bottom, evokes a damped oscillation of the membrane potential, which results in an oscillation of the firing probability. The natural period of such an oscillation is around 9 ms for the mesencephalic V neuron used in the figure. The effect of the second pulse depends on its timing relative to the first pulse: If the interval between the pulses is near the natural period, e.g., 10 ms in Fig. 7.18 and Fig. 7.20, the second pulse arrives during the rising phase of oscillation, and it increases the amplitude of oscillation even further. In this case the effects of the pulses add up. The third pulse increases the amplitude of oscillation even further thereby increasing the probability of an action potential, as in Fig. 7.20.

If the interval between pulses is near half the natural period, e.g., 5 ms in Fig. 7.18 and Fig. 7.20, the second pulse arrives during the falling phase of oscillation, and it leads to a decrease in oscillation amplitude. The spikes effectively cancel each other

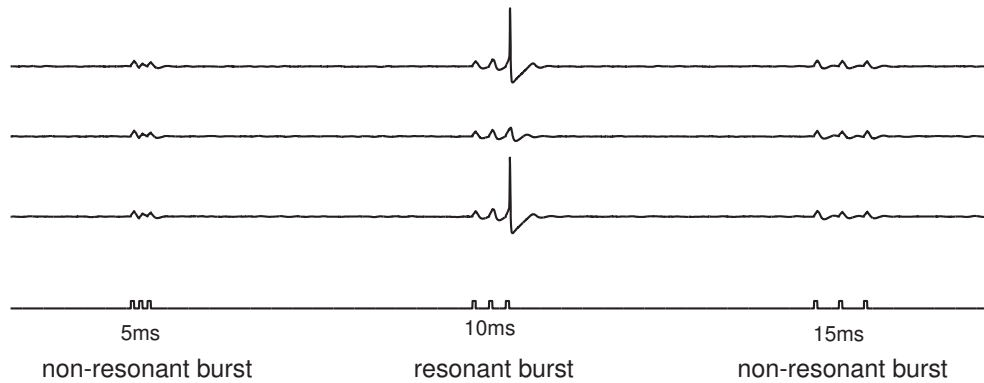


Figure 7.20: Experimental observations of selective response to a resonant (10 ms interspike period) burst in mesencephalic V neurons in brainstem having subthreshold membrane oscillations with natural period around 9 ms; see also Fig. 7.18. Three consecutive voltage traces are shown to demonstrate some variability of the result. Modified from Izhikevich et al. (2003).

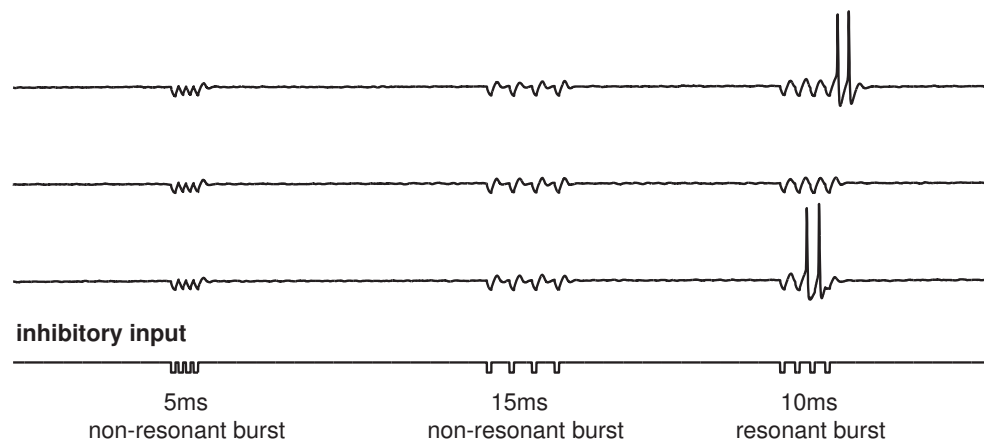


Figure 7.21: Experimental observations of selective response to inhibitory resonant burst in mesencephalic V neurons in brainstem having oscillatory potentials with the natural period around 9 ms. Modified from Izhikevich et al. (2003).

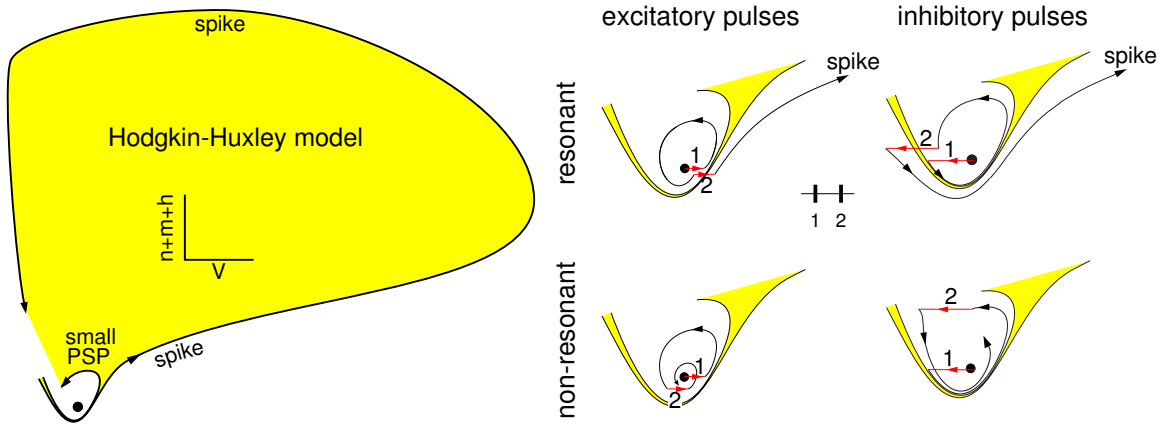


Figure 7.22: (Left) Projection of trajectories of the Hodgkin-Huxley model on a plane. (Right) Phase portrait and typical trajectories during resonant and non-resonant response of the model to excitatory and inhibitory doublets of spikes. Modified from Izhikevich (2000).

out in this case. Similarly, the spikes cancel each other when the interpulse period is 15 ms, which is 60 % greater than the natural period. The same phenomenon occurs for inhibitory synapses, as we illustrate in Fig. 7.21. Here the second pulse increases (decreases) the amplitude of oscillation if it arrives during the falling (rising) phase.

We study the mechanism of such frequency preference in Ex. 4, and present its geometrical illustration in Fig. 7.22. There, we depict a projection of the phase portrait of the Hodgkin-Huxley model having a stable focus equilibrium. The model does not have a true threshold, as we discuss in Sect. 7.2.4. To fire a spike, a perturbation must push the state of the model beyond the shaded figure that is bounded by two trajectories, one of which corresponds to a small post-synaptic potential (PSP), while the other corresponds to a spike.

Fig. 7.22, right, depicts responses of the model to pairs of pulses, called doublets. Pulse 1 in the excitatory doublet shifts the membrane potential from the equilibrium to the right, thereby initiating a subthreshold oscillation. The effect of pulse 2 depends on its timing: If it arrives when the trajectory finishes one full rotation around the equilibrium, then it pushes the voltage variable even more to the right, beyond the shaded area into the spiking zone, and the neuron fires an action potential. In contrast, if it arrives too soon, the trajectory does not finish the rotation, and it is still to the left of the equilibrium. In this case, pulse 2 pushes the state of the model closer to the equilibrium, thereby canceling the effect of pulse 1. Similarly, the effect of an inhibitory doublet depends on the interspike period between the inhibitory pulses. If the interpulse period is near the natural period of damped oscillations, pulse 2 arrives when the trajectory finishes one full rotation, and it adds to pulse 1, thereby firing the neuron. If it arrives too soon or too late, it cancels the effect of pulse 1.

Quite often, the frequency of subthreshold oscillations depends on their amplitudes, e.g., oscillations in the Hodgkin-Huxley model slow down as they become larger. In this

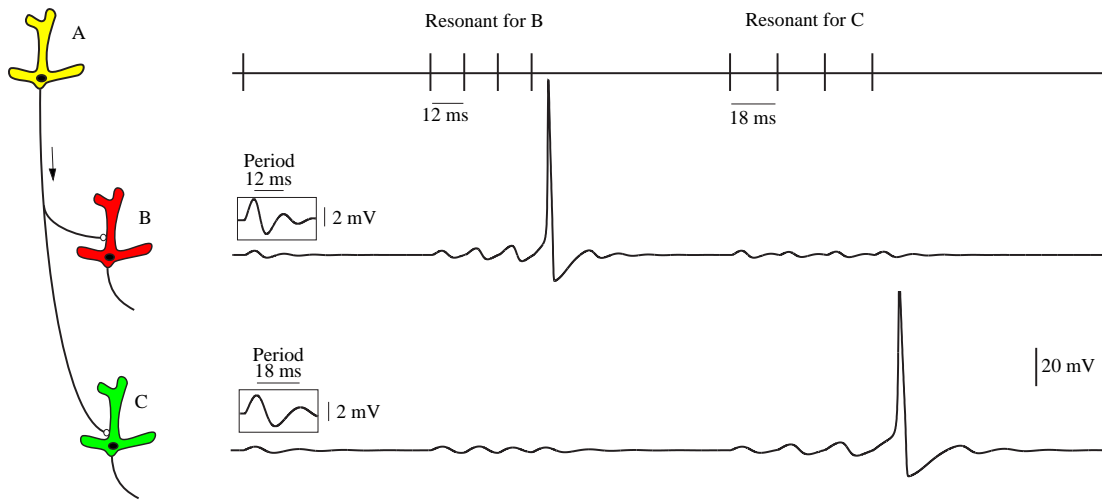


Figure 7.23: Selective communication via bursts: Neuron A sends bursts of spikes to neurons B and C that have different natural periods (12 ms and 18 ms, respectively; both are simulations of the Hodgkin-Huxley model). As a result of changing the interspike frequency, neuron A can selectively affect either B or C without changing the efficacy of synapses. Modified from Izhikevich (2002).

case, the most optimal input is a resonant burst with a slowly decreasing (adapting) interspike frequency. We will see many examples of such bursts in Chap. 9.

The fact that resonator neurons prefer inputs with “resonant” frequencies is not interesting by itself. What makes it interesting is the observation that the same input can be resonant for one neuron and non-resonant for another, depending on their natural periods. For example, in Fig. 7.23 neurons B and C have different periods of subthreshold oscillations: 12 and 18 ms, respectively. By sending a burst of spikes with interspike interval of 12 ms, neuron A can elicit a response in neuron B, but not in C. Similarly, the burst with interspike interval of 18 ms elicits a response in neuron C, but not in B. Thus, neuron A can selectively affect either neuron B or C by merely changing the intra-burst frequency without changing the efficacy of synaptic connections. In contrast, integrators do not have this property.

### 7.2.3 Frequency preference *in vivo*

Figure 7.20 and 7.21 demonstrate convincingly the essence of frequency preference and resonance phenomenon *in vitro*, i.e., when the neuron is quiescent and “waiting” for the resonant burst to come. What if the neuron is under a constant bombardment of synaptic input, as it happens *in vivo*, firing 10 or so spikes per second; Would it be able to tell the difference between the resonant and non-resonant inputs?

To address this question, we performed a frozen-noise experiment pioneered by Bryant and Segundo (1976) and depicted in Fig. 7.24. We generated a noisy signal

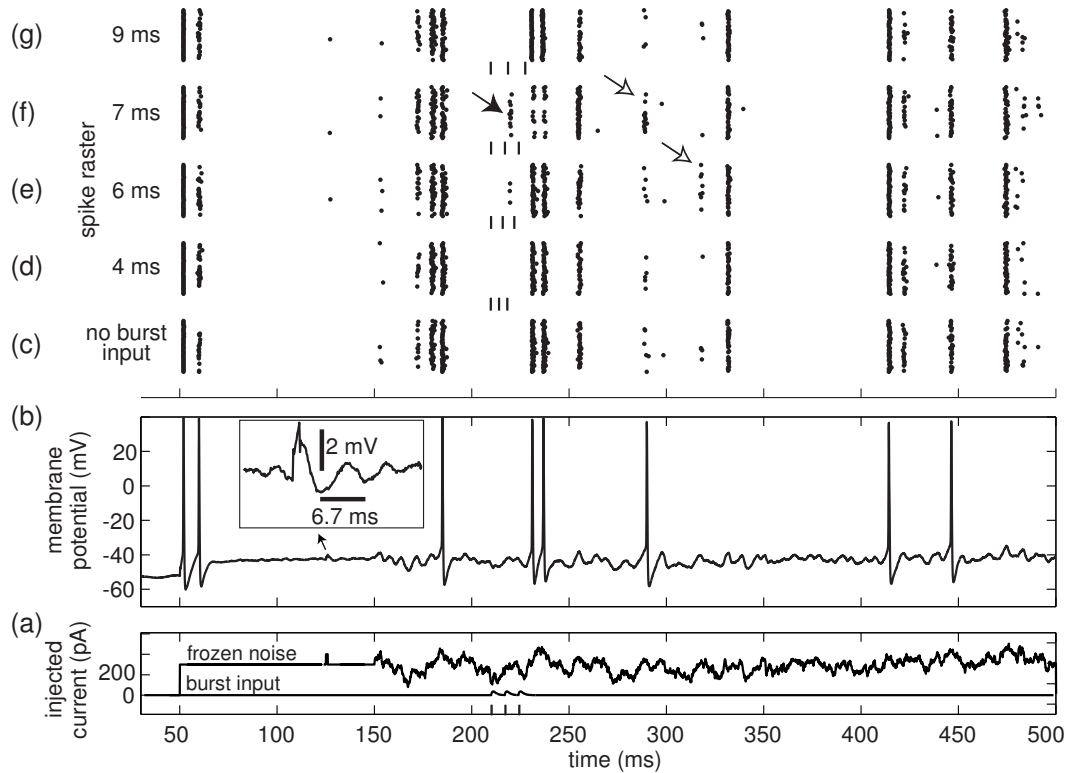


Figure 7.24: Frozen-noise experiments demonstrate frequency preference and resonance to embedded bursts. (a) A random signal (frozen noise) is injected into a neuron *in vitro* to simulate the *in vivo* conditions (b). The neuron responds with some spike-timing variability depicted in (c). (d-g) Burst input is added to the frozen noise. Notice that the neuron is most sensitive to the input having the resonant period 7 ms, which is near the period of subthreshold oscillation (6.7 ms). Shown are *in vitro* responses of mesencephalic V neuron of rats brainstem recorded by the author, Niraj S. Desai, and Betsy C. Walcott. The order of stimulation was first line of c,d,e,f,g, then second line of c,d,e,f,g, then third line, etc., to avoid slow artifacts.

(frozen noise in Fig. 7.24a) and saved it into the memory of the program that injects current into a neuron. Then we injected the stored signal into the neuron 50 times to see how reliable its spike response is. Despite the *in vivo*-like activity in Fig. 7.24b, the spike raster in Fig. 7.24c shows vertical clusters indicating that the neuron prefers to fire at certain “scheduled” moments of time corresponding to certain features of the frozen-noise input.

In Fig. 7.24d-g, we added bursts of 3 spikes to the frozen noise. The amplitudes of the bursts were constant (less than 10% of the frozen noise amplitude), but the interspike periods were different. The idea is to see whether the response of the neuron would be any different when the burst period is near the neuronal intrinsic period of 6.7 ms (see the inset in Fig. 7.24b). As one expects, the non-resonant bursts with 4 ms and 9 ms periods remained undetected by the neuron, since the spike rasters in Fig. 7.24d

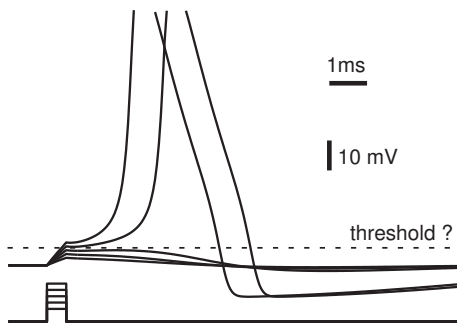


Figure 7.25: Finding threshold in Hodgkin-Huxley model.

and  $g$  are essentially the same as in Fig. 7.24c. The resonant burst with 7 ms period in Fig. 7.24f produced the most significant deviation from Fig. 7.24c marked by the black arrow, indicating that the neuron is most sensitive to the resonant input. Typically, the resonant burst does not make the neuron fire extra spikes, but only changes the timing of “scheduled” spikes. Injecting resonant bursts at different moments results in other interesting phenomena, such as extra spikes or the omission of “scheduled” spikes, not shown here, or no effect at all. Finally, there is a subtle but noticeable effect of the resonant (7 ms) and nearly-resonant (6 ms) bursts even 100 ms after the stimulation (white arrows in the figure), for which we have no explanation.

### 7.2.4 Thresholds and action potentials

A common misconception is that all neurons have firing thresholds. Moreover, great effort has been made to determine such thresholds experimentally. Typically, a neuron is stimulated with brief current pulses of various amplitudes to elicit various degrees of depolarization of the membrane potential, as we illustrate in Fig. 7.25 using the Hodgkin-Huxley model. Small “subthreshold” depolarizations decay while large “suprathreshold” or “suprathreshold” depolarizations result in action potentials. The maximal value of the subthreshold depolarization is taken to be the firing threshold value for that neuron. Indeed, the neuron will fire a spike if depolarized just above that value.

The notion of a firing threshold is simple and attractive, especially when we teach neuroscience to undergraduates. Everybody, including the author of this book, uses it to describe neuronal properties. Unfortunately, it is wrong. First, the problem is in the definition of an action potential. Are the two dashed curves in Fig. 7.26 action potentials? What about a curve in-between (not shown in the figure)? Suppose we define an action potential to be any deviation from the resting potential, say by 20 mV. Is the concept of firing threshold well-defined in this case? Unfortunately, the answer is still NO.

The membrane potential value that separates subthreshold depolarizations from action potentials (whatever the definition of an action potential is) depends on the prior activity of the neuron. For example, if a neuron having transient  $\text{Na}^+$  current just fired an action potential, the current is partially inactivated, and a subsequent depolarization above the firing threshold might not evoke another action potential.

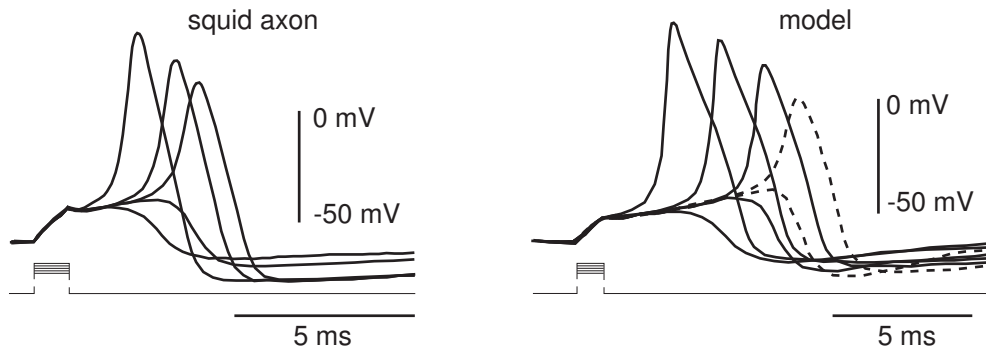


Figure 7.26: Variable-size action potentials in squid giant axon and revised Hodgkin-Huxley model (Clay 1998) in response to brief steps of currents of variable magnitudes (data was kindly provided by John Clay).

Conversely, if the neuron was briefly hyperpolarized and then released from hyperpolarization, it could fire a rebound post-inhibitory spike, as we discuss later in this chapter (see Fig. 7.29). Apparently, releasing from hyperpolarization does not qualify as a superthreshold stimulation. Why then the neuron fired?

### 7.2.5 Threshold manifolds

The problem of formulating a mathematical definition of firing thresholds was first tackled by FitzHugh (1955). Using geometrical analysis of neural models, he noticed that thresholds, if exist, are never numbers but manifolds, e.g., curves in two-dimensional systems. We illustrate his concept in Fig. 7.27 using phase plane analysis of the  $I_{Na,p}+I_K$ -model.

Integrators do have well-defined threshold manifolds. Since an integrator neuron is near a saddle-node bifurcation, whether on or off an invariant circle, there is a saddle point with its stable manifold; see Fig. 7.27a. This manifold separates two regions of the phase space, and for this reason often called a *separatrix*. Depending on the prior activity of the neuron and the size of the input, its state can end up in the shaded area and generate a subthreshold potential, or in the white area and generate an action potential. An intermediate-size input cannot reduce the size of the action potential, but can only delay its occurrence. In the extreme case, a perturbation can put the state vector precisely on the threshold manifold, and the system converges to the saddle, at least in theory. Since the saddle is unstable, small noise present in neurons pushes the state either to the left or to the right, resulting in either a long subthreshold potential or a large-amplitude spike with a long latency, as we discuss in Sect. 7.2.9 and show in Fig. 7.34. Finally, notice that a neuron has a single threshold value of membrane potential only when its threshold manifold is a straight vertical line.

Resonators may or may not have well-defined threshold manifolds, depending on the type of bifurcation. Consider a resonator neuron in the bistable regime; that is, sufficiently near a subcritical Andronov-Hopf bifurcation with an unstable limit cycle

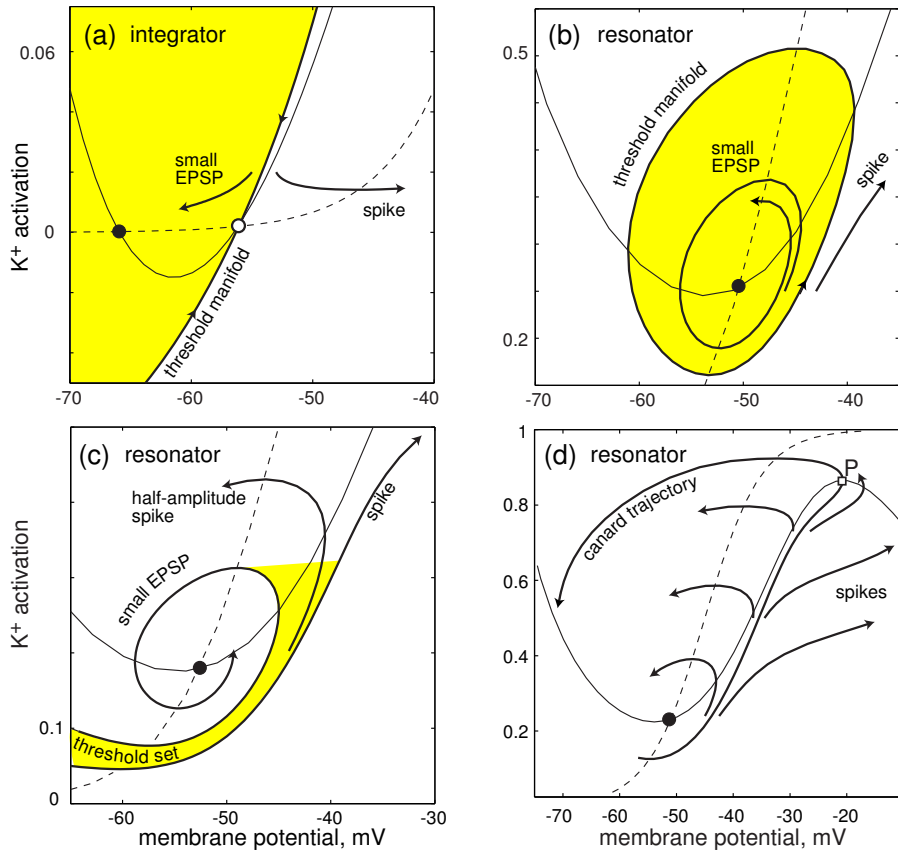


Figure 7.27: Threshold manifolds and sets in the  $I_{Na,p} + I_K$ -model. Parameters in (a) as in Fig. 4.1a, in (b), (c), and (d) as in Fig. 6.16 with  $I = 45$  (b) and  $I = 42$  (c and d).

separating the resting and the spiking states, as in Fig. 7.27b. Such an unstable cycle acts as a threshold manifold. Any perturbation that leaves the state of the neuron inside the attraction domain of the resting state, which is the shaded region bounded by the unstable cycle, results in subthreshold potentials. Any perturbation that pushes the state of the neuron outside the shaded region results in an action potential. In the extreme case, a perturbation may put the state right on the unstable limit cycle. Then, the neuron exhibits unstable "threshold" oscillations, at least in theory. In practice, such oscillations cannot be sustained because of noise, and they will either subside or result in spikes.

The bistable regime near subcritical Andronov-Hopf bifurcation is the only case when a resonator can have a well-defined threshold manifold. In all other cases, including the supercritical Andronov-Hopf bifurcation, resonators do not have well-defined thresholds. We illustrate this in Fig. 7.27c. A small deviation from the resting state produces a trajectory corresponding to a "subthreshold" potential. A large deviation produces a trajectory corresponding to an action potential. We refer to the shaded region between the two trajectories as a threshold set. It consists of trajectories corre-

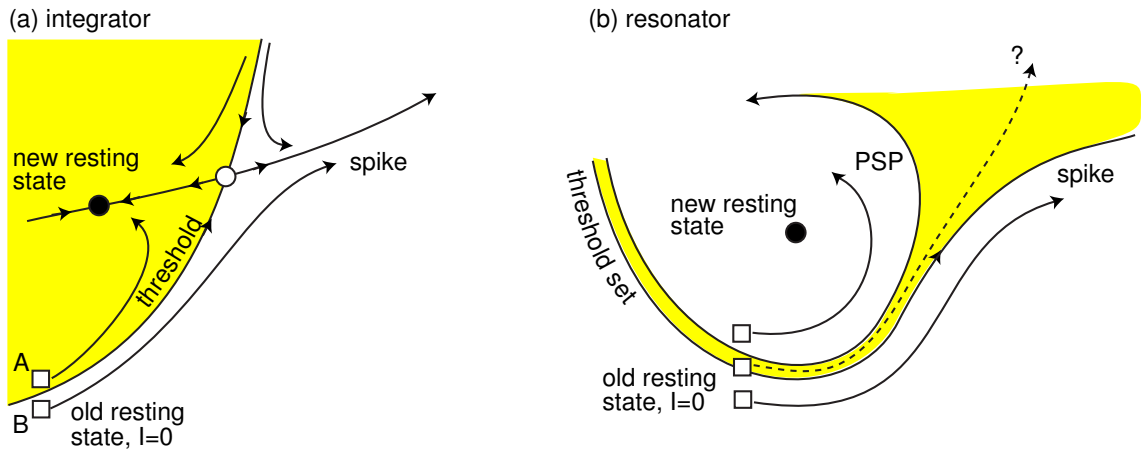


Figure 7.28: Integrators have well-defined rheobase current while resonators may not.

sponding to partial-amplitude action potentials, such as those in Fig. 7.26. No single curve separates small potentials from action potentials, so there is no well-defined threshold manifold.

FitzHugh (1955) noticed that the threshold set can be quite thin in some models, including the Hodgkin-Huxley model. In particular, the difference between the trajectories corresponding to small potentials and action potentials can be as small as 0.0001 mV, which is smaller than the noisy fluctuations of the membrane potential. Thus, to observe an intermediate-amplitude spike in such models, one needs to simulate the models with accuracy beyond the limits of uncertainty which appear when the physical interpretation of the model is considered. As a result, for any practical purpose such models exhibit all-or-none behavior with the threshold set looking like a threshold manifold. FitzHugh referred to this as being a *quasithreshold* phenomenon.

Quasi-thresholds are related to the special canard trajectory depicted in Fig. 7.27d. The trajectory follows the unstable branch of the cubic nullcline all the way to the right knee point P. The flow near the trajectory is highly unstable; any small perturbation pushes the state of the system to the left or to the right, resulting in a “subthreshold” or “superthreshold” response. The solutions depicted in Fig. 7.26, right, try to follow such a trajectory. An easy way to compute the trajectory in two-dimensional relaxation oscillators is to start with the point P and integrate the system backwards ( $t \rightarrow -\infty$ ). We discuss canard (French duck) solutions in detail in Sect. 6.3.4.

## 7.2.6 Rheobase

Neuronal rheobase, i.e., the minimal amplitude of a current of infinite duration that makes the neuron fire, measures the “current threshold” of the neuron. Integrators have a well-defined rheobase while resonators may not. To see this, consider an integrator neuron in Fig. 7.28a receiving a current step that changes instantly its phase portrait. In particular, the current moves the equilibrium from the old location corresponding

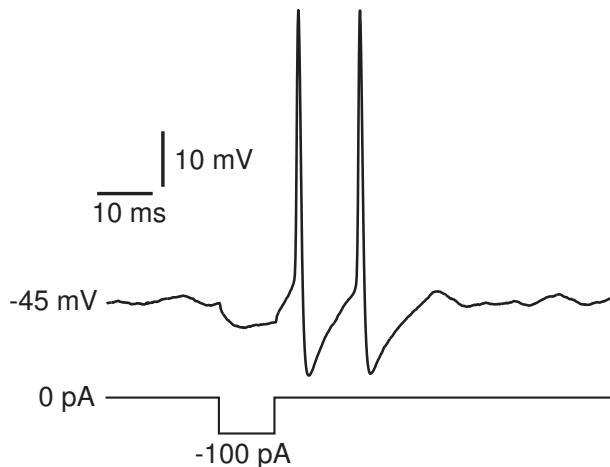


Figure 7.29: Rebound spikes in response to a brief hyperpolarizing pulse in a brainstem mesV neuron having fast subthreshold oscillations of membrane potential.

to  $I = 0$  (white square in the figure) to a new location (black circle). Whether the neuron fires or not depends on the location of the old equilibrium relative to the stable manifold to the saddle, which plays the role of the new threshold. In case A the neuron does not fire, in case B it fires even though the resting state is still stable. The neuronal rheobase is the amplitude of the current  $I$  that puts the threshold exactly on the location of the old equilibrium. Such a value of  $I$  always exists, and it often corresponds to the saddle-node bifurcation value. Notice that the rheobase current results in a spike with infinite latency, at least theoretically.

A resonator neuron may not have well-defined rheobase simply because it may not have well-defined threshold. Indeed, the dotted line in Fig. 7.28b may correspond to a subthreshold or superthreshold response depending on where it is in the threshold set. Stimulating such a neuron with “rheobase” current produces spikes with finite latencies but partial amplitudes. A bistable resonator (near subcritical Andronov-Hopf bifurcation) may have a well-defined rheobase because it has a well-defined threshold — the small-amplitude unstable limit cycle.

### 7.2.7 Post-inhibitory spike

Prolonged injection of a hyperpolarizing current and then sudden release from hyperpolarization can produce a rebound post-inhibitory response in many neurons. The hyperpolarizing current is often called anodal current, release from the hyperpolarization is called anodal break, so rebound spiking is called anodal break excitation (FitzHugh 1976). Notice that firing of a neuron follows a sudden increase of injected current, whether it is a positive step or release from a negative step.

Often, post-inhibitory responses are caused by the “hyperpolarization-activated” h-current, which slowly builds up and upon termination of the hyperpolarization drives the membrane potential over the threshold manifold (or threshold set). Alternatively, the rebound response can be caused by slow de-inactivation of  $\text{Na}^+$  or  $\text{Ca}^{2+}$  currents, or slow de-activation of a  $\text{K}^+$  current that is partially activated at rest and prevents firing. In any case, such a rebound response relies on slow currents and long or strong

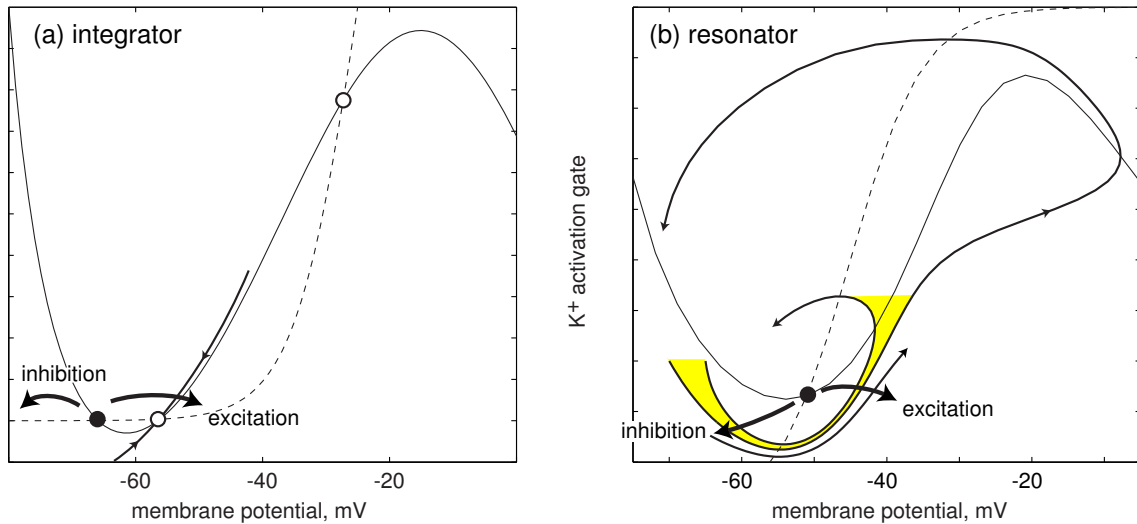


Figure 7.30: Direction of excitatory and inhibitory input in integrators (a) and resonators (b).

hyperpolarizing steps, it does not depend on the bifurcation mechanism of excitability, and it can occur in integrators or resonators.

Some neurons can exhibit rebound spikes after short and relatively weak hyperpolarizing currents, as we illustrate in Fig. 7.29. The negative pulse deactivates a fast low-threshold resonant current, e.g.,  $K^+$  current, which is partially activated at rest. Upon release from the hyperpolarization, there is a deficit of the outward current and the net membrane current results in rebound depolarization and possibly a spike. Such a response occurs on the fast time scale and it does depend on the bifurcation mechanism of excitability.

In Fig. 7.30 we show why integrators cannot fire rebound spikes to short stimulation, while resonators typically can. A brief excitatory pulse of current depolarizes the membrane and brings it closer to the threshold manifold, as in Fig. 7.30a. Consequently, an inhibitory pulse hyperpolarizes the membrane and increases the distance to the threshold manifold. The dynamics of such a neuron is consistent with our intuition that excitation facilitates spiking and inhibition prevents it.

Contrary to our intuition, inhibition can also facilitate spiking in resonator neurons because the threshold set may wrap around the resting state, as in Fig. 7.30b. A sufficiently strong inhibitory pulse can push the state of the neuron beyond the threshold set thereby evoking a rebound action potential. If the inhibitory pulse is not strong, it still can have an excitatory effect, since it brings the state of the system closer to the threshold set. For example, it can enhance the effect of subsequent excitatory pulses, as we illustrate in Fig. 7.31. The excitatory pulse here is subthreshold if applied alone. However, it becomes superthreshold if preceded by an inhibitory pulse. The timing of pulses is important here, as we discussed in Sect. 7.2.2. John Rinzel suggested to call this phenomenon a *post-inhibitory facilitation*.

### 7.2.8 Inhibition-induced spiking

In Fig. 7.32, top, we use the  $I_{Na,t}$ -model introduced in Chap. 5 to illustrate an interesting property of some resonators — inhibition-induced spiking. Recall, that the model consists of an Ohmic leak current and a transient  $\text{Na}^+$  current with instantaneous activation and relatively slow inactivation kinetics. It can generate action potentials due to the interplay between the amplifying gate  $m$  and the resonant gate  $h$ .

We widened the activation function  $h_\infty(V)$  so that  $\text{Na}^+$  current is largely inactivated at the resting state; see the inset in Fig. 7.32. Indeed,  $h = 0.27$  when  $I = 0$ . Even though such a system is excitable, it cannot fire repetitive action potentials when a positive step of current, e.g.,  $I = 10$ , is injected. Depolarization produced by the injected current inactivates  $\text{Na}^+$  current so much that no repetitive spikes are possible. Such a system is Class 3 excitable.

Remarkably, injection of a negative step of current, e.g.,  $I = -15$  in the figure, results in a periodic train of action potentials! How is it possible? Inhibition-induced spiking or bursting are possible in neurons having slow h-current or T-current, such as the thalamo-cortical relay neurons. (We discuss these and other examples in the next chapter.) The  $I_{Na,t}$ -model does not have such currents, yet it can fire in response to inhibition.

Figure 7.33 summarizes the ionic mechanism of inhibition-induced spiking. The resting state in the model corresponds to the balance of the outward leak current and a partially activated, partially inactivated inward  $\text{Na}^+$  current. When the membrane potential is hyperpolarized by the negative injected current, two processes take place:  $\text{Na}^+$  current deinactivates (variable  $h$  increases), and deactivates (variable  $m = m_\infty(V)$  decreases). Since  $m_\infty(V)$  is flatter than  $h_\infty(V)$ , deinactivation is stronger than deacti-

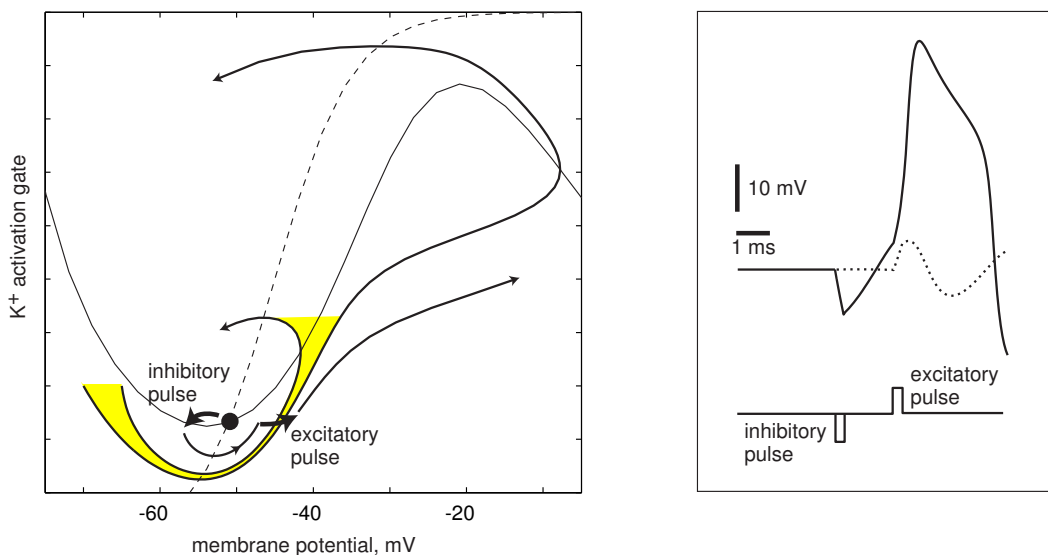


Figure 7.31: Post-inhibitory facilitation: A subthreshold excitatory pulse can become superthreshold if it is preceded by an inhibitory pulse.

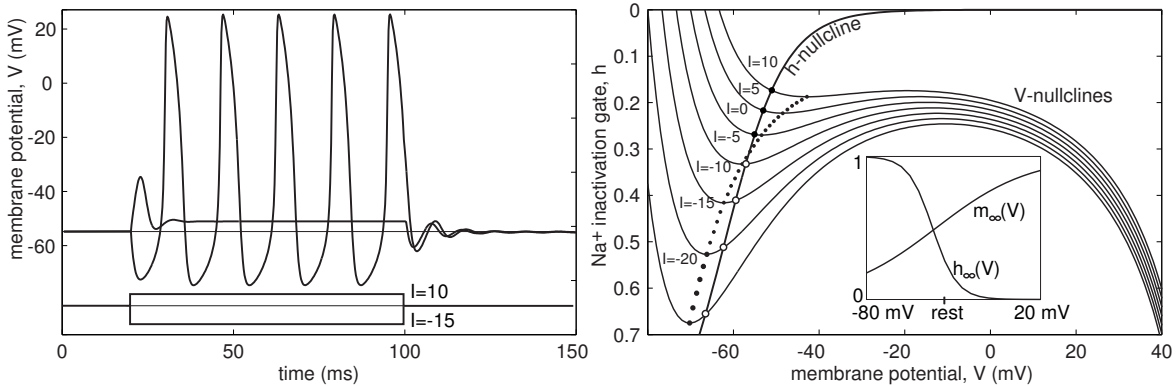


Figure 7.32: Inhibition-induced spiking in the  $I_{\text{Na},t}$ -model. Parameters are the same as in Fig. 5.6b, except  $g_{\text{leak}} = 1.5$  and  $m_\infty(V)$  has  $k = 27$ .

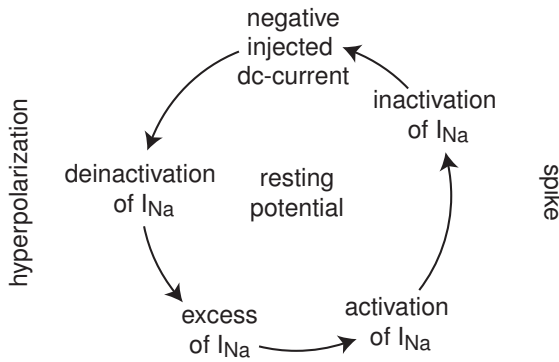


Figure 7.33: Mechanism of inhibition-induced spiking in the  $I_{\text{Na},t}$ -model.

vation and the  $\text{Na}^+$  conductance,  $g_{\text{Na}}mh$ , increases. This leads to an imbalance of the inward current and to the generation of the first spike. During the spike, the current inactivates completely, and the leak and negative injected currents repolarize and then hyperpolarize the membrane. During the hyperpolarization, clearly seen in the figure,  $\text{Na}^+$  current deinactivates and is ready for the generation of the next spike.

To understand the dynamic mechanism of such an inhibition-induced spiking, we need to consider the geometry of the nullclines of the model, depicted in Fig. 7.32, bottom. Notice how the position of the  $V$ -nullcline depends on  $I$ . Negative  $I$  shifts the nullcline down and leftward so that the vertex of its left knee, marked by a dot, moves to the left. As a result, the equilibrium of the system, which is the intersection of the  $V$ - and  $h$ -nullclines, moves toward the middle branch of the cubic  $V$ -nullcline. When  $I = -2$ , the equilibrium loses stability via supercritical Andronov-Hopf bifurcation, and the model exhibits periodic activity.

Instead of the  $I_{\text{Na},t}$ -model, we could have used the  $I_{\text{Na}} + I_{\text{K}}$ -model or any other model with a low-threshold resonant gating variable. The key point here is not the ionic basis of the spike-generation mechanism, but its dynamic attribute — the Andronov-Hopf bifurcation. Even the FitzHugh-Nagumo model (4.11, 4.12) can exhibit this phenomenon; see Ex. 1.

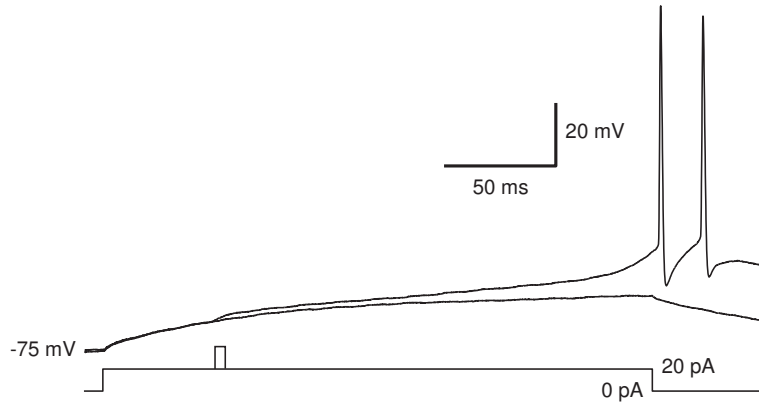


Figure 7.34: Long latencies and threshold crossing of layer 5 neuron recorded *in vitro* in rat motor cortex.

### 7.2.9 Spike latency

In Fig. 7.34 we illustrate an interesting neuronal property - *latency-to-first-spike*. A barely superthreshold stimulation evokes action potentials with a significant delay, which could be as large as a second in some cortical neurons. Usually, such a delay is attributed to slow charging of the dendritic tree or to the action of the A-current, which is a voltage-gated transient K<sup>+</sup> current with fast activation and slow inactivation. The current activates quickly in response to a depolarization and prevents the neuron from immediate firing. With time, however, the A-current inactivates and eventually allows firing. (A low-threshold slowly activating Na<sup>+</sup> or Ca<sup>2+</sup> current would achieve a similar effect.)

In Fig. 7.35 we explain the latency mechanism from dynamical systems point of view. Long latencies arise when neurons undergo saddle-node bifurcation depicted in Fig. 7.35, left. When a step of current is delivered, the V-nullcline moves up so that the saddle and node equilibria that existed when  $I = 0$  coalesce and annihilate each other. Although there are no equilibria, the vector field remains small in the shaded neighborhood, as if there were still a ghost of the resting equilibrium there (see Sect. 3.3.5). The voltage variable increases and passes that neighborhood. As we discussed in Ex. 3 at the end of the previous chapter, the passage time scales as  $1/\sqrt{I - I_b}$ , where  $I_b$  is the bifurcation point, see Fig. 6.8. Hence, the spike is generated with a significant latency. If the bifurcation is on an invariant circle, then the state of the neuron returns to the shaded neighborhood after each spike resulting in firing with small frequency, characteristic of Class 1 excitability; see Fig. 7.3. In contrast, if the saddle-node bifurcation is *off* an invariant circle, then the state does not return to the neighborhood, and the firing frequency can be large, as in Fig. 7.34 or in the neostriatal and basal ganglia neurons reviewed in Sect. 8.4.2.

We see that the existence of long spike latencies is an innate neuro-computational property of integrators. It is still not clear how or when the brain is using it. Two most plausible hypotheses are 1) Neurons encode the strength of input into spiking latency.

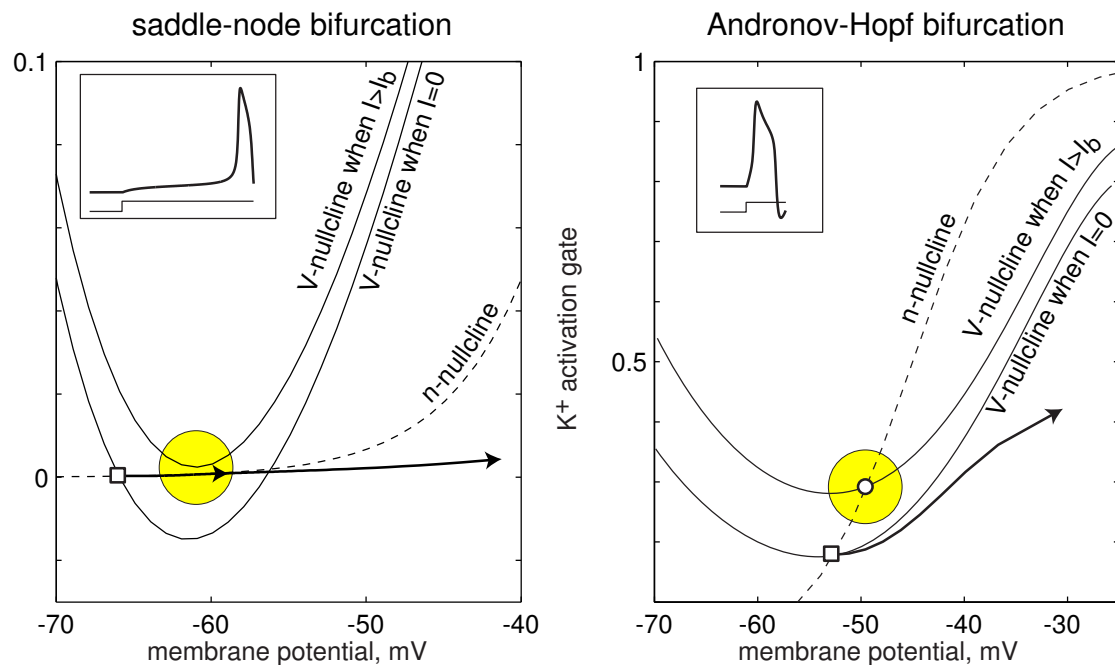


Figure 7.35: Bifurcation mechanism of latency to first spike when the injected dc-current steps from  $I = 0$  to  $I > I_b$ , where  $I_b$  is a bifurcation value. The shaded circle denotes the region where vector field is small. Shown are phase portraits of the  $I_{\text{Na,p}} + I_K$ -model.

2) Neuronal responses become less sensitive to noise, since only prolong inputs can cause spikes.

Interestingly, but resonators do not exhibit long latencies even though there is a neighborhood where the vector field is small and even zero, as we show in Fig. 7.35, right. When the current pulse is applied, the  $V$ -nullcline moves up and the voltage variable accelerates. However, it misses the shaded neighborhood, and the neuron fires an action potential practically without any latency. In Ex. 5 we discuss why some models near Andronov-Hopf bifurcation, including the Hodgkin-Huxley model in Fig. 7.26, seem to exhibit small but noticeable latencies. In Sect. 8.2.7 we show that latencies could result from slow charging of the dendritic compartment. In this case, integrators neurons exhibit latency to the first spike, while resonator neurons may exhibit latency to the second spike (after they fire the first, transient spike).

### 7.2.10 Flipping from an integrator to a resonator

One of the reasons we provided so many examples of neuronal systems in Chap. 5 is to convince the reader that all neuronal models can exhibit both saddle-node and Andronov-Hopf bifurcations, depending on the parameters describing the ionic currents. Since the kinetics of ionic currents in neurons could change during development or due to the action of neuromodulators, neurons could switch from being integrators to being resonators.

In Fig. 7.36 we illustrate an interesting case: Mitral cells in rat main olfactory bulb can exhibit bistability of membrane potential. That is, the potential can be in two states: down-state around  $-60$  mV, and up-state around  $-50$  mV (Heyward et al. 2001). A sufficiently strong synaptic input can shift the cell between these states in a matter of milliseconds. An amazing observation is that the down-state is a stable node and the up-state is a stable focus, as we illustrate at the bottom of the figure and study in detail in Sect. 8.4.5. As a result, mitral cells can be quickly switched from being integrators to being resonators by synaptic input.

Similar phenomenon was observed in a cerebella Purkinje neuron in Fig. 7.37. It acts as an integrator in the down-state, but has fast ( $> 100$  Hz) subthreshold oscillations in the up-state, and hence can act as a resonator.

Cortical pyramidal neurons can also exhibit up- and down-states, though the states are not intrinsic, but induced by the synaptic activity. Since the neurons are depolarized in the up-state, there is an interesting possibility that fast  $K^+$  conductances are partially activated and the fast  $Na^+$  inactivation gate is partially inactivated so that the neuron exhibits fast subthreshold oscillations and acts as a resonator. That is, integrator neurons could switch to the resonator mode when in the up-state. This possibility needs to be tested experimentally.

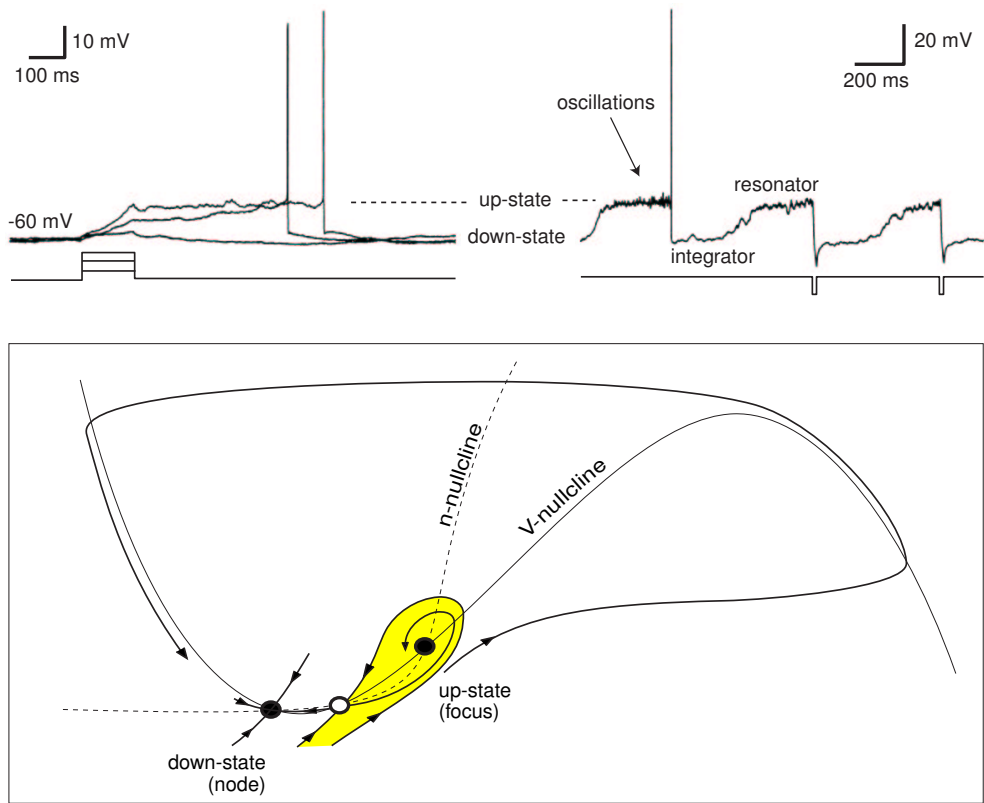


Figure 7.36: Bistability of the up- and down-state of mitral cells in rat main olfactory bulb. The cells are integrators in the down-state and resonators in the up-state. Membrane potential recordings are modified from Heyward et al. (2001). The shaded area denotes the attraction domain of the up-state.

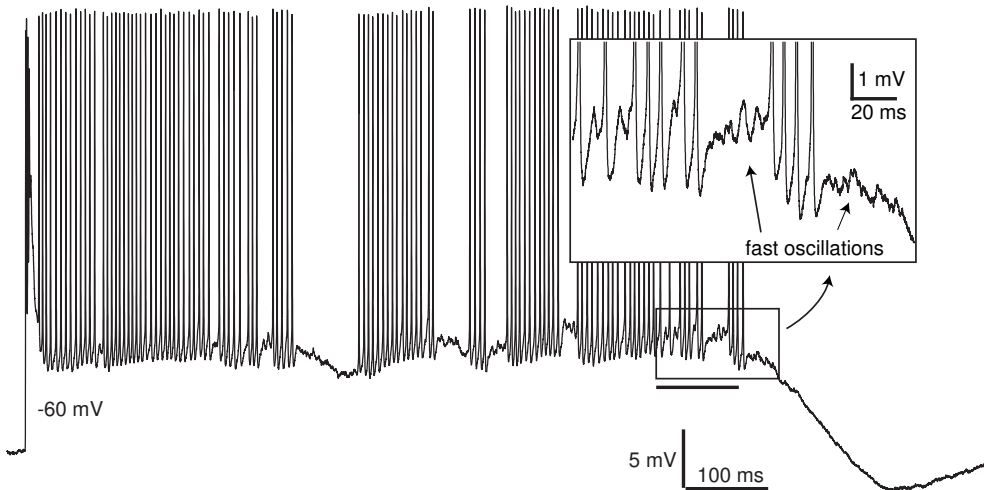


Figure 7.37: Fast subthreshold oscillations during complex spikes of cerebella Purkinje neuron of a guinea-pig (data was provided by Yonatan Loewenstein).

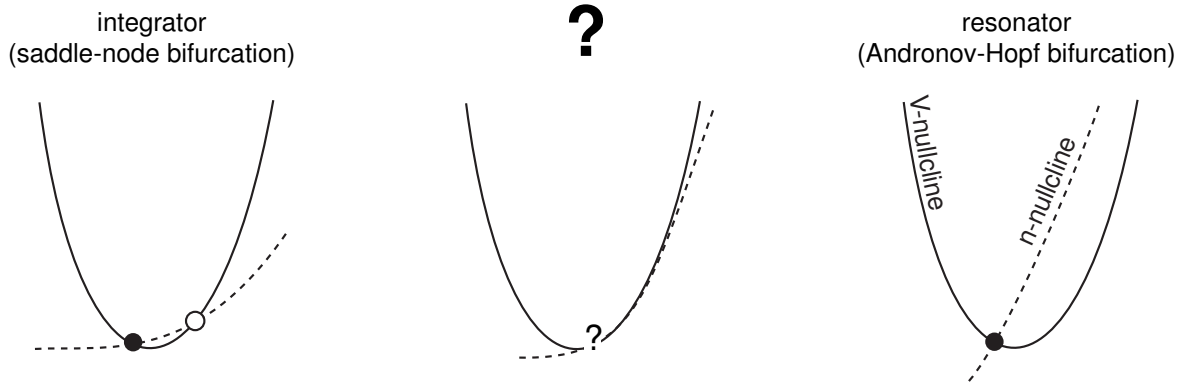


Figure 7.38: Is there an intermediate mode between integrators and resonators?

### 7.2.11 Transition between integrators and resonators

Consider the  $I_{\text{Na}} + I_{\text{K}}$ -model or any other minimal model from Chap. 5 that can exhibit saddle-node or Andronov-Hopf bifurcation, depending on the parameter values. Let us start with the  $I_{\text{Na}} + I_{\text{K}}$ -model near saddle-node bifurcation, and hence in the integrator mode. The intersection of its nullclines at the left knee is similar to the one in Fig. 7.38, left. Now, let us slowly change the parameters toward the values corresponding to the Andronov-Hopf bifurcation with the nullclines intersecting as in Fig. 7.38, right. At some point, the behavior of the model must change from integrator to a resonator mode. Is the change sudden, or is it gradual?

Any qualitative change of the behavior of the system is a bifurcation. Such a bifurcation should somehow combine the saddle-node and the Andronov-Hopf cases; That is, it should have a zero eigenvalue, and a pair of complex-conjugate eigenvalues with zero real part. Since the  $I_{\text{Na}} + I_{\text{K}}$ -model is two-dimensional, the only way these two conditions are satisfied is when the model undergoes the Bogdanov-Takens bifurcation considered in Sect. 6.3.3. This bifurcation has codimension 2, that is, it can be reliably observed when two parameters are changed, in our case  $E_{\text{leak}}$  and the half-voltage,  $V_{1/2}$ , of  $n_{\infty}(V)$ .

The top of Fig. 7.39 depicts the phase portrait of the  $I_{\text{Na}} + I_{\text{K}}$ -model at the Bogdanov-Takens bifurcation. Notice that the nullclines are tangent near the left knee, but the tangency is degenerate. A small change of the parameter  $V_{1/2}$  can result either in a saddle and a node (middle of the figure) or in a focus equilibrium (bottom of the figure). The neuron acts as an integrator in the former case and as a resonator in the latter case.

Due to the proximity to a codimension-2 bifurcation, the behavior of the  $I_{\text{Na}} + I_{\text{K}}$ -model is quite degenerate. That is, it could exhibit features that are normally not observed. For example, the integrator can exhibit post-inhibitory spiking, as in Fig. 7.40. This occurs because the shaded region in the figure, bounded by the stable manifold of the saddle, goes to the left of the resting state. An inhibitory pulse of current that hyperpolarizes the membrane potential to  $V < -65$  mV and deactivates

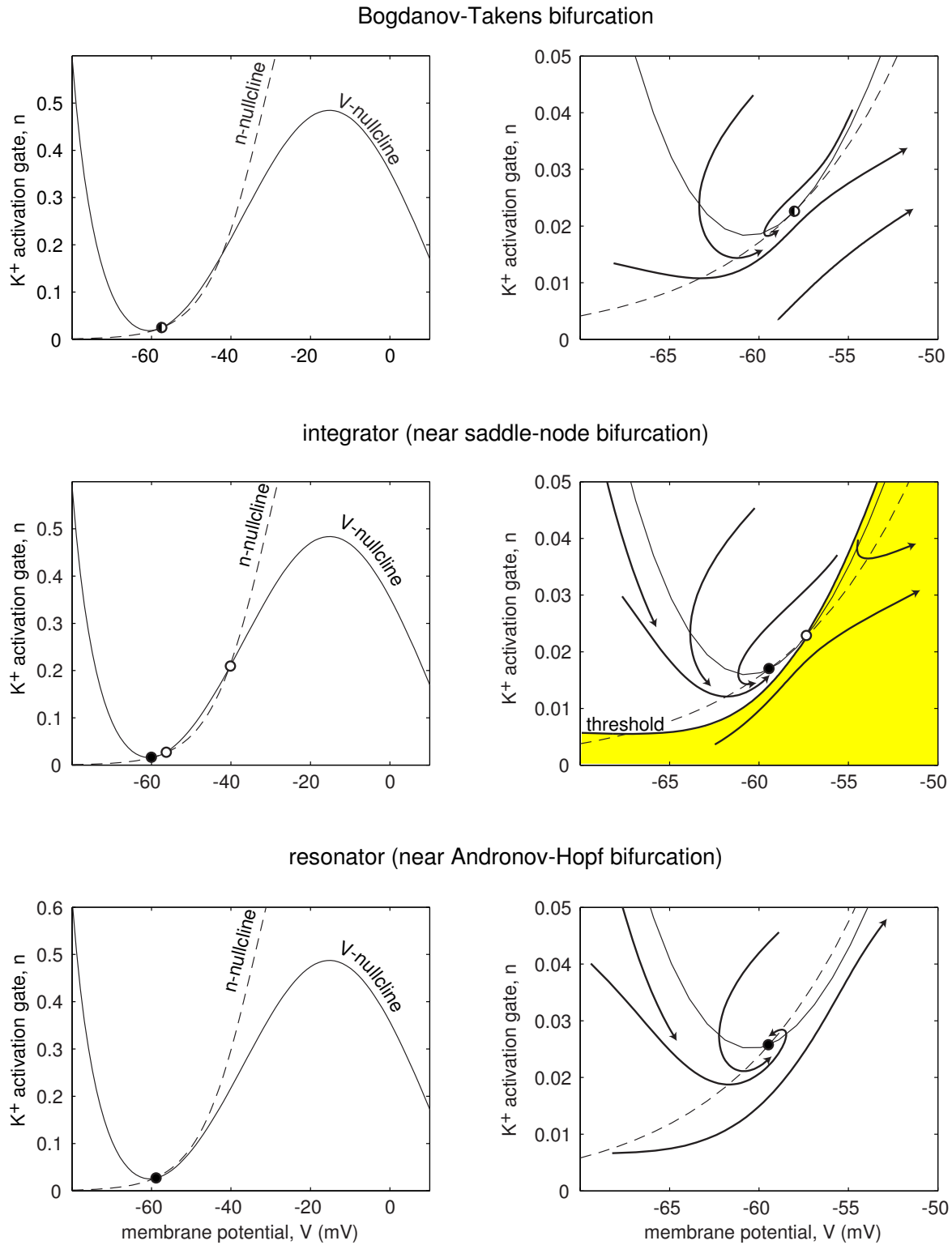


Figure 7.39: Bogdanov-Takens bifurcation in the  $I_{\text{Na}} + I_K$ -model (4.1, 4.2). Parameters as in Fig. 4.1a, except  $n_\infty(V)$  has  $k = 7$  mV and  $V_{1/2} = -31.64$  mV,  $E_{\text{leak}} = -79.42$  and  $I = 5$ . Integrator:  $V_{1/2} = -31$  mV and  $I = 4.3$ . Resonator:  $V_{1/2} = -34$  mV and  $I = 7$ .

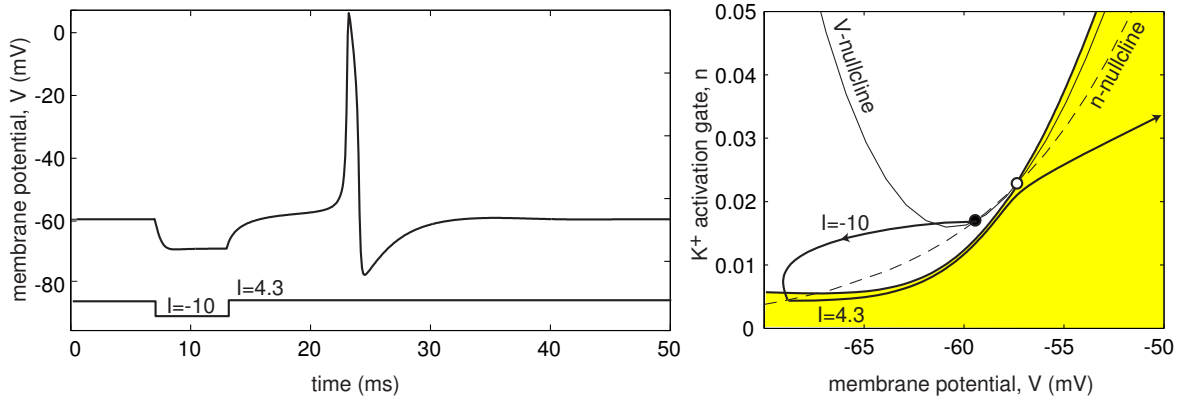


Figure 7.40: Post-inhibitory spike of an integrator neuron near Bogdanov-Takens bifurcation; see Fig. 7.39.

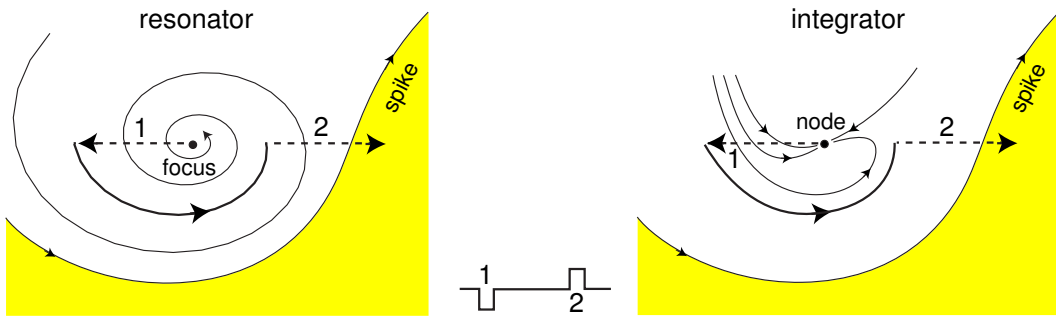


Figure 7.41: Post-inhibitory facilitation — enhancement of subthreshold depolarizing pulse (2) by preceding inhibitory pulse (1) — can occur in integrator neurons near Bogdanov-Takens bifurcation.

the  $K^+$  current to  $n < 0.005$  pushes the point  $(V, n)$  to the shaded region, i.e., beyond the threshold. Upon release from inhibition, the integrator neuron produces a rebound spike and then returns to the resting state.

Integrator neurons can also exhibit frequency preference and resonance, illustrated in Fig. 7.41. The post-inhibitory facilitation in resonator neurons in Fig. 7.41a was described in Sect. 7.2.7. It may happen in integrator neurons when the node equilibrium has nearly equal eigenvalues and nearly parallel eigenvectors, as in Fig. 7.41b. The former are about to become complex-conjugate resulting in rotation of the vector field around the equilibrium, and hence in the post-inhibitory rebound response to the first (inhibitory) pulse.

Resonator neurons near Bogdanov-Takens bifurcation can fire spikes with noticeable latencies. This occurs because the  $V$ -nullcline follows the  $n$ -nullcline at the focus equilibrium in Fig. 7.39, bottom. Such a proximity creates a “tunnel” with small vector field that slows down the spiking trajectory. Finally, the neuron can exhibit an oscillation (marked as P in Fig. 7.42, bottom) before firing a spike in response to

a pulse of current. Of course, these behaviors are difficult to catch experimentally, because the system must be near a codimension-2 bifurcation.

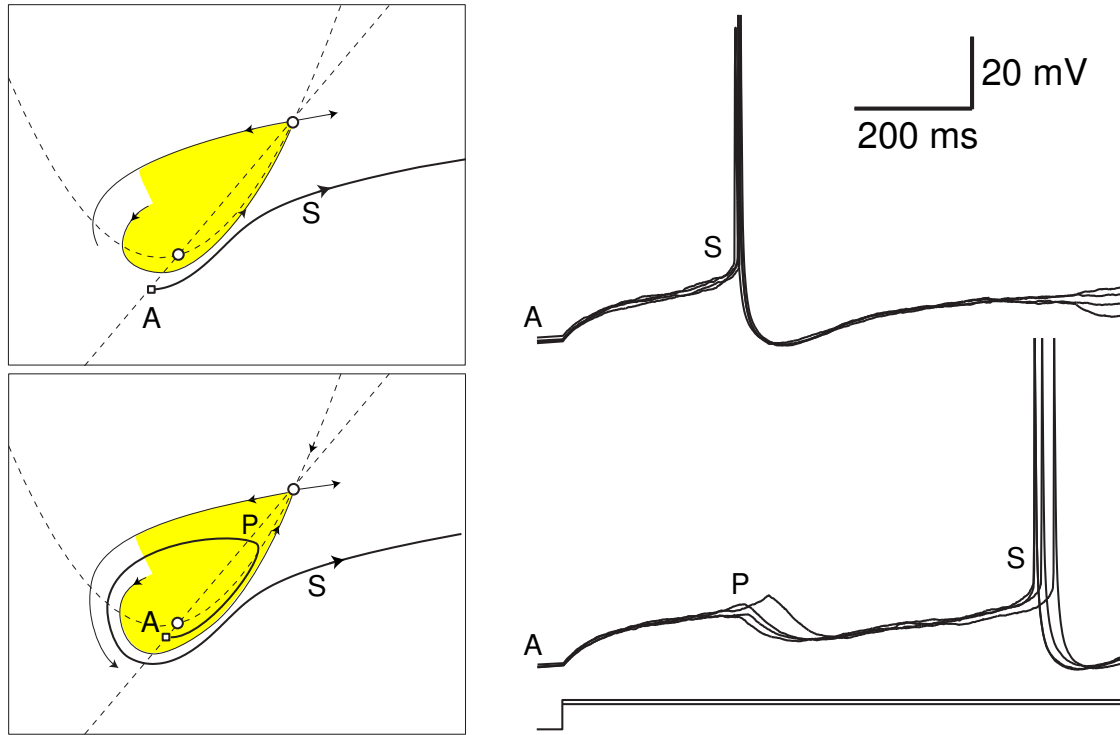


Figure 7.42: Proximity to Bogdanov-Takens bifurcation in layer 5 pyramidal neuron of rat primary visual cortex results in slow subthreshold oscillation before a spike. Shown are hand-drawn phase portrait and *in vitro* recordings obtained while an automated procedure was testing the neuronal rheobase.

### 7.3 Slow Modulation

So far we have considered neuronal models having voltage- or  $\text{Ca}^{2+}$ -gated conductances operating on a fast time scale comparable with the duration of a spike. Such conductances participate directly or indirectly in the generation of each spike and subsequent repolarization of the membrane potential. In addition, neurons have dendritic trees and some slow conductances and currents that may not be involved in the spike-generation mechanism directly, but rather modulate it. For example, some cortical pyramidal neurons have  $I_h$ , all thalamocortical neurons have  $I_h$  and  $I_{\text{Ca}(T)}$ . Activation and inactivation kinetics of these current is too slow to participate in the generation of up-stroke or down-stroke of a spike, but the currents can modulate spiking pattern, e.g., they can transform it into bursting.

To illustrate the phenomenon of slow modulation, we use the  $I_{\text{Na,p}} + I_K + I_{\text{K(M)}} -$

model

$$\begin{aligned} C\dot{V} &= \overbrace{I_{\text{Na,p}} + I_{\text{K-model}}}^{\text{I}_{\text{Na,p}} + \text{I}_{\text{K}}-\text{model}} - \overbrace{g_M n_M(V - E_K)}^{I_{\text{K(M)}}} \\ \dot{n} &= (n_\infty(V) - n)/\tau(V) \\ \dot{n}_M &= (n_{\infty,M}(V) - n_M)/\tau_M(V) \quad (\text{slow K}^+ \text{ M-current}) \end{aligned} \quad (7.1)$$

whose excitable and spiking properties are similar to those of the  $I_{\text{Na,p}} + I_{\text{K}}$ -submodel on a short time scale. However, the long-term behavior of the two models may be quite different. For example, the  $\text{K}^+$  M-current may result in frequency adaptation during a long train of action potentials. It can change the shape of the I-V relation of the model and result in slow oscillations, post-inhibitory spikes, and other resonator properties even when the  $I_{\text{Na,p}} + I_{\text{K}}$ -submodel is an integrator. All these interesting phenomena are discussed in this section.

In general, models having fast and slow currents, such as (7.1), can be written in the fast-slow form

$$\begin{aligned} \dot{x} &= f(x, u) && (\text{fast spiking}), \\ \dot{u} &= \mu g(x, u) && (\text{slow modulation}), \end{aligned} \quad (7.2)$$

where the vector  $x \in \mathbb{R}^m$  describes fast variables responsible for spiking. It includes the membrane potential  $V$ , activation and inactivation gating variables for fast currents, etc. The vector  $u \in \mathbb{R}^k$  describes relatively slow variables that modulate fast spiking, e.g., the gating variable of a slow  $\text{K}^+$  current, the intracellular concentration of  $\text{Ca}^{2+}$  ions, etc. The small parameter  $\mu$  represents the ratio of time scales between spiking and its modulation. Such systems often result in bursting activity, and we study them in detail in Chap. 9.

### 7.3.1 Spike-frequency modulation

Slow currents can modulate the instantaneous spiking frequency of a long train of action potentials, as we illustrate in Fig. 7.43a using recordings of a layer 5 pyramidal neuron. The neuron generates a train of spikes with increasing interspike interval (see inset in the figure) in response to a long pulse of injected dc-current. In Fig. 7.43b we plot the instantaneous interspike intervals  $T_i$ , i.e., the time intervals between spikes number  $i$  and  $i + 1$ , as a function of the magnitude of injected current  $I$ . Notice that  $T_i(I) < T_{i+1}(I)$ , meaning that the intervals increase with each spike. The function  $T_0(I)$  describes the latency of the first spike, and  $T_\infty(I)$  describes the steady-state (asymptotic) interspike period. The instantaneous frequencies are defined as  $F_i(I) = 1000/T_i(I)$  (Hz), and they are depicted in Fig. 7.43c. Since the neuron is Class 1 excitable, the F-I curves are square-root parabolas (see Sect. 6.1.2). Notice that  $F_0(I)$  is nearly a straight line, probably reflecting the passive charging of the dendritic tree.

Decrease of the instantaneous spiking frequency, as in Fig. 7.43, is referred to as *spike-frequency adaptation*. This is a prominent feature of cortical pyramidal neurons of the regular spiking (RS) type (Connors and Gutnick 1990), as well as many

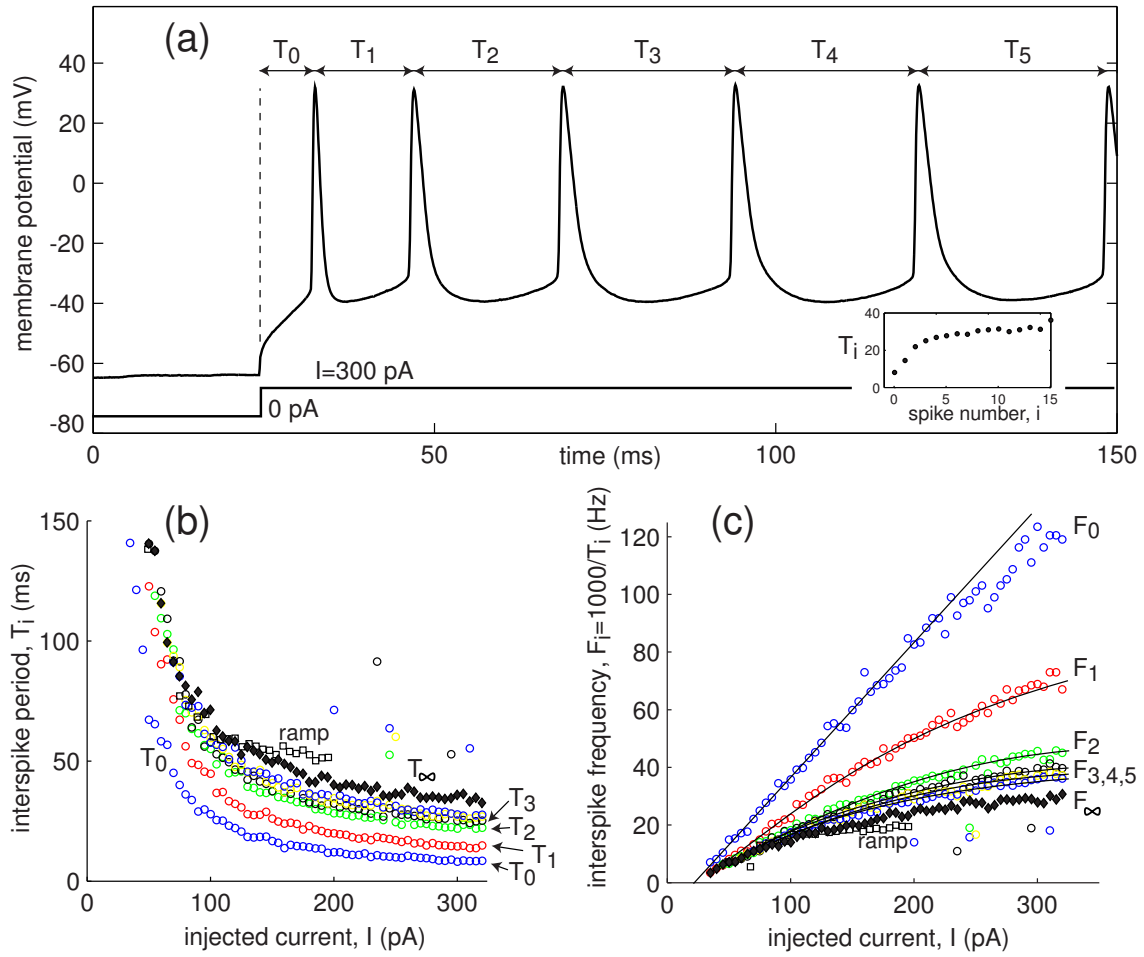


Figure 7.43: Spike-frequency adaptation in layer 5 pyramidal cell (see Fig. 7.3). Ramp data is from Fig. 7.6.

other types of neurons discussed in the next chapter. In contrast, cortical fast spiking (FS) interneurons (Gibson et al. 1999) exhibit *spike-frequency acceleration*, depicted in Fig. 7.44, i.e., the instantaneous interspike intervals decrease, and the frequency increases with each spike.

Whether a neuron exhibits spike frequency adaptation or acceleration depends on the nature of the slow current or currents and how they affect the spiking limit cycle of the fast subsystem. At the first glance, a resonant slow current, e.g., slowly activating  $K^+$  or slowly inactivating  $Na^+$  current, builds up during each spike and provides a negative feedback that should slow down spiking of the fast subsystem. Buildup of a slow amplifying current, e.g., slowly activating  $Na^+$  or inactivating  $K^+$  current, or slow charging of the dendritic tree should have the opposite effect. In Chap. 9, devoted to bursting, we will show that this simple rule works for many models, but there are also many exceptions. To understand how the slow subsystem modulates repetitive spiking, we need to consider bifurcations of the fast subsystem in (7.2), treating the

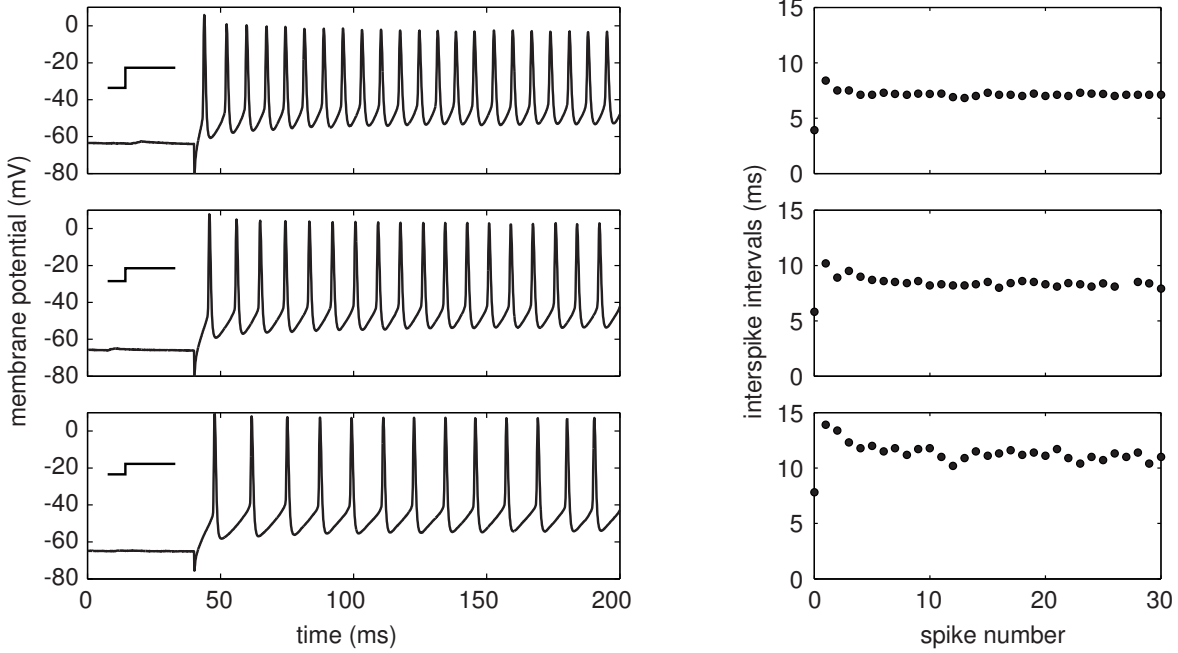


Figure 7.44: Spike-frequency acceleration of a cortical fast spiking (FS) interneuron. Data kindly provided by Barry Connors.

slow variable  $u$  as a bifurcation parameter.

### 7.3.2 I-V relation

Slow currents and conductances, though not responsible for the generation of spikes, can mask the true I-V relation of the fast subsystem in (7.2) responsible for spiking. Take, for example, the  $I_{Na,p}+I_K$ -model with parameters as in Fig. 4.1a (high-threshold  $K^+$  current), so that its I-V curve is non-monotonic with a region of negative slope depicted in Fig. 7.45a. Such a system is near saddle-node on invariant circle bifurcation and it acts as an integrator. Now add a slow  $K^+$  M-current with I-V relation depicted as a dashed curve in the figure and a time constant  $\tau_M = 100$  ms. The spike-generating mechanism of the combined  $I_{Na,p}+I_K+I_{K(M)}$ -model is described by the fast  $I_{Na,p}+I_K$ -submodel, so that the neuron continues to have integrator properties, at least on the millisecond time scale. However, the asymptotic I-V relation  $I_\infty(V)$  is dominated by the strong  $I_{K(M)}(V)$  and it is monotonic, as if the  $I_{Na,p}+I_K+I_{K(M)}$ -model is a resonator. The model can indeed exhibit some resonance properties, such as post-inhibitory (rebound) responses, but only on the long time scale of hundreds of milliseconds, i.e., on the time scale of the slow  $K^+$  M-current.

Similarly, we can take a resonator model with a monotonic I-V relation and add a slow amplifying current or a gating variable to get a non-monotonic  $I_\infty(V)$ , as if the model becomes an integrator. For example, in Fig. 7.45b we use the  $I_{Na,p}+I_K$ -model with parameters as in Fig. 4.1b (low-threshold  $K^+$  current) and add an inactivation

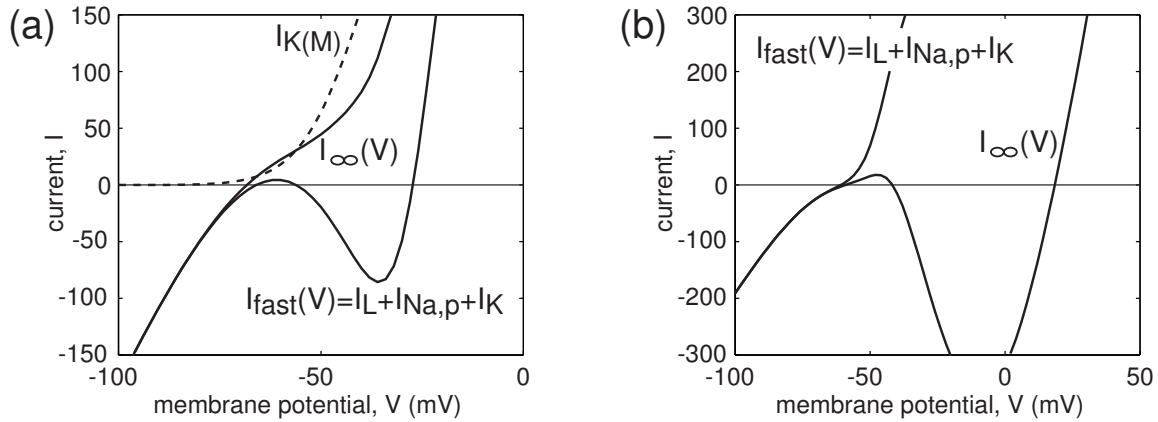


Figure 7.45: Slow conductances can mask the true I-V relation of the spike-generating mechanism. (a) The  $I_{\text{Na},p} + I_K$ -model with parameters as in Fig. 4.1a has a non-monotonic I-V curve  $I_{\text{fast}}(V)$ . Addition of the slow K<sup>+</sup> M-current with parameters as in Sect. 2.3.5 and  $g_M = 5$  (dashed curve) makes the asymptotic I-V relation,  $I_\infty(V)$ , of the full  $I_{\text{Na},p} + I_K + I_{K(M)}$ -model monotonic. (b) Addition of a slow inactivation gate to the K<sup>+</sup> current of the  $I_{\text{Na},p} + I_K$ -model with parameters as in Fig. 4.1b results in a non-monotonic asymptotic I-V relation of the full  $I_{\text{Na},p} + I_A$ -model.

gate to the persistent K<sup>+</sup> current, effectively transforming it into transient A-current. If the inactivation kinetics is sufficiently slow, the  $I_{\text{Na},p} + I_A$ -model retains resonator properties on the millisecond time scale, i.e., on the time scale of individual spikes. However, its asymptotic I-V relation, depicted in Fig. 7.45b, becomes non-monotonic. Besides spike-frequency acceleration, the model acquires another interesting property — bistability. A single spike does not deactivate  $I_A$  significantly. A burst of spikes could deactivate the K<sup>+</sup> A-current to such a degree that repetitive spiking becomes sustained. Slow inactivation of the A-current is believed to facilitate the transition from down- to up-states in neocortical and neostriatal neurons.

When a neuronal model consists of conductances operating on drastically different time scales, it has multiple I-V relations, one for each time scale. We illustrate this phenomenon in Fig. 7.46 using the  $I_{\text{Na},p} + I_K + I_{K(M)}$ -model with activation time constant of 0.01 ms for  $I_{\text{Na},p}$ , 1 ms for  $I_K$ , and 100 ms for  $I_{K(M)}$ . The up-stroke of an action potential is described only by leak and persistent Na<sup>+</sup> currents, since the K<sup>+</sup> currents do not have enough time to activate during such a short event. During the up-stroke, the model can be reduced to a one-dimensional system (see Chap. 3) with instantaneous I-V relation  $I_0(V) = I_{\text{leak}} + I_{\text{Na},p}(V)$  depicted in Fig. 7.46a. The dynamics during and immediately after the action potential is described by the fast  $I_{\text{Na},p} + I_K$ -subsystem with its I-V relation  $I_{\text{fast}}(V) = I_0(V) + I_K(V)$ . Finally, the asymptotic I-V relation,  $I_\infty(V) = I_{\text{fast}}(V) + I_{K(M)}(V)$ , takes into account all currents in the model.

The three I-V relations determine the fast, medium, and asymptotic behavior of a neuron in a voltage-clamp experiment. If the time scales are well separated (they are in Fig. 7.46), all three I-V relations can be measured from a simple voltage-clamp

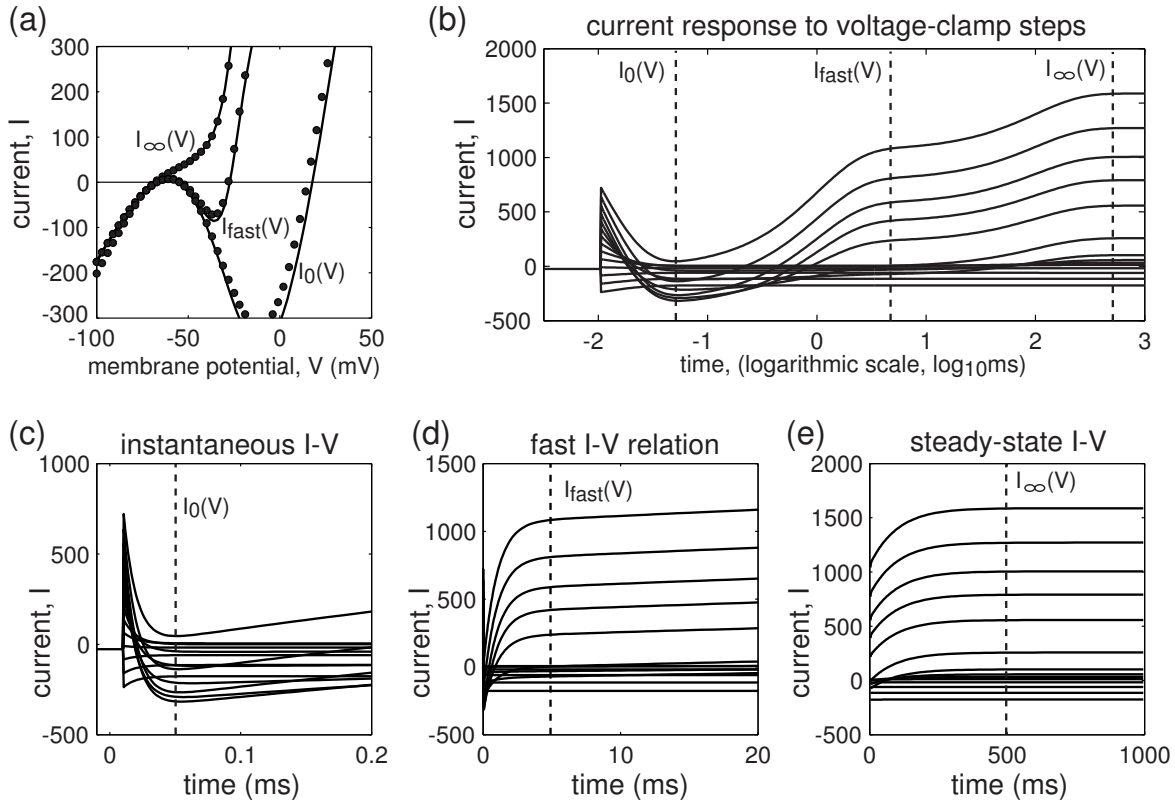


Figure 7.46: (a) The  $I_{\text{Na,p}} + I_K + I_{K(M)}$ -model in Fig. 7.45a has three I-V relations: Instantaneous  $I_0(V) = I_{\text{leak}}(V) + I_{\text{Na,p}}(V)$  describes spike upstroke dynamics. The curve  $I_{\text{fast}}(V) = I_0(V) + I_K(V)$  is the I-V relation of the fast  $I_{\text{Na,p}} + I_K$ -subsystem responsible for spike-generating mechanism. The curve  $I_\infty(V) = I_{\text{fast}}(V) + I_{K(M)}(V)$  is the steady-state (asymptotic) I-V relation of the full model. Dots denote values obtained from a simulated voltage-clamp experiment in (b); notice the logarithmic time scale. Magnifications of current responses are shown in (c,d,e). Simulated time constants:  $\tau_{\text{Na,p}}(V) = 0.01$  ms,  $\tau_K(V) = 1$  ms,  $\tau_M(V) = 100$  ms.

experiment, depicted in Fig. 7.46b. We hold the model at  $V = -70$  mV and step the command voltage to various values. The values of the current, taken at  $t = 0.05$  ms,  $t = 5$  ms, and  $t = 500$  ms in Fig. 7.46b, result in the instantaneous, fast, and steady-state I-V curves, respectively. Notice that the data in Fig. 7.46b are plotted on the logarithmic time scale. Various magnifications using the linear time scale are depicted in Fig. 7.46c,d, and e. Numerically obtained values of the three I-V relations are depicted as dots in Fig. 7.46a. They approximate the theoretical values quite well because there is a 100-fold separation of time scales in the model.

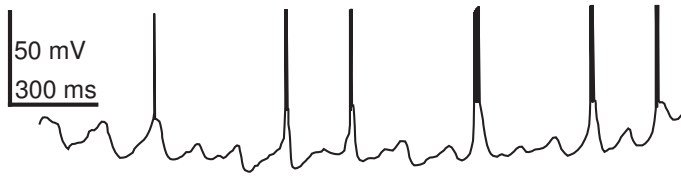


Figure 7.47: Slow subthreshold oscillation of membrane potential of cat thalamocortical neuron evoked by slow hyperpolarization (modified from Roy et al. 1984).

### 7.3.3 Slow Subthreshold oscillation

Interactions between fast and slow conductances can result in low-frequency subthreshold oscillation of membrane potential, such as the one in Fig. 7.47, even when the fast subsystem is near a saddle-node bifurcation, acts as an integrator, and cannot have subthreshold oscillations. The oscillation in Fig. 7.47 is caused by the interplay between activation and inactivation of the slow  $\text{Ca}^{2+}$  T-current and inward h-current, and it is a precursor of bursting activity, which we consider in detail in Chap. 9.

There exist three different mechanisms of *slow* subthreshold oscillations of membrane potential of a neuron.

- The fast subsystem responsible for spiking has a small-amplitude subthreshold limit cycle attractor. The period of the limit cycle may be much larger than the time scale of the slowest variable of the fast subsystem when the cycle is near saddle-node on invariant circle, saddle homoclinic orbit bifurcation, or Bogdanov-Takens bifurcation considered in Chap. 6. In this case, no slow currents or conductances modulating the fast subsystem are needed. However, such a cycle must be near the bifurcation, hence the low-frequency subthreshold oscillation exists in a narrow parameter range and it is difficult to be seen experimentally.
- The I-V relation of the fast subsystem has N-shape in the subthreshold voltage range, so that there are two stable equilibria corresponding to two resting states, as e.g., in Fig. 7.36. A slow resonant variable switches the fast subsystem between those two states via a hysteresis loop resulting in a subthreshold slow relaxation oscillation.
- If the fast subsystem has a monotonic I-V relation, then a stable subthreshold oscillation can result from the interplay between slow variables.

The first cases does not need any slow variables, the second case needs only one slow variable, whereas the third case needs at least two. Indeed, one slow variable is not enough because the entire system can be reduced to a one-dimensional slow equation.

### 7.3.4 Rebound response and voltage sag

A slow resonant current can cause a neuron to fire a rebound spike or a burst in response to a sufficiently long hyperpolarizing current, even when the spike-generating mecha-

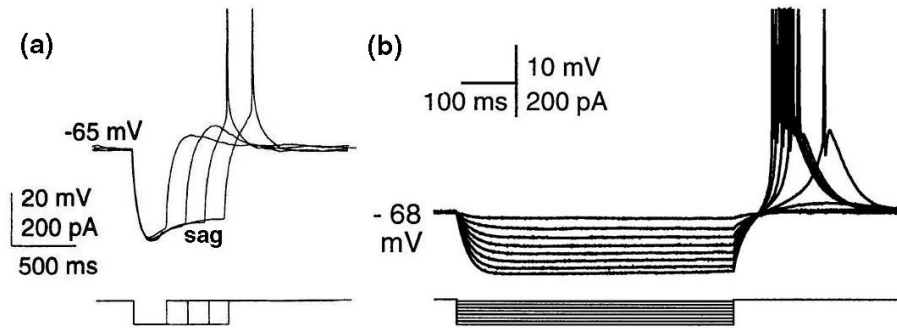


Figure 7.48: Rebound responses to long inhibitory pulses in (a) pyramidal neuron of sensorimotor cortex of juvenile rat (modified from Hutcheon et al. 1996) and (b) rat auditory thalamic neurons (modified from Tennigkeit et al. 1997).

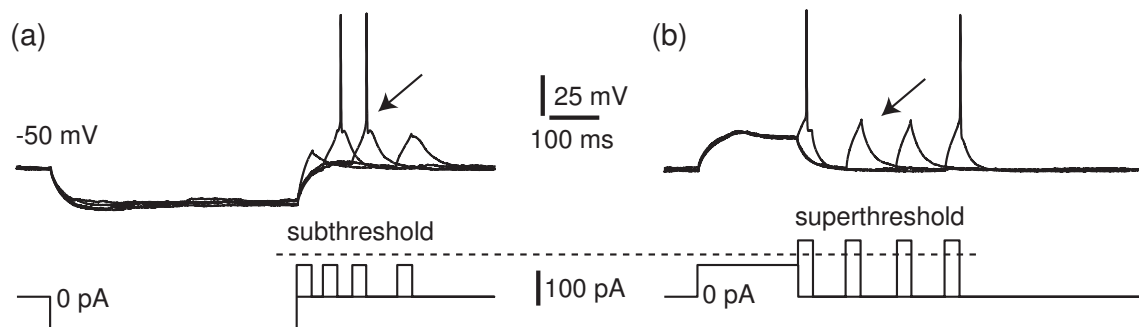


Figure 7.49: Post-inhibitory facilitation (a) and post-excitatory depression (b) in a layer 5 pyramidal neuron (IB type) of rat visual cortex recorded *in vitro* in response to a long hyperpolarizing pulse.

nism of the neuron is near a saddle-node bifurcation and hence has neuro-computational properties of an integrator. For example, the cortical pyramidal neuron in Fig. 7.48a has a slow resonant current  $I_h$ , which opens by hyperpolarization. A short pulse of current does not open enough of  $I_h$  and results only in a small subthreshold rebound potential. In contrast, a long pulse of current opens enough  $I_h$ , resulting in a strong inward current that produces the voltage sag and, upon termination of stimulation, drives the membrane potential over the threshold.

Similarly, the thalamocortical neuron in Fig. 7.48b has a low-threshold  $\text{Ca}^{2+}$  T-current  $I_{\text{Ca}(T)}$  that is partially activated but completely inactivated at rest. A negative pulse of current hyperpolarizes the neuron and deinactivates the T-current, thereby making it available to generate a spike. Notice that there is no voltage sag in Fig. 7.48b because the T-current is deactivated at low membrane potentials. Upon termination of the long pulse of current, the membrane potential returns to the resting state around  $-68 \text{ mV}$ , the  $\text{Ca}^{2+}$  T-current activates and drives the neuron over the threshold. A distinctive feature of thalamocortical neurons is that they fire a rebound burst of spikes in response to strong negative currents.

Even when the rebound depolarization is not strong enough to elicit a spike, it

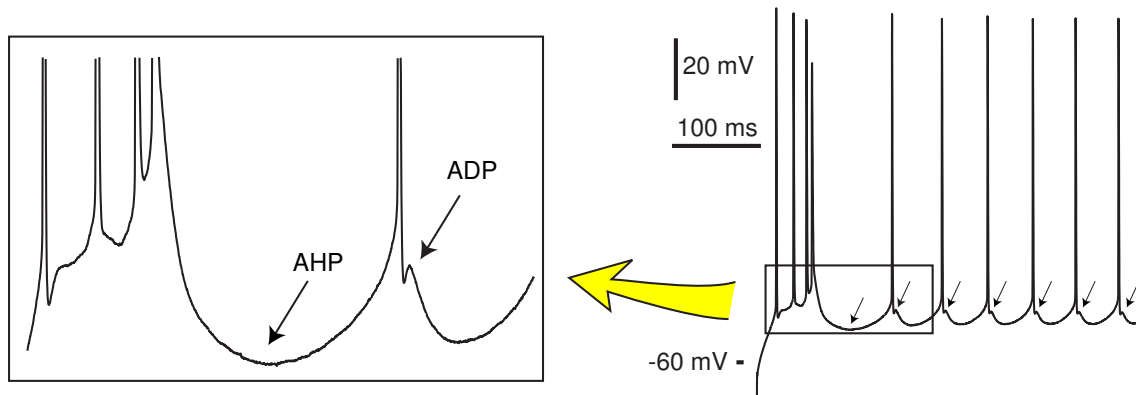


Figure 7.50: Afterhyperpolarizations (AHP) and afterdepolarizations (ADP) in intrinsically bursting (IB) pyramidal neurons of the rat motor cortex recorded *in vitro*.

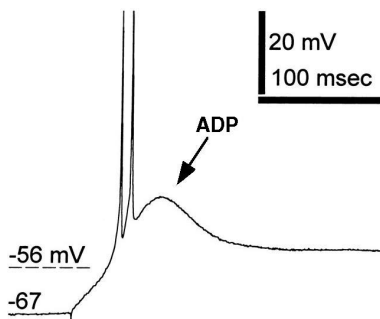


Figure 7.51: Rebound spikes and afterdepolarization (marked ADP) at the break of hyperpolarizing current in thalamocortical neurons of the cat dorsal lateral geniculate nucleus. (Data modified from Pirchio et al. 1997, resting potential is  $-56$  mV, holding potential is  $-67$  mV).

may increase the excitability of the neuron, so that it fires a spike to an otherwise subthreshold stimulus, as in Fig. 7.49a. This type of post-inhibitory facilitation relies on the slow currents, and not on the resonant properties of the spike-generation mechanism (as in Fig. 7.31). Figure 7.49b demonstrates the inverse property, post-excitatory depression, i.e., a decreased excitability after a transient depolarization. In this seemingly counterintuitive case, a superthreshold stimulation becomes subthreshold when it is preceded by a depolarized pulse, because the pulse partially inactivates  $\text{Na}^+$  current and/or activates  $\text{K}^+$  current.

### 7.3.5 AHP and ADP

The membrane potential may undergo negative and positive deflections right after the spike, as illustrated in Fig. 7.50 and Fig. 7.51. These are known as *afterhyperpolarizations* (AHP) and *afterdepolarizations* (ADP). The latter are sometimes called *depolarizing after-potentials* (DAP). A great effort is usually made to determine the ionic basis of AHPs and ADPs, since it is often implicitly assumed that they are generated by slow currents that turn on right after the spike, such as slow  $\text{Ca}^{2+}$ -gated  $\text{K}^+$  current  $I_{\text{AHP}}$  or slow persistent  $\text{Na}^+$  current, respectively. Below we discuss these and other alternative mechanisms.

Let us consider the AHP first. Each spike in the initial burst in Fig. 7.50 presumably

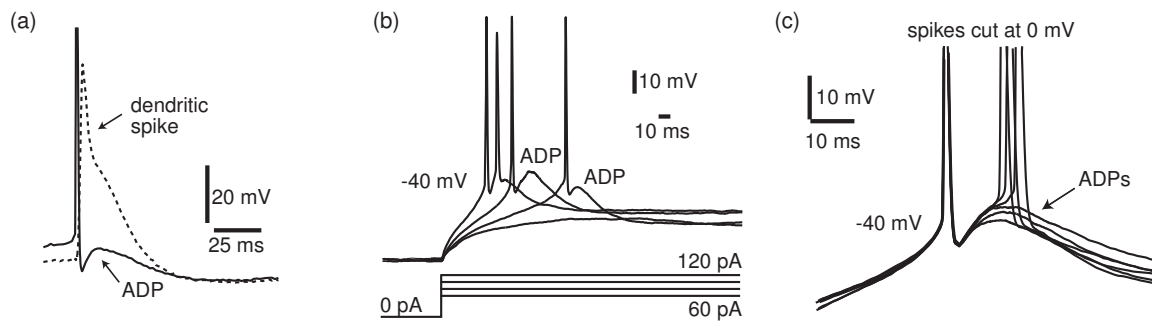


Figure 7.52: (a) Somatic spike evokes dendritic spike, which in turn produces afterdepolarization (ADP) in the soma of the pyramidal neuron of rat somatosensory cortex (*in vitro* recording was provided Greg Stuart and Maarten Kole). (b) and (c) Increased level of depolarization in another neuron (the same as in Fig. 7.49) converts ADP to a second spike.

activates a slow voltage- or  $\text{Ca}^{2+}$ -dependent outward  $\text{K}^+$  current, which eventually stops the burst and hyperpolarizes the membrane potential. During the AHP period, the slow outward current deactivates and the neuron can fire again. The neuron can switch from bursting to tonic spiking mode due to the incomplete deactivation of the slow current. The same explanation holds if we substitute “activation of outward” by “inactivation of inward” current.

Similarly, slow inactivation of the transient  $\text{Ca}^{2+}$  T-current explains the rebound response and the long afterdepolarization (marked ADP) in Fig. 7.51: The current was deinactivated by the preceding hyperpolarization, so upon release from the hyperpolarization, it quickly activates and slowly inactivates, thereby producing a slow depolarizing wave on which fast spikes can ride. The ADP seen in the figure is the tail of the wave.

Probably the most common mechanism of ADPs is due to the dendritic spikes, at least in pyramidal neurons of neocortex and hippocampus considered in the next chapter. In Fig. 7.52a we depict dual somatic/dendritic recording of membrane potential of a pyramidal neuron. The somatic spike backpropagates into the dendritic tree, activates voltage-gated conductances there, and results in a slower dendritic spike. The latter depolarizes the soma and produces a noticeable ADP. Recordings of another neuron in Fig. 7.52b and c show that if there is an additional source of depolarization, such as the injected dc-current, the ADPs can grow and result in a second spike. This may evoke another dendritic spike, another ADP or spike, etc., resulting in a bursting activity discussed in Sect. 8.2.2.

Slow ADPs can also be generated due to a nonlinear interplay of fast currents responsible for spiking, rather than due to slow currents or dendritic spikes. One obvious example is the damped oscillation of membrane potential of the  $I_{\text{Na,p}} + I_{\text{K}}$ -model in Fig. 7.53 right after the spike, with the trough and the peak corresponding to an AHP and an ADP, respectively. Notice that the duration of the ADP is ten times the duration of the spike even though the model does not have any slow currents. Such

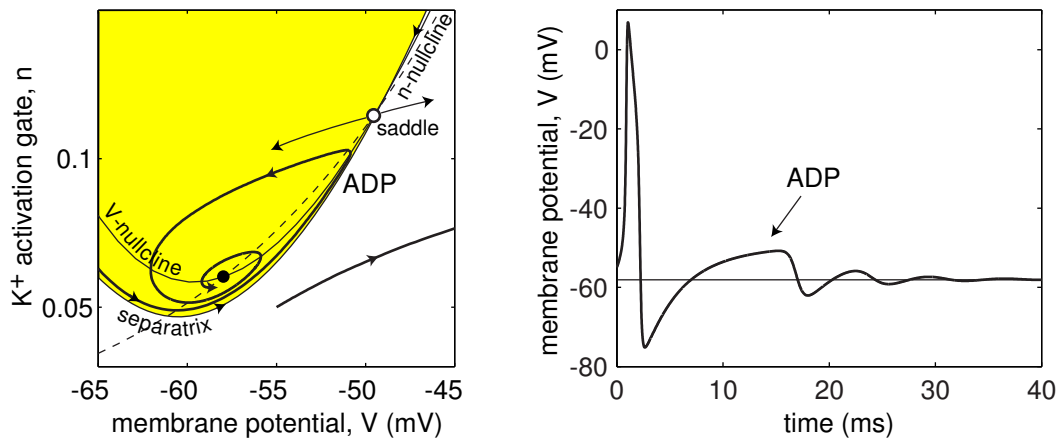


Figure 7.53: A long afterdepolarization (ADP) in the  $I_{Na,p} + I_K$ -model without any slow currents. Parameters as in Fig. 6.52.

a long-lasting effect appears because the trajectory follows the separatrix, comes close to the saddle point, and spends some time there before returning to the stable resting state.

An example in Fig. 7.54 shows the membrane potential of a model neuron slowly passing through a saddle-node on invariant circle bifurcation. Because the vector field is small at the bifurcation, which takes place around  $t = 70$  ms, the membrane potential is slowly increasing along the limit cycle and then slowly decreasing along the locus of stable node equilibria, thereby producing a slow ADP. In Chap. 9 we will show that such ADPs exist in 4 out of 16 basic types of bursting neurons, including thalamocortical relay neurons and R<sub>15</sub> bursting cells in the abdominal ganglion of the mollusk *Aplysia*.

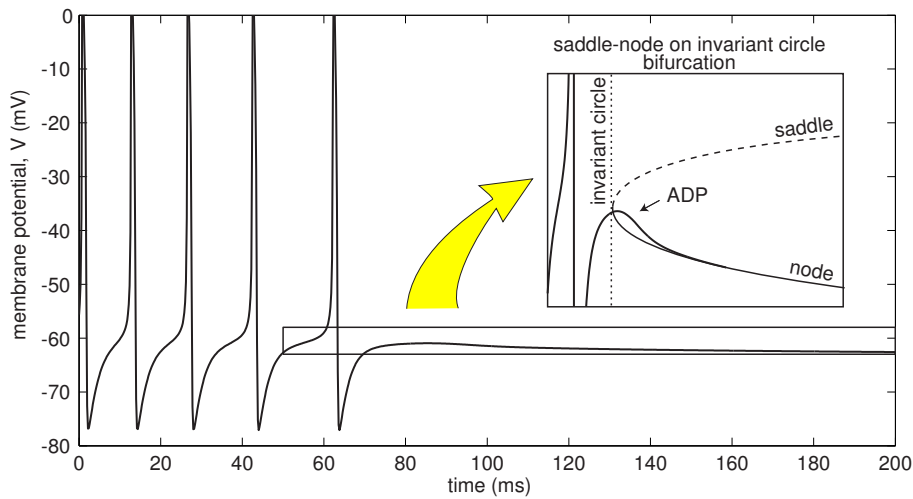


Figure 7.54: Afterdepolarization in the  $I_{Na,p}+I_K$ -model passing slowly through saddle-node on invariant circle bifurcation, as the magnitude of the injected current ramps down.

## Review of Important Concepts

- A neuron is excitable because, as a dynamical system, it is near a bifurcation from resting to spiking activity.
- The type of bifurcation determines the neuron's computational properties, summarized in Fig. 7.15.
- Saddle-node *on* invariant circle bifurcation results in Class 1 excitability: the neuron can fire with arbitrary small frequency and encode the strength of input into the firing rate.
- Saddle-node *off* invariant circle and Andronov-Hopf bifurcations result in Class 2 excitability: the neuron can fire only within a certain frequency range.
- Neurons near saddle-node bifurcation are integrators: they prefer high-frequency excitatory input, have well-defined thresholds, and fire all-or-none spikes with some latencies.
- Neurons near Andronov-Hopf bifurcation are resonators: they have oscillatory potentials, prefer resonant-frequency input, and can easily fire post-inhibitory spikes.

## Bibliographical Notes

There is no universally accepted definition of excitability. Our definition is consistent with the one involving  $\varepsilon$ -pseudo-orbits (Izhikevich 2000). R. FitzHugh (1955, 1960, 1976) pioneered geometrical analyses of phase portraits of neuronal models with the view to understand their neuro-computational properties. It is amazing that such important neuro-computational properties as all-or-none action potentials, firing thresholds, and integration of EPSPs are still introduced and illustrated using the Hodgkin-Huxley model, which according to FitzHugh, cannot have these properties. Throughout this chapter we follow Izhikevich (2000) to compare and contrast neuro-computational properties of integrators and resonators.

The frozen noise experiment in Fig. 7.24 was pioneered by Bryant and Segundo in 1976, but due to an interesting quirk of history, it is better known at present as the Mainen-Sejnowski (1995) experiment (despite the fact that the latter paper refers to the former). Post-inhibitory facilitation was pointed out by Luk and Aihara (2000), Izhikevich (2001). John Rinzel suggested to call it “post-inhibitory exaltation” (in a similar vein, the phenomenon in Fig. 7.49b may be called “post-excitatory hesitation”). Richardson et al. (2003) pointed out that frequency preference and resonance occurs without subthreshold oscillations when the system is near the transition from an integrator to a resonator.

The Hodgkin’s classification of neuronal excitability can be applied to classify any rhythmic system, e.g., contractions of uterus during labor. Typically, the contractions start with low frequency that gradually increases — Class 1 excitability. The author’s wife had to be induced pharmacologically to evoke labor contractions, which is a typical medical intervention when the baby is overdue. The contraction monitor showed a sinusoidal signal with constant period, around 2 minutes, but slowly growing amplitude — Class 2 excitability via supercritical Andronov-Hopf bifurcation! Since the mother had an advance degree in applied mathematics, the author waited for a 1-minute period of quiescence between the contractions and managed to explain to the delivering mother the basic relationship between bifurcations and excitability. Five years later, induced delivery of the author’s second daughter resulted in the same supercritical Andronov-Hopf bifurcation. The author reminded this concept to the mother and explained it to the obstetrician minutes after the delivery.

## Exercises

1. When can the FitzHugh-Nagumo model (4.11, 4.12) exhibit inhibition-induced spiking, such as the one in Fig. 7.32?
2. (French ducks) Numerically investigate the quasi-threshold in the FitzHugh-Nagumo model (4.11, 4.12). How is it related to the French duck (canard; see Eckhaus 1983) limit cycles discussed in Sect. 6.3.4?

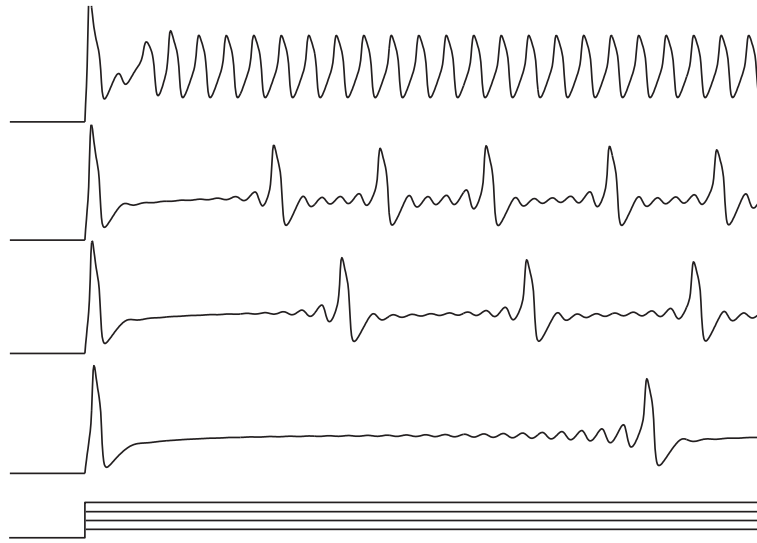


Figure 7.55: Ex. 6: Zero frequency firing near subcritical Andronov-Hopf bifurcation in the  $I_{\text{Na,p}}+I_K$ -model with parameters as in Fig. 6.16 and a high-threshold slow  $K^+$  current ( $g_{K,\text{slow}} = 25$ ,  $\tau_{K,\text{slow}} = 10$  ms,  $n_{\infty,\text{slow}}(V)$  has  $V_{1/2} = -10$  mV and  $k = 5$  mV.)

3. (Noise-induced oscillations) Consider the system

$$\dot{z} = (-\varepsilon + i\omega)z + \varepsilon I(t), \quad z \in \mathbb{C} \quad (7.3)$$

which has a stable focus equilibrium  $z = 0$  and is subject to a weak noisy input  $\varepsilon I(t)$ . Show that the system exhibits sustained noisy oscillations with an average amplitude  $|I^*(\omega)|$ , where

$$I^*(\omega) = \lim_{T \rightarrow \infty} \frac{1}{T} \int_0^T e^{-i\omega t} I(t) dt$$

is the Fourier coefficient of  $I(t)$  corresponding to the frequency  $\omega$ .

4. (Frequency preference) Show that a system exhibiting damped oscillation with frequency  $\omega$  is sensitive to an input having frequency  $\omega$  in its power spectrum. (Hint: use Ex. 3.)
5. (Rush and Rinzel 1996) Use the phase portrait of the reduced Hodgkin-Huxley model in Fig. 5.21 to explain some small but noticeable latencies in Fig. 7.26.
6. The neuronal model in Fig. 7.55 has a high-threshold slow persistent  $K^+$  current. Its resting state undergoes a subcritical Andronov-Hopf bifurcation, yet it can fire low-frequency spikes, and hence exhibits Class 1 excitability. Explain. (Hint: Show numerically that the model is near a certain codimension-2 bifurcation involving a homoclinic orbit).

7. Show that the resting state of a Class 3 excitable conductance-based model is near an Andronov-Hopf bifurcation if some other variable, not  $I$ , is used as a bifurcation parameter.

# Chapter 8

## Simple Models

The advantage of using conductance-based models, such as the  $I_{\text{Na}}+I_{\text{K}}$ -model, is that each variable and parameter has a well-defined biophysical meaning. In particular, they could be measured experimentally. The drawback is that the measurement procedures may not be accurate, that the parameters are usually measured in different neurons, averaged, and then fine-tuned (a fancy word meaning “to make arbitrary choices”). As a result, the model does not have the same behavior as one sees in experiments. And even if it “looks” OK, there is no guarantee that the model is accurate from the dynamical systems point of view, i.e., that it exhibits the same kind of bifurcations as the type of neuron under consideration.

Sometimes we do not need or cannot afford to have a biophysically detailed conductance-based model. Instead, we want a simple model that faithfully reproduces all the neuro-computational features of the neuron. In this chapter we review salient features of cortical, thalamic, and other neurons, and we present simple models that capture the essence of their behavior from the dynamical systems point of view.

### 8.1 Simplest Models

Let us start with reviewing the simplest possible models of neurons. As one can guess from their names, the integrate-and-fire and resonate-and-fire neurons capture the essence of integrators and resonators. The models are similar in many respects: both are described by linear differential equations, both have a hard firing threshold and a reset, both have a unique stable equilibrium at rest. The only difference is that the equilibrium is a node in the integrate-and-fire case, but it is a focus in the resonate-and-fire case. One can model the former using only one equation, and the latter using only two equations, though multi-dimensional extensions are straightforward. Both models are useful from the analytical point of view, i.e., to prove theorems.

Many scientists, including the author of this book, refer to these neural models as being “spiking models”. The models have a threshold, but they lack any spike-generation mechanism, i.e., they cannot produce a brief regenerative depolarization of membrane potential corresponding to the spike up-stroke. Therefore, they are not

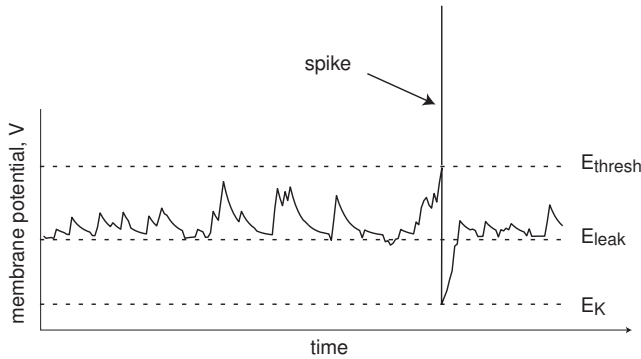


Figure 8.1: Leaky integrate-and-fire neuron with noisy input. The spike is added manually for aesthetic purposes and to fool the reader into believing that this is a spiking neuron.

“spiking models”; the spikes in the next two figures, as well as in hundreds of scientific papers devoted to these models, are drawn by hand. The quadratic integrate-and-fire model is the simplest truly spiking model.

### 8.1.1 Integrate-and-fire

The leaky integrate-and-fire model (Lapicque 1907, Stein 1967, Tuckwell 1988) is an idealization of a neuron having Ohmic leakage current and a number of voltage-gated currents that are completely de-activated at rest. Subthreshold behavior of such a neuron can be described by the linear differential equation

$$C\dot{V} = I - \underbrace{g_{\text{leak}}(V - E_{\text{leak}})}_{\text{Ohmic leakage}},$$

where all parameters have the same biophysical meanings as in the previous chapters. When the membrane potential  $V$  reaches the threshold value  $E_{\text{thresh}}$ , the voltage-sensitive currents instantaneously activate, the neuron is said to fire an action potential, and  $V$  is reset to  $E_K$ , as in Fig. 8.1. After appropriate re-scaling, the leaky integrate-and-fire model can be written in the form

$$\dot{v} = b - v, \quad \text{if } v = 1, \text{ then } v \leftarrow 0, \quad (8.1)$$

where the resting state is  $v = b$ , the threshold value is  $v = 1$  and the reset value is  $v = 0$ . Apparently, the neuron is excitable when  $b < 1$  and fires a periodic spike train when  $b > 1$  with period  $T = -\ln(1 - 1/b)$  (verify that).

The integrate-and-fire neuron illustrates a number of important neuro-computational properties:

- *All-or-none spikes.* Since the shape of the spike is not simulated, all spikes are implicitly assumed to be identical in size and duration.

- *Well-defined threshold.* A stereotypical spike is fired as soon as  $V = E_{\text{thresh}}$ , leaving no room for any ambiguity (see though Ex. 1).
- *Relative refractory period.* When  $E_K < E_{\text{leak}}$ , then neuron is less excitable right after the spike.
- *Distinction between excitation and inhibition.* Excitatory inputs ( $I > 0$ ) bring the membrane potential closer to the threshold and hence facilitate firing, while inhibitory inputs ( $I < 0$ ) do the opposite.
- *Class 1 excitability.* The neuron can continuously encode the strength of an input into the frequency of spiking.

In summary, the neuron seems to be a good model for an integrator.

However, a closer look reveals that the integrate-and-fire neuron has flaws. The transition from resting to repetitive spiking occurs neither via saddle-node nor via Andronov-Hopf bifurcation, but via some other weird type of a bifurcation that can be observed only in piece-wise continuous systems. As a result, the F-I curve has logarithmic scaling and not the expected square-root scaling of a typical Class 1 excitable system (see though Ex. 6.19). The integrate-and-fire model cannot have spike latency to a transient input because superthreshold stimuli evoke immediate spikes without any delays (compare with Fig. 8.8(I)). In addition, the model has some weird mathematical properties, such as non-uniqueness of solutions, as we show in Ex. 1. Finally, the integrate-and-fire model is not a spiking model: Technically, it did not fire a spike in Fig. 8.1, it was only “said to fire a spike”, which was added manually afterwards to fool the reader.

Despite all these drawbacks, the integrate-and-fire model is an acceptable sacrifice for a mathematician who wants to prove theorems and derive analytical expressions. However, using this model might be a waste of time for a computational neuroscientist who wants to simulate large-scale networks. At the end of this section we present alternative models that are as computationally efficient as the integrate-and-fire neuron, yet as biophysically plausible as Hodgkin-Huxley-type models.

### 8.1.2 Resonate-and-fire

The resonate-and-fire model is a two-dimensional extension of the integrate-and-fire model that incorporates an additional low-threshold persistent  $K^+$  current or h-current, or any other resonant current that is partially activated at rest. Let  $W$  denote the magnitude of such a current. In the linear approximation, the conductance-based equations describing neuronal dynamics can be written in the form

$$\begin{aligned} C\dot{V} &= I - g_{\text{leak}}(V - E_{\text{leak}}) - W, \\ \dot{W} &= (V - V_{1/2})/k - W. \end{aligned}$$

known as Young (1937) model (see also eq. 2-1 in FitzHugh 1969). Whenever the membrane potential reaches the threshold value,  $V_{\text{thresh}}$ , the neurons is said to fire a

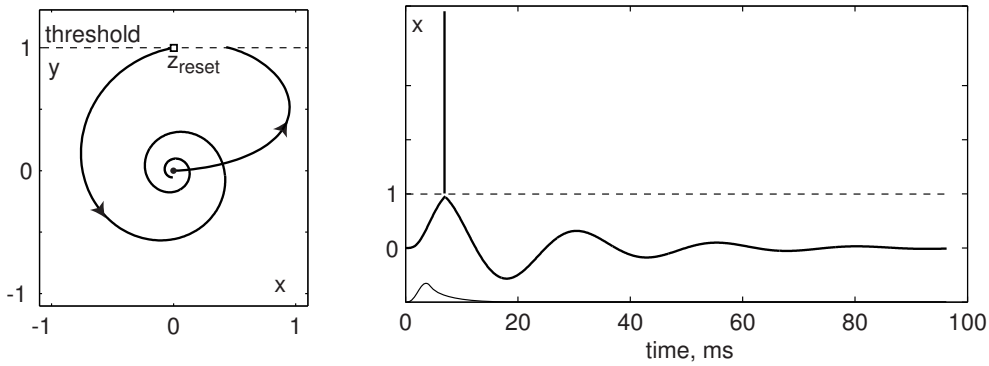


Figure 8.2: Resonate-and-fire model with  $b = -0.05$ ,  $\omega = 0.25$  and  $z_{\text{reset}} = i$ . The spike was added manually.

spike. Young did not specify what happens after the spike. The resonate-and-fire model is the Young model with the resetting: if  $V \geq V_{\text{thresh}}$ , then  $V \leftarrow V_{\text{reset}}$  and  $W \leftarrow W_{\text{reset}}$ , where  $V_{\text{rest}}$  and  $W_{\text{rest}}$  are some parameters.

When the resting state is a stable focus, the model can be recast in complex coordinates as

$$\dot{z} = (b + i\omega)z + I,$$

where  $b + i\omega \in \mathbb{C}$  is the complex eigenvalue of the resting state,  $z = x + iy \in \mathbb{C}$  is the complex-valued variable describing damped oscillations with frequency  $\omega$  around the resting state. The real part,  $x$ , is a current-like variable. It describes the dynamics of the resonant current and synaptic currents. The imaginary part,  $y$  is a voltage-like variable. The neuron is said to fire a spike when  $y$  reaches the threshold  $y = 1$ . Thus, the threshold is a horizontal line on the complex plane that passes through  $i \in \mathbb{C}$ , as in Fig. 8.2, though other choices are also possible. After firing the spike, the variable  $z$  is reset to  $z_{\text{reset}}$ .

The resonate-and-fire model illustrates the most important features of resonators: damped oscillations, frequency preference, post-inhibitory (rebound) spikes, and Class 2 excitability. It cannot have sustained subthreshold oscillations of membrane potential.

Integrate-and-fire and resonate-and-fire neurons do not contradict, but complement each other. Both are linear, and hence are useful when we prove theorems and derive analytical expressions. They have the same flaws limiting their applicability, which we discussed earlier. In contrast, two simple models described below are difficult to treat analytically, but because of their universality they should be the models of choice when large-scale simulations are concerned.

### 8.1.3 Quadratic integrate-and-fire

Substituting  $-v$  by  $+v^2$  in (8.1) results in the *quadratic integrate-and-fire* model

$$\dot{v} = b + v^2, \quad \text{if } v = v_{\text{peak}}, \text{ then } v \leftarrow v_{\text{reset}}, \quad (8.2)$$

which we considered in Sect. 3.3.8. Here  $v_{\text{peak}}$  is not a threshold, but the peak (cut off) of a spike, as we explain below. It is useful to use  $v_{\text{peak}} = +\infty$  in analytical studies. In simulations, the peak value is assumed to be large but finite, so it can be normalized to  $v_{\text{peak}} = 1$ .

Notice that  $\dot{v} = b + v^2$  is a topological normal form for the saddle-node bifurcation. That is, it describes dynamics of any Hodgkin-Huxley-type system near that bifurcation, as we discuss in Chap. 3 and 6. There we derived the normal form (6.3) for the  $I_{\text{Na,p}} + I_K$ -model and showed that the two systems agree quantitatively in a reasonably broad voltage range. By resetting  $v$  to  $v_{\text{reset}}$ , the quadratic integrate-and-fire model captures the essence of recurrence when the saddle-node bifurcation is on an invariant circle.

When  $b > 0$ , the right-hand side of the model is strictly positive, and the neuron fires a periodic train of action potentials. Indeed,  $v$  increases, reaches the peak, resets to  $v_{\text{reset}}$ , and then increases again, as we show in Fig. 3.35, top. In Ex. 3 we prove that the period of such spiking activity is

$$T = \frac{1}{\sqrt{b}} \left( \tan^{-1} \frac{v_{\text{peak}}}{\sqrt{b}} - \tan^{-1} \frac{v_{\text{reset}}}{\sqrt{b}} \right) < \frac{\pi}{\sqrt{b}},$$

so that the frequency scales as  $\sqrt{b}$ , as in Class 1 excitable systems.

When  $b < 0$ , the parabola  $b + v^2$  has two zeroes,  $\pm\sqrt{|b|}$ . One corresponds to the stable node equilibrium (resting state), the other corresponds to the unstable node (threshold state); see Ex. 2. Subthreshold perturbations are those that keep  $v$  below the unstable node. Superthreshold perturbations are those that push  $v$  beyond the unstable node, resulting in the initiation of an action potential, reaching the peak value  $v_{\text{peak}}$ , and then resetting to  $v_{\text{reset}}$ . If, in addition,  $v_{\text{reset}} > \sqrt{|b|}$ , then there is a co-existence of resting and periodic spiking states, as in Fig. 3.35, bottom. The period of the spiking state is provided in Ex. 4. A two-parameter bifurcation diagram of (8.2) is depicted in Fig. 8.3.

Unlike its linear predecessor, the quadratic integrate-and-fire neuron is a genuine integrator. It exhibits saddle-node bifurcation, it has a soft threshold, and it generates spikes with latencies, like many mammalian cells do. Besides, the model is canonical in the sense that the entire class of neuronal models near saddle-node on invariant circle bifurcation can be transformed into this model by a piece-wise continuous change of variables (see Sect. 8.1.5 and the Ermentrout-Kopell theorem in Hoppensteadt and Izhikevich 1997). In conclusion, the quadratic and not the leaky integrate-and-fire neuron should be used in simulations of large-scale networks of integrators. A generalization of this model is discussed next.

### 8.1.4 Simple model of choice

A striking similarity among many spiking models, discussed in Chap. 5, is that they can be reduced to two-dimensional systems having a fast voltage variable and a slower “recovery” variable, which may describe activation of  $K^+$  current or inactivation of  $Na^+$

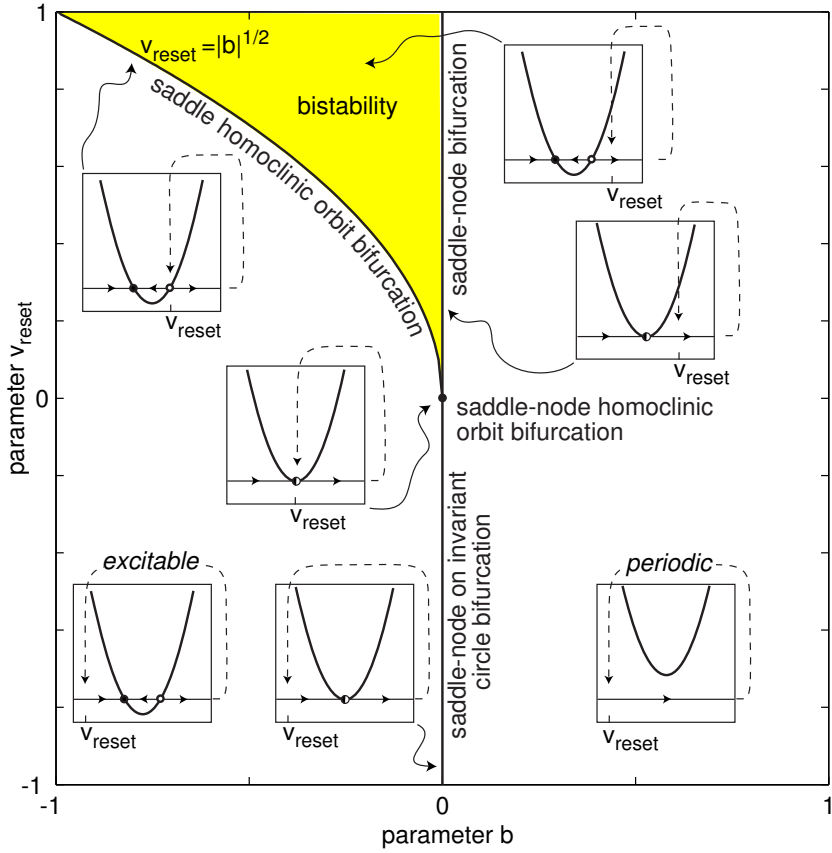


Figure 8.3: Bifurcation diagram of the quadratic integrate-and-fire neuron (8.2).

current or their combination. Typically, the fast variable has an N-shaped nullcline and the slower variable has a sigmoid-shaped nullcline. The resting state in such models is the intersection of the nullclines near the left knee, as we illustrate in Fig. 8.4a. There,  $V$  and  $u$  denote the fast and the slow variables, respectively. In Chap. 7 we showed that many computational properties of biological neurons could be explained by considering dynamics at the left knee.

In Sect. 5.2.4 we derive a simple model that captures the subthreshold behavior in a small neighborhood of the left knee confined to the shaded square in Fig. 8.4 and the initial segment of the up-stroke of an action potential. In many cases, especially involving large-scale simulations of spiking models, the shape of the action potential is less important than the subthreshold dynamics leading to this action potential. So, retaining detailed information about the left knee and its neighborhood and simplifying the vector field outside the neighborhood is justified.

The simple model

$$\dot{v} = I + v^2 - u \quad \text{if } v \geq 1, \text{ then} \quad (8.3)$$

$$\dot{u} = a(bv - u) \quad v \leftarrow c, u \leftarrow u + d. \quad (8.4)$$

has only four dimensionless parameters. Depending on the values of  $a$  and  $b$ , it can

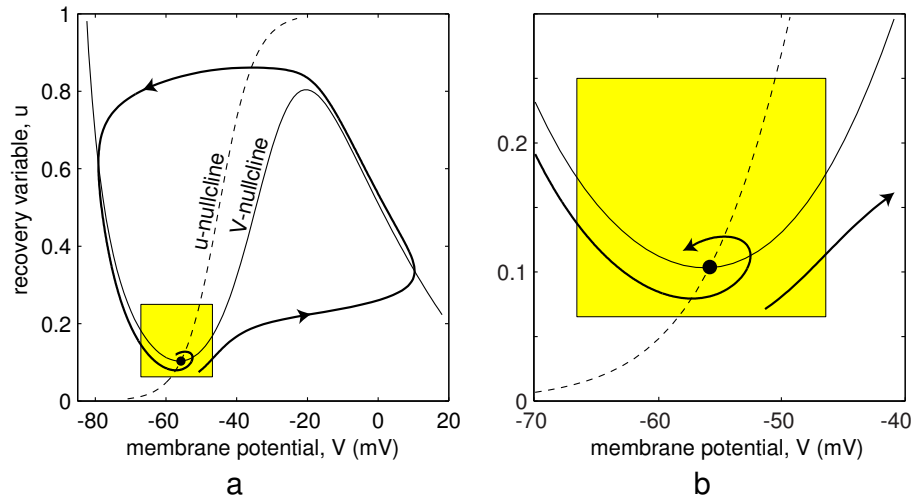


Figure 8.4: Phase portrait (a) and its magnification (b) of a typical neuronal model having voltage variable  $V$  and a recovery variable  $u$ .

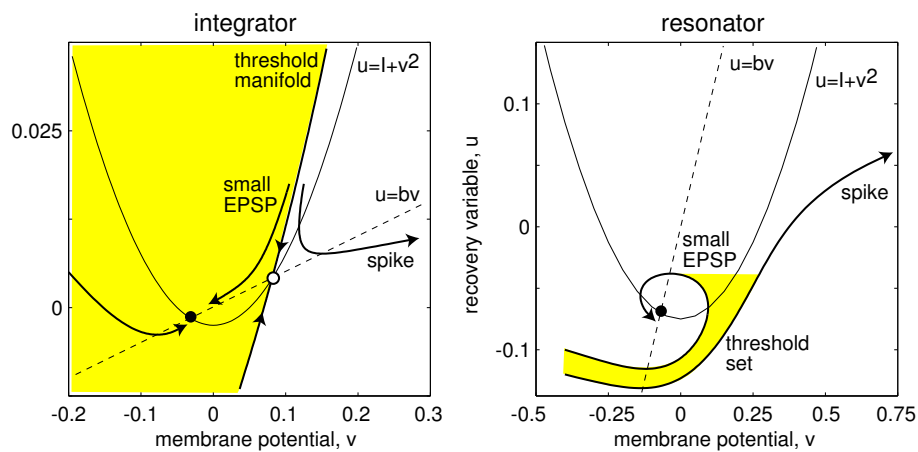


Figure 8.5: The simple model (8.3, 8.4) can be an integrator or a resonator. Compare with Fig. 7.27.

be an integrator or a resonator, as we illustrate in Fig. 8.5. The parameters  $c$  and  $d$  do not affect steady-state subthreshold behavior. Instead, they take into account the action of high-threshold voltage-gated currents activated during the spike and affect only the after-spike transient behavior. If there are many currents with diverse time scales, then  $u, a, b$ , and  $d$  are vectors, and the equation (8.3) contains  $\sum u$  instead of  $u$ .

The simple model may be treated as quadratic integrate-and-fire neuron with adaptation in the simplest case  $b = 0$ . When  $b < 0$ , the model can be treated as quadratic integrate-and-fire neuron with a passive dendritic compartment (see Ex. 10). When  $b > 0$ , the connection to the quadratic integrate-and-fire neuron is lost, and the simple model represents a novel class of spiking models.

In the rest of this chapter we tune the simple model to reproduce spiking and bursting behavior of many known types of neurons. It is convenient to use it in the form

$$C\dot{v} = k(v - v_r)(v - v_t) - u + I \quad \text{if } v \geq v_{\text{peak}}, \text{ then} \quad (8.5)$$

$$\dot{u} = a\{b(v - v_r) - u\} \quad v \leftarrow c, u \leftarrow u + d \quad (8.6)$$

where  $v$  is the membrane potential,  $u$  is the recovery current,  $C$  is the membrane capacitance,  $v_r$  is the resting membrane potential, and  $v_t$  is the instantaneous threshold potential. Though it looks like the model has ten parameters, but it is equivalent to (8.3,8.4) and hence it has only four independent parameters. As we described in Sect. 5.2.4, the parameters  $k$  and  $b$  can be found knowing the neuron's rheobase and input resistance. The sum of all slow currents that modulate the spike-generation mechanism are combined in the phenomenological variable  $u$  with outward currents taken with the plus sign.

The sign of  $b$  determines whether  $u$  is an amplifying ( $b < 0$ ) or a resonant ( $b > 0$ ) variable. In the latter case, the neuron sags in response to hyperpolarized pulses of current, peaks in response to depolarized subthreshold pulses, and produces rebound (post-inhibitory) responses. The recovery time constant is  $a$ . The spike cut-off value is  $v_{\text{peak}}$ , and the voltage reset value is  $c$ . The parameter  $d$  describes the total amount of outward minus inward currents activated during the spike and affecting the after-spike behavior. All these parameters can be easily fit to any particular neuron type, as we show in subsequent sections.

### Implementation and phase portrait

The following MATLAB code simulates the model and produces Fig. 8.6a.

```

C=100; vr=-60; vt=-40; k=0.7;      % parameters used for RS
a=0.03; b=-2; c=-50; d=100;          % neocortical pyramidal neurons
vpeak=35;                            % spike cutoff

T=1000; tau=1;                        % time span and step (ms)
n=round(T/tau);                      % number of simulation steps

```

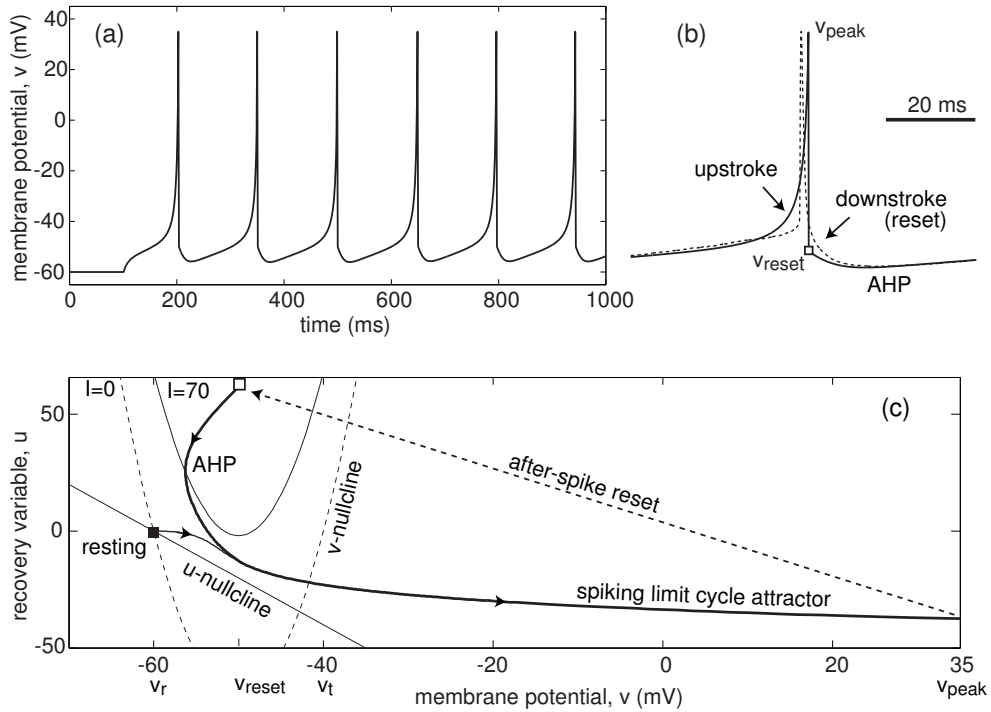


Figure 8.6: (a) Output of the MATLAB code simulating the simple model (8.5, 8.6). (b) Comparison of the simulated (continuous curve) and experimental (dashed curve) voltage traces shows two major discrepancies marked by arrows. (c) Phase portrait of the model.

```

v=vr*ones(1,n); u=0*v; % initial values
I=[zeros(1,0.1*n),70*ones(1,0.9*n)];% pulse of input dc-current

for i=1:n-1 % forward Euler method
    v(i+1)=v(i)+tau*(k*(v(i)-vr)*(v(i)-vt)-u(i)+I(i))/C;
    u(i+1)=u(i)+tau*a*(b*(v(i)-vr)-u(i));
    if v(i+1)>=vpeak % a spike is fired!
        v(i)=vpeak; % padding the spike amplitude
        v(i+1)=c; % membrane voltage reset
        u(i+1)=u(i+1)+d; % recovery variable update
    end;
end;
plot(tau*(1:n), v); % plot the result

```

Notice that the spikes were padded to  $v_{peak}$  to avoid amplitude jitter associated with the finite simulation time step  $\tau = 1$  ms. In Fig. 8.6b we magnify the simulated voltage trace and compare it with recording of a neocortical pyramidal neuron (dashed curve). There are two discrepancies, marked by arrows: (1) sharper spike upstroke and (2) smoother spike downstroke. The first discrepancy can be removed by assuming that the coefficient  $k$  of the square polynomial in (8.5)

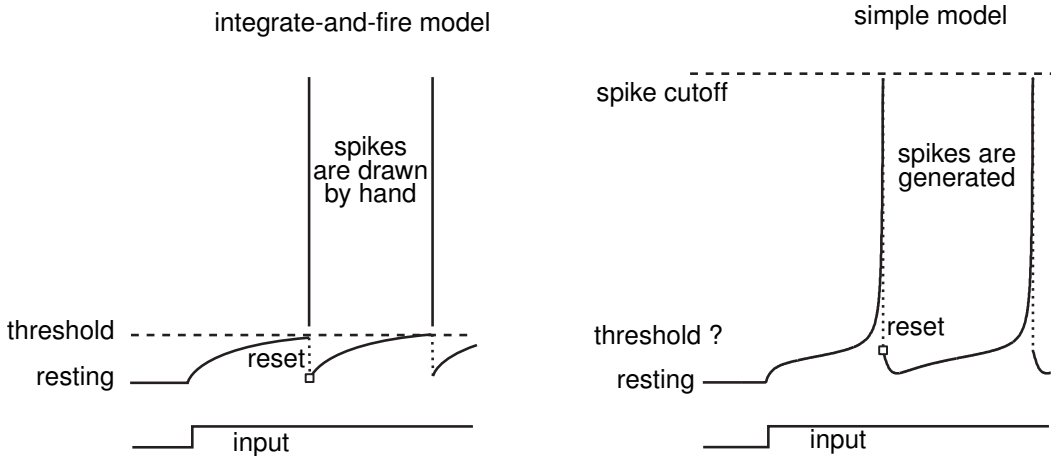


Figure 8.7: Voltage reset in the integrate-and-fire model and in the simple model.

is voltage-dependent, e.g.,  $k = 0.7$  for  $v \leq v_t$  and  $k = 7$  for  $v > v_t$ , or by using the modification of the simple model presented in Ex. 13 and Ex. 17. The second discrepancy results from the instantaneous after-spike resetting, and it is of a lesser importance because it does not affect the decision whether or when to fire. However, the slope of the downstroke may become important in studies of gap-junction-coupled spiking neurons.

The phase portrait of the simple model is depicted in Fig. 8.6c. Injection of the step of dc-current  $I = 70$  pA shifts the  $v$ -nullcline (square parabola) up and makes the resting state, denoted by a black square, disappear. The trajectory approaches the spiking limit cycle attractor, and when it crosses the cutoff vertical line  $v_{\text{peak}} = 35$  mV, it is reset to the white square, resulting in periodic spiking behavior. Notice the slow afterhyperpolarization (AHP) following the reset that is due to the dynamics of the recovery variable  $u$ . Depending on the parameters, the model can have other types of phase portraits, spiking, and bursting behavior, as we demonstrate in the rest of the chapter.

In Fig. 8.7 we illustrate the difference between the integrate-and-fire neuron and the simple model. The integrate-and-fire model is said to fire spikes when the membrane potential reaches a preset threshold value. The potential is reset to a new value, and the spikes are drawn by hand. In contrast, the simple model generates the up-stroke of the spike due to the intrinsic (regenerative) properties of the voltage equation. The voltage reset occurs not at the threshold, but at the peak of the spike. In fact, the firing threshold in the simple model is not a parameter, but a *property* of the bifurcation mechanism of excitability. Depending on the bifurcation of equilibrium, the model may not even have a well-defined threshold, similarly to conductance-based models.

When implementing numerically the voltage reset, whether at the threshold or the peak of the spike, one needs to be aware of the numerical errors, which translate into the errors of spike timing. These errors are inversely proportional to the slope of the voltage variable at the reset value. The slope is small in the integrate-and-fire model, so

clever numerical methods are needed to catch the exact moment of threshold crossing (Hansel et al. 1998). In contrast, the slope is nearly infinite in the simple model, so no special methods are needed to identify the peak of the spike.

In Fig. 8.8 we used the model to reproduce the 20 of the most fundamental neuro-computational properties of biological neurons. Let us check that the model is the simplest possible system that can exhibit the kind of behavior in the figure. Indeed, it has only one non-linear term, i.e.,  $v^2$ . Removing the term makes the model linear and equivalent to the resonate-and-fire neuron (though it becomes analytically solvable). Removing the recovery variable  $u$  makes the model equivalent to the quadratic integrate-and-fire neuron with all its limitations, such as inability to burst or to be a resonator. In summary, we found the simplest possible model capable of spiking, bursting, being an integrator or a resonator, and it should be the model of choice in simulations of large-scale networks of spiking neurons.

### 8.1.5 Canonical models

It is quite rare, if ever possible, to know precisely the parameters describing dynamics of a neuron (many erroneously think that the Hodgkin-Huxley model of squid axon is an exception). Indeed, even if all ionic channels expressed by the neuron are known, the parameters describing their kinetics are usually obtained via averaging over many neurons; there are measurement errors; the parameters change slowly, etc. Thus, we are forced to consider families of neuronal models with free parameters, e.g. the family of  $I_{\text{Na}}+I_{\text{K}}$ -models. It is more productive from computational neuroscience point of view to consider families of neuronal models having a common property, e.g., the family of all integrators, the family of all resonators, or the family of “fold/homoclinic” bursters considered in the next chapter. How can we study the behavior of the entire family of neuronal models if we have no information about most of its members?

The canonical model approach addresses this issue. Briefly, a model is *canonical* for a family if there is a piece-wise continuous change of variables that transforms any model from the family into this one, as we illustrate in Fig. 8.10. The change of variables does not have to be invertible, so the canonical model is usually lower-dimensional, simple, and tractable. Yet, it retains many important features of the family. For example, if the canonical model has multiple attractors, then each member of the family has multiple attractors. If the canonical model has a periodic solution, then each member of the family has a periodic (quasi-periodic or chaotic) solution. If the canonical model can burst, then each member of the family can burst. The advantage of this approach is that we can study universal neuro-computational properties that are shared by all members of the family since all such members can be put into the canonical form by a change of variables. Moreover, we need not actually present such a change of variables explicitly, so derivation of canonical models is possible even when the family is so broad that most of its members are given implicitly, e.g., the family of “all resonators”.

The process of deriving canonical models is more an art than a science, since a

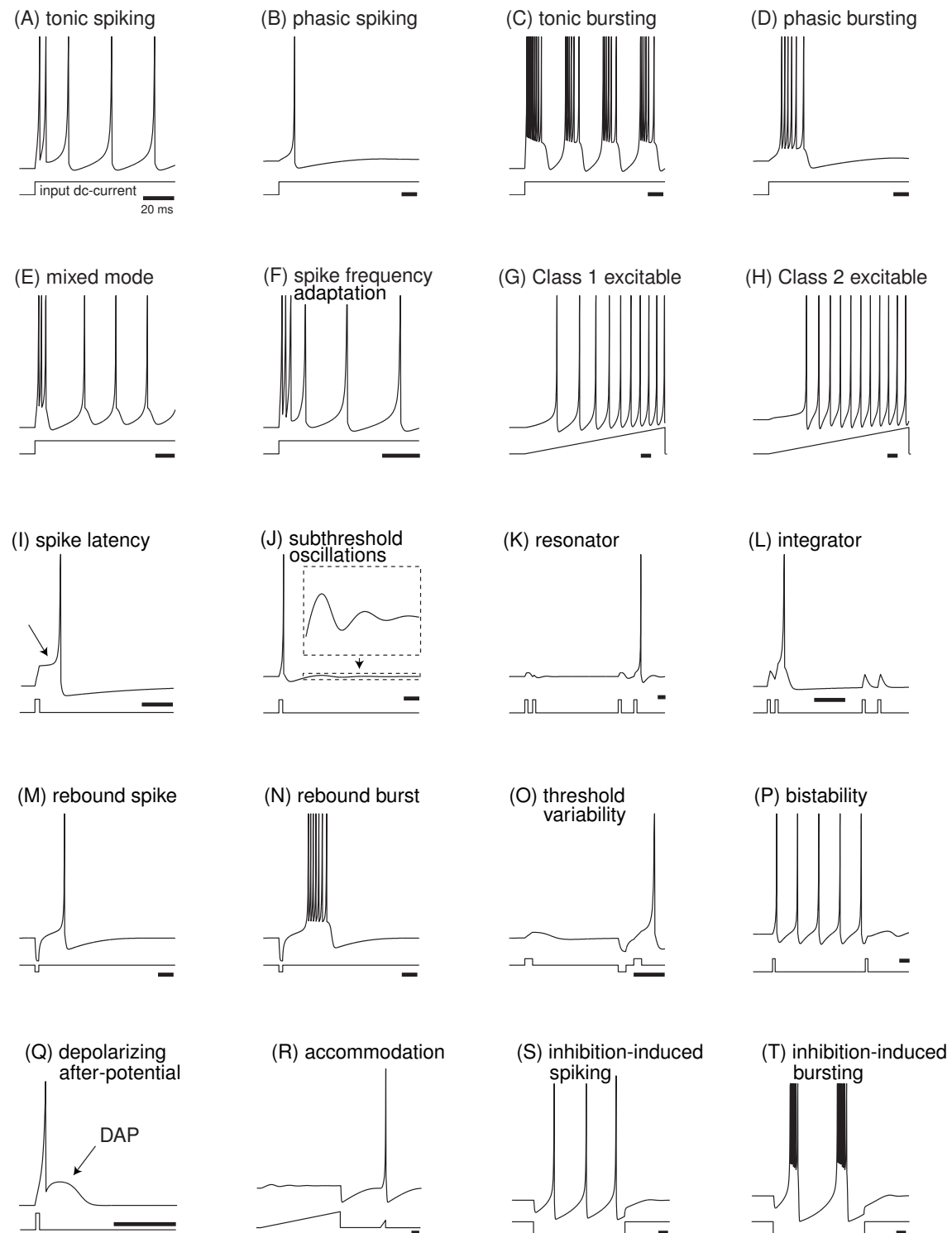


Figure 8.8: Summary of neuro-computational properties exhibited by the simple model; see Ex. 11. The figure is reproduced with permission from [www.izhikevich.com](http://www.izhikevich.com). (electronic version of the figure and reproduction permissions are freely available at [www.izhikevich.com](http://www.izhikevich.com))

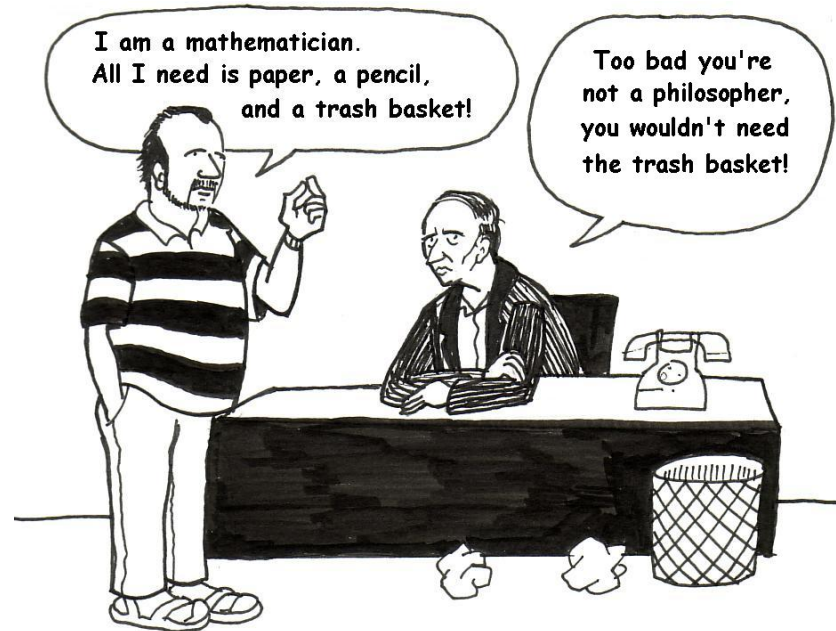


Figure 8.9:

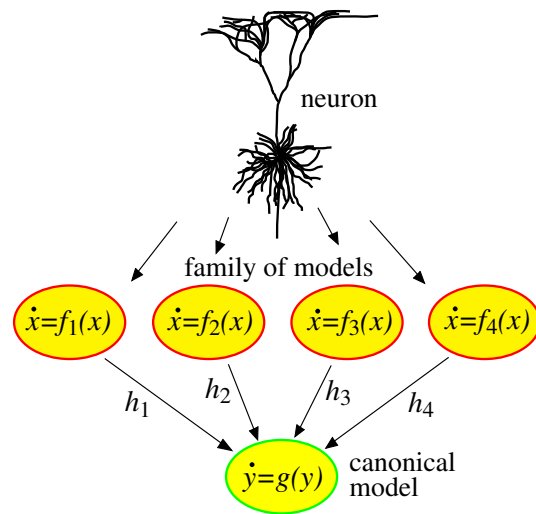


Figure 8.10: Dynamical system  $\dot{y} = g(y)$  is a canonical model for the family  $\{f_1, f_2, f_3, f_4\}$  of neural models  $\dot{x} = f(x)$  because each such model can be transformed into the form  $\dot{y} = g(y)$  by the piece-wise continuous change of variables  $h_i$ .

general algorithm for doing this is not known. However, much success has been achieved in some important cases. The canonical model for a system near an equilibrium is the topological normal form at the equilibrium (Kuznetsov 1995). Such canonical model is local, but it can be extended to describe global dynamics. For example, the quadratic integrate-and-fire model with a fixed  $v_{\text{reset}} < 0$  is a global canonical model for all Class 1 excitable systems, i.e., systems near saddle-node on invariant circle bifurcation. The same model with variable  $v_{\text{reset}}$  is a global canonical model for all systems near saddle-node homoclinic orbit bifurcation considered in Sect. 6.3.6. The phase model  $\dot{\vartheta} = 1$  derived in Chap. 10 is a global canonical model for the family of nonlinear oscillators having exponentially stable limit cycle attractors. Other examples of canonical models for spiking and bursting can be found in subsequent chapters of this book.

The vector-field of excitable conductance-based models in the subthreshold region and in the region corresponding to the up-stroke of the spike can be converted into the simple form (8.3, 8.4), possibly with  $u$  being a vector. Therefore, the simple model (8.3, 8.4) is a *local* canonical model for the spike-generation mechanism and the spike up-stroke of the Hodgkin-Huxley-type neuronal models. It is not a global canonical model because it ignores the spike downstroke. Yet, it describes remarkably well the spiking and bursting dynamics of many biological neurons, as we demonstrate next.

## 8.2 Cortex

In this section we consider the six most fundamental classes of firing patterns observed in the mammalian neocortex and depicted in Fig. 8.11 (Connors and Gutnick 1990, Gray and McCormick 1996, Gibson et al. 1999). Though most biologists agree with the classification in the figure, many would point out that it is greatly oversimplified (Markram et al. 2004), that the distinction between the classes is not sharp, that there are subclasses within each class (Nowak et al. 2003, Toledo-Rodriguez et al. 2004), and that neurons can change their firing classes depending on the state of the brain (Steriade 2004).

- (RS) Regular spiking neurons fire tonic spikes with adapting (decreasing) frequency in response to injected pulses of dc-current. Most of them have Class 1 excitability in the sense that the interspike frequency vanishes when the amplitude of the injected current decreases. Morphologically, these neurons are spiny stellate cells in layer 4 and pyramidal cells in layers 2,3,5, and 6.
- (IB) Intrinsically bursting neurons generate a burst of spikes at the beginning of a strong depolarizing pulse of current, and then switch to tonic spiking mode. Those are excitatory pyramidal neurons found in all cortical layers, but most abundant in layer 5.
- (CH) Chattering neurons fire high-frequency bursts of spikes with relatively short interburst periods, hence another name — FRB or fast rhythmic bursting. Output of such a cell fed to the loudspeaker “sounds a lot like a helicopter — cha,

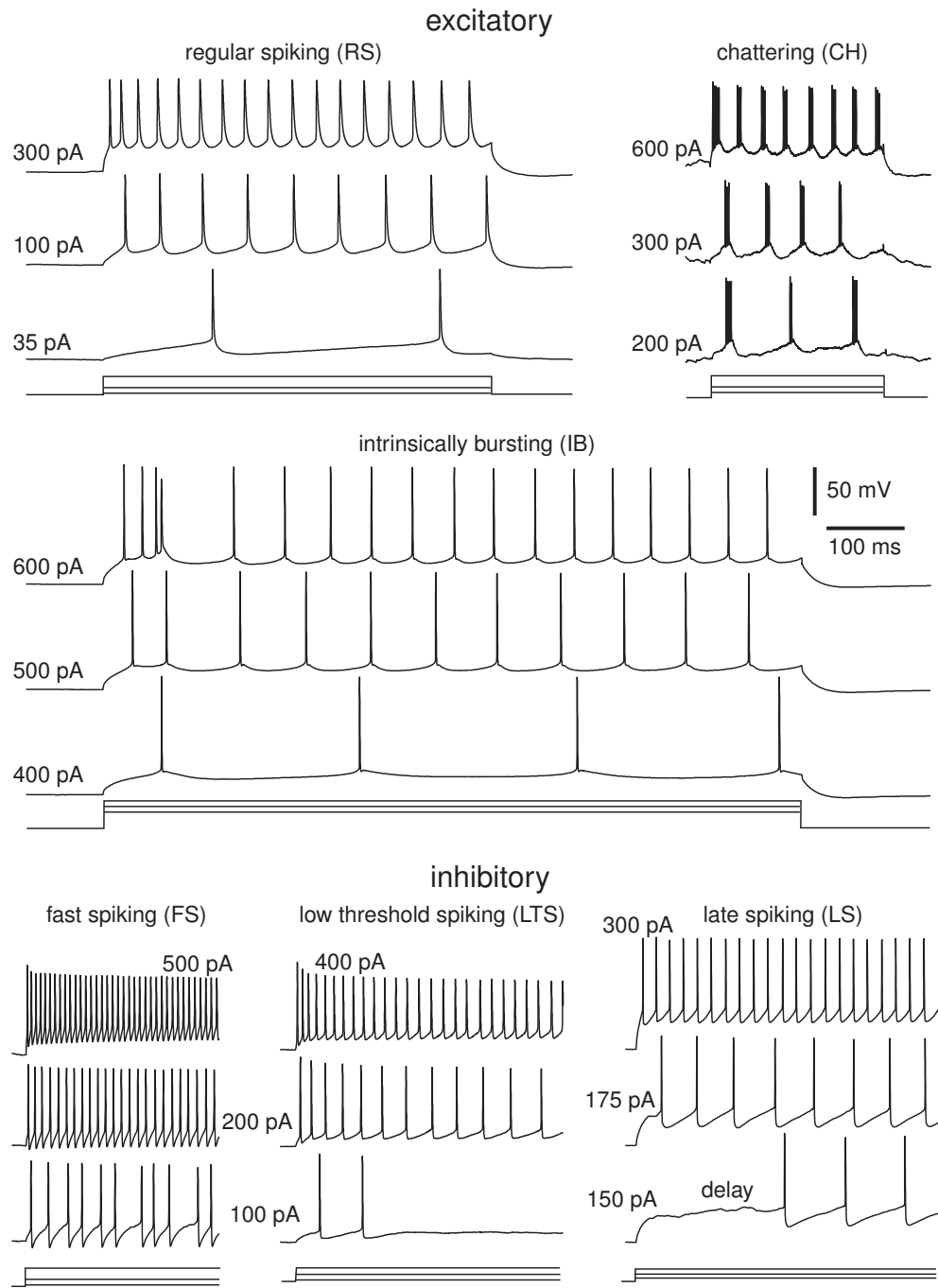


Figure 8.11: Six most fundamental classes of firing patterns of neocortical neurons in response to pulses of depolarizing dc-current. RS and IB are *in vitro* recordings of pyramidal neurons of layer 5 of primary visual cortex of a rat, CH was recorded *in vivo* in cat's visual cortex (area 17, data provided by D. McCormick). FS was recorded *in vitro* in rat's primary visual cortex, LTS was recorded *in vitro* in layer 4 or 6 of rat's barrel cortex (data provided by B. Connors). LS was recorded in layer 1 of rat's visual cortex (data provided by S. Hestrin). All recordings are plotted on the same voltage and time scale, and the data are available on the author's webpage ([www.izhikevich.com](http://www.izhikevich.com)).

cha, cha — real fast”, according to Gray and McCormick (1996). CH neurons were found in visual cortex of adult cats, and, morphologically, they are spiny stellate or pyramidal neurons of layer 2-4, mainly layer 3.

- (FS) Fast spiking interneurons fire high-frequency tonic spikes with relatively constant period. They exhibit Class 2 excitability (Tateno et al. 2004). When the magnitude of the injected current decreases below a certain critical value, they fire irregular spikes, switching randomly between resting and spiking states. Morphologically, FS neurons are sparsely spiny or aspiny nonpyramidal cells (basket or chandelier; see Kawaguchi and Kubota 1997) providing local inhibition along the horizontal (intra-laminar) direction of the neocortex (Bacci et al. 2003).
- (LTS) Low-threshold spiking neurons fire tonic spikes with pronounced spike frequency adaptation and rebound (post-inhibitory) spikes, often called “low-threshold spikes” by biologists (hence the name). They seem to be able to fire low-frequency spike trains, though their excitability class has not been determined yet. Morphologically, LTS neurons are nonpyramidal interneurons providing local inhibition along the vertical (inter-laminar) direction of the neocortex (Bacci et al. 2003).
- (LS) Late spiking neurons exhibit voltage ramp in response to injected dc-current near the rheobase, resulting in delayed spiking with latencies as long as 1 sec. There is a pronounced sub-threshold oscillation during the ramp, but the discharge frequency is far less than that of FS neurons. Morphologically, LS neurons are nonpyramidal interneurons (neurogliaform; see Kawaguchi and Kubota 1997) found in all layers of neocortex (Kawaguchi 1995), especially in layer 1 (Chu et al. 2003).

Our goal is to use the simple model (8.5, 8.6) presented in the previous section to reproduce each of the firing types. We want to capture the dynamic mechanism of spike generation of each neuron, so that the model reproduces the correct responses to many types of the inputs, and not only to the pulses of dc-current. We strive to have not only qualitative but also quantitative agreement with the published data on neuron’s resting potential, input resistance, rheobase, F-I behavior, the shape of the upstroke of the action potential, etc., though this is impossible in many cases mostly because the data are contradictory. To fine-tune the model, we use recordings of real neurons. We consider the tuning successful when quantitative difference between simulated and recorded responses is smaller than the difference between responses of two “sister” neurons recorded in the same slice. We do not want to claim that the simple model explains the mechanism of generation of any of the firing patterns recorded in real neurons (simply because the mechanism is usually not known). Although in many instances we must resist the temptation to use the Wolfram (2002) new-kind-of-science criterion: “if it looks the same — it must be the same”.

### 8.2.1 Regular spiking (RS) neurons

Regular spiking neurons are the major class of excitatory neurons in the neocortex. Many are Class 1 excitable, as we show in Fig. 7.3 using *in vitro* recordings of a layer 5 pyramidal cell of rat's primary visual cortex; see also Tateno et al. (2004). RS neurons have a transient K<sup>+</sup> current  $I_A$ , whose slow inactivation delays the onset of the first spike and increases the interspike period, and a persistent K<sup>+</sup> current  $I_M$ , which is believed to be responsible for the spike frequency adaptation seen in Fig. 7.43. Let us use the simple model (8.5, 8.6) to capture qualitative and some quantitative features of typical RS neurons.

We assume that the resting membrane potential is  $v_r = -60$  mV and the instantaneous threshold potential is  $v_t = -40$  mV; that is, instantaneous depolarizations above  $-40$  mV cause the neuron to fire, as in Fig. 3.15. Assuming that the rheobase is 50 pA, and the input resistance is 80 MΩ, we find  $k = 0.7$  and  $b = -2$ . We take the membrane capacitance  $C = 100$  pF, which yields a membrane time constant of 8 ms.

Since  $b < 0$ , depolarizations of  $v$  decrease  $u$  as if the major slow current is the inactivating K<sup>+</sup> current  $I_A$ . The inactivation time constant of  $I_A$  is around 30 ms in the subthreshold voltage range, hence we take  $a = 0.03 \approx 1/30$ . The membrane potential of a typical RS neuron reaches the peak value  $v_{\text{peak}} = +35$  mV during a spike (the precise value has little effect on dynamics) and then repolarizes to  $c = -50$  mV or below, depending on the firing frequency. The parameter  $d$  describes the total amount of outward minus inward currents activated during the spike and affecting the after-spike behavior. Trying different values, we find that  $d = 100$  gives a reasonable F-I relationship, at least in the low-frequency range.

As it follows from Ex. 10, we can also interpret  $u$  as the membrane potential of a passive dendritic compartment, taken with the minus sign. Thus, when  $b < 0$ , the variable  $u$  represents the combined action of slow inactivation of  $I_A$  and slow charging of the dendritic tree. Both processes slow down the frequency of somatic spiking.

Notice that we round-up all the parameters, e.g., we use  $d = 100$  and not 93.27. Nevertheless, the simulated voltage responses in Fig. 8.12 agree quantitatively with the *in vitro* recordings of the layer 5 pyramidal neuron used in Fig. 7.3. Tweaking the parameters, considering multidimensional  $u$ , or adding multiple dendritic compartments, one can definitely improve the quantitative correspondence between the model and the *in vitro* data of that particular neuron, but this is not our goal here. Instead, we want to understand the qualitative dynamics of RS neurons using the geometry of their phase portraits.

#### Phase plane analysis

Figure 8.13 shows recordings of two pyramidal RS neurons from the same slice while an automated procedure injects pulses of dc-current to determine their rheobase. The neuron on the left exhibits monotonically increasing (ramping) or decreasing responses of membrane potential to weak input pulses, long latencies of the first spike and no rebound spikes, whereas the neuron on the right exhibits non-monotone overshooting

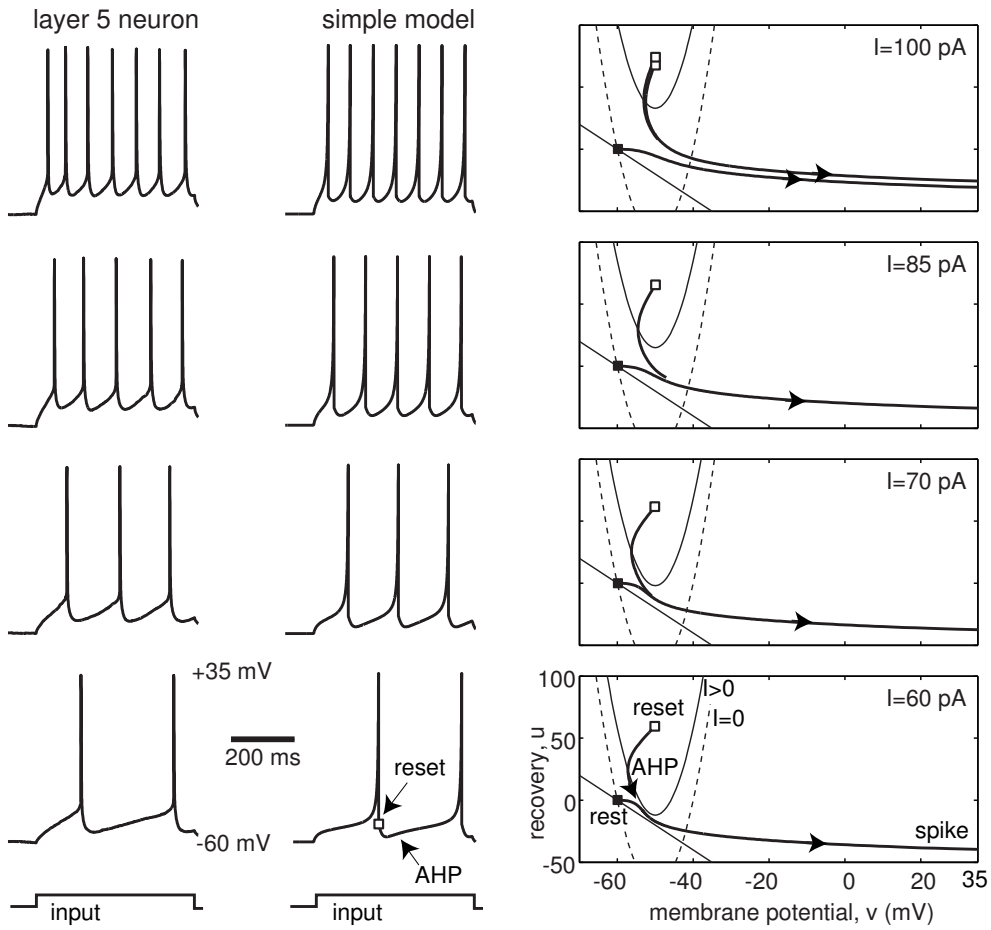


Figure 8.12: Comparison of *in vitro* recordings of a regular spiking (RS) pyramidal neurons with simulations of the simple model  $100\dot{v} = 0.7(v + 60)(v + 40) - u + I$ ,  $\dot{u} = 0.03\{-2(v + 60) - u\}$ , if  $v \geq +35$ , then  $v \leftarrow -50$ ,  $u \leftarrow u + 100$ .

responses to positive pulses, sags and rebound spikes to negative pulses (as in Fig. 7.48), relatively short latencies of the first spike, and other resonance phenomena. The even more extreme example in Fig. 7.42 shows a pyramidal neuron executing a subthreshold oscillation before switching to a tonic spiking mode.

The difference between the types in Fig. 8.13 can be explained by the sign of the parameter  $b$  in the simple model (8.5, 8.6), which depends on the relative contributions of amplifying and resonant slow currents and gating variables. When  $b < 0$  (or  $b \approx 0$ , e.g.,  $b = 0.5$  in Fig. 8.14), the neuron is a pure integrator near saddle-node on invariant circle bifurcation. Greater values of  $b > 0$  put the model near the transition from an integrator to a resonator via co-dimension-2 Bogdanov-Takens bifurcation studied in Sect. 6.3.3 and 7.2.11.

The sequence of bifurcations when  $b > 0$  is depicted in Fig. 8.15. Injection of depolarizing current below the neuron's rheobase transforms the resting state into a stable focus and results in damped oscillations of the membrane potential. The

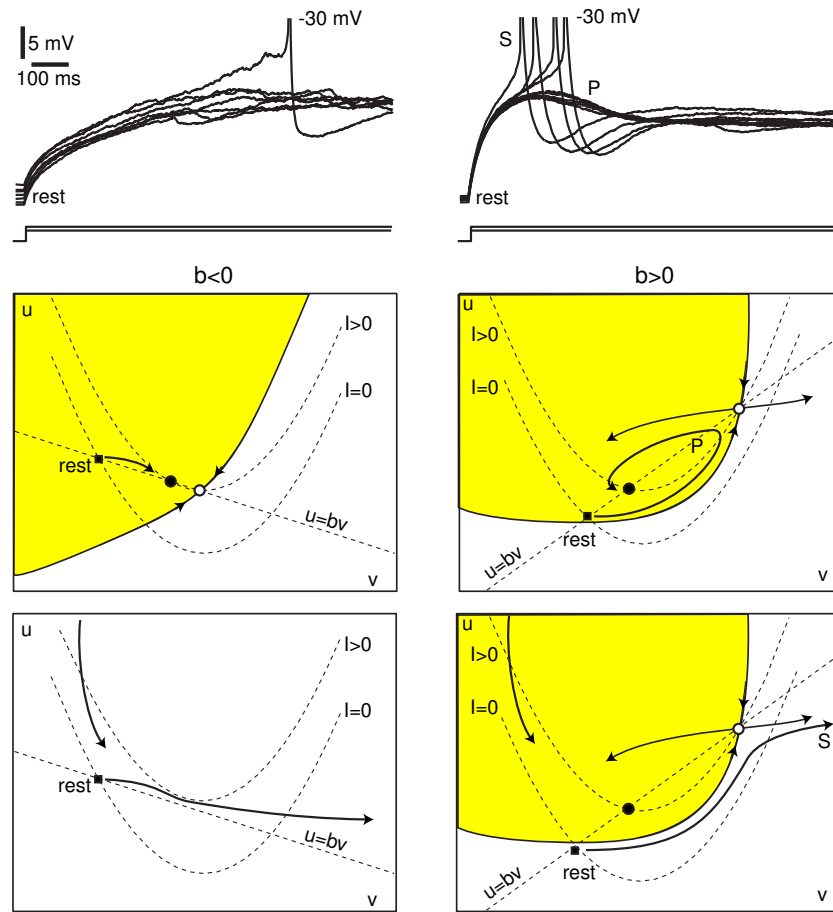


Figure 8.13: Two types of qualitative behavior of RS neurons. Some exhibit monotone responses to weak injected currents (case  $b < 0$ ), others exhibit non-monotone overshooting responses (case  $b > 0$ ). Shown are *in vitro* recordings of two RS neurons from the same slice of rat's primary visual cortex while an automated procedure was trying to determine the neurons' rheobase. Phase portraits are drawn by hand and they illustrate a possible dynamic mechanism of the phenomenon.

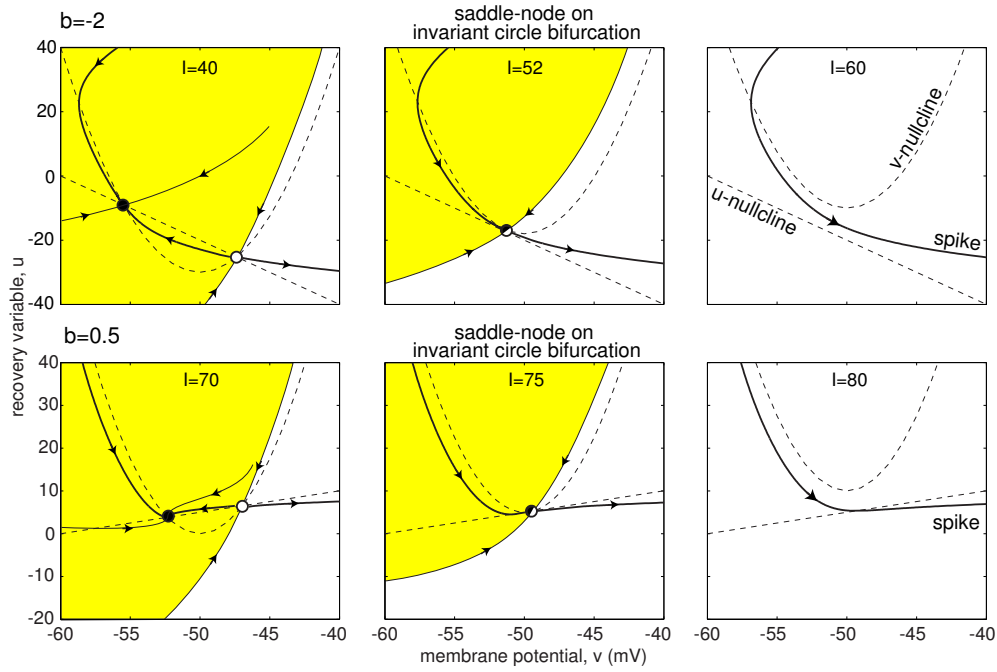


Figure 8.14: Saddle-node on invariant circle bifurcations in the RS neuron model as the magnitude of the injected current  $I$  increases.

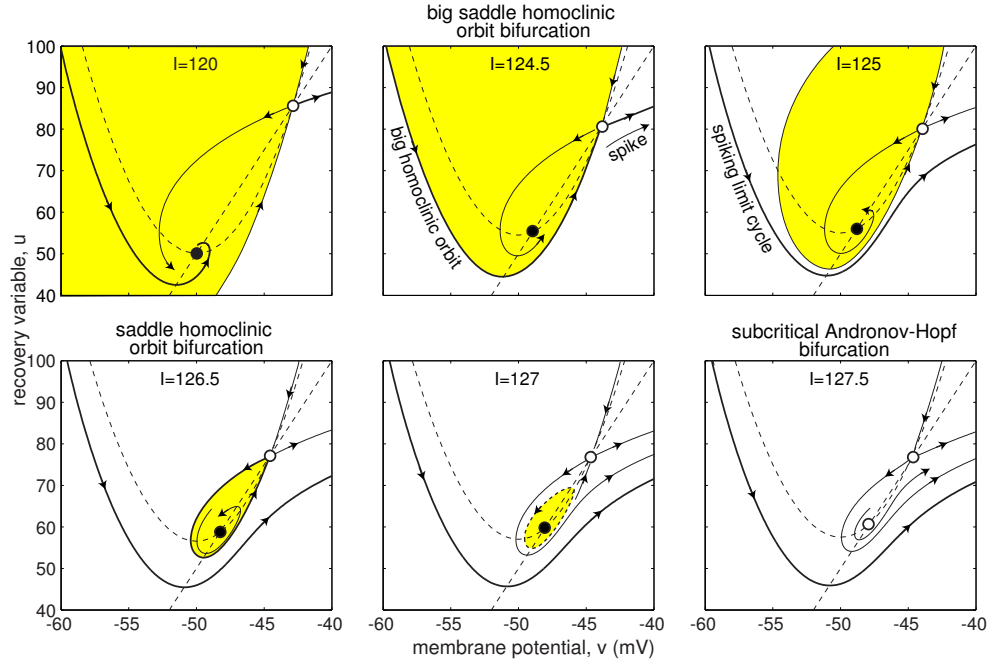


Figure 8.15: The sequence of bifurcations of the RS model neuron (8.5, 8.6) in resonator regime. Parameters as in Fig. 8.12 and  $b = 5$ ; see also Fig. 6.40.

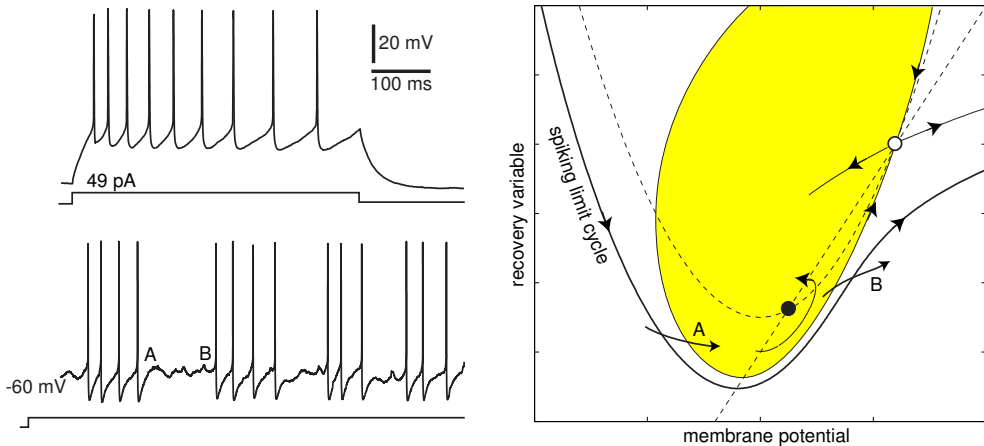


Figure 8.16: Stuttering behavior of an RS neuron (data were provided by Dr. Klaus M. Stiefel, P28-36 adult mouse, coronal slices, 300 $\mu$ m, layer II/III pyramid, visual cortex).

attraction domain of the focus (shaded region in the figure) is bounded by the stable manifold of the saddle. As  $I$  increases, the stable manifold makes a loop and becomes a big homoclinic orbit giving birth to a spiking limit cycle attractor. When  $I = 125$ , stable resting and spiking states co-exist, which plays an important role in explaining the paradoxical stuttering behavior of some neocortical neurons discussed later. As  $I$  increases, the saddle quantity, i.e., the sum of eigenvalues of the saddle, becomes positive. When the stable manifold makes another, smaller loop, it gives birth to an unstable limit cycle, which then shrinks to the resting equilibrium and results in subcritical Andronov-Hopf bifurcation.

What is the excitability class of the RS model neuron in Fig. 8.15? If a slow ramp of current is injected, the resting state of the neuron becomes a stable focus and then loses stability via subcritical Andronov-Hopf bifurcation. Hence the neuron is a resonator exhibiting Class 2 excitability. Now suppose steps of dc-current of amplitude  $I = 125$  pA or less are injected. The trajectory starts at the initial point  $(v, u) = (-60, 0)$ , which is the resting state when  $I = 0$ , and then approaches the spiking limit cycle. Because the limit cycle was born via a homoclinic bifurcation to the saddle, it has a large period and hence the neuron is Class 1 excitable. Thus, depending on the nature of stimulation, i.e., ramps vs. pulses, we can observe small or large spiking frequencies, at least in principle.

In practice, it is quite difficult to catch homoclinic orbits to saddles because they are sensitive to noise. Injection of a constant current just below the neuron's rheobase in Fig. 8.15 would result in random transitions between the resting state and a periodic spiking state. Indeed, the two attractors co-exist and are near each other, so weak membrane noise can push the trajectory in and out of the shaded region resulting in a stuttering spiking, illustrated in Fig. 8.16, mingled with subthreshold oscillations. Such a behavior is also exhibited by FS interneurons studied later in this section.

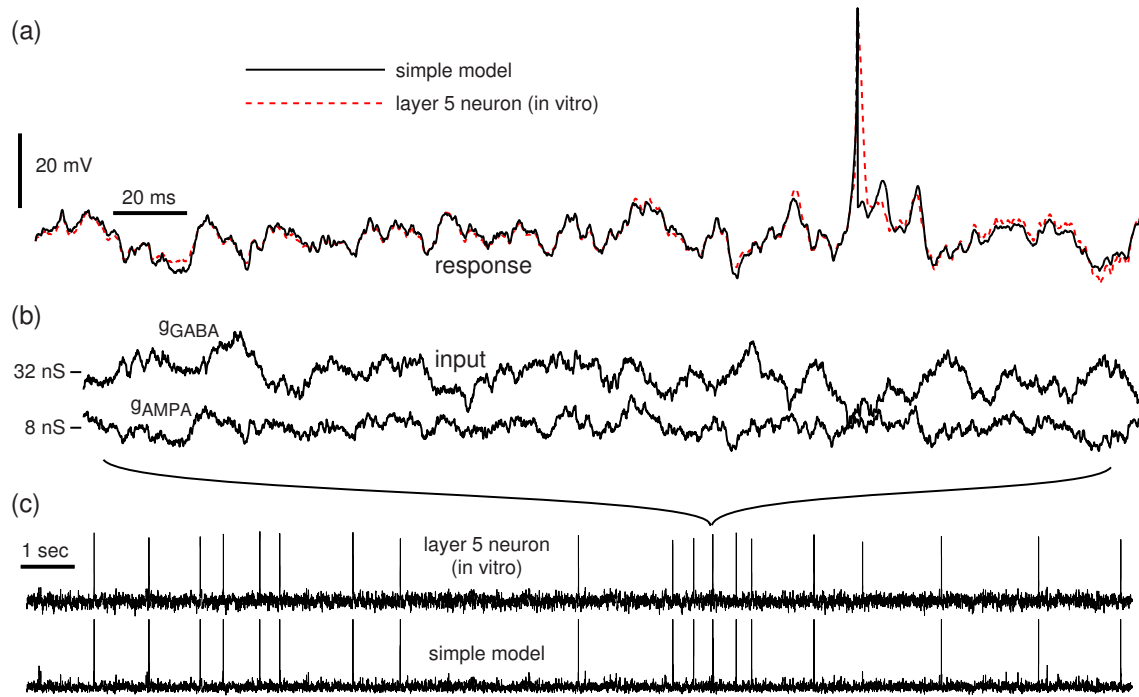


Figure 8.17: (a) Comparison of responses of a rat motor cortex layer 5 pyramidal neuron of RS type and the simple model (8.5, 8.6) to *in vivo*-like stochastic input (8.7) with the random conductances in (b). Part (a) is a magnification of a small region in (c). Shown are simulations of  $30\dot{v} = 3(v+55)(v+42)-u+I(t)$ ,  $\dot{u} = 0.01\{-0.25(v+55)-u\}$ , if  $v \geq +10$ , then  $v \leftarrow -40$ ,  $u \leftarrow u + 90$ . Data was kindly provided by Niraj S. Desai and Betsy C. Walcott.

### In vivo-like conditions

In Fig. 8.17a (dashed curve) we show the response of *in vitro* recorded layer 5 pyramidal neuron of rat motor cortex to fluctuating *in vivo*-like input. First, random excitatory and inhibitory conductances,  $g_{\text{AMPA}}(t)$  and  $g_{\text{GABA}}(t)$  (Fig. 8.17b), were generated using the Ornstein-Uhlenbeck stochastic process (Uhlenbeck and Ornstein 1930), which was originally developed to describe Brownian motion, but can equally well describe *in vivo*-like fluctuating synaptic conductances produced by random firings (Destexhe et al. 2001). Let  $E_{\text{AMPA}} = 0$  mV and  $E_{\text{GABA}} = -65$  mV denote the reverse potentials of excitatory and inhibitory synapses, respectively. The corresponding current

$$I(t) = \underbrace{g_{\text{AMPA}}(t)(E_{\text{AMPA}} - V(t))}_{\text{excitatory input}} + \underbrace{g_{\text{GABA}}(t)(E_{\text{GABA}} - V(t))}_{\text{inhibitory input}}, \quad (8.7)$$

was injected into the neuron using the dynamic clamp protocol (Sharp et al. 1993), where  $V(t)$  denotes the instantaneous membrane potential of the neuron. The same conductances were injected into the simple model (8.5, 8.6), whose parameters were adjusted to fit this particular neuron. The superimposed voltage traces, depicted in

Fig. 8.17a, show a reasonable fit. The simple model predicts more than 90% of spikes of the *in vitro* neuron, often with a submillisecond precision, see Fig. 8.17c. Of course, we should not expect to get a total fit, since we do not explicitly model the sources of intrinsic and synaptic noise present in the cortical slice. In fact, presentation of the same input to the same neuron a few minutes later produces a response with spike jitter, missing spikes, and extra spikes (as in Fig. 7.24) comparable with those in the simulated response.

### 8.2.2 Intrinsically bursting (IB) neurons

The class of intrinsically bursting (IB) neurons forms a continuum of cells that differ in their degree of “burstiness”, and it probably should consist of subclasses. On one extreme, responses of IB neurons to injected pulses of dc-current have initial stereotypical bursts (Fig. 8.18a) of high-frequency spikes followed by low-frequency tonic spiking. Many IB neurons bursts even when the current is barely superthreshold and not strong enough to elicit a sustained response (as in Fig. 8.21, bottom). On the other extreme, bursts could be seen only in response to sufficiently strong current, as in Fig. 8.11 or Fig. 9.1b. Weaker stimulation elicits regular spiking responses. In comparison with typical RS neurons, the regular spiking response of IB neurons has lower firing frequency, higher rheobase (threshold) current, exhibit shorter latency to the first spike and noticeable afterdepolarizations (ADPs), compare RS and IB cell in Fig. 8.11.

Magnifications of the responses of two IB neurons in Fig. 8.18b and c show that the interspike intervals within the burst may be increasing or decreasing, reflecting possibly different ionic mechanisms of burst generation and termination. In any case, the initial high-frequency spiking is caused by the excess of the inward current or the deficit of the outward current needed to repolarize the membrane potential below the threshold. As a result, many spikes are needed to build-up outward current to terminate the high-frequency burst. After the neuron recovers, it fires low frequency tonic spikes because there is a residual outward current (or residual inactivation of inward current) that prevents the occurrence of another burst. Many IB neurons can actually fire two or more bursts before they switch into tonic spiking mode, as in Fig. 8.18a. Below we present two models of IB neurons, one relying on the interplay of voltage-gated currents, another relying on the interplay of fast somatic and slow dendritic spikes.

Let us use the available data on the IB neuron in Fig. 8.11 to build a simple one-compartment model (8.5, 8.6) exhibiting IB firing patterns. The neuron has resting state at  $v_r = -75$  mV and instantaneous threshold at  $v_t = -45$  mV. Its rheobase is 350 pA, and the input resistance is around  $30 \text{ M}\Omega$ , resulting in  $k = 1.2$  and  $b = 5$ . The peak of the spike is at +50 mV, and the after-spike resetting point is around  $c = -56$  mV. The parameters  $a = 0.01$  and  $d = 130$  give a reasonable fit of the neuron’s current-frequency relationship.

The phase portraits in Fig. 8.19 explain the mechanism of firing of IB patterns in the simple model. When  $I = 0$ , the model has an equilibrium at -75 mV, which is

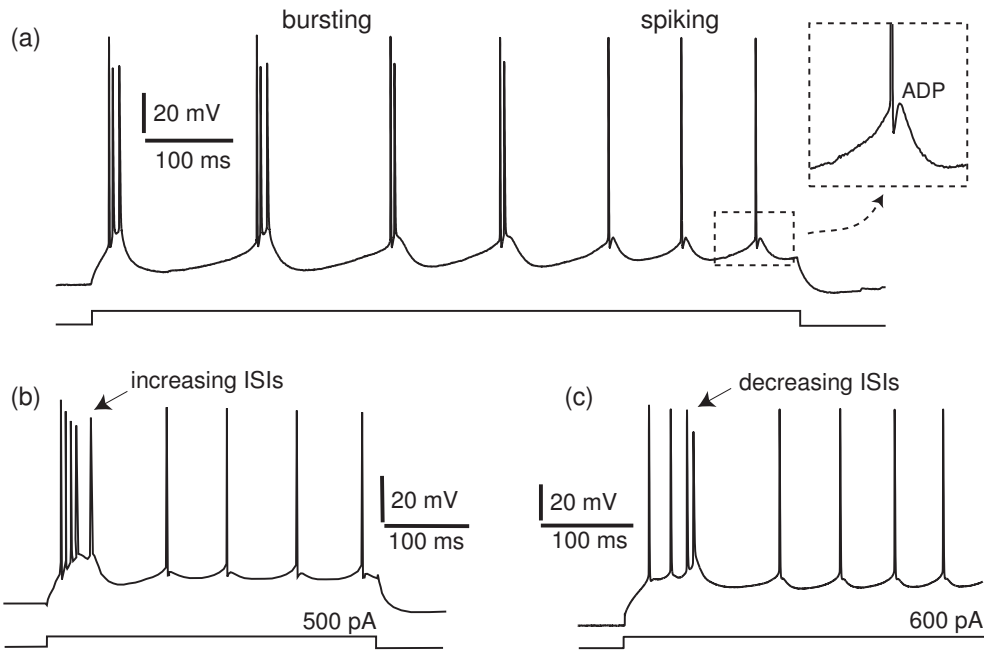


Figure 8.18: (a) bursting and spiking in an IB neuron (layer 5 of somatosensory cortex of a 4 week old rat at 35°C; data was kindly provided by Greg Stuart and Maarten Kole). Notice the afterdepolarization (ADP). (b) IB neuron of a cat (modified from Fig. 2 of Timofeev et al. (2000)). (c) pyramidal neuron of rat's visual cortex. Notice that IB neurons may exhibit bursts with increasing or decreasing inter-spike intervals (ISIs).

the intersection of the  $v$ -nullcline (dashed parabola) and the  $u$ -nullcline (straight line). Injection of a depolarizing current moves the  $v$ -nullcline up. The pulse of current of magnitude  $I = 300$  pA is below the neuron's rheobase, so the trajectory moves from the old resting state (black square) to the new one (black circle). Since  $b > 0$ , the trajectory overshoots the new equilibrium. The pulse of magnitude  $I = 370$  pA is barely above the rheobase, so that the model exhibits low-frequency tonic firing with some spike frequency adaptation. Elevating the fast nullcline by injecting  $I = 500$  pA transforms the first spike into a doublet. Indeed, the after-the-first-spike resetting point (white square marked “1”) is below the parabola, so the second spike is fired immediately. Similarly, injection of an even stronger current of magnitude  $I = 550$  pA transforms the doublet into a burst of three spikes, each raising the after-spike resetting point. Once the resetting point is inside the parabola, the neuron is in tonic spiking mode.

Figure 8.20a shows simultaneous recording of somatic and dendritic membrane potentials of a layer 5 pyramidal neuron. Somatic spike backpropagates into the dendrite, activates voltage-gated dendritic  $\text{Na}^+$  and  $\text{Ca}^{2+}$  currents (Stuart et al. 1999, Häusser et al. 2000), and results in a slower dendritic spike clearly seen in the figure. The slow dendritic spike depolarizes the soma resulting in an ADP, which is typical in many

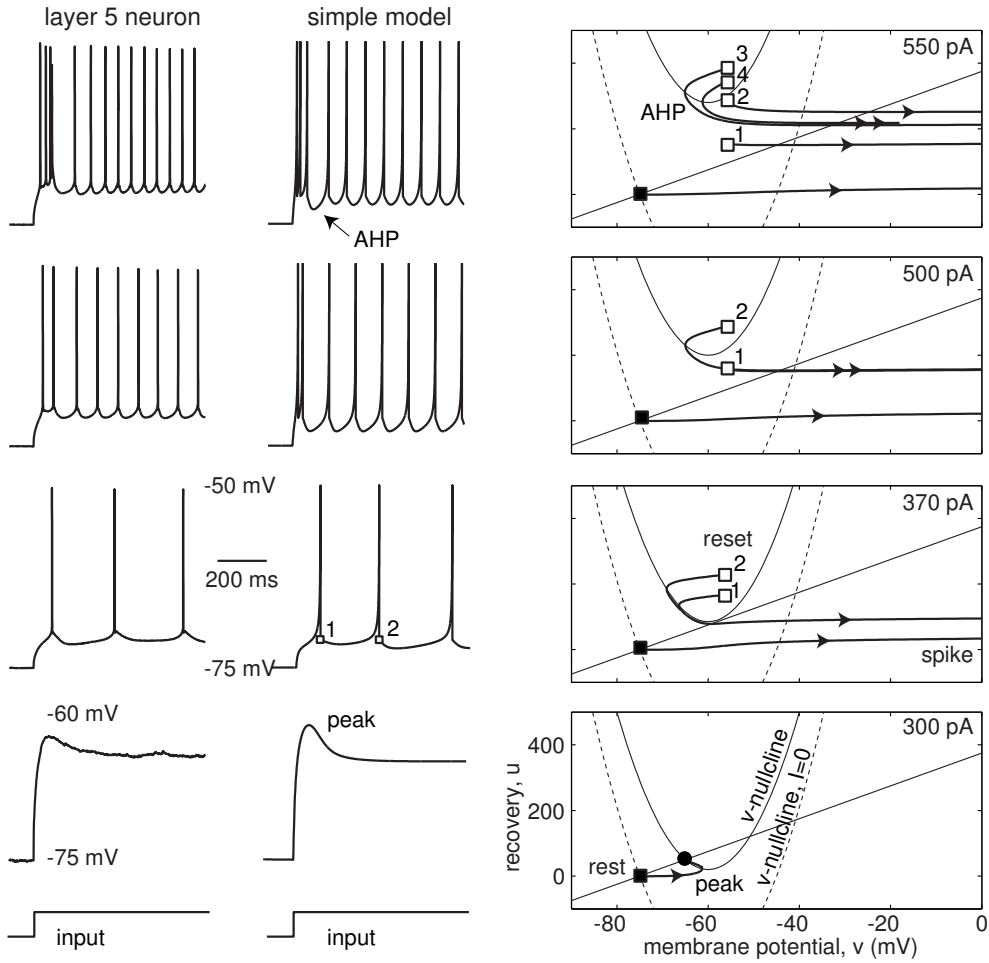


Figure 8.19: Comparison of *in vitro* recordings of an intrinsically bursting (IB) neuron with the simple model  $150\dot{v} = 1.2(v + 75)(v + 45) - u + I$ ,  $\dot{u} = 0.01\{5(v + 75) - u\}$ , if  $v \geq +50$ , then  $v \leftarrow -56$ ,  $u \leftarrow u + 130$ . White squares denote the reset points numbered according to the spike number.

IB cells. Depending on the strength of the injected dc current and the state of the neuron, the AHP can be large enough to cause another somatic spike, as we illustrate in Fig. 7.52. The somatic spike may initiate another dendritic spike, etc., resulting in a burst in Fig. 8.20b. This mechanism is known as the dendritic-somatic ping-pong (Wang 1999) and it occurs in the Pinsky-Rinzel (1994) model of hippocampal CA3 neuron, the sensory neuron of weakly electric fish (Doiron et al. 2002), and in chattering neurons considered below.

Let us build a two-compartment simple model that simulates the somatic and dendritic spike generation of IB neurons. Since we do not know the rheobase, input resistance, resting and instantaneous threshold potentials of dendritic tree of IB neurons, we cannot determine parameters of the dendritic compartment. Instead, we feed the somatic recording  $V(t)$  in Fig. 8.20a into the model dendritic compartment and

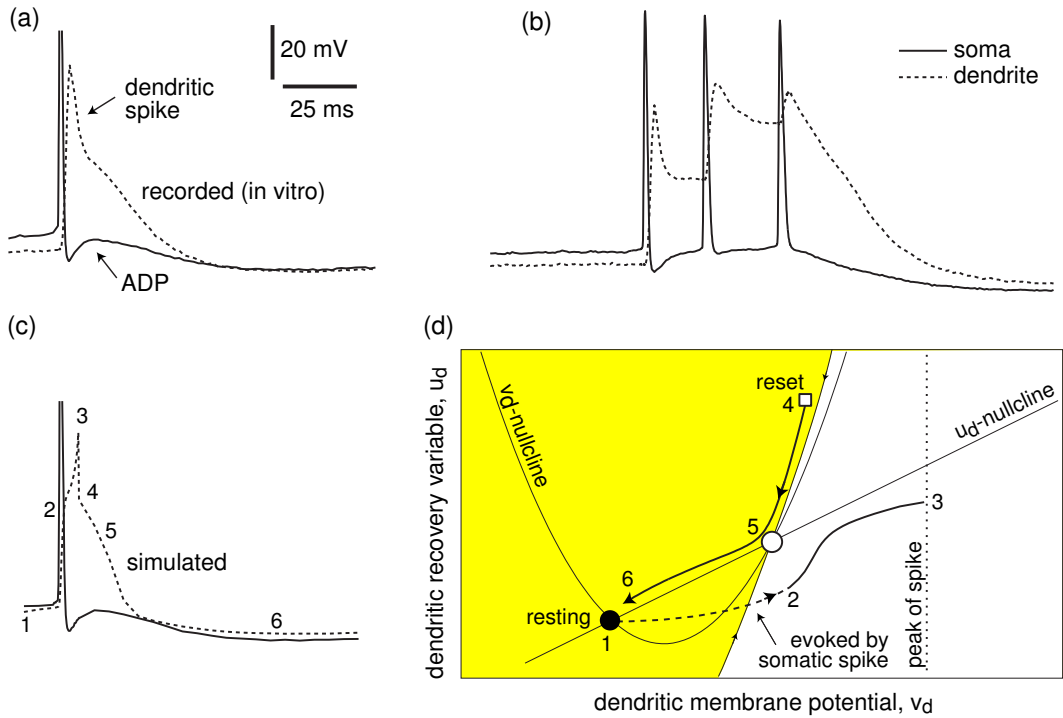


Figure 8.20: Somatic and dendritic spike (a) and burst (b) in an IB neuron. The dendritic spike in (a) is simulated in (c) using the simple model described in Fig. 8.20. Phase portrait (d) describes the geometry of dendritic spike-generation mechanism. (Recordings are from layer 5 of somatosensory cortex of a 4 week old rat at 35C; dendritic electrode is 0.43mm from the soma; data was kindly provided by Greg Stuart and Maarten Kole).

fine-tune the parameters so that simulated dendritic spike in Fig. 8.20c “looks like” the recorded one in Fig. 8.20a.

The phase portrait in Fig. 8.20d explains the peculiarities of the shape of simulated dendritic spike. Recorded somatic spike quickly depolarizes the dendritic membrane potential from point 1 to point 2, and starts the regenerative process — the up-stroke of a spike. Upon reaching the peak of the spike (3), the dendritic membrane potential and the recovery variable are reset by the action of fast voltage-gated  $K^+$  currents, which are not modeled here explicitly. The reset point (4) is near the stable manifold of the saddle, so the membrane potential slowly repolarizes (5) and returns to the resting state (6).

In Fig. 8.21 we put the somatic and dendritic compartment together, adjust some of the parameters, and simulate the response of the IB neuron to pulses of current of various amplitudes. Notice that the model correctly reproduces the transient burst of 2 closely spaced spikes when stimulation is weak, and the rhythmic bursting with decreasing number of spikes per burst when stimulation is strong. Using this approach, one can build models of pyramidal neurons having multiple dendritic compartments,

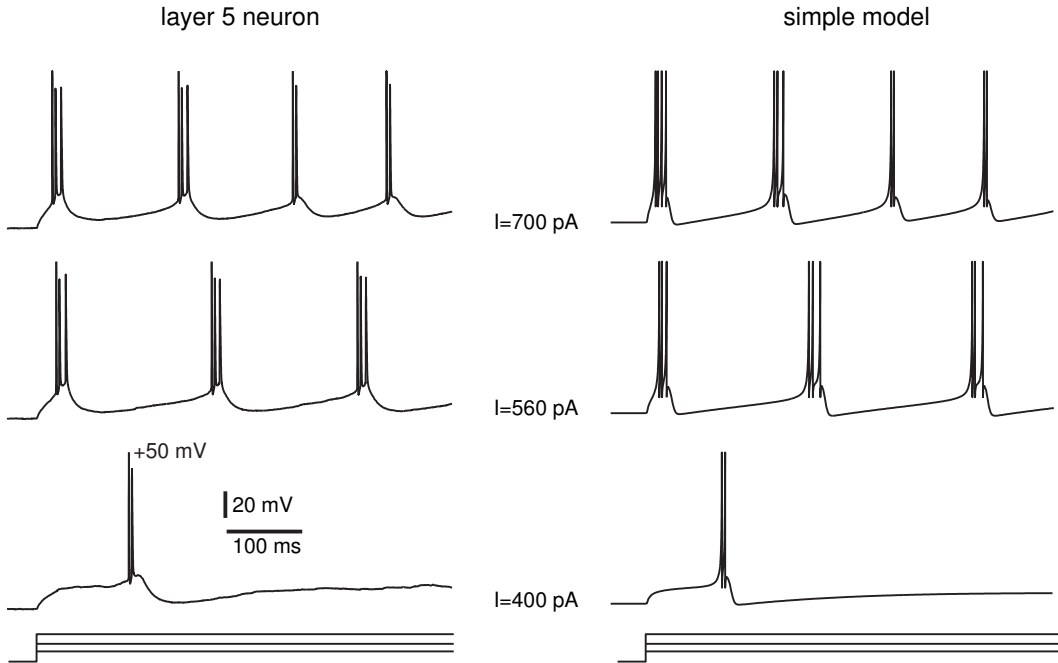


Figure 8.21: Comparison of *in vitro* recordings of an intrinsically bursting (IB) neuron (layer 5 of somatosensory cortex of a 4 week old rat at 35C; data was kindly provided by Greg Stuart and Maarten Kole) with the two-compartment simple model. Soma:  $150\dot{v} = 3(v + 70)(v + 45) + 50(v_d - v) - u + I$ ,  $\dot{u} = 0.01\{5(v + 70) - u\}$ , if  $v \geq +50$ , then  $v \leftarrow -52$ ,  $u \leftarrow u + 240$ . Active dendrite:  $30\dot{v}_d = (v_d + 50)^2 + 20(v - v_d) - u_d$ ,  $\dot{u}_d = 3\{15(v_d + 50) - u_d\}$ , if  $v_d \geq +20$ , then  $v_d \leftarrow -20$ ,  $u_d \leftarrow u_d + 500$ .

as we do next.

### 8.2.3 Multi-compartment dendritic tree

In Fig. 8.22 we simulate an IB pyramidal neuron having 47 compartments (Fig. 8.22a,b), each described by a simple model with parameters provided in the caption of the figure. Our goal is to illustrate a number of interesting phenomena that occur in neuronal models having active dendrites, i.e., dendrites capable of generating action potentials.

In Fig. 8.22c we inject a current into compartment 4 on the apical dendrite to evoke an excitatory post-synaptic potential (EPSP) of 4 mV, which is subthreshold for the spike-generation mechanism. This depolarization produces a current that passively spreads to neighboring compartments, and eventually into the somatic compartment. However, the somatic EPSP is much weaker, only 1 mV, reflecting the distance-dependent attenuation of dendritic synaptic inputs. Notice also that somatic EPSP is delayed and it has a wider time course, which is the result of dendritic low-pass filtering, or smoothing, of subthreshold neuronal signals. The further the stimulation site is from the soma, the weaker, more delayed, and longer lasting is the somatic EPSP. For many years, dendrites were thought to be passive conductors whose sole

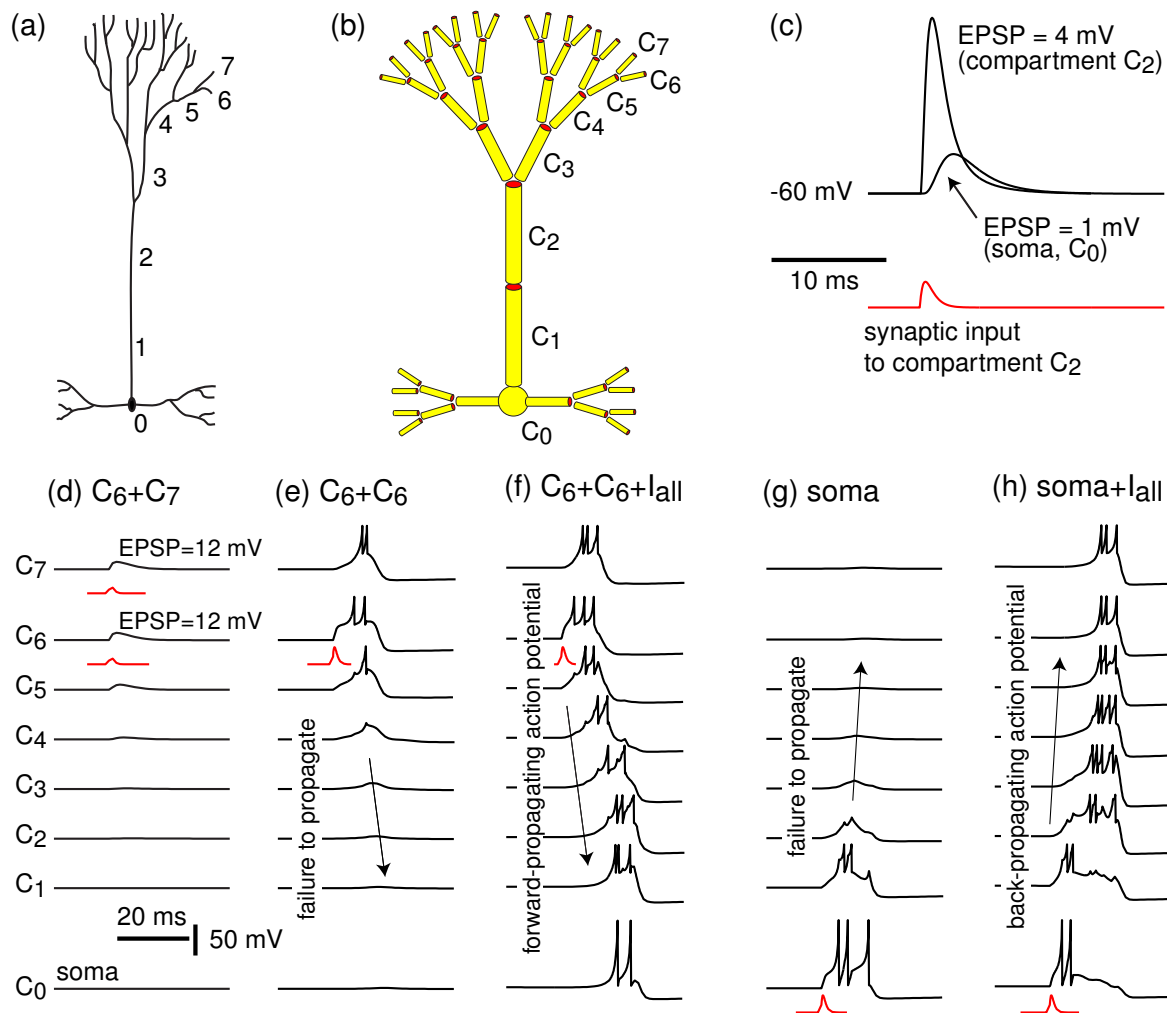


Figure 8.22: (a) Hand drawing and (b) a 47-compartment representation of a layer 5 pyramidal neuron. (c) Injection of excitatory synaptic input into the compartment 2 evokes a large excitatory postsynaptic potential (EPSP) in that compartment, but much smaller EPSP in the somatic compartment. (d) Synaptic inputs to compartments 6 and 7 result in large EPSPs there, but no dendritic spike. (e) The same synaptic inputs into compartment 6 result in dendritic spike, which fails to propagate forward to the soma. (f) The same input combined with background excitation  $I_{\text{all}} = 60 \text{ pA}$  to all compartments results in forward propagating dendritic spikes. (g) Strong synaptic input to the soma results in a spike that fails to propagate into the dendritic tree. (h) The same input combined with injection of  $I_{\text{all}} = 70 \text{ pA}$  to all compartments (to simulate *in vivo* tonic background input) promotes back-propagation of spike into the dendritic tree. Each compartment is simulated by the simple model  $100\dot{v} = 3(v + 60)(v + 50) - u + I$ ,  $\dot{u} = 0.01\{5(v + 60) - u\}$ . Soma: if  $v \geq +50$ , then  $v \leftarrow -55$ ,  $u \leftarrow u + 500$ . Dendrites: if  $v \geq +10$ , then  $v \leftarrow -35$ ,  $u \leftarrow u + 1000$ . The conductance between any two adjacent compartments is 70 nS.

purpose is to collect and low-pass filter the synaptic input.

Now, we explore the active properties of dendrites and their dependence on the location, timing, and strength of synaptic input. First, let us stimulate two synapses that innervate two sister dendritic compartments, e.g., compartments 6 and 7 in Fig. 8.22d that could interact via their mother compartment 5. Each synaptic input evokes a strong EPSP of 12 mV, but due to their separation, the EPSPs do not add up and no dendritic spike is fired. The resulting somatic EPSP is only 0.15 mV due to the passive attenuation. In Fig. 8.22e we provide exactly the same synaptic input, but into the same compartment, i.e., compartment 6. The EPSPs add up and result in a dendritic spike, which propagates into the mother compartment 5 and then into the sister compartment 7 (which was not stimulated), but it fails to propagate along the apical dendrite into the soma. Nevertheless, the somatic compartment exhibits an EPSP of 1.5 mV, hardly seen in the figure. Thus, the location of synaptic stimulation, with all other conditions being equal, made a difference. In Fig. 8.22f we combine the synaptic stimulation to compartment 6 with injection of a weak current,  $I_{\text{all}}$ , to all compartments of the neuron. This current represents a tonic background excitation to the neuron that is always present *in vivo*. It depolarizes the membrane potential by 2.5 mV and facilitates the propagation of the dendritic spike along the apical dendrite all the way into the soma. The same effect could be achieved by an appropriately timed excitatory synaptic input arriving to an intermediate compartment, e.g., compartment 3 or 2. Not surprisingly, an appropriately timed inhibitory input to an intermediate compartment on the apical dendrite could stop the forward-propagating dendritic spike in Fig. 8.22f.

In Fig. 8.22g and h we illustrate the opposite phenomenon — back-propagating spikes from soma to dendrites. A superthreshold stimulation of the somatic compartment evokes a burst of three spikes, which fails to propagate along the apical dendrites alone, but can propagate if combined with a tonic depolarization of the dendritic tree.

We see that dendritic trees can do more than just averaging and low-pass filtering of distributed synaptic inputs. Separate parts of the tree can perform independent local signal processing and even fire dendritic spikes. Depending on the synaptic inputs to other parts of the tree, the spikes can be localized or they can forward-propagate into the soma, causing the cell to fire. Spikes at the soma can backpropagate into the dendrites, triggering spike-time-dependent processes, such as synaptic plasticity.

#### 8.2.4 Chattering (CH) neurons

Chattering neurons, also known as fast rhythmic bursting (FRB) neurons, generate high-frequency repetitive bursts in response to injected depolarizing currents. The magnitude of the dc-current determines the interburst period, which could be as long as 100 ms or as short as 15 ms, and the number of spikes within each burst, typically 2 to 5, as we illustrate in Fig. 8.23 using *in vivo* recordings of pyramidal neuron of cat visual cortex.

An RS model neuron as shown in Fig. 8.12 can be easily transformed into a CH

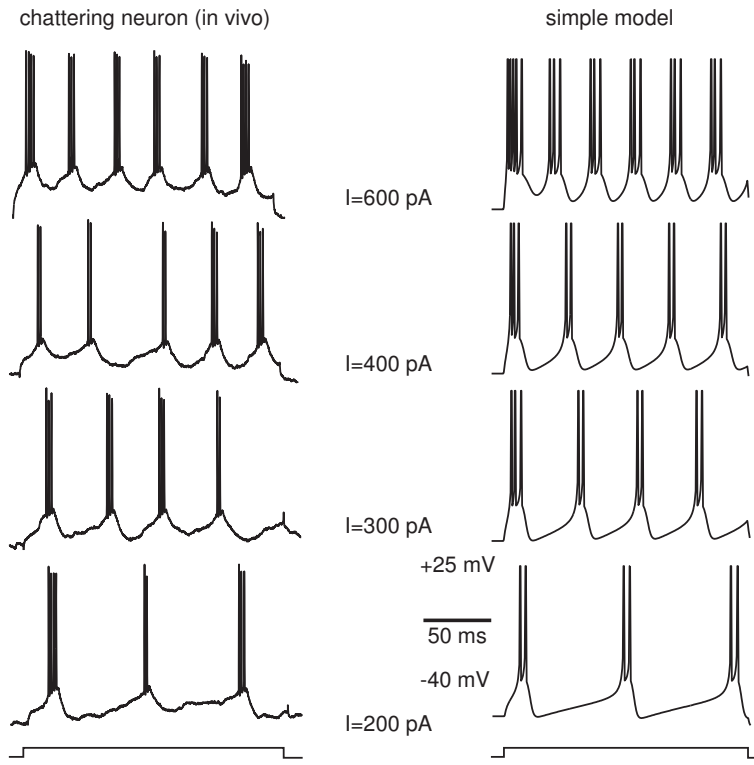


Figure 8.23: Comparison of *in vivo* recordings from cat's primary visual cortex with simulations of the simple model  $50\dot{v} = 1.5(v+60)(v+40) - u + I$ ,  $\dot{u} = 0.03\{(v+60) - u\}$ , if  $v \geq +25$ , then  $v \leftarrow -40$ ,  $u \leftarrow u + 150$ . Data were kindly provided by D. McCormick, and are available on the author's webpage.

neuron by increasing the after-spike reset voltage to  $c = -40$  mV, mimicking decreased  $K^+$  and increased  $Na^+$  currents activated during each spike. The phase portrait in Fig. 8.24 explains the mechanism of chattering of the simple model (8.5, 8.6). A step of depolarizing current shifts the fast quadratic nullcline up and the trajectory quickly moves rightward to fire a spike. The after-spike reset point (white square marked “1” in the figure) is outside the parabola nullcline, so another spike is fired immediately, etc., until the total amount of outward current is large enough to stop the burst, that is, until the variable  $u$  moves the reset point (white square marked “5”) inside the quadratic parabola. The trajectory makes a brief excursion to the left knee (afterhyperpolarization) and then moves rightward again, initiating another burst. Since the second burst starts with an elevated value of  $u$ , it has fewer spikes — a phenomenon exhibited by many CH neurons.

### 8.2.5 Low-threshold spiking (LTS) interneurons

Low-threshold spiking interneurons behave similarly to RS excitatory neurons ( $b > 0$ ) in the sense that they exhibit regular spiking patterns in response to injected pulses of

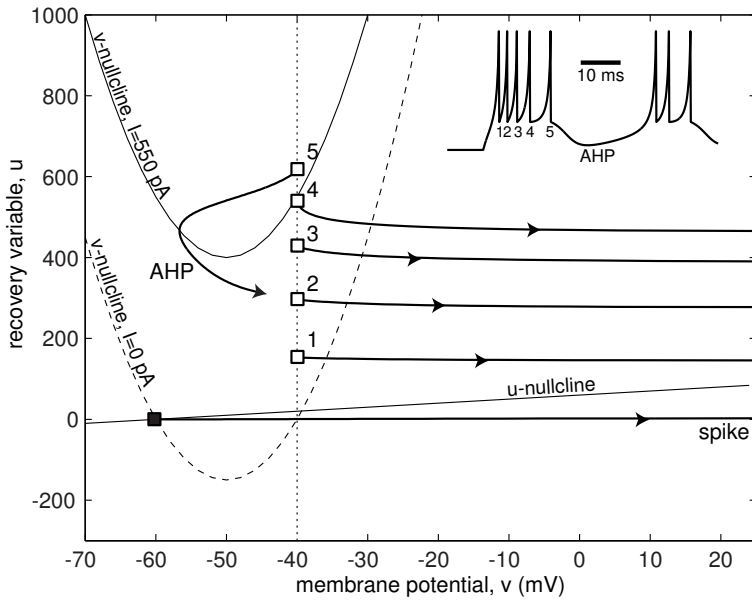


Figure 8.24: Phase portrait of the simple model in Fig. 8.23 exhibiting CH firing pattern.

current. There are some subtle differences: The response of an LTS cell to a weak depolarizing current consists of a phasic spike or a doublet with a relatively short latency followed by low-frequency (less than 10 Hz) subthreshold oscillation of membrane potential. Stronger pulses elicit tonic spikes with slow frequency adaptation, decreasing amplitudes and decreasing after-hyperpolarizations, as one can see in Fig. 8.11.

LTS neurons have more depolarized resting potentials, lower threshold potentials, and lower input resistances than those of RS neurons. To match the *in vitro* firing patterns of LTS interneuron of rat's barrel cortex in Fig. 8.25, we take the simple model of RS neuron and adjust the resting and instantaneous threshold potentials  $v_r = -56$  mV and  $v_t = -42$  mV, and the values  $p = 1$  and  $b = 8$  resulting in the rheobase current of 120 pA and the input resistance of 50 M $\Omega$ . To model the decreasing nature of the spike and AHP amplitudes, we assume that the peak of the spike and the after-spike resetting point depend on the value of the recovery variable  $u$ . This completely unnecessary cosmetic adjustment has a mild effect on the quantitative behavior of the model but renders a more “realistic” look to the simulated voltage traces in Fig. 8.25.

The class of excitability of LTS neurons has not been studied systematically, though the neurons seem to be able to fire periodic spike trains with a frequency as low as that of RS neurons (Beierlein et al. 2003, Tateno and Robinson, personal communication). The conjecture that they are near saddle-node on invariant circle bifurcation, and hence are Class 1 excitable integrators, seems to be at odds with the observation that their membrane potential exhibits slow damped oscillation and that they can fire post-inhibitory rebound spikes (Bacci et al. 2003), called low-threshold spikes (hence the name). They are better characterized as being at the transition from integrators to

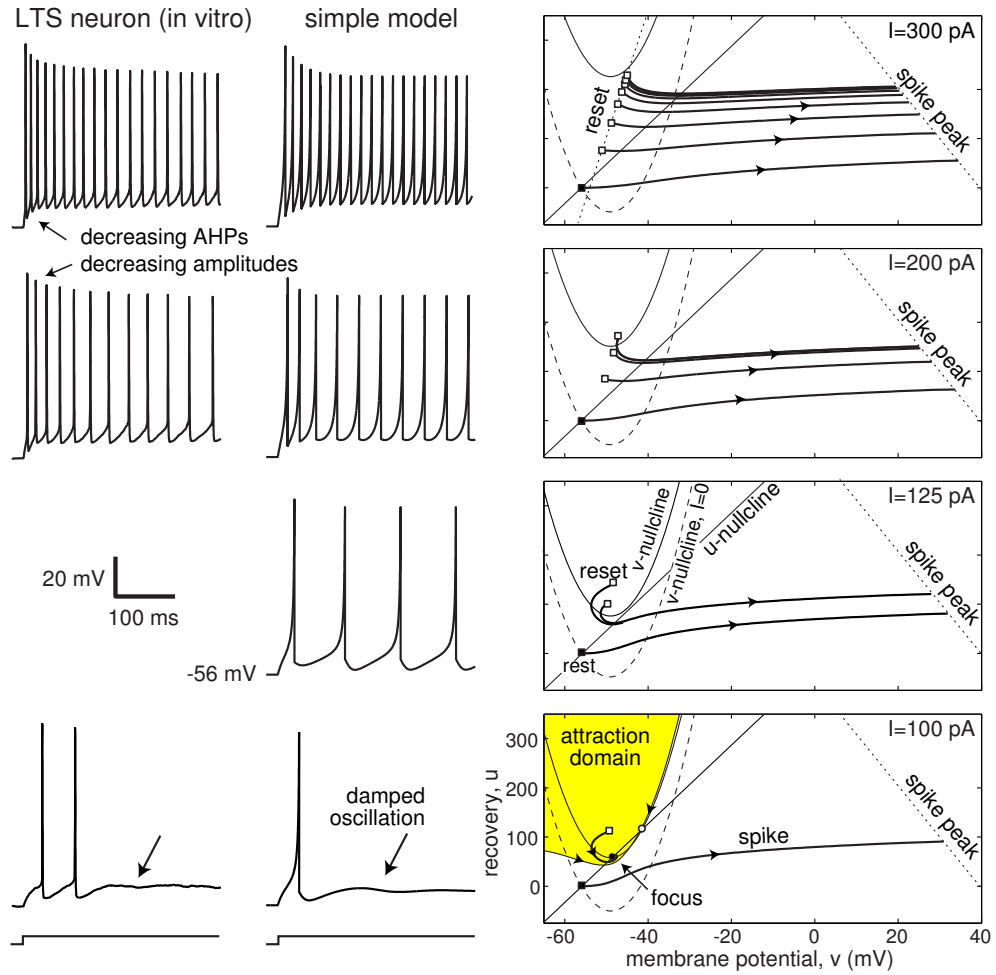


Figure 8.25: Comparison of *in vitro* recordings of a low threshold spiking (LTS) interneuron (rat's barrel cortex, data provided by B. Connors) with simulations of the simple model  $100\dot{v} = (v + 56)(v + 42) - u + I$ ,  $\dot{u} = 0.03\{8(v + 56) - u\}$ , if  $v \geq 40 - 0.1u$ , then  $v \leftarrow -53 + 0.04u$ ,  $u \leftarrow u + 20$ .

resonators, with phase portraits as in Fig. 8.15.

A possible explanation for the subthreshold oscillations in LTS (and some RS) neurons is given in Fig. 8.13, case  $b > 0$ . The resting state is a stable node when  $I = 0$ , but it becomes a stable focus when the magnitude of the injected current is near the neuron's rheobase. After firing a phasic spike, the trajectory spirals in to the focus exhibiting damped oscillation. Its frequency is the imaginary part of the complex-conjugate eigenvalues of the equilibrium, and it is small because the system is near Bogdanov-Takens bifurcation.

A possible explanation for the rebound spike in LTS (or some RS) neurons is given in Fig. 8.26. The shaded region is the attraction domain of the resting state (black circle), which is bounded by the stable manifold of the saddle (white circle). A sufficiently strong hyperpolarized pulse moves the trajectory to the new, hyperpolarized

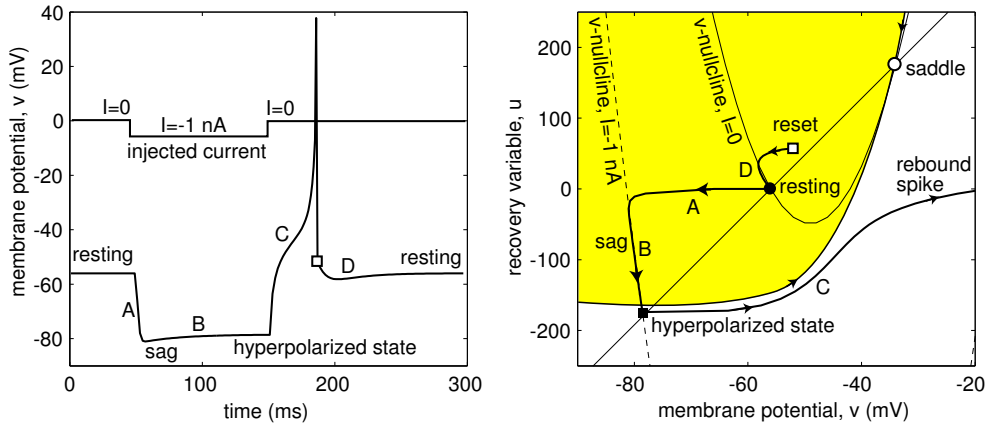


Figure 8.26: The mechanism of sag and rebound spike of the model in Fig. 8.25.

equilibrium (black square), which is outside the attraction domain. Upon release from the hyperpolarization, the trajectory fires a phasic spike and then returns to the resting state. Some LTS interneurons fire bursts of spikes, and for that reason are called burst-spiking non-pyramidal (BSNP) neurons.

### 8.2.6 Fast spiking (FS) interneurons

Fast spiking neurons fire “fast” tonic spike trains of relatively constant amplitude and frequency in response to depolarized pulses of current. In a systematic study, Tateno et al. (2004) have shown that FS neurons have Class 2 excitability in the sense that their frequency-current (F-I) relation has a discontinuity around 20 Hz. When stimulated with barely superthreshold current, such neurons exhibit irregular firing randomly switching between spiking and fast subthreshold oscillatory mode (Kubota and Kawaguchi 1999, Tateno et al. 2004).

The absence of spike frequency adaptation in FS neurons is mostly due to the fast  $K^+$  current that activates during the spike, produces deep AHP, completely deinactivates  $Na^+$  current, and thereby facilitates the generation of the next spike. Blocking the  $K^+$  current by TEA (Erisir et al. 1999) removes AHP, leaves residual inactivation of the  $Na^+$  current and slows down the spiking, essentially transforming the FS firing pattern into LTS.

The existence of fast subthreshold oscillations of membrane potential suggest that the resting state of the FS neurons is near Andronov-Hopf bifurcation. Stuttering behavior at the threshold currents points to the co-existence of resting and spiking states, as in Fig. 8.16, and suggests that the bifurcation is of the subcritical type. However, FS neurons do not fire post-inhibitory (rebound) spikes — the feature used to distinguish them experimentally from LTS types. Thus, we cannot use the simple model (8.5, 8.6) in its present form to simulate FS neurons because the model with linear slow nullcline would fire rebound spikes according to the mechanism depicted in Fig. 8.26. In addition, the simple model has a non-monotone I-V relation, whereas FS

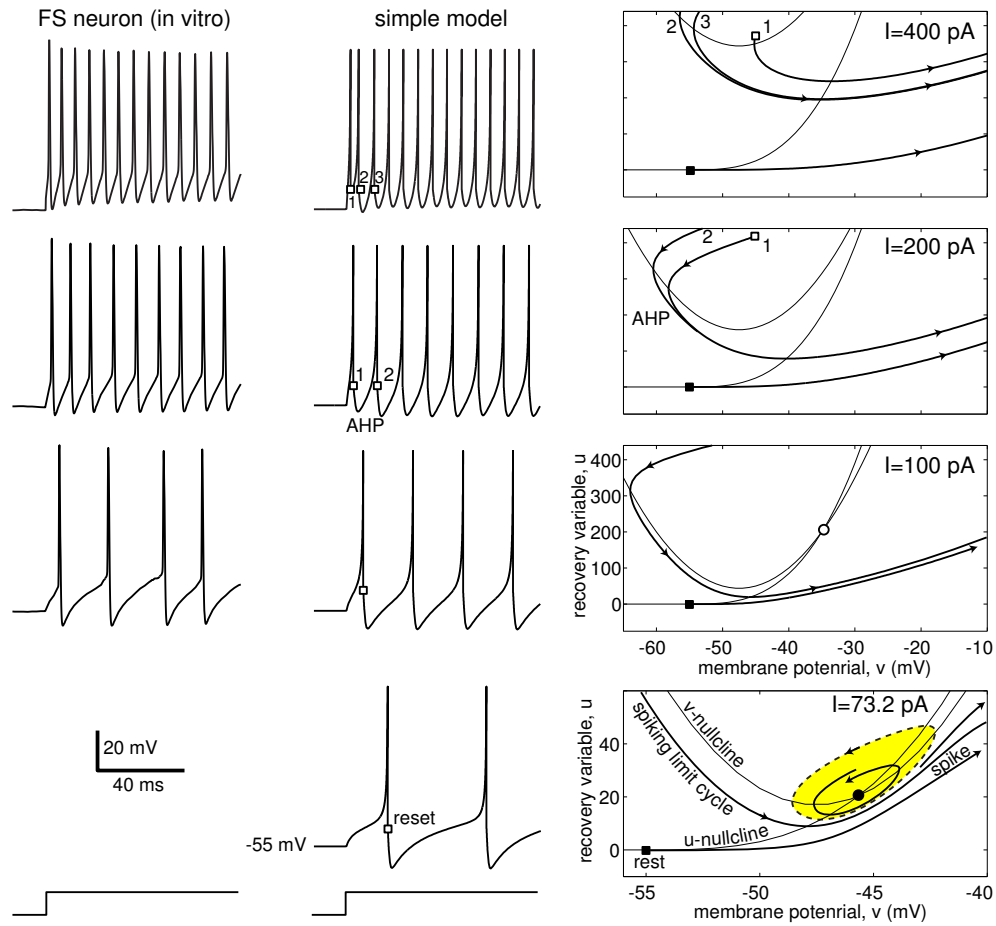


Figure 8.27: Comparison of *in vitro* recordings of a fast spiking (FS) interneuron of layer 5 rat's visual cortex with simulations of the simple model  $20\dot{v} = (v+55)(v+40)-u+I$ ,  $\dot{u} = 0.2\{U(v) - u\}$ , if  $v \geq 25$ , then  $v \leftarrow -45$  mV. Slow nonlinear nullcline  $U(v) = 0$  when  $v < v_b$  and  $U(v) = 0.025(v - v_b)^3$  when  $v \geq v_b$  with  $v_b = -55$  mV. Shaded area denotes the attraction domain of the resting state.

neurons have monotone relation.

The absence of rebound responses in FS neurons means that the phenomenological recovery variable (activation of fast  $K^+$  current) does not decrease significantly below the resting value when the membrane potential is hyperpolarized. That is, the slow  $u$ -nullcline becomes horizontal in the hyperpolarized voltage range. Accordingly, we simulate FS neuron in Fig. 8.27 using the simple model (8.5) with nonlinear  $u$ -nullcline.

The phase portraits and bifurcation diagram of the FS neuron model are qualitatively similar to the fast subsystem of a “subHopf/fold cycle” burster: Injection of dc-current  $I$  creates a stable and unstable limit cycles via fold limit cycle bifurcation. The frequency of the newborn stable cycle is around 20 Hz, hence the discontinuity of the F-I curve and Class 2 excitability. There is a bistability of resting and spiking states, as in Fig. 8.27, bottom, so that noise can switch the state of the neuron back

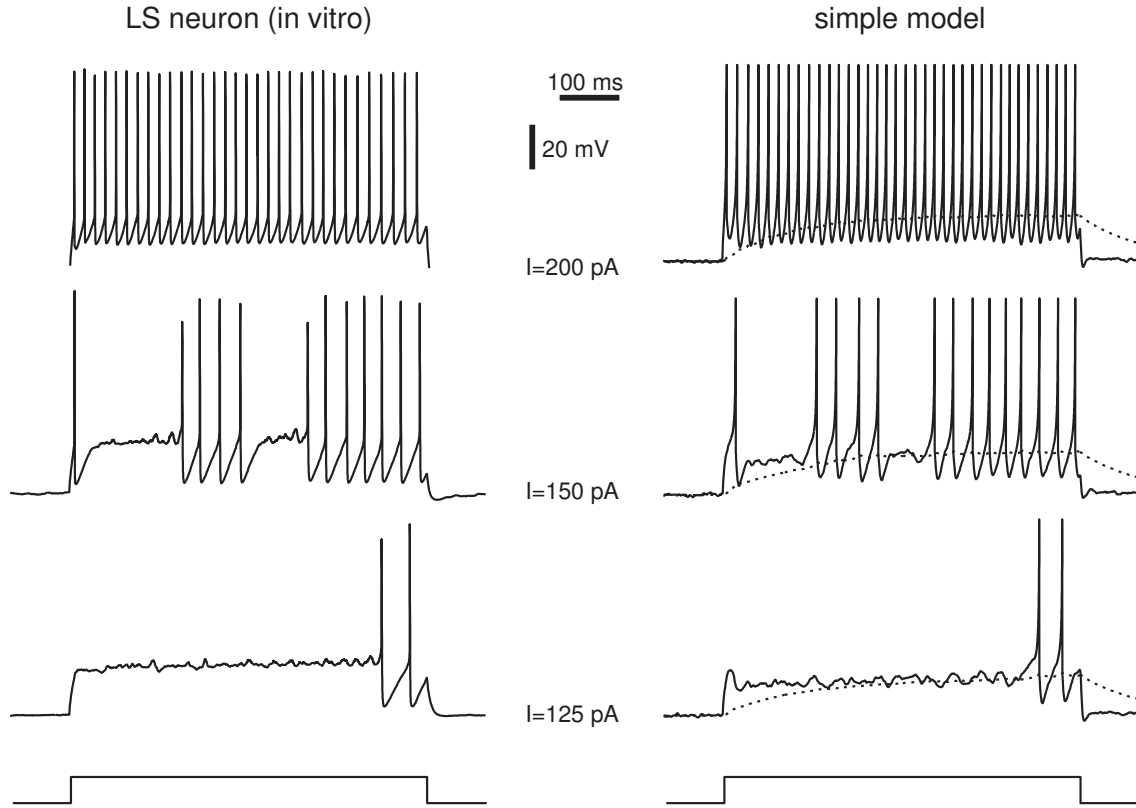


Figure 8.28: Comparison of *in vitro* recordings of a late spiking (LS) interneuron of layer 1 rat's neocortex with simulations of the simple two-compartment model. Soma:  $20\dot{v} = 0.3(v + 66)(v + 40) + 1.2(v_d - v) - u + I$ ,  $\dot{u} = 0.17\{5(v + 66) - u\}$ , if  $v \geq 30$ , then  $v \leftarrow -45$ ,  $u \leftarrow u + 100$ . Passive dendrite (dotted curve):  $\dot{v}_d = 0.01(v - v_d)$ . Weak noise was added to simulations to unmask the subthreshold oscillations. (Recordings were kindly provided by Zhiguo Chu, Mario Galarreta and Shaul Hestrin. Traces  $I = 125$  and  $I = 150$  are from one cell, trace  $I = 200$  is from another cell.)

and forth and result in irregular stuttering spiking with subthreshold oscillations in the 10-40 Hz range between the spike trains. Further increase of  $I$  shrinks the amplitude of the unstable limit cycle, results in the subcritical Andronov-Hopf bifurcation of the resting state, removes the co-existence of attractors, and leaves only tonic spiking mode.

### 8.2.7 Late spiking (LS) interneurons

When stimulated with long pulses of dc-current, late spiking neurons exhibit a long voltage ramp, barely seen in Fig. 8.28, bottom, and then switch into a tonic firing mode. A stronger stimulation may evoke an immediate (transient) spike followed by a long ramp and a long latency to the second spike. There are pronounced fast subthreshold oscillations during the voltage ramp indicating the existence of at least two time scales:

(1) fast oscillations resulting from the interplay of amplifying and resonant currents, and (2) slow ramp resulting from the slow kinetic of an amplifying variable, such as slow inactivation of an outward current (e.g.,  $K^+$  A-current) or slow activation of an inward current, or both. In addition, the ramp could result from the slow charging of the dendritic compartment of the neuron.

The exact mechanism responsible for the slow ramp in LS neurons is not known at present. Fortunately, we do not need to know the mechanism to simulate LS neurons using the simple model approach. Indeed, simple models with passive dendrites are equivalent to simple models with linear amplifying currents. For example, the model in Fig. 8.28 consists of a 2-dimensional system  $(v, u)$  responsible for the spike-generation mechanism at the soma and a linear equation for the passive dendritic compartment  $v_d$ .

When stimulated with the threshold current, i.e., just above the neuronal rheobase, LS neurons often exhibit stuttering behavior seen in Fig. 8.28, middle. Subthreshold oscillations, voltage ramps, and stuttering are consistent with the following geometrical picture: Abrupt onset of stimulation evokes a transient spike followed by brief hyperpolarization and then sustained depolarization. While depolarized, the fast subsystem affects the slow subsystem, e.g., slowly charges the dendritic tree or slowly inactivates the  $K^+$  current. In any case, there is a slow decrease of the outward current, or equivalently, slow increase of the inward current that drives the fast subsystem through the subcritical Andronov-Hopf bifurcation. Because of the co-existence of resting and spiking states near the bifurcation, the neuron can be switched from one state to the other by the membrane noise. Once the bifurcation is passed, the neuron is in the tonic spiking mode. Overall, LS neurons can be thought of as being FS neurons with a slow subsystem that damps any abrupt changes, delays the onset of spiking, and slows down its frequency.

### 8.2.8 Diversity of inhibitory interneurons

In contrast to excitatory neocortical pyramidal neurons, which have stereotypical morphological and electrophysiological classes (RS, IB, CH), inhibitory neocortical interneurons have wildly diverse classes with various firing patterns that cannot be classified as FS, LTS, or LS. Markram et al. (2004) reviewed recent results on the relationship between electrophysiology, pharmacology, immunohistochemistry and gene-expression patterns of inhibitory interneurons. An extreme interpretation of their findings is that there is a continuum of different classes of interneurons rather than a set of 3 classes.

Figure 8.29 summarizes five of the most ubiquitous groups in the continuum:

- (NAC) non-accommodating interneurons fire repetitively without frequency adaptation in response to a wide range of sustained somatic current injections. Many FS and LS neurons are of this type.
- (AC) accommodating interneurons fire repetitively with frequency adaptation and therefore do not reach high firing rates of NAC neurons. Some FS and LS

cells, but mostly LTS cells are of this type.

- (STUT) stuttering interneurons fire high-frequency clusters of regular spikes intermingled with unpredictable periods of quiescence. Some FS and LS cells exhibit this firing type.
- (BST) bursting interneurons fire a cluster of 3 to 5 spikes riding on a slow depolarizing wave followed by a strong slow AHP.
- (IS) irregular spiking interneurons fire single spikes randomly with pronounced frequency accommodation.

NAC and AC are the most common response types found in neocortex. Each group can be divided into three subgroups depending on the type of the onset of the response to a step depolarization:

- (c) classical response is when the first spike has the same shape as any other spike in the response.
- (b) burst response is when the first three or more spikes are clustered into a burst.
- (d) delayed response is when there is noticeable delay before the onset of spiking.

The BST type has a different subdivision: repetitive (r), initial (i), or transient (t) bursting.

In Fig. 8.30 we use the simple model (8.5, 8.6) to reproduce all firing patterns of the interneurons, including the delayed irregular spiking (d-IS) pattern that was omitted in Fig. 8.29. We use one-fit-all set of parameters  $C = 100$ ,  $k = 1$ ,  $v_r = -60$  mV and  $v_t = -40$  mV, and we vary the parameters  $a$ ,  $b$ ,  $c$ , and  $d$ . We do not strive to reproduce the patterns quantitatively, but only qualitatively.

The parameters for the NAC and AC cells were similar to those for RS neurons, with an additional passive dendritic compartment for the delayed response. The parameters for the STUT and IS cells were similar to those of LS interneuron with some minor modifications that affect the initial burstiness and delays. Irregular stuttering in these types results from the co-existence of stable resting equilibrium and spiking limit cycle attractor, as in the case of FS and LS neurons considered above. The level of intrinsic noise controls the probabilities of transitions between the attractors. The parameters for the BST cells were similar to those of IB and CH pyramidal cells. Varying the parameters  $a$ ,  $b$ ,  $c$ , and  $d$ , we indeed can get all the firing patterns in Fig. 8.29 plus many intermediate patterns, thereby creating a continuum of types of inhibitory interneurons.

## 8.3 Thalamus

Thalamus is the major gateway to the neocortex in the sense that no sensory signal, such as vision, hearing, touch, taste, etc., can reach the neocortex without first passing

through an appropriate thalamic nucleus. Anatomically, the thalamic system consists of three major types of neurons: thalamocortical (TC) neurons, which relay signals into the neocortex, reticular thalamic nucleus (RTN) neurons, and thalamic interneurons, which provide local reciprocal inhibition (Shepherd 2004). The three types have distinct electrophysiological properties and firing patterns.

There are undoubtedly subtypes with each type of thalamic neurons, however, the classification is not as elaborate as the one in neocortex. This, and the difference between species, age and various thalamic nuclei, explains the contradictory reports of different firing patterns in presumably the same types of thalamic neurons. Below we use the simple model (8.5, 8.6) to simulate a “typical” TC, TRN, and interneuron. The reader should realize, though, that our attempt is as incomplete as the attempt to simulate a “typical” neocortical neuron ignoring the fact that there are RS, IB, CH, FS, etc., cells.

### 8.3.1 Thalamo-cortical (TC) relay neurons

Thalamocortical (TC) relay neurons, the type of thalamic neurons that project sensory input to the cortex, have two prominent models of firing, illustrated in Fig. 8.31: tonic and burst mode. Both modes are ubiquitous *in vitro* and *in vivo*, including awake and behaving animals, and both represent different patterns of relay of sensory information into the cortex (Sherman 2001). The transition between the firing modes depend on the degree of inactivation of low-threshold  $\text{Ca}^{2+}$  T-current (Jahnsen and Llinas 1984, McCormick and Huguenard 1992), which in turn depends on the holding membrane potential of the TC neuron.

In tonic mode, the resting membrane potential of a TC neuron is around  $-60$  mV, which is above the inactivation threshold of the T-current. The slow  $\text{Ca}^{2+}$  current is inactivated and is not available to contribute to spiking behavior. The neuron fires  $\text{Na}^+$ - $\text{K}^+$  tonic spikes with a relatively constant frequency that depends on the amplitude of the injected current and could be as low as a few Hertz (Zhan et al. 1999). Such a cell, illustrated in Fig. 8.31, is a typical Class 1 excitable system near a saddle-node on invariant circle bifurcation. It exhibits regular spiking behavior similar to that of RS neocortical neurons. It relays transient inputs into outputs, and for this reason, many refer to the tonic mode as relay mode of firing.

To switch a TC neuron into the burst mode, an injected dc-current or inhibitory synaptic input must hyperpolarize the membrane potential to around  $-80$  mV for at least 50-100 ms. While hyperpolarized, the  $\text{Ca}^{2+}$  T-current deinactivates and becomes available. As soon as the membrane potential is returned to the resting or depolarized state, there is an excess of the inward current that drives the neuron over threshold and results in a rebound burst of high-frequency spikes, as in Fig. 8.31, called a low-threshold (LT) spike or a  $\text{Ca}^{2+}$  spike.

In Fig. 8.31, right, we simulate TC neuron using simple model (8.5, 8.6), treating  $u$  as the low-threshold  $\text{Ca}^{2+}$  current. Since the current is inactivated in the tonic mode, i.e.,  $u \approx 0$ , we take  $b = 0$ . The resting and threshold voltages of the neuron in the

figure are  $v_r = -60$  mV and  $v_t = -50$  mV. The value  $p = 1.6$  results in 40 pA rheobase current and  $60\text{ M}\Omega$  input resistance, and the membrane capacitance  $C = 200$  pF gives the right current-frequency (F-I) relationship. Thus, in the tonic mode, our model is essentially the quadratic integrate-and-fire neuron  $200\dot{v} = 1.6(v + 60)(v + 50) + I$  with the after-spike reset from +35 mV to -60 mV.

To model slow  $\text{Ca}^{2+}$  dynamics in the burst mode, we assume that hyperpolarizations below the  $\text{Ca}^{2+}$  inactivation threshold of -65 mV decrease  $u$ , thereby creating inward current. In the linear case, we take  $\dot{u} = 0.01\{b(v + 65) - u\}$  with  $b = 0$  when  $v \geq -65$  and  $b = 15$  when  $v < -65$ , resulting in the piecewise linear  $u$ -nullcline depicted in Fig. 8.31, bottom. Prolonged hyperpolarization below -65 mV decreases  $u$  and moves the trajectory outside the attraction domain of the resting state (shaded region in the figure). Upon release from the hyperpolarization, the model fires a rebound burst of spikes, variable  $u \rightarrow 0$  reflecting inactivation of  $\text{Ca}^{2+}$ , and the trajectory reenters the attraction domain of the resting state. Steps of depolarized current produce rebound bursts followed by tonic spiking with adapting frequency. A better quantitative agreement with TC recordings can be achieved when two slow variables,  $u_1$  and  $u_2$ , are used.

### 8.3.2 Reticular thalamic nucleus (RTN) neurons

Reticular thalamic nucleus (RTN) neurons provide reciprocal inhibition to TC relay neurons. RTN and TC cells are similar in the sense that they have two firing modes, illustrated in Fig. 8.32: They fire trains of single spikes following stimulation from resting or depolarized potentials in the tonic mode, and rebound bursts upon release from hyperpolarized potentials in the burst mode.

The parameters of the simple model in Fig. 8.32 are adjusted to match the *in vitro* recording of the RTN cell in the figure, and they differ from the parameters of the TC model cell. Nevertheless, the mechanism of rebound bursting of RTN neuron is the same as that of the TC neuron in Fig. 8.31, bottom. In contrast, the tonic mode of firing is different. Since  $b > 0$ , the model neuron is near the transition from an integrator to a resonator; It can fire transient spikes followed by slow subthreshold oscillations of membrane potential; It has co-existence of stable resting and spiking states, with the bifurcation diagram similar to the one in Fig. 8.15, and it can stutter and produce clustered spikes when stimulated with barely threshold current. Interestingly, similar behavior of TC neurons was reported by Pirchio et al. (1997), Pedroarena and Llinas (1997) and Li et al. (2003). We will return to the issue of subthreshold oscillations and stuttering spiking when we consider stellate cells of entorhinal cortex in Sect. 8.4.4.

### 8.3.3 Thalamic interneurons

In contrast to TC and RTN neurons, thalamic interneurons do not have a prominent burst mode, though they can fire rebound spikes upon release from hyperpolarization (Pape and McCormick 1995). They have action potentials with short duration, and

they are able to generate high-frequency trains of spikes reaching 800 Hz, like cortical FS interneurons. The simple model in Fig. 8.33 reproduces all these features. Its phase portrait and bifurcation diagram is similar to the one in Fig. 8.15, but its dynamics has a much faster time scale.

## 8.4 Other interesting cases

The neocortical and thalamic neurons span an impressive range of dynamic behavior. Many neuronal types found in other brain regions have dynamics quite similar to some of the types discussed above, while many do not.

### 8.4.1 Hippocampal CA1 pyramidal neurons

Hippocampal pyramidal neurons and interneurons are similar to those of the neocortex, and hence could be simulated using the simple model presented in Sect. 8.2. Let us elaborate using the pyramidal neurons of CA1 region of hippocampus as an example.

Jensen et al. (1994) suggested to classify all CA1 pyramidal neurons according to their propensity to fire bursts of spikes, often called *complex spikes*. The majority (more than 80%) of CA1 pyramidal neurons are non-bursting cells, whereas the remaining exhibit some form of bursts, which are defined in this context as sets of three or more closely spaced spikes. There are five different classes:

- (NB) Non-bursting cells generate accommodating trains of tonic spikes in response to depolarizing pulses of dc-current and a single spike in response to a brief superthreshold pulse of current, as in Fig. 8.34A.
- (HTB) High-threshold bursters fire bursts only in response to strong long pulses of current, but fire single spikes in response to weak or brief pulses of current, as in Fig. 8.34B.
- (LTB I) Grade I low-threshold bursters fire bursts in response to long pulses, but single spikes in response to brief pulses of current, as in Fig. 8.34C.
- (LTB II) Grade II low-threshold bursters fire stereotypical bursts also in response to brief pulses, as in Fig. 8.34D.
- (LTB III) Finally, grade III low-threshold bursters fire rhythmic bursts spontaneously, which are depicted in Fig. 8.34E using two time scales.

NB neurons are equivalent to neocortical pyramidal neurons of RS type, whereas HTB and LTB I neurons are equivalent to neocortical pyramidal neurons of IB type. The author is not aware of any systematic studies of the ability of IB neurons to fire stereotypical bursts in response to brief pulses, as in Fig. 8.34Db, or to have intrinsic rhythmic activity, as in Fig. 8.34E. Therefore, it is not clear whether there are any analogues of LTB grade II and III neurons in the neocortex.

The classification of hippocampal CA1 pyramidal neurons into five different classes does not imply a fundamental difference in the ionic mechanism of spike-generation, but only a quantitative difference. This follows from the observation that pharmacological manipulations can gradually and reversibly transform an NB neuron into LTB III neuron and visa-versa by elevating the extracellular concentration of  $K^+$  (Jensen et al. 1994), reducing extracellular  $Ca^{2+}$  (Su et al. 2001), or blocking  $K^+$  M-current (Yue and Yaari 2004), or manipulating  $Ca^{2+}$  current dynamics in apical dendrites (Magee and Carruth 1999).

In Fig. 8.35 we modify the simple model for neocortical RS neuron to reproduce firing patterns of hippocampal pyramidal cells. To get the continuum of responses, from NB to LTB II, we fix all the parameters and vary only the after-spike reset parameter  $c$  in an increment of 5 mV, and the parameter  $d$ . These phenomenological parameters describe the effect of high-threshold inward and outward currents activated during each spike and affecting the after-spike behavior. Increasing  $c$  corresponds to up-regulating slow  $I_{Na,p}$  or down-regulating slow  $K^+$  currents, which leads to transition from NB to LTB III in the CA1 slice (Su et al. 2001) and in the simple model in Fig. 8.35. Interestingly, the same procedure results in transitions from RS to IB and possibly to CH classes in neocortical pyramidal neurons (Izhikevich 2003). This is consistent with the observation by Steriade (2004) that many neocortical neurons can change their firing classes *in vivo* depending on the state of the brain.

#### 8.4.2 Spiny projection neurons of neostriatum and basal ganglia

Spiny projection neurons, the major class of neurons in neostriatum and basal ganglia, display a prominent bistable behavior *in vivo* shown in Fig. 8.36 (Wilson and Groves 1981, Wilson 1993): They shift the membrane potential from hyperpolarized to depolarized states in response to synchronous excitatory synaptic input from cortex and/or thalamus. *In vitro* studies of such neurons reveal a slowly inactivating  $K^+$  A-current, which is believed to be responsible for the maintenance of the up- and down-states, in addition to the synaptic input. Indeed, the  $K^+$  current is completely deinactivated at the hyperpolarized potentials (down-states), and reduces the response of the neuron to any synaptic input. In contrast, prolonged depolarization (up-state) inactivates the current and makes the neuron more excitable and ready to fire spikes.

The most remarkable feature of neostriatal spiny neurons is depicted in Fig. 8.37. In response to depolarizing current pulses, the neurons display a prominent slowly depolarizing (ramp) potential, and hence long latency to spike discharge (Nisenbaum et al. 1994). The ramp is mostly due to the slow inactivation of  $K^+$  A-current and slow charging of the dendritic tree. The delay to spike could be as long as 1 sec, but the subsequent spike train has a shorter relatively constant period that depends on the magnitude of the injected current.

Let us use the simple model (8.5, 8.6) to simulate the responses of spiny neurons to current pulses. The resting membrane potential of the neuron in Fig. 8.37 is around

$v_r = -80$  mV, and we set  $v_t = -25$  mV,  $p = 1$ , and  $b = -20$  to get  $30\text{ M}\Omega$  input resistance and  $300\text{ pA}$  rheobase current. We take  $a = 0.01$  to reflect the slow inactivation of the  $\text{K}^+$  A-current in the subthreshold voltage range. The membrane potential in the figure reaches the peak of  $+40$  mV during the spike and then resets to  $-55$  mV or lower, depending on the firing frequency. The value  $d = 150$  provides a reasonable match of the interspike frequencies for all magnitudes of injected current. Notice that  $b < 0$ , so that  $u$  represents either slow inactivation of  $I_A$  or slow charging of the passive dendritic compartment, or both. In any case, it is a slow amplifying variable, which is consistent with the observation that spiny neurons do not “sag” in response to hyperpolarizing current pulses, do not “peak” in response to depolarizing pulses (Nisenbaum et al. 1994), and do not generate rebound (post-inhibitory) spikes.

Injection of a depolarizing current shifts the  $v$ -nullcline of the simple model up, and the resting state disappears via saddle-node bifurcation. The trajectory slowly moves through the ghost of the bifurcation point (shaded rectangle in the figure), resulting in the long latency to the first spike. The spike resets the trajectory to a point (white square) below the ghost, resulting in significantly smaller delays to subsequent spikes. Because the resetting point is so close to the saddle-node bifurcation point, the simple model, and probably the spiny projection neuron in the figure, is near the co-dimension-2 saddle-node homoclinic orbit bifurcation discussed in Sect. 6.3.6.

### 8.4.3 Mesencephalic V neurons of brainstem

The best examples of resonators, with fast subthreshold oscillations, Class 2 excitability, rebound spikes, etc., are mesencephalic V (mesV) neurons of brainstem (Wu et al. 2001) and primary sensory neurons of dorsal root ganglion (Amir et al. 2002, Jian et al. 2004). Mes V neurons of the brainstem have monotone I-V curves, whereas the simple model with linear equation for  $u$  does not. In Fig. 8.38 we use a modification of the simple model to simulate the responses of mesV neuron (data from Fig. 7.3) to pulses of depolarizing current.

The model’s phase portrait is qualitatively similar to that of the FS interneurons in Fig. 8.27. The resting state is a stable focus, resulting in damped or noise-induced sustained oscillations of the membrane potential. Their amplitude and frequency depend on  $I$  and could be larger than  $5$  mV and  $100$  Hz, respectively. The focus loses stability via subcritical Andronov-Hopf bifurcation. Because of the co-existence of the resting and spiking states, the mesV neuron can burst, and so can the simple model if noise or a slow resonant variable is added.

### 8.4.4 Stellate cells of entorhinal cortex

The entorhinal cortex occupies a privileged anatomical position that allows it to gate the main flow of information to and out of the hippocampus. *In vitro* studies show that stellate cells, a major class of neurons in entorhinal cortex, exhibit intrinsic subthreshold oscillations with a slow dynamics of the kind shown in Fig. 8.39b (Alonso and Llinas

1989, Alonso and Klink 1993, Klink and Alonso 1993, Dickson et al. 2000). The oscillations are generated by the interplay between persistent  $\text{Na}^+$  current and h-current, and they are believed to set the theta rhythmicity in the entorhinal-hippocampal network.

The caption of Fig. 8.39 provides parameters of the simple model (8.5, 8.6) that captures the slow oscillatory dynamics of an entorhinal stellate cell recorded *in vitro* in adult rat. The cell sags to injected hyperpolarizing current in Fig. 8.39a and then fires a rebound spike upon release from hyperpolarization. From a neurophysiological point of view, the sag and rebound response are due to the opening of the h-current; From a mathematical point of view, they are caused by the resonant slow variable  $u$ , which could also describe deinactivation of a transient  $\text{Na}^+$  current and deactivation of low-threshold  $\text{K}^+$  current. The geometrical explanation of these responses is similar to the one provided for LTS interneurons in Fig. 8.26. Positive steps of current evoke a transient or sustained spiking activity. Notice that the first spike is actually a doublet in the recording and in the simulation in Fig. 8.39a ( $I = 200 \text{ pA}$ ).

Stellate cells in the entorhinal cortex of adult animals can exhibit damped or sustained subthreshold oscillations in a frequency range from 5 to 15 Hz. The oscillations can be clearly seen when the cell is depolarized by injected dc-current, as in Fig. 8.39b. The stronger the current, the higher the amplitude and frequency of oscillations, which occasionally result in spikes or even bursts of spikes (Alonso and Klink 1993). The simple model also exhibits slow damped oscillations because its resting state is a stable focus. The focus loses stability via subcritical Andronov-Hopf bifurcation, and hence it coexists with a spiking limit cycle. To enable sustained oscillations and random spikes, we add channel noise to the  $v$ -equation (White et al. 2000).

In Fig. 8.39c we explain the mechanism of random transitions between subthreshold oscillations and spikes, which is similar to the mechanism of stuttering in RS and FS neurons. When weak dc-current is injected (left), the attraction domain of the resting state (shaded region) is separated from the rest of the phase space by the stable manifold to the saddle equilibrium (denoted separatrix). Noisy perturbations evoke small sustained noisy oscillations around the resting state with an occasional spike when the separatrix is crossed. Increasing the level of injected dc-current results in the series of bifurcations similar to those in Fig. 8.15. As a result, there is a co-existence of a large amplitude (spiking) limit cycle attractor and a small unstable limit cycle, which encompasses the attraction domain of the resting state (right). Noisy perturbations can randomly switch the activity between these attractors, resulting in the random bursting activity in Fig. 8.39b.

#### 8.4.5 Mitral neurons of olfactory bulb

Mitral cells recorded in slices of rat main olfactory bulb exhibit intrinsic bistability of membrane potentials (Heyward et al. 2001). They spontaneously alternate between two membrane potentials separated by 10 mV: a relatively depolarized (up-state) and hyperpolarized (down-state) potentials. The membrane potential could be switched between the states by a brief depolarizing or hyperpolarizing pulse of current, as we

show in Fig. 7.36. In response to stimulation, the cells are more likely to fire in the up-state than in the down-state.

Current-voltage (I-V) relations of such mitral cells have three zeros in the subthreshold voltage range confirming that there are three equilibria, two stable corresponding to the up- and down-state, and one unstable — saddle. There are no subthreshold oscillations in the down-state, hence it is a node, and the cell is an integrator. There are small-amplitude 40 Hz oscillations in the up-state, hence it is a focus and the cell is a resonator.

To model the bistability, we use the simple model with a piece-wise linear slow nullcline that approximates non-linear activation functions  $n_\infty(v)$  near the “threshold” of the current and a passive dendritic compartment. In many respects, the model is similar to the one for late spiking (LS) cortical interneurons. In Fig. 8.40 we fine-tune the model to simulate responses of a rat mitral cell to pulses of current of various amplitude. To prevent noise-induced spontaneous transitions between the up- and down-states, the cell in the figure was held at  $-75$  mV by injection of a large negative current. Its responses to weak positive pulses of current show a fast rising phase followed by an abrupt step (arrow in the figure) to a constant value corresponding to the up-state. Increasing the magnitude of stimulation elicits trains of spikes with a considerable latency, whose cause has yet to be determined experimentally. The latency could be the result of slow activation of an inward current, slow inactivation of an outward current, e.g.  $K^+$  A-current, or just slow charging of the dendritic compartment. All three cases correspond to an additional slow variable in the simple model, which we interpret as a membrane potential of a passive dendritic compartment.

To understand the dynamics of the simple model, and hopefully of the mitral cell, we simulate its responses in Fig. 8.41 to the activation of the olfactory nerve (ON). In the top of Fig. 8.41, the cell is held at  $I = 0$  pA. Its phase portrait clearly shows the co-existence of stable node and focus equilibria separated by a saddle. The shaded region corresponds to the attraction domain of the focus equilibrium. To fire a spike from the up-state, noise or external stimulation must push the state of the system from the shaded region over the threshold to the right. The cell returns to the down-state right after the spike. Much stronger stimulation is needed to fire the cell from the down-state. Typically, the cell is switched to the up-state first, spend some time oscillating at 40 Hz, and then fire a spike (Heyward et al. 2001).

In the bottom of Fig. 8.41, the cell is held at a slightly depolarizing current  $I = 7$  pA. The node equilibrium disappeared via saddle-node bifurcation, so there is no down-state, but only its ghost. Stimulation at the up-state results in a spike, after-hyperpolarization, and slow transition through the ghost of the down-state back to the up-state. Further increasing the holding current results in the stable manifold to the upper saddle (marked “threshold” in the figure) to make a loop, and then become a homoclinic trajectory to the saddle giving birth to an unstable limit cycle, which shrinks to the focus and makes it lose stability via subcritical Andronov-Hopf bifurcation. Notice that this phase portrait and the bifurcation scenario is different from the one in Fig. 7.36. However, in both cases, the neuron is an integrator in

the down-state and a resonator in the up-state! The same property is exhibited by cerebella Purkinje cells (see Fig. 7.37), and possibly by other neurons kept in the up-state (intrinsically or extrinsically).

## Review of Important Concepts

- Integrate-and-fire neuron is a linear model having a stable *node* equilibrium, an artificial threshold, and a reset.
- Resonate-and-fire neuron is a linear model having a stable *focus* equilibrium, an artificial threshold, and a rest.
- Though technically not spiking neurons, these models are useful for analytical studies, i.e., to prove theorems.
- The quadratic integrate-and-fire model captures the non-linearity of the spike-generation mechanism of real neurons having Class 1 excitability (saddle-node on invariant circle bifurcation).
- Its simple extension, model (8.5, 8.6), reproduces quantitatively sub-threshold, spiking, and bursting activity of all known types of cortical and thalamic neurons in response to pulses of dc-current.
- The simple model makes testable hypotheses on the dynamic mechanisms of excitability in these neurons.
- The model is especially suitable for simulations of large-scale models of the brain.

## Bibliographical Notes

Many people have used the integrate-and-fire neuron, treating it as a folklore model. It was Tuckwell's (1988) "*Introduction to Theoretical Neurobiology*" that gave appropriate credit to its inventor — Lapique (1907). Although better models, such as the quadratic integrate-and-fire model, are available now, many scientists continue to favor the leaky integrate-and-fire neuron mostly because of its simplicity. Such an attitude is understandable when one wants to derive analytical results. However, purely computa-

tional papers can actually suffer from using the model because of its weird properties, such as the logarithmic F-I curve and fixed threshold.

The resonate-and-fire model was introduced by Izhikevich (2001), and then by Richardson, Brunel, and Hakim (2003) and Brunel, Hakim, and Richardson (2003). These authors initially called the model “resonate-and-fire”, but then changed its name to “generalized integrate-and-fire” (GIF), possibly to avoid confusion.

A better choice is the quadratic integrate-and-fire neuron in the normal form (8.2) or in the  $\vartheta$ -form (8.8); see Ex. 7. The  $\vartheta$ -form was first suggested in the context of circle/circle (parabolic) bursting by Ermentrout and Kopell (1986a,b). Later, Ermentrout (1996) used this model to generalize numerical results by Hansel et al. (1995) on synchronization of Class 1 excitable systems, discussed in Chap. 10. Hoppensteadt and Izhikevich (1997) introduced the canonical model approach, provided many examples of canonical models, and proved that the quadratic integrate-and-fire model was canonical in the sense that all Class 1 excitable systems could be transformed into this model by a piece-wise continuous change of variables. They also suggested to call the model “Ermentrout-Kopell canonical model”, but most scientists follow Ermentrout and call it “theta-neuron”.

The model presented in Sect. 8.1.4 was first suggested by Izhikevich (2000; Eq. (4) and (5) with voltage reset discussed in Sect. 2.3.1) in the  $\vartheta$ -form. The form presented here first appeared in Izhikevich (2003). The representation of the function  $I + v^2$  in the form  $(v - v_r)(v - v_t)$  was suggested by Latham et al. (2000).

We stress that the simple model is useful only when one wants to simulate large-scale networks of spiking neurons. He or she still needs to use the Hodgkin-Huxley-type conductance based models to study the behavior of one neuron or a small network of neurons. The parameter values that match firing patterns of biological neurons presented in this chapter are only educated guesses (the same is true for conductance-based models). More experiments are needed to reveal the true spike-generation mechanism of any particular neuron. An additional insights into the question “which model is more realistic” is in Fig. 1.8.

Looking at the simple model, one gets an impression that the spike generation mechanism of RS neurons is the simplest in the neocortex. This is probably true, however, the complexity of the RS neurons, most of which are pyramidal cells, is hidden in their extensive dendritic trees having voltage- and  $\text{Ca}^{2+}$ -gated currents. Studying dendritic dynamics is a subject of a 500-page book by itself, and we purposefully omitted this subject. We recommend reading *Dendrites* by Stuart et al. (1999), recent reviews by Hausser and Mel (2003) and Williams and Stuart (2003), and the seminal paper by Arshavsky et al. (1971; Russian language edition - 1969).

## Exercises

1. (Integrate-and-fire network) The simplest implementation of a pulse-coupled integrate-and-fire neural network has the form

$$\dot{v}_i = b_i - v_i + \sum_{j \neq i} c_{ij} \delta(t - t_j) ,$$

where  $t_j$  is the moment of firing of the  $j$ th neuron, i.e., the moment  $v_j(t_j) = 1$ . Thus, whenever the  $j$ th neuron fires, the membrane potentials of the other neurons are adjusted instantaneously by  $c_{ij}$ ,  $i \neq j$ . Show that the same initial conditions may result in different solutions, depending on the implementation details.

2. (Latham et al. 2000) Determine the relationship between the normal form for saddle-node bifurcation (6.2) and the equation

$$\dot{V} = a(V - V_{\text{rest}})(V - V_{\text{thresh}}) .$$

3. Show that the period of oscillations in the quadratic integrate-and-fire model (8.2) is

$$T = \frac{1}{\sqrt{b}} \left( \tan \frac{v_{\text{peak}}}{\sqrt{b}} - \tan \frac{v_{\text{reset}}}{\sqrt{b}} \right)$$

when  $b > 0$ .

4. Show that the period of oscillations in the quadratic integrate-and-fire model (8.2) with  $v_{\text{peak}} = 1$  is

$$T = \frac{1}{2\sqrt{|b|}} \left( \ln \frac{1 - \sqrt{|b|}}{1 + \sqrt{|b|}} - \ln \frac{v_{\text{reset}} - \sqrt{|b|}}{v_{\text{reset}} + \sqrt{|b|}} \right)$$

when  $b < 0$  and  $v_{\text{reset}} > \sqrt{|b|}$ .

5. Justify the bifurcation diagram in Fig. 8.3.
6. Brizzi et al. (2004) have shown that shunting inhibition of cat motoneurons raises the firing threshold, rheobase current, and shifts the F-I curve to the right without changing the shape of the curve. Use the quadratic integrate-and-fire model to explain the effect. (Hint: Consider  $\dot{v} = b - gv + v^2$  with  $g \geq 0$ ,  $v_{\text{reset}} = -\infty$ , and  $v_{\text{peak}} = +\infty$ .)
7. (Theta neuron) Determine when the quadratic integrate-and-fire neuron (8.2) is equivalent to the theta neuron

$$\dot{\vartheta} = (1 - \cos \vartheta) + (1 + \cos \vartheta)r , \quad (8.8)$$

where  $r$  is the bifurcation parameter and  $\vartheta \in [-\pi, \pi]$  is a phase variable on the unit circle.

8. (Another theta neuron) Show that the quadratic integrate-and-fire neuron (8.2) is equivalent to

$$\dot{\vartheta} = \vartheta^2 + (1 - |\vartheta|)^2 r .$$

where  $\vartheta \in [-1, 1]$  and  $r$  have the same meaning as in the previous exercise. Are there any other “theta neurons”?

9. When is the linear version of (8.3, 8.4),

$$\begin{aligned}\dot{v} &= I - v - u && \text{if } v = 1, \text{ then} \\ \dot{u} &= a(bv - u) && v \leftarrow 0, u \leftarrow u + d,\end{aligned}$$

equivalent to the integrate-and-fire or resonate-and-fire model?

10. Show that the simple model (8.3, 8.4) with  $b < 0$  is equivalent to the quadratic integrate-and-fire neuron with a passive dendritic compartment.
11. All membrane potential responses in Fig. 8.8 were obtained using model (8.3, 8.4) with appropriate values of the parameters. Use MATLAB to experiment with the model and reproduce the figure.
12. Simulate the FS spiking neuron in Fig. 8.27 using simple model (8.5, 8.6) with linear equation for  $u$ . What can you say about its possible bifurcation structure?
13. Fit the recordings of RS neuron in Fig. 8.12 using the following model

$$\begin{aligned}C\dot{v} &= I - g(v - v_r) + p(v - v_t)_+^2 - u && \text{if } v = v_{\text{peak}}, \text{ then} \\ \dot{u} &= a(b(v - v_r) - u) && v \leftarrow c, u \leftarrow u + d\end{aligned}$$

where  $x_+ = x$  when  $x > 0$  and  $x_+ = 0$  when otherwise. This model better fits the upstroke of the action potential.

14. Explore numerically the model (8.3, 8.4) with a nonlinear after-spike reset  $v \leftarrow f(u)$ ,  $u \leftarrow g(u)$ , where  $f$  and  $g$  are some functions.
15. [M.S.] Analyze the generalization of the system (8.3, 8.4)

$$\begin{aligned}\dot{v} &= I + v^2 + evu - u && \text{if } v = 1, \text{ then} \\ \dot{u} &= a(bv - u) && v \leftarrow c, u \leftarrow u + d\end{aligned}$$

where  $e$  is another parameter.

16. [M.S.] Analyze the generalization of the following system, related to the exponential integrate-and-fire model

$$\begin{aligned}\dot{v} &= I - v + ke^v - u && \text{if } v = 1, \text{ then} \\ \dot{u} &= a(bv - u) && v \leftarrow c, u \leftarrow u + d\end{aligned}$$

where  $k$  is another parameter.

17. [M.S.] Analyze the following system

$$\begin{aligned}\dot{v} &= I - v + kv_+^2 - u && \text{if } v = 1, \text{ then} \\ \dot{u} &= a(bv - u) && v \leftarrow c, u \leftarrow u + d\end{aligned}$$

where  $v_+ = v$  when  $v > 0$  and  $v_+ = 0$  otherwise.

18. [M.S.] Find an analytical solution to the system (8.3, 8.4) with time-dependent input,  $I = I(t)$ .
19. [M.S.] Determine the complete bifurcation diagram of the system (8.3, 8.4).

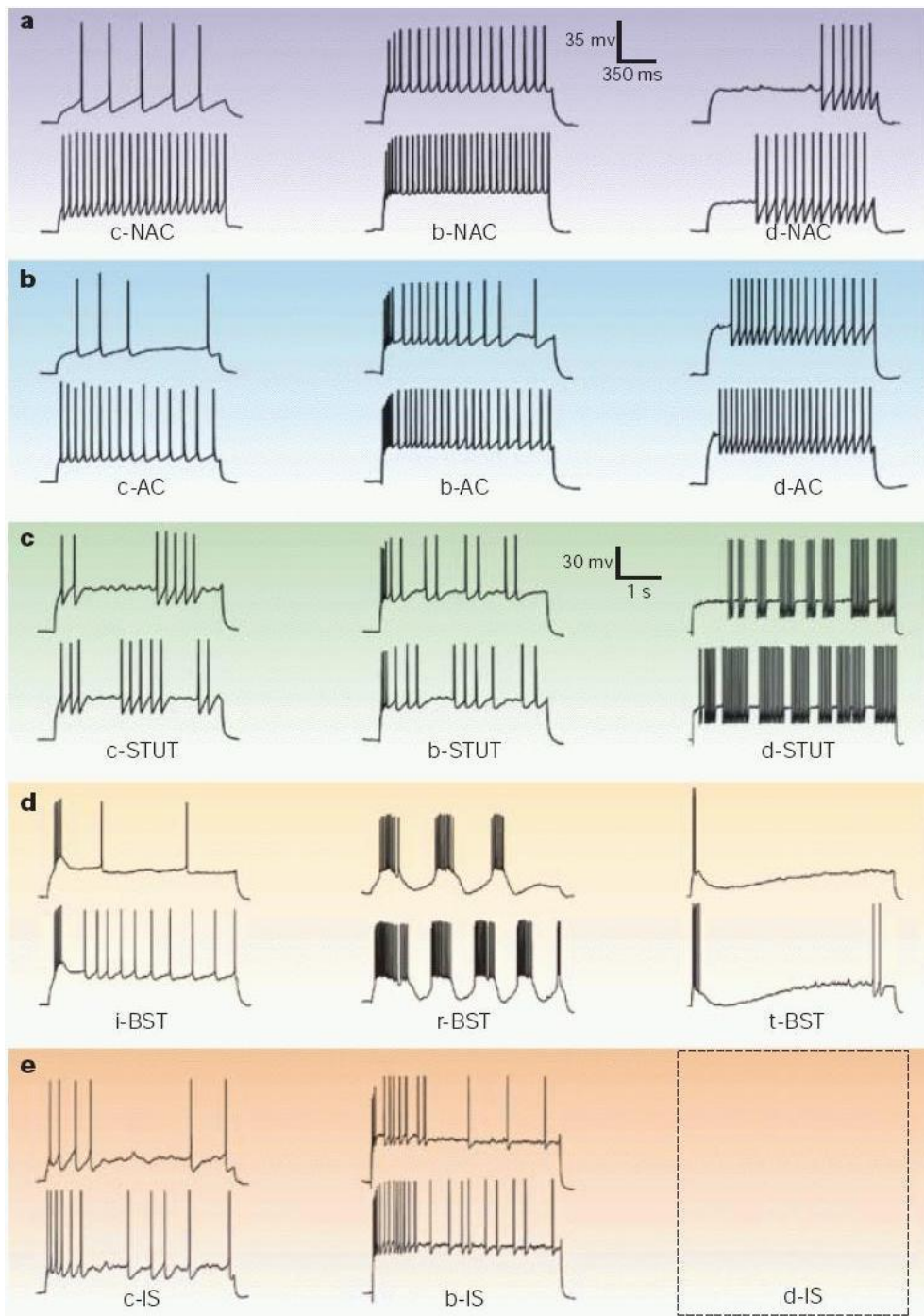


Figure 8.29: An alternative classification of neocortical inhibitory interneurons (modified from Markram et al. 2004). Five major classes: non-accommodating (NAC), accommodating (AC), stuttering (STUT), bursting (BST), and irregular spiking (IS). Most classes contain subclasses: delay (d), classic (c), and burst (b). For bursting interneurons, the three types are repetitive (r), initial (i), and transient (t). Subclass d-IS is not provided in the original picture by Markram et al. (2004).

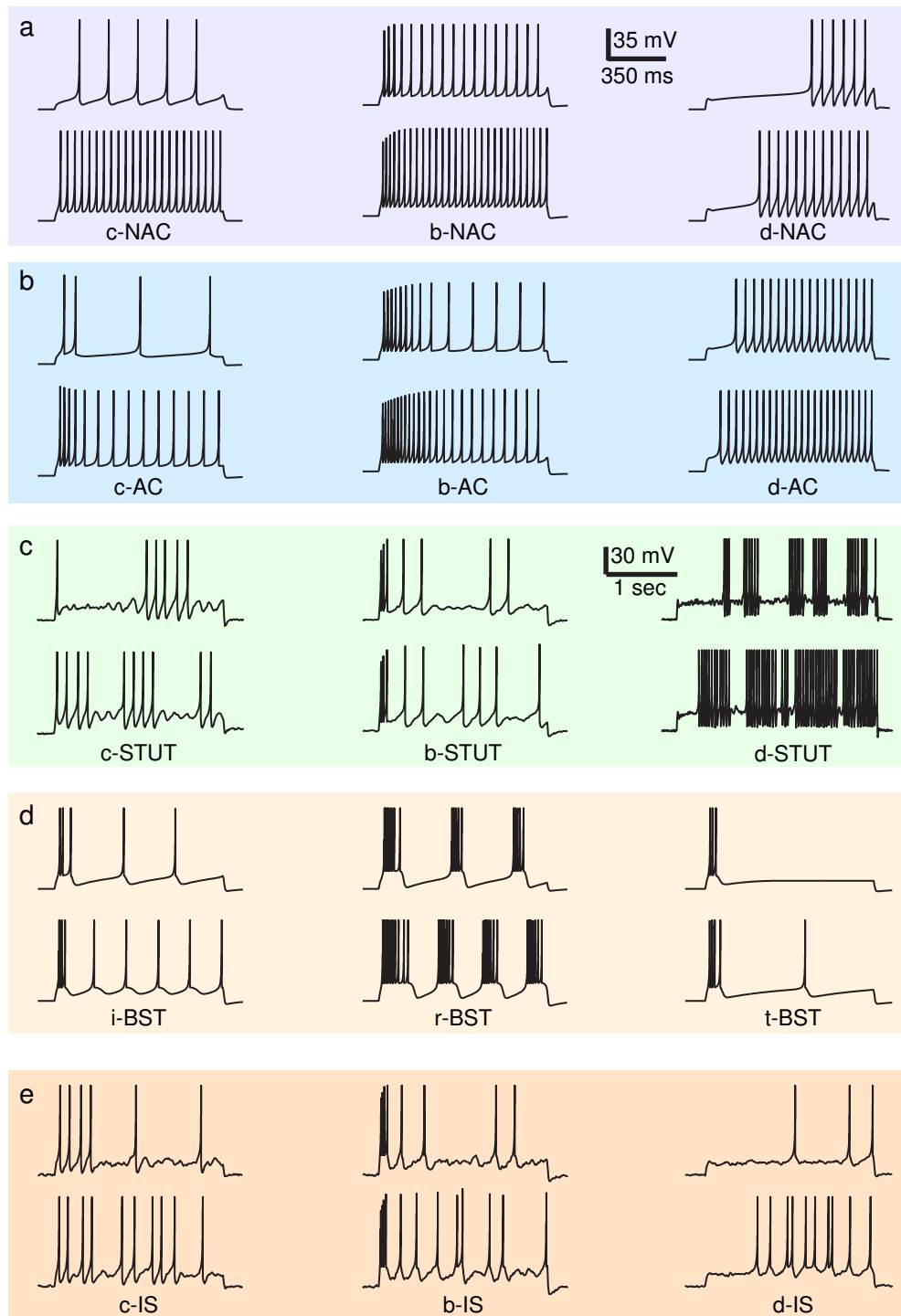


Figure 8.30: Simulations of the simple model with various parameters can reproduce all firing patterns of neocortical inhibitory interneurons in Fig. 8.29.

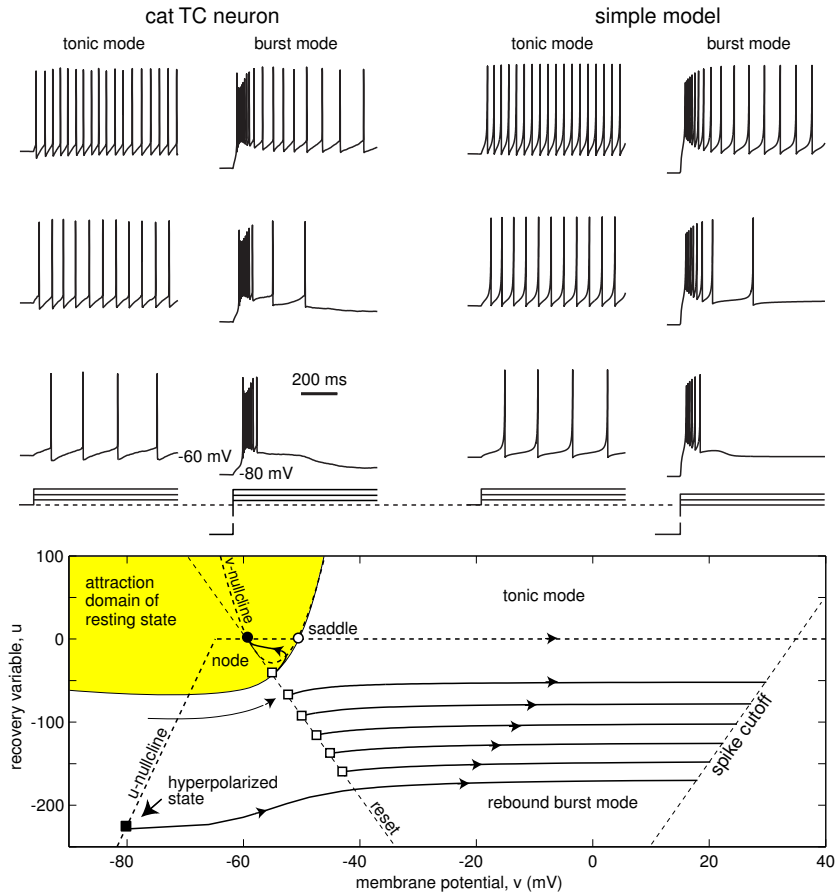


Figure 8.31: Comparison of *in vitro* recordings of a thalamocortical (TC) cell of cat dorsal lateral geniculate nucleus with simulations of the simple model  $200\dot{v} = 1.6(v + 60)(v + 50) - u + I$ ,  $\dot{u} = 0.01\{b(v + 65) - u\}$ ,  $b = 15$  if  $v \leq -65$  and  $b = 0$  otherwise. When  $v \geq 35 + 0.1u$ , then  $v \leftarrow -60 - 0.1u$ ,  $u \leftarrow u + 10$ . Injected current pulses are in 50 pA increments. In burst mode, the cell was hyperpolarized to  $-80$  mV prior to injecting a depolarizing pulse of current (data provided by C. L. Cox and S. M. Sherman)

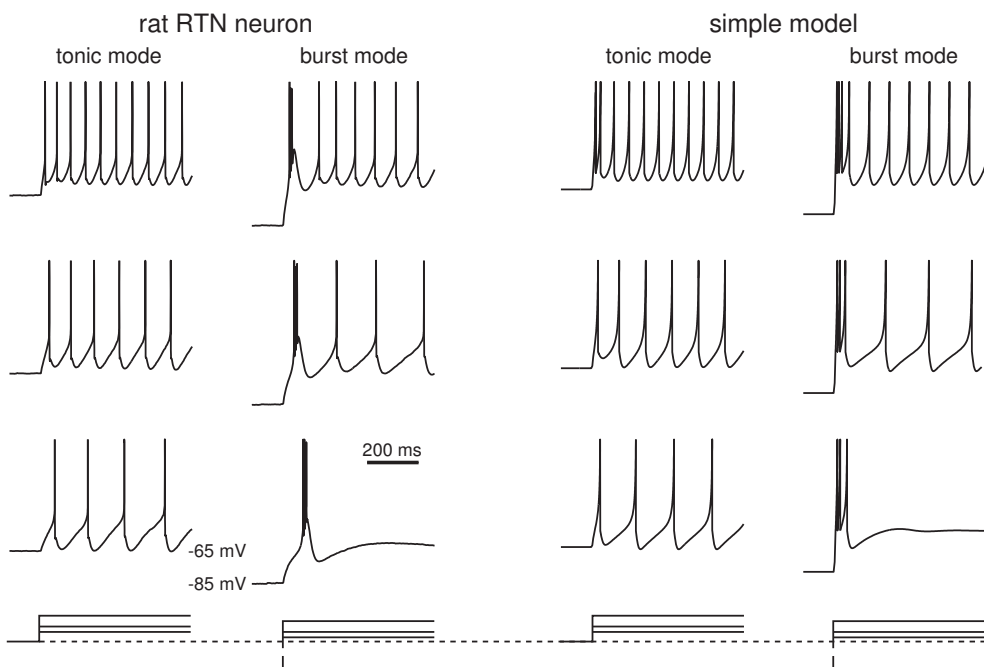


Figure 8.32: Comparison of *in vitro* recordings of a reticular thalamic nucleus (RTN) neuron of a rat with simulations of the simple model  $40\dot{v} = 0.25(v + 65)(v + 45) - u + I$ ,  $\dot{u} = 0.015\{b(v + 65) - u\}$ ,  $b = 10$  if  $v \leq -65$  and  $b = 2$  otherwise. When  $v \geq 0$  (spike cutoff), then  $v \leftarrow -55$ ,  $u \leftarrow u + 50$ . Injected current pulses are 50, 70, 110 pA. In burst mode, the cell was hyperpolarized to  $-80$  mV prior to injecting a depolarizing pulse of current (data provided S.H. Lee and C.L. Cox).

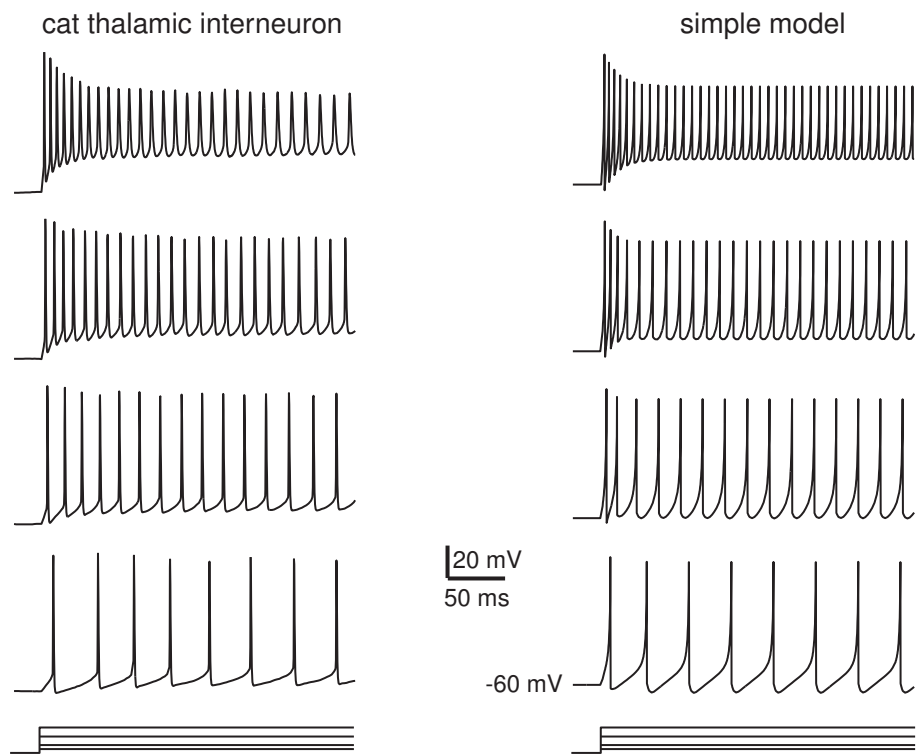


Figure 8.33: Comparison of *in vitro* recordings of dorsal lateral geniculate nucleus interneuron of a cat with simulations of the simple model  $20\dot{v} = 0.5(v + 60)(v + 50) - u + I$ ,  $\dot{u} = 0.05\{7(v + 60) - u\}$ . When  $v \geq 20 - 0.08u$  (spike cutoff), then  $v \leftarrow -65 + 0.08u$ ,  $u \leftarrow u + 50$ . Injected current pulses are 50, 100, 200, 250 pA (data provided by C. L. Cox and S. M. Sherman)

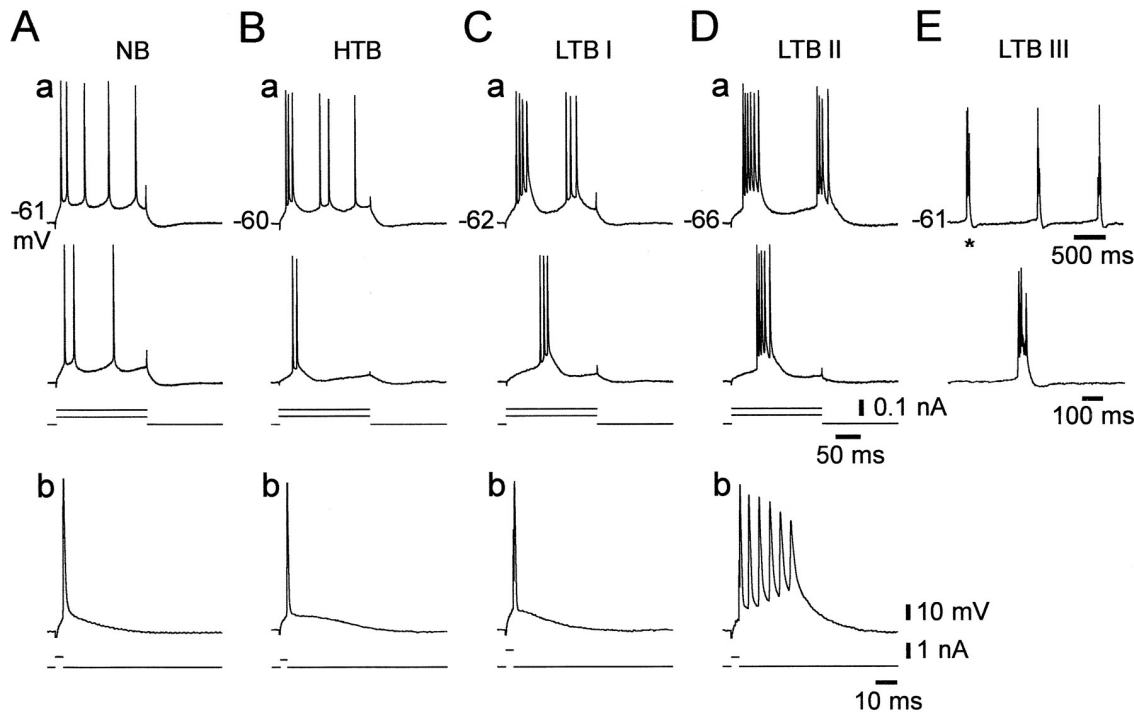


Figure 8.34: Classification of hippocampal CA1 pyramidal neurons. A-E, *in vitro* recordings from five different pyramidal neurons arranged according to a gradient of increasing propensity to burst. The neurons were stimulated with current pulses of 200 ms duration and amplitude 50 pA and 100 pA (a), or brief (3-5 ms) superthreshold pulses (b). Non-burster (NB) neuron fires tonic spikes in response to long pulses and a single spike in response to brief pulses. High-threshold burster (HTB) fires bursts only in response to strong long pulses, and single spikes in response to weak or brief pulses. Grade I low-threshold burster (LTB I) generates bursts in response to long pulses of current, but single spikes in response to brief pulses. Grade II LTB (LTB II) fires bursts in response to both long (a) and brief (b) current pulses. Grade III LTB (LTB III), in addition to firing bursts in response to long and brief pulses of current (not shown) also fires spontaneous rhythmic bursts, shown in contracted and expanded time scales (reproduced from Su et al. (2001) with permission).

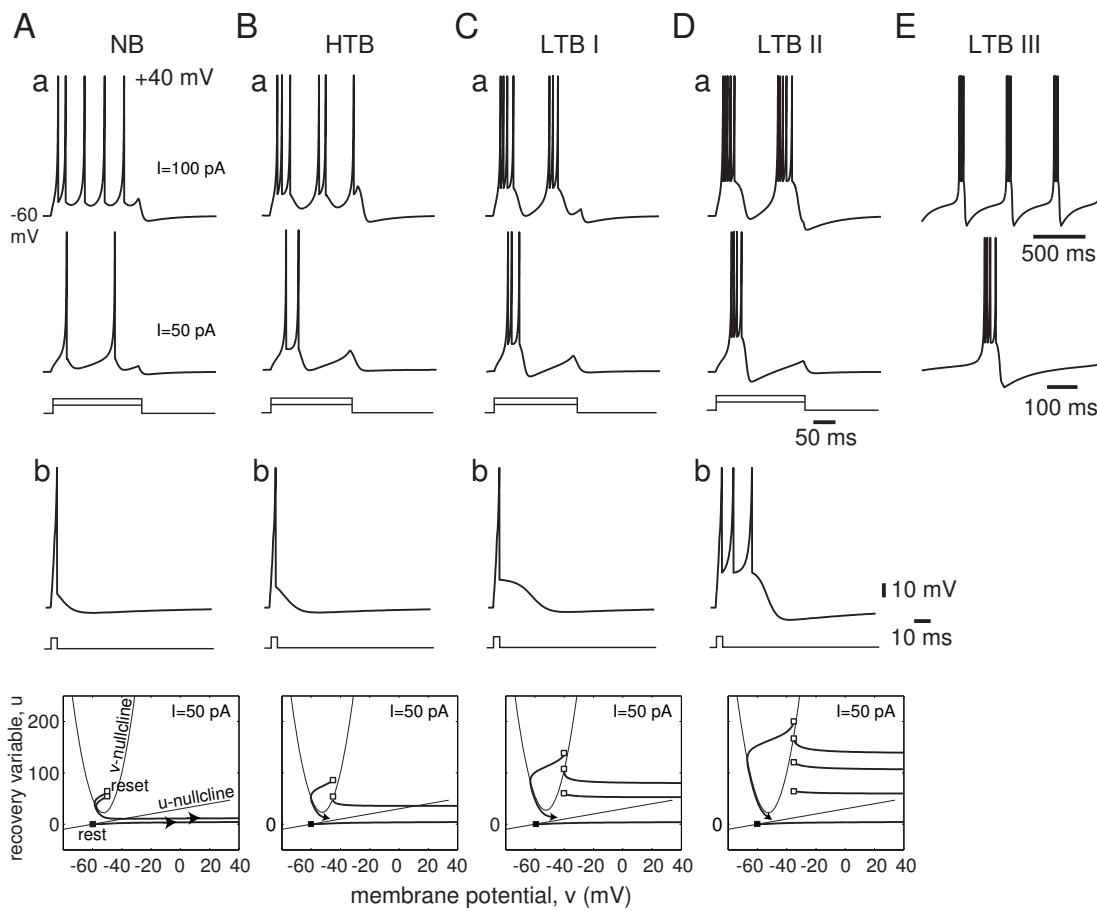


Figure 8.35: Simulations of hippocampal CA1 pyramidal neurons (compare with Fig. 8.34) using simple model  $50\dot{v} = 0.5(v+60)(v+45)-u+I$ ,  $\dot{u} = 0.02\{0.5(v+60)-u\}$ . When  $v \geq 40$  (spike cutoff), then  $v \leftarrow c$  and  $u \leftarrow u + d$ . Here  $c = -50, -45, -40, -35$  mV and  $d = 50, 50, 55, 60$  for A-D, respectively. Parameters in E are the same as in D, but  $I = 33$  pA.

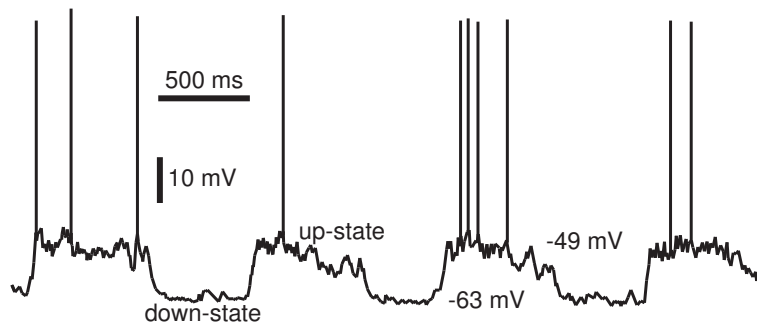


Figure 8.36: Neostriatal spiny neurons have two-state behavior *in vivo* (data provided by Charles Wilson).

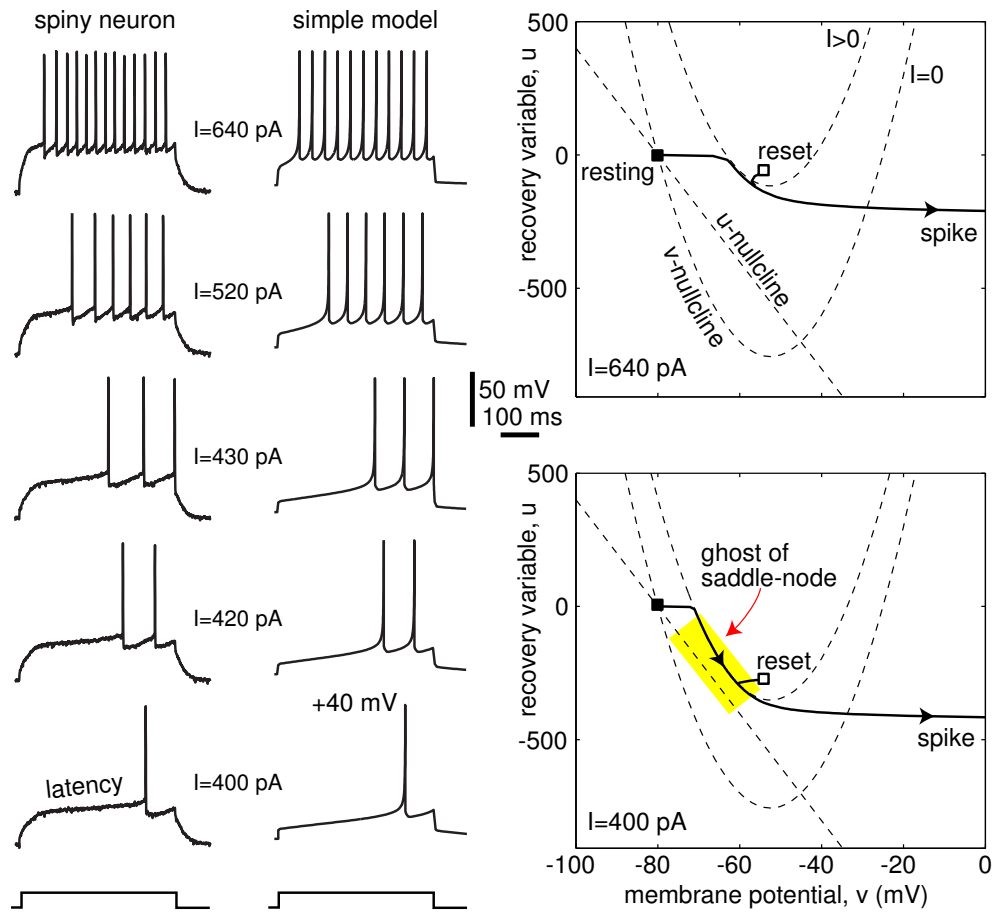


Figure 8.37: Comparison of *in vitro* recordings of a neostriatal spiny projection neuron of a rat with simulations of the simple model  $50\dot{v} = (v + 80)(v + 25) - u + I$ ,  $\dot{u} = 0.01\{-20(v + 80) - u\}$ , if  $v \geq 40$ , then  $v \leftarrow -55$ ,  $u \leftarrow u + 150$  (*in vitro* data were kindly provided by C. Wilson).

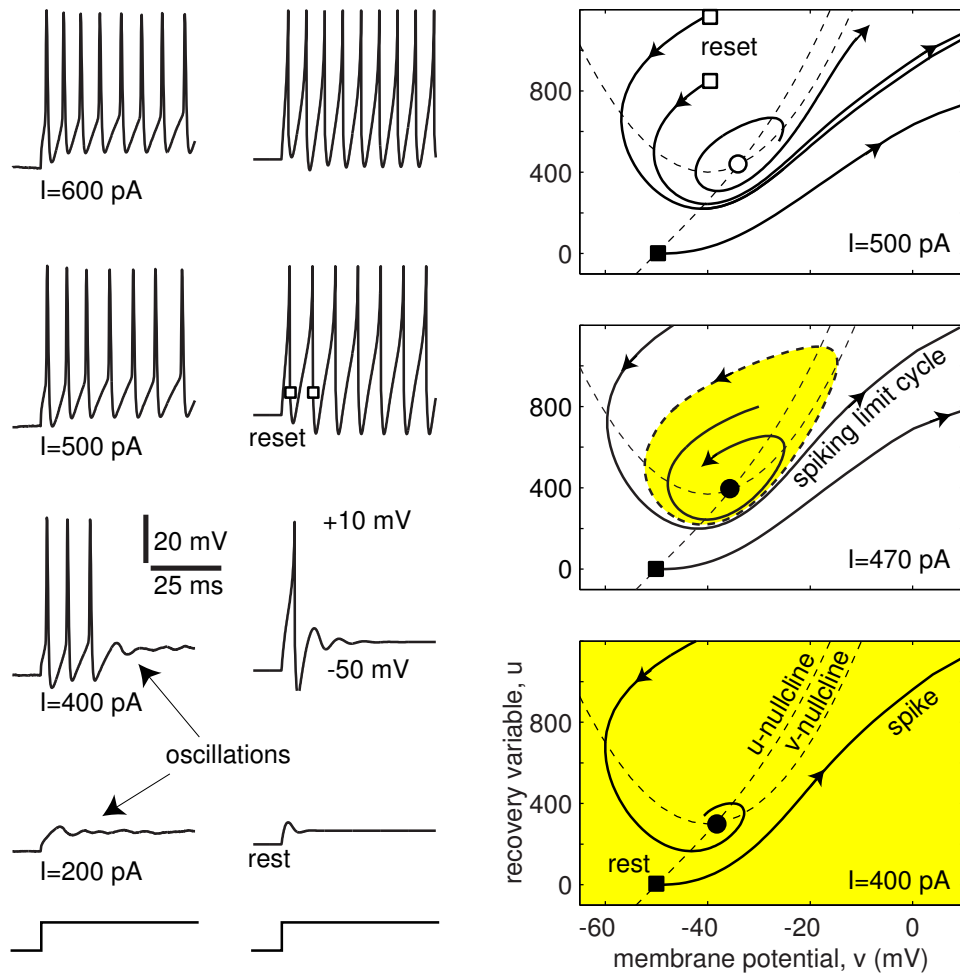


Figure 8.38: Comparison of *in vitro* recordings of rat's brainstem mes V neuron (from Fig. 7.3) with simulations of the simple model  $25\dot{v} = (v + 50)(v + 30) - u + I$ ,  $\dot{u} = 0.5\{U(v + 50) - u\}$ , with cubic slow nullcline  $U(x) = 25x + 0.009x^3$ . If  $v \geq 10$ , then  $v \leftarrow -40$ .

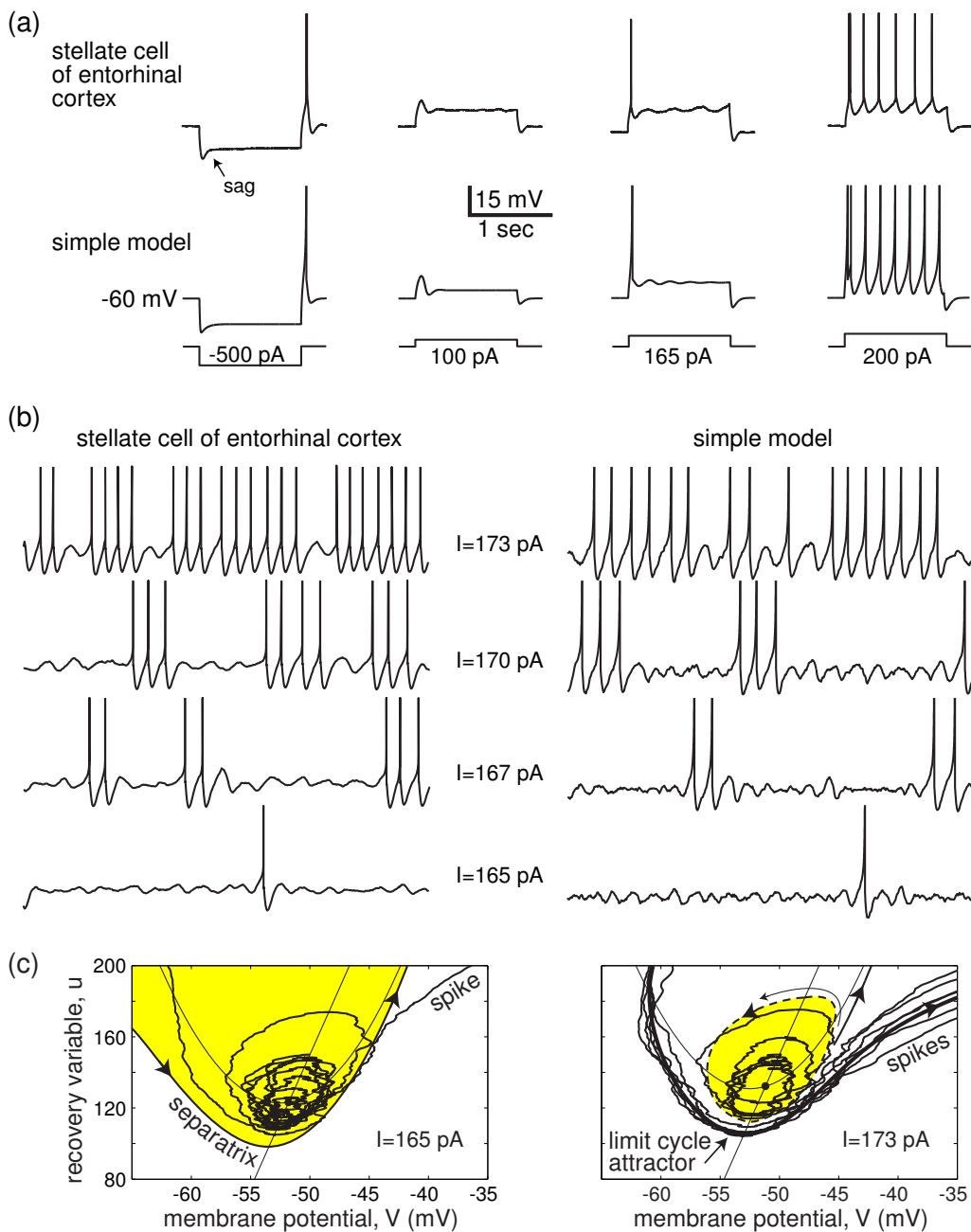


Figure 8.39: Comparison of *in vitro* recordings of stellate neurons of rat's entorhinal cortex with simulations of the simple model  $200\dot{v} = 0.75(v + 60)(v + 45) - u + I$ ,  $\dot{u} = 0.01\{15(v + 60) - u\}$ , if  $v \geq 30$ , then  $v \leftarrow -50$ . (a) Responses to steps of dc-current. (b) Subthreshold oscillations and occasional spikes at various levels of injected dc-current. (c) Phase portraits corresponding to two levels of injected dc-current. Weak noise was added to simulations to unmask subthreshold oscillations. (Data were kindly provided by Brian Burton and John A. White. All recordings are from the same neuron except steps of  $-500 \text{ pA}$  and  $200 \text{ pA}$  were recorded from a different neuron. Spikes are cut at  $0 \text{ mV}$ .)

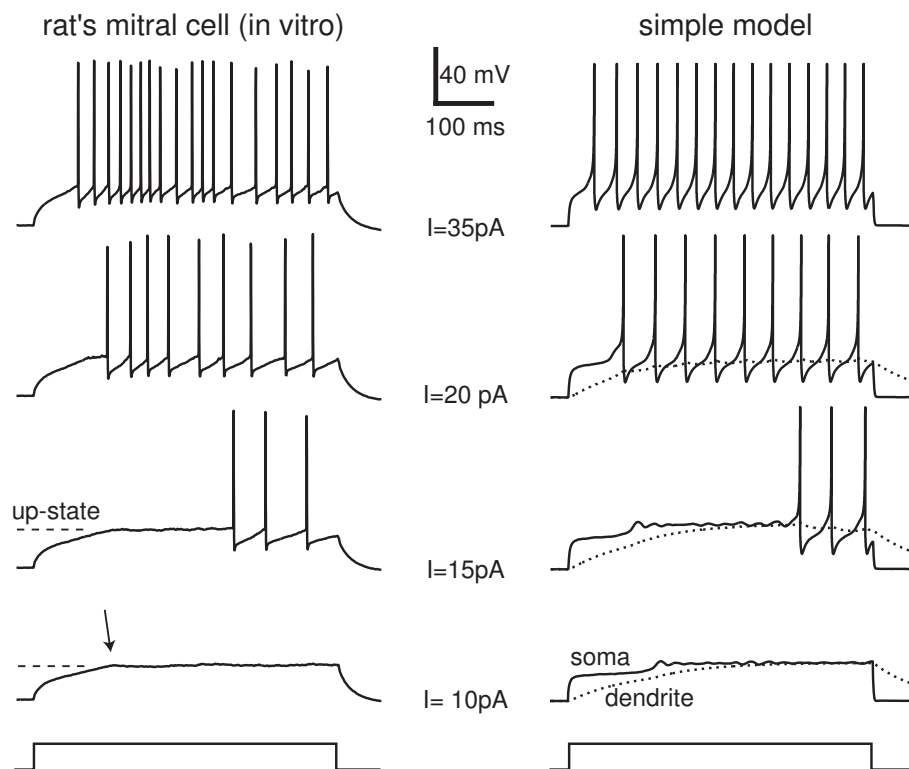


Figure 8.40: Comparison of *in vitro* recordings of mitral neurons of rat's olfactory bulb with simulations of the simple two-compartment model. Soma:  $40\dot{v} = (v+55)(v+50) + 0.5(v_d - v) - u + I$ ,  $\dot{u} = 0.4\{(U(v) - u)\}$  with  $U(v) = 0$  when  $v < v_b$  and  $U(v) = 20(v - v_b)$  when  $v \geq v_b = -48$  mV. If  $v \geq 35$ , then  $v \leftarrow -50$ . Passive dendrite (dotted curve):  $\dot{v}_d = 0.0125(v - v_d)$ . Weak noise was added to simulations to unmask subthreshold oscillations in the up-state. The membrane potential of the neuron is held at -75 mV by injecting a strong negative current, and then stimulated with steps of positive current. (Data were kindly provided by Philip Heyward.)

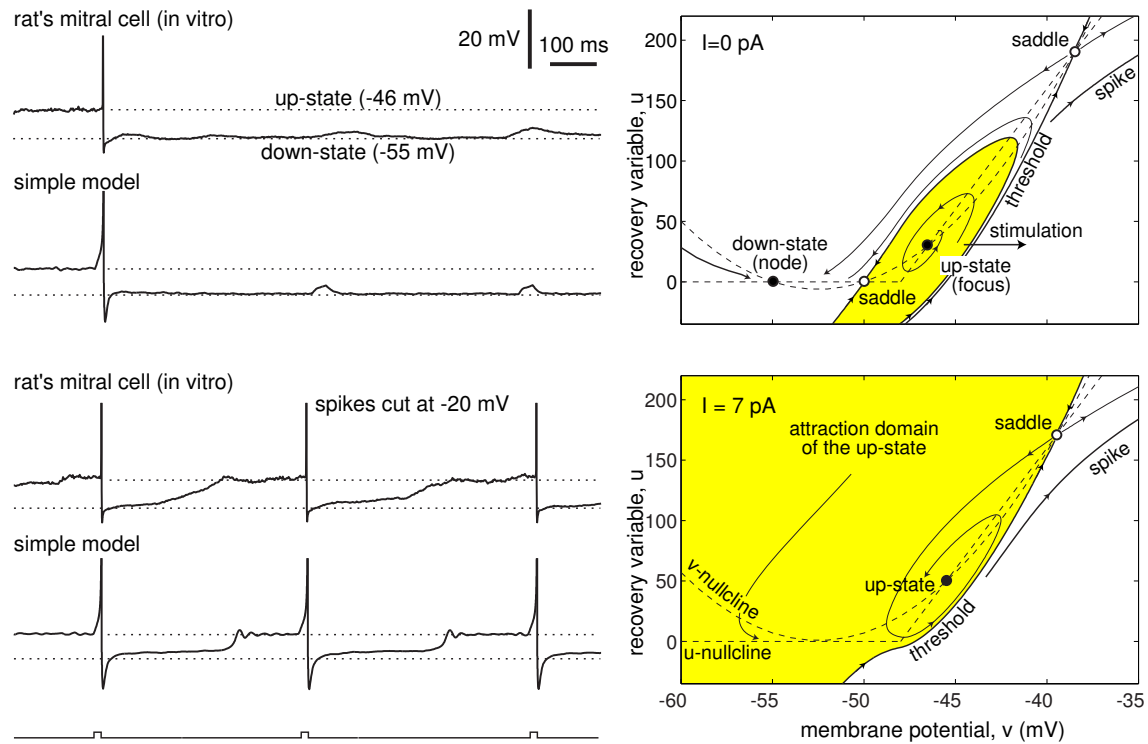


Figure 8.41: Voltage responses of a rat's mitral cell and a simple model from Fig. 8.40 at two different values of the holding current. *Right:* Phase portraits of somatic compartments show coexistence of stable node (down-state) and stable focus (up-state) equilibria. Spikes are emitted only from the up-state.



Figure 8.42: Louis Lapicque — the inventor of the integrate-and-fire neuron.

# Chapter 9

## Bursting

A neuron can fire a single spike or a stereotypical burst of spikes, depending on the nature of stimulation and the intrinsic neuronal properties. Typically, bursting occurs due to the interplay of fast currents responsible for spiking activity, and slow currents that modulate the activity. In this chapter we study this interplay in detail.

To understand the geometry of bursting, it is customary to assume that the fast and slow currents have drastically different time scales. In this case we can dissect a burster, i.e., freeze its slow currents and use them as parameters that control the fast spiking subsystem. During bursting, the slow parameters drive the fast subsystem through bifurcations of equilibria and limit cycles. We provide a topological classification of bursters based on these bifurcations, and show that different topological types have different neuro-computational properties.

### 9.1 Electrophysiology

Many spiking neurons can exhibit bursting activity if manipulated, e.g., pharmacologically. In Fig. 9.1 we depict a few well-known examples of neurons that burst under natural conditions without any manipulation. Some require an injected dc-current to bias the membrane potential, others do not. One can only be amazed by the diversity of bursting patterns and time scales. In this chapter we consider electrophysiological and bifurcation mechanisms responsible for the generation of these patterns.

Is zebra a black animal with white stripes or a white animal with black stripes? This seemingly silly question is pertinent to every bursting pattern: Does bursting activity correspond to an infinite period of quiescence interrupted by groups of spikes or does it correspond to an infinite spike train interrupted by short periods of quiescence? Biologists are mostly concerned with the question of what makes the neuron fire the first spike in a burst and what keeps it in the spiking regime afterwards. The question of why the spiking stops is often forgotten. It turns out that to fully understand the ionic mechanism of bursting, we need to concentrate on the second question, i.e., we need to treat bursting as an infinite spike train that is chopped into short bursts by a slow (resonant) current that builds up during the spiking phase and recovers during the

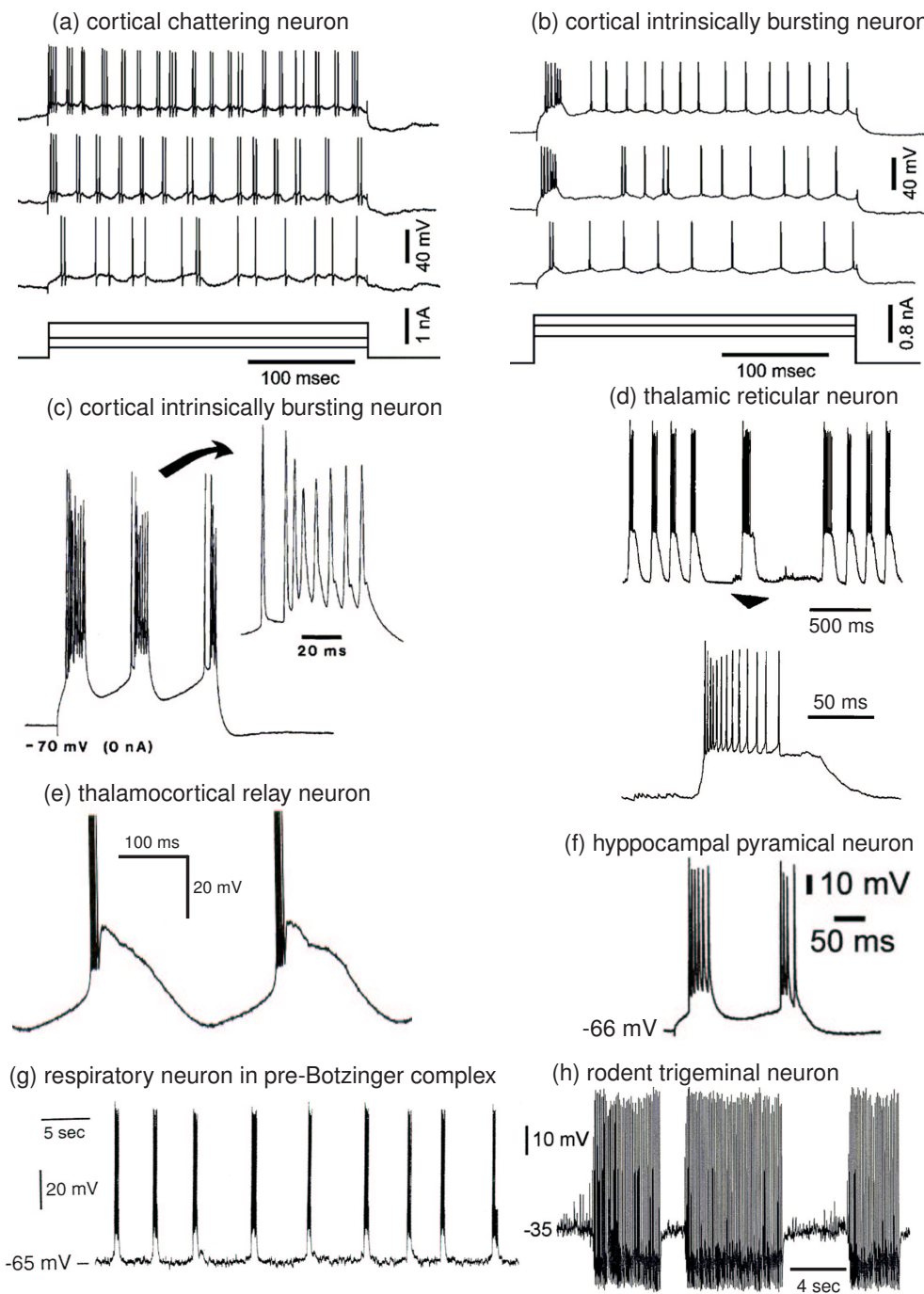


Figure 9.1: Examples of intrinsic bursters. (a) and (b) cat primary visual cortical neurons (modified from Nowak et al. 2003). (c) cortical neuron in anesthetized cat (modified from Timofeev et al. 2000). (d) thalamic reticular (RE) neuron (modified from Steriade 2003). (e) Cat thalamocortical relay neuron (modified from McCormick and Pape 1990). (f) CA1 pyramidal neuron exhibiting grade II low-threshold bursting pattern (modified from Su et al. 2001). (g) respiratory neuron in the pre-Botzinger complex (modified from Butera et al. 1999). (h) Trigeminal interneuron from rat brainstem (modified from Del Negro et al. 1998).



Figure 9.2: Is bursting a spiking state interrupted by periods of quiescence or is it a quiescent state interrupted by groups of spikes?

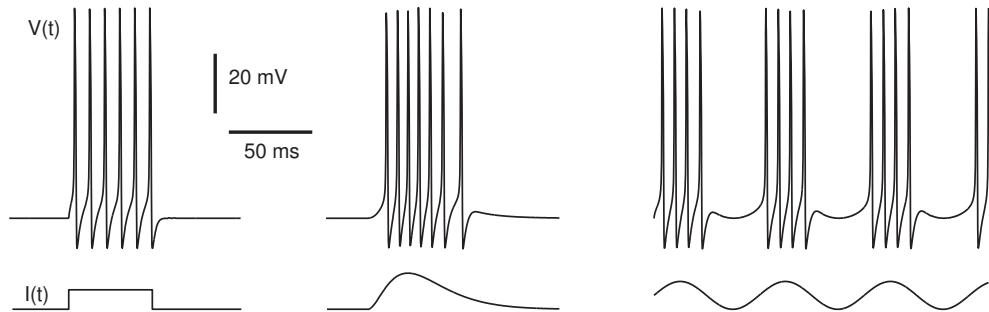


Figure 9.3: Forced bursting in the  $I_{Na,p}+I_K$ -model with parameters as in Fig. 4.1a and time-dependent injected current  $I(t)$ .

quiescent phase. Before proceeding to a general case, let us consider a simple example.

### 9.1.1 Example: The $I_{Na,p}+I_K+I_{K(M)}$ -model

Any model neuron capable of spiking can also burst, as e.g., the  $I_{Na,p}+I_K$ -model in Fig. 9.3. However, this example is not interesting because the neuron is forced to burst by the time-dependent input  $I(t)$ .

In contrast, a modification of the  $I_{Na,p}+I_K$ -model in Fig. 9.4 fires a burst of spikes in response to a brief pulse of current. The first spike in the burst is caused by the stimulation, but the subsequent spikes are generated autonomously due to the intrinsic properties of the neuron, and they outlast the stimulation. Such a burst is stereotypical and fairly independent of the amplitude or the duration of the pulse that triggered it.

To make the  $I_{Na,p}+I_K$ -model burst, we took parameters as in Fig. 6.7a, so that

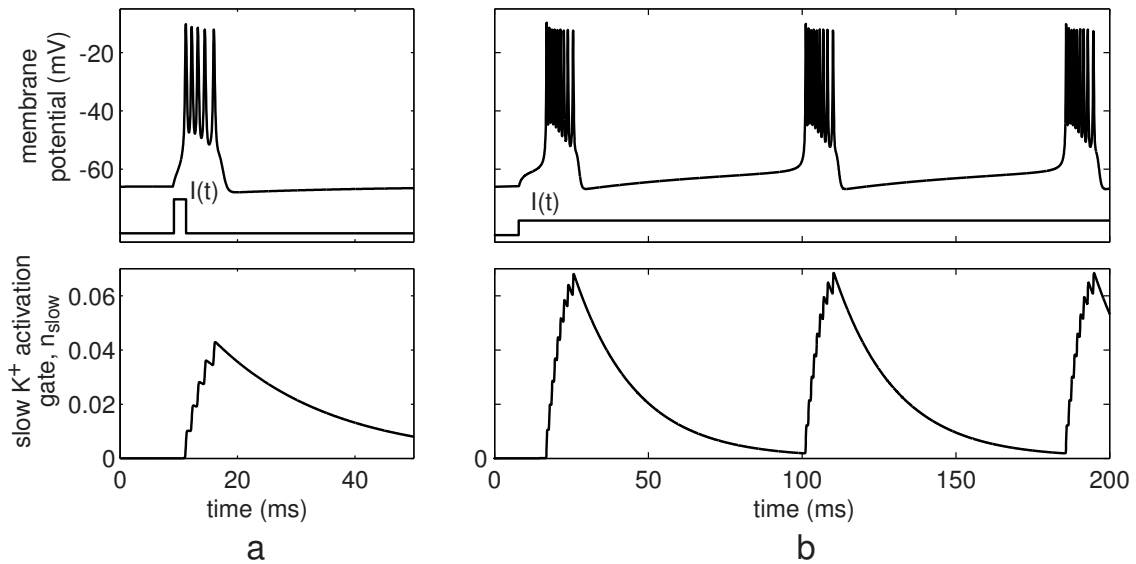


Figure 9.4: Intrinsic bursting in the  $I_{\text{Na,p}} + I_K + I_{\text{K(M)}}$ -model (7.1) consisting of the  $I_{\text{Na,p}} + I_K$ -model with parameters as in Fig. 4.1a and fast K<sup>+</sup> current ( $g_K = 9, \tau(V) = 0.152$ ) and a slow K<sup>+</sup> current with  $g_{\text{slow}} = 5, V_{1/2} = -20$  mV,  $k = 5$  mV and  $\tau_{\text{slow}}(V) = 20$  ms. (a) Burst excitability when  $I = 0$ . (b) Periodic bursting when  $I = 5$ .

there is a coexistence of the resting and spiking states. The brief pulse of current excites the neuron, i.e., moves its state into the attraction domain of the spiking limit cycle and initiates periodic activity. Without any other modification, the model would produce an infinite spike train. To stop the train, we added a slower high-threshold persistent K<sup>+</sup> current similar to  $I_{\text{K(M)}}$  that provides a negative feedback. This M-current is deactivated at rest. However, during the active (spiking) phase, the current slowly activates, as indicated by the slow build-up of its gating variable  $n_{\text{slow}}$  in the figure. The neuron becomes less and less excitable, and eventually cannot sustain spiking activity. If, instead of a pulse of current, a constant current is applied, the neuron can burst periodically, as in Fig. 9.4b.

This model presents only one of many possible examples of bursters, which we study in this chapter. However, it illustrates a number of important issues common to all bursters. For instance, in contrast to the forced bursting in Fig. 9.3, this bursting is *intrinsic* or *autonomous*. This stereotypical bursting pattern results from the intrinsic voltage-sensitive currents, and not from a time-dependent input. The behavior in Fig. 9.4a is called *burst excitability* to emphasize that the model is an excitable system with the exception that superthreshold stimulation elicits a burst of spikes instead of a single spike. Hippocampal pyramidal neurons of the type “grade III bursters” depicted in Fig. 8.34Eb exhibit burst excitability.

Biologists sometimes refer to the bursting in Fig. 9.4b as being *conditional*, because repetitive bursting occurs when a certain condition is satisfied, e.g., positive  $I$  is in-

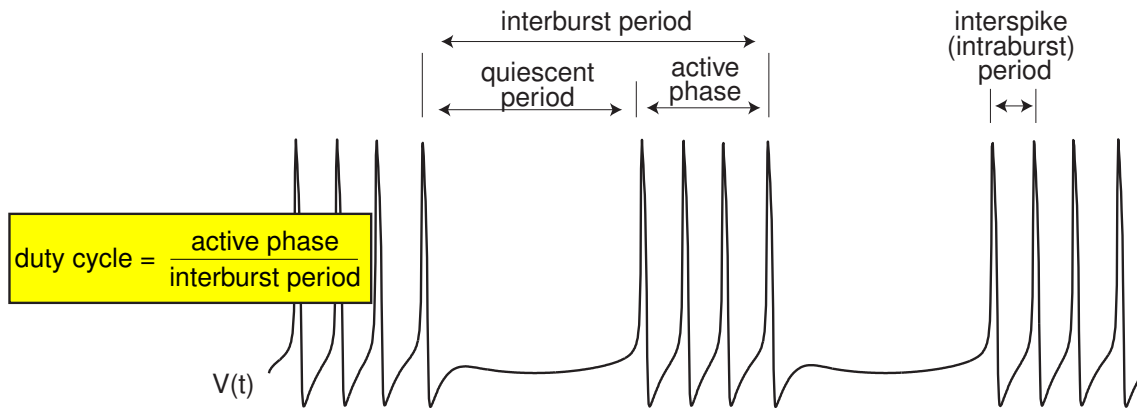


Figure 9.5: Basic characteristics of bursting dynamics.

jected. From a mathematical point of view, every burster is conditional, since it exists for some values of the parameters but not others.

### 9.1.2 Fast-Slow Dynamics

In general, every bursting pattern consists of oscillations with two time scales: fast spiking oscillation within a single burst (*intraburst* oscillation, or spiking), modulated by a slow oscillation between the bursts (*interburst* oscillation); see Fig. 9.5. Typically, though not necessarily (see exercises at the end of this chapter), two time scales result from two interacting processes involving fast and slow currents. For example, the spiking in Fig. 9.4 is generated by the fast  $I_{Na,p}+I_K$ -subsystem and modulated by the slow  $I_{K(M)}$ -subsystem.

There are two questions associated with each bursting pattern:

- What *initiates* sustained spiking during the burst?
- What *terminates* sustained spiking temporarily and ends the burst?

The answer to the first question is relatively simple: Repetitive spiking is initiated and sustained by the positive injected current  $I$ , or some other source of persistent inward current that causes the neuron to fire (most biologists are interested in identifying this source). Surprisingly, the second question is the most important for building a model of bursting. While the neuron fires, relatively slow processes somehow make it non-excitible and eventually terminate the firing. Such slow processes result in a slow buildup of an outward current or in a slow decrease of an inward current needed to sustain the spiking. During the quiescent phase, the neuron slowly recovers and regains the ability to generate action potentials again.

Let us discuss possible ionic mechanisms responsible for the termination of spiking within a burst. Suppose we are given a neuronal model that is capable of sustained spiking activity, at least when a positive  $I$  is injected. To transform an infinite spike train into a finite burst of spikes, it suffices to add a slow *resonant* current or gating

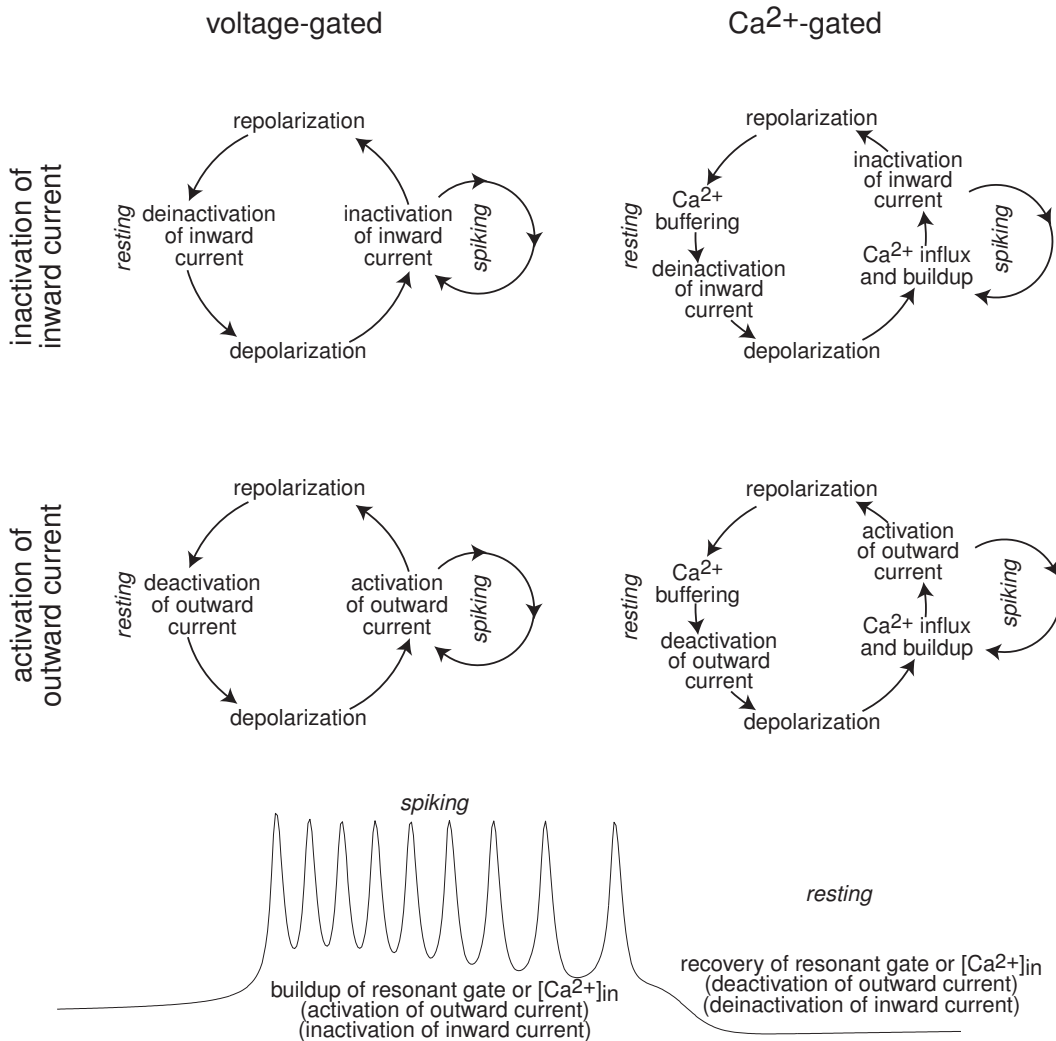


Figure 9.6: Four major classes of bursting models are defined by the slow resonant gating variable that modulates spiking activity.

variable (see Sect. 5.1.1) that modulates the spiking via a slow negative feedback. The resonant gating variable can describe inactivation of an inward current or activation of an outward current, both voltage- or Ca<sup>2+</sup>-dependent (see Fig. 5.17). Hence, there are four major classes of bursting models, summarized in Fig. 9.6:

- *Voltage-gated inactivation of an inward current*, e.g., slow inactivation of persistent Na<sup>+</sup> current or inactivation of Ca<sup>2+</sup> transient T-current, or inactivation of the h-current (most biologists refer to this as activation of the h-current by hyperpolarization). Repetitive spiking slowly inactivates (turns off) the inward current and makes the neuron less excitable and unable to sustain spiking activity. After a while, the spiking stops and the membrane potential repolarizes. The inward current slowly de-inactivates (turns on) and depolarizes the membrane potential,

possibly resulting in a new burst.

- *Voltage-gated activation of an outward current*, e.g., slow activation of persistent  $K^+$  current, such as M-current. Repetitive spiking slowly activates the outward current, which eventually terminates the spiking activity. While at rest, the outward current slowly deactivates (turns off) and unmasks inward currents that can depolarize the membrane potential, possibly initiating another burst.
- *$Ca^{2+}$ -gated inactivation of an inward current*, e.g., slow inactivation of high-threshold  $Ca^{2+}$ -currents  $I_{Ca(L)}$  or  $I_{Ca(N)}$ . Calcium entry during repetitive spiking leads to its intracellular accumulation and slow inactivation of  $Ca^{2+}$ -channels that provide an inward current needed for repetitive spiking. As a result, the neuron cannot sustain spiking activity and becomes quiescent. During this period, intracellular  $Ca^{2+}$  ions are removed,  $Ca^{2+}$  channels are de-inactivated, and the neuron is primed to start a new burst.
- *$Ca^{2+}$ -gated activation of an outward current*, e.g., slow activation of  $Ca^{2+}$ -dependent  $K^+$ -current  $I_{AHP}$ . Calcium entry and buildup during repetitive spiking slowly activates the outward current and makes the neuron less and less excitable. When the spiking stops, intracellular  $Ca^{2+}$  ions are removed,  $Ca^{2+}$ -gated outward current deactivates (turns off), the neuron is no longer hyperpolarized and ready to fire a new burst of spikes.

In addition, the slow process may include  $Na^+$ -,  $K^+$ -, or  $Cl^-$ -gated currents, such as the “slack and slick” family of  $Na^+$ -gated  $K^+$  currents, or slow change of ionic concentrations in the vicinity of the cell membrane (so called Hodgkin-Frankenhaeuser layer), which leads to slow change of the Nernst potential for ionic species. We do not elaborate these cases in the book.

Notice that in some cases, the slow process modulates fast currents responsible for spiking, while in other cases it produces an independent slow current that impedes spiking. In any case, the slow process is directly responsible for the termination of continuous spiking, and indirectly for its initiation and maintenance.

The four mechanisms in Fig. 9.6 and their combinations are ubiquitous in neurons, as we summarize in Fig. 9.7. However, there could be other, less obvious bursting mechanisms. In Ex. 8–10 we provide examples of bursters having slowly activating persistent inward current, such as  $I_{Na,p}$ . These surprising examples show that buildup of the inward current (or any other amplifying gate) can also be responsible for the termination of the active phase and for the repolarization of the membrane potential. To understand these mechanisms, one needs to study the geometry of bursting.

### 9.1.3 Minimal models

Let us follow the ideas presented in Sect. 5.1 and determine minimal models for bursting. That is, we are interested in classification of all fast-slow electrophysiological models that can exhibit sustained bursting activity, as in Fig. 9.4b, at least for some

neuron	slow dynamics				references	
	voltage-gated		Ca <sup>2+</sup> -gated			
	activation of outward	inactivation of inward	activation of outward	inactivation of inward		
neocortical chattering neurons	$I_{K(M)}$ $I_{K_{slow}}$				Wang (1999)	
pre-Botzinger complex (respiratory rhythm)	$I_{K_{slow}}$	$I_{Na_{slow}}$			Butera et al. (1999)	
thalamic relay neurons		$I_{Ca(T)}$ $I_h$			Huguenard and McCormick (1992)	
thalamic reticular neurons		$I_{Ca(T)}$			Destexhe et al. (1994)	
hippocampal CA3 neurons			$I_{AHP}$		Traub et al. (1991)	
subiculum bursting neurons			$I_{AHP}$		Stanford et al. (1998)	
midbrain dopaminergic neurons			$I_{K(Ca)}$	$I_{Ca(L)}$	Amini et al. (1999)	
anterior bursting (AB) neuron in lobster stomatogastric ganglion			$I_{K(Ca)}$	$I_{Ca(L)}$	Harris-Warrick and Flamm (1987)	
Aplysia abdominal ganglion R15 neuron				$I_{Ca(L)}$	Canavier et al. (1991)	

Figure 9.7: Slow dynamics in bursting neurons.

values of parameters. A bursting model is *minimal* if removal of any current or gating variable eliminates the ability to burst.

One way to build a fast-slow minimal model for bursting is to take a minimal model for spiking, which consists of an amplifying and a resonant gate, see Fig. 5.17, and add another slow resonant gate. Since there are many minimal spiking models in Fig. 5.17 and four choices of slow resonant gates in Fig. 9.6, there are quite a few combinations, which fill out the squares in Fig. 9.8. We present only a few reasonable models in the figure and ask the reader to fill in the blanks. Completing the table is an excellent test of one's knowledge and understanding of how different currents interact to produce non-trivial firing patterns.

Some of the minimal models for bursting might seem too bizarre at first glance. Yet the table in Fig. 9.8, upon completion, might prove to be a valuable tool that could allow experimenters to formulate various ionic hypotheses. For example, if one uses pharmacological agents, e.g., TEA or Ba<sup>2+</sup>, to block Ca<sup>2+</sup>-gated K<sup>+</sup> channels and show that bursting persists, then the possible electrophysiological mechanisms of

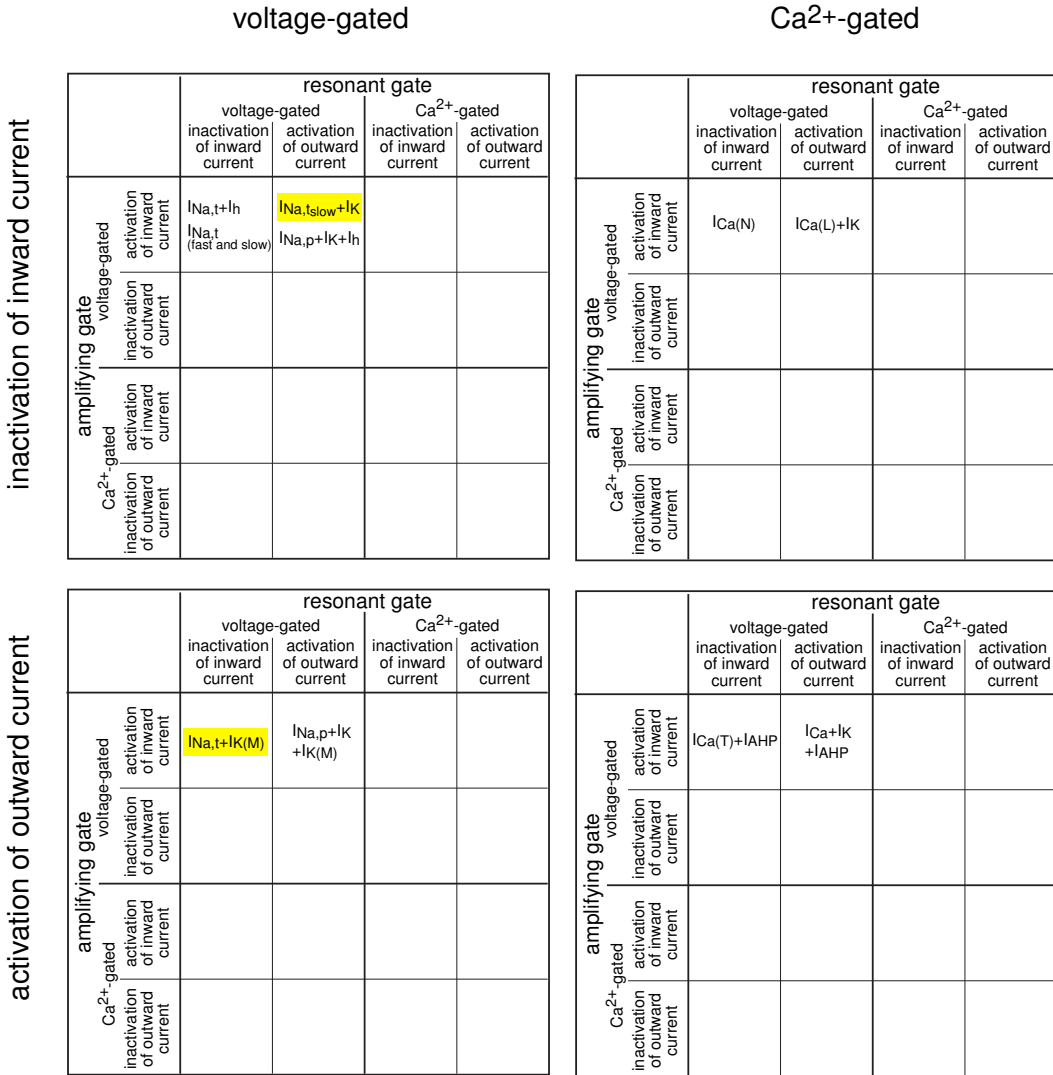


Figure 9.8: Some minimal models for bursting.

bursting are confined to the left column in Fig. 9.8. Minimal models in this column would provide testable hypotheses on the ionic basis of bursting, and they could guide novel experiments. If block abolishes bursting, we cannot conclude that the blocked current drives the bursting — it may merely be necessary for providing background stimulation.

Notice that the  $I_{\text{Na,t}_{\text{slow}}} + I_K$ -model and the  $I_{\text{Na,t}} + I_{K(M)}$ -model in the figure (see the shaded rectangles) consist of the same gating variables:  $\text{Na}^+$  activation gate  $m$ , inactivation gate  $h$ , and  $\text{K}^+$  activation gate  $n$ . Both models are equivalent to the Hodgkin-Huxley model, the only difference being the choice of the slow gate. Thus, in contrast to the common biophysical folklore, the Hodgkin-Huxley model is a minimal model for bursting, and there are two fundamentally different ways in which one can make it burst without any additional currents, as we show in Fig. 9.9. Of course, one

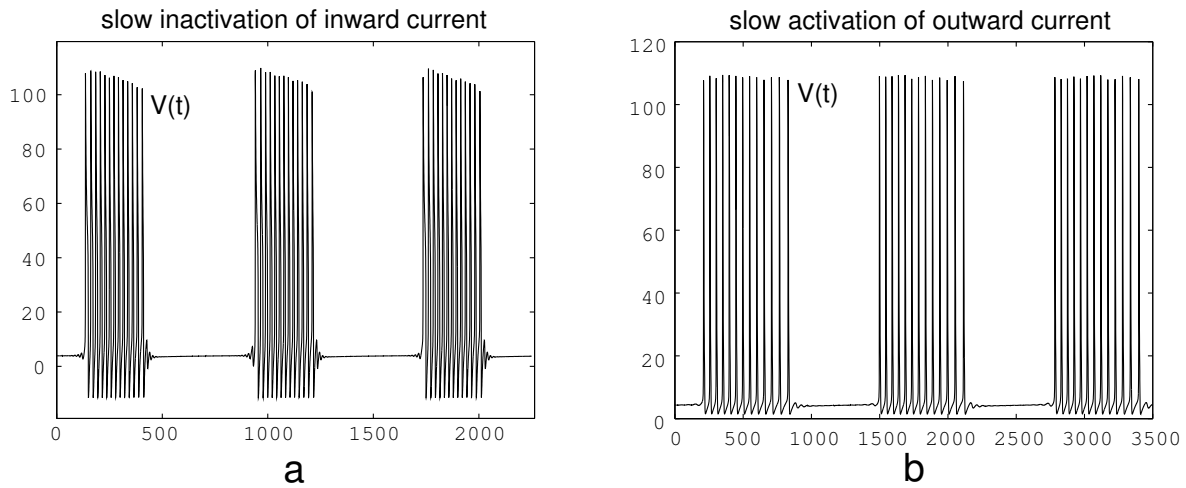


Figure 9.9: Hodgkin-Huxley (1952) model with three gating variables is minimal for bursting (modified from Fig. 1.10 in Izhikevich 2001).

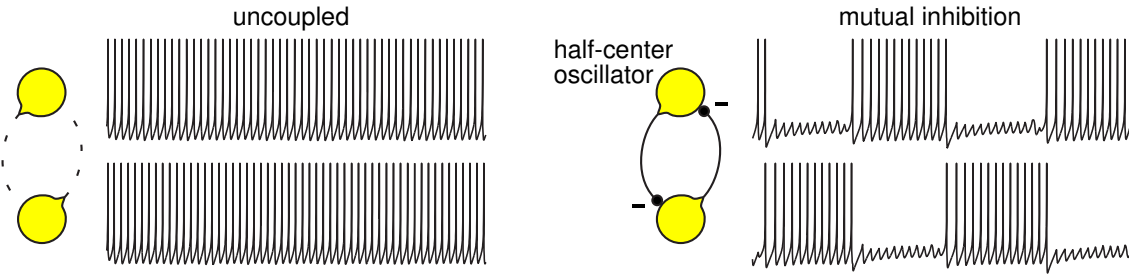


Figure 9.10: Central pattern generation by mutually inhibitory oscillators.

may argue that the model in the figure is not Hodgkin-Huxley at all, since we changed the kinetics of some currents by an order of magnitude.

Thinking in terms of minimal models, we can understand what is essential for spiking and bursting and what is not. In addition, we can clearly see that some well-known conductance-based models form partially-ordered set. For example, the chain of neuronal models *Morris-Lecar* ( $I_{\text{Ca}}+I_K$ )  $\prec$  *Hodgkin-Huxley* ( $I_{\text{Na,t}}+I_K$ )  $\prec$  *Butera-Rinzel-Smith* ( $I_{\text{Na,t}}+I_K+I_{\text{K,slow}}$ ) is obtained by adding a conductance or gating variable to one model to get the next one. Here,  $A \prec B$  means  $A$  is a subsystem of  $B$ .

Understanding the ionic bases of bursting is an important step in analysis of bursting dynamics. However, such an understanding may not provide sufficient information on why the bursting pattern looks as it does, what the neuro-computational properties of the neuron are, and how they depend on the parameters of the system. Indeed, we showed in Chap. 5 that spiking models based on quite different ionic mechanisms can have identical dynamics and vice versa. This is true for bursting models as well.

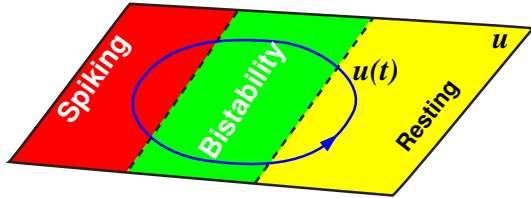


Figure 9.11: Parameter  $u$  can control spiking behavior of the fast subsystem in (9.1). When  $u$  changes slowly, the model exhibits bursting behavior.

### 9.1.4 Central pattern generators and half-center oscillators

Bursting can also appear in small circuits of coupled spiking neurons, such as the two mutually inhibitory oscillators in Fig. 9.10, called half-center oscillators. While one cell fires, the other is inhibited, then they switch roles, and so on. Such small circuits, suggested by Brown (1911), are the building blocks of central pattern generators in pyloric network of the lobster stomatogastric ganglion, medicine leech heartbeat, fictive motor patterns and swimming patterns of many vertebrates and invertebrates (Marder and Bucher 2001).

What makes the oscillators in Fig. 9.10 alternate? Wang and Rinzel (1992) suggested two mechanisms, *release* and *escape*, which were later refined to *intrinsic* or *synaptic* by Skinner et al. (1994):

- INTRINSIC RELEASE: The active cell stops spiking, terminates inhibition and allows inhibited cell to fire.
- INTRINSIC ESCAPE: Inhibited cell recovers, starts to fire and shuts off the active cell.
- SYNAPTIC RELEASE: The inhibition weakens, e.g., due to spike frequency adaptation or short-term synaptic depression, and allows the inhibited cell to fire.
- SYNAPTIC ESCAPE: Inhibited cell depolarizes above certain threshold and starts to inhibit the active cell.

All four mechanisms assume that in addition to fast variables responsible for spiking, there are also slow adaptation variables responsible for slowing down or termination of spiking, recovery, or synaptic depression. Thus, similarly to the minimal models above, the circuit has at least two time scales, i.e., it is a fast-slow system.

## 9.2 Geometry

To understand the neuro-computational properties of bursters, we need to study the geometry of their phase portraits. In general, it is quite a difficult task. However, it can be accomplished in the special case of fast-slow dynamics.

### 9.2.1 Fast-slow bursters

We say that a neuron is a *fast-slow burster* if its behavior can be described by a fast-slow system of the form

$$\begin{aligned}\dot{x} &= f(x, u) && \text{(fast spiking),} \\ \dot{u} &= \mu g(x, u) && \text{(slow modulation).}\end{aligned}\tag{9.1}$$

The vector  $x \in \mathbb{R}^m$  describes fast variables responsible for spiking. It includes the membrane potential  $V$ , activation and inactivation gating variables for fast currents, etc. The vector  $u \in \mathbb{R}^k$  describes relatively slow variables that modulate fast spiking, e.g., gating variable of a slow  $K^+$  current, intracellular concentration of  $\text{Ca}^{2+}$  ions, etc. The small parameter  $\mu$  represents the ratio of time scales between spiking and modulation. When we analyze models, we assume that  $\mu \ll 1$ ; that is, it could be as small as we wish. The results obtained via such an analysis may not have any sense when  $\mu$  is of the order 0.1 or greater.

To analyze bursters, we first assume that  $\mu = 0$ , so that we can consider the fast and slow systems separately. This constitutes the method of *dissection* of neural bursting pioneered by Rinzel (1985). In fact, we have done this many times in the previous chapters when we substituted  $m = m_\infty(V)$  into the voltage equation. The fast subsystem can be resting (but excitable), bistable, or spiking depending on the value of  $u$ ; see Fig. 9.11. Bursting occurs when  $u$  visits the spiking and quiescent areas periodically. Many important aspects of bursting behavior can be understood via phase portrait analysis of the fast subsystem

$$\dot{x} = f(x, u), \quad x \in \mathbb{R}^m,$$

treating  $u \in \mathbb{R}^k$  as a vector of slowly changing bifurcation parameters.

We say that the burster is of the “ $m+k$ ” type when the fast subsystem is  $m$ -dimensional and the slow subsystem is  $k$ -dimensional. There are some “1+1” and “2+0” bursters, see Ex. 1 — Ex. 4, though they do not correspond to any known neuron. Most of the bursting models in this chapter are of the “2+1” and “2+2” type.

### 9.2.2 Phase portraits

Since most bursting models are at least of the “2+1” type, their phase space is at least three-dimensional. Analyzing and depicting multi-dimensional phase portraits is challenging. Even understanding the geometry of a single bursting trajectory depicted in Fig. 9.12 is difficult unless one uses a stereoscope.

In Fig. 9.13 we investigate geometrically the  $I_{\text{Na,p}} + I_K + I_{K(M)}$ -model, which is a fast-slow burster of the “2+1” type. The naked bursting trajectory is shown in the lower left corner. We set  $\mu = 0$  (i.e.,  $\tau_{\text{slow}}(V) = +\infty$ ) and slice the three-dimensional space by planes  $n_{\text{slow}} = \text{const}$ , shown in the top right corner. Phase portraits of the two-dimensional fast subsystem with fixed  $n_{\text{slow}}$  are shown in the middle of the figure. Notice how the limit cycle attractors and the equilibria of the fast subsystem depend on

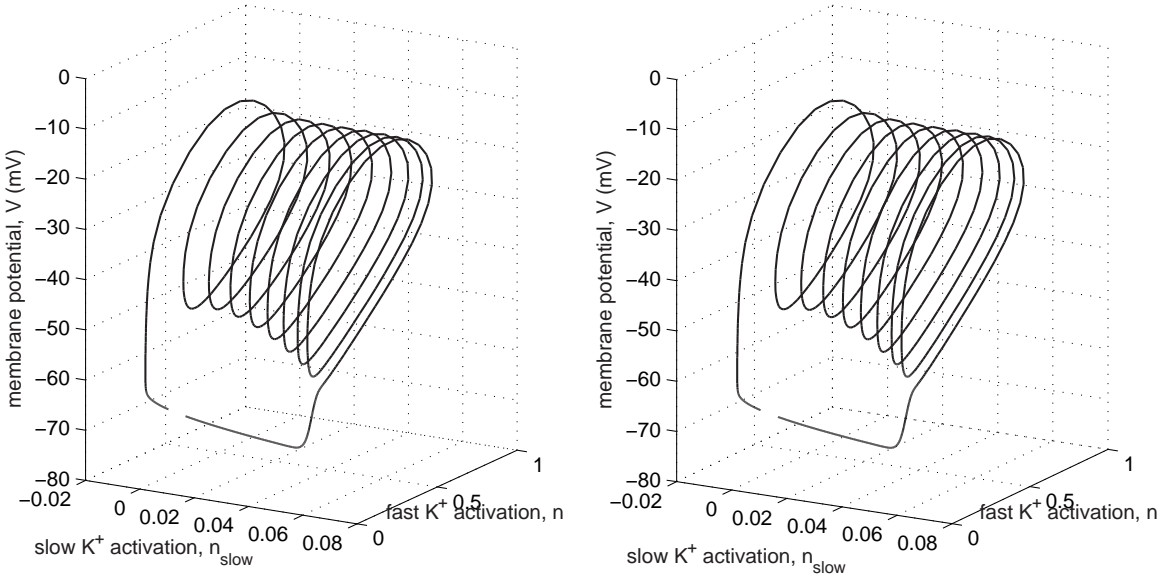


Figure 9.12: Stereoscopic image of a bursting trajectory of the  $I_{Na,p} + I_K + I_{K(M)}$ -model in the three-dimensional phase space ( $V, n, n_{slow}$ ) (for cross-eye viewing).

the value of  $n_{slow}$ . Gluing the phase portraits together, we see that there is a manifold of limit cycle attractors (shaded cylinder) that starts when  $n_{slow} < 0$  and ends in a saddle homoclinic orbit bifurcation when  $n_{slow} = 0.066$ . There is also a locus of stable and unstable equilibria that appears via a saddle-node bifurcation when  $n_{slow} = 0.0033$ .

Once we understand the transitions from one phase portrait to another as the slow variable changes, we can understand the geometry of the burster. Suppose  $\mu > 0$  (i.e.,  $\tau_{slow}(V) = 20$  ms) so that  $n_{slow}$  can evolve according to its gating equation.

Let us start with the membrane potential at the stable equilibrium corresponding to resting state. The parameters of the  $I_{Na,p} + I_K + I_{K(M)}$ -model (see caption to Fig. 9.4) are such that slow K<sup>+</sup> M-current deactivates at rest, i.e.,  $n_{slow}$  slowly decreases, and the bursting trajectory slides along the bold half-parabola corresponding to the locus of stable equilibria. After a while, the K<sup>+</sup> current becomes so small, that it cannot hold the membrane potential at rest. This happens when  $n_{slow}$  passes the value 0.0033, the stable equilibrium coalesces with an unstable equilibrium (saddle), and they annihilate each other via saddle-node bifurcation. Since the resting state no longer exists (see the phase portrait at the top left of Fig. 9.13) the trajectory jumps up to the stable limit cycle corresponding to repetitive spiking. This jumping corresponds to the transition from resting to spiking behavior.

While the fast subsystem fires spikes, the K<sup>+</sup> M-current slowly activates, i.e.,  $n_{slow}$  slowly increases. The bursting trajectory winds up around the cylinder corresponding to the manifold of limit cycles. Each rotation corresponds to firing a spike. After the 9th spike in the figure, the K<sup>+</sup> current becomes so large that repetitive spiking cannot be sustained. This happens when  $n_{slow}$  passes the value 0.066, the limit cycle becomes a homoclinic orbit to a saddle, and then disappears. The bursting trajectory jumps down

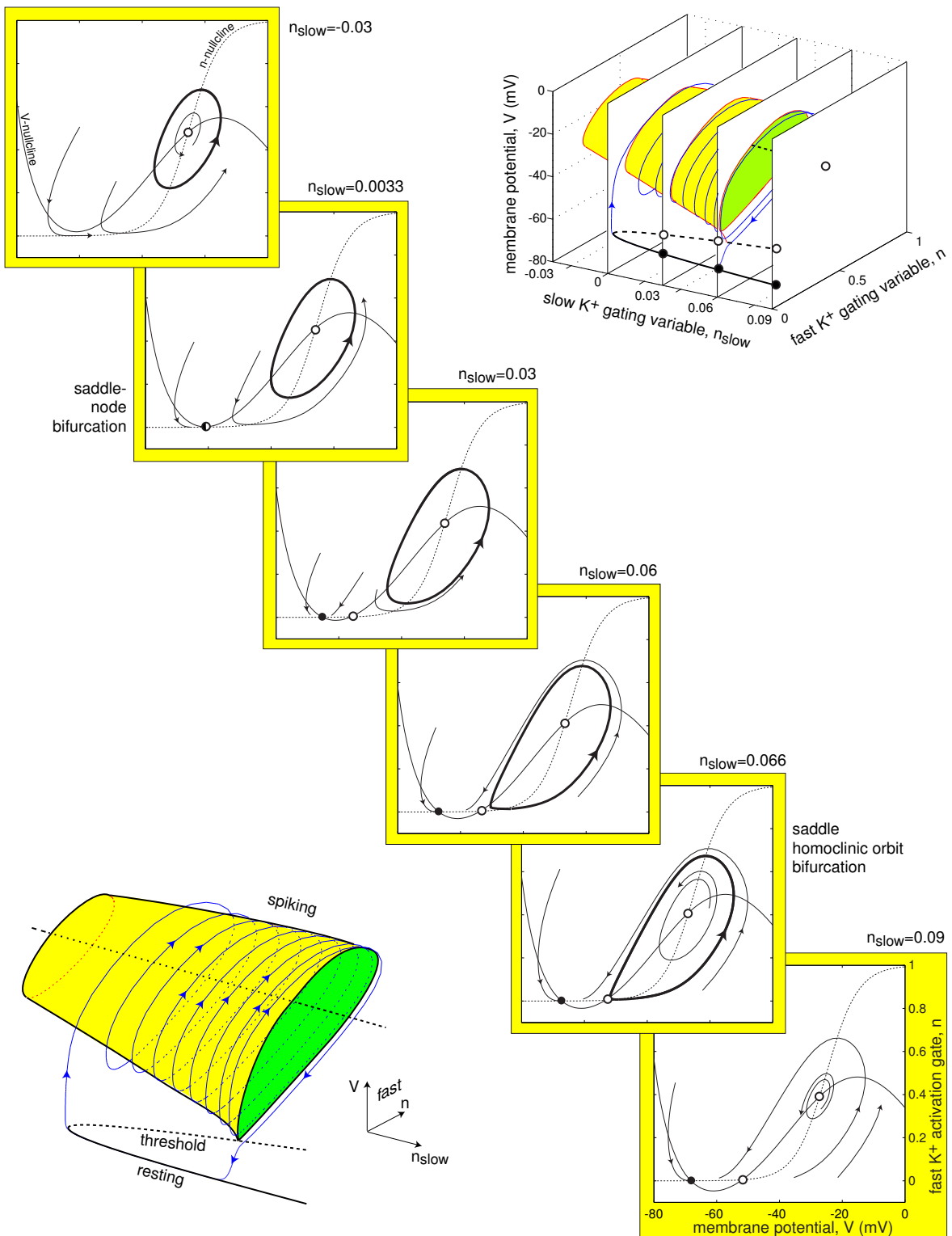


Figure 9.13: Bursting trajectory of the  $I_{\text{Na},p} + I_K + I_{\text{K(M)}}$ -model in three-dimensional phase space and its slices  $n_{\text{slow}} = \text{const}$ .

to the stable equilibrium corresponding to the resting state. This jumping corresponds to the termination of the active phase of bursting and transition to resting. While at rest,  $K^+$  current deactivates,  $n_{\text{slow}}$  decreases, and so on.

Figure 9.13 presents the inner structure of the geometrical mechanism of bursting of the  $I_{\text{Na,p}}+I_K+I_{K(M)}$ -model with parameters as in Fig. 9.4. Other values of the parameters can result in different geometrical mechanisms, summarized in Sect. 9.3. In all cases, our approach is the same: freeze the slow subsystem by setting  $\mu = 0$ ; analyze phase portraits of the fast subsystem treating the slow variable as a bifurcation parameter; then glue the phase portraits, let  $\mu \neq 0$  but small, and see how the evolution of the slow subsystem switches the fast subsystem between spiking and resting states. The method usually breaks down if  $\mu$  is not small enough, because evolution of the “slow” variable starts to interfere with that of the fast variable. How small is *small* depends on the particulars of the equations describing bursting activity. One should worry when  $\mu$  is greater than 0.1.

### 9.2.3 Averaging

What governs the evolution of the slow variable  $u$ ? To study this question, we describe a well-known and widely used method that reduces the fast-slow system (9.1) to its slow component. In fact, we have already used this method in Chapters 3 and 4 to reduce the dimension of neuronal models via substitution  $m = m_\infty(V)$ . Using essentially the same ideas, we take advantage of the two time scales in (9.1) and get rid of the fast subsystem by means of a substitution  $x = x(u)$ .

When the neuron is resting, its membrane potential is at an equilibrium and all fast gating variables are at their steady-state values, so that  $x = x_{\text{rest}}(u)$ . Using this function in the slow equation in (9.1) we obtain

$$\dot{u} = \mu g(x_{\text{rest}}(u), u) \quad (\text{reduced slow subsystem}), \quad (9.2)$$

which can easily be studied using the geometrical methods presented in Chapters 3 or 4.

Let us illustrate all the steps involved using the  $I_{\text{Na,p}}+I_K+I_{K(M)}$ -model with  $n_{\text{slow}}$  being the gating variable of the slow  $K^+$  M-current. First, we freeze the slow subsystem, i.e., set  $\tau_{\text{slow}}(V) = \infty$  so that  $\mu = 1/\tau_{\text{slow}} = 0$ , and determine numerically the resting potential  $V_{\text{rest}}$  as a function of the slow variable  $n_{\text{slow}}$ . The function  $V = V_{\text{rest}}(n_{\text{slow}})$  is depicted in Fig. 9.14, top, and it coincides with the solid half-parabola in Fig. 9.13. Then, we use this function in the gating equation for the M-current to obtain (9.2)

$$\dot{n}_{\text{slow}} = (n_{\infty,\text{slow}}(V_{\text{rest}}(n_{\text{slow}})) - n_{\text{slow}})/\tau_{\text{slow}}(V_{\text{rest}}(n_{\text{slow}})) = \bar{g}(n_{\text{slow}})$$

depicted in Fig. 9.14, bottom. Notice that  $\bar{g} < 0$ , meaning that  $n_{\text{slow}}$  decreases while the fast subsystem rests. The rate of decrease is fairly small when  $n_{\text{slow}} \approx 0$ .

A similar method of reduction, with an extra step, can be used when the fast subsystem fires spikes. Let  $x(t) = x_{\text{spike}}(t, u)$  be a periodic function corresponding to

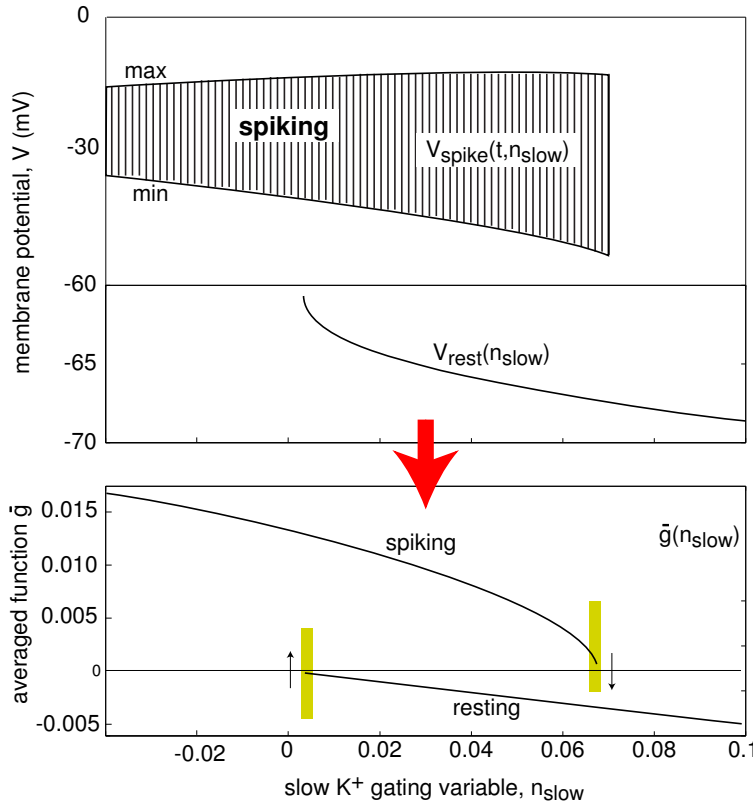


Figure 9.14: Spiking solutions  $V(t) = V_{\text{spike}}(t, u_{\text{slow}})$ , resting membrane potential  $V = V_{\text{rest}}(n_{\text{slow}})$ , and the reduced slow subsystem  $\dot{n}_{\text{slow}} = \bar{g}(n_{\text{slow}})$  of the  $I_{\text{Na,p}} + I_K + I_{K(M)}$ -model. The reduction is not valid in the shaded regions.

an infinite spike train of the fast subsystem when  $u$  is frozen. Slices of this function are shown in Fig. 9.14, top. Let  $T(u)$  be the period of spiking oscillation. The periodically forced slow subsystem

$$\dot{u} = \mu g(x_{\text{spike}}(t, u), u) \quad (\text{slow subsystem}) \quad (9.3)$$

can be averaged and reduced to a simpler model

$$\dot{w} = \mu \bar{g}(w) \quad (\text{averaged slow subsystem}) \quad (9.4)$$

by a near-identity change of variables  $w = u + o(\mu)$ , where  $o(\mu)$  denotes small terms of order  $\mu$  or less. Here

$$\bar{g}(w) = \frac{1}{T(w)} \int_0^{T(w)} g(x_{\text{spike}}(t, w), w) dt$$

is the average of  $g$ , shown in Fig. 9.14, bottom, for the  $I_{\text{Na,p}} + I_K + I_{K(M)}$ -model. Check that  $\bar{g}(w) = g(x_{\text{rest}}(w), w)$  when the fast subsystem is resting. Limit cycles of the

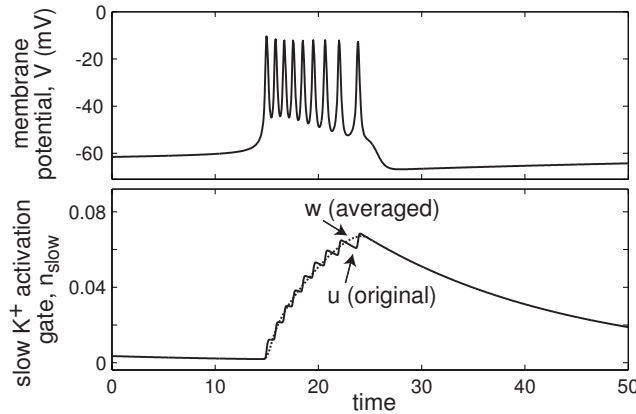


Figure 9.15: The  $I_{\text{Na,p}} + I_{\text{K}} + I_{\text{K(M)}}$ -model burster with original and averaged slow variable.

averaged slow subsystem corresponds to bursting dynamics, whereas equilibria correspond to either resting or periodic spiking states of the full system (9.1) — the result known as Pontryagin–Rodygin (1960) theorem. Interesting regimes correspond to the co-existence of limit cycles and equilibria of the slow averaged system.

The main purpose of averaging consists in substituting the wiggle trajectory of  $u(t)$  by a smooth trajectory of  $w(t)$ , as we illustrate in Fig. 9.15. We purposely used a different letter,  $w$ , for the new slow variable to stress that (9.4) is not equivalent to (9.3). Their solutions are  $o(\mu)$ -close to each other only when certain conditions are satisfied, see Guckenheimer and Holmes (1983) or Hoppensteadt and Izhikevich (1997). In particular, this straightforward averaging breaks down when  $u$  passes slowly the bifurcation values. For example, the period,  $T(u)$ , of  $x_{\text{spike}}(t, u)$  may go to infinity, as happens near saddle-node on invariant circle and saddle homoclinic orbit bifurcations, or transients may take as long as  $1/\mu$ , or the averaged system (9.4) is not smooth. All these cases are encountered in bursting models. Thus, one can use the reduced slow subsystem only when the fast subsystem is sufficiently far away from a bifurcation, e.g., away from the shaded regions in Fig. 9.14.

### 9.2.4 Equivalent voltage

Let us consider a “2+1” burster with a slow subsystem depending only on the slow variable and the membrane potential  $V$ , as in the  $I_{\text{Na,p}} + I_{\text{K}} + I_{\text{K(M)}}$ -model. The nonlinear equation

$$g(V, u) = \bar{g}(u) \quad (9.5)$$

can be solved for  $V$ . The solution,  $V = V_{\text{equiv}}(u)$ , is referred to as being the *equivalent voltage* (Kepler et al. 1992, Bertram et al. 1995), because it replaces the periodic function  $x_{\text{spike}}(t, u)$  in (9.3) by an “equivalent” value of the membrane potential, so that the reduced slow subsystem (9.3) has the same form,

$$\dot{u} = \mu g(V_{\text{equiv}}(u), u) \quad (\text{slow subsystem}), \quad (9.6)$$

as in (9.1). Check that  $V_{\text{equiv}}(u) = V_{\text{rest}}(u)$  when the fast subsystem is resting. An interesting mathematical possibility is when  $V_{\text{equiv}}$  during spiking is below  $V_{\text{rest}}$ , leading

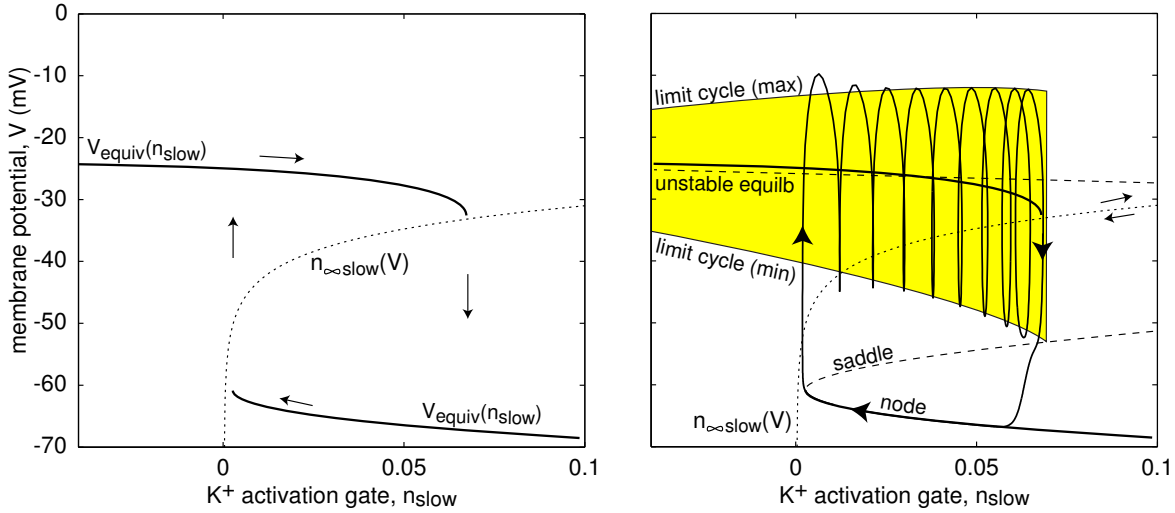


Figure 9.16: Projection of bursting trajectory of the  $I_{\text{Na,p}} + I_K + I_{K(M)}$ -model onto the  $(n_{\text{slow}}, V)$  plane.

to bizarre bursters having amplifying slow currents, such as the one in Ex. 10.

We depict the equivalent voltage of the  $I_{\text{Na,p}} + I_K + I_{K(M)}$ -model in Fig. 9.16, left (variable  $u$  corresponds to  $n_{\text{slow}}$ ). In the same figure, we depict the steady-state activation function  $n = n_{\infty, \text{slow}}(V)$  (notice the flipped coordinate system). We interpret the two curves as fast and slow nullclines of the reduced  $(V, n_{\text{slow}})$ -system. During the active (spiking) phase of bursting, the reduced system slides along the upper branch of  $V_{\text{equiv}}(n_{\text{slow}})$  to the right. When it reaches the end of the branch, it falls down to the lower branch corresponding to resting, and slides along this branch to the left. When it reaches the left end of the lower branch, it jumps up to the upper branch, and thereby closes the hysteresis loop. Fig. 9.16, right, summarizes all the information needed to understand the transitions between resting and spiking states in this model. It depicts the bursting trajectory, loci of equilibria of the fast subsystem, and the voltage range of spiking limit cycle as a function of the slow gate  $n_{\text{slow}}$ . With some experience, one can read this complicated figure and visualize the three-dimensional geometry underlying bursting dynamics.

### 9.2.5 Hysteresis loops and slow waves

Sustained bursting activity of the fast-slow system (9.1) corresponds to periodic (or chaotic) activity of the reduced slow subsystem (9.6). Depending on the dimension of  $u$ , i.e., on the number of slow variables, there could be two fundamentally different ways the slow subsystem oscillates.

If the slow variable  $u$  is one-dimensional, then there must be a bistability of resting and spiking states of the fast subsystem so that  $u$  oscillates via a hysteresis loop. That is, the reduced equation (9.6) consists of two parts, one for  $V_{\text{equiv}}(u)$  corresponding to spiking, and one for  $V_{\text{equiv}}(u)$  corresponding to resting of the fast subsystem, as

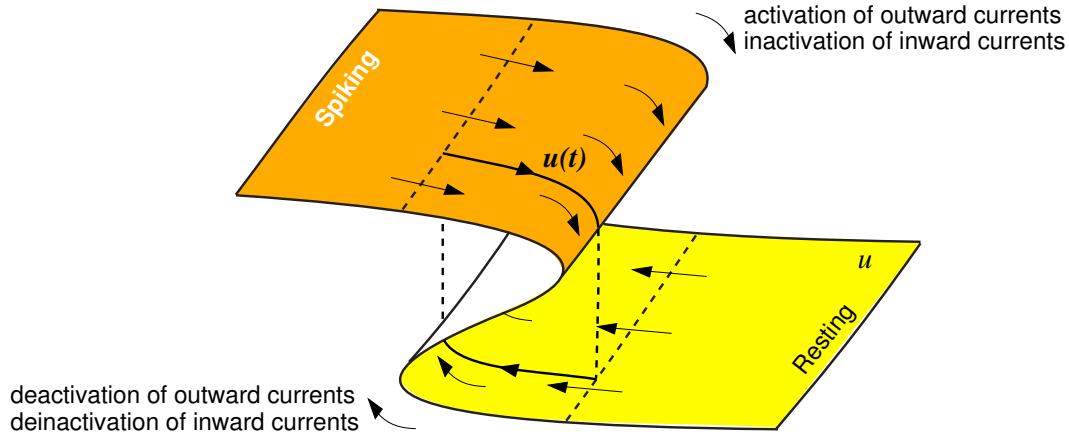


Figure 9.17: Hysteresis-loop periodic bursting.

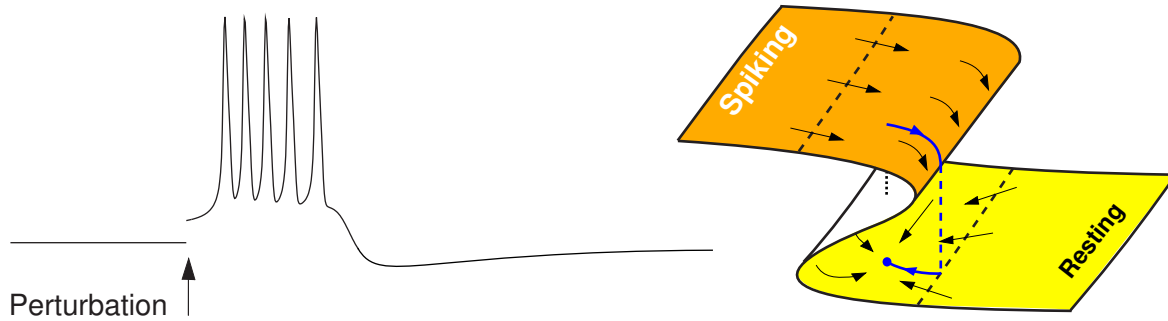


Figure 9.18: Burst excitability: A perturbation causes a burst of spikes.

in Fig. 9.16, left. Such a hysteresis loop bursting can also occur when  $u$  is multi-dimensional, as we illustrate in Fig. 9.17. The vector-field on the top (spiking) leaf pushes  $u$  outside the spiking area, whereas the vector-field on the bottom (resting) leaf pushes  $u$  outside the resting area. As a result,  $u$  visits the spiking and resting areas periodically, and the model exhibits *hysteresis-loop* bursting.

If resting  $x$  does not push  $u$  into the spiking area, but leaves it in the bistable area, then the neuron exhibits *burst excitability*: It has quiescent excitable dynamics, but its response to perturbations is not a single spike, but a burst of spikes, as we illustrate in Fig. 9.18. Grade III bursters of hippocampus (Fig. 8.34Eb) produce such a response, often called *complex spike* response, to brief stimuli. In general, many bistable models are bistable only because they neglect slow currents and other homeostatic processes present in real neurons. If the currents are taken into account, then the models become bistable on a short time scale and burst-exitable on a longer time scale. This justifies why many researchers refer to bistable systems as excitable, implicitly assuming that the response to superthreshold perturbations is either a single spike or a long train of spikes.

If the fast subsystem does not have a coexistence of resting and spiking states, then the reduced slow subsystem (9.6) must be at least two-dimensional to exhibit

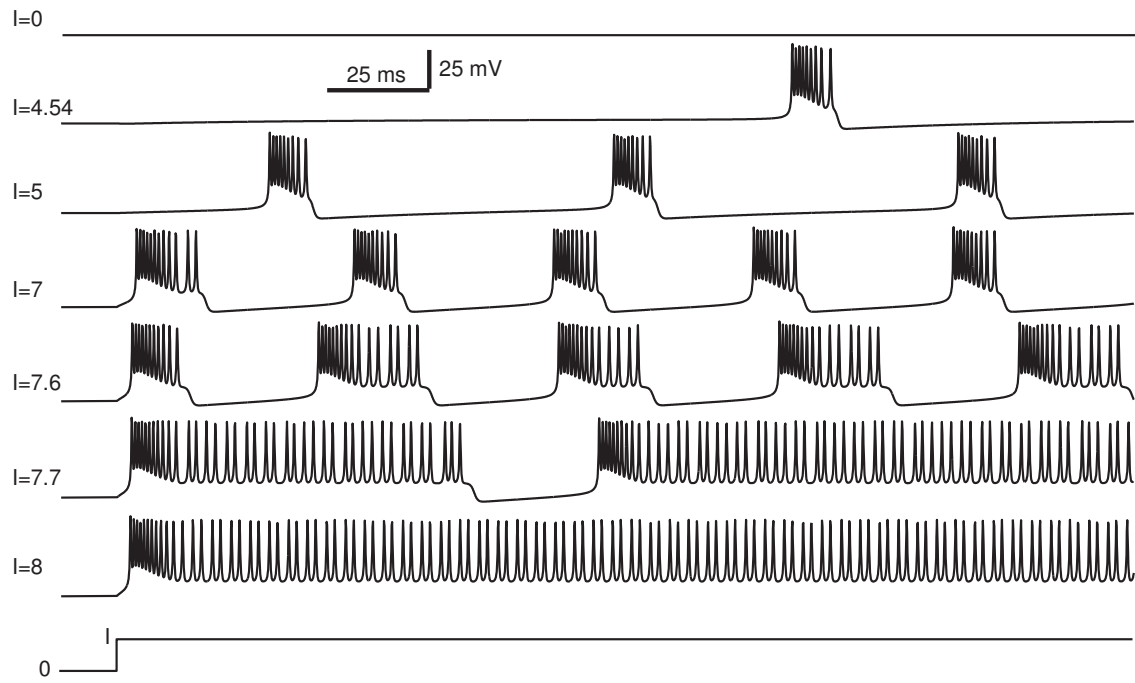


Figure 9.19: Bifurcations of bursting solutions in the  $I_{\text{Na},p} + I_K + I_{\text{K}(\text{M})}$ -model as the magnitude of the injected dc-current  $I$  changes.

sustained autonomous oscillation (however, see Ex. 6). Such an oscillation produces a depolarization wave that drives the fast subsystem to spiking and back, as in Fig. 9.3. We refer to such bursters as *slow-wave* bursters. Quite often, however, the slow subsystem of a slow-wave burster needs the feedback from the fast subsystem to oscillate. For example, in Sect. 9.3.2 we consider slow-wave bursting in the  $I_{\text{Na},p} + I_K + I_{\text{Na,slow}} + I_{\text{K}(\text{M})}$ -model, whose slow subsystem consists of two uncoupled equations, and hence cannot oscillate by itself unless the fast subsystem is present.

### 9.2.6 Bifurcations “resting $\leftrightarrow$ bursting $\leftrightarrow$ spiking”

Switching between spiking and resting states during bursting occurs because the slow variable drives the fast subsystem through bifurcations of equilibria and limit cycle attractors. These bifurcations play an important role in our classification of bursters and in understanding their neuro-computational properties. We discuss them in detail in the next section.

Since the fast subsystem goes through bifurcations, *does this mean that the entire system (9.1) undergoes bifurcations during bursting?* The answer is NO. As long as parameters of (9.1) are fixed, the system as a whole does not undergo any bifurcations, no matter how small  $\mu$  is. The system can exhibit periodic, quasi-periodic or even chaotic bursting activity, but its  $(m+k)$ -dimensional phase portrait does not change.

The only way to make system (9.1) undergo a bifurcation is to change its param-

eters. For example, in Fig. 9.19 we change the magnitude of the injected dc-current  $I$  in the  $I_{\text{Na,p}}+I_{\text{K}}+I_{\text{K(M)}}$ -model. Apparently, no bursting exists when  $I = 0$ . Then, repetitive bursting appears with a large interburst period that decreases as  $I$  increases. The value  $I = 5$  was used to obtain bursting solutions in Fig. 9.12 and Fig. 9.13. Increasing  $I$  further increases the duration of each burst, until it becomes infinite, i.e., bursting turns into tonic spiking. When  $I > 8$ , the slow K<sup>+</sup> current is not enough to stop spiking.

In Fig. 9.20 we depict the geometry of bursting in the  $I_{\text{Na,p}}+I_{\text{K}}+I_{\text{K(M)}}$ -model when  $I = 3$ , i.e., just before periodic bursting appears, and when  $I = 10$ , i.e., just after bursting turns into tonic spiking.

When  $I = 3$ , the nullcline of the slow subsystem  $n_{\text{slow}} = n_{\infty,\text{slow}}(V)$  intersects the locus of stable equilibria of the fast subsystem. The intersection point is a globally stable equilibrium of the full system (9.1). Small perturbations, whether in the  $V$  direction,  $n$  direction, or  $n_{\text{slow}}$  direction subside, whereas a large perturbation, e.g., in the  $V$  direction, that moves the membrane potential to the open square in the figure, initiates a transient (phasic) burst of 7 spikes. Increasing the magnitude of the injected current  $I$  shifts the saddle-node parabola to the right. When  $I \approx 4.54$ , the nullcline of the slow subsystem does not intersect the locus of stable equilibria, and the resting state no longer exists, as in Fig. 9.16, right. (There is still a global steady state, but it is not stable.)

Further increase of the magnitude of the injected current  $I$  results in the intersection of the nullcline of the slow subsystem with the equivalent voltage function  $V_{\text{equiv}}(n_{\text{slow}})$ . The intersection, marked by the black circle in Fig. 9.20, right, corresponds to a globally stable (spiking) limit cycle of the full system (9.1). A sufficiently strong perturbation can push the state of the fast subsystem into the attraction domain of the stable (resting) equilibrium. While the fast subsystem is resting, the slow variable decreases, i.e., K<sup>+</sup> current deactivates, the resting equilibrium disappears and repetitive spiking resumes.

Figures 9.19 and Fig. 9.20 illustrate possible transitions between bursting and resting, and bursting and tonic spiking. There could be other routes of emergence of bursting solutions from resting or spiking, some of them are in Fig. 9.21. Each such route corresponds to a bifurcation in the full system (9.1) with some  $\mu > 0$ . For example, the case  $a \rightarrow 0$  corresponds to supercritical Andronov-Hopf bifurcation; the case  $c \rightarrow \infty$  corresponds to a saddle-node on invariant circle or saddle homoclinic orbit bifurcation; the case  $d \rightarrow \infty$  corresponds to a periodic orbit with a homoclinic structure, e.g., blue-sky catastrophe, fold limit cycle on homoclinic torus bifurcation, or something more complicated. The transitions “bursting  $\leftrightarrow$  spiking often exhibit chaotic (irregular) activity, so Fig. 9.21 if probably a great oversimplification. Understanding and classifying all possible bifurcations leading to bursting dynamics is an important but open problem; see Ex. 27.

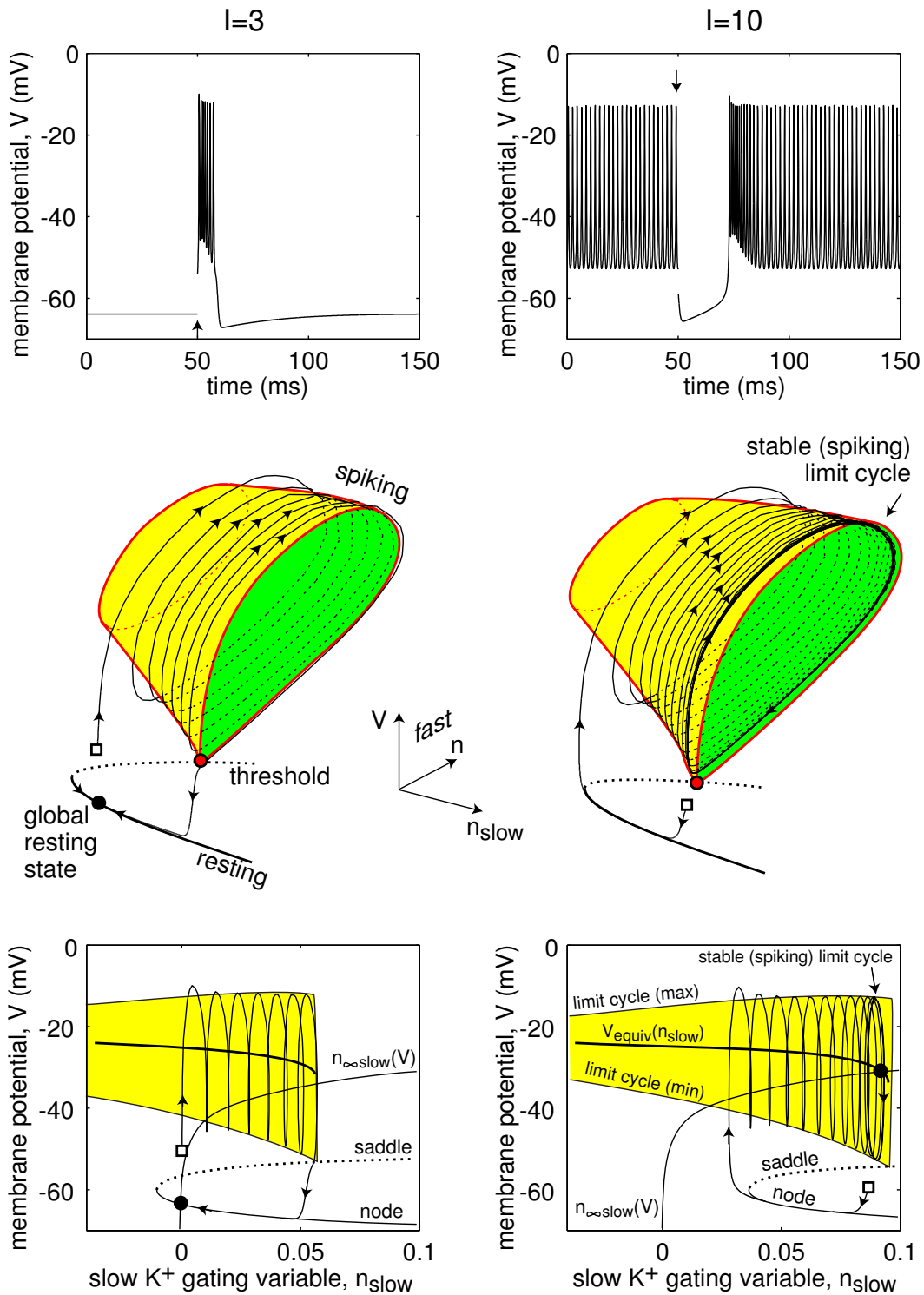


Figure 9.20: Burst excitability ( $I = 3$ , left) and periodic spiking ( $I = 10$ , right) in the  $I_{Na,p} + I_K + I_{K(M)}$ -model.

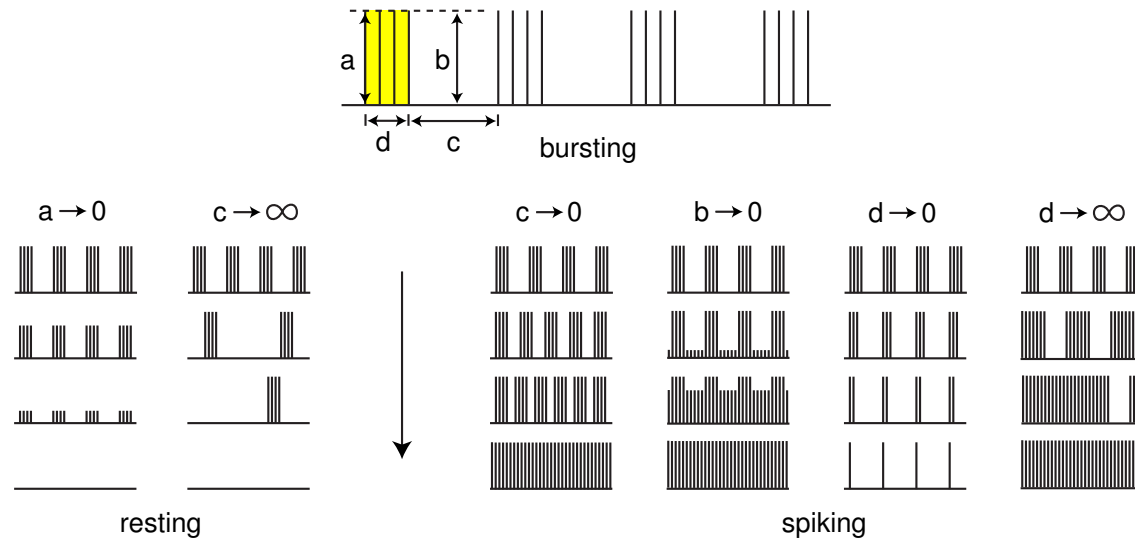


Figure 9.21: Possible transitions between repetitive bursting and resting, and repetitive bursting and repetitive spiking.

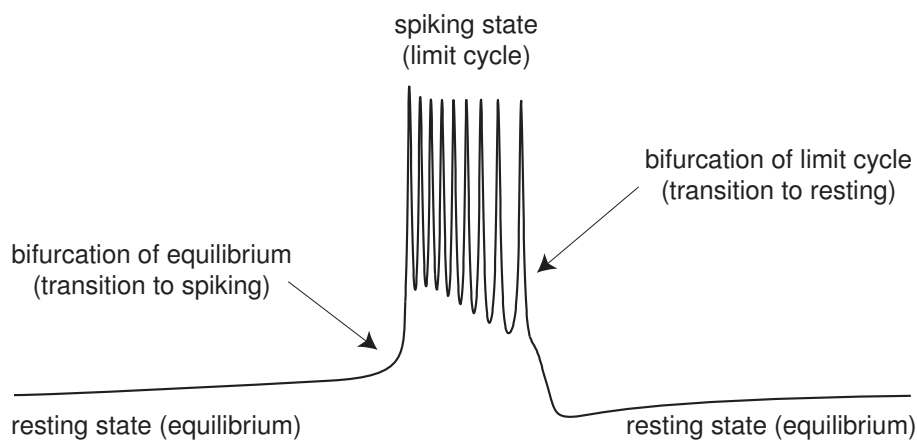


Figure 9.22: Two important bifurcations associated with fast-slow bursting.

### 9.3 Classification

In Fig. 9.22 we identify two important bifurcations of the fast subsystem that are associated with bursting activity in the fast-slow burster (9.1):

- (**resting → spiking**) Bifurcation of an equilibrium attractor that results in transition from resting to repetitive spiking.
- (**spiking → resting**) Bifurcation of the limit cycle attractor that results in transition from spiking to resting.

The ionic basis of bursting, i.e., the fine electrophysiological details, determine the kind of bifurcations in Fig. 9.22. The bifurcations, in turn, determine the neuro-computational properties of fast-slow bursters, discussed in Sect. 9.4.

A complete topological classification of bursters based on these two bifurcations is provided by Izhikevich (2000), who identified 120 different topological types. Here, we consider only 16 planar point-cycle co-dimension-1 fast-slow bursters. We say that a fast-slow burster is *planar* when its fast subsystem is two-dimensional. We emphasize planar bursters because they have a greater chance to be encountered in computer simulations (but not necessarily in nature). We say that a burster is of the *point-cycle* type when its resting state is a stable equilibrium point and its spiking state is a stable limit cycle. All bursters considered so far, including those in Fig. 9.1, are of the point-cycle type. Other, less common types, such as cycle-cycle and point-point, are considered as exercises.

We consider here only bifurcations of co-dimension 1, i.e. those that need only one parameter and hence are more likely to be encountered in nature. Having a two-dimensional fast subsystem imposes severe restriction on possible co-dimension-1 bifurcations of the resting and spiking states. In particular, there are only 4 bifurcations of equilibria and 4 bifurcations of limit cycles, which we consider in Chap. 6 and summarize in Figures 6.46 and 6.47. Any combination of them results in a distinct topological type of fast-slow bursting, hence there are  $4 \times 4 = 16$  such bursters, summarized in Fig. 9.23.

We name the bursters according to the type of the bifurcations of the resting and spiking states. To keep the names short, we refer to saddle-node on invariant circle bifurcation as just a “circle” bifurcation because it is the only co-dimension-1 bifurcation on a circle manifold  $\mathbb{S}^1$ . We refer to supercritical Andronov-Hopf bifurcation as just “Hopf” bifurcation, to subcritical Andronov-Hopf as “subHopf”, to fold limit cycle bifurcation as “fold cycle”, and to saddle homoclinic orbit bifurcation as “homoclinic” bifurcation. Thus, the bursting pattern exhibited by the  $I_{\text{Na,p}} + I_K + I_{K(M)}$ -model in Fig. 9.13 is of the “fold/homoclinic” type because the resting state disappears via “fold” bifurcation and the spiking limit cycle attractor disappears via saddle “homoclinic” orbit bifurcation.

Similarly to Fig. 9.13, we depict the geometry of the other bursters in Fig. 9.24. This figure gives only examples and it does not exhaust all possibilities. Let us consider some most common bursting types in detail.

bifurcations of equilibria

bifurcations of limit cycles				
	saddle-node on invariant <b>circle</b>	saddle <b>homoclinic</b> orbit	supercritical Andronov- Hopf	<b>fold</b> limit cycle
saddle-node <b>(fold)</b>	fold/ circle	fold/ homoclinic	fold/ Hopf	fold/ fold cycle
saddle-node on invariant <b>circle</b>	circle/ circle	circle/ homoclinic	circle/ Hopf	circle/ fold cycle
supercritical Andronov- <b>Hopf</b>	Hopf/ circle	Hopf/ homoclinic	Hopf/ Hopf	Hopf/ fold cycle
<b>subcritical</b> Andronov- <b>Hopf</b>	subHopf/ circle	subHopf/ homoclinic	subHopf/ Hopf	subHopf/ fold cycle

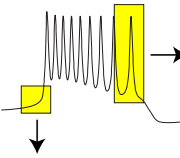


Figure 9.23: Classification of planar point-cycle fast-slow bursters based on the co-dimension-1 bifurcations of the resting and spiking states of the fast subsystem.

### 9.3.1 fold/homoclinic

When the resting state disappears via a saddle-node (fold) bifurcation and the spiking limit cycle disappears via saddle homoclinic orbit bifurcation, the burster is said to be of the “fold/homoclinic” type depicted in Fig. 9.25. Notice the bistability of resting and spiking states, resulting in hysteresis loop oscillation of the slow subsystem.

“Fold/homoclinic” bursting is quite common in neuronal models, for example in the  $I_{Na,p} + I_K + I_{K(M)}$ -model considered in this chapter; see Fig. 9.13. It was first characterized in the context of the insulin-producing pancreatic  $\beta$ -cells in Fig. 9.26, with intracellular concentration of  $\text{Ca}^{2+}$  ions being the slow resonant variable (Chay and Keizer 1983). Neurons located in the pre-Botzinger complex, a region that is associated with generating the rhythm for breathing, also exhibit this kind of bursting (Butera et al. 1999), as shown in Fig. 9.27. Intrinsic bursting (IB) and chattering (CH) behavior of the simple model in Sect. 8.2 could be of the “fold/homoclinic” type too, provided that the parameter  $a$  is sufficiently small. Because of the distinct square-wave shape of oscillations of the membrane potential in Figures 9.26 and Fig. 9.27, this bursting was called “square-wave” bursting in earlier studies. Since many types of bursters resemble square waves, referring to a burster by its shape is misleading and should be avoided.

In Fig. 9.25, bottom, we depict a typical configuration of nullclines of the fast subsystem during “fold/homoclinic” bursting. The resting state of the membrane po-

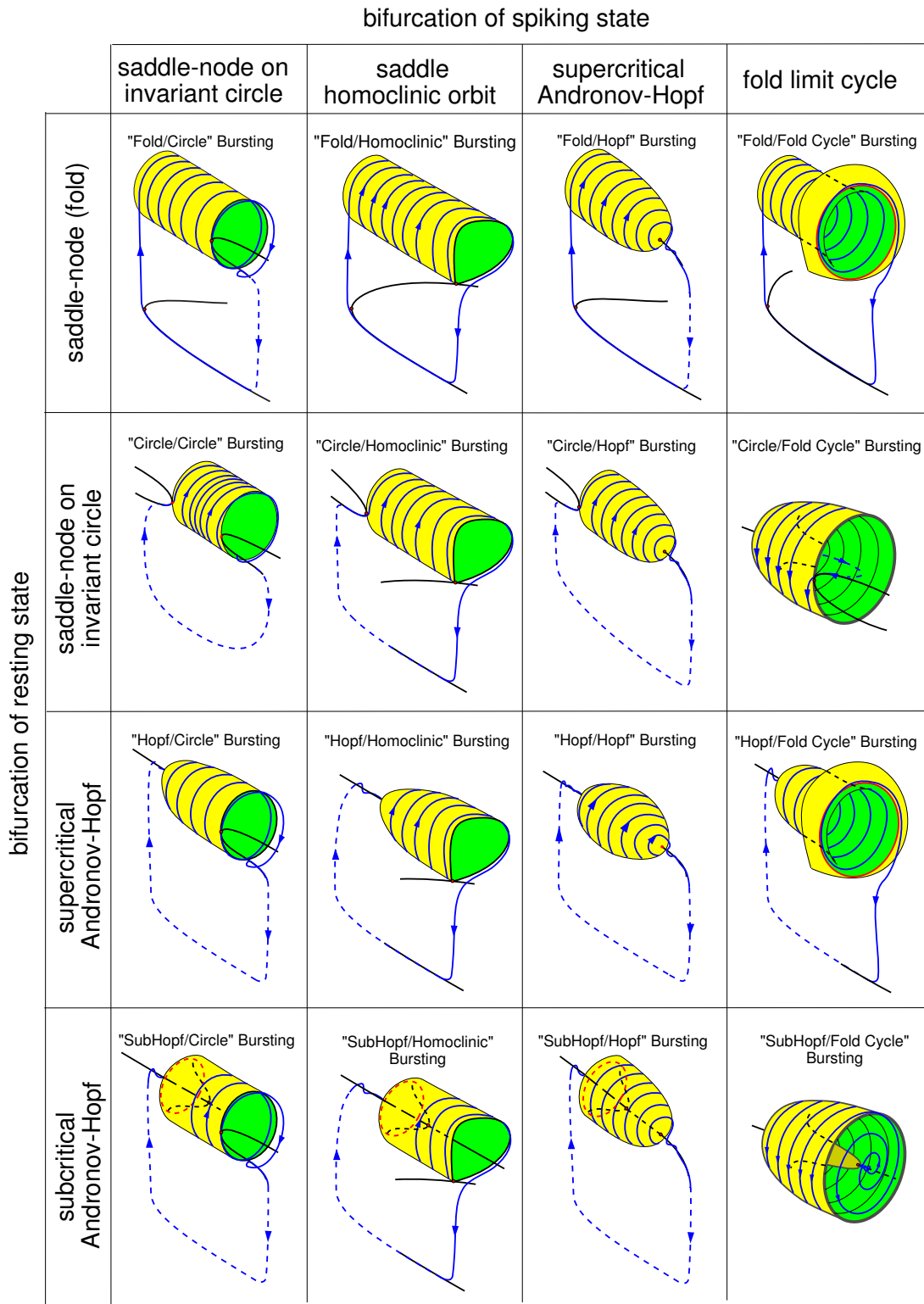


Figure 9.24: Examples of “2+1” point-cycle fast-slow co-dimension-1 bursters of hysteresis-loop type (modified from Izhikevich 2000). Dashed chains of arrows show transitions that might involve other bifurcations not relevant to the bursting type.

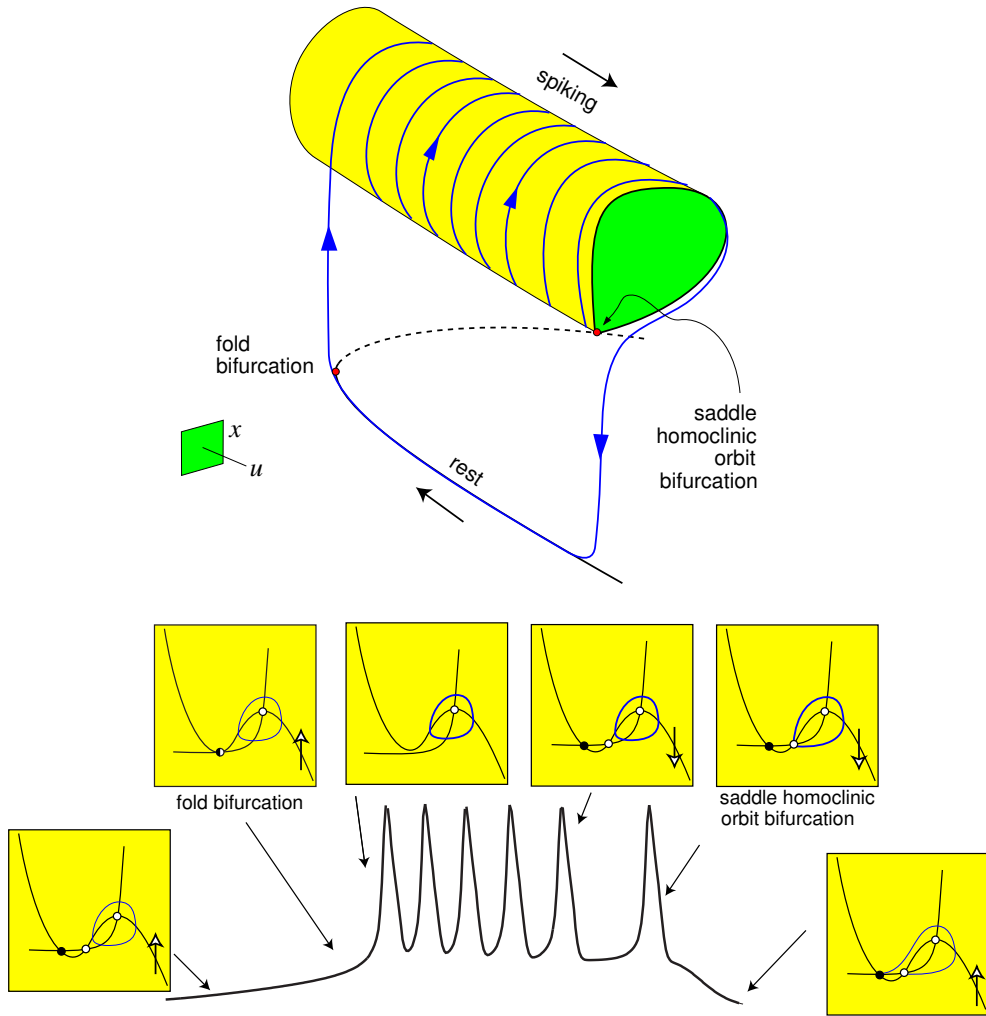


Figure 9.25: “Fold/homoclinic” bursting: The resting state disappears via saddle-node (fold) bifurcation and the spiking limit cycle disappears via saddle homoclinic orbit bifurcation.

tential corresponds to the left stable equilibrium, which is the intersection of the left knee of the fast N-shaped nullcline with the slow nullcline. During resting, the N-shape nullcline slowly moves up, until its knee touches the slow nullcline at a saddle-node point. Right after this moment, the resting state disappears via saddle-node (fold) bifurcation, hence the part “fold” in the name of the burster. After the fold bifurcation, the membrane potential jumps up to the stable limit cycle corresponding to repetitive spiking. During the spiking state, the N-shaped nullcline slowly moves down, and the middle (saddle) equilibrium moves away from the resting state toward the limit cycle. After a while, the limit cycle becomes a homoclinic trajectory to the saddle, and then the cycle disappears via saddle homoclinic orbit bifurcation, hence the part “homoclinic” in the name of the burster. After this bifurcation, the membrane potential jumps down to the resting state and closes the hysteresis loop.



Figure 9.26: Putative “fold/homoclinic” bursting in a pancreatic  $\beta$ -cell (modified from Kinard et al. 1999).

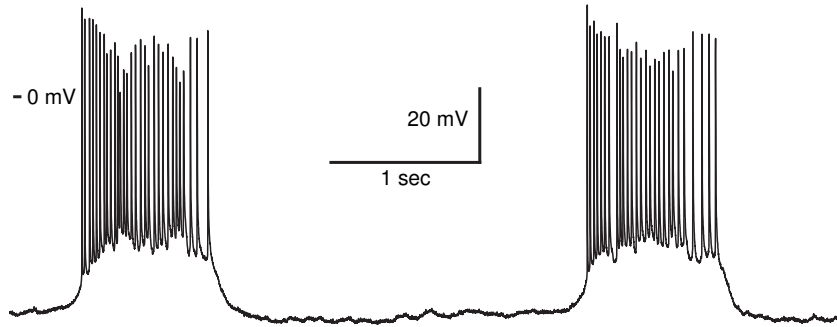


Figure 9.27: Putative ”fold/homoclinic” bursting in a cell located in pre-Botzinger complex of rat brain stem (data kindly shared by Christopher A. Del Negro and Jack L. Feldman, Systems Neurobiology Laboratory, Department of Neurobiology, UCLA.)

Suppose that the hysteresis loop oscillation of the slow variable  $u$  has a small amplitude. That is, the saddle-node bifurcation and the saddle homoclinic orbit bifurcation occur for nearby values of the parameter  $u$ . In this case, the fast subsystem of (9.1) is near co-dimension-2 saddle-node homoclinic orbit bifurcation, depicted in Fig. 9.28 and studied in Sect. 6.3.6. The figure shows a two-parameter unfolding of the bifurcation, treating  $u \in \mathbb{R}^2$  as the parameter. A stable equilibrium (resting state) exists in the left half-plane, and a stable limit cycle (spiking state) exists in the right half-plane of the figure and in the shaded (bistable) region. “Fold/homoclinic” bursting occurs when the bifurcation parameter, being a slow variable, oscillates between the resting and spiking states through the shaded region. Due to the bistability, the parameter could be one-dimensional. Other trajectories of the slow parameter correspond to other types of bursting.

In Ex. 16 we prove that there is a piece-wise continuous change of variables that transforms any “fold/homoclinic” burster with fast subsystem near such a bifurcation into the canonical model (see Sect. 8.1.5)

$$\begin{aligned}\dot{v} &= I + v^2 - u, \\ \dot{u} &= -\mu u,\end{aligned}\tag{9.7}$$

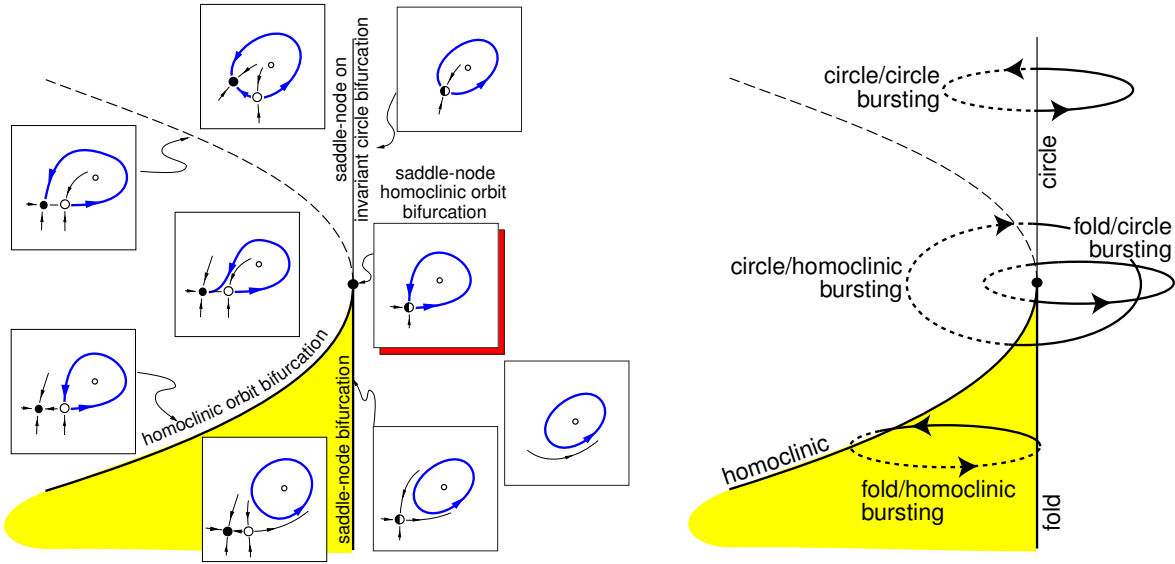


Figure 9.28: A neural system near co-dimension-2 saddle-node homoclinic orbit bifurcation (center dot) can exhibit four different types of fast-slow bursting, depending on the trajectory of the slow variable  $u \in \mathbb{R}^2$  in the two-dimensional parameter space. Solid (dotted) lines correspond to spiking (resting) regimes.

with an after-spike resetting:

$$\text{if } v = +\infty, \text{ then } v \leftarrow 1 \text{ and } u \leftarrow u + d.$$

Here  $v \in \mathbb{R}$  is the re-scaled membrane potential of the neuron,  $u \in \mathbb{R}$  is the re-scaled net outward (resonant) current that provides a negative feedback to  $v$ , and  $I, d$  and  $\mu \ll 1$  are parameters. This model is related to the canonical model considered in Sect. 8.1.4, and it is simplified further in Ex. 15.

The fast subsystem  $\dot{v} = (I - u) + v^2$  is the normal form for the saddle-node bifurcation, and with the resetting it is known as the quadratic integrate-and-fire neuron (Sect. 3.3.8). When  $u > I$ , there is a stable equilibrium  $v_{\text{rest}} = -\sqrt{u - I}$  corresponding to the resting state. While the parameter  $u$  slowly decreases toward  $u = 0$ , the stable equilibrium and the saddle equilibrium  $v_{\text{thresh}} = +\sqrt{u - I}$  approach and annihilate each other at  $u = I$  via saddle-node (fold) bifurcation. When  $u < I$ , the membrane potential  $v$  increases and escapes to infinity in a finite time, i.e., it fires a spike. (Instead of infinity, any large value can be used in simulations.) The spike activates fast outward currents and resets  $v$  to 1, as in Fig. 9.29. It also activates slow currents and increments  $u$  by  $d$ . If the reset value 1 is greater than the threshold potential  $v_{\text{thresh}}$ , the fast subsystem fires another spike, and so on, even when  $u > I$ ; see Fig. 9.29. Since each spike increases  $u$ , the repetitive spiking stops when  $u = I + 1$  via saddle homoclinic orbit bifurcation. The membrane potential jumps down to the resting state, the hysteresis loop is closed, and the variable  $u$  decreases (recovers) to initiate another “fold/homoclinic” burst. One can vary  $I$  in the canonical model (9.7) to study transitions from quiescence to bursting to tonic spiking, as in Fig. 9.20.

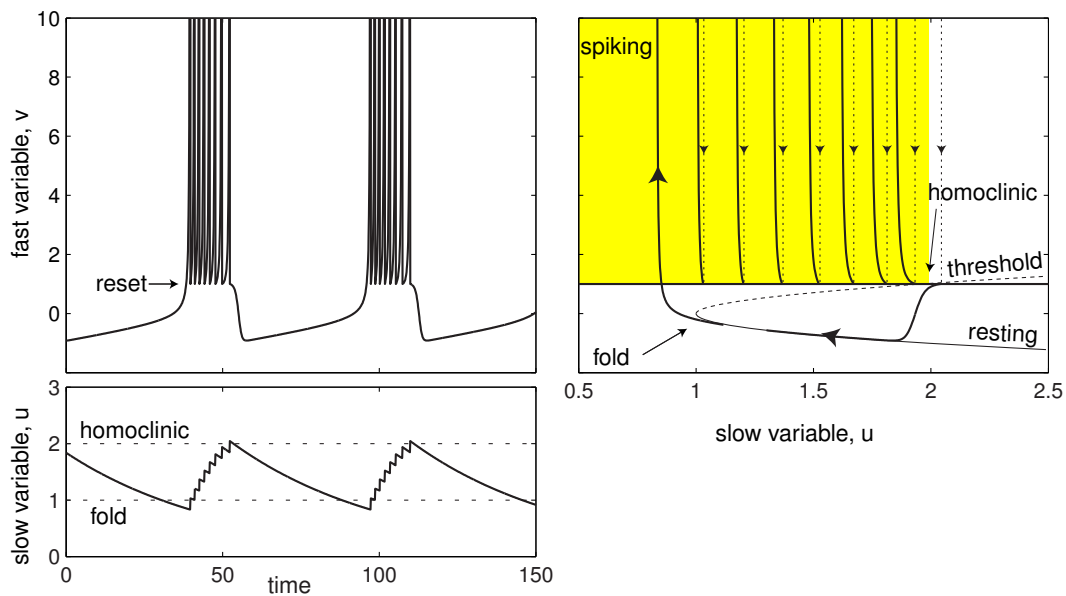


Figure 9.29: “Fold/homoclinic” bursting in the canonical model (9.7) with parameters  $\mu = 0.02$ ,  $I = 1$  and  $d = 0.2$ .

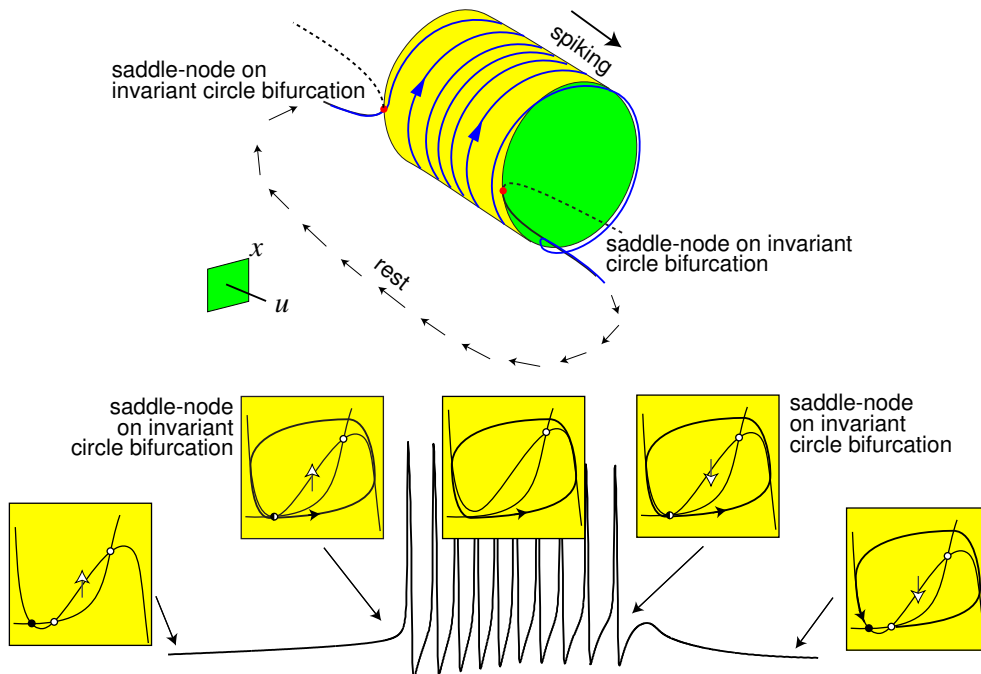


Figure 9.30: “Circle/circle” bursting: The resting state disappears via saddle-node on invariant circle bifurcation and the spiking limit cycle disappears via saddle-node on invariant circle bifurcation.

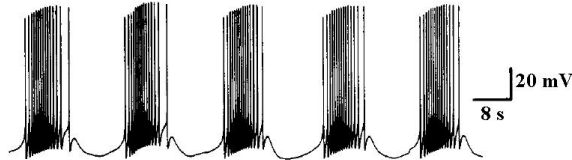


Figure 9.31: Putative “circle/circle” bursting pacemaker activity of neuron R<sub>15</sub> in abdominal ganglion of the mollusk *Aplysia* (modified from Levitan and Levitan 1988).

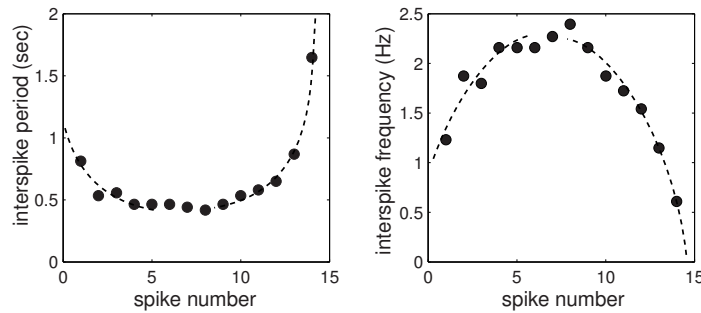


Figure 9.32: The interspike period in the “circle/circle” bursting in Fig. 9.31 resembles a parabola, which motivates the name “parabolic bursting” used in earlier studies.

### 9.3.2 circle/circle

When the equilibrium corresponding to the resting state disappears via a saddle-node on invariant *circle* bifurcation, and the limit cycle attractor corresponding to spiking state disappears via another saddle-node on invariant *circle* bifurcation, the burster is said to be of the “circle/circle” type shown in Fig. 9.30. Since the bifurcation does not produce a co-existence of attractors, there is usually no hysteresis loop, and the bursting is of the slow-wave type with at least two slow variables. (An example of “circle/circle” hysteresis loop bursting in a “2+1” system is provided by Izhikevich (2000)).

“Circle/circle” bursting is a prominent feature of the R<sub>15</sub> cells in the abdominal ganglion of the mollusk *Aplysia*, shown in Fig. 9.31 (Plant 1981). It was called “parabolic” bursting in earlier studies because the interspike period depicted in Fig. 9.32 was erroneously thought to be a parabola. In Sect. 6.1.2 we showed that when a system undergoes a saddle-node on invariant circle bifurcation, its period scales as  $1/\sqrt{\lambda}$ , where  $\lambda$  is the distance to the bifurcation. Two pieces of this function, put together as in Fig. 9.32, do indeed resemble a parabola. But so does the interspike period of a “circle/homoclinic” burster.

To transform the  $I_{\text{Na,p}} + I_K$ -model to a “circle/circle” burster, we take the parameters as in Fig. 4.1a so that there is a saddle-node on invariant circle bifurcation when  $I = 4.51$  (see Sect. 6.1.2). Its nullclines and phase portrait look similar to those in Fig. 9.30. Then, we add one amplifying and one resonant current with gating variables

$$\begin{aligned}\dot{m}_{\text{slow}} &= (m_{\infty, \text{slow}}(V) - m_{\text{slow}})/\tau_{\text{Na,slow}}(V) \quad (\text{slow } I_{\text{Na,slow}}), \\ \dot{n}_{\text{slow}} &= (n_{\infty, \text{slow}}(V) - n_{\text{slow}})/\tau_{K(M)}(V) \quad (\text{slow } I_{K(M)}),\end{aligned}$$

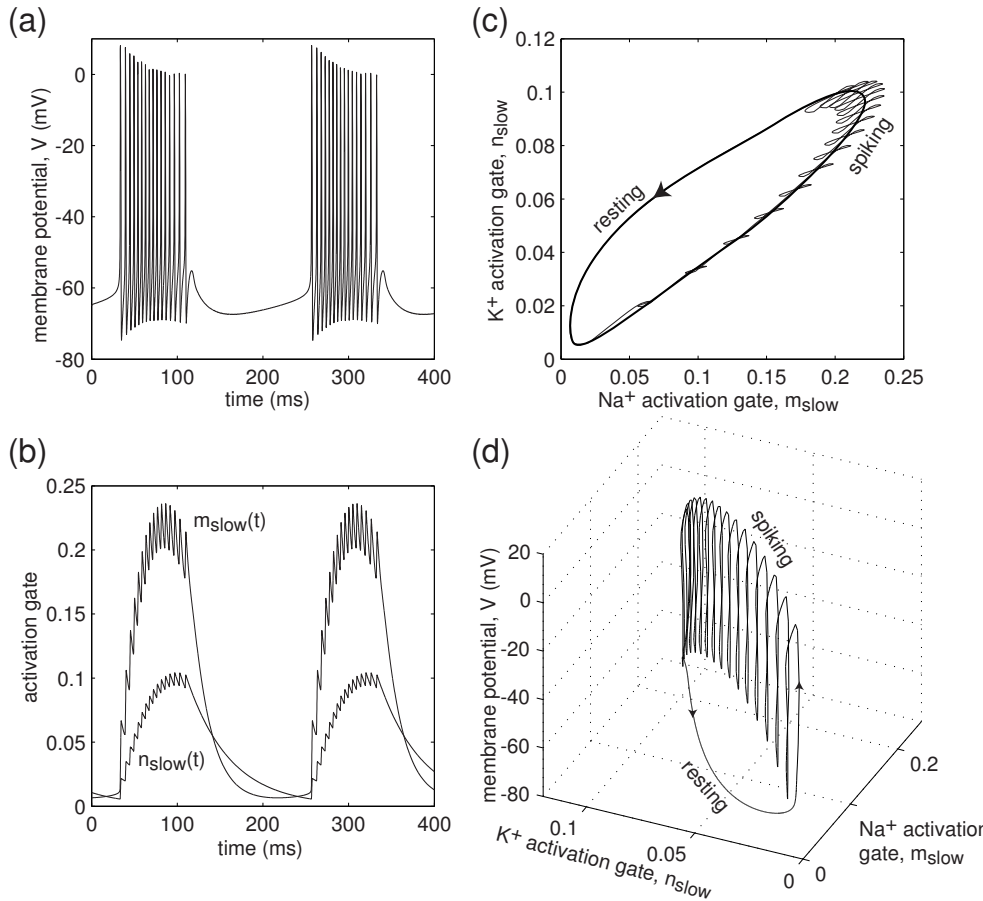


Figure 9.33: “Circle/circle” bursting in the  $I_{\text{Na},p} + I_K + I_{\text{Na,slow}} + I_{\text{K}(\text{M})}$ -model. Parameters of the fast  $I_{\text{Na},p} + I_K$ -subsystem are the same as in Fig. 4.1a with  $I = 5$ . Slow  $Na^+$  current has  $V_{1/2} = -40$  mV,  $k = 5$  mV,  $g_{\text{Na,slow}} = 3$ ,  $\tau_{\text{Na,slow}}(V) = 20$  ms. Slow  $K^+$  current has  $V_{1/2} = -20$  mV,  $k = 5$  mV,  $g_{\text{K}(\text{M})} = 20$ ,  $\tau_{\text{K}(\text{M})}(V) = 50$  ms.

having parameters as in Fig. 9.33. Notice that these equations are uncoupled and hence cannot oscillate by themselves without the feedback from variable  $V$ .

Let us describe the bursting mechanism in the full  $I_{\text{Na},p} + I_K + I_{\text{Na,slow}} + I_{\text{K}(\text{M})}$ -model with  $I = 5$ . Since  $I > 4.51$ , the resting state of the fast subsystem does not exist, and the model generates action potentials, depicted in Fig. 9.33a. Each spike activates  $I_{\text{Na,slow}}$ , produces even more inward current and hence more spikes. This, however, activates a much slower  $K^+$  current, see Fig. 9.33b, and produces a net outward current that moves the fast nullcline down and eventually terminates spiking. The transition from spiking to resting occurs via saddle-node on invariant circle bifurcation. While at rest, both currents deactivate and the fast nullcline slowly moves up. The net inward current, consisting mostly of the injected dc-current  $I = 5$ , drives the fast subsystem via the same saddle-node on invariant circle bifurcation and initiates another burst, as shown in Fig. 9.33a.

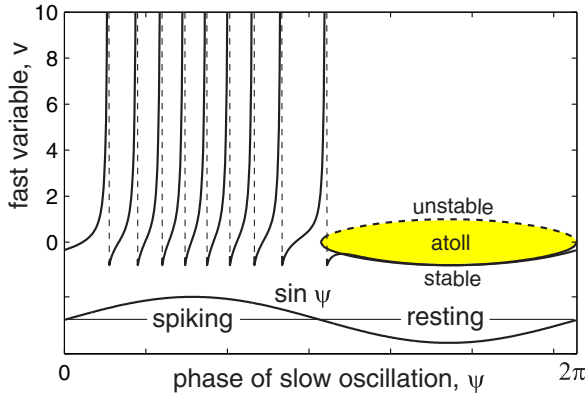


Figure 9.34: “Circle/circle” bursting in the Ermentrout-Kopell canonical model (9.8) with  $r(\psi) = \sin \psi$  and  $\omega = 0.1$ . The fast variable fires spikes while  $\sin \psi > 0$  and quiescent while  $\sin \psi < 0$ . Shaded atoll is surrounded by the equilibria curves  $\pm\sqrt{|\sin \psi|}$ . The fast subsystem undergoes saddle-node on invariant circle bifurcation when  $\sin \psi = 0$ .

Using the averaging technique described above in Sect. 9.2.3, we can reduce the four-dimensional  $I_{\text{Na,p}} + I_K + I_{\text{Na,slow}} + I_{\text{K(M)}}$ -model to a simpler, two-dimensional slow  $I_{\text{Na,slow}} + I_{\text{K(M)}}$ -subsystem of the form (9.4). Bursting of the full model corresponds to a limit cycle attractor of the averaged slow subsystem depicted as a bold curve on the  $(m_{\text{slow}}, n_{\text{slow}})$  plane in Fig. 9.33c. Superimposed is the projection of the bursting solution of the full system (thin wobbly curve). In Fig. 9.33d we project a four-dimensional bursting trajectory onto the three-dimensional subspace  $(V, m_{\text{slow}}, n_{\text{slow}})$ .

The  $I_{\text{Na,p}} + I_K + I_{\text{Na,slow}} + I_{\text{K(M)}}$ -model in Fig. 9.33 enjoys a remarkable property: It generates slow-wave bursts even though its slow  $I_{\text{Na,slow}} + I_{\text{K(M)}}$ -subsystem consists of two uncoupled equations, and hence cannot oscillate by itself! Another example of this phenomenon is presented in Ex. 12. Thus, the slow wave that drives the fast  $I_{\text{Na,p}} + I_K$ -subsystem through the two circle bifurcations is not autonomous: it needs a feedback from  $V$ . In particular, the oscillation would disappear in a voltage-clamp experiment, i.e., when the membrane potential is fixed.

Now consider a “circle/circle” burster with a slow subsystem performing small-amplitude oscillations so that the fast subsystem is always near the saddle-node on invariant circle bifurcation. If the slow subsystem has an autonomous limit cycle attractor that exists without feedback from  $V$ , then such a burster can be reduced to the Ermentrout-Kopell (1986) canonical model

$$\begin{aligned} \dot{v} &= v^2 + r(\psi), & \text{if } v = +\infty, \text{ then } v = -1, \\ \dot{\psi} &= \omega, \end{aligned} \tag{9.8}$$

which was originally written in the  $\vartheta$ -form; see Ex. 13. Here,  $\psi$  is the phase of autonomous oscillation of the slow subsystem,  $\omega \approx 0$  is the frequency of slow oscillation, and  $r(\psi)$  is a periodic function that changes sign and slowly drives the fast quadratic integrate-and-fire neuron (9.8) back and forth through the bifurcation, as we illustrate in Fig. 9.34.

Alternatively, suppose that the slow subsystem cannot have sustained oscillations without the fast subsystem, i.e., the slow subsystem has a stable equilibrium if  $v$  is fixed. In Ex. 17 we prove that there is a piece-wise continuous change of variables that transforms any such “circle/circle” burster into one of the two canonical models below,

depending on the type of the equilibrium. If the equilibrium of the slow subsystem is a stable node, then the canonical model has the form

$$\begin{aligned}\dot{v} &= I + v^2 + u_1 - u_2, \\ \dot{u}_1 &= -\mu_1 u_1, \\ \dot{u}_2 &= -\mu_2 u_2.\end{aligned}\tag{9.9}$$

If the equilibrium of the slow subsystem is a stable focus, the canonical model has the form

$$\begin{aligned}\dot{v} &= I + v^2 + u_1, \\ \dot{u}_1 &= -\mu_1 u_2, \\ \dot{u}_2 &= -\mu_2(u_2 - u_1),\end{aligned}\tag{9.10}$$

with  $\mu_2 < 4\mu_1$ . In both cases, there is an after-spike resetting:

$$\text{if } v = +\infty, \text{ then } v \leftarrow -1, \text{ and } (u_1, u_2) \leftarrow (u_1, u_2) + (d_1, d_2).$$

Similarly to (9.7), the variable  $v \in \mathbb{R}$  is the re-scaled membrane potential of the neuron. The positive feedback variable  $u_1 \in \mathbb{R}$  describes activation of slow amplifying currents or potential at a dendritic compartment, whereas the negative feedback variable  $u_2 \in \mathbb{R}$  describes activation of slow resonant currents.  $I, d_1, d_2$ , and  $\mu_1, \mu_2 \ll 1$  are parameters.

When  $\mu_2 > 4\mu_1$ , the equilibrium of the slow subsystem in (9.10) is a stable node, so (9.10) can be transformed into (9.9) by a linear change of slow variables. If  $d_1 = 0$ , then  $u_1 \rightarrow 0$  and (9.9) is equivalent to (9.7).

Both canonical models above exhibit “circle/circle” slow-wave bursting, as depicted in Fig. 9.35. When  $I > 0$ , the equilibrium of the slow subsystem is in the shaded area corresponding to spiking dynamics of the fast subsystem. When the slow vector  $(u_1, u_2)$  enters the shaded area, the fast subsystem fires spikes, prevents the vector from converging to the equilibrium, and eventually pushes it out of the area. While outside, the vector follows the curved trajectory of the linear slow subsystem and then reenters the shaded area again. Such a slow wave oscillation corresponds to the thick limit cycle attractor in Fig. 9.35, which looks remarkably similar to the one for the  $I_{Na,p} + I_K + I_{Na,slow} + I_{K(M)}$ -model in Fig. 9.33.

### 9.3.3 subHopf/fold cycle

When the resting state loses stability via subcritical Andronov-Hopf bifurcation, and the spiking state disappears via fold limit cycle bifurcation, the burster is said to be of the “subHopf/fold cycle” type depicted in Fig. 9.36. Because there is a co-existence of resting and spiking states, such bursting usually occurs via a hysteresis loop with only one slow variable.

This kind of bursting was one of the three basic types identified by Rinzel (1987). It was called “elliptic” in earlier studies because the profile of oscillation of the membrane potential resembles ellipses, or at least half-ellipses; see Fig. 9.37. Rodent trigeminal interneurons in Fig. 9.38, dorsal root ganglion and mesV neurons in Fig. 9.39 are all

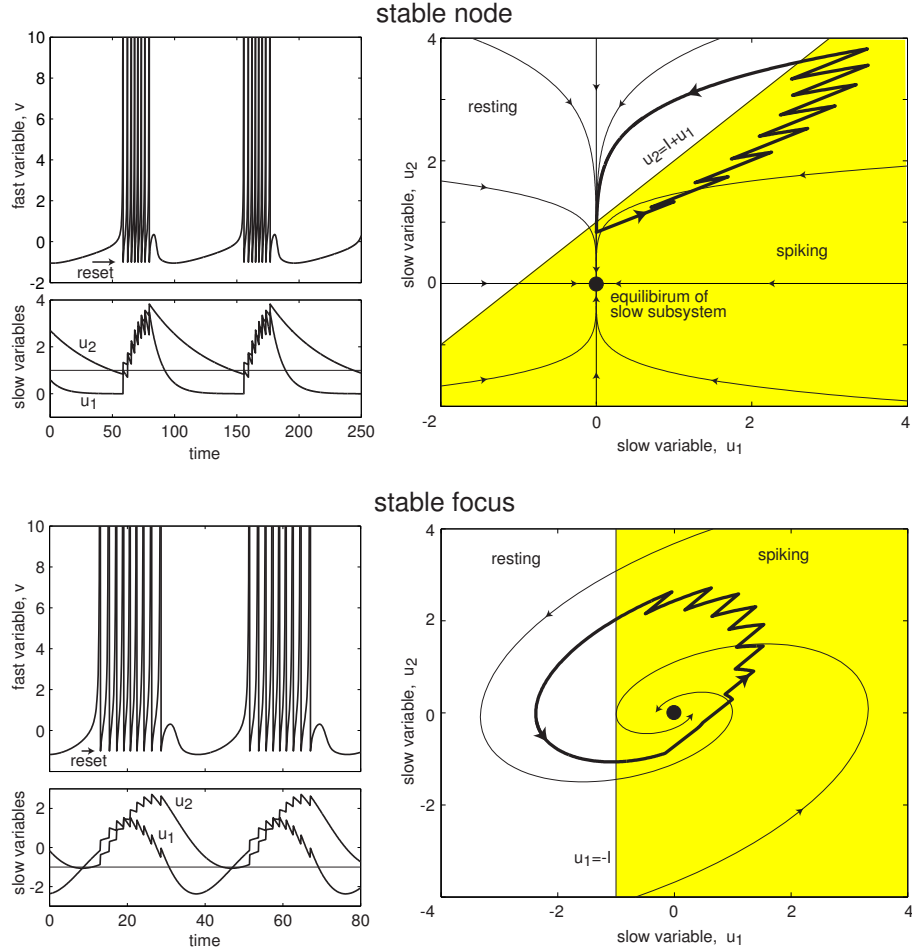


Figure 9.35: “Circle/circle” bursting in the canonical models (9.9) (*top*, parameters:  $I = 1$ ,  $\mu_1 = 0.1$ ,  $\mu_2 = 0.02$ ,  $d_1 = 1$ ,  $d_2 = 0.5$ ) and (9.10) (*bottom*, parameters:  $I = 1$ ,  $\mu_1 = 0.2$ ,  $\mu_2 = 0.1$ ,  $d_1 = d_2 = 0.5$ ).

“subHopf/fold cycle” bursters, yet the bursting profiles do not look like ellipses. Many models of “subHopf/fold cycle” bursters do not generate elliptic profiles either, hence referring to this type of bursting by its shape is misleading and should be avoided.

It is quite easy to transform the  $I_{\text{Na,p}} + I_K$ -model into a “subHopf/fold cycle” burster. First, we chose the parameters of the model as in Fig. 6.16 so that the phase portrait depicted in Fig. 9.40 is the same as in Fig. 9.36, bottom. The co-existence of the stable equilibrium, an unstable limit cycle and a stable limit cycle is essential for producing the hysteresis loop oscillation. Then, we add a slow  $K^+$  M-current that activates while the fast subsystem fires spikes and deactivates while it is resting. Such a resonant current provides a negative feedback to the fast subsystem, and the full  $I_{\text{Na,p}} + I_K + I_{K(M)}$ -model exhibits “subHopf/fold cycle” bursting, shown in Fig. 9.41.

As in the previous examples, the burster in this figure is conditional: It needs an injection of a dc-current  $I$ , so that the equilibrium corresponding to the resting state of

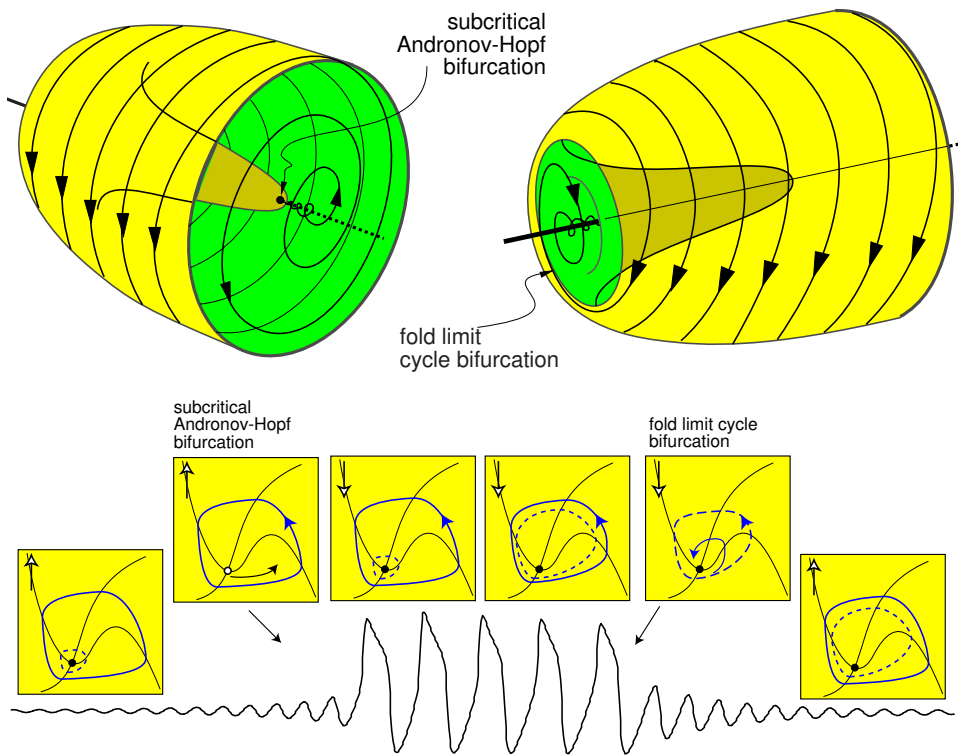


Figure 9.36: “SubHopf/fold cycle” burster: The middle equilibrium corresponding to the resting state loses stability via subcritical Andronov-Hopf bifurcation, and the outer limit cycle attractor corresponding to repetitive spiking disappears via fold limit cycle bifurcation. Top two images are different views of the same 3-D structure.

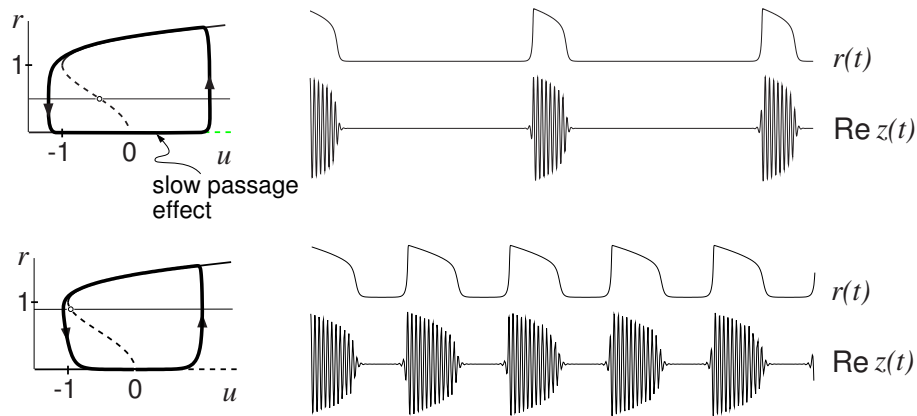


Figure 9.37: Phase portrait and solution of the canonical model (9.11) for  $\mu = 0.1$ ,  $\omega = 3$ , and  $a = 0.25$  (top) and  $a = 0.8$  (bottom), where  $r = |z|$  is the amplitude of oscillation (modified from Izhikevich 2000).

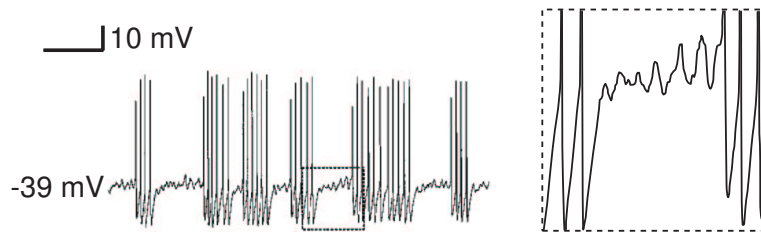


Figure 9.38: Putative “subHopf/fold cycle” bursting in rodent trigeminal neurons (modified from Del Negro et al. 1998).

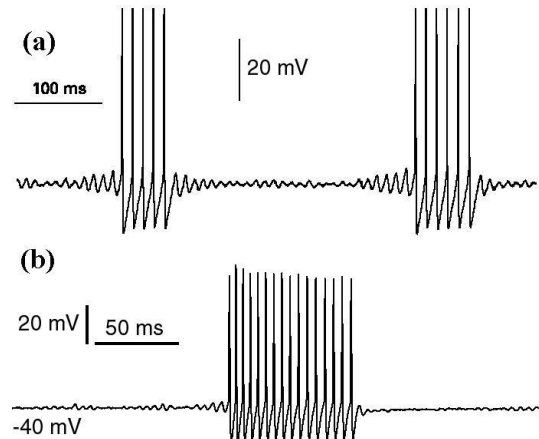


Figure 9.39: Putative “subHopf/fold cycle” bursting in (a) injured dorsal root ganglion (data modified from Jian et al. 2004) and in (b) rat mesencephalic layer 5 neurons.

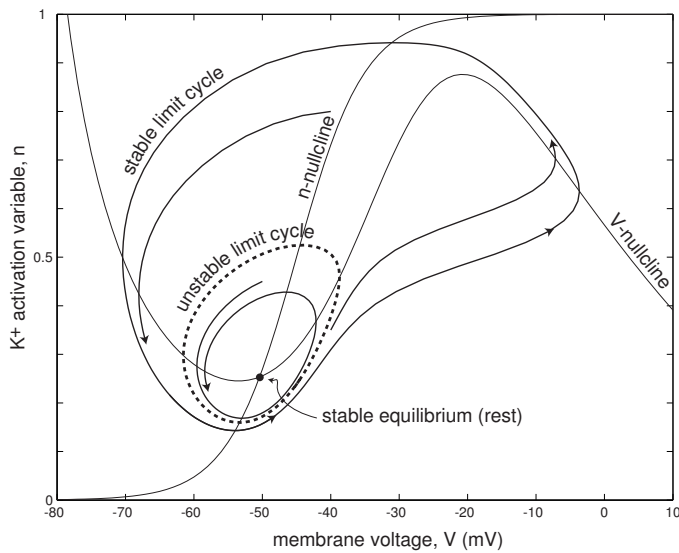


Figure 9.40: Phase portrait of the  $I_{Na,p} + I_K$ -model with parameters corresponding to subcritical Andronov-Hopf bifurcation and fold limit cycle bifurcation.

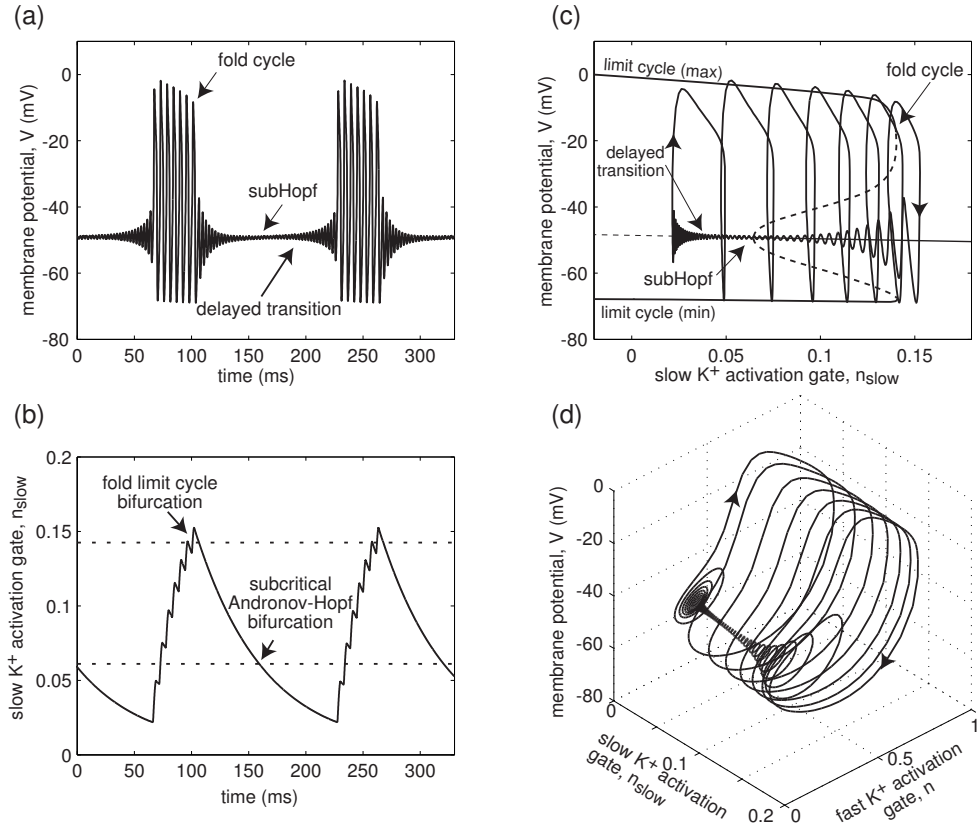


Figure 9.41: “SubHopf/fold cycle” bursting in the  $I_{Na,p} + I_K + I_{K(M)}$ -model. Parameters of the fast  $I_{Na,p} + I_K$ -subsystem are the same as in Fig. 6.16 with  $I = 55$ . Slow  $K^+$  M-current has  $V_{1/2} = -20$  mV,  $k = 5$  mV,  $\tau(V) = 60$  ms and  $g_{K(M)} = 1.5$ .

the fast subsystem is unstable. If the subsystem is near such an equilibrium, it slowly diverges from the equilibrium and jumps to the large-amplitude limit cycle attractor corresponding to spiking behavior, as one can see in Fig. 9.41a. Each spike activates slow  $K^+$  M-current, see Fig. 9.41b, and results in build-up of a net outward current that makes the fast subsystem less and less excitable. Geometrically, the large-amplitude limit cycle attractor is approached by a smaller amplitude unstable limit cycle, they coalesce, and annihilate each other via fold limit cycle bifurcation at  $n_{slow} \approx 0.14$ , see Fig. 9.41c. The trajectory jumps to the stable equilibrium corresponding to the resting state. At this moment, the slow  $K^+$  current starts to deactivate and the net outward current decreases. Since the activation gate  $n_{slow}$  moves in the opposite direction, the fold limit cycle bifurcation gives birth to large-amplitude stable and unstable limit cycles, but the trajectory remains on the steady-state branch. The unstable limit cycle slowly shrinks and makes the resting equilibrium lose stability via subcritical Andronov-Hopf bifurcation. Once the resting state becomes unstable, the trajectory diverges from it and jumps back to the large-amplitude limit cycle, thereby closing the hysteresis loop.

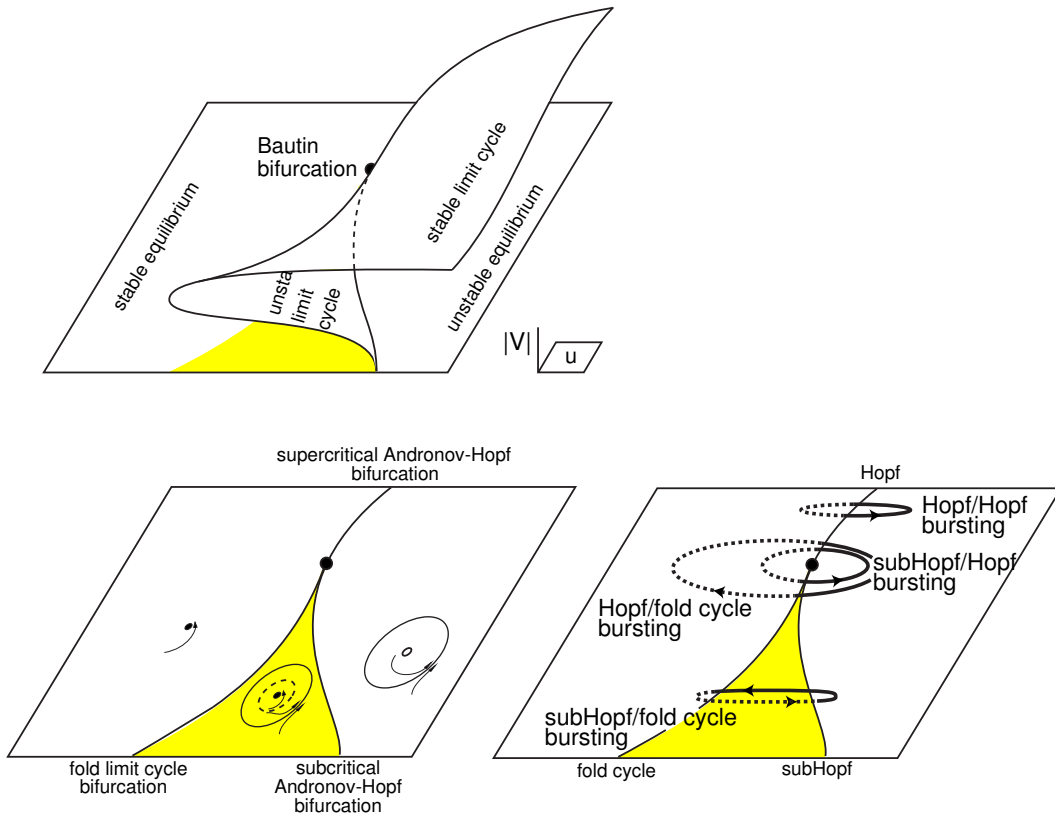


Figure 9.42: A neural system near co-dimension-2 Bautin bifurcation (central dot) can exhibit 4 different types of fast-slow bursting, depending on the trajectory of the slow variable  $u \in \mathbb{R}^2$  in the parameter space. The “subHopf/fold cycle” bursting occurs via a hysteresis loop and requires only one slow variable. Solid (dotted) lines correspond to spiking (resting) regimes (modified from Izhikevich 2000).

A prominent feature of “subHopf/fold cycle” bursting, as well as any other type of fast-slow bursting involving Andronov-Hopf bifurcation (“subHopf/\*” or “Hopf/\*”, where the wildcard “\*” means any bifurcation) is that the transition from resting to spiking does not occur at the moment the resting state becomes unstable. The fast subsystem continues to dwell at the unstable equilibrium for quite some time before it jumps rather abruptly to a spiking state, as we can clearly see in Fig. 9.41. This delayed transition is due to the slow passage through Andronov-Hopf bifurcation, discussed in Sect. 6.1.4. Delayed transitions through Andronov-Hopf bifurcation are ubiquitous in neuronal models, but they have never been seen in real neurons. Conductance noise, always present at physiological temperatures, constantly kicks the membrane potential away from the stable equilibrium, as one can see in the inset in Fig. 9.38, so transition to spiking in real neurons is never delayed. Instead, it can occur even before the equilibrium becomes unstable, as we show in Sect. 6.1.4.

Suppose that the hysteresis loop oscillation of the slow variable has a small amplitude. That is, the subcritical Andronov-Hopf bifurcation and the fold limit cycle

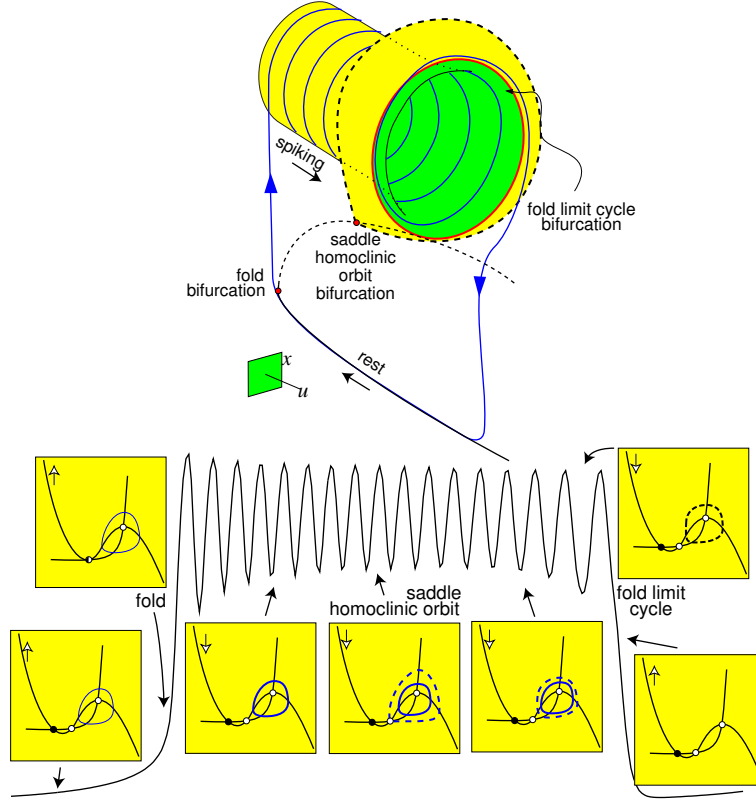


Figure 9.43: “Fold/fold cycle” bursting: The resting state disappears via saddle-node (fold) bifurcation and the spiking limit cycle disappears via fold limit cycle bifurcation (modified from Izhikevich 2000).

bifurcation of the fast subsystem in (9.1) occur for nearby values of the parameter  $u$ . In this case, the fast subsystem is near a co-dimension-2 Bautin bifurcation, which was studied in Sect. 6.3.5. Its two-parameter unfolding is depicted in Fig. 9.42, left. “SubHopf/fold cycle” bursting occurs when the bifurcation parameter, being a slow variable, oscillates between the resting and spiking regions through the shaded region. Due to the bistability, the parameter could be one-dimensional. Other trajectories of the slow parameter correspond to other types of bursting shown in Fig. 9.42, right.

If the slow variable has an equilibrium near the Bautin bifurcation point, then the fast-slow burster (9.1) can be transformed into the following canonical “2+1” model by a continuous change of variables

$$\begin{aligned}\dot{z} &= (u + i\omega)z + 2z|z|^2 - z|z|^4, \\ \dot{u} &= \mu(a - |z|^2),\end{aligned}\tag{9.11}$$

where  $z \in \mathbb{C}$  and  $u \in \mathbb{R}$  are the canonical fast and slow variables, respectively, and  $a, \omega$  and  $\mu \ll 1$  are parameters. In Ex. 14 we show that the model exhibits hysteresis loop periodic point-cycle bursting behavior depicted in Fig. 9.37 when  $0 < a < 1$ .

### 9.3.4 fold/fold cycle

When the stable equilibrium corresponding to the resting state disappears via saddle-node (fold) bifurcation and the limit cycle attractor corresponding to the spiking state disappears via fold limit cycle bifurcation, the burster is said to be of the “fold/fold cycle” type, as in Fig. 9.43. This type was first discovered in the Chay-Cook (1988) model of a pancreatic  $\beta$ -cell by Bertram et al. (1995), who referred to it as being Type IV bursting (the three bursters we considered so far were referred to as being Type I, II, and III, respectively). Since both bifurcations result in a co-existence of resting and spiking states, the “fold/fold cycle” bursting can occur via a hysteresis loop in a “2+1” system.

An interesting geometrical feature of the “fold/fold cycle” bursting is that there is an unstable limit cycle that appears in the middle of a burst and that participates in the “fold cycle” bifurcation to terminate the burst. The cycle appears via saddle homoclinic orbit bifurcation in Fig. 9.43, but other scenarios are possible too. It is a good exercise of one’s geometrical intuition and understanding of the fast-slow bursting mechanisms to come up with alternative scenarios of the “fold/fold cycle” bursting. For example, consider the case of the unstable limit cycle being inside the stable one.

### 9.3.5 fold/Hopf

When the stable equilibrium corresponding to the resting state disappears via saddle-node (fold) bifurcation and the limit cycle attractor corresponding to the spiking state shrinks to a point via supercritical Andronov-Hopf bifurcation, the burster is said to be of the “fold/Hopf” type; see Fig. 9.44. This type of bursting, called “tapered” in some earlier studies, was found in models of insulin-producing pancreatic  $\beta$ -cells (Smolen et al. 1993, Pernarowski 1994) and in models of certain enzymatic systems (Holden and Erneux 1993a,b).

As one can see in the figure, the fast subsystem undergoes two bifurcations while it is in the excited state: One corresponds to the termination of repetitive spiking via supercritical Andronov-Hopf bifurcation, and the other one corresponds to the transition from the excited equilibrium to resting equilibrium via saddle-node (fold) bifurcation. The first bifurcation, i.e., bifurcation of a spiking limit cycle attractor, determines the topological type of bursting. The second bifurcation is essential for the “fold/fold” hysteresis loop, and it only determines the subtype of the “fold/Hopf” bursting. Using ideas described in Ex. 19, one can come up with another subtype of “fold/Hopf” burster having “fold/subHopf” hysteresis loop.

### 9.3.6 fold/circle

When the stable equilibrium corresponding to the resting state disappears via saddle-node (fold) bifurcation and the limit cycle attractor corresponding to the spiking state disappears via saddle-node on invariant circle bifurcation, the burster is said to be of the “fold/circle” type, as in Fig. 9.45. This type was first discovered in the model of

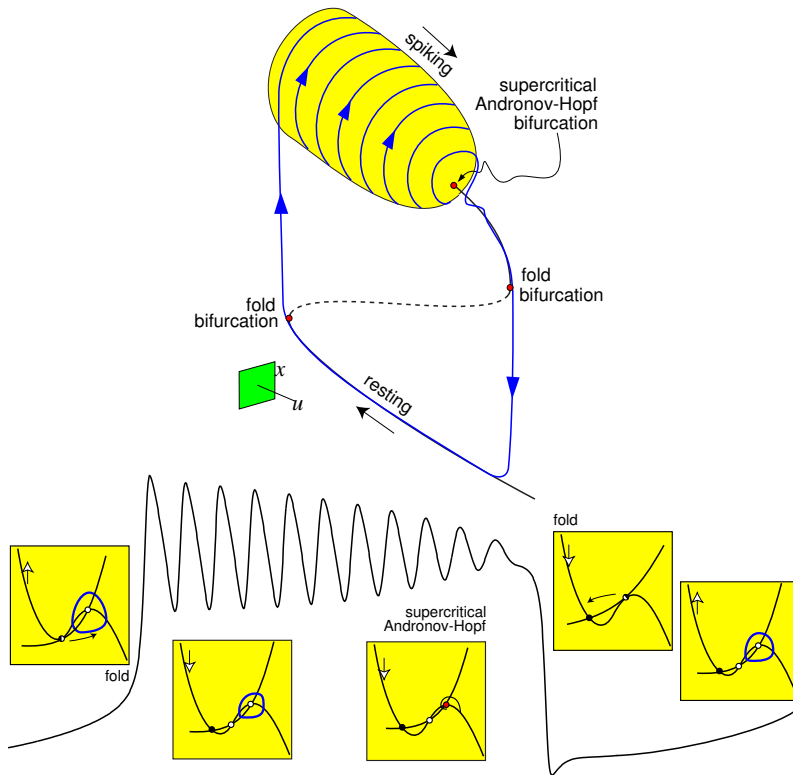


Figure 9.44: “Fold/Hopf” bursting: The resting state disappears via saddle-node (fold) bifurcation and the spiking limit cycle shrinks to a point via supercritical Andronov-Hopf bifurcation (modified from Izhikevich 2000).

thalamo-cortical relay neuron by Rush and Rinzel (1994), and it was called “triangular” in earlier studies (Wang and Rinzel 1995) because of the shape of the voltage envelope.

As one can see in the figure, the fast subsystem can have five equilibria, two of which are stable nodes. This is a consequence of the quintic shape of the  $V$ -nullcline of the fast subsystem. While the trajectory is at the lower equilibrium, the  $V$ -nullcline moves up, the equilibrium disappears via fold bifurcation, and the fast subsystem starts to fire spikes. During this active period, the  $V$ -nullcline slowly moves down, and the spiking limit cycle disappears via saddle-node on invariant circle bifurcation. The fast subsystem, however, is at the second stable equilibrium corresponding to a depolarized state. The slow  $V$ -nullcline continues to move down, and this equilibrium disappears via another fold bifurcation, thereby closing the “fold/fold” hysteresis loop. Alternatively, “fold/circle” bursting can be of the slow-wave type depicted in Fig. 9.28 having only three equilibria. The slow subsystem needs to be at least two-dimensional in this case, though.

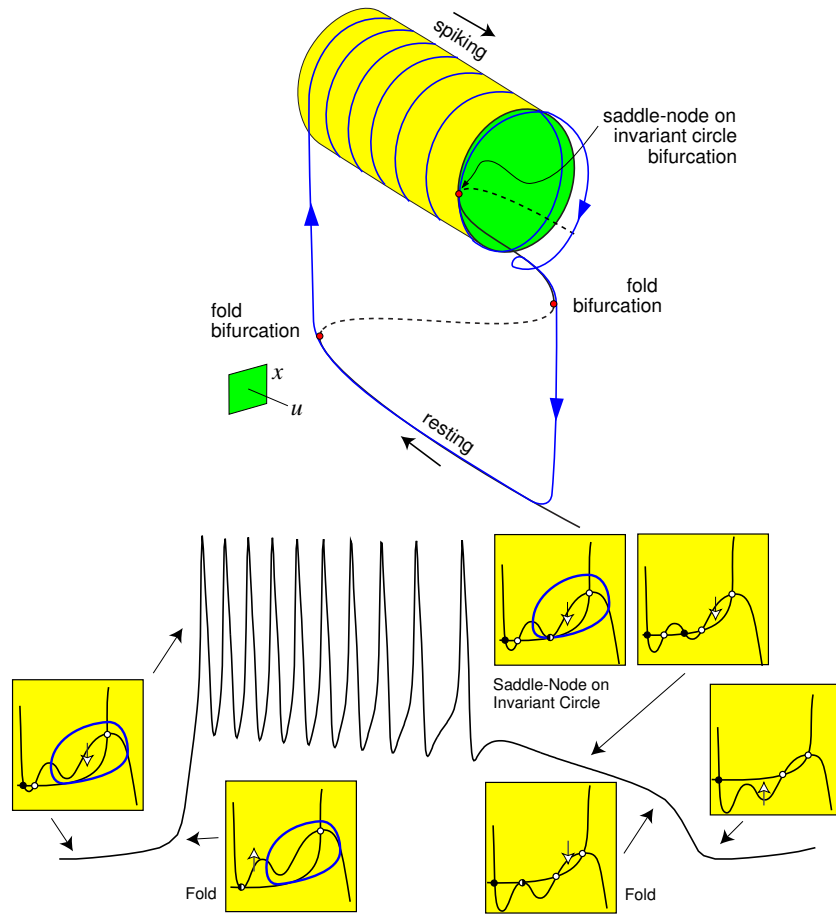


Figure 9.45: “Fold/circle” bursting: The resting state disappears via fold bifurcation and the spiking state disappears via saddle-node on invariant circle bifurcation (modified from Izhikevich 2000).

## 9.4 Neuro-Computational Properties

There is more to the topological classification of bursters than just a mathematical exercise. Indeed, in Chap. 7 we have shown that the neuro-computational properties of an excitable system depend on the type of bifurcation of the resting state. The same is valid for a burster: Its neuro-computational properties depend on the kind of bifurcations of the resting and spiking states, that is, on the burster’s type. Knowing the topological type of a given bursting neuron, we know what the neuron can do and more importantly what it cannot do, regardless of the model that describes its dynamics.

### 9.4.1 How to distinguish?

First, we stress that the topological classification of bursters provided in the previous section is defined for mathematical models, and not for real neurons. Moreover, the

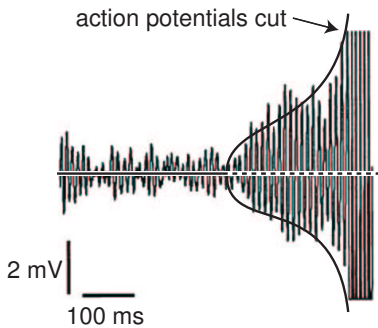


Figure 9.46: The conductance noise destabilizes the focus equilibrium in a mesencephalic V neuron before subcritical Andronov-Hopf bifurcation takes place, thereby giving an impression of a supercritical Andronov-Hopf bifurcation (data modified from Wu et al. 2001).

types are defined for models of the fast-slow form (9.1) assuming that the ratio of time scales,  $\mu$ , is sufficiently small. Not all neurons can be described adequately by such models, hence extending the classification to those neurons may be worthless. Typical example when the classification fails is the model of bursting of the sensory processing neuron in weakly electric fish, known as the “ghostburster” (Doiron et al. 2002) in which  $\mu > 0.1$ .

If a bursting neuron can be described accurately by a model having fast-slow form (9.1), then there is no problem to determine its topological type — just freeze the slow subsystem, i.e., set  $\mu = 0$ , and find bifurcations of the fast subsystem treating  $u$  as a parameter. Software packages, such as XPPAUT, AUTO, or MATLAB based MATCONT, are helpful in bifurcation analyses of such systems.

What if a neuron has an apparent fast-slow dynamics but its model is not known at present? To determine the types of bifurcations of the fast subsystem, we first use non-invasive observations: presence or absence of fast subthreshold oscillations, changes in intraburst (interspike) frequency, changes in spike amplitudes, etc. Each piece of information excludes some bifurcations and narrows the set of possible types of bursting. Then, we can use invasive methods, e.g., small perturbations, to test the co-existence of resting and spiking states, and narrow down the choice of bifurcations further. With some luck, we can exclude sufficiently many bifurcations and determine exactly the type of bursting without even knowing the details of the mathematical model that describes it.

#### 9.4.2 Integrators vs. Resonators

A conspicuous feature of neuronal systems near Andronov-Hopf bifurcation, whether subcritical or supercritical, is the existence of fast subthreshold oscillations of the membrane potential. Quite often, these oscillations are visible in recordings of the membrane potential. If not, then they could be evoked by a brief small pulse of current. Apparently, a bursting neuron exhibiting such oscillations in the quiescent state is either of the “Hopf/\*” type or “subHopf/\*” type, where the wildcard “\*” denotes any appropriate bifurcation of the spiking state. All such bursters are in the lower half of the table in Fig. 9.23.

To discern whether the bifurcation is supercritical or subcritical, one needs to study

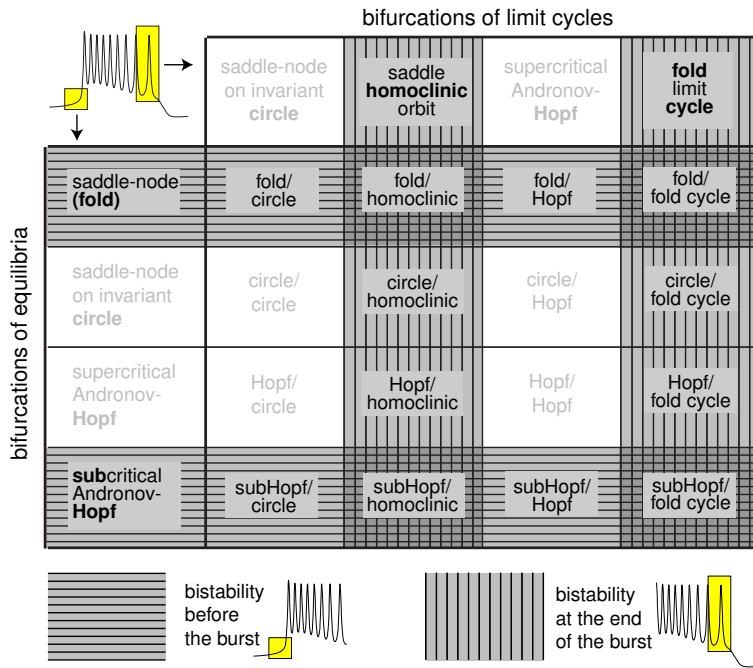


Figure 9.47: Bistability, i.e., co-existence of resting and spiking states, depends on the topological type of bursting.

the amplitude of emerging oscillations, which could be tricky. In models, slow passage through supercritical Andronov-Hopf bifurcations often results in a delayed transition to oscillations with an intermediate or large amplitude, hence such a bifurcation may look like subcritical. In recordings, like the one in Fig. 9.39a or in Fig. 9.46, noise destabilizes the focus equilibrium before the subcritical Andronov-Hopf bifurcation takes place and gives the impression that the amplitude increases gradually, i.e., as if the bifurcation were supercritical.

The existence of fast subthreshold oscillations indicates that the bursting neuron acts as a resonator, at least right before the onset of a burst. In Sect. 7.2.2 we showed that such neurons prefer a certain resonant frequency of stimulation that matches the frequency of subthreshold oscillations. A resonant input may excite the neuron and initiate a burst or it may delay the transition to the burst, depending on its phase relative to the phase of subthreshold oscillations.

In contrast, all bursters in the upper half of the table in Fig. 9.23, i.e., “fold/\*” and “circle/\*” types, do not have fast subthreshold oscillations, at least before the onset of each burst (see Ex. 5). The fast subsystem of such bursters acts as an integrator: It prefers high-frequency inputs; the higher the frequency, the sooner the transition to the spiking state. The phase of the input does not play any role here.

### 9.4.3 Bistability

Suppose the transition from resting to spiking state occurs via saddle-node bifurcation (off an invariant circle) or subcritical Andronov-Hopf bifurcation of the fast subsystem, as in Fig. 6.46. In these cases, the trajectory jumps to a pre-existing limit cycle attractor corresponding to the spiking state, not shown in the figure. In contrast, saddle-node on invariant circle bifurcation or supercritical Andronov-Hopf bifurcation creates such a limit cycle attractor. Thus, there must be a co-existence of stable resting and stable spiking states in the former case, but not necessarily in the latter case. This simple observation has far reaching consequences described below. In particular, it implies that all “fold/\*” and “subHopf/\*” bursters exhibit bistability, at least before the onset of a burst, while “circle/\*” and “Hopf/\*” bursters may not; see Fig. 9.47.

Similarly, if the transition from spiking to resting state of the fast subsystem occurs via saddle homoclinic orbit bifurcation or fold limit cycle bifurcation, then there is a pre-existing stable equilibrium, and hence a co-existence of attractors. Thus, “\*/homoclinic” and “\*/fold cycle” bursters also exhibit bistability, at least at the end of a burst, while “\*/circle” and “\*/Hopf” bursters may not, as we summarize in Fig. 9.47.

An obvious consequence of bistability is that an appropriate stimulus can switch the system from resting to spiking and back. We illustrate this phenomenon in Fig. 9.48 using the  $I_{Na,p} + I_K + I_{K(M)}$ -model, which exhibits a hysteresis loop “fold/homoclinic” bursting when  $I = 5$ . All three simulations in the figure start with the same initial conditions. In Fig. 9.48b we apply a brief pulse of current while the fast subsystem is at the resting state. This stimulation pushes the membrane potential over the threshold state into the attraction domain of the spiking limit cycle of the fast subsystem, thereby evoking a burst.

Notice that the evoked burst is one spike shorter than the control one in Fig. 9.48a. This is expected, since the  $K^+$  M-current did not have enough time to recover from the previous burst (not shown in the figure), therefore, there is a residual outward current that shortens the active phase. From the geometrical point of view, this occurs because the transition to the spiking manifold in Fig. 9.48b, right, occurs before the slow variable reaches the fold knee, hence the distance to the homoclinic bifurcation is shorter. An interesting observation is that the first spike in the evoked burst actually corresponds to the second spike in the control burst in Fig. 9.48a. The earlier the stimulation acts, the sooner the trajectory jumps to the spiking manifold and the fewer spikes the evoked burst has.

In Fig. 9.48c we applied a brief pulse of current in the middle of a burst to switch the system to the resting state. Notice that the quiescent period, i.e., the time period to the second burst, is shorter than the control one in Fig. 9.48a or in Fig. 9.48b. This is also to be expected, since the  $K^+$  M-current was not fully activated during the interrupted burst, therefore it does not need that much time to deactivate during the resting period. Geometrically, the short duration of the resting phase is a consequence of the distance the slow variable needs to travel to get to the fold knee being small.

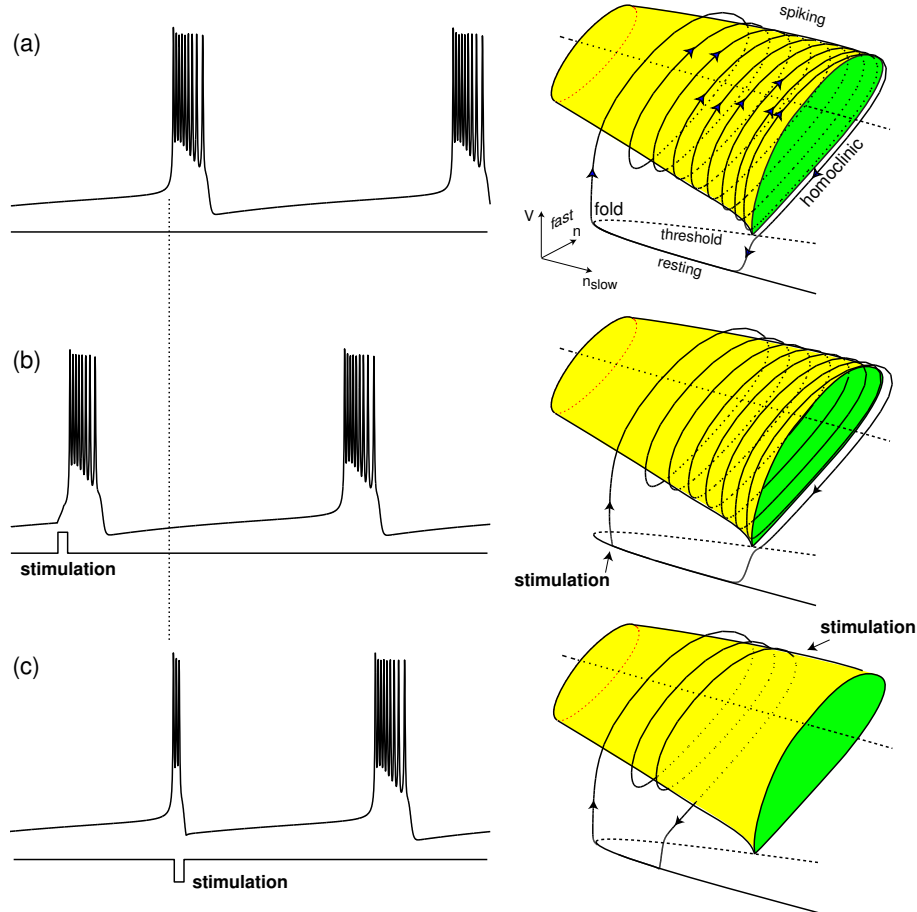


Figure 9.48: Bistability of resting and spiking states in a “fold/homoclinic” burster. A brief stimulus can initiate a premature transition to spiking state (b) or to quiescent state (c). Shown are simulations of the  $I_{\text{Na,p}}+I_{\text{K}}+I_{\text{K(M)}}$ -model with parameters as in Fig. 9.4b.

#### 9.4.4 Bursts as a unit of neuronal information

Mammalian neurons may fire bursts to increase the reliability of synaptic transmission (Lisman 1997). Indeed, if a presynaptic neuron sends a burst of spikes instead of a single spike, then the chances that at least one of them overcomes the synaptic transmission failure increase. If two or more spikes go through, then the postsynaptic effect is much stronger than the one for a single spike.

In addition, important information may be carried in the intraburst frequency. Consider the effect of a burst on a postsynaptic resonator neuron, i.e., a neuron with resting state near an Andronov-Hopf bifurcation. Such a neuron cares about the frequency content of the burst, i.e., whether it is resonant or not, as we discussed in Sect. 7.2.2. Some types of bursters have relatively constant intraburst (instantaneous interspike) frequencies, as in Fig. 9.49b, which may be resonant for some postsynaptic

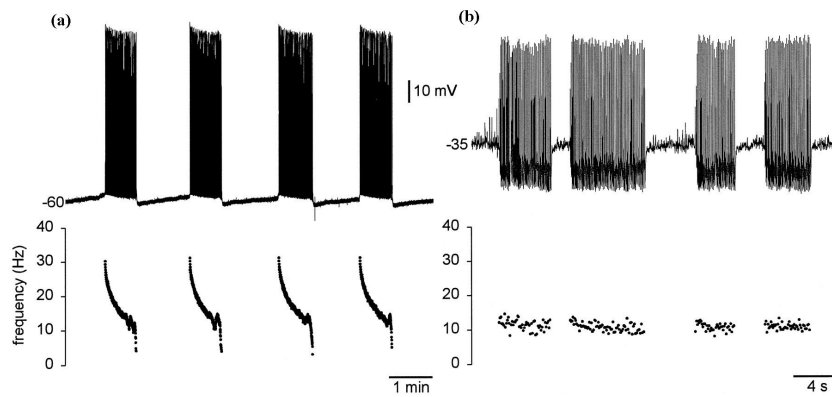


Figure 9.49: The instantaneous spike frequency of a trigeminal motor neuron (a) and trigeminal interneuron (b) of a rodent (modified from Del Negro et al. 1998).

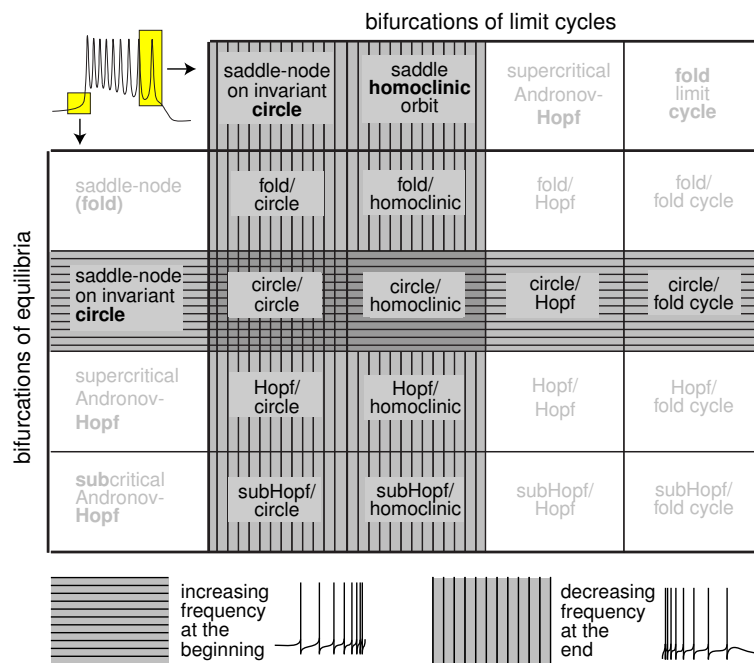


Figure 9.50: Topological types of bursters in the shaded regions can produce chirp-bursts that sweep a frequency range.

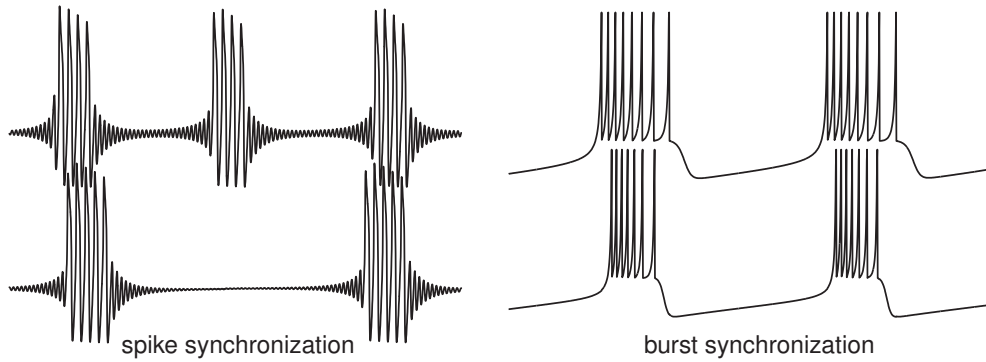


Figure 9.51: Various regimes of synchronization of bursters.

neurons but not for others. In contrast, other topological types of bursters have widely varying instantaneous interspike frequencies, as in Fig. 9.49a, that scan or sweep a broad frequency range going all the way to zero.

When the bifurcation from resting to spiking state is of the saddle-node on invariant circle type, i.e., the system is Class 1 excitable, the frequency of emerging spiking is first small, and then increases. Therefore, all “circle/\*” bursters generate chirps with instantaneous interspike frequencies increasing from zero to a relatively large value, at least at the beginning of the burst. Similarly, when the bifurcation of the spiking state is of the saddle-node on invariant circle or saddle homoclinic orbit type, the frequency of spiking at the end of the burst decreases to zero, so all “\*/circle” and “\*/homoclinic” bursters also generate chirps, as in Fig. 9.49a. In summary, all shaded bursters in Fig. 9.50 have sweeping interspike frequencies, so that one part of the burst is resonant for one neuron and another part of the same burst is resonant for another neuron.

#### 9.4.5 Synchronization

Consider two coupled bursting neurons of the fast-slow type. Since each burster has two time scales, one for rhythmic spiking and one for repetitive bursting, there are two synchronization regimes:

- Spike synchronization, as in Fig. 9.51, left.
- Burst synchronization, as in Fig. 9.51, right.

One of them does not imply the other. Of course, there is an additional regime when spikes and bursts are synchronized. We will study synchronization phenomena in detail in Chap. 10; here we just mention how they depend on the topological type of bursting.

Let us consider spike synchronization first. Since we are interested in the fast time scale, we neglect the slow variable dynamics for a while and treat two bursters as coupled oscillators. A necessary condition for synchronization of two weakly coupled oscillators is that they have nearly equal frequencies. How near is “near” depends on the strength of the coupling. Thus, spike synchronization depends crucially on

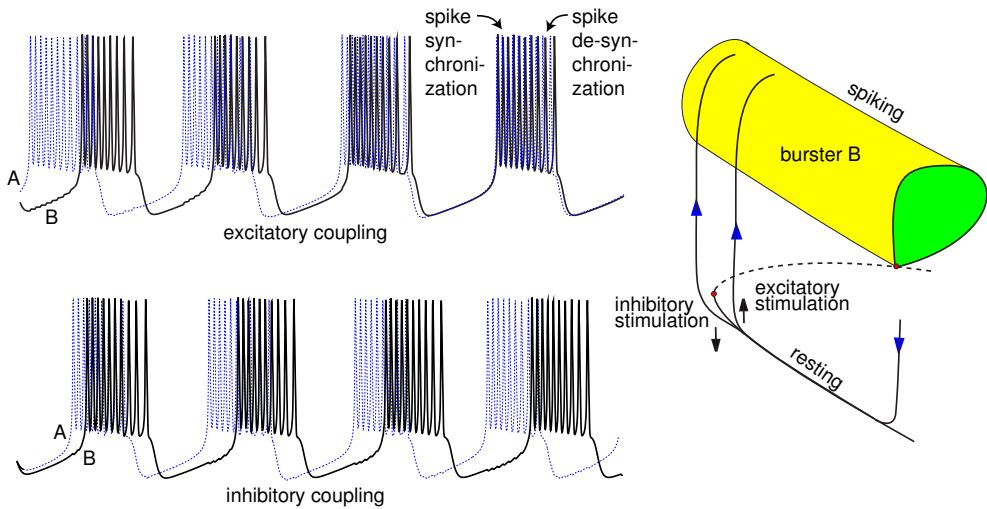


Figure 9.52: Burst synchronization and de-synchronization of two coupled “fold/homoclinic” bursters (modified from Izhikevich 2000).

the instantaneous interspike frequency, which may vary substantially during a burst. Indeed, a small perturbation of the slow variable may result in large perturbations of the interspike frequency in any shaded burster in Fig. 9.50, hence such a burster would be reluctant to exhibit spike synchronization, unless the coupling is strong.

Studying burst synchronization of weakly coupled neurons involves the same mathematical methods as studying synchronization of strongly coupled relaxation oscillators, which we consider in detail in Chap. 10. The mechanisms of synchronization depend on whether the bursting is of the hysteresis loop type or of the slow wave type, and whether the resting state is an integrator or a resonator.

In Fig. 9.52 we illustrate the geometry of burst synchronization of two coupled “fold/homoclinic” bursters of hysteresis loop type. Burster A is slightly ahead of burster B so that A starts the spiking phase while B is still resting. If the synaptic connections between the bursters are excitatory, firing of A causes B to jump to the spiking state prematurely, thereby shortening the time difference between the bursts. In addition, the evoked burst of B is shorter, which also speeds up the synchronization process. In contrast, when the connections are inhibitory, firing of A delays the transition of B to the spiking state, thereby increasing the time difference between the bursts and desynchronizing the bursters. Thus, the “fold/homoclinic” burster behaves according to the principle *excitation means synchronization, inhibition means de-synchronization*. Since the instantaneous interspike frequency of “fold/homoclinic” bursting decays to zero, small deviations of the slow variable result in large deviations of the period of oscillation. Typically, the periods of fast oscillations of the two bursters can slowly diverge from each other. As a result, spikes start synchronized and then de-synchronize during the burst, as we indicate in the figure.

If the bursting neuron is a resonator, i.e., it is of the “Hopf/\*” or “subHopf/\*” type, then both excitation and inhibition may evoke premature spiking, as we have shown

in Chap. 7, and lead to burst synchronization. An important feature here is that the interspike frequency of one burster be resonant to the subthreshold oscillations of the other one. We study these and other issues related to synchronization in Chap. 10.

## Review of Important Concepts

- A burst of spikes is a train of action potentials followed by a period of quiescence.
- Bursting activity typically involves two time scales: fast spiking and slow modulation via a resonant current.
- Many mathematical models of bursters have fast-slow form

$$\begin{aligned}\dot{x} &= f(x, u) && \text{(fast spiking),} \\ \dot{u} &= \mu g(x, u) && \text{(slow modulation).}\end{aligned}$$

- To dissect a burster, one freezes its slow subsystem (i.e., sets  $\mu = 0$ ) and uses the slow variable  $u$  as a bifurcation parameter to study the fast subsystem.
- The fast subsystem undergoes two important bifurcations during a burst: (1) bifurcation of an equilibrium resulting in transition to spiking state, and (2) bifurcation of a limit cycle attractor resulting in transition to resting state.
- Different types of bifurcations result in different topological types of bursting.
- There are 16 basic types of bursting, summarized in Fig. 9.23.
- Different topological types of bursters have different neuro-computational properties.

## Bibliographical Notes

The history of formal classification of bursting starts with the seminal paper by Rinzel (1987), who contrasted the bifurcation mechanism of the “square-wave”, “parabolic”, and “elliptic” bursters. Then, Bertram et al. (1995) followed Rinzel’s suggestion and referred to the bursters using Roman numbers, adding a new, Type IV burster. Another, “tapered” type of bursting was studied simultaneously and independently by Holden and Erneux (1993a,b), Smolen et al. (1993), and Pernarowski (1994). Later de Vries (1998) suggested to refer to it as Type V burster. Yet another, “triangular” type of bursting was studied by Rush and Rinzel (1994), making the total number of identified bursters to be 6. To honor these pioneers, we described these six *classical* bursters in the order consisted with the numbering nomenclature of Bertram et al. (1995). Their bifurcation mechanisms are summarized in Fig. 9.53.

<i>Bifurcations</i>	<i>Saddle-Node on Invariant Circle</i>	<i>Saddle Homoclinic Orbit</i>	<i>Supercritical Andronov-Hopf</i>	<b>Fold Limit Cycle</b>
<b>Fold</b>	triangular	square-wave Type I	tapered Type V	Type IV
<i>Saddle-Node on Invariant Circle</i>	parabolic Type II			
<i>Supercritical Andronov-Hopf</i>				
<b>Subcritical Andronov-Hopf</b>				elliptic Type III

Figure 9.53: Bifurcation mechanisms and classical nomenclature of the 6 bursters known in the XX century. Compare with Fig. 9.23 and Fig. 9.24.

The complete classification of bursters was provided by Izhikevich (2000), and it was actually motivated by the paper of Guckenheimer et al. (1997). There is a drastic difference between Izhikevich's approach, and that of the scientists mentioned above. They used a *bottom-up* approach; that is, they considered biophysically plausible conductance based models describing experimentally observable cellular behavior and then they determined the types of bursting these models exhibited. In contrast, Izhikevich (2000) used the *top-down* approach and considered all possible pairs of co-dimension-1 bifurcations of rest and spiking states, which resulted in different types of bursting. It was an easy task to provide a conductance-based model exhibiting each bursting type. Thus, many of the bursters are “theoretical” in the sense that they have yet to be seen in experiments.

Interestingly, a challenging problem was to suggest a naming scheme for the bursters. The names should be self-explanatory and easy to remember and understand. Thus, the numbering scheme suggested by Bertram et al. (1995) would lead, e.g., to bursters of Type XXVII, Type LXIII, Type LCXVI, etc. We cannot use descriptions such as “elliptic”, “parabolic”, “hyperbolic”, “triangular”, “rectangular”, etc., since they are misleading. In this book we follow Izhikevich (2000) and name the bursters according to the two bifurcations involved, as in Fig. 9.23.

Not all bursters can be represented in the fast-slow form with a clear separation

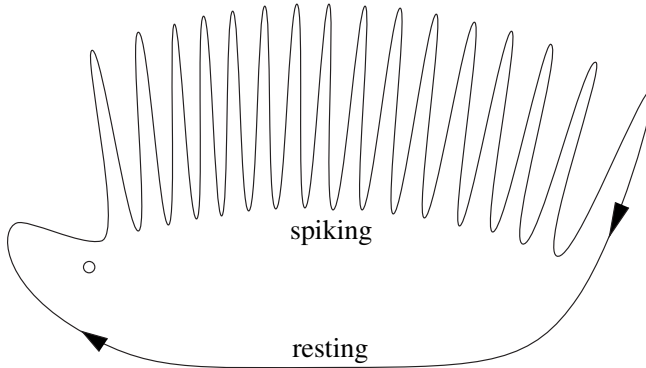


Figure 9.54: A hedgehog-like limit cycle attractor results in bursting dynamics even in two-dimensional systems; see Ex. 1 (modified from Hoppensteadt and Izhikevich 1997).

of the time scales. Those that cannot are referred to as hedgehog bursters (Izhikevich 2000), since they have a limit cycle (or a more complicated attractor) with some spiky parts corresponding to repetitive spiking and some smooth parts corresponding to quiescence, as in Fig. 9.54. An interesting example of the hedgehog burster is the model of sensory processing neuron of weakly electric fish (Doiron et al. 2002). The authors refer to the model as “ghostburster” because repetitive spiking corresponds to a slow transition of the full system through the ghost of a fold limit cycle attractor. As a dynamical system, the ghostburster is near a co-dimension-2 bifurcation of limit cycle attractor, and it exhibits chaotic dynamics.

Betram et al. (1995) noticed that bursting often occurs when the fast subsystem is near a co-dimension-2 bifurcation. Izhikevich (2000) suggested that many simple models of bursters could be obtained by considering unfoldings of various degenerate bifurcations of high co-dimension (organizing centers) and treating the unfolding parameters as slow variables rotating around the bifurcation point, as in Fig. 9.28 or Fig. 9.42. Considering the Bautin bifurcation, Izhikevich (2001) obtained the canonical model for “elliptic” burster (9.11). Golubitsky et al. (2001) applied this idea to other local bifurcations (spiking with infinitesimal amplitude). Global bifurcations are considered in Ex. 26.

Izhikevich and Hoppensteadt (2004) extend the classification of bursters to one- and two-dimensional mappings, identifying 3 and 20 different classes, respectively. A collection of chapters “Bursting: The Genesis of Rhythm in the Nervous System” edited by Coombes and Bressloff (2005) provides recent developments in the field of bursting dynamics.

Studying bursting dynamics is still one of the hardest problems in applied mathematics. The method of dissection of fast-slow bursters of the form (9.1), pioneered by Rinzel (1987), is part of the asymptotic theory of singularly perturbed dynamical systems (Mishchenko et al. 1994). One would expect the theory to suggest other, quantitative methods of analyses of fast-slow bursters. However, the basic assumption of the theory is that the fast subsystem has only equilibria, e.g., up- and down-states as

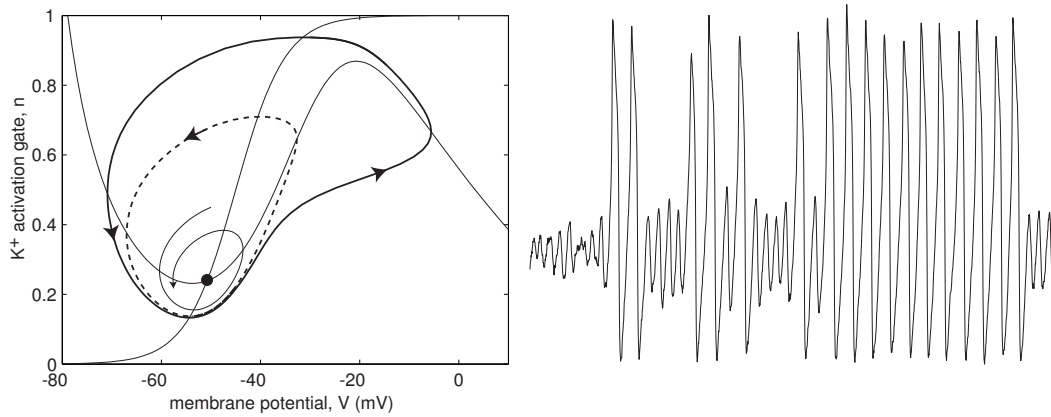


Figure 9.55: Bursting in two-dimensional  $I_{\text{Na,p}}+I_K$ -model with parameters as in Fig. 6.16 and  $I = 43$ .

in the point-point hysteresis loops in Ex. 19. This assumption is violated when the neuron fires a burst of spikes. Thus, the theory is helpless in studying fast-slow point-cycle bursters. An exception is Pontryagin's problem, which is related to "fold cycle/fold cycle" bursting; see Ex. 21 below and Sect. 7 in Mishchenko et al. (1994). Pontryagin and Rodygin (1960) pioneered the method of averaging of the fast subsystem, which was used in the context of bursters by Rinzel and Lee (1986), Pernarowski et al. (1992), Smolen et al. (1993), Baer et al. (1995). Shilnikov et al. (2005) introduced an average nullcline of the slow subsystem, and showed how the averaging method can be used to study co-existence of spiking and bursting states in a model neuron, and bifurcations in bursters in general. Some of the transitions "resting  $\leftrightarrow$  bursting  $\leftrightarrow$  tonic spiking" were also considered by Ermentrout and Kopell (1986a), Terman (1991), Destexhe and Gaspard (1993), Shilnikov and Cymbalyuk (2004, 2005), and Medvedev (2005).

The averaging method, as many other classical methods of analysis of dynamical systems, breaks down when the fast subsystem slowly passes a bifurcation point. The development of early dynamical system theory was largely motivated by studies of periodic oscillators. It is reasonable to expect that the next major developments of this theory will be coming from studies of bursters.

## Exercises

1. (Planar burster) Invent a planar system of ODEs having a hedgehog limit cycle attractor, as in Fig. 9.54, and capable of exhibiting periodic bursting activity.
2. (Noise-induced bursting) Explain why the  $I_{\text{Na,p}}+I_K$ -model with the phase portrait as in Fig. 9.55 bursts even though it has only two dimensions.
3. (Noise-induced bursting) Explore numerically the  $I_{\text{Na,p}}+I_K$ -model with phase portrait as in Fig. 6.7, top, and make it burst as in Fig. 9.56 without adding any new current or gating variable.

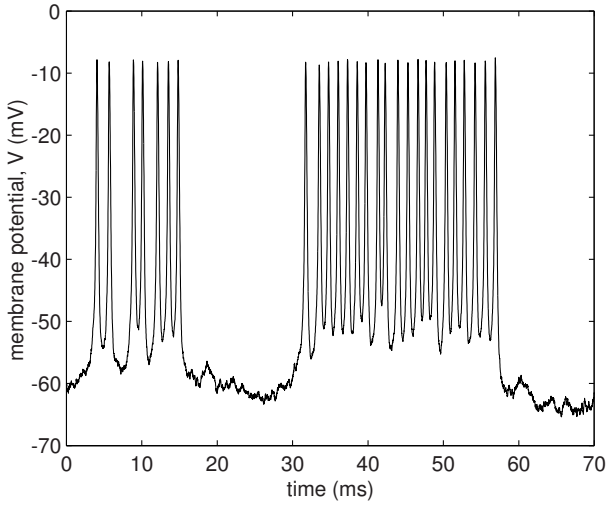


Figure 9.56: Bursting in a two-dimensional  $I_{Na,p}+I_K$ -model; see Ex. 3.

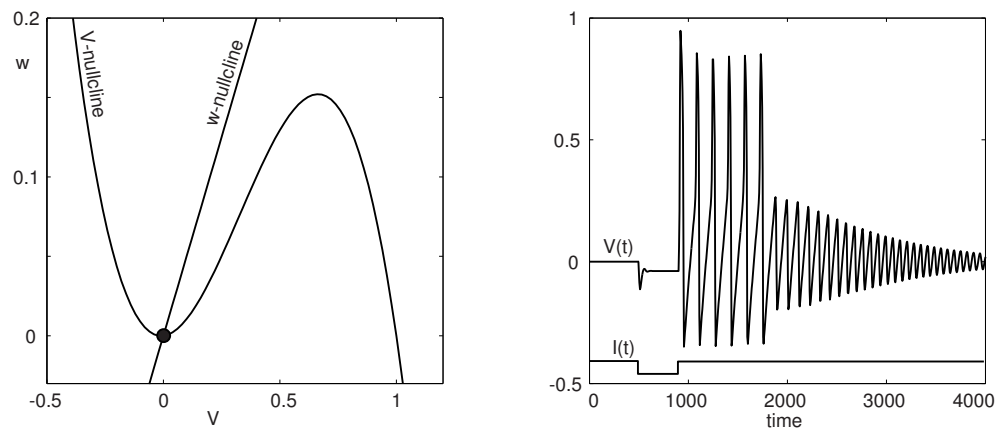


Figure 9.57: Rebound bursting in the FitzHugh-Nagumo oscillator; see Ex. 4.

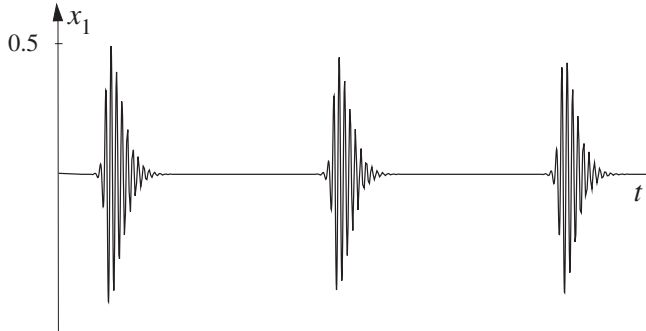


Figure 9.58: Hopf/Hopf bursting without co-existence of attractors; see Ex. 6 (modified from Hoppensteadt and Izhikevich 1997).

4. (Rebound bursting) Explain the mechanism of rebound bursting in the two-dimensional FitzHugh-Nagumo oscillator (4.11,4.12) shown in Fig. 9.57.
5. Can “circle/\*” and “fold/\*” bursters have fast subthreshold oscillations of membrane potential? Explain.
6. (Hopf/Hopf bursting) The system

$$\dot{x} = (y + i)x - x|x|^2, \quad x = x_1 + ix_2 \in \mathbb{C},$$

has a unique attractor for any value of the parameter  $y \in \mathbb{R}$ . If

$$\dot{y} = \mu(2aS(\frac{y}{a} - a) - |x|), \quad \mu = 0.05, \quad a = \sqrt{\mu/20}, \quad S(u) = \frac{1}{1 + e^{-u}}$$

then the “2+1” system above can burst, as we show in Fig. 9.58. Explore the system numerically and explain the origin of bursting.

7. (Hopf/Hopf canonical model) Consider the “2+1” fast-slow burster (9.1) and suppose that  $x_0$  is the supercritical Andronov-Hopf bifurcation point of the fast subsystem when  $u = u_0$ . Also suppose that  $u_0$  is a stable equilibrium of the slow subsystem when  $x = x_0$  is fixed. Show that there is a continuous change of variables that transforms (9.1) into the canonical model

$$\begin{aligned} z' &= (u + i\omega)z - z|z|^2, \\ u' &= \mu(\pm 1 \pm u - a|z|^2), \end{aligned}$$

where  $z \in \mathbb{C}$  is the new fast variable,  $u \in \mathbb{R}$  is a slow variable, and  $\omega, a$  and  $\mu$  are parameters.

8. (Bursting in the  $I_{Na,t} + I_{Na,slow}$ -model) Take advantage of the phenomenon of inhibition-induced spiking described in Sect. 7.2.8 to show that a slow persistent inward current, say  $I_{Na,slow}$ , can make a spiking model burst.
9. Modify the example above to obtain repetitive bursting in a model consisting of fast  $I_{Na,t}$  current, leak current, and a slow passive dendritic compartment.

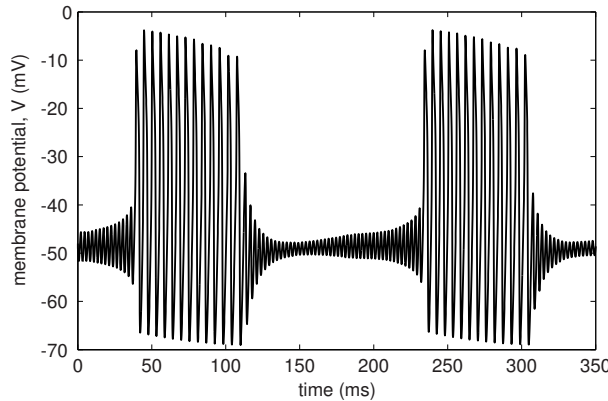


Figure 9.59: Bursting in the  $I_{Na,p} + I_K + I_{Na,slow}$ -model; see Ex. 10.

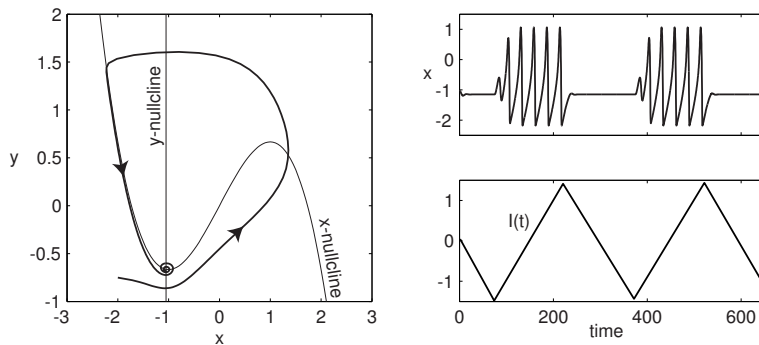


Figure 9.60: The phase portrait of the system in Ex. 11 shows that there is only one stable equilibrium for any value of  $I$ . Yet, the system bursts when  $I$  is periodically modulated.

10. (Bursting in the  $I_{Na,p} + I_K + I_{Na,slow}$ -model) Explore numerically this model with the fast subsystem as in Fig. 6.16 and a slow  $\text{Na}^+$  current with parameters:  $g_{\text{Na,slow}} = 0.5$ ,  $m_{\infty,\text{slow}}(V)$  with  $V_{1/2} = -50$  mV and  $k = 10$  mV, and  $\tau_{\text{slow}}(V) = 5 + 100 \exp(-(V + 20)^2/25^2)$ . Explain the origin of bursting oscillations when  $I = 27$  in Fig. 9.59.

11. The Bonhoeffer-van der Pol oscillator

$$\begin{aligned}\dot{x} &= I + x - x^3/3 - y, \\ \dot{y} &= 0.2(1.05 + x),\end{aligned}$$

with nullclines as in Fig. 9.60, is Class 3 excitable. It has a unique stable equilibrium for any value of  $I$  (check). Periodic modulations of  $I$  shift the  $x$ -nullcline up and down but do not change the stability of the equilibrium. Why does the system burst in Fig. 9.60? Explore the phenomenon numerically and explain the existence of repetitive spikes without a limit cycle.

12. Prove that the fast-slow “2+2” system

$$\dot{z} = (1 + u + i\omega)z - z|z|^2, \quad z \in \mathbb{C},$$

$$\begin{aligned}\dot{u} &= \mu(u - u^3 - w) , \\ \dot{w} &= \mu(|z|^2 - 1) ,\end{aligned}$$

is a slow-wave burster, even though the slow subsystem cannot oscillate for any fixed value of the fast subsystem  $z$ .

13. (Ermentrout and Kopell 1986) Consider the system

$$\begin{aligned}\dot{\vartheta} &= 1 - \cos \vartheta + (1 + \cos \vartheta)r(\psi) , \\ \dot{\psi} &= \omega ,\end{aligned}$$

with  $\vartheta$  and  $\psi$  being phase variables on the unit circle  $\mathbb{S}^1$  and  $r(\psi)$  being any continuous function that changes sign. Show that this system exhibits bursting activity when  $\omega$  is sufficiently small but positive. What type of bursting is that?

14. Prove that the canonical model for “subHopf/fold cycle” bursting (9.11) exhibits sustained bursting activity when  $0 < a < 1$ . What happens when  $a$  approaches 0 or 1?
15. Show that the canonical model for “fold/homoclinic” bursting (9.7) is equivalent to a simpler model (eq.27 in Izhikevich 2000 and Chap. 8)

$$\begin{aligned}\dot{v} &= v^2 + w , \\ \dot{w} &= \mu ,\end{aligned}$$

with after-spike ( $v = +\infty$ ) resetting  $v \leftarrow 1$  and  $w \leftarrow w - d$ , when  $I$  is sufficiently large and  $\mu$  and  $d$  are sufficiently small.

16. Derive the canonical model for “fold/homoclinic” bursting (9.7) assuming that the fast subsystem is near a saddle-node homoclinic orbit bifurcation point at some  $u = u_0$ , which is an equilibrium of the slow subsystem.
17. Derive the canonical models (9.9) and (9.10) for “circle/circle” bursting.
18. Show that the averaged slow subsystems of the canonical models for “circle/circle” bursters (9.9) and (9.10) have the form

$$\begin{aligned}\dot{u}_1 &= -\mu_1 u_1 + d_1 f(I + u_1 - u_2) , \\ \dot{u}_2 &= -\mu_2 u_2 + d_2 f(I + u_1 - u_2) ,\end{aligned}$$

and

$$\begin{aligned}\dot{u}_1 &= -\mu_1 u_2 + d_1 f(I + u_1) , \\ \dot{u}_2 &= -\mu_2(u_2 - u_1) + d_2 f(I + u_1) ,\end{aligned}$$

respectively, where

$$f(u) = \frac{\sqrt{u}}{\pi/2 + \arccot \sqrt{u}}$$

is the frequency of spiking of the fast subsystem (in Hz).

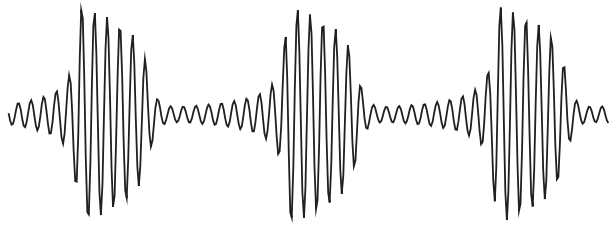


Figure 9.61: A cycle-cycle bursting: The resting state is not an equilibrium, but a small-amplitude limit cycle attractor.

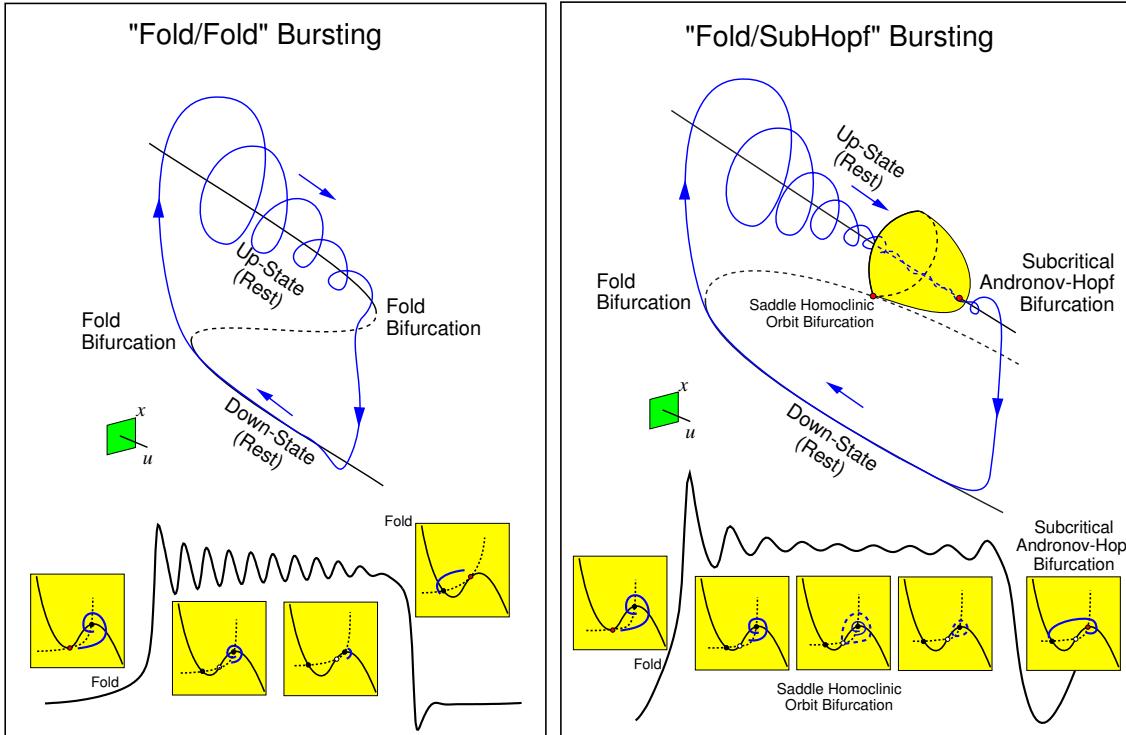
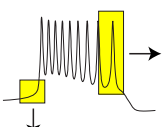


Figure 9.62: Two examples of point-point (not fast-slow) bursters (modified from Izhikevich 2000).

19. (Point-point hysteresis loops) Consider (9.1) and suppose that the fast subsystem has only equilibria for any value of the one-dimensional slow variable  $u$ . If there is a co-existence of equilibrium points of the fast subsystem, then (9.1) can exhibit point-point hysteresis loop oscillation. Classify all co-dimension-1 point-point hysteresis loops.
20. (Point-point bursting) In Fig. 9.62 we present two geometrical examples of point-point bursters that have no limit cycle attractors, yet are capable of exhibiting spike-like dynamics in the active phase. Construct a model for each type of point-point burster in the figure. Use phase portrait snapshots at the bottom of the figure as hints. What makes such bursting possible?
21. (Cycle-cycle bursters) Consider a fast-slow burster (9.1) and suppose that the resting state is not an equilibrium, but a limit cycle attractor, as in Fig. 9.61.



		bifurcations of limit cycles			
		saddle-node on invariant circle	saddle homoclinic orbit	supercritical Andronov-Hopf	fold limit cycle
bifurcations of equilibria	saddle-node (fold)	saddle-node homoclinic orbit $v' = l + v^2 \cdot u$ $u' = -\mu u$			
	saddle-node on invariant circle	$v' = l + v^2 + u_1$ $u_1' = -\mu_1 u_2$ $u_2' = -\mu_2(u_2 - u_1)$			
	supercritical Andronov-Hopf			Bautin	
	subcritical Andronov-Hopf				$z' = (u + i\omega)z$ $+ 2z z ^2 z z ^4$ $u' = \mu(a -  z ^2)$

Figure 9.63: Some canonical models of fast-slow bursters; see Ex. 26.

Such a bursting is called cycle-cycle. Classify all co-dimension-1 planar cycle-cycle fast-slow bursters. Is bursting in Fig. 9.10 of cycle-cycle type?

22. (Minimal models for bursting) Fill in the blank squares in Fig. 9.8.
23. Choose a minimal model from Fig. 9.8 and simulate it. Change the parameters to get as many different bursting types as possible.
24. [M.S.] Determine the bifurcation diagram of the canonical model for “fold/homoclinic” bursting (9.7).
25. [M.S.] Determine the bifurcation diagrams of the canonical models for “circle/circle” bursters (9.9) and (9.10).
26. [Ph.D.] Consider fast-slow bursters of the form (9.1) and assume that the fast subsystem is near a bifurcation of high co-dimension, as in Fig. 9.28 or in Fig. 9.42. Treating the bifurcation point as an organizing center for the fast subsystem (Bertram et al. 1995, Izhikevich 2000, Golubitsky et al. 2001), use unfolding theory to derive canonical models for the remaining fast-slow bursters in Fig. 9.63. Do not assume that the slow subsystem has an autonomous oscillation or that the fast oscillations have small amplitude.
27. [Ph.D.] Classify all possible mechanisms of emergence of bursting oscillations from resting or spiking, as in Fig. 9.19.

28. [Ph.D.] Develop an asymptotic theory of singularly perturbed systems of the form

$$\begin{aligned}\dot{x} &= f(x, u) && \text{(fast subsystem)}, \\ \dot{u} &= \mu g(x, u) && \text{(slow modulation)},\end{aligned}$$

that can deal with transitions between equilibria and limit cycle attractors of the fast subsystem.

# Chapter 10

## Synchronization (see [www.izhikevich.com](http://www.izhikevich.com))

This chapter, found on the author's webpage [www.izhikevich.com](http://www.izhikevich.com), considers networks of tonically spiking neurons. As any other kind of physical, chemical, or biological oscillators, such neurons could synchronize and exhibit collective behavior that is not intrinsic to any individual neuron. For example, partial synchrony in cortical networks is believed to generate various brain oscillations, such as the alpha and gamma EEG rhythms. Increased synchrony may result in pathological types of activity, such as epilepsy. Coordinated synchrony is needed for locomotion and swim pattern generation in fish. There is an ongoing debate on the role of synchrony in neural computation, see e.g., the special issue of *Neuron* (September 1999) devoted to the binding problem.

Depending on the circumstances, synchrony could be good or bad, and it is important to know what factors contribute to synchrony and how to control it. This is the subject of the present chapter – the most advanced chapter of the book. It provides a nice application of the theory developed earlier and hopefully gives some insight into why the previous chapters might be worth mastering. Unfortunately, it is too long to be included into the book, so reviewers recommended to put it on the web.

Our goal is to understand how the behavior of two coupled neurons depends on their intrinsic dynamics. First, we introduce the method of description of an oscillation by its phase. Then, we describe various methods of reduction of coupled oscillators to phase models. The reduction method and the exact form of the phase model depends on the type of coupling, i.e., whether it is pulsed, weak, or slow, and on the type of

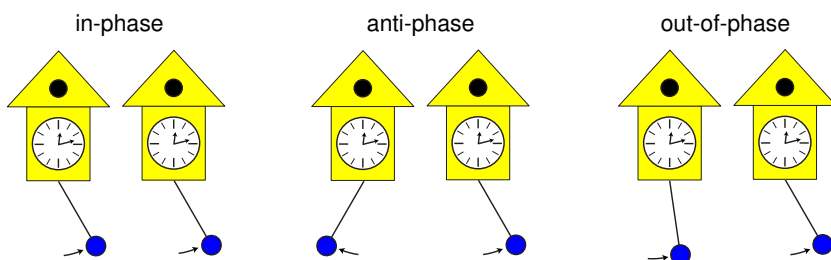


Figure 10.1: Different types of synchronization.

bifurcations of the limit cycle attractor generating tonic spiking. Finally, we show how to use phase models to understand the collective dynamics of many coupled oscillators.

## Review of Important Concepts

- Oscillations are described by their phase variables  $\vartheta$  rotating on a circle  $\mathbb{S}^1$ . We define  $\vartheta$  as the time since the last spike.
- The phase response curve,  $PRC(\vartheta)$ , describes the magnitude of the phase shift of an oscillator caused by a strong pulsed input arriving at phase  $\vartheta$ .
- PRC depends on the bifurcations of spiking limit cycle, and it defines synchronization properties of an oscillator.
- Two oscillators are synchronized in-phase, anti-phase, or out-of-phase, when their phase difference,  $\vartheta_2 - \vartheta_1$ , equals 0, half-period, or some other value, respectively; see Fig. 10.1.
- Synchronized states of pulse-coupled oscillators are fixed points of the corresponding Poincare phase map.
- Weakly coupled oscillators

$$\dot{x}_i = f(x_i) + \varepsilon \sum g_{ij}(x_j)$$

can be reduced to phase models

$$\dot{\vartheta}_i = 1 + \varepsilon Q(\vartheta_i) \sum g_{ij}(x_j(\vartheta_j)) ,$$

where  $Q(\vartheta)$  is the infinitesimal PRC defined by Malkin's equation.

- Weak coupling induces a slow phase deviation of the natural oscillation,  $\vartheta_i(t) = t + \varphi_i$ , described by the averaged model

$$\dot{\varphi}_i = \varepsilon \left( \omega_i + \sum H_{ij}(\varphi_j - \varphi_i) \right) ,$$

where the  $\omega_i$  denote the frequency deviations, and

$$H_{ij}(\varphi_j - \varphi_i) = \frac{1}{T} \int_0^T Q(t) g_{ij}(x_j(t + \varphi_j - \varphi_i)) dt$$

describe the interactions between the phases.

- Synchronization of two coupled oscillators correspond to equilibria of the one-dimensional system

$$\dot{\chi} = \varepsilon(\omega + G(\chi)) , \quad \chi = \varphi_2 - \varphi_1 ,$$

where  $G(\chi) = H_{21}(-\chi) - H_{12}(\chi)$  describes how the phase difference  $\chi$  compensates for the frequency mismatch  $\omega = \omega_2 - \omega_1$ .



# Solutions to Exercises

## Solutions to Chapter 2

1.  $T = 20^\circ\text{C} \approx 293^\circ\text{F}$ .

$$E_{\text{Ion}} = \frac{RT}{zF} \ln \frac{[\text{Ion}]_{\text{out}}}{[\text{Ion}]_{\text{in}}} = \frac{8315 \cdot 293 \cdot \ln 10}{z \cdot 96480} \log_{10} \frac{[\text{Ion}]_{\text{out}}}{[\text{Ion}]_{\text{in}}} = \pm 58 \log_{10} \frac{[\text{Ion}]_{\text{out}}}{[\text{Ion}]_{\text{in}}}$$

when  $z = \pm 1$ . Therefore,

$$\begin{aligned} E_K &= 58 \log(20/430) = -77 \text{ mV} \\ E_{\text{Na}} &= 58 \log(440/50) = 55 \text{ mV} \\ E_{\text{Cl}} &= -58 \log(560/65) = -54 \text{ mV} \end{aligned}$$

2.

$$\begin{aligned} I &= \bar{g}_{\text{Na}} p(V - E_{\text{Na}}) + \bar{g}_K p(V - E_K) = p\{\bar{g}_{\text{Na}} + \bar{g}_K\} V - \bar{g}_{\text{Na}} E_{\text{Na}} - \bar{g}_K E_K \\ &= (\underbrace{\bar{g}_{\text{Na}} + \bar{g}_K}_\bar{g}) p \left( V - \underbrace{\frac{\bar{g}_{\text{Na}} E_{\text{Na}} + \bar{g}_K E_K}{\bar{g}_{\text{Na}} + \bar{g}_K}}_E \right) \end{aligned}$$

3. The answer follows from the equation

$$I - g_L(V - E_L) = -g_L(V - \hat{E}_L), \quad \text{where } \hat{E}_L = E_L + I/g_L.$$

4. See Fig. 10.1.

Function	$V_{1/2}$	$k$	Function	$V_{\max}$	$\sigma$	$C_{\text{amp}}$	$C_{\text{base}}$
$n_\infty(V)$	12	15	$\tau_n(V)$	-14	50	4.7	1.1
$m_\infty(V)$	25	9	$\tau_m(V)$	27	30	0.46	0.04
$h_\infty(V)$	3	-7	$\tau_h(V)$	-2	20	7.4	1.2

Remark: Hodgkin and Huxley shifted  $V_{1/2}$  and  $V_{\max}$  by 65 mV so that the resting potential is at  $V = 0$  mV.

5. (Willms et al. 1999)

$$\begin{aligned} \tilde{V}_{1/2} &= V_{1/2} - k \ln(2^{1/p} - 1), \\ \tilde{k} &= \frac{k}{2p(1 - 2^{-1/p})}. \end{aligned}$$

The first equation is obtained from the condition  $m_\infty^p(\tilde{V}_{1/2}) = 1/2$ . The second equation is obtained from the condition that the two functions have the same slope at  $V = \tilde{V}_{1/2}$ .

6. See author's webpage.

7. See author's webpage.

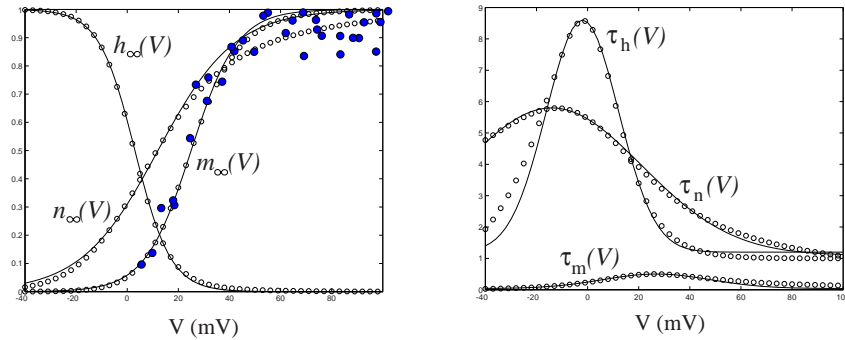


Figure 10.1: *Open dots:* The steady-state (in)activation functions and voltage-sensitive time constants in the Hodgkin-Huxley model. *Filled dots:* steady-state  $\text{Na}^+$  activation function  $m_\infty(V)$  in the squid giant axon (experimental results by Hodgkin and Huxley, 1952, Fig. 8). *Continuous curves:* Approximations by Boltzmann and Gaussian functions. See Ex. 4.

## Solutions to Chapter 3

- Consider the limit case: (1) activation of  $\text{Na}^+$  current is instantaneous, and (2) conductance kinetics of the other currents are frozen. Then, the  $\text{Na}^+$  current will result in the nonlinear term  $g_{\text{Na}} m_\infty(V)(V - E_{\text{Na}})$  with the parameter  $h_\infty(V_{\text{rest}})$  incorporated into  $g_{\text{Na}}$ , and all the other currents will result in the linear leak term.

In Fig. 3.15, the activation of the  $\text{Na}^+$  current is not instantaneous, hence the sag right after the pulses. In addition, its inactivation, as well as the kinetics of the other currents are not slow enough, hence the membrane potential quickly reaches the excited state and then slowly repolarizes back to the resting state.

- See Fig. 10.2. The eigenvalues are negative at each equilibrium marked as filled circle (stable), and positive at each equilibrium marked as open circle (unstable). The eigenvalue at the bifurcation point (left equilibrium in Fig. 10.2b) is zero.

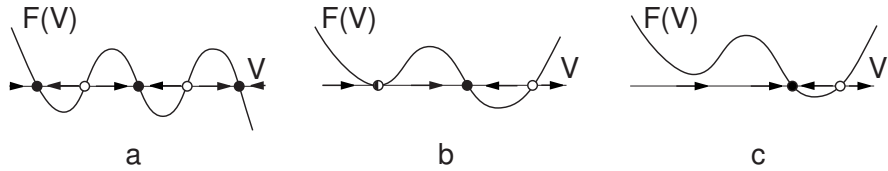


Figure 10.2: Phase portraits of the system  $\dot{V} = F(V)$  with given  $F(V)$ .

- Phase portraits are shown in Fig. 10.3.

- The equation  $0 = -1 + x^2$  has two solutions:  $x = -1$  and  $x = +1$ , hence there are two equilibria in the system (a). The eigenvalues are the derivatives at each equilibrium,  $\lambda = (-1 + x^2)' = 2x$ , where  $x = \pm 1$ . Equilibrium  $x = -1$  is stable because  $\lambda = -2 < 0$ . Equilibrium  $x = +1$  is unstable because  $\lambda = +2 > 0$ . The same fact follows from the geometrical analysis in Fig. 10.3.

- (b) The equation  $0 = x - x^3$  has three solutions:  $x = \pm 1$  and  $x = 0$ , hence there are three equilibria in the system (b). The eigenvalues are the derivatives at each equilibrium,  $\lambda = (x - x^3)' = 1 - 3x^2$ . The equilibria  $x = \pm 1$  are stable because  $\lambda = 1 - 3(\pm 1)^2 = -2 < 0$ . The equilibrium  $x = 0$  is unstable because  $\lambda = 1 > 0$ . The same conclusions also follow from the geometrical analysis in Fig. 10.3.

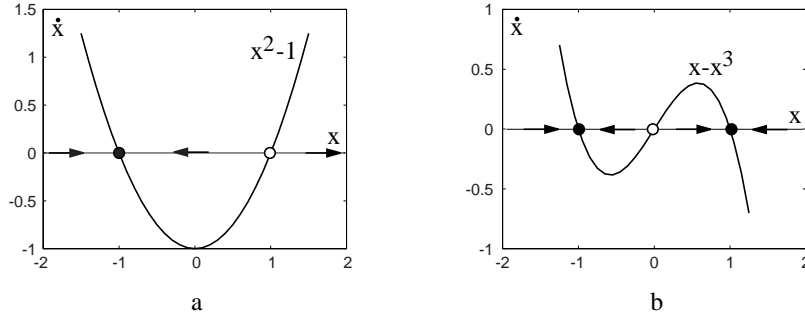


Figure 10.3: Phase portraits of the systems (a)  $\dot{x} = -1 + x^2$ , (b)  $\dot{x} = x - x^3$ .

4. The equilibrium  $x = 0$  is stable in all three cases.
5. See Fig. 10.4. Topologically equivalent systems are in (a), (b), and (c). In (d) there are different numbers of equilibria; no stretching or shrinking of the rubber phase line can produce new equilibria. In (e) the right equilibrium is unstable in  $\dot{V} = F_1(V)$ , but stable in  $\dot{V} = F_2(V)$ ; no stretching or shrinking can change the stability of an equilibrium. In (f) the flow between the two equilibria is directed rightward in  $\dot{V} = F_1(V)$  and leftward in  $\dot{V} = F_2(V)$ ; no stretching or shrinking can change the direction of the flow.
6. (Saddle-node (fold) bifurcation in  $\dot{x} = a + x^2$ ) The equation  $0 = a + x^2$  has no real solutions when  $a > 0$ , and two solutions  $x = \pm\sqrt{|a|}$  when  $a \leq 0$ . Hence there are two branches of equilibria, depicted in Fig. 10.5. The eigenvalues are

$$\lambda = (a + x^2)' = 2x = \pm 2\sqrt{|a|}.$$

The lower branch  $-\sqrt{|a|}$  is stable ( $\lambda < 0$ ), and the upper branch  $+\sqrt{|a|}$  is unstable ( $\lambda > 0$ ). They meet at the saddle-node (fold) bifurcation point  $a = 0$ .

- 7.
- (a)  $x = -1$  at  $a = 1$ , (b)  $x = -1/2$  at  $a = 1/4$  (c)  $x = 1/2$  at  $a = 1/4$   
 (d)  $x = \pm 1/\sqrt{3}$  at  $a = \pm 2/(3\sqrt{3})$  (e)  $x = \pm 1$  at  $a = \mp 2$  (f)  $x = -1$  at  $a = 1$
8. (Pitchfork bifurcation in  $\dot{x} = bx - x^3$ ) The equation  $0 = bx - x^3$  has one solution  $x = 0$  when  $b \leq 0$ , and three solutions  $x = 0$ ,  $x = \pm\sqrt{b}$  when  $b > 0$ . Hence there is only one branch of equilibria for  $b < 0$  and three branches for  $b > 0$  of the pitchfork curve depicted in Fig. 10.6. The eigenvalues are

$$\lambda = (bx - x^3)' = b - 3x^2.$$

The branch  $x = 0$  exists for any  $b$  and its eigenvalue is  $\lambda = b$ . Thus, it is stable for  $b < 0$  and unstable for  $b > 0$ . The two branches  $x = \pm\sqrt{b}$  exist only for  $b > 0$ , but they are always stable because  $\lambda = b - 3(\pm\sqrt{b})^2 = -2b < 0$ . We see that the branch  $x = 0$  loses stability when  $b$  passes the pitchfork bifurcation value  $b = 0$ , at which point a pair of new stable branches bifurcates (hence the name *bifurcation*). In other words, the stable branch  $x = 0$  divides (bifurcates) into two stable branches when  $b$  passes 0.

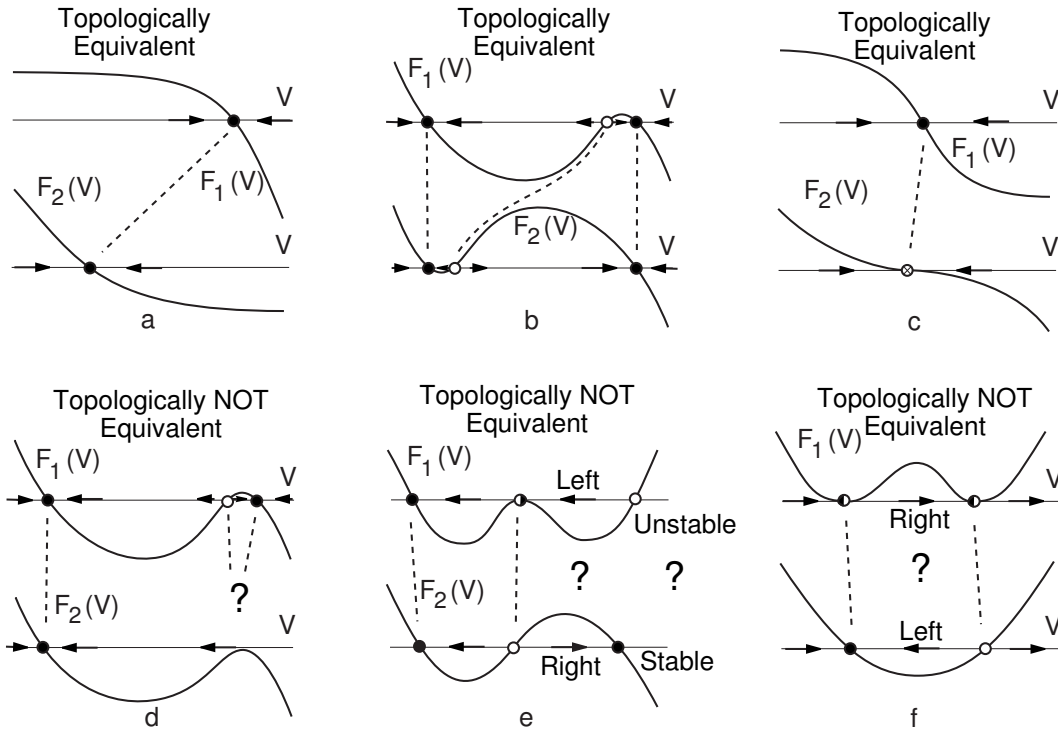


Figure 10.4: Answer to Chap. 3, Ex. 5.

9. Recall that the current  $I_{\text{Kir}}$  is turned off by depolarization and turned on by hyperpolarization. The dynamics of the  $I_{\text{Kir}}$ -model is similar to that of the  $I_{\text{Na,p}}$ -model in many respects. In particular, this system can also have co-existence of two stable equilibria separated by an unstable equilibrium, which follows from the N-shaped I-V relation. Indeed, when  $V$  is hyperpolarized, the current  $I_{\text{Kir}}$  is turned on (deinactivated) and it pulls  $V$  toward  $E_K$ . In contrast, when  $V$  is depolarized, the current is turned off (inactivated) and does not obstruct further depolarization of  $V$ .

We use (3.11) to find the curve

$$I = g_L(V - E_L) + g_{\text{Kir}}h_\infty(V)(V - E_K),$$

in Fig. 10.8. (The curve might not be S-shaped if a different bifurcation parameter is used, as in Ex. 12a).

The bifurcation diagram of the  $I_{\text{Kir}}$ -model (3.11) in Fig. 10.8 has three branches corresponding to the three equilibria. When the parameter  $I$  is relatively small, the outward  $I_{\text{Kir}}$  current dominates and the system has only one equilibrium in the low voltage range — the “down-state”. When the parameter  $I$  is relatively large, the injected inward current  $I$  dominates, and the system has one equilibrium in the intermediate voltage range — the “up-state”. When the parameter  $I$  is in neighborhood of  $I = 6$ , the system exhibits bistability of the “up-” and “down-states”. The states appear and disappear via saddle-node bifurcations. We see that the behavior of the  $I_{\text{Kir}}$ -model is conceptually (and qualitatively) similar to the behavior of the  $I_{\text{Na,p}}$ -model (3.5) even though the models have completely different ionic mechanisms for bistability.

10. The equilibrium satisfies the one-dimensional equation

$$0 = I - g_K n_\infty^4(V)(V - E_K) - g_{\text{Na}} m_\infty^3(V) h_\infty(V)(V - E_{\text{Na}}) - g_L(V - E_L),$$

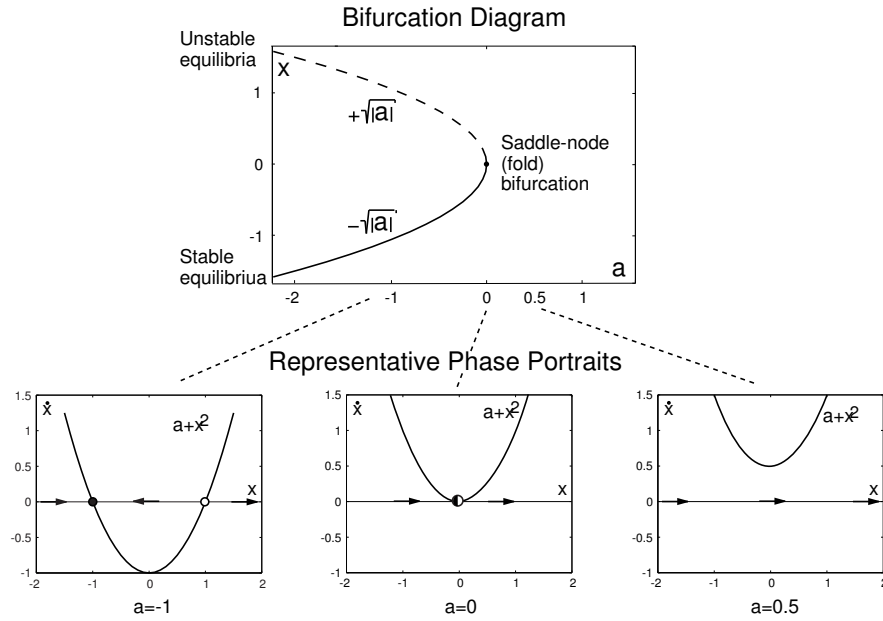


Figure 10.5: Saddle-node (fold) bifurcation diagram and representative phase portraits of the system  $\dot{x} = a + x^2$  (see Chap. 3, Ex. 6).

where all gating variables assume their asymptotic values. The solution

$$I = g_K n_\infty^4(V)(V - E_K) + g_{Na} m_\infty^3(V) h_\infty(V)(V - E_{Na}) + g_L(V - E_L)$$

is depicted in Fig. 10.9. Since the curve in Fig. 10.9 does not have folds, there are no saddle-node bifurcations in the Hodgkin-Huxley model (with the original values of parameters).

11. The curves

$$(a) \quad g_L(V) = -g_{Na} m_\infty(V)(V - E_{Na})/(V - E_L)$$

and

$$(b) \quad E_L(V) = V + g_{Na} m_\infty(V)(V - E_{Na})(V - E_L)/g_L$$

are depicted in Fig. 10.7.

12. The curves

$$(a) \quad g_L(V) = \{I - g_{Kir} h_\infty(V)(V - E_K)\}/(V - E_L)$$

and

$$(b) \quad g_{Kir}(V) = \{I - g_L(V - E_L)\}/\{h_\infty(V)(V - E_K)\}$$

are depicted in Fig. 10.10. Notice that the curve in Fig. 10.10a does not have the S shape.

- 13.

$$F'(V) = -g_L - g_K m_\infty^4(V) - g_{K4} m_\infty^3(V) m'_\infty(V)(V - E_K) < 0$$

because  $g_L > 0$ ,  $m_\infty(V) > 0$ ,  $m'_\infty(V) > 0$ , and  $V - E_K > 0$  for all  $V > E_K$ .

- 14.

$$F'(V) = -g_L - g_h h_\infty(V) - g_h h'_\infty(V)(V - E_h) < 0$$

because  $g_L > 0$ ,  $h_\infty(V) > 0$ , but  $h'_\infty(V) < 0$  and  $V - E_h < 0$  for all  $V < E_h$ .

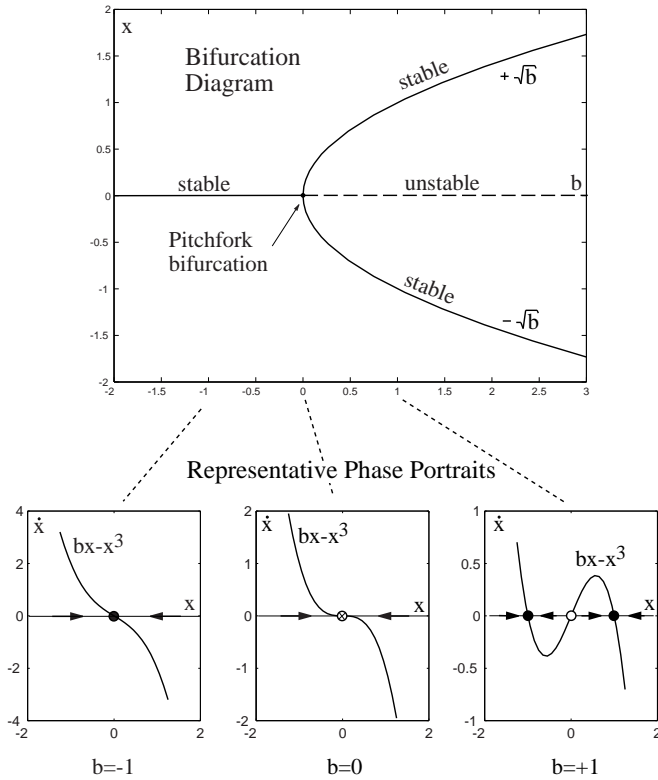


Figure 10.6: Pitchfork bifurcation diagram and representative phase portraits of the system  $\dot{x} = bx - x^3$  (see Chap. 3, Ex. 8).

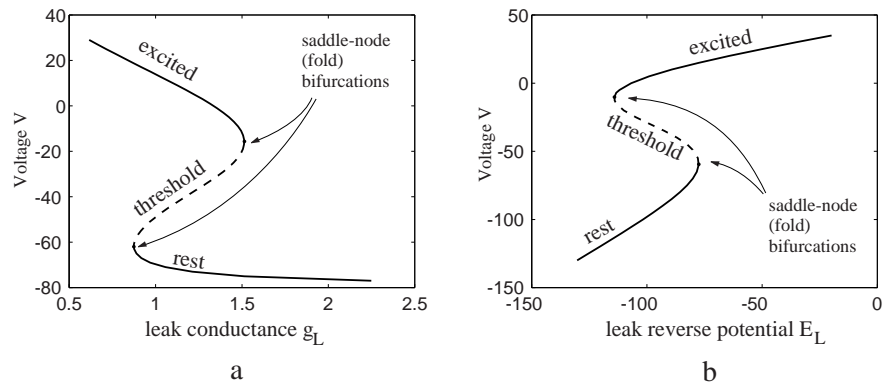


Figure 10.7: Bifurcation diagrams of the  $I_{Na,P}$ -model (3.5) with bifurcation parameters (a)  $g_L$  and (b)  $E_L$  (see Chap. 3, Ex. 11).

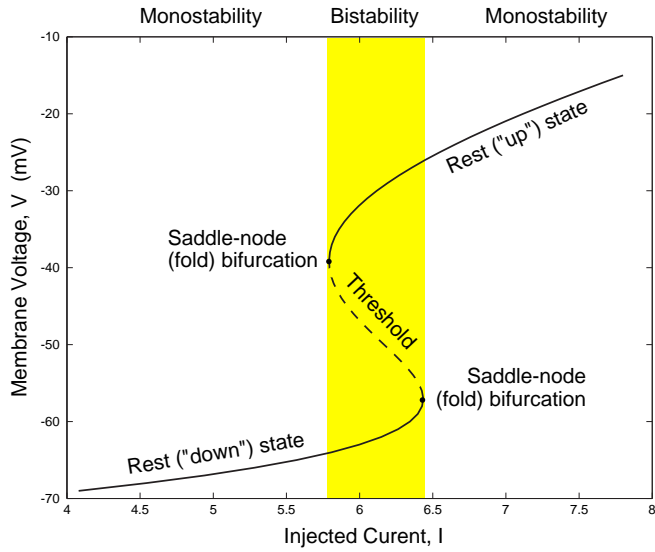
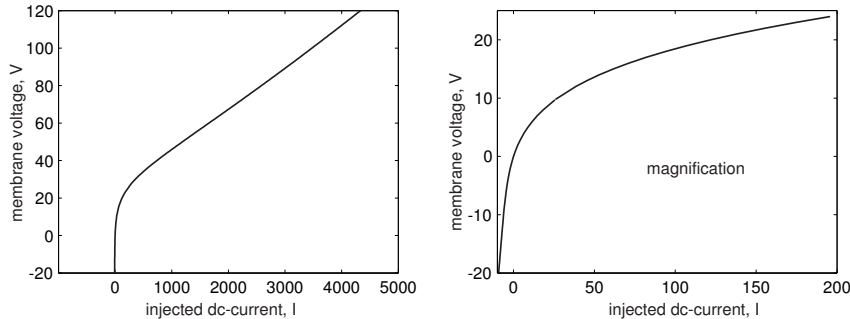
Figure 10.8: Bifurcation diagram of the  $I_{\text{Kir}}$ -model (3.11).

Figure 10.9: Dependence of the position of equilibrium in the Hodgkin-Huxley model on the injected dc-current; see Ex. 10.

15. When  $V$  is sufficiently large,  $\dot{V} \approx V^2$ . The solution of  $\dot{V} = V^2$  is  $V(t) = 1/(c-t)$  (check by differentiating), where  $c = 1/V(0)$ . Another way to show this is to solve (3.9) for  $V$  and find the asymptote of the solution.
16. Each equilibrium of the system  $\dot{x} = a + bx - x^3$  is a solution to the equation  $0 = a + bx - x^3$ . Treating  $x$  and  $b$  as free parameters, the set of all equilibria is given by  $a = -bx + x^3$ , and it looks like the cusp surface in Fig. 6.34. Each point where the cusp surface folds corresponds to a saddle-node (fold) bifurcation. The derivative with respect to  $x$  at each such point is zero; alternatively, the tangent vector to the cusp surface at each such point is parallel to the  $x$ -axis. The set of all bifurcation points is projected to the  $(a, b)$ -plane at the bottom of the figure, and it looks like a curve having two branches. To find the equation for the bifurcation curves one needs to remember that each bifurcation point satisfies two conditions:
  - It is an equilibrium; that is,  $a + bx - x^3 = 0$ .
  - The derivative of  $a + bx - x^3$  with respect to  $x$  is zero; that is,  $b - 3x^2 = 0$ .

Solving the second equation for  $x$  and using the solution  $x = \pm\sqrt{b/3}$  in the first equation yields  $a = \mp 2(b/3)^{3/2}$ . The point  $a = b = 0$  is called a cusp bifurcation point.

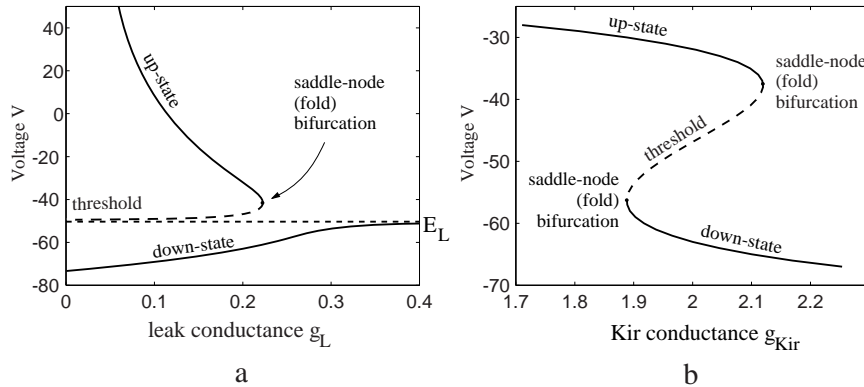


Figure 10.10: Bifurcation diagrams of the  $I_{\text{Kir}}$ -model (3.11),  $I = 6$ , with bifurcation parameters (a)  $g_L$  and (b)  $g_{\text{Kir}}$  (see Chap. 3, Ex. 12).

17. (Gradient systems) For  $\dot{V} = F(V)$  take

$$E(V) = - \int_c^V F(v) dv ,$$

where  $c$  is any constant.

- |                       |                            |                     |
|-----------------------|----------------------------|---------------------|
| a. $E(V) = 1$         | b. $E(V) = -V$             | c. $E(V) = V^2/2$   |
| d. $E(V) = V - V^3/3$ | e. $E(V) = -V^2/2 + V^4/4$ | f. $E(V) = -\cos V$ |

18. (c) implies (b) because  $|x(t) - y| < \exp(-at)$  implies that  $x(t) \rightarrow y$  as  $t \rightarrow \infty$ . (b) implies (a) according to the definition.

(a) does not imply (b) because  $x(t)$  might not approach  $y$ . For example,  $y = 0$  is an equilibrium in the system  $\dot{x} = 0$  (any other point is also an equilibrium). It is stable, since  $|x(t) - 0| < \varepsilon$  for all  $|x_0 - 0| < \varepsilon$  and all  $t \geq 0$ . However, it is not asymptotically stable because  $\lim_{t \rightarrow \infty} x(t) = x_0 \neq 0$  regardless of how close  $x_0$  is to 0 (unless  $x_0 = 0$ ).

(b) does not imply (c). For example, the equilibrium  $y = 0$  in the system  $\dot{x} = -x^3$  is asymptotically stable (check by differentiating that  $x(t) = (2t + x_0^{-2})^{-1/2} \rightarrow 0$  is a solution with  $x(0) = x_0$ ), however  $x(t)$  approaches 0 with a slower than exponential rate,  $\exp(-at)$ , for any constant  $a > 0$ .

## Solutions to Chapter 4

1. See figures 10.11 through 10.15.
2. See Fig. 10.16.
3. See figures 10.17 through 10.21.
4. The diagram follows from the form of the eigenvalues

$$\lambda = \frac{\tau \pm \sqrt{\tau^2 - 4\Delta}}{2} .$$

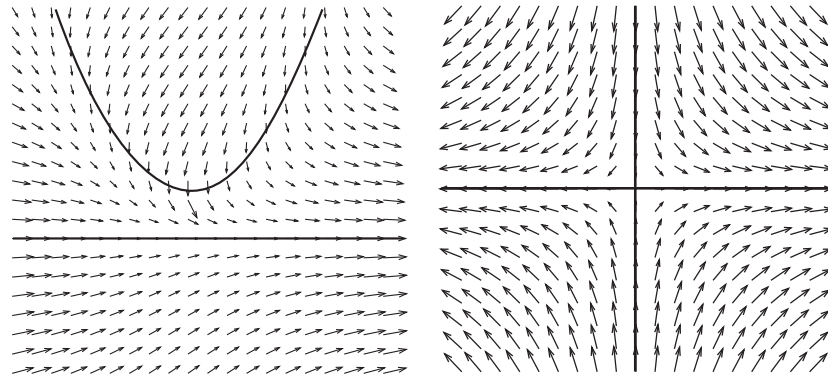


Figure 10.11: Nullclines of the vector field; see also Fig. 10.17.

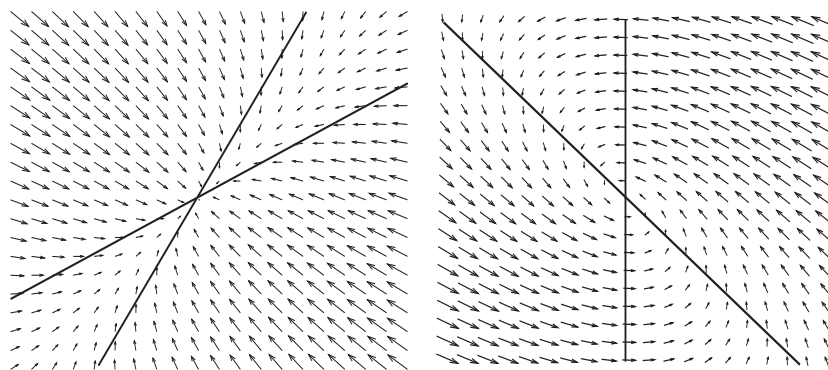


Figure 10.12: Nullclines of the vector field; see also Fig. 10.18.

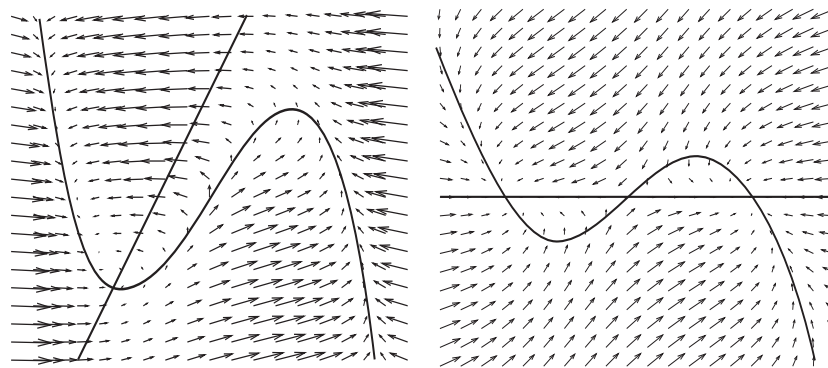


Figure 10.13: Nullclines of the vector field; see also Fig. 10.19.

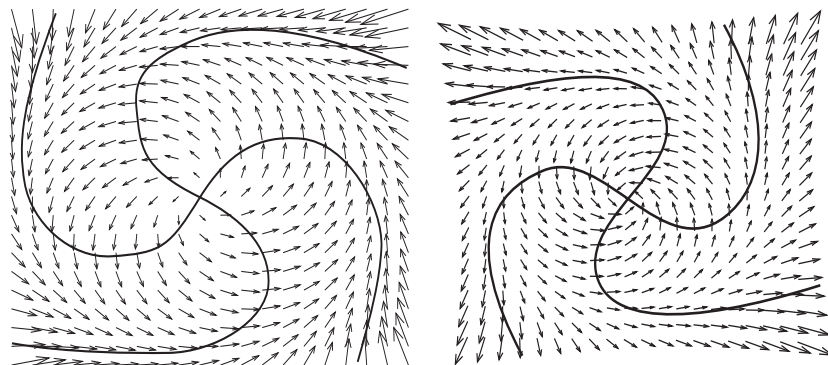


Figure 10.14: Nullclines of the vector field; see also Fig. 10.20.

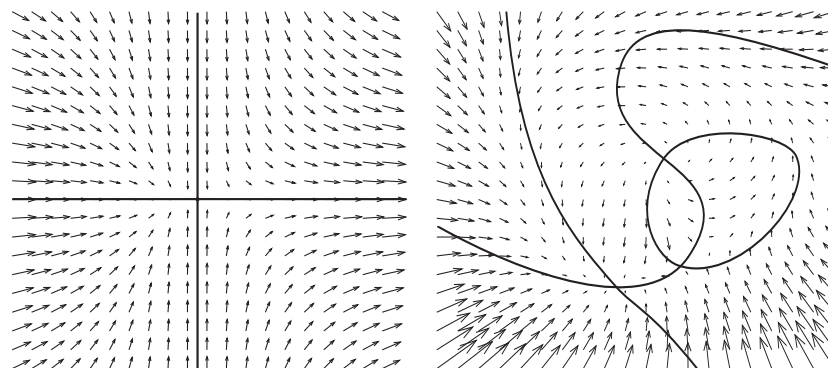


Figure 10.15: Nullclines of the vector field; see also Fig. 10.21.

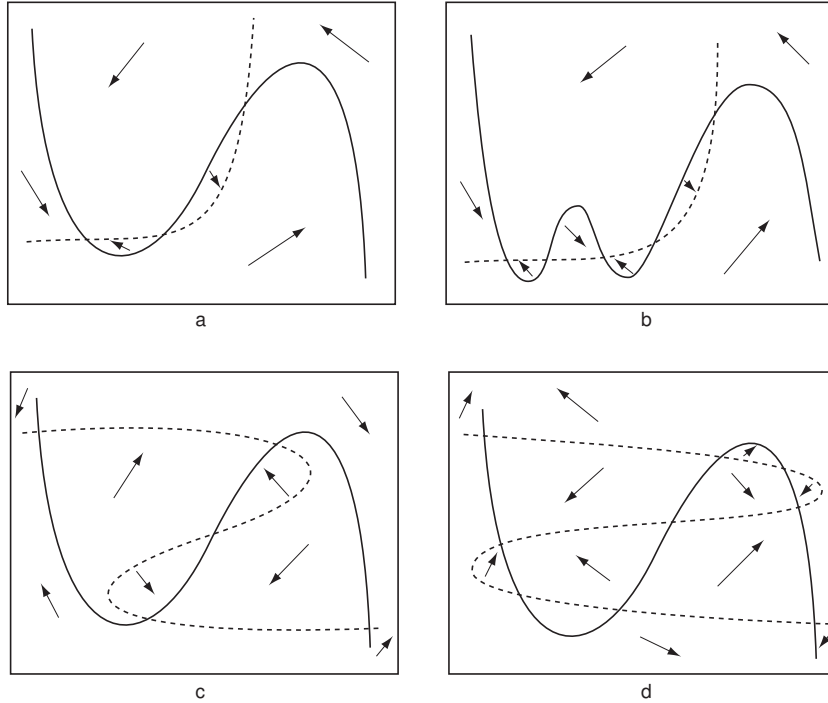


Figure 10.16: Approximate directions of the vector in each region between the nullclines.

If  $\Delta < 0$  (left half-plane in Fig. 4.15), then the eigenvalues have opposite signs. Indeed,

$$\sqrt{\tau^2 - 4\Delta} > \sqrt{\tau^2} = |\tau| ,$$

whence

$$\tau + \sqrt{\tau^2 - 4\Delta} > 0 \quad \text{and} \quad \tau - \sqrt{\tau^2 - 4\Delta} < 0 .$$

The equilibrium is a saddle in this case. Now consider the case  $\Delta > 0$ . When  $\tau^2 < 4\Delta$  (inside the parabola in Fig. 4.15), the eigenvalues are complex-conjugate, hence the equilibrium is a focus. It is stable (unstable) when  $\tau < 0$  ( $\tau > 0$ ). When  $\tau^2 > 4\Delta$  (outside the parabola in Fig. 4.15), the eigenvalues are real. They both are negative (positive) when  $\tau < 0$  ( $\tau > 0$ ).

5. (van der Pol oscillator) The nullclines of the van der Pol oscillator,

$$\begin{aligned} y &= x - x^3/3 && (\text{x-nullcline}) , \\ x &= 0 && (\text{y-nullcline}) , \end{aligned}$$

are depicted in Fig. 10.22. There is a unique equilibrium  $(0, 0)$ . The Jacobian matrix at the equilibrium has the form

$$L = \begin{pmatrix} 1 & -1 \\ b & 0 \end{pmatrix} .$$

Since  $\text{tr } L = 1 > 0$  and  $\det L = b > 0$ , the equilibrium is always an unstable focus.

6. (Bonhoeffer–van der Pol oscillator) The nullclines of the Bonhoeffer–van der Pol oscillator with  $c = 0$  have the form

$$\begin{aligned} y &= x - x^3/3 && (\text{x-nullcline}) , \\ x &= a && (\text{y-nullcline}) , \end{aligned}$$

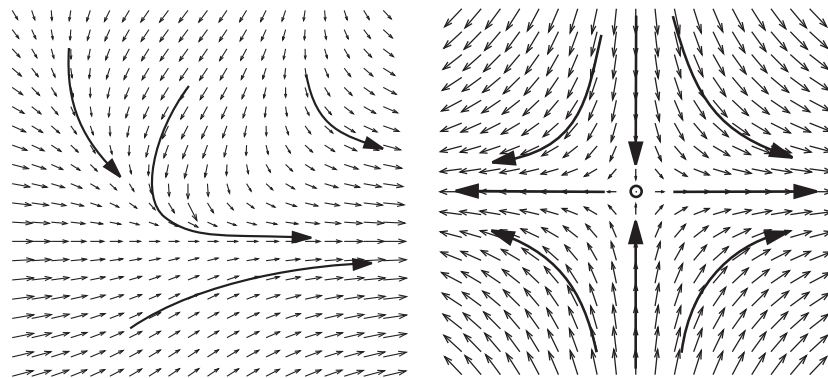


Figure 10.17: *Left:* No equilibria. *Right:* Saddle equilibrium.

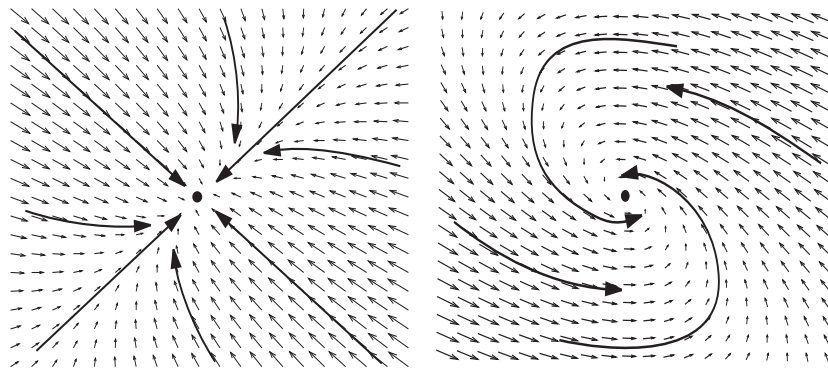


Figure 10.18: *Left:* Stable node. *Right:* Stable focus.

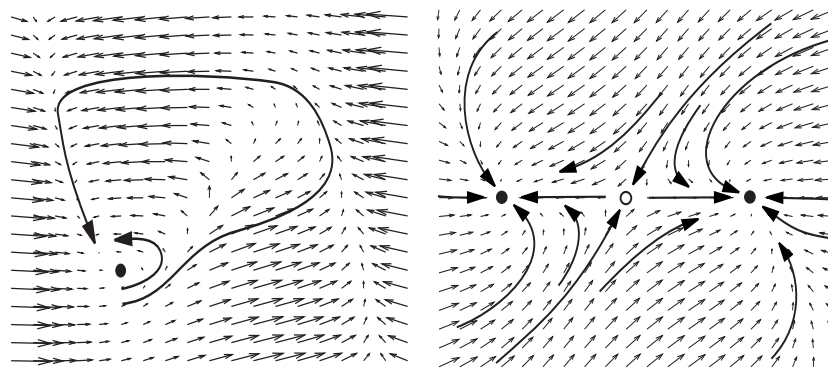


Figure 10.19: *Left:* Excitable system having one stable equilibrium. *Right:* Two stable nodes separated by a saddle equilibrium.

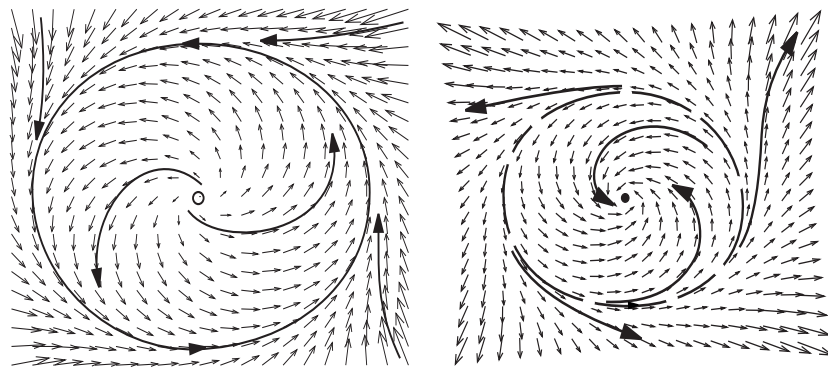


Figure 10.20: *Left:* Unstable focus inside a stable limit cycle. *Right:* Stable focus inside an unstable limit cycle.

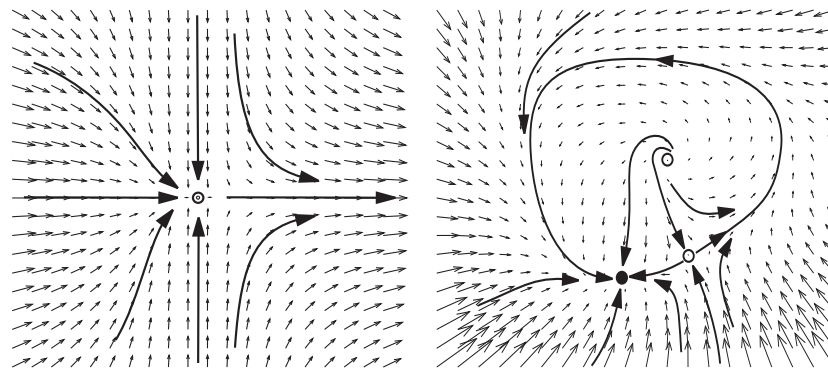


Figure 10.21: *Left:* Saddle-node equilibrium. *Right:* Stable node and saddle equilibria connected by two heteroclinic trajectories, which form an invariant circle with an unstable focus inside.

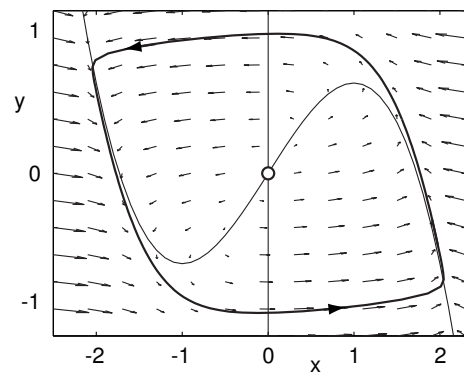


Figure 10.22: Nullclines and phase portrait of the van der Pol oscillator ( $b = 0.1$ ).

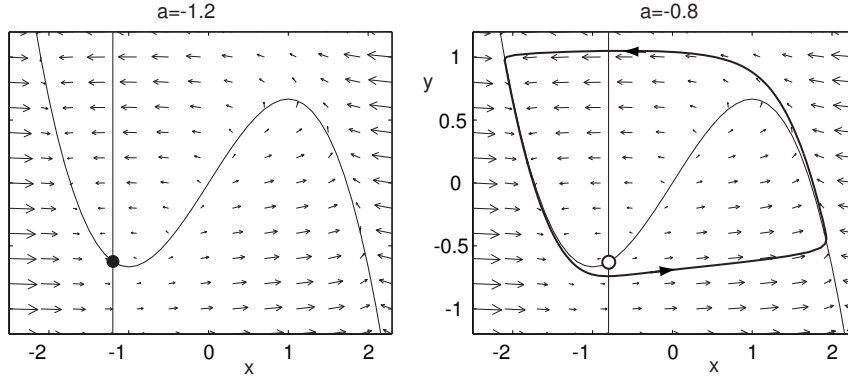


Figure 10.23: Nullclines and phase portrait of the Bonhoeffer–van der Pol oscillator ( $b = 0.05$  and  $c = 0$ ).

shown in Fig. 10.23. They intersect at the point  $x = a$ ,  $y = a - a^3/3$ . The Jacobian matrix at the equilibrium  $(a, a - a^3/3)$  has the form

$$L = \begin{pmatrix} 1 - a^2 & -1 \\ b & 0 \end{pmatrix}.$$

Since  $\text{tr } L = 1 - a^2$  and  $\det L = b > 0$ , the equilibrium is a stable (unstable) focus when  $|a| > 1$  ( $|a| < 1$ ), as we illustrate in Fig. 10.23.

7. (Hindmarsh-Rose spiking neuron) The Jacobian matrix at the equilibrium  $(\bar{x}, \bar{y})$  is

$$L = \begin{pmatrix} f' & -1 \\ g' & -1 \end{pmatrix},$$

therefore

$$\text{tr } L = f' - 1 \quad \text{and} \quad \det L = -f' + g'.$$

The equilibrium is a saddle ( $\det L < 0$ ) when  $g' < f'$ , i.e., in the region below the diagonal in Fig. 10.24. When  $g' > f'$ , the equilibrium is stable ( $\text{tr } L < 0$ ) when  $f' < 1$ , which is the left half-plane in Fig. 10.24. Using the classification in Fig. 4.15, we conclude that it is focus when  $(f' - 1)^2 - 4(g' - f') < 0$ , i.e., when

$$g' > \frac{1}{4}(f' + 1)^2$$

which is the upper part of the parabola in Fig. 10.24.

8. ( $I_K$ -model) The steady-state I-V relation of the  $I_K$ -model is monotone, hence it has a unique equilibrium, which we denote here as  $(\bar{V}, \bar{m}) \in \mathbb{R}^2$ , where  $\bar{V} > E_K$  and  $\bar{m} = m_\infty(\bar{V})$ . The Jacobian at the equilibrium has the form

$$L = \begin{pmatrix} -(g_L + \bar{g}_K \bar{m}^4)/C & -4\bar{g}_K \bar{m}^3(\bar{V} - E_K)/C \\ m'_\infty(\bar{V})/\tau(\bar{V}) & -1/\tau(\bar{V}) \end{pmatrix},$$

with the signs

$$L = \begin{pmatrix} - & - \\ + & - \end{pmatrix}.$$

Obviously,  $\det L > 0$  and  $\text{tr } L < 0$ , hence the equilibrium (focus or node) is always stable.

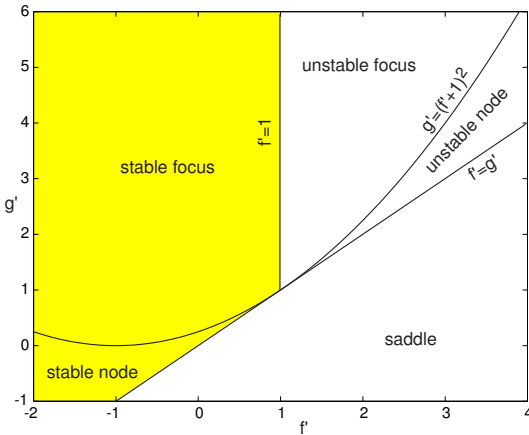


Figure 10.24: Stability diagram of the Hindmarsh-Rose spiking neuron model; see Ex. 7.

9. ( $I_h$ -model) The steady-state I-V relation of the  $I_h$ -model is monotone, hence it has a unique equilibrium denote here as  $(\bar{V}, \bar{h}) \in \mathbb{R}^2$ , where  $\bar{V} < E_h$  and  $\bar{h} = h_\infty(\bar{V})$ . The Jacobian at the equilibrium has the form

$$L = \begin{pmatrix} -(g_L + \bar{g}_h \bar{h})/C & -\bar{g}_h(\bar{V} - E_h)/C \\ h'_\infty(\bar{V})/\tau(\bar{V}) & -1/\tau(\bar{V}) \end{pmatrix},$$

with the signs

$$L = \begin{pmatrix} - & + \\ - & - \end{pmatrix}.$$

Obviously,  $\det L > 0$  and  $\text{tr } L < 0$ , hence the equilibrium is always stable.

10. (Bendixson's criterion) The divergence of the vector field of the  $I_K$ -model

$$\underbrace{\frac{\partial f(x,y)/\partial x}{(-g_L - \bar{g}_K m^4)/C}}_{+} + \underbrace{\frac{\partial g(x,y)/\partial y}{-1/\tau(V)}}$$

is always negative, hence the model cannot have a periodic orbit. Therefore, it cannot have sustained oscillations.

11. The  $x$ -nullcline is  $y = a + x^2$  and the  $y$ -nullcline is  $y = bx/c$ , as in Fig. 10.25. The equilibria (intersections of the nullclines) are

$$\bar{x} = \frac{b/c \pm \sqrt{(b/c)^2 - 4a}}{2}, \quad \bar{y} = b\bar{x}/c,$$

provided that  $a < \frac{1}{4}(b/c)^2$ . The Jacobian matrix at  $(\bar{x}, \bar{y})$  has the form

$$L = \begin{pmatrix} 2\bar{x} & -1 \\ b & -c \end{pmatrix}$$

with  $\text{tr } L = 2\bar{x} - c$  and

$$\det L = -2\bar{x}c + b = \mp\sqrt{b^2 - 4ac^2}.$$

Thus, the right equilibrium (i.e.,  $(b/c + \sqrt{(b/c)^2 - 4a})/2$ ) is always a saddle and the left equilibrium (i.e.,  $(b/c - \sqrt{(b/c)^2 - 4a})/2$ ) is always a focus or a node. It is always stable when it lies on the left branch of the parabola  $y = a + x^2$  (i.e., when  $\bar{x} < 0$ ), and can also be stable on the right branch if it is not too far from the parabola knee (i.e., if  $\bar{x} < c/2$ ); see Fig. 10.25.

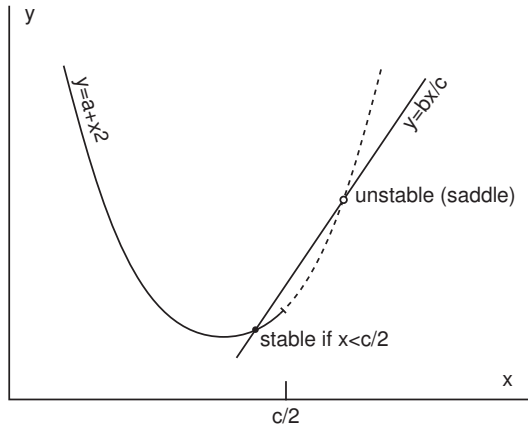


Figure 10.25: The left equilibrium is stable when  $x < c/2$ ; see Ex. 11.

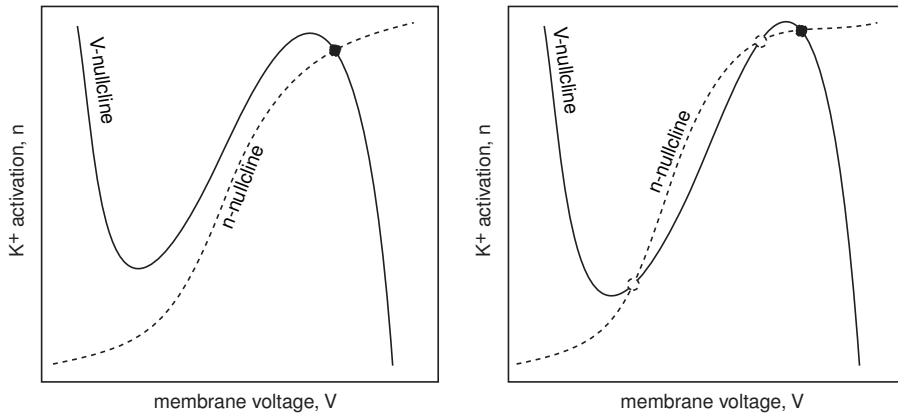


Figure 10.26: Answer to Ex. 2.

## Solutions to Chapter 5

- The  $I_A$ -model with instantaneous activation has the form

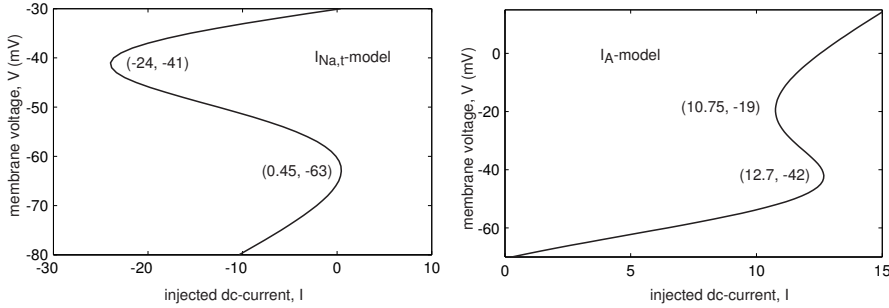
$$\begin{aligned} C \dot{V} &= I - \overbrace{g_L(V - E_L)}^{\text{leak}} - \overbrace{\bar{g}_A m_\infty(V) h(V - E_K)}^{I_A} \\ \dot{h} &= (h_\infty(V) - h)/\tau(V). \end{aligned}$$

To apply the Bendixson criterion (Chap. 4, Ex. 10), we first determine the divergence of this vector field

$$\frac{\partial \dot{V}}{\partial V} + \frac{\partial \dot{h}}{\partial h} = -\{g_L + \bar{g}_A m'_\infty(V)h(V - E_K) + \bar{g}_A m_\infty(V)h\}/C - 1/\tau(V) < 0.$$

Since it is always negative, the  $I_A$ -model cannot have limit cycle attractors (or any other closed loop orbit).

- See Fig. 10.26.

Figure 10.27: The saddle-node bifurcation diagrams of the  $I_{\text{Na},t}$ - and  $I_A$ -minimal models.

3. The curves

$$I = g_L(V - E_L) + \bar{g}_{\text{Na}} m_\infty^3(V) h_\infty(V)(V - E_{\text{Na}})$$

and

$$I = g_L(V - E_L) + \bar{g}_A m_\infty(V) h_\infty(V)(V - E_K)$$

are depicted in Fig. 10.27.

4.  $g$  is not an absolute conductance, but is taken relative to the conductance at resting state. Negative values occur because the initial holding voltage value in the voltage-clamp experiment described in Fig. 5.22a corresponds to the resting potential, at which the  $K^+$  conductance is partially activated. Indeed, in the  $I_{\text{Na},p} + I_K$ -model the  $K^+$  gating variable  $n \approx 0.04$ , hence the  $K^+$  conductance is approximately 0.4 (because  $\bar{g}_K = 10$ ). According to the procedure, this value corresponds to  $g = 0$ . Any small decrease in conductance would result in negative values of  $g$ . If the initial holding voltage were very negative, say below  $-100$  mV, then the slow conductance  $g$  would have non-negative values in the relevant voltage range (above  $-100$  mV).
5. The curve  $I_{\text{slow}}(V)$  defines slow changes of the membrane voltage. The curve  $I - I_{\text{fast}}(V)$  defines fast changes. Its middle part, which has positive slope, is unstable. If the I-V curves intersect in the middle part, the equilibrium is unstable, and the system exhibits periodic spiking: The voltage slides down slowly along the left branch of the fast I-V curve toward the slow I-V curve until it reaches the left knee, and then it jumps quickly to the right branch. After the jump, the voltage slides up slowly along the right branch until it reaches the right knee, and then it quickly jumps to the left branch along the straight line that connects the knee and the point  $(E_K, 0)$  (see also previous exercise). Notice that the direction of the jump is not horizontal, as in relaxation oscillators, but along a sloped line. On that line the slow conductance  $g$  is constant, but the slow current  $I_{\text{slow}}(V) = g(V - E_K)$  changes fast because the driving force  $V - E_K$  changes fast. When the I-V curves intersect at the stable point (negative slope of  $I - I_{\text{fast}}(V)$ ), the voltage variable may produce a single action potential, and then slides slowly toward the intersection, which is a stable equilibrium.

## Solutions to Chapter 6

1. There are two equilibria:  $x = 0$  and  $x = b$ . The stability is determined by the sign of the derivative

$$\lambda = (x(b-x))'_x = b - 2x$$

at the equilibrium. Since  $\lambda = b$  when  $x = 0$ , this equilibrium is stable (unstable) when  $b < 0$  ( $b > 0$ ). Since  $\lambda = -b$  when  $x = b$ , this equilibrium is unstable (stable) when  $b < 0$  ( $b > 0$ ).

2. (a) The system

$$\dot{x} = bx^2, \quad b \neq 0$$

cannot exhibit saddle-node bifurcation: It has one equilibrium for any non-zero  $b$ , or an infinite number of equilibria when  $b = 0$ . The equilibrium  $x = 0$  is non-hyperbolic and the non-degeneracy condition is satisfied ( $a = b \neq 0$ ). However, the transversality condition is not satisfied at the equilibrium  $x = 0$ . Another example is  $\dot{x} = b^2 + x^2$ .

- (b) The system

$$\dot{x} = b - x^3$$

has a single stable equilibrium for any  $b$ . However, the point  $x = 0$  is non-hyperbolic when  $b = 0$ , and the transversality condition is also satisfied. The non-degeneracy condition is violated, though.

3. It is easy to check (by differentiating) that

$$V(t) = \frac{\sqrt{c(b - b_{\text{sn}})}}{\sqrt{a}} \tan(\sqrt{ac(b - b_{\text{sn}})}t)$$

is a solution to the system. Since  $\tan(-\pi/2) = -\infty$  and  $\tan(+\pi/2) = +\infty$ , it takes

$$T = \frac{\pi}{\sqrt{ac(b - b_{\text{sn}})}}$$

for the solution to go from  $-\infty$  to  $+\infty$ .

4. The first system can be transformed into the second one if we use complex coordinates  $z = u + iv$ . To obtain the third system, we use polar coordinates

$$re^{i\varphi} = z = u + iv \in \mathbb{C},$$

so that

$$\underbrace{\dot{r}e^{i\varphi} + re^{i\varphi}i\dot{\varphi}}_{\dot{r} - c(b)r - ar^3} = \underbrace{(c(b) + i\omega(b))re^{i\varphi} + (a + id)r^3e^{i\varphi}}_{(c(b) + i\omega(b))z + (a + id)z|z|^2}.$$

Next, we divide both sides of this equation by  $e^{i\varphi}$  and separate the real and imaginary parts to obtain

$$\{\dot{r} - c(b)r - ar^3\} + ir\{\dot{\varphi} - \omega(b) - dr^2\} = 0,$$

which we can write in the polar-coordinates form.

5. (a) The equilibrium  $r = 0$  of the system

$$\begin{aligned}\dot{r} &= br^3, \\ \dot{\varphi} &= 1,\end{aligned}$$

has a pair of complex-conjugate eigenvalues  $\pm i$  for any  $b$ , and the non-degeneracy condition is satisfied for any  $b \neq 0$ . However, the transversality condition is violated, and the system does not exhibit Andronov-Hopf bifurcation (no limit cycle exists near the equilibrium).

- (b) The equilibrium  $r = 0$  for  $b = 0$

$$\begin{aligned}\dot{r} &= br, \\ \dot{\varphi} &= 1,\end{aligned}$$

has a pair of complex-conjugate eigenvalues  $\pm i$  and the transversality condition is satisfied. However, the bifurcation is not of the Andronov-Hopf type because no limit cycle exists near the equilibrium for any  $b$ .

6. The Jacobian matrix at the equilibrium  $(u, v) = (0, 0)$  has the form

$$L = \begin{pmatrix} b & -1 \\ 1 & b \end{pmatrix}.$$

It has eigenvalues  $b \pm i$ . Therefore, the loss of stability occurs at  $b = 0$ , and the non-hyperbolicity and transversality conditions are satisfied. Since the model can be reduced to the polar-coordinate system (see Ex. 4), and  $a \neq 0$ , the non-degeneracy condition is also satisfied, and the system undergoes an Andronov-Hopf bifurcation.

7. Since

$$(cr + ar^3)'_r = c + 3ar^2 = c + 3a|c/a| = \begin{cases} c + 3|c| & \text{when } a > 0, \\ c - 3|c| & \text{when } a < 0, \end{cases}$$

the limit cycle is stable when  $a < 0$

8. The sequence of bifurcations is similar to that of the RS neuron in Fig. 8.15. The resting state is a globally asymptotically stable equilibrium for  $I < 5.64$ . At this value a stable (spiking) limit cycle appears via a big saddle homoclinic orbit bifurcation. At  $I = 5.8$  a small-amplitude unstable limit cycle is born via another saddle homoclinic orbit bifurcation. This cycle shrinks to the equilibrium and makes it lose stability via subcritical Andronov-Hopf bifurcation at  $I = 6.5$ . This unstable focus becomes an unstable node when  $I$  increases, and then it coalesces with the saddle (at  $I = 7.3$ ) and disappears. Notice that there is a saddle-node bifurcation according to the I-V relation, but it corresponds to the disappearance of an unstable equilibrium.

9. The Jacobian matrix of partial derivatives has the form

$$L = \begin{pmatrix} -I'_V(V, x) & -I'_x(V, x) \\ x'_\infty(V)/\tau(V) & -1/\tau(V) \end{pmatrix},$$

so that

$$\text{tr } L = -\{I'_V(V, x) + 1/\tau(V)\}$$

and

$$\det L = \{I'_V(V, x) + I'_x(V, x)x'_\infty(V)\}/\tau(V) = I'_\infty(V)/\tau(V).$$

The characteristic equation

$$\lambda^2 - \lambda \text{tr } L + \det L = 0$$

has two solutions

$$\overbrace{(\text{tr } L)/2}^c \pm \overbrace{\sqrt{\{(\text{tr } L)/2\}^2 - \det L}}^\omega$$

which might be complex-conjugate.

10. Let  $z = re^{\varphi i}$ , then

$$\begin{aligned} r' &= ar + r^3 - r^5, \\ \varphi' &= \omega. \end{aligned}$$

Any limit cycle is an equilibrium of the amplitude equation, i.e.,

$$a + r^2 - r^4 = 0.$$

The system undergoes fold limit cycle bifurcation when the amplitude equation undergoes a saddle-node bifurcation, i.e., when

$$a + 3r^2 - 5r^4 = 0$$

(check the non-degeneracy and transversality conditions). The two equations have the non-trivial solution  $(a, r) = (-1/4, 1/\sqrt{2})$ .

11. The projection onto the  $v_1$ -axis is described by the equation

$$\dot{x} = \lambda_1 x, \quad x(0) = a.$$

The trajectory leaves the square when  $x(t) = ae^{\lambda_1 t} = 1$ ; that is, when

$$t = -\frac{1}{\lambda_1} \ln a = -\frac{1}{\lambda_1} \ln \tau(I - I_b).$$

12. Equation (6.13) has two bifurcation parameters,  $b$  and  $v$ , and the saddle-node homoclinic bifurcation occurs when  $b = b_{\text{sn}}$  and  $v = V_{\text{sn}}$ . The saddle-node bifurcation curve is the straight line  $b = b_{\text{sn}}$  (any  $v$ ). This bifurcation is *on* an invariant circle when  $v < V_{\text{sn}}$  and *off* otherwise. When  $b > b_{\text{sn}}$ , there are no equilibria and the normal form exhibits periodic spiking. When  $b < b_{\text{sn}}$ , the normal form has two equilibria,

$$\underbrace{V_{\text{sn}} - \sqrt{c|b - b_{\text{sn}}|/a}}_{\text{node}} \quad \text{and} \quad \underbrace{V_{\text{sn}} + \sqrt{c|b - b_{\text{sn}}|/a}}_{\text{saddle}}.$$

The saddle homoclinic orbit bifurcation occurs when the voltage is reset to the saddle, i.e., when

$$v = V_{\text{sn}} + \sqrt{c|b - b_{\text{sn}}|/a}.$$

13. The Jacobian matrix at an equilibrium is

$$L = \begin{pmatrix} 2v & -1 \\ ab & -a \end{pmatrix}.$$

Saddle-node condition  $\det L = -2va + ab = 0$ , results in  $v = b/2$ . Since  $v$  is an equilibrium, it satisfies  $v^2 - bv + I = 0$ , hence  $b^2 = 4I$ . Andronov-Hopf condition  $\text{tr } L = 2v - a = 0$  results in  $v = a/2$ , hence  $a^2/4 - ab/2 + I = 0$ . The bifurcation occurs when  $\det L > 0$ , resulting in  $a < b$ . Combining the saddle-node and Andronov-Hopf conditions results in the Bogdanov-Takens conditions.

14. Change of variables (6.5),  $v = x$  and  $u = \sqrt{\mu}y$ , transforms the relaxation oscillator into the form

$$\begin{aligned} \dot{x} &= f(x) - \sqrt{\mu}y \\ \dot{y} &= \sqrt{\mu}(x - b) \end{aligned} \quad \text{with the Jacobian} \quad L = \begin{pmatrix} f'(b) & -\sqrt{\mu} \\ \sqrt{\mu} & 0 \end{pmatrix}$$

at the equilibrium  $v = x = b$ ,  $u = \sqrt{\mu}y = f(b)$ . The Andronov-Hopf bifurcation occurs when  $\text{tr } L = f'(b) = 0$  and  $\det L = \mu > 0$ . Using (6.7), we find that it is supercritical when  $f'''(b) < 0$  and subcritical when  $f'''(b) > 0$ .

15. The Jacobian matrix at the equilibrium, which satisfies  $F(v) - bv = 0$ , is

$$L = \begin{pmatrix} F' & -1 \\ \mu b & -\mu \end{pmatrix}.$$

The Andronov-Hopf bifurcation occurs when  $\text{tr } L = F' - \mu = 0$  (hence  $F' = \mu$ ) and  $\det L = \omega^2 = \mu b - \mu^2 > 0$  (hence  $b > \mu$ ). The change of variables (6.5),  $v = x$  and  $u = \mu x + \omega y$ , transforms the system into the form

$$\begin{aligned} \dot{x} &= -\omega y + f(x) \\ \dot{y} &= \omega x + g(x) \end{aligned}$$

where  $f(x) = F(x) - \mu x$  and  $g(x) = \mu[bx - F(x)]/\omega$ . The result follows from (6.7).

16. The change of variables (6.5) converts the system into the form

$$\begin{aligned}\dot{x} &= F(x) + \text{linear terms} \\ \dot{y} &= \mu(G(x) - F(x))/\omega + \text{linear terms}\end{aligned}$$

The result follows from (6.7).

17. The change of variables (6.5),  $v = x$  and  $u = \mu x + \omega y$ , converts the system into

$$\begin{aligned}\dot{x} &= F(x) - x(\mu x + \omega y) + \text{linear terms} \\ \dot{y} &= \mu[G(x) - F(x) + x(\mu x + \omega y)]/\omega\end{aligned}$$

The result follows from (6.7).

18. The system undergoes Andronov-Hopf bifurcation when  $F_v = -\mu G_u$  and  $F_u G_v < -\mu G_u^2$ . We perform all the steps from (6.4) to (6.7) disregarding linear terms (they do not influence  $a$ ) and the terms of the order  $\mathcal{O}(\mu)$ . Let  $\omega = \sqrt{-\mu F_u G_v} + \mathcal{O}(\mu)$ , then  $u = (\mu G_u x - \omega y)/F_u = -\omega y/F_u + \mathcal{O}(\mu)$ , and

$$f(x, y) = F(x, -\omega y/F_u + \mathcal{O}(\mu)) = F(x, 0) - F_u(x, 0)\omega y/F_u + \mathcal{O}(\mu)$$

and

$$g(x, y) = (\mu/\omega)[G_u F(x, 0) - F_u G(x, 0)] + \mathcal{O}(\mu).$$

The result follows from (6.7).

## Solutions to Chapter 7

1. Take  $c < 0$  so that the slow  $w$ -nullcline has a negative slope.
2. The quasi-threshold contains the union of canard solutions.
3. The change of variables  $z = e^{i\omega t}u$  transforms the system into the form

$$\dot{u} = \varepsilon\{-u + e^{-i\omega t}I(t)\},$$

which can be averaged, yielding

$$\dot{u} = \varepsilon\{-u + I^*(\omega)\}.$$

Apparently, the stable equilibrium  $u = I^*(\omega)$  corresponds to the sustained oscillation  $z = e^{i\omega t}I^*(\omega)$ .

4. The existence of damped oscillations with frequency  $\omega$  implies that the system has a focus equilibrium with eigenvalues  $-\varepsilon \pm i\omega$ , where  $\varepsilon > 0$ . The local dynamics near the focus can be represented in the form (7.3). The rest of the proof is the same as the one for Ex. 3.
5. Even though the slow and the fast nullclines in Fig. 5.21 intersect only in one point, they continue to be close and parallel to each other in the voltage range 10 mV to 30 mV. Such a proximity creates a tunneling effect (Rush and Rinzel 1996) that prolongs the time spent near those nullclines.
6. (Shilnikov-Hopf bifurcation) The model is near a co-dimension-2 bifurcation having a homoclinic orbit to an equilibrium undergoing subcritical Andronov-Hopf bifurcation, as we illustrate in Fig. 10.28. Many weird phenomena could happen near bifurcations of co-dimension 2 or higher.

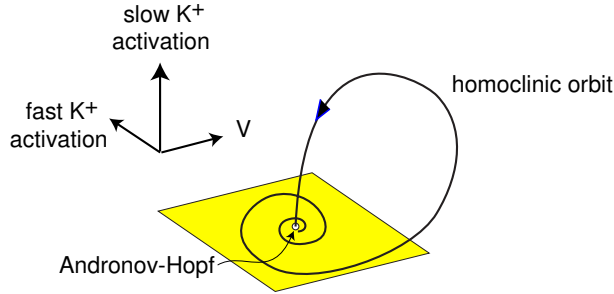


Figure 10.28: Co-dimension-2 Shilnikov-Hopf bifurcation.

## Solutions to Chapter 8

1. Consider two mutually coupled neurons firing together.
2. The equation

$$\dot{V} = c(b - b_{\text{sn}}) + a(V - V_{\text{sn}})^2,$$

can be written in the form

$$\dot{V} = a(V - V_{\text{rest}})(V - V_{\text{thresh}}).$$

with

$$V_{\text{rest}} = V_{\text{sn}} - \sqrt{c(b_{\text{sn}} - b)/a} \quad \text{and} \quad V_{\text{thresh}} = V_{\text{sn}} + \sqrt{c(b_{\text{sn}} - b)/a}$$

provided that  $b < b_{\text{sn}}$ .

3. The system  $\dot{v} = b + v^2$  with  $b > 0$  and the initial condition  $v(0) = v_{\text{reset}}$  has the solution (check by differentiating)

$$v(t) = \sqrt{b} \tan(\sqrt{b}(t + t_0))$$

where

$$t_0 = \frac{1}{\sqrt{b}} \operatorname{atan} \frac{v_{\text{reset}}}{\sqrt{b}}.$$

From the condition  $v(T) = v_{\text{peak}} = 1$ , we find

$$T = \frac{1}{\sqrt{b}} \operatorname{atan} \frac{1}{\sqrt{b}} - t_0 = \frac{1}{\sqrt{b}} \left( \operatorname{atan} \frac{1}{\sqrt{b}} - \operatorname{atan} \frac{v_{\text{reset}}}{\sqrt{b}} \right),$$

which can be alternatively written as

$$T = \frac{1}{\sqrt{b}} \operatorname{atan} \left( \sqrt{b} \frac{v_{\text{reset}} - 1}{v_{\text{reset}} + b} \right).$$

4. The system  $\dot{v} = -|b| + v^2$  with the initial condition  $v(0) = v_{\text{reset}} > \sqrt{|b|}$  has the solution (check by differentiating)

$$v(t) = \sqrt{|b|} \frac{1 + e^{2\sqrt{|b|}(t+t_0)}}{1 - e^{2\sqrt{|b|}(t+t_0)}},$$

where

$$t_0 = \frac{1}{2\sqrt{|b|}} \ln \frac{v_{\text{reset}} - \sqrt{|b|}}{v_{\text{reset}} + \sqrt{|b|}}.$$

From the condition  $v(T) = 1$ , we find

$$T = \frac{1}{2\sqrt{|b|}} \left( \ln \frac{1 - \sqrt{|b|}}{1 + \sqrt{|b|}} - \ln \frac{v_{\text{reset}} - \sqrt{|b|}}{v_{\text{reset}} + \sqrt{|b|}} \right).$$

5. The saddle-node bifurcation occurs when  $b = 0$  regardless of the value of  $v_{\text{reset}}$ , which is a straight vertical line in Fig. 8.3. If  $v_{\text{reset}} < 0$ , then the saddle-node bifurcation is on an invariant circle. When  $b < 0$ , the unstable node (saddle) equilibrium is at  $v = \sqrt{|b|}$ . Hence, the saddle homoclinic orbit bifurcation occurs when  $v_{\text{reset}} = \sqrt{|b|}$ .
6. The change of variables  $v = g/2 + V$ ,  $b = g^2/4 + B$  transforms  $\dot{v} = b - gv + v^2$  to  $\dot{V} = B + V^2$  with  $V_{\text{reset}} = -\infty$  and  $V_{\text{peak}} = +\infty$ . It has threshold  $V = \sqrt{B}$ , rheobase  $B = 0$  and the same F-I curve as in the original model with  $g = 0$ . In  $v$ -coordinates, the threshold is  $v = g/2 + \sqrt{b - g^2/4}$ , which is greater than  $\sqrt{b}$ , the new rheobase is  $b = g^2/4$ , which is greater than  $b = 0$ , and the new F-I curve is the same as the old one, just shifted to the right by  $g^2/4$ .
7. Let  $b = \varepsilon r$  with  $\varepsilon \ll 1$  be a small parameter. The change of variables

$$v = \sqrt{\varepsilon} \tan \frac{\vartheta}{2}$$

transforms (8.2) into the theta-neuron form

$$\dot{\vartheta} = \sqrt{\varepsilon} \{(1 - \cos \vartheta) + (1 + \cos \vartheta)r\} .$$

uniformly on the unit circle except the small interval  $|\vartheta - \pi| < 2\sqrt[4]{\varepsilon}$  corresponding to the action potential ( $v > 1$ ); see Hoppensteadt and Izhikevich (1997) for more details.

8. Use the change of variables

$$v = \frac{\sqrt{\varepsilon} \vartheta}{1 - |\vartheta|} .$$

To obtain other theta neuron models, use the change of variables

$$v = \sqrt{\varepsilon} h(\vartheta) ,$$

where the monotone function  $h$  maps  $(-\pi, \pi)$  to  $(-\infty, \infty)$  and scales like  $1/(\vartheta \pm \pi)$  when  $\vartheta \rightarrow \pm\pi$ . The corresponding model has the form

$$\dot{\vartheta}' = h^2(\vartheta)/h'(\vartheta) + r/h'(\vartheta) .$$

In particular,  $h^2(\vartheta)/h'(\vartheta)$  exists and is bounded and  $1/h'(\vartheta) = 0$  when  $\vartheta \rightarrow \pm\pi$ . These imply a uniform velocity independent from the input  $r$  when  $\vartheta$  passes the value  $\pm\pi$  corresponding to firing a spike.

9. The equilibrium  $v = I/(b+1)$ ,  $u = bI/(b+1)$  has the Jacobian matrix

$$L = \begin{pmatrix} -1 & -1 \\ ab & -a \end{pmatrix}$$

with  $\text{tr}L = -(a+1)$  and  $\det L = a(b+1)$ . It is a stable node (integrator) when  $b < (a+1)^2/(4a) - 1$  and a stable focus (resonator) otherwise.

10. The quadratic integrate-and-fire neuron with a dendritic compartment

$$\begin{aligned} \dot{V} &= B + V^2 + g_1(V_d - V) \\ \dot{V}_d &= g_{\text{leak}}(E_{\text{leak}} - V_d) + g_2(V - V_d) \end{aligned}$$

can be written in the form (8.3, 8.4), with  $v = V - g_1/2$ ,  $u = -g_1 V_d$ ,  $I = B - g_1^2/4 - (g_1^2 g_2 + g_{\text{leak}} E_{\text{leak}})/(g_{\text{leak}} + g_2)$ ,  $a = g_{\text{leak}} + g_2$ , and  $b = -g_1 g_2/a$ .

11. A MATLAB program generating the figure is provided on the author's webpage.
12. An example is in Fig. 10.29.
13. An example is in Fig. 10.30.

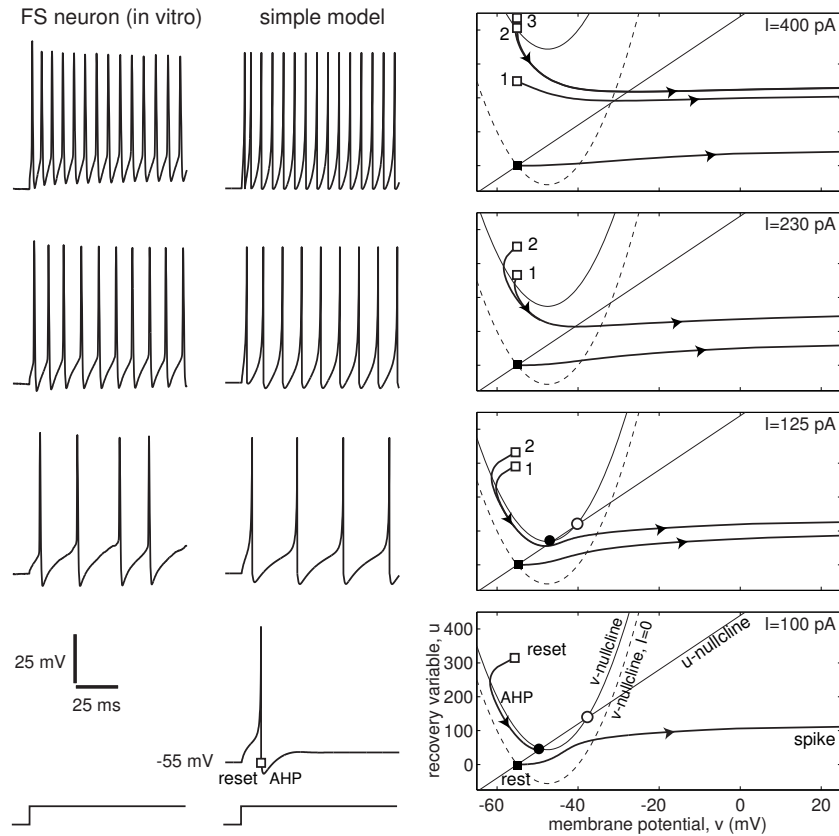


Figure 10.29: Comparison of *in vitro* recordings of a fast spiking (FS) interneuron of layer 5 rat's visual cortex with simulations of the simple model with linear slow nullcline  $20\dot{v} = (v + 55)(v + 40) - u + I$ ,  $\dot{u} = 0.15\{8(v + 55) - u\}$ , if  $v \geq 25$ , then  $v \leftarrow -55$ ,  $u \leftarrow u + 200$ .

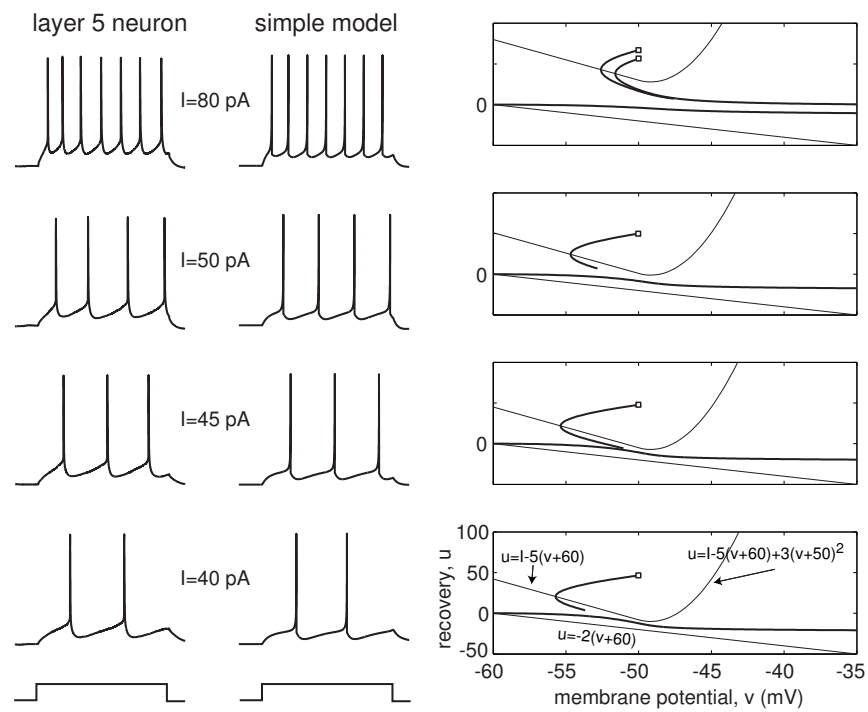


Figure 10.30: Comparison of *in vitro* recordings of a regular spiking (RS) neuron with simulations of the simple model  $100\dot{v} = I - 5(v + 60) + 3(v + 50)_+^2 - u$ ,  $\dot{u} = 0.02\{-2(v + 60) - u\}$ , if  $v \geq 35$ , then  $v \leftarrow -50$ ,  $u \leftarrow u + 70$ .

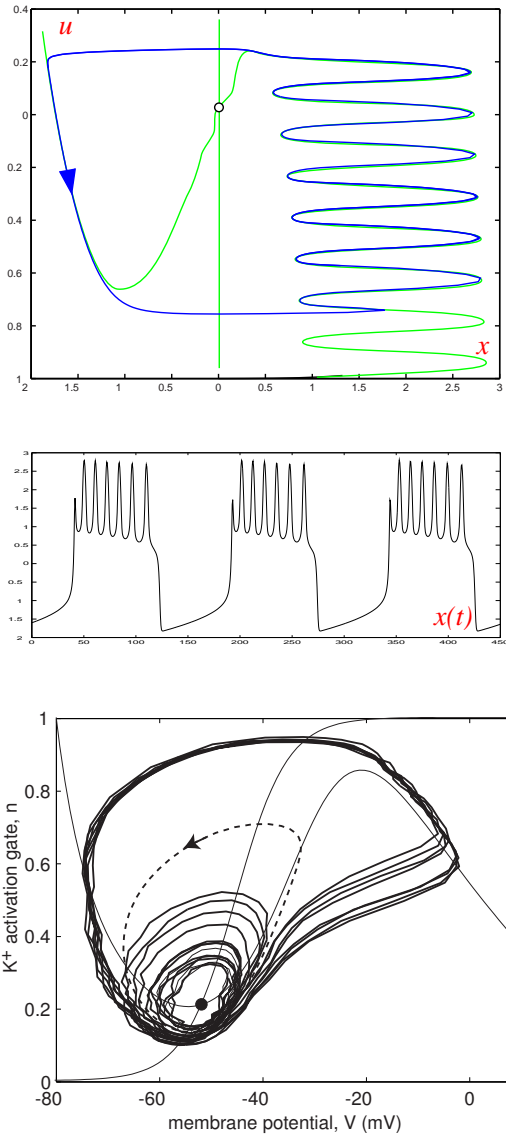


Figure 10.31: Solution to Ex. 1. Nullclines, hedgehog limit cycle and a bursting solution of a planar system (modified from Izhikevich 2000).

Figure 10.32: Noise-induced bursting in two-dimensional system; See Ex. 2.

## Solutions to Chapter 9

1. (Planar burster) Izhikevich (2000) suggested the system

$$\begin{aligned}\dot{x} &= x - x^3/3 - u + 4S(x) \cos 40u, \\ \dot{u} &= \mu x,\end{aligned}$$

with  $S(x) = 1/(1 + e^{5(1-x)})$  and  $\mu = 0.01$ . It has a hedgehog limit cycle depicted in Fig. 10.31.

2. (Noise-induced bursting) Noise can induce bursting in a two-dimensional system with co-existence of resting and spiking states. Indeed, noisy perturbations can randomly push the state of the system into the attraction domain of the resting state or into the attraction domain of the limit cycle attractor, as in Fig. 10.32. The solution meanders between the states, exhibiting a random bursting pattern as in Fig. 9.55,right. neocortical neurons of RS and FS type, as well as stellate neurons of the entorhinal cortex exhibit such bursting; see Chap. 8.

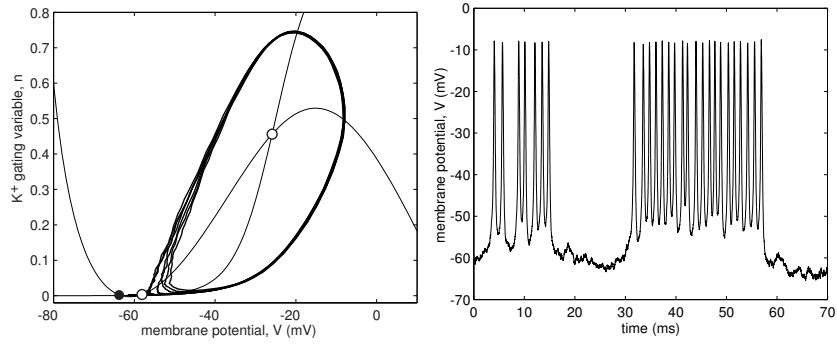


Figure 10.33: Noise-induced bursting a two-dimensional system with co-existence of an equilibrium and a limit cycle attractor; see Ex. 3.

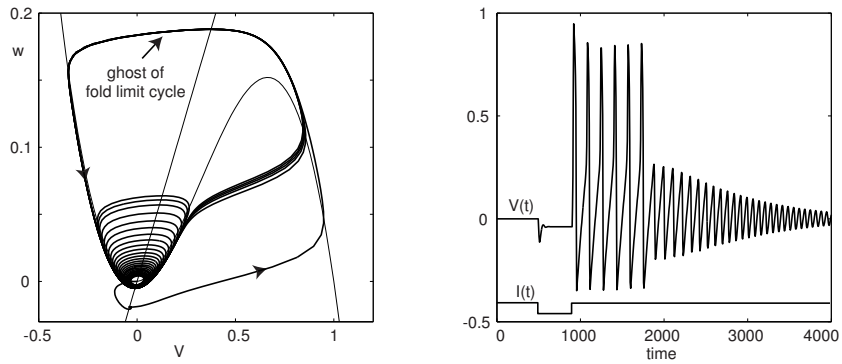


Figure 10.34: Rebound bursting in the FitzHugh-Nagumo oscillator; see Ex. 4.

3. (Noise-induced bursting) Bursting occurs because noisy perturbations push the trajectory into and out of the attraction domain of the limit cycle attractor, which coexists with the resting equilibrium; see the phase portrait in Fig. 10.33.
4. (Rebound bursting in the FitzHugh-Nagumo oscillator) The oscillator is near fold limit cycle bifurcation. The solution makes a few rotations along the ghost of the cycle before returning to rest; see Fig. 10.34.
5. Yes, they can, at the end of a burst. Think of a “fold/Hopf” or “circle/Hopf” burster. The resting equilibrium is a stable focus right after the termination of a burst, and then it is transformed into a stable node to be ready for the circle or fold bifurcation. Even “circle/circle” bursters could exhibit such oscillations, if the resting equilibrium turns into a focus for a short period of time somewhere in the middle of a quiescent phase. In any case, the oscillations should disappear just before the transition to the spiking state.
6. (Hopf/Hopf bursting) Even though there is no co-existence of attractors, there is a hysteresis loop due to the slow passage effect through the supercritical Andronov-Hopf bifurcation; see Fig. 10.35. The delayed transition to spiking creates the hysteresis loop and enables bursting.
7. (Hopf/Hopf canonical model) First, we restrict the fast subsystem to its center manifold and transform it to the normal form for supercritical Andronov-Hopf bifurcation, which after appropriate re-scaling, has the form

$$\dot{z} = (u + i\omega)z - z|z|^2 .$$

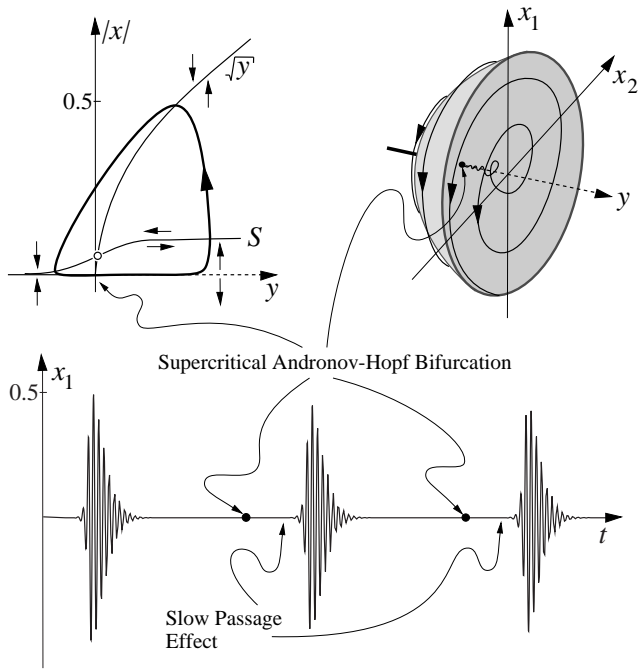


Figure 10.35: Hopf/Hopf bursting without co-existence of attractors; see Ex. 6 (modified from Hoppensteadt and Izhikevich 1997).

Here,  $u$  is the deviation from the slow equilibrium  $u_0$ . The slow subsystem

$$\dot{u} = \mu g(ze^{i\omega t} + \text{complex-conjugate}, u)$$

can be averaged and transformed into the canonical form.

8. (Bursting in the  $I_{Na,t}+I_{Na,\text{slow}}$ -model) First, determine the parameters of the  $I_{Na,t}$ -model corresponding to the subcritical Andronov-Hopf bifurcation, and hence the co-existence of the resting and spiking states. Then, add a slow high-threshold persistent  $\text{Na}^+$  current that activates during spiking, depolarizes the membrane potential and stops the spiking. During resting, the current deactivates, the membrane potential hyperpolarizes and the neuron starts to fire again.
9. Substitute the slow  $\text{Na}^+$  current in the exercise above with a slow dendritic compartment with dendritic resting potential far below the somatic resting potential. As the dendritic compartment hyperpolarizes the somatic compartment, the soma starts to fire (due to the inhibition-induced firing described in Sect. 7.2.8). As the somatic compartment fires, dendritic compartment slowly depolarizes, removes the hyperpolarization and stops firing.
10. (Bursting in the  $I_{Na,p}+I_K+I_{Na,\text{slow}}$ -model) The time constant  $\tau_{\text{slow}}(V)$  is relatively small in the voltage range corresponding to the spike after-hyperpolarization (AHP). Deactivation of the  $\text{Na}^+$  current during each AHP is much stronger than its activation during the spike peak. As a result,  $\text{Na}^+$  current deactivates (turns off) during the burst, and then slowly reactivates to its baseline level during the resting period, as one can see in Fig. 10.36.
11. The mechanism of spiking, illustrated in Fig. 10.37, is closely related to the phenomenon of accommodation and anodal break excitation. The key feature is that this bursting is not fast-slow.

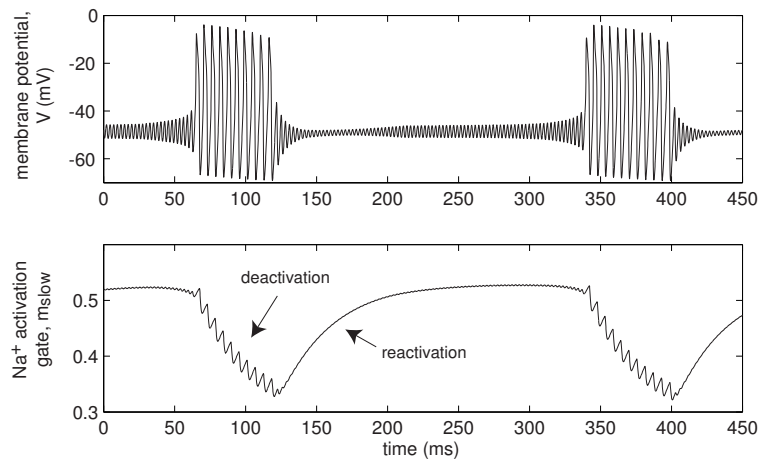


Figure 10.36: Bursting in the  $I_{\text{Na,p}} + I_K + I_{\text{Na,slow}}$ -model. See Ex. 10.

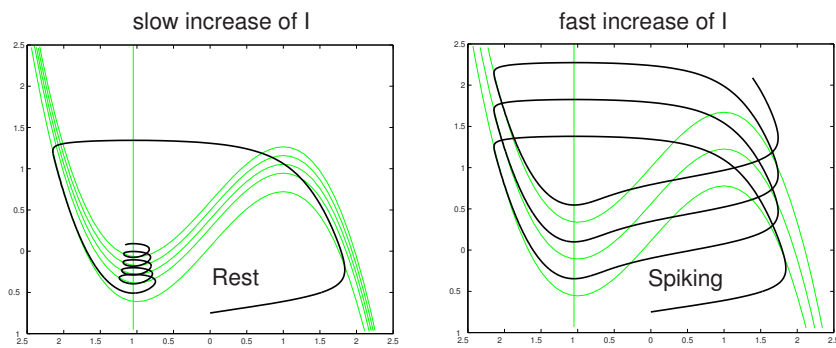


Figure 10.37: The system has a unique attractor — equilibrium, yet it can exhibit repetitive spiking activity when the N-shaped nullcline is moved up not very slow.

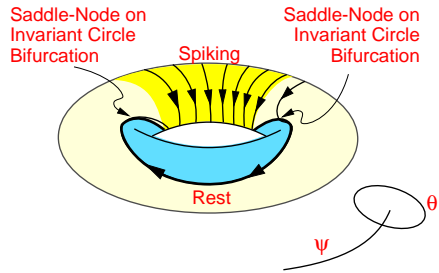


Figure 10.38: Answer to Ex. 13.

The system has a unique attractor — a stable equilibrium, and the solution always converges to it. The slow variable  $I$  controls the vertical position of the N-shaped nullcline. If  $I$  increases, the nullcline moves up slowly, and so does the solution because it tracks the equilibrium. However, if the rate of change of  $I$  is not small enough, the solution cannot catch up with the equilibrium and starts to oscillate with a large amplitude. Thus, the system exhibits spiking behavior even though it does not have a limit cycle attractor for any fixed  $I$ .

12. From the first equation, we find the equivalent voltage

$$|z|^2 = |1 + u|_+ = \begin{cases} 1 + u & \text{if } 1 + u > 0, \\ 0 & \text{if } 1 + u \leq 0, \end{cases}$$

so that the reduced slow subsystem has the form

$$\begin{aligned} \dot{u} &= \mu[u - u^3 - w], \\ \dot{w} &= \mu[|1 + u|_+ - 1], \end{aligned}$$

and it has essentially the same dynamics as the van der Pol oscillator.

13. The fast equation

$$\dot{\vartheta} = 1 - \cos \vartheta + (1 + \cos \vartheta)r$$

is the Ermentrout-Kopell canonical model for Class 1 excitability, also known as the theta neuron (Ermentrout 1996). It is quiescent when  $r < 0$  and fires spikes when  $r > 0$ . As  $\psi$  oscillates with frequency  $\omega$ , the function  $r = r(\psi)$  changes sign. The fast equation undergoes a saddle-node on invariant circle bifurcation, hence the system is a “circle/circle” burster of the slow-wave type; see Fig. 10.38.

14. To understand the bursting dynamics of the canonical model, we rewrite it in polar coordinates  $z = re^{i\varphi}$ :

$$\begin{aligned} \dot{r} &= ur + 2r^3 - r^5, \\ \dot{u} &= \mu(a - r^2), \\ \dot{\varphi} &= \omega. \end{aligned}$$

Apparently, it is enough to consider the first two equations, which determine the oscillation profile. Nontrivial ( $r \neq 0$ ) equilibria of this system correspond to limit cycles of the canonical model, which may look like periodic (tonic) spiking with frequency  $\omega$ . Limit cycles of this system correspond to quasi-periodic solutions of the canonical model, which look like bursting; see Fig. 9.37.

The first two equations above have a unique equilibrium

$$\begin{pmatrix} r \\ u \end{pmatrix} = \begin{pmatrix} \sqrt{a} \\ a^2 - 2a \end{pmatrix}$$

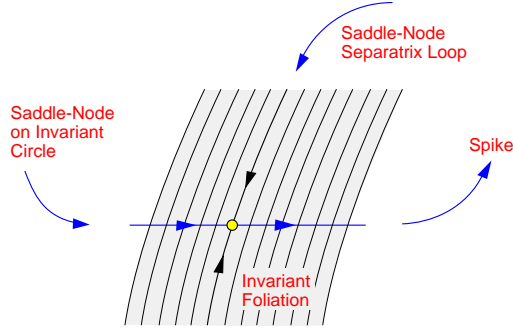


Figure 10.39: A small neighborhood of the saddle-node point can be invariantly foliated by stable submanifolds.

for all  $\mu$  and  $a > 0$ , which is stable when  $a > 1$ . When  $a$  decreases and passes an  $\mu$ -neighborhood of  $a = 1$ , the equilibrium loses stability via Andronov-Hopf bifurcation. When  $0 < a < 1$ , the system has a limit cycle attractor. Therefore, the canonical model exhibits bursting behavior. The smaller the value of  $a$ , the longer the interburst period. When  $a \rightarrow 0$ , the interburst period becomes infinite.

15. Take  $w = I - u$ . Then (9.7) becomes

$$\begin{aligned}\dot{v} &= v^2 + w, \\ \dot{w} &= \mu(I - w) \approx \mu I.\end{aligned}$$

16. Let us sketch the derivation. Since the fast subsystem is near saddle-node homoclinic orbit bifurcation for some  $u = u_0$ , a small neighborhood of the saddle-node point  $v_0$  is invariantly foliated by stable submanifolds, as in Fig. 10.39. Because the contraction along the stable submanifolds is much stronger than the dynamics along the center manifold, the fast subsystem can be mapped into the normal form  $\dot{v} = q(u) + p(v - v_0)^2$  by a continuous change of variables. When  $v$  escapes the small neighborhood of  $v_0$ , the neuron is said to fire a spike, and  $v$  is reset  $v \leftarrow v_0 + c(u)$ . Such a stereotypical spike also resets  $u$  by a constant  $d$ . If  $g(v_0, u_0) \approx 0$ , then all functions are small, and linearization and appropriate re-scaling yields the canonical model. If  $g(v_0, u_0) \neq 0$ , then the canonical model has the same form as in the previous exercise.

17. The derivation proceeds as in the previous exercise, yielding

$$\begin{aligned}\dot{v} &= I + v^2 + (a, u), \\ \dot{u} &= \mu Au.\end{aligned}$$

where  $(a, u)$  is the scalar (dot) product of vectors  $a, u \in \mathbb{R}^2$ , and  $A$  is the Jacobian matrix at the equilibrium of the slow subsystem. If the equilibrium is a node, it has generically two distinct eigenvalues, and two real eigenvectors. In this case, the slow subsystem uncouples into two equations, each along the corresponding eigenvector. Appropriate re-scaling gives the first canonical model. If the equilibrium is a focus, the linear part can be made triangular to get the second canonical model.

18. The solution of the fast subsystem

$$\dot{v} = u + v^2, \quad v(0) = -1,$$

with fixed  $u > 0$  is

$$v(t) = \sqrt{u} \tan \left( \sqrt{u}t - \arctan \frac{1}{\sqrt{u}} \right)$$

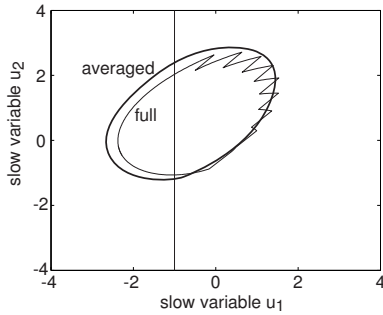


Figure 10.40: Ex. 18.

The interspike period,  $T$ , is defined by  $v(T) = +\infty$ , given by the formula

$$T(u) = \frac{1}{\sqrt{u}} \left( \frac{\pi}{2} + \arctan \frac{1}{\sqrt{u}} \right).$$

The result follows from the integral

$$\frac{1}{T(u)} \int_0^{T(u)} d_i \delta(t - T(u)) dt = \frac{d_i}{T(u)}$$

and the relationships

$$f(u) = \frac{1}{T(u)} \quad \text{and} \quad \arctan \frac{1}{\sqrt{u}} = \text{arcot } \sqrt{u}.$$

Periodic solutions of the averaged system (focus case) and the full system are depicted in Fig. 10.40. The deviation is due to the finite size of the parameters  $\mu_1$  and  $\mu_2$  in Fig. 9.35.

19. There are only two co-dimension-1 bifurcations of an equilibrium that result in transitions to another equilibrium: saddle-node *off* limit cycle and subcritical Andronov-Hopf bifurcation. Hence, there are four point-point hysteresis loops, depicted in Fig. 10.41. More details are provided in Izhikevich (2000).
20. This figure is modified from (Izhikevich 2000), where one can find two models exhibiting this phenomenon. The key feature is that the slow subsystem is not too slow, and the rate of attraction to the upper equilibrium is relatively weak. The spikes are actually damped oscillations that are generated by the fast subsystem while it converges to the equilibrium. Periodic bursting is generated via the point-point hysteresis loop.
21. There are only two co-dimension-1 bifurcations of a small limit cycle attractor (subthreshold oscillation) on a plane that result in sharp transitions to a large-amplitude limit cycle attractor (spiking): Fold limit cycle bifurcation and saddle-homoclinic orbit bifurcation; see Fig. 10.42. These two bifurcations paired with any of the four bifurcations of the large-amplitude limit cycle attractor result in 8 planar co-dimension-1 cycle-cycle bursters; see Fig. 10.43. More details are provided by Izhikevich (2000).

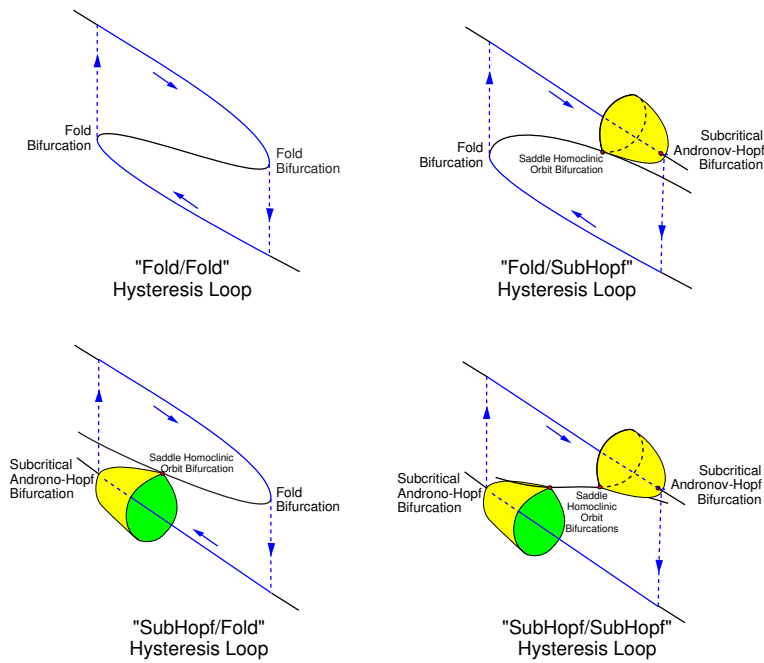


Figure 10.41: Classification of point-point co-dimension-1 hysteresis loops.

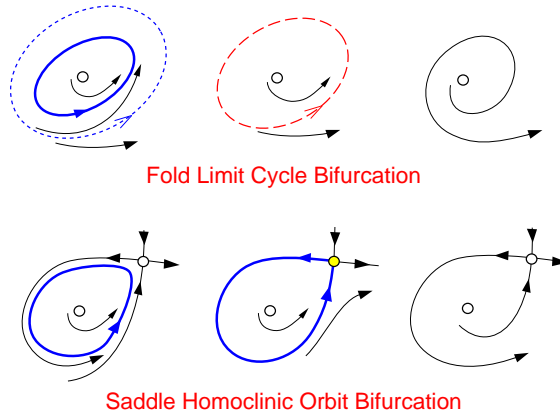


Figure 10.42: Co-dimension-1 bifurcations of a stable limit cycle in planar systems that result in sharp loss of stability and transition to a large-amplitude (spiking) limit cycle attractor, not shown in the figure. *Fold limit cycle*: Stable limit cycle is approached by an unstable one, they coalesce, and then disappear. *Saddle homoclinic orbit*: A limit cycle grows into a saddle. The unstable manifold of the saddle makes a loop and returns via the stable manifold (separatrix).

<i>Bifurcations</i>	<i>Saddle-Node on Invariant Circle</i>	<i>Saddle <b>Homoclinic</b> Orbit</i>	<i>Supercritical Andronov- Hopf</i>	<b>Fold Limit Cycle</b>
<b>Fold Limit Cycle</b>	fold cycle/ circle	fold cycle/ homoclinic	fold cycle/ Hopf	fold cycle/ fold cycle
<i>Saddle <b>Homoclinic</b> Orbit</i>	homoclinic/ circle	homoclinic/ homoclinic	homoclinic/ Hopf	homoclinic/ fold cycle

Figure 10.43: Classification of co-dimension-1 cycle-cycle planar bursters.

# References

- Acebron J. A., Bonilla L.L., Vincente C.J. P., Ritort F., Spigler R. (2005) The Kuramoto model: a simple paradigm for synchronization phenomena. *Review of Modern Physics.* 77:137–185
- Alonso A. and Klink R. (1993) Differential Electroresponsiveness of Stellate and Pyramidal-Like Cells of Medial Entorhinal Cortex Layer II. *Journal of Neurophysiology,* 70:128–143.
- Alonso A and Llinas R. R. (1989) Subthreshold  $\text{Na}^+$ -dependent theta-like rhythmicity in stellate cells of entorhinal cortex layer II. *Nature,* 342:175–177.
- Amini, B., Clark J. W. Jr., and Canavier C. C. (1999) Calcium Dynamics Underlying Pacemaker-Like and Burst Firing Oscillations in Midbrain Dopaminergic Neurons: A Computational Study. *J. Neurophysiol.* 82:2249–2261,
- Amir R., Michaelis M., Devor M. (2002) Burst Discharge in Primary Sensory Neurons: Triggered by Subthreshold Oscillations, Maintained by Depolarizing Afterpotentials. *Journal of Neuroscience,* 22:1187–1198.
- Armstrong C.M. and Hille B. (1998) Voltage-Gated Ion Channels and Electrical Excitability. *Neuron* 20:371–380.
- Arnold V.I. (1965) Small denominators. I. Mappings of the circumference onto itself. *Trans. of the AMS Series 2,* 46:213–284.
- Arnold V.I. (1982) Geometrical Methods in the Theory of Ordinary Differential Equations. Springer-Verlag, New York, [Russian original: Additional Chapters of the Theory of Ordinary Differential Equations, Moscow 1977].
- Arnold V.I., Afraimovich V.S., Il'yashenko Yu.S., Shil'nikov L.P. (1994) Dynamical Systems V. Bifurcation Theory and Catastrophe Theory. Springer-Verlag, Berlin Heidelberg.
- Aronson D.G., Ermentrout G.B., and Kopell N. (1990) Amplitude response of coupled oscillators. *Physica D* 41:403–449.
- Arshavsky Y.I., Berkinblit M.B., Kovalev S.A., Smolyaninov V.V., and Chaylakhyan L.M. (1971) An analysis of the functional properties of dendrites in relation to their structure, in: I.M. Gelfand, Gurinskii, S.V. Fomin, M.L. Zetlin (Eds.), *Models of the Structural and Functional Organization of Certain Biological Systems,* MIT Press, Cambridge, Massachusetts, 1971, pp. 25–71.
- Bacci, A., Rudolph, U., Huguenard, J.R. and Prince, D.A. (2003) Major differences in inhibitory synaptic transmission onto two neocortical interneuron subclasses. *J. Neurosc.* 23:9664–9674.
- Bacci A., Huguenard J.R., Prince D.A. (2003) Long-lasting self-inhibition of neocortical in-

- terneurons mediated by endocannabinoids. *nature*, 431:312–316.
- Baer S.M., Erneux T., and Rinzel J. (1989) The slow passage through a Hopf bifurcation: delay, memory effects, and resonances. *SIAM Journal on Applied Mathematics* 49:55–71.
- Baer S.M., Rinzel J., and Carrillo H. (1995) Analysis of an autonomous phase model for neuronal parabolic bursting. *Journal of Mathematical Biology* 33:309–333.
- Baesens, C., Guckenheimer, J., Kim, S. and MacKay, R. S. (1991) Three coupled oscillators: mode-locking, global bifurcations and toroidal chaos. *Physica D*, 49, 387–475.
- Baker M.D. and Bostock H. (1997) Low-threshold, Persistent Sodium Current in Rat Large Dorsal Root Ganglion Neurons in Culture, *J. Neurophysiol.*, 77:1503-1513.
- Baker M.D. and Bostock H. (1998) Inactivation of Macroscopic Late  $\text{Na}^+$  Current and Characteristics of Unitary Late  $\text{Na}^+$  Currents in Sensory Neurons, *J. Neurophysiol.*, 80:2538-2549.
- Bautin N.N. (1949) The behavior of dynamical systems near to the boundaries of stability. *Gostekhizdat.*, Moscow-Leningrad, 2nd edition, Nauka, Moscow (1984).
- Beierlein M., Gibson J.R., and Connors B.W. (2003) Two Dynamically Distinct Inhibitory Networks in Layer 4 of the Neocortex. *Journal of Neurophysiology*, 90:2987–3000.
- Bekkers J.M. (2000) Properties of voltage-gated potassium currents in nucleated patches from large layer 5 pyramidal neurons of the rat. *Journal of Physiology*, 525.3:593–609
- Benoit E. (1984) Canards de  $\mathbb{R}^3$ . These d'etat, Universite de Nice.
- Benoit E., Callot J.-L., Diener F., Diener M. (1981) Chasse au canards. *Collectanea Mathematica*, 31–32(1–3):37–119.
- Bertram R., Butte M.J., Kiemel T., and Sherman A. (1995) Topological and phenomenological classification of bursting oscillations. *Bulletin of Mathematical Biology* 57:413–439.
- Blechman I.I. (1971) Synchronization of Dynamical Systems. [in Russian: “Sinchronizatzia Dinamicheskikh Sistem”, Science, Moscow].
- Bower J. M. and Beeman D. (1995) The Book of GENESIS. New York Springer-Verlag.
- Bressloff P.C. and Coombes S. (2000) Dynamics of strongly coupled spiking neurons. *Neural Computation*, 12:91–129.
- Brizzi L., Meunier C., Zytnicki D., Donnet M., Hansel D., Lamotte d’Incamps B., and van Vreeswijk C. (2004) How shunting inhibition affects the discharge of lumbar motoneurons: a dynamic clamp study in anaesthetized cats. *J. Physiol*, 558:671–683.
- Brown E., Moehlis J., Holmes P. (2004) On the phase reduction and response dynamics of neural oscillator populations. *Neural Computation* 16:673–715.
- Brown T.G. (1911) The intrinsic factors in the act of progression in the mammal. *Proc. Roy. Soc. Lond. B*, 84:308–319
- Brunel N., Hakim V., and Richardson M.J. (2003) Firing-rate resonance in a generalized integrate-and-fire neuron with subthreshold resonance. *Phys Rev E*, 67:051916.
- Bryant H.L., Segundo J.P. (1976) Spike initiation by transmembrane current: a white-noise analysis. *J. Physiol*, 260:279-314.
- Butera, R. J., Rinzel J., and Smith J. C. (1999) Models of Respiratory Rhythm Generation in the Pre-Botzinger Complex. I. Bursting Pacemaker Neurons. *J. Neurophysiol.* 82: 382-397.

- Canavier C. C. , Clark J. W. and Byrne J. H. (1991) Simulation of the bursting activity of neuron R15 in Aplysia: role of ionic currents, calcium balance, and modulatory transmitters. *J Neurophysiol* 66:2107–2124
- Cartwright M.L. and Littlewood J.E. (1945) On Nonlinear Differential Equations of the Second Order: I. The Equation  $\ddot{y} - k(1 - y^2)\dot{y} + y = b\lambda k \cos(\lambda t + \alpha)$ ,  $k$  large. *J. London Math Soc.* 20:180–189.
- del Castillo J. and Morales T. (1967) The Electrical and Mechanical Activity of the Esophageal Cell of Ascaris lumbricoides. *The Journal of General Physiology*, 50:603–629.
- Chay, T. R., and D. L. Cook. (1988) Endogenous bursting patterns in excitable cells. *Math. Biosci.* 90:139 -153.
- Chay T.R. and Keizer J. (1983) Minimal Model for Membrane Oscillations in the Pancreatic  $\beta$ -cell. *Biophys. J.* 42:181–190
- Chow C.C. and Kopell N. (2000) Dynamics of Spiking Neurons with Electrical Coupling. *Neural Computation*, 12:1643–1678
- Clay J. R. (1998) Excitability of the Squid Giant Axon Revisited. *J. Neurophysiol.* 80: 903-913.
- Cohen A.H., Holmes P.J., and Rand R.H. (1982) The nature of the coupling between segmental oscillators of the lamprey spinal generator for locomotion: A mathematical model. *Journal of Mathematical Biology*, 13:345–369.
- Cole K.S., Guttman R., and Bezanilla F. (1970) Nerve excitation without threshold. *PNAS*, 65:884–891.
- Collins J.J. and Stewart I. (1994) A group-theoretic approach to rings of coupled biological oscillators. *Biol. Cybern.* 71:95–103
- Collins, J. J. and Stewart, I. (1993) Coupled nonlinear oscillators and the symmetries of animal gaits. *J. Nonlin. Sci.* 3:349–392.
- Connor J.A., Walter D. and McKown R. (1977) Modifications of the Hodgkin-Huxley Axon Suggested by Experimental Results from Crustacean Axons, *Biophysical Journal* 18:81–102.
- Connors B.W. and Gutnick M.J. (1990) Intrinsic firing patterns of diverse neocortical neurons, *Trends in Neuroscience*, 13:99–104.
- Daido H. (1996) Onset of cooperative entrainment in limit-cycle oscillators with uniform all-to-all interactions: bifurcation of the order function. *Physica D*, 91:24–66.
- Del Negro C.A., Hsiao C.-F. Chandler S.H., and Garfinkel A. (1998) Evidence for a Novel Bursting Mechanism in Rodent Trigeminal Neurons. *Biophys Journal*, 75:174–182.
- Denjoy A. (1932) Sur les courbes definies par les equations differentielles a la surface du tore. *J. Math. Pures et Appl.* 11:333-375.
- Destexhe A. , Contreras D., Sejnowski T. J., and Steriade M. (1994) A model of spindle rhythmicity in the isolated thalamic reticular nucleus. *J Neurophysiol*, 72: 803–818.
- Destexhe A. and Gaspard P. (1993) Bursting oscillations from a homoclinic tangency in a time delay system. *Phys. Lett. A.* 173:386–391.
- Destexhe A., Rudolph M., Fellous J.M., and Sejnowski T.J. (2001) Fluctuating synaptic conductances recreate in vivo-like activity in neocortical neurons. *Neuroscience*, 107: 13–24.

- Dickson C.T., Magistretti J., Shalinsky M.H., Fransen E., Hasselmo M.E., Alonso A. (2000) Properties and Role of  $I_h$  in the Pacing of Subthreshold Oscillations in Entorhinal Cortex Layer II Neurons. *Journal of Neurophysiology*, 83:2562–2579.
- Doiron B., Laing C., Longtin A./, and Maler L. (2002) Ghostbursting: a novel neuronal burst mechanism, *J. Comput. Neurosci.* 12:5–25.
- Dong C.-J. and Werblin F.S. (1995) Inwardly Rectifying Potassium Conductance Can Accelerate the Hyperpolarization Response in Retinal Horizontal Cells. *Journal of Neurophysiology*, 74:2258–2265
- Eckhaus W. (1983) Relaxation Oscillations Including a Standard Chase of French Ducks. *Lecture Notes in Math.*, 985:432–449.
- Ermentrout G. B. (1981)  $n : m$  Phase-Locking of Weakly Coupled Oscillators. *Journal of Mathematical Biology*, 12:327–342.
- Ermentrout G. B. (1985) Losing Amplitude and Saving Phase. In Othmer H. G. (ed) *Nonlinear Oscillations in Biology and Chemistry*. Springer-Verlag.
- Ermentrout G. B. (1992) Stable Periodic Solutions to Discrete and Continuum Arrays of Weakly Coupled Nonlinear Oscillators. *SIAM Journal on Applied Mathematics*, 52:1665–1687.
- Ermentrout G. B. (1994) An Introduction to Neural Oscillators. In *Neural Modeling and Neural Networks*, F Ventruglia, (ed.), Pergamon Press, Oxford, pp.79–110.
- Ermentrout G. B. (1996) Type I Membranes, Phase Resetting Curves, and Synchrony. *Neural Computation* 8:979–1001.
- Ermentrout G. B. (1998) Linearization of F-I Curves by Adaptation. *Neural Computation* 10:1721–1729.
- Ermentrout, G. B. (2003) Dynamical Consequences of Fast-Rising, Slow-Decaying Synapses in Neuronal Networks *Neural Computation* 15:2483–2522
- Ermentrout G. B. (2002) *Simulating, Analyzing, and Animating Dynamical Systems: A Guide to XPPAUT for Researchers and Students (Software, Environments, Tools)*. SIAM
- Ermentrout G. B. and Kopell N. (1984) Frequency Plateaus in a Chain of Weakly Coupled Oscillators, I. *SIAM Journal on Applied Mathematics* 15:215–237.
- Ermentrout G. B. and Kopell N. (1986a) Parabolic Bursting in an Excitable System Coupled With a Slow Oscillation. *SIAM Journal on Applied Mathematics* 46:233–253.
- Ermentrout G. B. and Kopell N. (1986b) Subcellular Oscillations and Bursting. *Mathematical Biosciences* 78:265–291.
- Ermentrout G. B. and Kopell N. (1990) Oscillator death in systems of coupled neural oscillators. *SIAM Journal on Applied Mathematics* 50:125–146.
- Ermentrout G. B. and Kopell N. (1991) Multiple pulse interactions and averaging in systems of coupled neural oscillators. *Journal of Mathematical Biology* 29:195–217.
- Ermentrout G. B. and Kopell N. (1994) Learning of phase lags in coupled neural oscillators. *Neural Computation* 6:225–241.
- FitzHugh R. (1955) Mathematical Models of Threshold Phenomena in the Nerve Membrane, *Bulletin of Mathematical Biophysics*, 7:252–278.

- FitzHugh R. (1960) Threshold and Plateaus in the Hodgkin-Huxley Nerve Equations. *The Journal of General Physiology*, 43:867–896.
- FitzHugh, R.A. (1961) Impulses and physiological states in theoretical models of nerve membrane. *Biophys. J.*, 1:445–466.
- FitzHugh R. (1969) Mathematical Models of Excitation and Propagation in Nerve. In Schwan (ed.) *Biological Engineering*, McGraw-Hill Book Co., Inc., N.Y.
- FitzHugh R. (1976) Anodal excitation in the Hodgkin-Huxley nerve model. *Biophys J.* 16:209–226.
- Fourcaud-Trocme N., Hansel D., van Vreeswijk C., and Brunel N. (2003) How Spike Generation Mechanisms Determine the Neuronal Response to Fluctuating Inputs. *The Journal of Neuroscience*, 23(37):11628–11640.
- Frankel P. and Kiemel T. (1993) Relative Phase Behavior of Two Slowly Coupled Oscillators. *SIAM J. Appl. Math.*, 53, pp. 1436–1446.
- Geiger J.R.P. and Jonas P. (2000) Dynamic Control of Presynaptic Ca Inflow by Fast-Inactivating K Channels in Hippocampal Mossy Fiber Boutons. *Neuron*, 28:927–939.
- Gerstner W. and Kistler W.M. (2002) Spiking Neuron Models: Single Neurons, Populations, Plasticity. Cambridge University Press.
- George R. M. (1914) On Circulating Excitations on Heart Muscles and Their Possible Relation to Tachycardia and Fibrillation. *Trans. R. Soc. Can.* 4:43–53.
- Gibson J.R., Belerlein M. and Connors B.W. (1999) Two networks of electrically coupled inhibitory neurons in neocortex, *Nature*, 402:75–79
- Glass L. and MacKey M.C. (1988) From Clocks to Chaos. Princeton University Press.
- Goel P. and Ermentrout B. (2002) Synchrony, stability, and firing patterns in pulse-coupled oscillators. *Physica D*, 163:191–216.
- Golubitsky M., Josic K. and Kaper T.J. (2001) An unfolding theory approach to bursting in fast-slow systems. In: *Global Analysis of Dynamical Systems: Festschrift dedicated to Floris Takens on the occasion of his 60th birthday*. (H.W. Broer, B. Krauskopf and G. Vegter, eds.) Institute of Physics Publ., 277–308
- Golubitsky M. and Stewart I. (2002) Patterns of oscillation in coupled cell systems. In: Geometry, Dynamics, and Mechanics: 60th Birthday Volume for J.E. Marsden. (P. Holmes, P. Newton and A. Weinstein, eds.) Springer-Verlag, 243–286.
- Gray C.M. and McCormick D.A. (1996) Chattering cells: superficial pyramidal neurons contributing to the generation of synchronous oscillations in the visual cortex. *Science*. 274 (5284): 109–113
- Grundfest H. (1971) Biophysics and Physiology of Excitable Membranes. Ed. WJ Adelman, Van Nostrand Reinhold Co, New York,
- Guckenheimer J, Harris-Warrick R, Peck J, Willms A. (1997) Bifurcation, Bursting, and Spike Frequency Adaptation. *J Comput Neurosci.* 4:257–277.
- Guckenheimer J. and Holmes D. (1983) Nonlinear Oscillations, Dynamical Systems, and Bifurcations of Vector Fields. Springer-Verlag, New York.

- Guckenheimer J. (1975) Isochrons and Phaseless Sets. *Journal of Mathematical Biology*, 1:259–273.
- Guevara M.R. and Glass L. (1982) Phase locking, periodic doubling bifurcations and chaos in a mathematical model of a periodically driven oscillator: a theory for the entrainment of biological oscillators and the generation of cardiac dysrhythmias. *Math. Biol.* 14: 1-23.
- Guttman R., Lewis S., Rinzel J. (1980) Control of repetitive firing in squid axon membrane as a model for a neuroneoscillator. *J. Physiology.* 305: 377-395.
- Hansel D., Mato G., and Meunier C. (1995) Synchrony in excitatory neural networks. *Neural Computations* 7:307–335.
- Hansel D. and Mato G. (2003) Asynchronous States and the Emergence of Synchrony in Large Networks of Interacting Excitatory and Inhibitory Neurons. *Neural Computation*, 15:1–56.
- Hansel D., Mato G., Meunier C., and Neltner L. (1998) On Numerical Simulations of Integrate-and-Fire Neural Networks. *Neural Computation*, 10:467–483.
- Harris-Warrick R.M. and Flamm R.E. (1987) Multiple mechanisms of bursting in a conditional bursting neuron. *J. Neurosci.*, 7:2113–2128
- Hastings J.W. and Sweeney B.M. (1958) A persistent diurnal rhythms of luminescence in *Gonyaulax polyedra*. *Biol. Bull.* 115:440-458.
- Hausser M., Spruston N., and Stuart G.J. (2000) Diversity and Dynamics of Dendritic Signaling. *Science*, 290:739–744
- Hausser M. and Mel B. (2003) Dendrites: bug or feature? *Current Opinion in Neurobiology*, 13:372–383
- Heyward P., Ennis M., Keller A., and Shipley M.T. (2001) Membrane Bistability in Olfactory Bulb Mitral Cells *The Journal of Neuroscience*, 21:5311–5320
- Hille B. (2001) Ion Channels of Excitable Membranes. (2nd edition) Sinauer, Sunderland, MA.
- Hindmarsh J.L. and Rose R.M. (1982) A model of the nerve impulse using two first-order differential equations. *Nature* 296:162–164
- Hines M.A. (1989) Program for simulation of nerve equations with branching geometries. *Int J Biomed Comput* 24:55–68.
- Hodgkin A.L. (1948) The local electric changes associated with repetitive action in a non-medulated axon. *Journal of Physiology* 107:165–181.
- Hodgkin A.L. and Huxley A.F. (1952) A quantitative description of membrane current and application to conduction and excitation in nerve. *Journal Physiol.*, 117:500–544.
- Holden L. and Erneux T. (1993a) Slow passage through a Hopf bifurcation: form oscillatory to steady state solutions. *SIAM Journal on Applied Mathematics* 53:1045–1058
- Holden L. and Erneux T. (1993b) Understanding bursting oscillations as periodic slow passages through bifurcation and limit points. *J. Math. Biol.* 31:351–365
- Hopf E. (1942) Abzweigung einer periodischen Losung von einer stationaren Losung eines Differentialsystems. *Ber. Math.-Phys. Kl. Sachs. Aca. Wiss. Leipzig*, 94:1–22.
- Hoppensteadt F.C. (1997) An Introduction to the Mathematics of Neurons. Second edition: Modeling in the Frequency Domain. Cambridge Univ. Press, Cambridge, U. K.

- Hoppensteadt F.C. (2000) Analysis and simulations of chaotic systems. Springer-Verlag, New York.
- Hoppensteadt F.C. and Izhikevich E.M. (1996) Synaptic Organizations and Dynamical Properties of Weakly Connected Neural Oscillators. II. Learning of Phase Information. *Biological Cybernetics*, 75:129–135
- Hoppensteadt F.C. and Izhikevich E.M. (1996) Synaptic Organizations and Dynamical Properties of Weakly Connected Neural Oscillators: I. Analysis of Canonical Model. *Biological Cybernetics*, 75:117–127
- Hoppensteadt F.C. and Izhikevich E.M. (1997) Weakly Connected Neural Networks. Springer-Verlag, NY
- Hoppensteadt F.C. and Keener J.P. (1982) Phase Locking of Biological Clocks. *J. MATH. Biology*, 15:339–349.
- Hoppensteadt F.C. and Peskin C.S. (2002) Modeling and Simulation in Medicine and the Life Sciences. Second edition. Springer-Verlag, NY
- Hughes S.W., Cope D.W., Toth T.L., Williams S.R., and Crunelli V. (1999) All thalamocortical neurones possess a T-type  $\text{Ca}^{2+}$  'window' current that enables the expression of bistability-mediated activities. *The Journal of Physiology*, 517:805–815.
- Huguenard J.R. and McCormick D.A. (1992) Simulation of the Currents Involved in Rhythmic Oscillations in Thalamic Relay Neurons. *Journal of Neurophysiology*, 68:1373–1383
- Hutcheon, B., Miura, R.M., Puil, E., (1996). Subthreshold membrane resonance in neocortical neurons. *Journal of Neurophysiology* 76:683–697.
- Izhikevich E.M. (2003) Simple Model of Spiking Neurons IEEE Transactions on Neural Networks, 14:1569- 1572.
- Izhikevich E.M. (2002) Resonance and Selective Communication Via Bursts in Neurons Having Subthreshold Oscillations. *BioSystems*, 67:95-102
- Izhikevich E.M. (2001) Resonate-and-Fire Neurons. *Neural Networks*, 14:883-894
- Izhikevich E.M. (2001) Synchronization of Elliptic Bursters SIAM Review, 43:315-344
- Izhikevich E.M. (2000) Neural Excitability, Spiking, and Bursting. *International Journal of Bifurcation and Chaos*. 10:1171-1266.
- Izhikevich E.M. (2000) Phase Equations For Relaxation Oscillators SIAM Journal on Applied Mathematics, 60:1789-1805
- Izhikevich E.M. (1999) Class 1 Neural Excitability, Conventional Synapses, Weakly Connected Networks, and Mathematical Foundations of Pulse-Coupled Models. *IEEE Transactions On Neural Networks*,10:499-507
- Izhikevich E.M. (1999) Weakly Connected Quasiperiodic Oscillators, FM Interactions, and Multiplexing in the Brain. *SIAM Journal on Applied Mathematics*, 59:2193-2223
- Izhikevich E.M. (1998) Phase Models With Explicit Time Delays. *Physical Review E*, 58:905-908
- Izhikevich E.M., Desai N.S., Walcott E.C., Hoppensteadt F.C. (2003) Bursts as a unit of neural information: selective communication via resonance . *Trends in Neuroscience* 26:161-167
- Izhikevich E.M. and Hoppensteadt F.C. (2004) Classification of Bursting Mappings. Interna-

- tional Journal of Bifurcation and Chaos, 14:3847–3854
- Jahnsen H. and Llinas R. (1984) Electrophysiological properties of guinea-pig thalamic neurons: an in vitro study. *Journal of Physiology London*, 349:205–226.
- Jensen M.S., Azouz R., and Yaari Y. (1994) Variant Firing Patterns in RAt Hippocampal Pyramidal Cells Modulated by Extracellular Potassium. *Journal of Neurophysiology*, 71:831–839
- Jian Z., Xing J.L., Yang G.S., and Hu S.J. (2004) A novel Bursting Mechanism of Type A Neurons in Injured Dorsal Root Ganglia. *NeuroSignals*, 13:150-156.
- Johnson C.H. (1999) Forty Years of PRC — What Have We Learned?. *Chronobiology International*, 16:711-743.
- Johnston D. and Wu S.M. (1995) Foundations of Cellular Neurophysiology. The MIT Press.
- Katriel G. (2005) Stability of Synchronized Oscillations in Networks of Phase-Oscillators. Discrete and Continuous Dynamical Systems-Series B. 5:353–364.
- Kay A.R., Sugimori M., and Llinas R. (1998) Kinetic and Stochastic Properties of a Persistent Sodium Current in Mature Guinea Pig Cerebellar Purkinje Cells, *J. Neurophysiology*, 80:1167–1179.
- Keener J. and Sneyd J. (1998) Mathematical Physiology. Springer-Verlag, New York
- Kepler T.B., Abbott L.F., and Marder E. (1992) Reduction of conductance based neuron models. *Biological Cybernetics*, 66:381–387.
- Kinard T.A., de Vries G., Sherman A., Satin L.S. (1999) Modulation of the bursting properties of single mouse pancreatic beta-cells by artificial conductances. *Biophys J.* 76:1423-35
- Klink R. and Alonso A. (1993) Ionic Mechanisms for the Subthreshold Oscillations and Differential Electroresponsiveness of Medial Entorhinal Cortex Layer II Neurons. *Journal of Neurophysiology*, 70:144–157.
- Koch C. (1999) Biophysics of Computation: Information Processing in Single Neurons. Oxford University Press.
- Kopell N. (1986) Coupled oscillators and locomotion by fish. In Othmer HG (Ed) Nonlinear Oscillations in Biology and Chemistry. Lecture Notes in Biomathematics, Springer-Verlag.
- Kopell N. (1995) Chains of Coupled Oscillators. In Arbib M.A. (Ed) Brain Theory and Neural Networks, The MIT press, Cambridge, MA.
- Kopell N. and Ermentrout G.B. (1990) Phase transitions and other phenomena in chains of coupled oscillators. *SIAM Journal on Applied Mathematics* 50:1014–1052.
- Kopell N., Ermentrout G.B., Williams T.L. (1991) On Chains of Oscillators Forced at One End. *SIAM Journal on Applied Mathematics* 51:1397–1417.
- Kopell N. and Somers D. (1995) Anti-phase solutions in relaxation oscillators coupled through excitatory interactions. *J. Math. Biol.* 33:261–280.
- Korngreen A. and Sakmann B. (2000) Voltage-gated K<sup>+</sup> channels in layer 5 neocortical pyramidal neurones from young rats: subtypes and gradients. *Journal of Physiology*, 525.3:621–639
- Krinskii V.I. and Kokoz Yu.M. (1973) Analysis of Equations of Excitable Membranes - I. Reduction of the Hodgkin-Huxley Equations to a Second Order System. *Biofizika*, 18 3, 506–511

- Kuramoto, Y., (1975) in H. Araki (Ed) International Symposium on Mathematical Problems in Theoretical Physics, Lecture Notes in Physics, Vol. 39, Springer, New York, p. 420-422.
- Kuramoto Y. (1984) Chemical Oscillations, Waves, and Turbulence. Springer-Verlag, New York.
- Kuznetsov Yu. (1995) Elements of Applied Bifurcation Theory. Springer-Verlag, New York.
- Lapicque, L (1907) Recherches quantitatives sur l'excitation électrique des nerfs traitée comme une polarisation. *J Physiol Pathol Gen* 9:620-635.
- Latham PE, Richmond BJ, Nelson PG, Nirenberg S. Intrinsic dynamics in neuronal networks. I. Theory. *J Neurophysiol* 2000 Feb;83(2):808-27
- Levitin E.S., Kramer R.H., and Levitan I.B. (1987) Augmentation of bursting pacemaker activity by egg-laying hormone in Aplysia neuron R15 is mediated by a cyclic AMP-dependent increase in Ca<sup>2+</sup> and K<sup>+</sup> currents. *Proc Natl Acad Sci U S A*. 84 (17): 6307–6311.
- Levitin E.S. and Levitan I.B. (1988) A Cyclic GMP Analog Decreases the Currents Underlying Bursting Activity in the Aplysia Neuron R15. *J. Neuroscience*, 8:1162–1171
- Li, J., Bickford M.E., and Guido W. (2003) Distinct firing properties of higher order thalamic relay neurons. *Journal of Neurophysiology*, 90: 291–299.
- Liénard A. (1928) Etude des oscillations entretenues, *Rev. Gen. Elec.* 23:901–912, 946–954
- Lisman J. (1997) Bursts as a unit of neural information: making unreliable synapses reliable, *Trends Neurosci.* 20:38–43
- Lopatin A.N., Makhina E.N., Nichols C.G. (1994) Potassium channel block by cytoplasmic polyamines as the mechanism of intrinsic rectification. *Nature* 373:366–369
- Luk W.K. and Aihara K. (2000) Synchronization and sensitivity enhancement of the Hodgkin-Huxley neurons due to inhibitory inputs. *Biological Cybernetics*, 82:455–467.
- Magee J.C. (1998) Dendritic Hyperpolarization-Activated Currents Modify the Integrative Properties of Hippocampal CA1 Pyramidal Neurons. *The Journal of Neuroscience*, 18:7613–7624.
- Magee J.C. and Carruth M. (1999) Dendritic Voltage-Gated Ion Channels Regulate the Action Potential Firing Mode of Hippocampal CA1 Pyramidal neurons. *J. Neurophysiology*, 82:1895–1901.
- Magistretti J. and Alonso A. (1999) Biophysical Properties and Slow Voltage- dependent Inactivation of a Sustained Sodium Current in Entorhinal Cortex Layer-II Principal Neurons. *J.Gen.Physiol.*, 114:491-509.
- Mainen Z.F., Sejnowski T.J. (1995) Reliability of spike timing in neocortical neurons. *Science*, 268(5216):1503–1506.
- Mainen Z.F., Sejnowski T.J. (1996) Influence of dendritic structure on firing pattern in model neocortical neurons. *Nature*. 382:363-366.
- Malkin I.G. (1949) Methods of Poincare and Liapunov in theory of non-linear oscillations. [in Russian: “Metodi Puankare i Liapunova v teorii nelineinix kolebanii” Gostexizdat, Moscow].
- Malkin I.G. (1956) Some Problems in Nonlinear Oscillation Theory. [in Russian: “Nekotorye zadachi teorii nelineinix kolebanii” Gostexizdat, Moscow].
- Marder E. and Bucher D. (2001) Central pattern generators and the control of rhythmic movements. *Current Biology*, 11:986–996.

- Markram H, Toledo-Rodriguez M, Wang Y, Gupta A, Silberberg G, and Wu C. (2004) Interneurons of the neocortical inhibitory system. *Nature Review Neuroscience* 5:793–807
- Medvedev G. (2005) Reduction of a model of an excitable cell to a one-dimensional map. *Physica D*, 202:37–59.
- Melnikov V.K. (1963) On the stability of the center for time periodic perturbations. *Trans. Moscow Math. Soc.* 12:1-57.
- McCormick D.A. (2004) Membrane Properties and Neurotransmitter Actions, in Shepherd G.M. *The Synaptic Organization of the Brain*. Oxford University Press, New York, Fifth Edition.
- McCormick D.A. and Pape H.-C. (1990) Properties of a Hyperpolarization-Activated Cation Current and Its Role in Rhythmic Oscillation in Thalamic Relay Neurones. *Journal of Physiology*, 431:291–318
- Miroollo R.E. and Strogatz S.H. (1990) Synchronization of pulse-coupled biological oscillators. *SIAM J. Appl. Math.* 50:1645–1662
- Mishchenko E.F., Kolesov Yu.S., Kolesov A.Yu., and Rozov N.K. (1994) Asymptotic Methods in Singularly Perturbed Systems. Plenum Press, New York.
- Morris C. and Lecar H. (1981) Voltage Oscillations in the Barnacle Giant Muscle Fiber, *Bioophysical Journal* 35:193–213.
- Murray J.D. (1993). Mathematical Biology, Springer-Verlag.
- Nagumo, J., S. Arimoto, and S. Yoshizawa (1962) An active pulse transmission line simulating nerve axon. *Proc IRE*. 50:2061–2070.
- Nejshtadt A. (1985) Asymptotic investigation of the loss of stability by an equilibrium as a pair of eigenvalues slowly cross the imaginary axis. *Usp. Mat. Nauk* 40:190-191.
- Neu J.C. (1979) Coupled chemical oscillators. *SIAM Journal of Applied Mathematics* 37:307–315.
- Nisenbaum E. S., Xu Z.C., and Wilson C.J. (1994) Contribution of a slowly inactivating potassium current to the transition to firing of neostriatal spiny projection neurons. *Journal of Neurophysiology*, 71:1174–1189
- Noble D. (1966) Applications of Hodgkin-Huxley equations to excitable tissues. *Physiol Rev* 1966 46:1–50
- Nowak L.G., Azouz R., Sanchez-Vives M.V., Gray C.M., and McCormick D.A. (2003) Electrophysiological Classes of Cat Primary Visual Cortical Neurons In Vivo as Revealed by Quantitative Analyses. *J Neurophysiol* 89: 1541-1566
- Parri H. R. and Crunelli V. (1999) Sodium Current in Rat and Cat Thalamocortical Neurons: Role of a Non-Inactivating Component in Tonic and Burst Firing, *The Journal of Neuroscience*, February 1, 1998, 18(3):854-867
- Pape, H.-C., and McCormick, D.A. (1995) Electrophysiological and pharmacological properties of interneurons in the cat dorsal lateral geniculate nucleus. *Neuroscience*, 68: 1105–1125.
- Pernarowski M., Miura R.M., and Kevorkian J. (1992) Perturbation techniques for models of bursting electrical activity in pancreatic  $\beta$ -cells. *SIAM Journal on Applied Mathematics* 52:1627–1650.

- Pernarowski M. (1994) Fast Subsystem Bifurcations in a Slowly Varied Liénard System Exhibiting Bursting. SIAM Journal on Applied Mathematics, 54:814–832.
- Pfeuty B., Mato G., Golomb D., Hansel D. (2003) Electrical Synapses and Synchrony: The Role of Intrinsic Currents. J. Neuroscience, 23:6280–6294.
- Pinsky P. and Rinzel J. (1994) Intrinsic and network rhythmogenesis in a reduced Traub model of CA3 neurons. J. Comput. Neurosci. 1:39–60.
- Pikovsky A., Rosenblum M., Kurths J. (2001) Synchronization: A Universal Concept in Nonlinear Science. CUP, Cambridge.
- Pirchio M., Turner J. P., Williams S. R., Asprodini E. and Crunelli V. (1997) Postnatal Development of Membrane Properties and delta Oscillations in Thalamocortical Neurons of the Cat Dorsal Lateral Geniculate Nucleus. J. Neurosci. 17 :5428–5444.
- Plant R.E. (1981) Bifurcation and Resonance in a Model for Bursting Nerve Cells. Journal of Mathematical Biology, 11:15–32.
- Pontryagin L.S. and Rodygin L.V. (1960) Periodic solution of a system of ordinary differential equations with a small parameter in the terms containing derivatives Sov. Math. Dokl. 1: 611–614.
- Rall W. (1959) Branching dendritic trees and motoneuron membrane resistivity. Exp. Neurol. 1:491–527.
- Reuben J. P., Werman R., and Grundfest H. (1961) The Ionic Mechanisms of Hyperpolarizing Responses in Lobster Muscle Fibers. The Journal of General Physiology, 45:243–265
- Reyes A.D. and Fetz E.E. (1993) Two modes of interspike interval shortening by brief transient depolarizations in cat neocortical neurons. Journal of Neurophysiology 69: 1661–1672.
- Richardson, M.J.E., Brunel, N. and Hakim, V. (2003) From Subthreshold to Firing-Rate Resonance. Journal of Neurophysiology 89:2538–2554
- Rinzel J. and Ermentrout G.B. (1989) Analysis of Neural Excitability and Oscillations. In Koch C., Segev I. (eds) Methods in Neuronal Modeling, The MIT Press, Cambridge, Mass.
- Rinzel J. (1978) On repetitive activity in nerve. Fed. Proc. 37:2793-2802.
- Rinzel J. (1985) Bursting oscillations in an excitable membrane model. In: Sleeman BD, Jarvis RJ, eds. *Ordinary and partial Differential Equations Proceedings of the 8th Dundee Conference* Lecture Notes in Mathematics **1151**. Berlin: Springer, 304–316.
- Rinzel J. (1987) A formal classification of bursting mechanisms in excitable systems. In: E. Teramoto, M. Yamaguti, eds. Mathematical Topics in Population Biology, Morphogenesis, and Neurosciences, vol. 71 of Lecture Notes in Biomathematics, Springer-Verlag, Berlin.
- Rinzel J. and Lee Y.S. (1986) On different mechanisms for membrane potential bursting. In Othmer H.G. (Ed) Nonlinear Oscillations in Biology and Chemistry. Lecture Notes in Biomathematics, Springer-Verlag.
- Rinzel J. and Lee Y.S. (1987) Dissection of a model for neuronal parabolic bursting. Journal of Mathematical Biology, 25:653–675.
- Robbins J., Trousdale J., Marsh S.J., and Brown D.A. (1992) Kinetic and Pharmacological Properties of the M-current in Rodent Neuroblastoma  $\times$  Glioma Hybrid Cells, Journal of Physiology, 451:159-185.

- Rosenblum M.G. and Pikovsky A.S. (2001) Detecting direction of coupling in interacting oscillators. *Physical Review E*, 64, p. 045202.
- Roy J. P., Clercq M. , Steriade M. , and Deschenes M. (1984) Electrophysiology of neurons of lateral thalamic nuclei in cat: mechanisms of long-lasting hyperpolarizations. *J Neurophysiol*, 51:1220–1235.
- Rubin J. and Terman D. (2000) Analysis of clustered firing patterns in synaptically coupled networks of oscillators. *J. Math. Biology*, 41:513–545.
- Rubin J. and Terman D. (2002) Geometric singular perturbation analysis of neuronal dynamics. *Handbook of Dynamical systems*, vol. 2: Toward Applications (B. Fiedler, G. Iooss, eds.) Elsevier, Amsterdam
- Rush M. E. and Rinzel J. (1995) The Potassium A-Current, Low Firing Rates and Rebound Excitation in Hodgkin-Huxley Models. *Bulletin of Mathematical Biology*, 57:899–929.
- Rush M. E. and Rinzel J. (1994) Analysis of bursting in a thalamic neuron model, *Biological Cybernetics* 71:281–291.
- Samborskij S.N. (1985) Limit trajectories of singularly perturbed differential equations. *Dokl. Akad. Nauk Ukr. SSR. Ser. A*, 9:22–25.
- Sanabria E.R.G., Su H., and Yaari Y. (2001) Initiation of network bursts by  $\text{Ca}^{2+}$ -dependent intrinsic bursting in the rat pilocarpine model of temporal lobe epilepsy. *Journal of Physiology*, 532:205–216
- Sharp A.A., O'Neil M.B., Abbott L.F., Marder E. (1993) Dynamic clamp: computer-generated conductances in real neurons. *J Neurophysiol*, 69:992-995
- Shilnikov, A. L., Calabrese R. and Cymbalyuk, G. (2005) Mechanism of bi-stability: tonic spiking and bursting in a neuron model. *Phys Review E*, 71, 056214.
- Shilnikov A.L. and Cymbalyuk G (2005) Transition between Tonic Spiking and Bursting in a Neuron Model via the Blue-Sky Catastrophe. *Physical Review Letters*, 94, 048101.
- Shilnikov A.L. and Cymbalyuk G (2004) Homoclinic bifurcations of periodic orbits en a route from tonic spiking to bursting in neuron models. *Regular and Chaotic Dynamics*, vol. 9, [2004-11-19]
- Shilnikov L.P., Shilnikov A.L., Turaev D., Chua L.O. (2001) Methods of qualitative theory in nonlinear dynamics. Part II, World Scientific, Singapore
- Shilnikov L.P., Shilnikov A.L., Turaev D., Chua L.O. (1998) Methods of qualitative theory in nonlinear dynamics. Part I, World Scientific, Singapore
- Shilnikov, A.L. and Shilnikov, L.P, (1995) Dangerous and safe stability boundaries of equilibria and periodic orbits" in NDES'95, University College Dublin, Ireland, 55-63.
- Shishkova M.A. (1973) Investigation of a system of differential equations with a small parameter in highest derivatives. *Dokl. Adad. Nauk SSSR* 209. No.3, 576–579. English transl. Sov. Math., Dokl. 14,483–487
- Shepherd G.M. (2004) The Synaptic Organization of the Brain. Oxford University Press, New York, Fifth Edition.
- Skinner F.K., Kopell N., Marder E. (1994) Mechanisms for oscillation and frequency control in reciprocal inhibitory model neural networks. *J. Comput. Neurosci.*, 1:69–87.

- Smolen P., Terman D., and Rinzel J. (1993) Properties of a bursting model with two slow inhibitory variables. *SIAM Journal on Applied Mathematics* 53:861–892.
- Somers D. and Kopell N. (1993) Rapid synchronization through fast threshold modulation. *Biological Cybernetics*, 68:393–407
- Somers D. and Kopell N. (1995) Waves and synchrony in networks of oscillators or relaxation and non-relaxation type. *Physica D*, 89:169–183
- Stanford, I. M., Traub R. D., and Jefferys J. G.R. (1998) Limbic gamma rhythms. II. Synaptic and intrinsic mechanisms underlying spike doublets in oscillating subicular neurons. *J. Neurophysiol.* 80:162–171
- Stein RB. Some models of neuronal variability. *Biophys J* 7: 37-68, 1967
- Steriade M. (2003) Neuronal Substrates of Sleep and Epilepsy. Cambridge University Press.
- Steriade M. (2004) Neocortical Cell Classes Are Flexible Entities. *Nature Reviews Neuroscience*, 5:121–134.
- Strogatz S.H. (1994) Nonlinear Dynamics and Chaos. Cambridge, Mass.
- Strogatz S. H. (2000) From Kuramoto to Crawford: exploring the onset of synchronization in populations of coupled oscillators. *Physica D*, 143: 1–20.
- Stuart G., Spruston N., Häusser M. (1999) Dendrites. Oxford University Press.
- Su H, Alroy G, Kirson ED, Yaari Y. (2001) Extracellular calcium modulates persistent sodium current-dependent burst-firing in hippocampal pyramidal neurons. *Journal of Neuroscience* 21:4173-4182.
- Szmolyan P. and Wechselberger M. (2001) Canards in  $\mathbb{R}^3$ . *Journal of Differential Equations*, 177:419–453.
- Szmolyan P. and Wechselberger M. (2004) Relaxation oscillations in  $\mathbb{R}^3$ . *Journal of Differential Equations*, 200:69–104.
- Tateno T., Harsch A., and Robinson H.P.C. (2004) Threshold firing frequency-current relationships of neurons in rat somatosensor cortex: type 1 and type 2 dynamics. *Journal of Neurophysiology* 92: 2283–2294.
- Tennigkeit F., Ries C.R., Schwarz D.W.F., and Puil E. (1997) Isoflurane attenuates resonant responses of auditory thalamic neurons. *J. Neurophysiol.* 78:591–596
- Terman D. (1991) Chaotic spikes arising from a model of bursting in excitable membranes. *SIAM J. Appl. Math.* 51:1418–1450.
- Timofeev I., Grenier F., Bazhenov M., Sejnowski T.J. and Steriade M. (2000) Origin of Slow Cortical Oscillations in Deafferented Cortical Slabs Cerebral Cortex, Vol. 10, No. 12, 1185–1199
- Toledo-Rodriguez M., Blumenfeld B., Wu C., Luo J., Attali B., Goodman P., and Markram H. (2004) Correlation Maps Allow Neuronal Electrical Properties to be Predicted from Single-cell Gene Expression Profiles in Rat Neocortex. *Cerebral Cortex*, 14:1310–1327.
- Traub R. D., Wong R. K., Miles R., and Michelson H. (1991) A model of a CA3 hippocampal pyramidal neuron incorporating voltage-clamp data on intrinsic conductances. *Journal of Neurophysiology*, 66:635–650

- Tuckwell H.C. (1988) Introduction to Theoretical Neurobiology. Cambridge, UK, Cambridge University Press.
- Uhlenbeck G.E. and Ornstein L.S. (1930) On the theory of the Brownian motion. *Phys. Rev.* 36:823–841.
- van Vreeswijk C., Abbott L.F., Ermentrout G.B. (1994) When inhibition not excitation synchronizes neural firing. *Journal of Computational Neuroscience*, 1:313–321
- van Vreeswijk C. and Hansel D. (2001) Patterns of Synchrony in Neural Networks with Spike Adaptation. *Neural Comp.* 13:959–992
- van Vreeswijk C. (2000) Analysis of the Asynchronous State in Networks of Strongly Coupled Oscillators. *Physical Review Letters*, 84, 5110–5113.
- de Vries G. (1998) Multiple Bifurcations in a Polynomial Model of Bursting Oscillations. *Journal of Nonlinear Science*, 8:281–316.
- Wang X.-J. (1999) Fast burst firing and short-term synaptic plasticity: a model of neocortical chattering neurons. *Neuroscience* 89:347–362.
- Wang X.-J. and Rinzel J. (1992) Alternating and synchronous rhythms in reciprocally inhibitory model neurons. *Neural Computation*. 4:84–97.
- Wechselberger M. (2005) Existence and Bifurcation of Canards in  $\mathbb{R}^3$  in the Case of a Folded Node. *SIAM J. Appl. Dynamical Systems*, 4:101–139.
- Wessel R., Kristan W.B., and Kleinfeld D. (1999) Supralinear Summation of Synaptic Inputs by an Invertebrate Neuron: Dendritic Gain Is Mediated by an “Inward Rectifier”  $K^+$  Current. *The Journal of Neuroscience*, 19:5875–5888.
- White J.A., Rubinstein J. T., and Kay A. R. (2000) Channel noise in neurons. *Trends in Neuroscience*, 23:131–137.
- Williams J.T., North R.A., and Tokimasa T. (1988) Inward Rectification of Resting and Opiate-Activated Potassium Currents in Rat Locus Coeruleus Neurons. *The Journal of Neuroscience*, 8:4299–4306
- Williams S.R. and Stuart G.J. (2003) Role of dendritic synapse location in the control of action potential. *TINS*, 26:147–154.
- Willms A.R., Baro D.J., Harris-Warrick R.M., and Guckenheimer J. (1999) An Improved Parameter Estimation Method for Hodgkin-Huxley Models, *Journal of Computational Neuroscience*, 6:145–168.
- Wilson C.J. (1993) The generation of natural firing patterns in neostriatal neurons. In *Progress in Brain Research*. (Arbuthnott G., Emson P.C. eds), 277–297. Amsterdam. Elsevier
- Wilson C. J. and Groves P. M. (1981) Spontaneous firing patterns of identified spiny neurons in the rat neostriatum. *Brain Research*, 220:67–80
- Wilson H.R. and Cowan J.D. (1972) Excitatory and inhibitory interaction in localized populations of model neurons. *Biophys J* 12:1–24.
- Wilson H.R. and Cowan J.D. (1973) A Mathematical theory of the functional dynamics of cortical and thalamic nervous tissue. *Kybernetik* 13:55–80.
- Wilson H.R. (1999) Spikes, Decisions, and Actions: The dynamical foundations of neuroscience.

- Oxford University Press.
- Winfree A. (1967) Biological Rhythms and the Behavior of Populations of Coupled Oscillators. *Journal of Theoretical Biology*, 16:15–42.
- Winfree A. (1974) Patterns of Phase Compromise in Biological Cycles. *Journal of Math. Biology* 1:73–95.
- Winfree A. (2001) The Geometry of Biological Time. Springer-Verlag, New York, second edition.
- Wolfram S. (2002) A New Kind of Science. Wolfram Media.
- Wu N., Hsiao C.-F., Chandler S. (2001) Membrane resonance and subthreshold membrane oscillations in mesencephalic V neurons: participants in burst generation. *J. Neurosci* 21:3729–3739.
- Young G. (1937) *Psychometrika*, 2:103.
- Yuan A., Dourado M., Butler A., Walton N., Wei A., Salkoff L. (2000) SLO-2, a K<sup>+</sup> channel with an unusual Cl<sup>-</sup> dependence. *Nature Neuroscience*, 3:771–779.
- Yuan A., Santi C.M., Wei A., Wang Z.W., Pollak K., Nonet M., Kaczmarek L., Crowder C.M., Salkoff L. (2003) The sodium-activated potassium channel is encoded by a member of the Slo gene family. *Neuron*. 37:765–773.
- Yue C. and Yaari Y. (2004) KCNQ/M Channels Control Spike Afterdepolarization and Burst Generation in Hippocampal Neurons. *J. Neuroscience*, 24:4614–4624.
- Zhan, X. J., Cox C. L., Rinzel J., and Sherman S. M. (1999) Current clamp and modeling studies of low-threshold calcium spikes in cells of the cat's lateral geniculate nucleus. *J. Neurophysiol.* 81:2360–2373.



# Chapter 10

## Synchronization (see [www.izhikevich.com](http://www.izhikevich.com))

In this chapter we consider networks of tonically spiking neurons. As any other kind of physical, chemical, or biological oscillators, such neurons could synchronize and exhibit collective behavior that is not intrinsic to any individual neuron. For example, partial synchrony in cortical networks is believed to generate various brain oscillations, such as the alpha and gamma EEG rhythms. Increased synchrony may result in pathological types of activity, such as epilepsy. Coordinated synchrony is needed for locomotion and swim pattern generation in fish. There is an ongoing debate on the role of synchrony in neural computation, see e.g., the special issue of *Neuron* (September 1999) devoted to the binding problem.

Depending on the circumstances, synchrony could be good or bad, and it is important to know what factors contribute to synchrony and how to control it. This is the subject of the present chapter – the most advanced chapter of the book. It provides a nice application of the theory developed earlier and hopefully gives some insight into why the previous chapters might be worth mastering.

Our goal is to understand how the behavior of two coupled neurons depends on their intrinsic dynamics. First, we introduce the method of description of an oscillation by its phase. Then, we describe various methods of reduction of coupled oscillators to simple phase models. The reduction method and the exact form of the phase model depends on the type of coupling, i.e., whether it is pulsed, weak, or slow, and on the type of bifurcations of the limit cycle attractor generating tonic spiking. Finally, we show how to use phase models to understand the collective dynamics of many coupled oscillators.

### 10.1 Pulsed Coupling

In this section we consider oscillators of the form

$$\dot{x} = f(x) + A\delta(t - t_s) , \quad x \in \mathbb{R}^m , \quad (10.1)$$

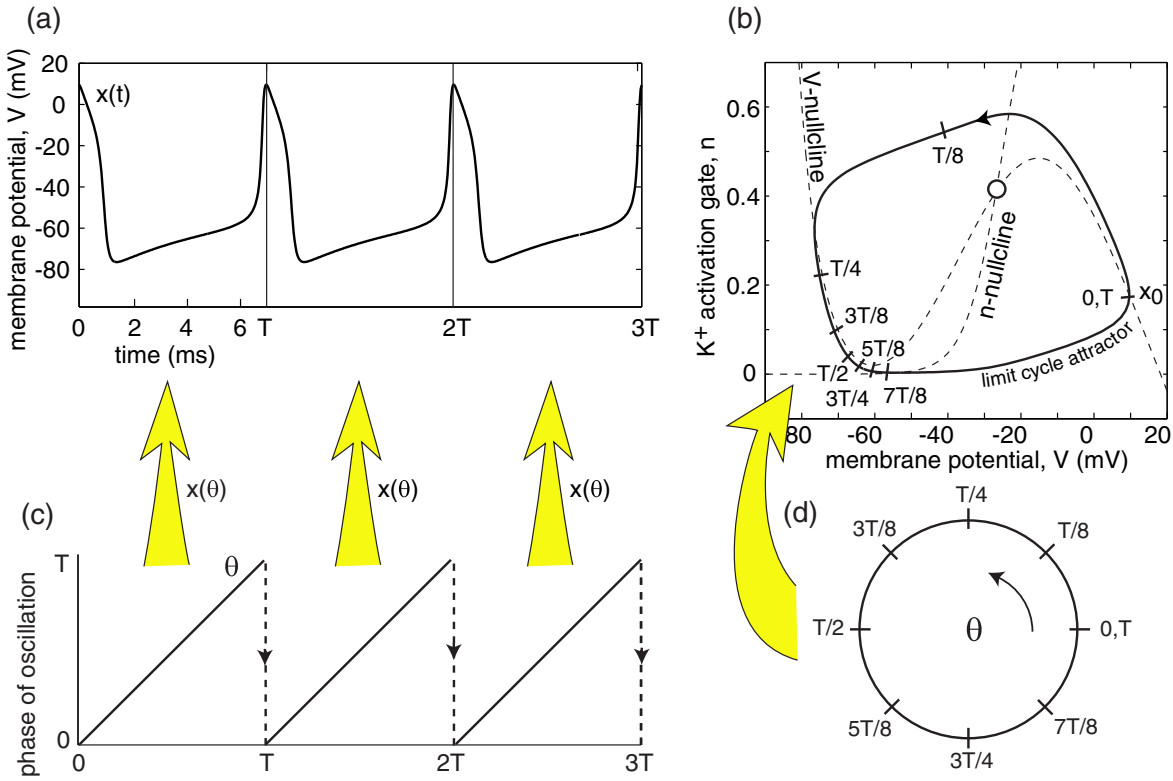


Figure 10.1: Definition of a phase of oscillation,  $\vartheta$ , in the  $I_{Na} + I_K$ -model with parameters as in Fig. 4.1a and  $I = 10$ .

having exponentially stable limit cycles and experiencing pulsed stimulation at times  $t_s$  that instantaneously increases the state variable by constant  $A$ . The Dirac delta function  $\delta(t)$  is a mathematical shorthand notation for resetting  $x$  by  $A$ . The strength of pulsed stimulation,  $A$ , is not assumed to be small. Most of the results of this section can also be applied to the case when the action of input pulse is not instantaneous, but smeared over an interval of time, typically shorter than the period of oscillation.

### 10.1.1 Phase of oscillation

Many types of physical, chemical, and biological oscillators share an astonishing feature: They can be described by a single phase variable  $\vartheta$ . In the context of tonic spiking, the phase is just the time since the last spike, as in Fig. 10.1a.

In general, the notion of the phase is related to the notion of parametrization of a limit cycle attractor, as in Fig. 10.1b. Take a point  $x_0$  on the attractor and plot the trajectory  $x(t)$  with  $x(0) = x_0$ . Then, the phase of  $x(t)$  is just  $\vartheta = t$ . As  $t$  increases past the period  $T$ , then  $2T$ , etc., the phase variable  $\vartheta$  wraps around the interval  $[0, T]$ , jumping from  $T$  to 0; see Fig. 10.1c. Gluing together the points 0 and  $T$ , as in Fig. 10.1d, we can treat the interval  $[0, T]$  as a circle, denoted as  $\mathbb{S}^1$ , with circumference  $T$ . The parametrization is the mapping of  $\mathbb{S}^1$  in Fig. 10.1d into the

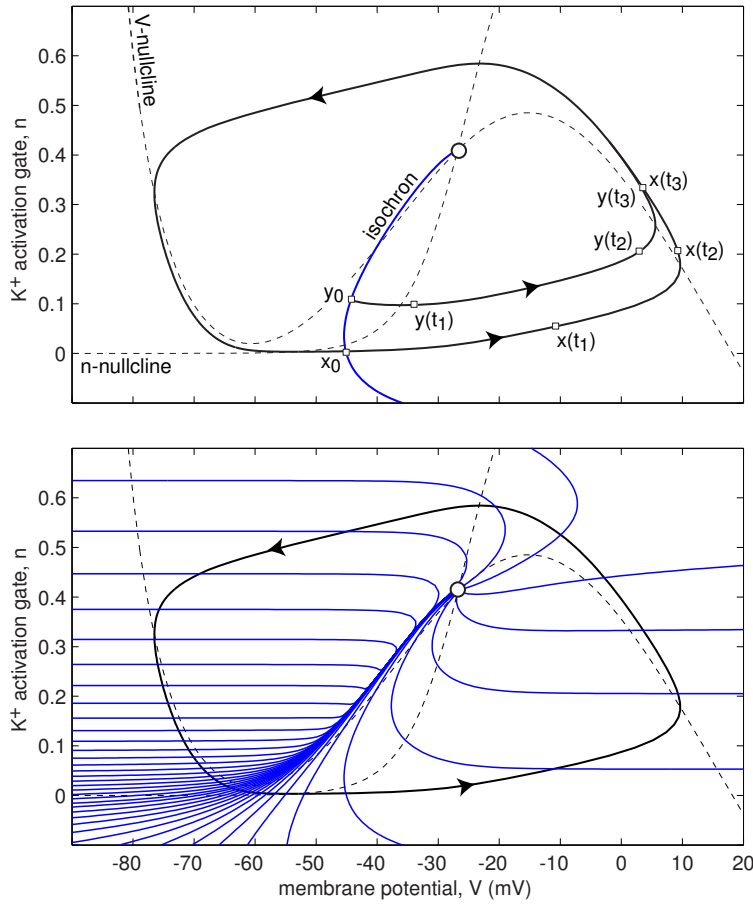


Figure 10.2: *Top:* An isochron, or a stable manifold, of a point  $x_0$  on the limit cycle attractor is the set of all initial conditions  $y_0$  such that  $y(t) \rightarrow x(t)$  as  $t \rightarrow +\infty$ . *Bottom:* Isochrons of the limit cycle attractor in Fig. 10.1 corresponding to 40 evenly distributed phases  $nT/40$ ,  $n = 1, \dots, 40$ .

phase space  $\mathbb{R}^2$  in Fig. 10.1b given by  $\vartheta \mapsto x(\vartheta)$ .

We could put the initial point  $x_0$  corresponding to the zero phase anywhere else on the limit cycle, and not necessarily at the peak of the spike. The choice of the initial point introduces an ambiguity in parameterizing the phase of oscillation. Different parametrizations, however, are equivalent up to a constant phase shift, i.e., translation in time. In the rest of the chapter,  $\vartheta$  always denotes the phase of oscillation, the parameter  $T$  denotes the period of oscillation, and  $\vartheta = 0$  corresponds to the peak of the spike unless stated otherwise. If the system has two or more co-existing limit cycle attractors, then a separate phase variable needs to be defined for each attractor.

### 10.1.2 Isochrons

The phase of oscillation can also be introduced outside the limit cycle. Consider, for example, point  $y_0$  in Fig. 10.2, top. Since the trajectory  $y(t)$  is not on a limit cycle,

it is not periodic. However, it approaches the cycle as  $t \rightarrow +\infty$ . Hence, there is some point  $x_0$  on the limit cycle, not necessarily the closest to  $y_0$ , such that

$$y(t) \rightarrow x(t) \quad \text{as } t \rightarrow +\infty. \quad (10.2)$$

Now take the phase of the non-periodic solution  $y(t)$  to be the phase of its periodic proxy  $x(t)$ .

Alternatively, we can consider a point on the limit cycle  $x_0$  and find all the other points  $y_0$  that satisfy (10.2). The set of all such points is called *the stable manifold* of  $x_0$ . Since any solution starting on the stable manifold has an asymptotic behavior indistinguishable from that of  $x(t)$ , its phase is the same as that of  $x(t)$ . For this reason, the manifold represents solutions having equal phases, and it is often referred to as being the *isochron* of  $x_0$  (*iso*: equal and *chronos*: time), a notion going back to Bernoulli and Leibniz.

Every point on the plane in Fig. 10.2, except the unstable equilibrium, gives rise to a trajectory that approaches the limit cycle. Therefore, every point has some phase. Let  $\vartheta(x)$  denote the phase of the point  $x$ . Then, isochrons are level contours of the function  $\vartheta(x)$ , since the function is constant on each isochron.

The entire plane is foliated by isochrons. We depict only 40 representative ones in Fig. 10.2. In this chapter we consider neighborhoods of exponentially stable limit cycles, where the foliation is continuous and invariant (Guckenheimer 1975):

- *Continuity:* The function  $\vartheta(x)$  is continuous so that nearby points have nearby phases.
- *Invariance:* If  $\vartheta(x(0)) = \vartheta(y(0))$ , then  $\vartheta(x(t)) = \vartheta(y(t))$  for all  $t$ . Isochrons are mapped to isochrons by the flow of the vector-field.

Fig. 10.3 shows the geometry of isochrons of various oscillators. The Andronov-Hopf oscillator in the figure is often called a radial isochron clock for the obvious reason. It is simple enough to be solved explicitly, see Ex. 1. In general, finding isochrons is a daunting mathematical task. In Ex. 3 we present a MATLAB program that finds isochrons numerically.

### 10.1.3 PRC

Consider a periodically spiking neuron (10.1) receiving a single brief pulse of current that increases the membrane potential by  $A = 1$  mV, as in Fig. 10.4, left. Such a perturbation may not elicit an immediate spike, but it can change the timing, i.e., the phase, of the following spikes. For example, the perturbed trajectory (solid line in Fig. 10.4, left) fires earlier than the free-running unperturbed trajectory (dashed line). That is, right after the perturbation, the phase,  $\vartheta_{\text{new}}$ , is greater than the old phase,  $\vartheta$ . The magnitude of the phase shift of the spike train depends on the exact timing of the stimulus relative to the phase of oscillation  $\vartheta$ . Stimulating the neuron at different

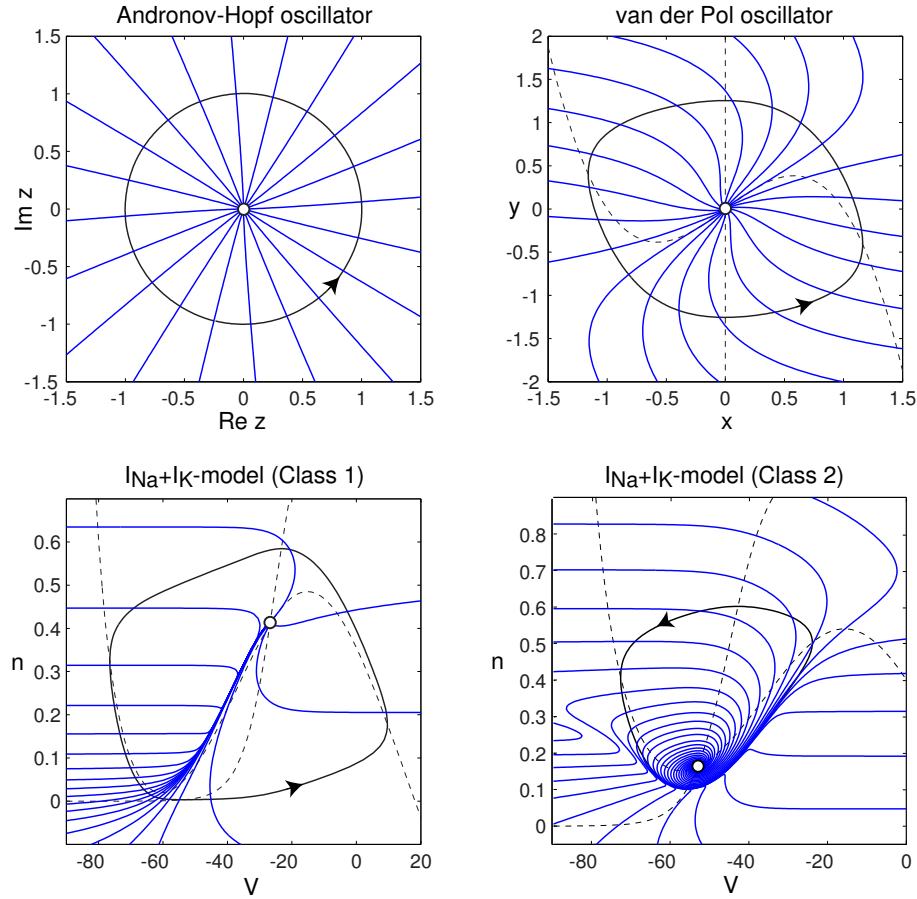


Figure 10.3: Isochrones of various oscillators. Andronov-Hopf oscillator:  $\dot{z} = (1 + i)z - z|z|^2$ ,  $z \in \mathbb{C}$ . van der Pol oscillator:  $\dot{x} = x - x^3 - y$ ,  $\dot{y} = x$ . The  $I_{\text{Na}} + I_{\text{K}}$ -model with parameters as in Fig. 4.1a and  $I = 10$  (Class 1) and  $I = 35$  (Class 2). Only isochrons corresponding to phases  $nT/20$ ,  $n = 1, \dots, 20$ , are shown.

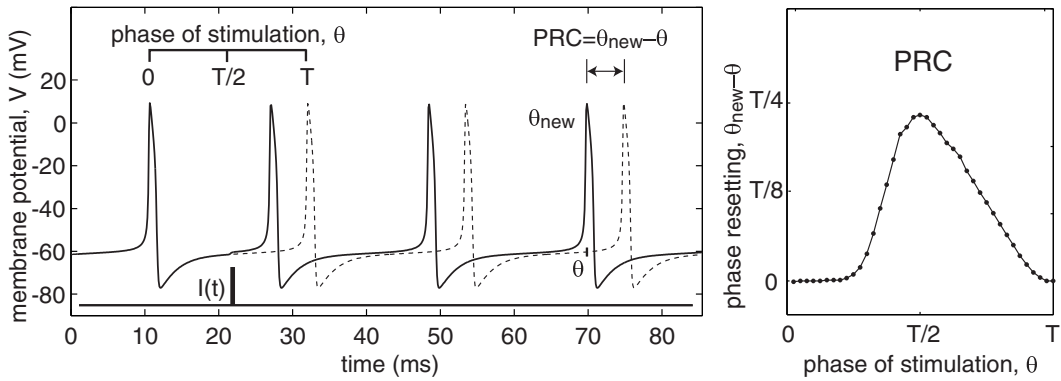


Figure 10.4: Phase response of the  $I_{\text{Na}} + I_{\text{K}}$ -model with parameters as in Fig. 4.1a and  $I = 4.7$ . The dashed voltage trace is the free-running trajectory.

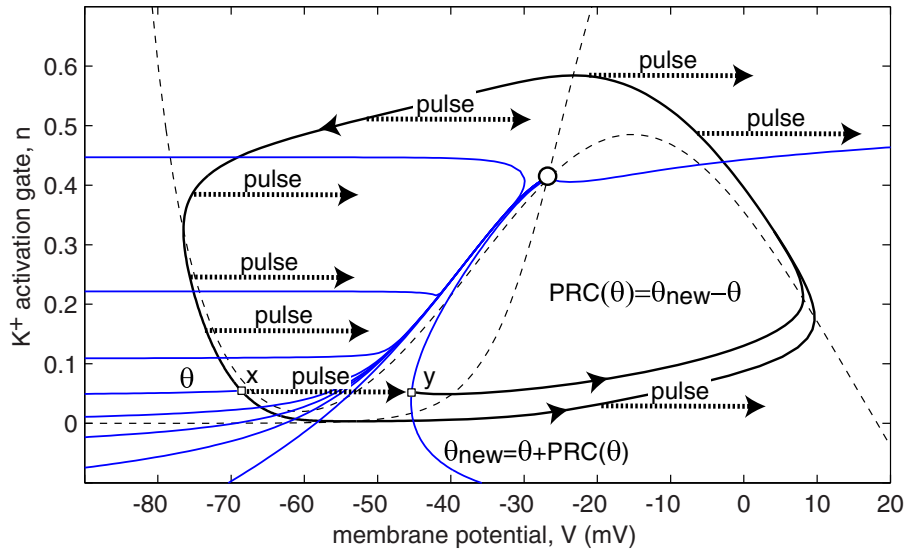


Figure 10.5: The geometrical relationship between isochrons and the phase response curve (PRC) of the  $I_{\text{Na}} + I_{\text{K}}$ -oscillator in Fig. 10.1.

phases, we can measure the *phase response curve* (also called phase resetting curve PRC, or spike time response curve STRC)

$$\text{PRC}(\vartheta) = \{\vartheta_{\text{new}} - \vartheta\} \bmod T \quad (\text{shift} = \text{new phase} - \text{old phase}),$$

depicted in Fig. 10.4, right. Positive (negative) values of the function correspond to phase advances (delays) in the sense that they advance (delay) the timing of the next spike.

In contrast to the common folklore, the function  $\text{PRC}(\vartheta)$  can be measured for an arbitrary stimulus, not necessarily weak or brief. The only caveat is that to measure the new phase of oscillation we need to wait long enough for transients to subside. This becomes a limiting factor when PRCs are used to study synchronization of oscillators to periodic pulses, as we do in Sect. 10.1.5.

There is a simple geometrical relationship between the structure of isochrons of an oscillator and its PRC, illustrated in Fig. 10.5, see also Ex. 6. Let us stimulate the oscillator at phase  $\vartheta$  by a pulse, which moves the trajectory from point  $x$  lying on the intersection of isochron  $\vartheta$  and the limit cycle attractor to a point  $y$  lying on some isochron  $\vartheta_{\text{new}}$ . From the definition of PRC, it follows that  $\vartheta_{\text{new}} = \vartheta + \text{PRC}(\vartheta)$ .

In general, one uses simulations to determine PRCs, as we do in Fig. 10.4. Using the MATLAB program presented in Ex. 5, we can determine PRCs of all four oscillators in Fig. 10.3 and plot them in Fig. 10.6. It is a good exercise to explain the shape of each PRC in the figure, or at least its sign, using the geometry of isochrons of corresponding oscillators. In Sect. 10.2.4 we discuss pitfalls of using the straightforward method in Fig. 10.4 to measure PRCs in biological neurons, and we present a better technique.

Notice that PRC of the  $I_{\text{Na}} + I_{\text{K}}$ -model in Fig. 10.6 is mainly positive in the Class 1 regime, i.e., when the oscillations appear via saddle-node on invariant circle bifurcation,

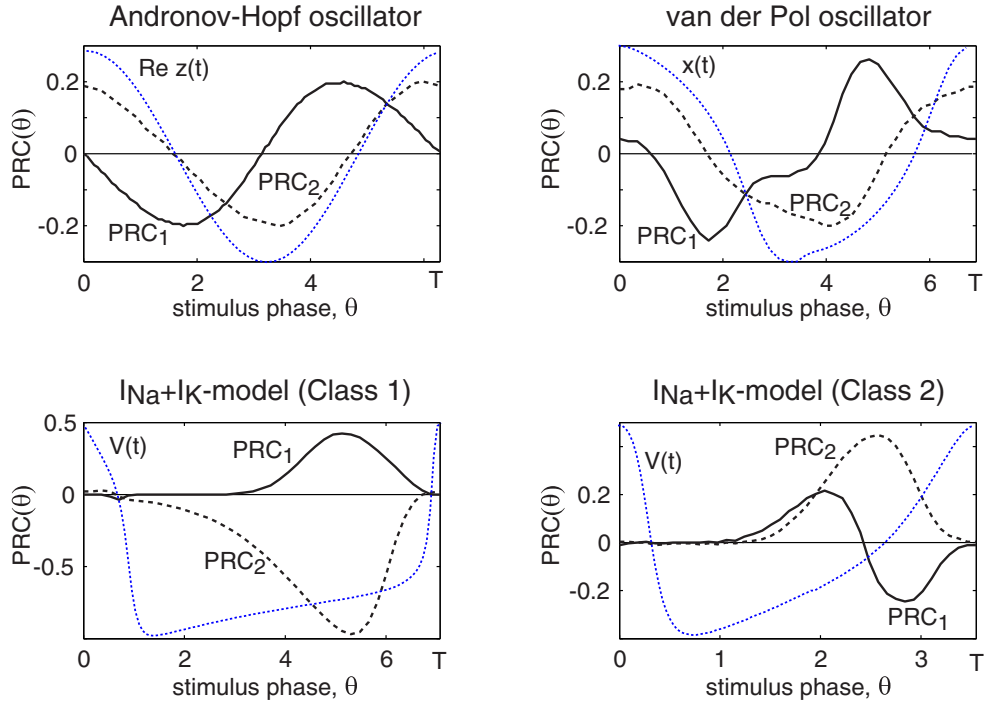


Figure 10.6: Examples of phase response curves (PRC) of the oscillators in Fig. 10.3.  $\text{PRC}_1(\vartheta)$ : Horizontal pulses (along the first variable) with amplitudes 0.2, 0.2, 2, 0.2 for Andronov-Hopf, van der Pol, Class 1 and Class 2 oscillators, respectively.  $\text{PRC}_2(\vartheta)$ : Vertical pulses (along the second variable) with amplitudes 0.2, 0.2, 0.02, 0.002, respectively. An example of oscillation is plotted as a dotted curve in each subplot (not to scale).

but it changes sign in the Class 2 regime, corresponding in this case to the supercritical Andronov-Hopf bifurcation. In Sect. 10.4 we find PRCs analytically in the case of weak coupling, and show that PRC of a Class 1 oscillator has the shape  $\sin^2 \vartheta$  (period  $T = \pi$ ) or  $1 - \cos \vartheta$  (period  $T = 2\pi$ ), whereas that of Class 2 oscillator has the shape  $\sin \vartheta$  (period  $T = 2\pi$ ). We show in Sect. 10.1.7 how the synchronization properties of an oscillator depend on the shape of its PRC.

#### 10.1.4 Type 0 and 1 phase response

Instead of phase resetting curves, many researchers in the field of circadian rhythms consider *phase transition curves* (Winfree 1980)

$$\vartheta_{\text{new}} = \text{PTC}(\vartheta_{\text{old}}).$$

Since

$$\text{PTC}(\vartheta) = \{\vartheta + \text{PRC}(\vartheta)\} \bmod T,$$

the two approaches are equivalent. PRCs are convenient when the phase shifts are small, so that they can be magnified and clearly seen. PTCs are convenient when the

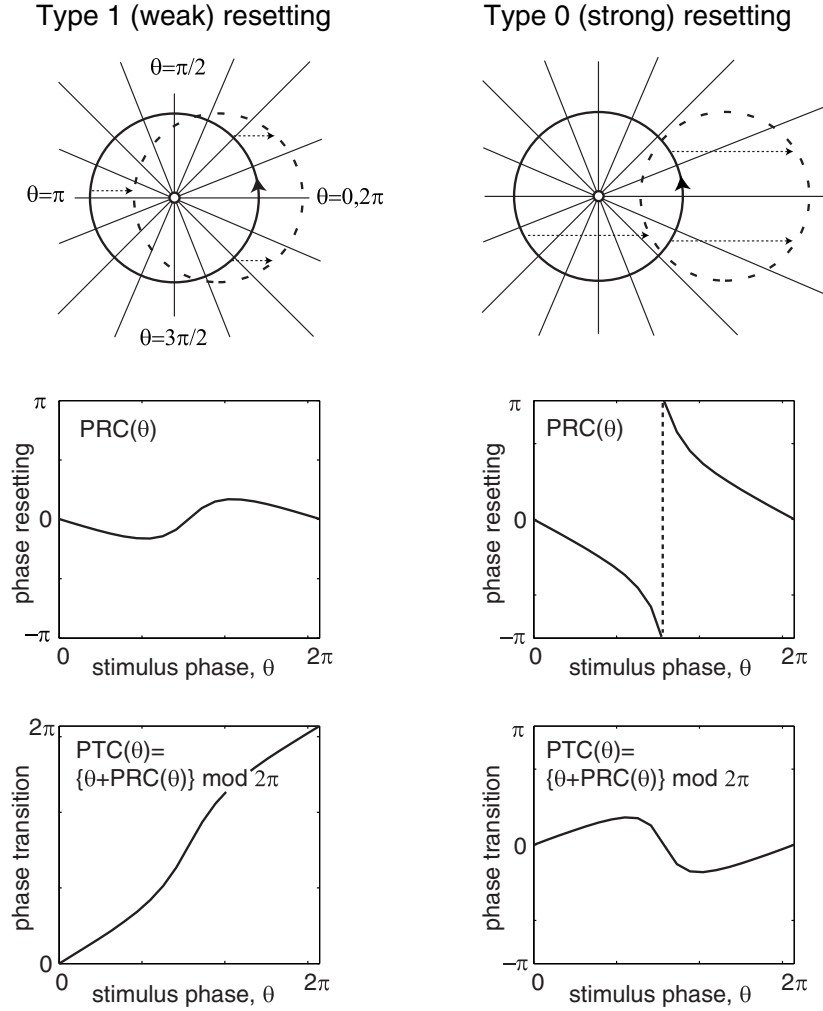


Figure 10.7: Types of phase resetting of the Andronov-Hopf oscillator in Fig. 10.3.

phase shifts are large and comparable with the period of oscillation. We present PTCs in this section solely for the sake of review, and we use PRCs throughout the rest of the chapter.

In Fig. 10.7, top, we depict phase portraits of the Andronov-Hopf oscillator having radial isochrons and receiving pulses of magnitude  $A = 0.5$  (left) and  $A = 1.5$  (right). Notice the drastic difference between the corresponding PRCs or PTCs. Winfree (1980) distinguishes two cases:

- *Type 1 (weak) resetting* results in continuous PRCs and PTCs with mean slope 1.
- *Type 0 (strong) resetting* results in discontinuous PRCs and PTCs with mean slope 0.

(Do not confuse these classes with Class 1, 2, and 3 excitability.) The discontinuity

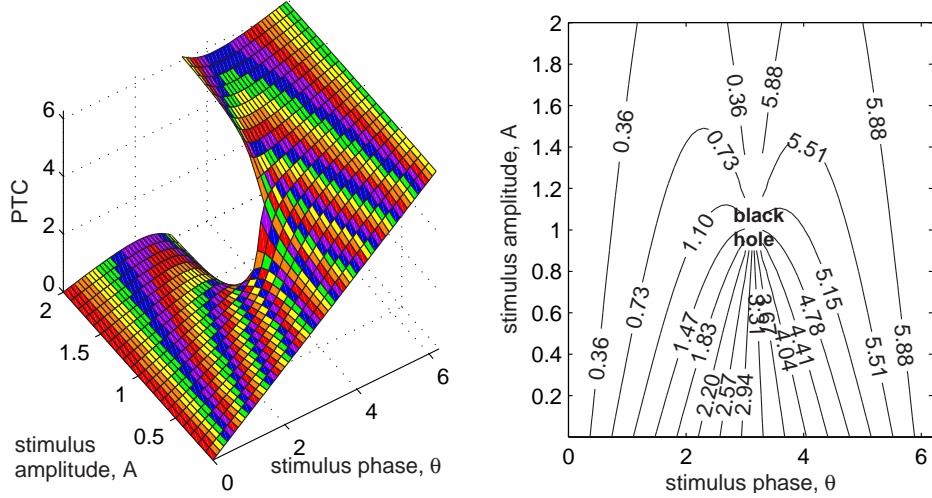


Figure 10.8: Time crystal (left) and its contour plot (right). Shown is the  $\text{PTC}(\vartheta, A)$  of the Andronov-Hopf oscillator (see Ex. 4).

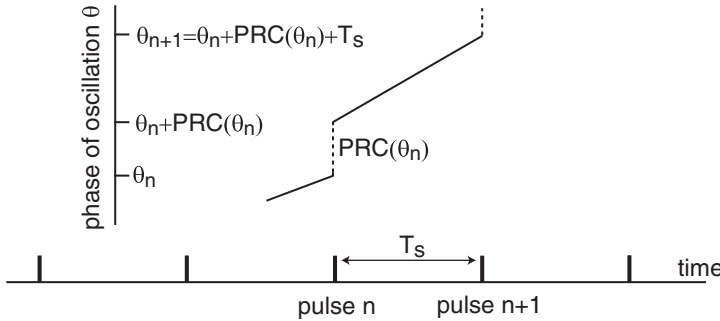


Figure 10.9: Calculation of the Poincare phase map.

of Type 0 PRC in Fig. 10.7 is a topological property that cannot be removed by reallocating the initial point  $x_0$  that corresponds to zero phase. As an exercise, prove that the discontinuity stems from the fact that the shifted image of the limit cycle (dashed circle) goes beyond the central equilibrium at which the phase is not defined.

If we vary not only the phase  $\vartheta$  of the applied stimulus, but also its amplitude  $A$ , then we obtain parameterized PRC and PTC. In Fig. 10.8 we plot  $\text{PTC}(\vartheta, A)$  of the Andronov-Hopf oscillator (the corresponding PRC is derived in Ex. 4). The surface is called *time crystal* and it can take quite amazing shapes (Winfree 1980). The contour plot of  $\text{PTC}(\vartheta, A)$  in the figure contains the singularity point (black hole) that corresponds to the phaseless equilibrium of the Andronov-Hopf oscillator. Stimulation at phase  $\vartheta = \pi$  with magnitude  $A = 1$  pushes the trajectory into the equilibrium and stalls the oscillation.

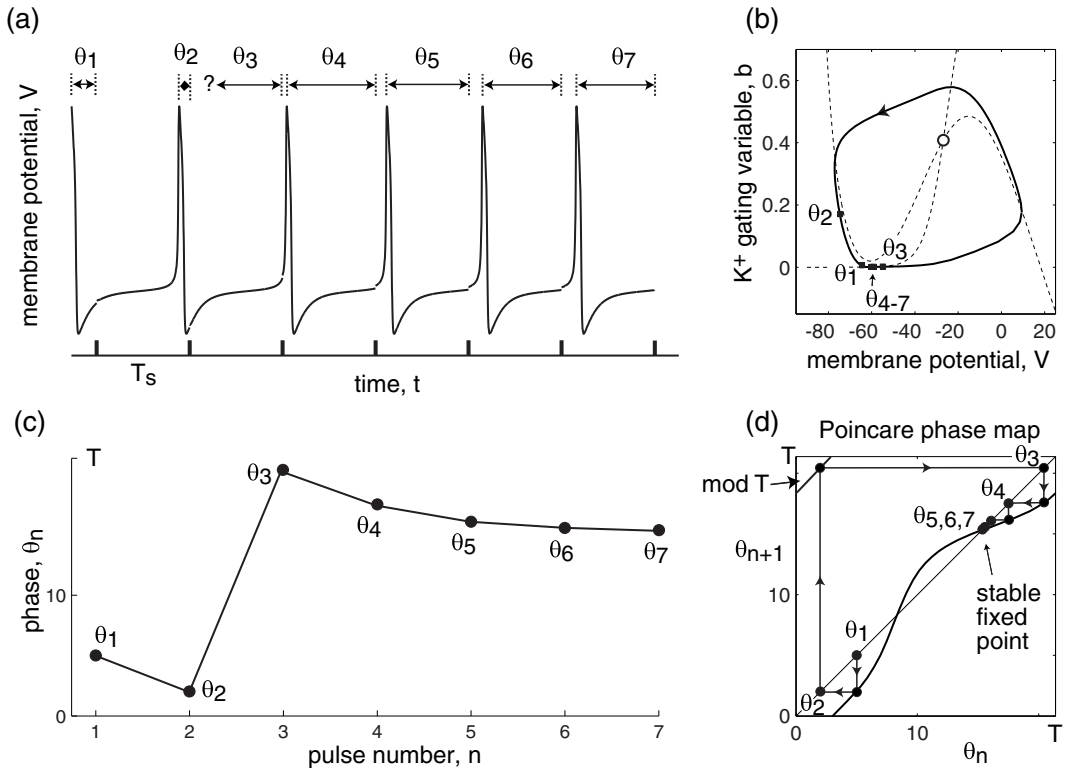


Figure 10.10: Description of synchronization of  $I_{Na} + I_K$ -oscillator in Fig. 10.4 using Poincare phase map.

### 10.1.5 Poincare phase map

The phase resetting curve (PRC) describes the response of an oscillator to a single pulse, but it can be used to study its response to a periodic pulse train using the following “stroboscopic” approach. Let  $\vartheta_n$  denote the phase of oscillation at the time the  $n$ th input pulse arrives. Such a pulse resets the phase by  $PRC(\vartheta_n)$ , so that the new phase right after the pulse is  $\vartheta_n + PRC(\vartheta_n)$ ; see Fig. 10.9. Let  $T_s$  denote the period of pulsed stimulation. Then the phase of oscillation before the next,  $(n+1)$ th pulse, is  $\vartheta_n + PRC(\vartheta_n) + T_s$ . Thus, we have a stroboscopic mapping of a circle to itself

$$\vartheta_{n+1} = (\vartheta_n + PRC(\vartheta_n) + T_s) \bmod T \quad (10.3)$$

called *Poincare phase map* (two pulse-coupled oscillators are considered in Ex. 11). Knowing the initial phase of oscillation  $\vartheta_1$  at the first pulse, we can determine  $\vartheta_2$ , then  $\vartheta_3$ , etc. The sequence  $\{\vartheta_n\}$  with  $n = 1, 2, \dots$ , is called the *orbit* of the map, and it is quite easy to find numerically.

Let us illustrate this concept using the  $I_{Na} + I_K$ -oscillator with PRC shown in Fig. 10.4. Its free-running period is  $T \approx 21.37$  ms, and the period of stimulation in Fig. 10.10a is  $T_s = 18.37$ , which results in the Poincare phase map depicted in Fig. 10.10d. The cobweb in the figure is the orbit going from  $\vartheta_1$  to  $\vartheta_2$  to  $\vartheta_3$ , etc. Notice

that the phase  $\vartheta_3$  cannot be measured directly from the voltage trace in Fig. 10.10a because pulse 2 changes the phase, so it is not the time since the last spike when pulse 3 arrives. The Poincare phase map (10.3) takes into account such multiple pulses. The orbit approaches a point (called fixed point, see below) that corresponds to a synchronized or phase-locked state.

A word of caution is in order. Recall that PRCs are measured on the limit cycle attractor. However, each pulse displaces the trajectory away from the attractor, as in Fig. 10.5. To use the PRC formalism to describe the effect of the next pulse, the oscillator must be given enough time to relax back to the limit cycle attractor. Thus, if the period of stimulation  $T_s$  is too small, or the attraction to the limit cycle is too slow, or the stimulus amplitude is too large, then the Poincare phase map may be not an appropriate tool to describe the phase dynamics.

### 10.1.6 Fixed points

To understand the structure of orbits of the Poincare phase map (10.3), or any other map

$$\vartheta_{n+1} = f(\vartheta_n), \quad (10.4)$$

we need to find its fixed points

$$\vartheta = f(\vartheta) \quad (\vartheta \text{ is a fixed point}),$$

which are analogues of equilibria of continuous dynamical systems. Geometrically, a fixed point is the intersection of the graph of  $f(\vartheta)$  with the diagonal line  $\vartheta_{n+1} = \vartheta_n$ ; see Fig. 10.10d or Fig. 10.11. At such a point, the orbit  $\vartheta_{n+1} = f(\vartheta_n) = \vartheta_n$  is fixed. A fixed point  $\vartheta$  is *asymptotically stable* if it attracts all nearby orbits, i.e., if  $\vartheta_1$  is in a sufficiently small neighborhood of  $\vartheta$ , then  $\vartheta_n \rightarrow \vartheta$  as  $n \rightarrow \infty$ , as in Fig. 10.11, left. The fixed point is *unstable* if any small neighborhood of the point contains an orbit diverging from it, as in Fig. 10.11, right.

The stability of the fixed point is determined by the slope

$$m = f'(\vartheta)$$

of the graph of  $f$  at the point, which is called *Floquet multiplier* of the mapping. It plays the same role as the eigenvalue  $\lambda$  of an equilibrium of a continuous dynamical system. Mnemonically, the relationship between them is  $\mu = e^\lambda$ , so that the fixed point is stable when  $|m| < 1$  ( $\lambda < 0$ ) and unstable when  $|m| > 1$  ( $\lambda > 0$ ). Fixed points bifurcate when  $|m| = 1$  ( $\lambda$  is zero or purely imaginary). They lose stability via flip bifurcation (a discrete analogue of Andronov-Hopf bifurcation) when  $m = -1$  and disappear via fold bifurcation (a discrete analogue of saddle-node bifurcation) when  $m = 1$ . The former plays an important role in the period-doubling phenomenon illustrated in Fig. 10.14, bottom trace. The latter plays an important role in the cycle slipping phenomenon illustrated in Fig. 10.16.

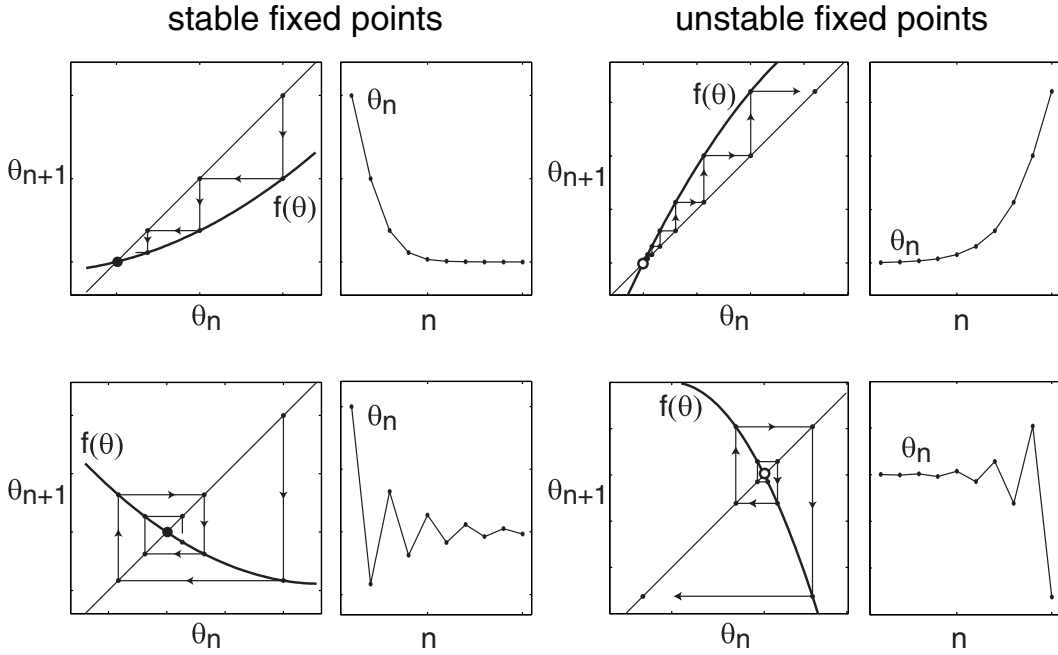


Figure 10.11: The stability of fixed points of the mapping (10.4) depends on the slope of the function  $f$ .

### 10.1.7 Synchronization

We say that two periodic pulse trains are synchronous, when the pulses occur at the same times or with a constant phase shift, as in Fig. 10.12a. Each subplot in the figure contains an input pulse train (bottom) and an output spike train (top), assuming that spikes are fired at zero crossings of the phase variable, as in Fig. 10.1. Such a synchronized state corresponds to a stable fixed point of the Poincare phase map (10.3). The in-phase, anti-phase, or out-of-phase synchronization corresponds to the phase shift  $\vartheta = 0$ ,  $\vartheta = T/2$ , or  $\vartheta$  equal some other value, respectively. Many scientist refer to the in-phase synchronization as just “synchronization”, and use the adjectives anti-phase or out-of-phase to denote the other types of synchronization.

When the period of stimulation,  $T_s$ , is near the free-running period of tonic spiking,  $T$ , then the fixed point of (10.3) satisfies

$$\text{PRC}(\vartheta) = T - T_s ,$$

i.e., it is the intersection of the PRC and the horizontal line, as in Fig. 10.13. Thus, synchronization occurs with such a phase shift  $\vartheta$  that compensates the input period mismatch  $T - T_s$ . The maxima and the minima of the PRC determine the tolerance of the oscillator to the mismatch. As an exercise, check that stable fixed points lie on the side of the graph with the slope

$$-2 < \text{PRC}'(\vartheta) < 0 \quad (\text{stability region})$$

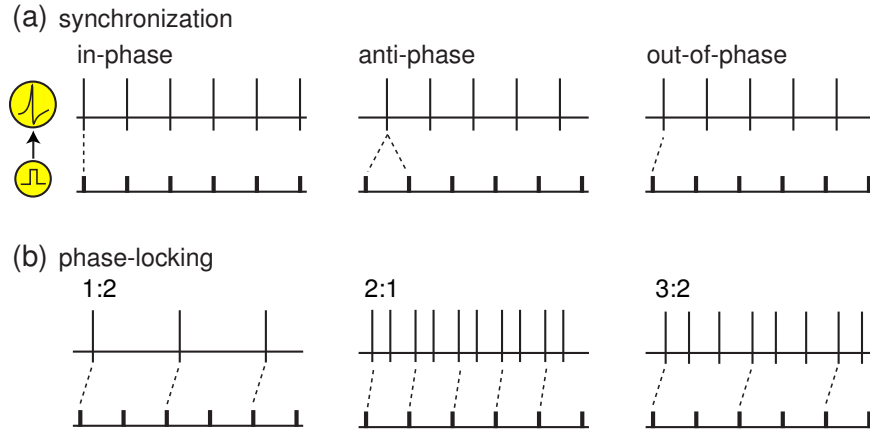


Figure 10.12: Examples of fundamental types of synchronization of spiking activity to periodic pulsed inputs (synchronization is 1:1 phase-locking).

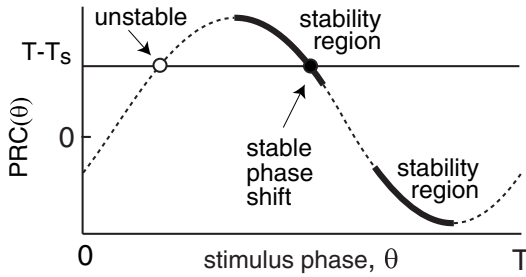


Figure 10.13: Fixed points of the Poincare phase map (10.1.5).

marked by the bold curves in Fig. 10.13.

Now consider the Class 1 and Class 2  $I_{\text{Na}} + I_K$ -oscillators shown in Fig. 10.6. The PRC in Class 1 regime is mostly positive, implying that such an oscillator can easily synchronize with faster inputs ( $T - T_s > 0$ ) but cannot synchronize with slower inputs. Indeed, the oscillator can only advance its phase to catch up faster pulse trains, but it cannot delay the phase to wait for the slower input. Synchronization with the input having  $T_s \approx T$  is only marginal. In contrast, Class 2  $I_{\text{Na}} + I_K$ -oscillator does not have this problem because its PRC has well-defined positive and negative regions.

### 10.1.8 Phase locking

*p:q-phase-locking* occurs when the oscillator fires  $p$  spikes for every  $q$  input pulses, such as the 3:2-phase-locking in Fig. 10.12b or 2:2 phase-locking in Fig. 10.14, which typically occurs when  $pT \approx qT_s$ . The integers  $p$  and  $q$  need not be relatively prime in the case of pulsed-coupled oscillators. Synchronization, i.e., 1:1 phase-locking, as well as  $p:1$  phase-locking corresponds to a fixed point of the Poincare phase map (10.3) with  $p$  fired spikes per one input pulse. Indeed, the map tells only the phase of the oscillator at each pulse, but does not tell the number of oscillations made between the pulses.

Each  $p:q$ -locked solution corresponds to a stable periodic orbit of the Poincare phase map with the period  $q$  (so that  $\vartheta_n = \vartheta_{n+q}$  for any  $n$ ). Such orbits in maps (10.4)

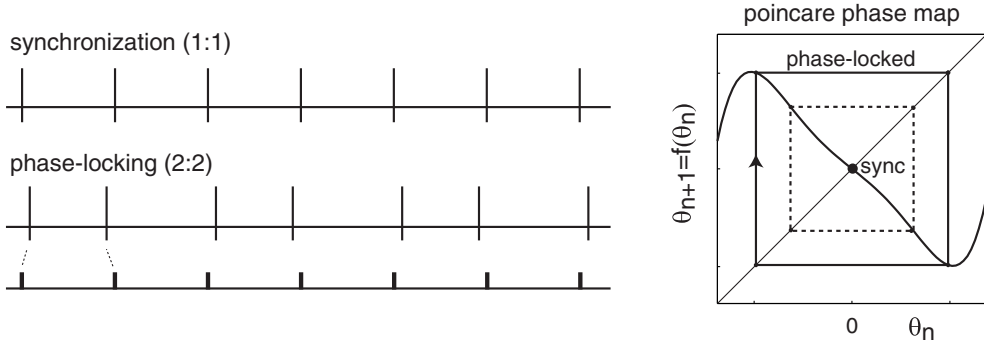


Figure 10.14: Co-existence of synchronized and phase-locked solutions corresponds to co-existence of stable fixed point and a stable periodic orbit of the Poincare phase map.

correspond to stable equilibria in the iterates  $\vartheta_{k+1} = f^q(\vartheta_k)$ , where  $f^q = f \circ f \circ \dots \circ f$  is the composition of  $f$  with itself  $q$  times. Geometrically, studying such maps is like considering every  $q$ -th input pulse in Fig. 10.12b and ignoring all the intermediate pulses.

Since maps can have co-existence of stable fixed points and periodic orbits, various synchronized and phase-locking states can co-exist in response to the same input pulse train, as in Fig. 10.14. The oscillator converges to one of the states depending on the initial phase of oscillation, but could be switched between the states by a transient input.

### 10.1.9 Arnold tongues

To synchronize an oscillator, the input pulse train must have period  $T_s$  sufficiently near the oscillator's free-running period  $T$  so that the graph of PRC and the horizontal line in Fig. 10.13 intersect. The amplitude of the function  $|\text{PRC}(\vartheta, A)|$  decreases as the strength of the pulse  $A$  decreases, because weaker pulses produce weaker phase shifts. Hence the region of existence of a synchronized state shrinks as  $A \rightarrow 0$ , and it looks like a horn or a tongue on the  $(T_s, A)$ -plane depicted in Fig. 10.15, called *Arnold tongue*. Each  $p:q$ -phase-locked state has its own region of existence ( $p:q$ -tongue in the figure), also shrinking to a point  $pT/q$  on the  $T_s$ -axis. The larger the order of locking,  $p + q$ , the narrower the tongue, and the more difficult it is to observe such a phase-locked state numerically, let alone experimentally.

The tongues can overlap, leading to the co-existence of phase-locked states, as in Fig. 10.14. If  $A$  is sufficiently large, the Poincare phase map (10.3) becomes non-invertible, i.e., it has a region of negative slope, and there is a possibility of chaotic dynamics (Glass and MacKey 1988).

In Fig. 10.16 we illustrate the *cycle slipping* phenomenon that occurs when the input period  $T_s$  drifts away from the 1:1 Arnold tongue. The fixed point of the Poincare phase map corresponding to the synchronized state undergoes a fold bifurcation and disappears. Similarly to the case of saddle-node on invariant circle bifurcation, the

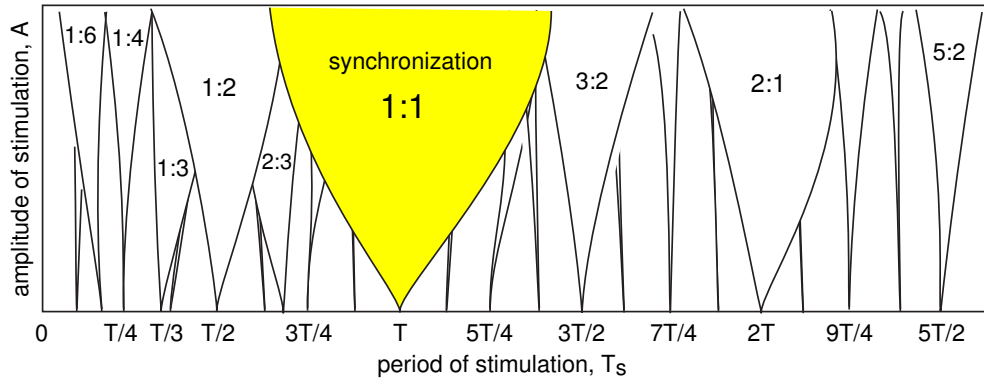


Figure 10.15: Arnold tongues are regions of existence of various phase-locked states on the “period-strength” plane.

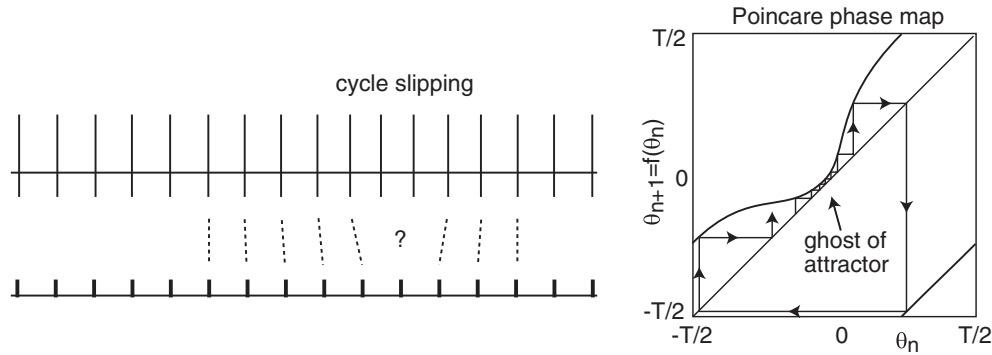


Figure 10.16: Cycle slipping phenomenon at the edge of the Arnold tongue corresponding to a synchronized state.

fold fixed point becomes a ghost attractor that traps orbits and keeps them near the synchronized state for a long period of time. Eventually the orbit escapes, the synchronized state is briefly lost, and then the orbit returns to the ghost attractor to be trapped again. Such an intermittently synchronized orbit typically corresponds to a  $p:q$ -phase-locked state with high order of locking  $p + q$ .

## 10.2 Weak Coupling

In this section we consider dynamical systems of the form

$$\dot{x} = f(x) + \varepsilon p(t), \quad (10.5)$$

describing periodic oscillators,  $\dot{x} = f(x)$ , forced by a time-depended input  $\varepsilon p(t)$ , e.g., from other oscillators in a network. The positive parameter  $\varepsilon$  measures the overall strength of the input, and it is assumed to be sufficiently small, denoted as  $\varepsilon \ll 1$ . We do not assume  $\varepsilon \rightarrow 0$  here. In fact, most of the results in this section can be cast in

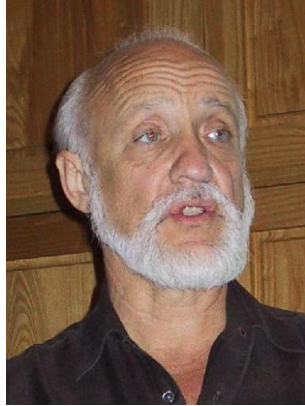


Figure 10.17: Arthur Winfree, 2001.

the form “there is an  $\varepsilon_0$  such that for all  $\varepsilon < \varepsilon_0$ , the following holds...” (Hoppensteadt and Izhikevich 1997), with  $\varepsilon_0$  depending on the function  $f(x)$  in (10.5) and sometimes taking not so small values, e.g.,  $\varepsilon_0 = 1$ .

Notice that if  $\varepsilon = 0$  in (10.5), then we can transform  $\dot{x} = f(x)$  to  $\dot{\vartheta} = 1$  using the theory presented in the previous section. What happens when we apply the same transformation to (10.5) with  $\varepsilon \neq 0$ ? In this section we present three different but equivalent approaches that transform (10.5) into the phase model

$$\dot{\vartheta} = 1 + \varepsilon \text{PRC}(\vartheta)p(t) + o(\varepsilon).$$

Here, the Landau’s “little oh” function  $o(\varepsilon)$  denotes the error terms smaller than  $\varepsilon$  so that  $o(\varepsilon)/\varepsilon \rightarrow 0$  if  $\varepsilon \rightarrow 0$ . For the sake of clarity of notation, we omit  $o(\varepsilon)$  throughout the book, and implicitly assume that all equalities are valid up to the terms of order  $o(\varepsilon)$ .

Since we do not impose restrictions on the form of  $p(t)$ , the three methods are readily applicable to the case

$$p(t) = \sum_s g_s(x(t), x_s(t)),$$

where the set  $\{x_s(t)\}$  denotes oscillators in the network connected to  $x$ , and  $p(t)$  is the postsynaptic current.

### 10.2.1 Winfree’s approach

A sufficiently small neighborhood of the limit cycle attractor of the unperturbed ( $\varepsilon = 0$ ) oscillator (10.5), magnified in Fig. 10.18, has nearly collinear uniformly spaced isochrons. Collinearity implies that a point  $x$  on the limit cycle in Fig. 10.18 has the same phase-resetting as any other point  $y$  on the isochron of  $x$  near the cycle. Uniform density of isochrons implies that the phase resetting scales linearly with the strength of the pulse, i.e., a half-pulse at the point  $z$  in Fig. 10.18 produces a half-resetting of the phase.

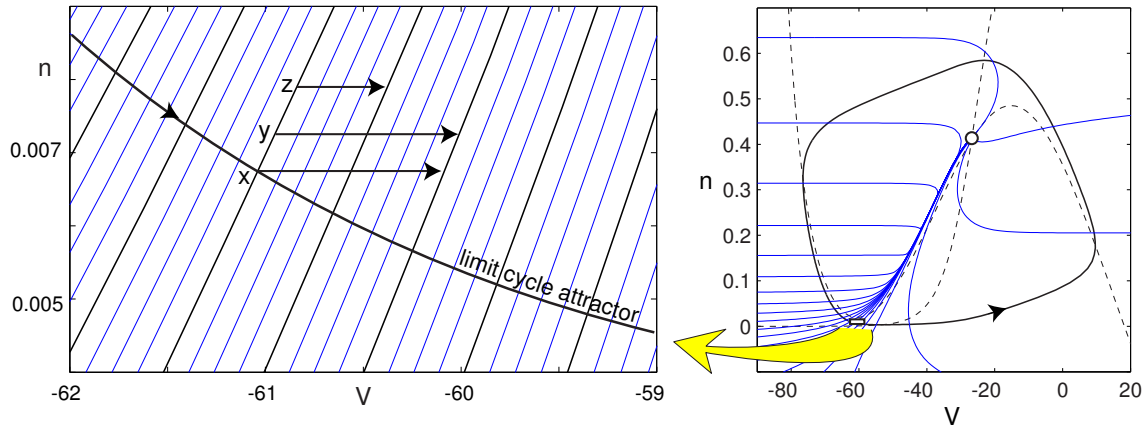


Figure 10.18: Magnification of isochrons in a small neighborhood of the limit cycle of the  $I_{Na} + I_K$ -model in Fig. 10.3. Isochron time step: 0.025 ms on the left, 0.35 ms on the right.

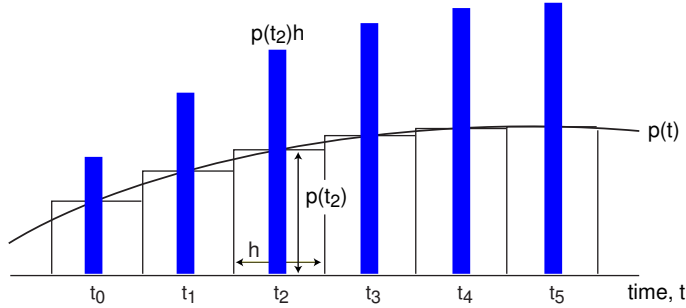


Figure 10.19: A continuous function  $p(t)$  is replaced by an equivalent train of pulses of variable amplitudes.

Linear scaling of PRC with respect to the strength of the pulse motivates the substitution

$$\text{PRC}(\vartheta, A) \approx Z(\vartheta)A,$$

where  $Z(\vartheta) = \partial \text{PRC}(\vartheta, A)/\partial A$  at  $A = 0$  is the *linear response* or *sensitivity* function (Winfree 1967) describing the slight alteration of rate, or of instantaneous frequency of oscillation, accompanying application of a small stimulus. Some call it the *infinitesimal PRC*.

Now suppose  $\varepsilon \neq 0$  but sufficiently small, so that the trajectory of the weakly perturbed oscillator (10.5) remains near the limit cycle attractor all the time. Let us replace the continuous input function  $\varepsilon p(t)$  by the equivalent train of pulses of strength  $A = \varepsilon p(t_n)h$ , where  $h$  is a small interpulse interval (denoted as  $T_s$  in the previous section), and  $t_n = nh$  is the timing of the  $n$ -th pulse, see Fig. 10.19. We



Figure 10.20: Yoshiki Kuramoto in 1988, while he was visiting Jim Murray's institute at University of Oxford.

rewrite the corresponding Poincare phase map (10.3)

$$\vartheta(t_{n+1}) = \{\vartheta(t_n) + \underbrace{Z(\vartheta(t_n)) \varepsilon p(t_n) h}_{A} + h\} \bmod T$$

in the form

$$\frac{\vartheta(t_n + h) - \vartheta(t_n)}{h} = Z(\vartheta(t_n)) \varepsilon p(t_n) + 1 ,$$

which is a discrete version of

$$\dot{\vartheta} = 1 + \varepsilon Z(\vartheta) \cdot p(t) , \quad (10.6)$$

in the limit  $h \rightarrow 0$ .

To be consistent with all the examples in the previous section, we implicitly assume here that  $p(t)$  perturbs only the first, voltage-like variable  $x_1$  of the state vector  $x = (x_1, \dots, x_m) \in \mathbb{R}^m$  and  $Z(\vartheta)$  is the corresponding sensitivity function. However, the phase model (10.6) is also valid for an arbitrary input  $p(t) = (p_1(t), \dots, p_m(t))$ . Indeed, let  $Z_i$  describe the linear response to perturbations of the  $i$ th state variable  $x_i$ , and  $Z(\vartheta) = (Z_1(\vartheta), \dots, Z_m(\vartheta))$  denote the corresponding linear response vector-function. Then, the combined phase shift  $Z_1 p_1 + \dots + Z_m p_m$  is just the dot product  $Z \cdot p$  in (10.6).

### 10.2.2 Kuramoto's approach

Consider the unperturbed ( $\varepsilon = 0$ ) oscillator (10.5), and let the function  $\vartheta(x)$  denote the phases of points near its limit cycle attractor. Obviously, isochrons are the level contours of  $\vartheta(x)$  since the function is constant on each isochron. Differentiating the function using the chain rule yields

$$\frac{d\vartheta(x)}{dt} = \text{grad } \vartheta \cdot \frac{dx}{dt} = \text{grad } \vartheta \cdot f(x) ,$$

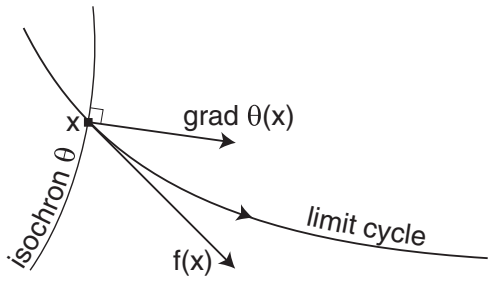


Figure 10.21: Geometrical interpretation of the vector  $\text{grad } \vartheta$ .

where  $\text{grad } \vartheta = (\vartheta_{x_1}(x), \dots, \vartheta_{x_m}(x))$  is the gradient of  $\vartheta(x)$  with respect to the state vector  $x = (x_1, \dots, x_m) \in \mathbb{R}^m$ . However,

$$\frac{d\vartheta(x)}{dt} = 1$$

near the limit cycle, because isochrons are mapped to isochrons by the flow of the vector-field  $f(x)$ . Therefore, we get a useful equality

$$\text{grad } \vartheta \cdot f(x) = 1 . \quad (10.7)$$

Figure 10.21 shows a geometrical interpretation of  $\text{grad } \vartheta(x)$ : it is the vector based at point  $x$ , normal to the isochron of  $x$  and with the length equal to the number density of isochrons at  $x$ . Its length can also be found from (10.7).

Kuramoto (1984) applied the chain rule to the perturbed system (10.5)

$$\frac{d\vartheta(x)}{dt} = \text{grad } \vartheta \cdot \frac{dx}{dt} = \text{grad } \vartheta \cdot \{f(x) + \varepsilon p(t)\} = \text{grad } \vartheta \cdot f(x) + \varepsilon \text{grad } \vartheta \cdot p(t) ,$$

and, using (10.7), obtained the phase model

$$\dot{\vartheta} = 1 + \varepsilon \text{grad } \vartheta \cdot p(t) , \quad (10.8)$$

which has the same form as (10.6). Subtracting (10.8) from (10.6) yields  $(Z(\vartheta) - \text{grad } \vartheta) \cdot p(t) = 0$ . Since this is valid for any  $p(t)$ , we conclude that  $Z(\vartheta) = \text{grad } \vartheta$ ; see also Ex. 6. Thus, Kuramoto's phase model (10.8) is indeed equivalent to Winfree's model (10.8).

### 10.2.3 Malkin's approach

Yet another equivalent method of reduction of weakly perturbed oscillators to their phase models follows from Malkin theorem (1949,1956), which we state in the simplest form below. The most abstract form and its proof is provided by Hoppensteadt and Izhikevich (1997).

*Malkin's theorem.* Suppose the unperturbed ( $\varepsilon = 0$ ) oscillator in (10.5) has an exponentially stable limit cycle of period  $T$ . Then its phase is described by the equation

$$\dot{\vartheta} = 1 + \varepsilon Q(\vartheta) \cdot p(t) , \quad (10.9)$$



Figure 10.22: Ioel Gil'evich Malkin (Иоэль Гильевич Малкин, 1907-1958).

where the  $T$ -periodic function  $Q$  is the solution to the linear “adjoint” equation

$$\dot{Q} = -\{Df(x(t))\}^\top Q , \quad \text{with } Q(0) \cdot f(x(0)) = 1 , \quad (10.10)$$

where  $Df(x(t))^\top$  is the transposed Jacobian of  $f$  (matrix of partial derivatives) at the point  $x(t)$  on the limit cycle, and the normalization condition can be replaced by  $Q(t) \cdot f(x(t)) = 1$  for any and hence all  $t$  (prove it). Here  $Q \cdot f$  is the dot product of two vectors, which is the same as  $Q^\top f$ .

Though this theorem looks less intuitive than the methods of Winfree and Kuramoto, it is actually more useful because (10.10) can be solved numerically quite easily. Applying the MATLAB procedure in Ex. 12 to the four oscillators in Fig. 10.3, we plot their functions  $Q$  in Fig. 10.23. It is not a coincidence that each component of  $Q$  looks like PRC along the first or the second state variable, respectively, shown in Fig. 10.6. Subtracting (10.9) from (10.8) or from (10.6), we conclude that

$$Z(\vartheta) = \text{grad } \vartheta(x) = Q(\vartheta) ,$$

(see also Ex. 7), so that we can determine the linear response function of the phase model using any of the three alternative methods: via PRCs, via isochrons, or solving the adjoint equation (10.10). This justifies why many refer to the function as just PRC, implicitly assuming that it is measured to the infinitesimal stimuli and then normalized by the stimulus amplitude.

#### 10.2.4 Measuring PRCs experimentally

In Fig. 10.24 we exploit the relationship (10.9) and measure the infinitesimal PRCs of a layer 5 pyramidal neuron of mouse visual cortex. First, we stimulate the neuron with 40 pA dc-current to elicit periodic spiking. Initially, the firing period starts at 50 ms, and then relaxes to the averaged value of 110 ms (Fig. 10.24a). The standard method of finding PRCs consists in stimulating the neuron by brief pulses of current at different phases of the cycle and measuring the induced phase shift, which could be approximated by the difference between two successive periods of oscillation. The method works fine in models, see Ex. 5, but should be used with caution in real neurons because their firing is too noisy, as we demonstrate in Fig. 10.24b. Thus, one needs

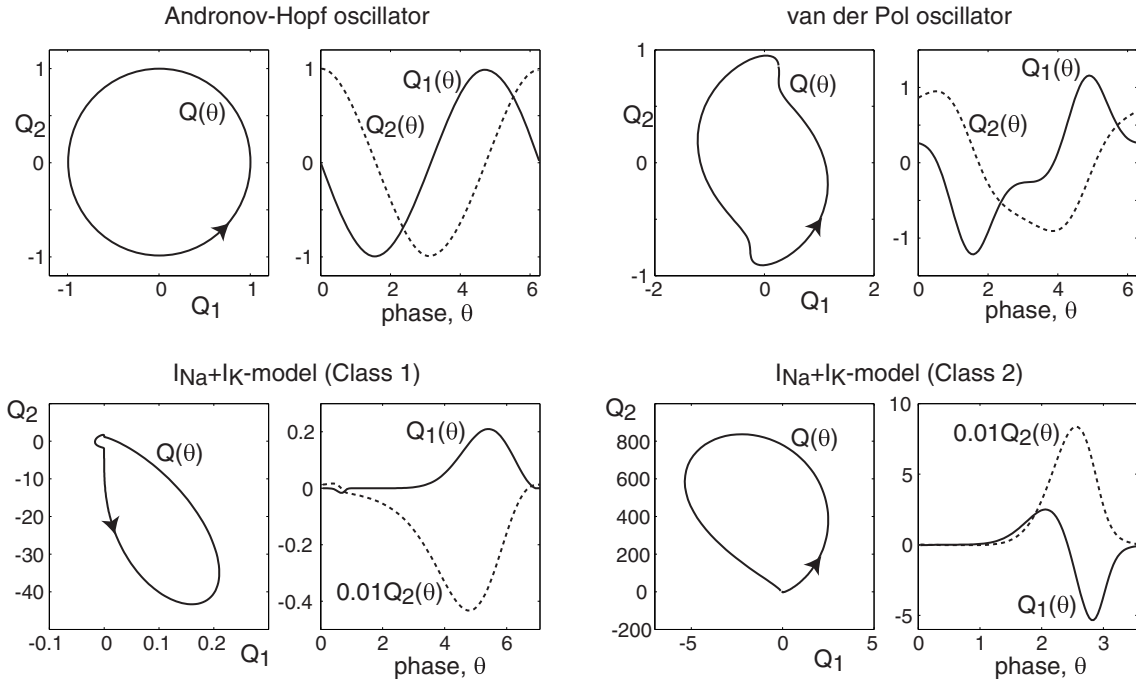


Figure 10.23: Solutions  $Q = (Q_1, Q_2)$  to adjoint problem (10.10) for oscillators in Fig. 10.3.

to apply hundreds if not thousands of pulses and then average the resulting phase deviations (Reyes and Fetz 1993).

Starting with time 10s we inject a relatively weak noisy current  $\varepsilon p(t)$  that continuously perturbs the membrane potential (Fig. 10.24c) and hence the phase of oscillation (the choice of  $p(t)$  is important; its Fourier spectrum must span a range of frequencies that depends on the frequency of firing of the neuron). Knowing  $\varepsilon p(t)$ , the moments of firing of the neuron, i.e., zero crossings  $\vartheta(t) = 0$ , and the relationship

$$\dot{\vartheta} = 1 + \text{PRC}(\vartheta)\varepsilon p(t),$$

we solve the inverse problem for the infinitesimal PRC  $\text{PRC}(\vartheta)$  and plot the solution in Fig. 10.24d. As one expects, the PRC is mostly positive, maximal just before the spike and almost zero during the spike. It would resemble the PRC in Fig. 10.23 ( $Q_1(\vartheta)$  in Class 1) if not for the dip in the middle, for which we have no explanation (probably it is due to overfitting). The advantage of this method is that it is more immune to noise, because intrinsic fluctuations are spread over the entire  $p(t)$  and not concentrated at the moments of pulses, unless of course  $p(t)$  consists of random pulses, in which case this method is equivalent to the standard one. The drawback is that we need to solve the equation above, which we do in Ex. 13 using an optimization technique.

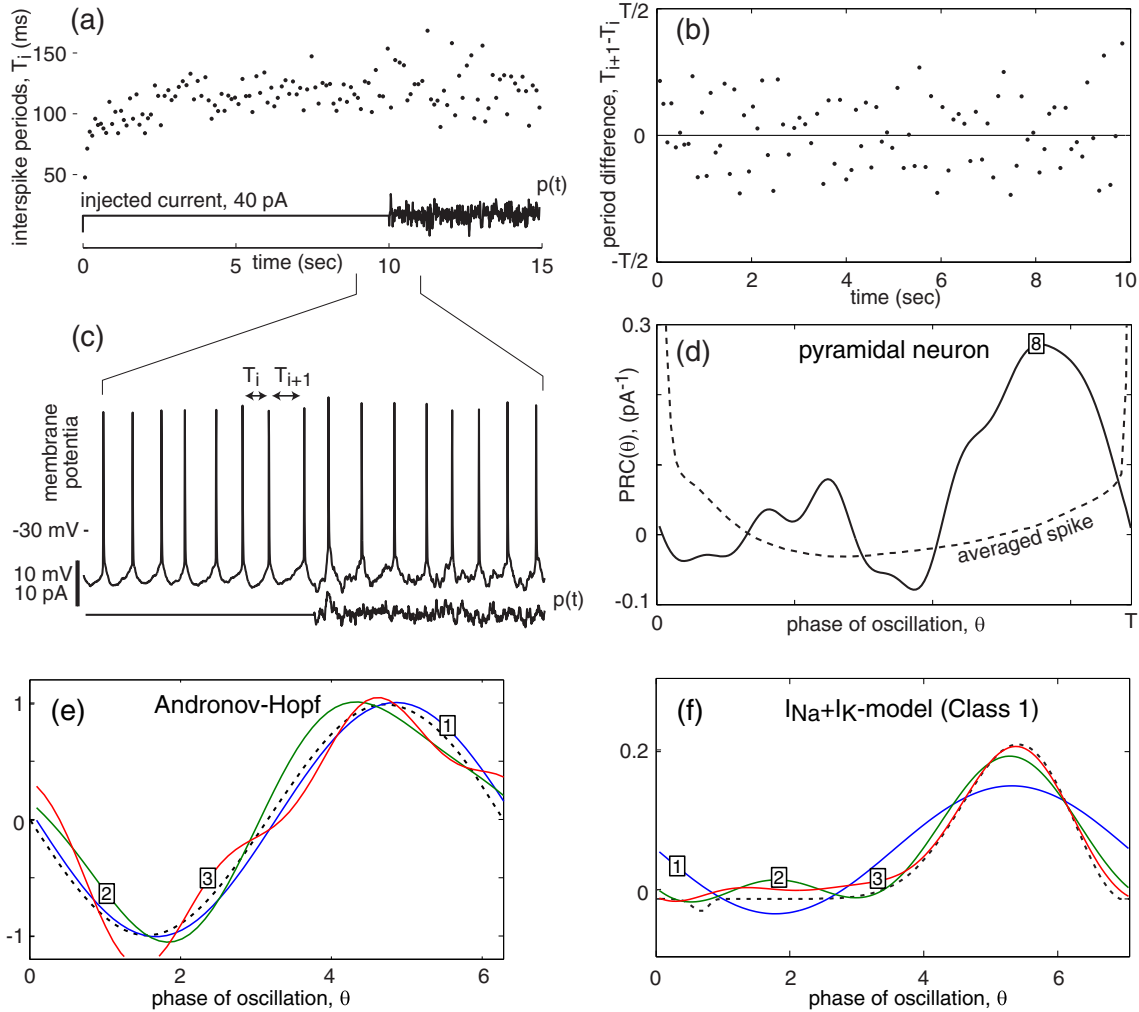


Figure 10.24: Measuring the infinitesimal PRC experimentally in a layer 5 pyramidal neuron of mouse visual cortex. (a) Interspike periods in response to the injection of dc-current. (b) Differences between successive periods. (c) Spiking 1 second before and after the noisy current  $p(t)$  is injected. (d) Infinitesimal PRC of the neuron (continuous curve) obtained from 40 cycles and the MATLAB program in Ex. 13 (first 8 Fourier terms). Averaged voltage trace during the spike (dotted curve) is plotted for reference. The same procedure applied to (e) the Andronov-Hopf oscillator and (f) the  $I_{\text{Na,p}} + I_K$ -model (Class 1). Numbers in boxes show the number of Fourier terms used to fit the curve, theoretical curves (functions  $Q_1(\vartheta)$  from Fig. 10.23) are dashed.

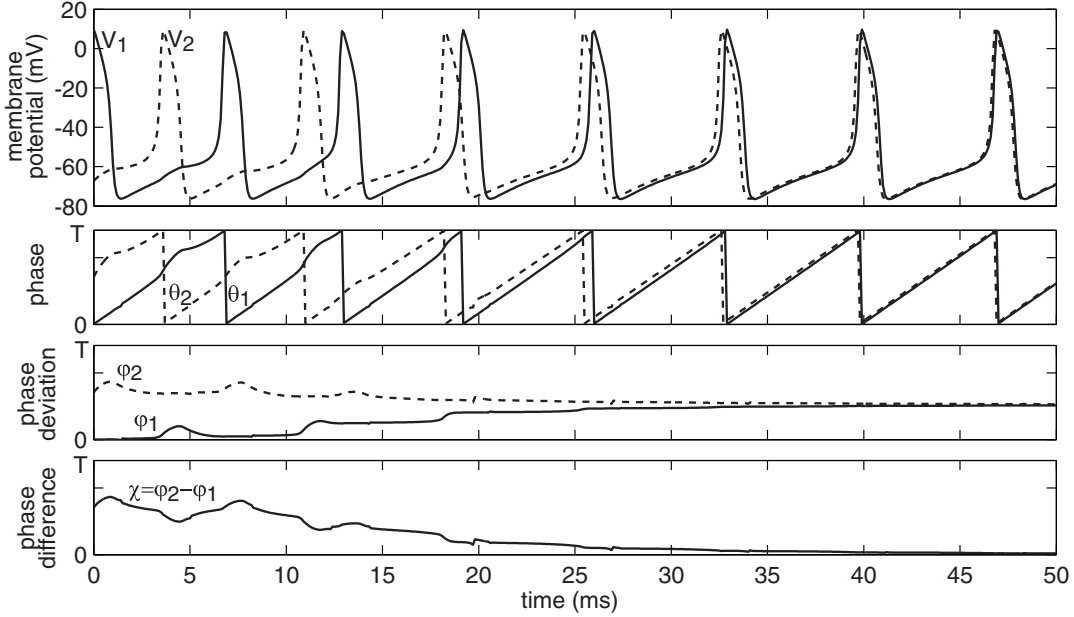


Figure 10.25: The relationship between membrane potential oscillation of two neurons,  $V_1$  (solid) and  $V_2$  (dashed), their phases, phase deviations, and phase difference. Shown are simulation of two  $I_{\text{Na}} + I_{\text{K}}$ -models with parameters as in Fig. 10.3 and coupled symmetrically via gap junctions  $0.1(V_j - V_i)$  (see Sect. 2.3.4).

### 10.2.5 Phase model for coupled oscillators

Now consider  $n$  weakly coupled oscillators of the form

$$\dot{x}_i = f_i(x_i) + \varepsilon \underbrace{\sum_{j=1}^n g_{ij}(x_i, x_j)}_{p_i(t)}, \quad x_i \in \mathbb{R}^m, \quad (10.11)$$

and assume that the oscillators, when uncoupled ( $\varepsilon = 0$ ), have equal free-running periods  $T_1 = \dots = T_n = T$ . Applying any of the three methods above to such a weakly perturbed system, we obtain the corresponding phase model

$$\dot{\vartheta}_i = 1 + \varepsilon Q_i(\vartheta_i) \cdot \underbrace{\sum_{j=1}^n g_{ij}(x_i(\vartheta_i), x_j(\vartheta_j))}_{p_i(t)}, \quad (10.12)$$

where each  $x_i(\vartheta_i)$  is the point on the limit cycle having phase  $\vartheta_i$ . Note that (10.11) is defined in  $\mathbb{R}^{nm}$ , whereas the phase model (10.12) is defined on the  $n$ -torus, denoted as  $\mathbb{T}^n$ .

To study collective properties of the network, such as synchronization, it is convenient to represent each  $\vartheta_i(t)$  as

$$\vartheta_i(t) = t + \varphi_i, \quad (10.13)$$

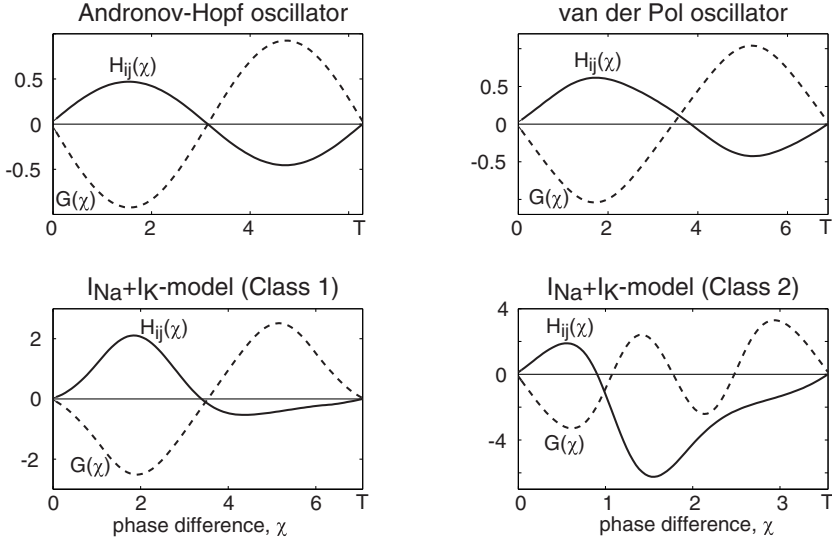


Figure 10.26: *Solid curves:* Functions  $H_{ij}(\chi)$  defined by (10.16) with the input  $g(x_i, x_j) = (x_{j1} - x_{i1}, 0)$  corresponding to electrical synapse via gap-junction. *Dashed curves:* Functions  $G(\chi) = H_{ji}(-\chi) - H_{ij}(\chi)$ . Parameters as in Fig. 10.3.

with the first term capturing *fast* free-running natural oscillation  $\dot{\vartheta}_i = 1$ , and the second term capturing *slow* network-induced build-up of *phase deviation* from the natural oscillation. The relationship between  $x_i(t)$ ,  $\vartheta_i(t)$  and  $\varphi_i(t)$  is illustrated in Fig. 10.25.

Substituting (10.13) into (10.12) results in

$$\dot{\varphi}_i = \varepsilon Q_i(t + \varphi_i) \cdot \sum_{j=1}^n g_{ij}(x_i(t + \varphi_i), x_j(t + \varphi_j)) . \quad (10.14)$$

Notice that the right hand-side is of order  $\varepsilon$ , reflecting the slow dynamics of phase deviations  $\varphi_i$  seen in Fig. 10.25. Thus, it contains two time scales: fast oscillations (variable  $t$ ) and slow phase modulation of phase (variables  $\varphi$ ). The classical method of averaging, reviewed by Hoppensteadt and Izhikevich (1997, Chap. 9) consists in a near-identity change of variables that transforms the system into the form

$$\dot{\varphi}_i = \varepsilon \omega_i + \varepsilon \sum_{j \neq i}^n H_{ij}(\varphi_j - \varphi_i) , \quad (10.15)$$

where

$$H_{ij}(\varphi_j - \varphi_i) = \frac{1}{T} \int_0^T Q_i(t) \cdot g_{ij}(x_i(t), x_j(t + \varphi_j - \varphi_i)) dt , \quad (10.16)$$

and each  $\omega_i = H_{ii}(\varphi_i - \varphi_i) = H_{ii}(0)$  describes a constant frequency deviation from the free-running oscillation. Figure 10.26 depicts the functions  $H_{ij}$  corresponding to gap-junction (i.e., electrical; see Sect. 2.3.4) coupling of oscillators in Fig. 10.3. Prove

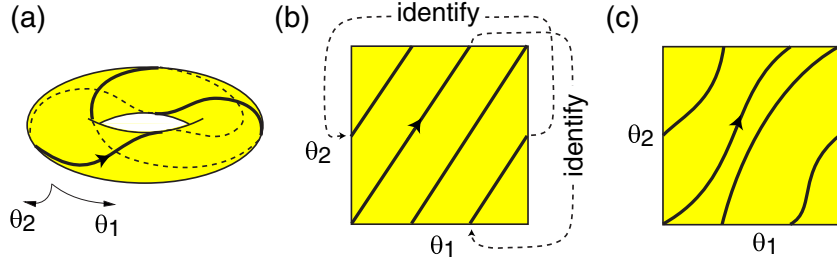


Figure 10.27: Torus knot of type (2,3) (a) and its representation on the square (b). The knot produces frequency locking and phase locking. (c) Torus knot that does not produce phase locking.

that  $H(\chi) = Q(\chi) \cdot A/T$  in the case of pulse-coupling (10.1), so that  $H(\chi)$  is just re-scaled PRC.

A special case of (10.15) is when  $H$  is replaced by its first Fourier term,  $\sin$ . The resulting system written in the slow time  $\tau = \varepsilon t$

$$\varphi'_i = \omega_i + \sum_{j=1}^n c_{ij} \sin(\varphi_j - \varphi_i + \psi_{ij})$$

is called the *Kuramoto phase model* (Kuramoto 1975). Here, the frequency deviations  $\omega_i$  are interpreted as intrinsic frequencies of oscillators. The strengths of connections  $c_{ij}$  are often assumed to be equal to  $K/n$  for some constant  $K$ , so that the model can be studied in the limit  $n \rightarrow \infty$ . The phase deviations  $\psi_{ij}$  are often neglected for the sake of simplicity.

To summarize, we transformed the weakly coupled system (10.11) into the phase model (10.15) with  $H$  given by (10.16) and each  $Q$  being the solution to the adjoint problem (10.10). This constitutes the Malkin theorem for weakly coupled oscillators (Hoppensteadt and Izhikevich 1997, Theorem 9.2).

## 10.3 Synchronization

Consider two coupled phase variables (10.12) in a general form

$$\begin{aligned}\dot{\vartheta}_1 &= h_1(\vartheta_1, \vartheta_2), \\ \dot{\vartheta}_2 &= h_2(\vartheta_1, \vartheta_2),\end{aligned}$$

with some positive functions  $h_1$  and  $h_2$ . Since each phase variable is defined on the circle  $\mathbb{S}^1$ , the state space of this system is the 2-torus  $\mathbb{T}^2 = \mathbb{S}^1 \times \mathbb{S}^1$  depicted in Fig. 10.27, with  $\vartheta_1$  and  $\vartheta_2$  being the longitude and the latitude, respectively. The torus can be represented as a square with vertical and horizontal sides identified, so that a solution disappearing at the right side of the square appears at the left side.

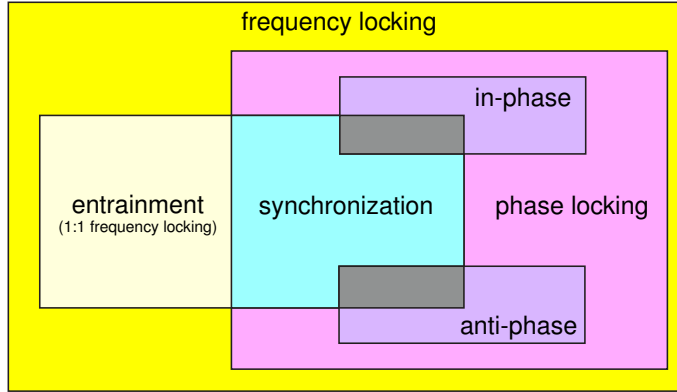


Figure 10.28: Various degrees of locking of oscillators.

The coupled oscillators above are said to be *frequency locked* when there is a periodic trajectory on the 2-torus, which is called a *torus knot*. It is said to be of type  $(p, q)$  if  $\vartheta_1$  makes  $p$  rotations while  $\vartheta_2$  makes  $q$  rotations, and  $p$  and  $q$  are relatively prime integers, i.e., do not have a common divisor greater than 1. Torus knots of type  $(p, q)$  produce  $p:q$  frequency locking, e.g., 2:3 frequency locking in Fig. 10.27. A 1:1 frequency locking is called *entrainment*. There could be many periodic orbits on the torus, with stable orbits between unstable ones. Since the orbits on the 2-torus cannot intersect, they all are knots of the same type, resulting in the same  $p:q$  frequency locking.

Let us follow a trajectory on the torus and count the number of rotations of the phase variables. The limit of the ratio of rotations as  $t \rightarrow \infty$  is independent on the trajectory we follow, and it is called the *rotation number* of the torus flow. It is rational if and only if there is a  $(p, q)$  periodic orbit, in which case the rotation number is  $p/q$ . An irrational rotation number implies there are no periodic orbits, and it corresponds to a *quasi-periodic* or *multiperiodic* torus flow. Oscillators exhibit *phase drifting* in this case. Denjoy (1932) proved that such coupled oscillators are topologically equivalent to the uncoupled system  $\dot{\vartheta}_1 = r$ ,  $\dot{\vartheta}_2 = 1$  with irrational  $r$ .

Suppose the oscillators are frequency locked; that is, there is a  $p : q$  limit cycle attractor on the torus. We say that the oscillators are  $p : q$  *phase locked* if

$$q\vartheta_1(t) - p\vartheta_2(t) = \text{const}$$

on the cycle. The value of the constant determines whether the locking is in-phase (const= 0), anti-phase (const=  $T/2$ , half-period), or out-of-phase. Frequency locking does not necessarily imply phase locking: The (2, 3) torus knot in Fig. 10.27b corresponds to phase locking, whereas that in Fig. 10.27c does not. Frequency locking without phase locking is called *phase trapping*. Finally, *synchronization* is a 1:1 phase locking. The phase difference  $\vartheta_2 - \vartheta_1$  is also called *phase lag* or *phase lead*. The relationships between all these definitions are shown in Fig. 10.28.

Frequency locking, phase locking, entrainment, and synchronization of a network of  $n > 2$  oscillators is the same as pair-wise locking, entrainment, and synchronization

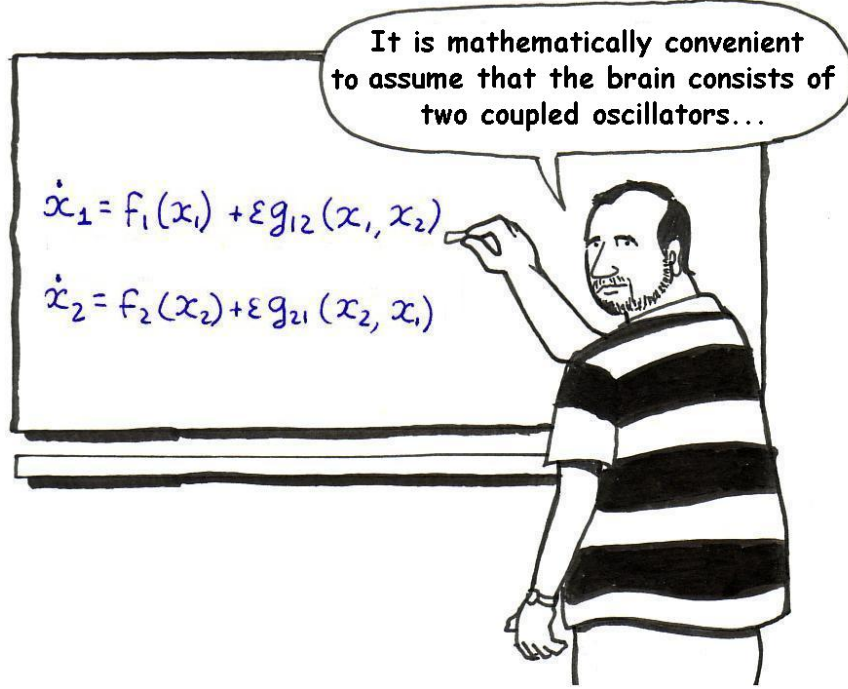


Figure 10.29: A major part of computational neuroscience concerns coupled oscillators.

of the oscillators comprising the network. In addition, a network can exhibit partial synchronization, when only a subset of oscillators is synchronized.

Synchronization of oscillators with nearly identical frequencies is described by the phase model (10.15). Existence of one equilibrium of (10.15) implies the existence of the entire circular family of equilibria, since translation of all  $\varphi_i$  by a constant phase shift does not change the phase differences  $\varphi_j - \varphi_i$  and hence the form of (10.15). This family corresponds to a limit cycle of (10.11), on which all oscillators,  $x_i(t + \varphi_i)$ , have equal frequencies and constant phase shifts, i.e., they are synchronized, possibly out-of-phase.

### 10.3.1 Two oscillators

Consider (10.11) with  $n = 2$ , describing two coupled oscillators, as in Fig. 10.29. Let us introduce the “slow” time  $\tau = \varepsilon t$  and rewrite the corresponding phase model (10.15) in the form

$$\begin{aligned}\varphi'_1 &= \omega_1 + H_1(\varphi_2 - \varphi_1) , \\ \varphi'_2 &= \omega_2 + H_2(\varphi_1 - \varphi_2) ,\end{aligned}$$

where  $' = d/d\tau$  is the derivative with respect to slow time. Let  $\chi = \varphi_2 - \varphi_1$  denote the phase difference between the oscillators. Then the two-dimensional system above becomes one-dimensional

$$\chi' = \omega + G(\chi) , \quad (10.17)$$

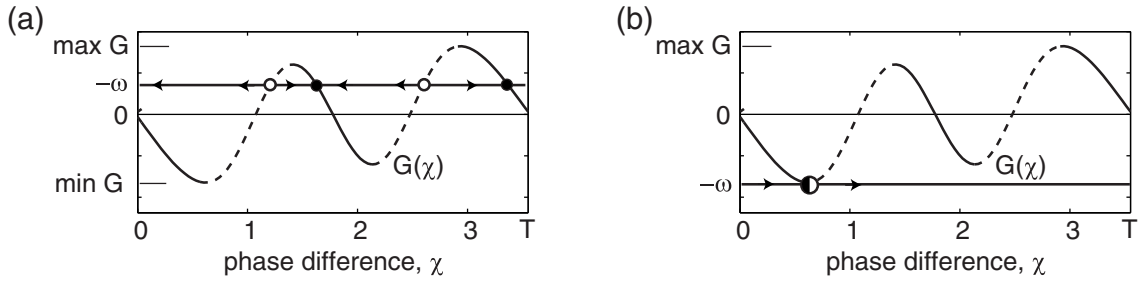


Figure 10.30: Geometrical interpretation of equilibria of the phase model (10.17) for gap-junction-coupled Class 2  $I_{\text{Na}} + I_{\text{K}}$ -oscillators (see Fig. 10.26).

where

$$\omega = \omega_2 - \omega_1 \quad \text{and} \quad G(\chi) = H_2(-\chi) - H_1(\chi) ,$$

is the frequency mismatch and the anti-symmetric part of the coupling, respectively, illustrated in Fig. 10.26, dashed curves. A stable equilibrium of (10.17) corresponds to a stable limit cycle of the phase model.

All equilibria of (10.17) are solutions to  $G(\chi) = -\omega$ , and they are intersections of the horizontal line  $-\omega$  with the graph of  $G$ , as illustrated in Fig. 10.30a. They are stable if the slope of the graph is negative at the intersection. If the oscillators are identical, then  $G(\chi) = H(-\chi) - H(\chi)$  is an odd function (i.e.,  $G(-\chi) = -G(\chi)$ ), and  $\chi = 0$  and  $\chi = T/2$  are always equilibria, possibly unstable, corresponding to the in-phase and anti-phase synchronized solutions. The stability condition of the in-phase synchronized state is

$$G'(0) = -2H'(0) < 0 \quad (\text{stability of in-phase synchronization})$$

The in-phase synchronization of electrically (gap-junction) coupled oscillators in Fig. 10.26 is stable because the slope of  $G$  (dashed curves) is negative at  $\chi = 0$ . Simulation of two coupled  $I_{\text{Na}} + I_{\text{K}}$ -oscillators in Fig. 10.25 confirms that. Coupled oscillators in Class 2 regime also have a stable anti-phase solution, since  $G' < 0$  at  $\chi = T/2$  in Fig. 10.30a.

The max and min values of the function  $G$  determine the tolerance of the network to the frequency mismatch  $\omega$ , since there are no equilibria outside this range. Geometrically, as  $\omega$  increases (the second oscillator speeds up), the horizontal line  $-\omega$  in Fig. 10.30a slides down, and the phase difference  $\chi = \varphi_2 - \varphi_1$  increases, compensating for the frequency mismatch  $\omega$ . When  $\omega > -\min G$ , the second oscillator becomes too fast, and the synchronized state is lost via saddle-node on invariant circle bifurcation; see Fig. 10.30b. This bifurcation corresponds to the annihilation of stable and unstable limit cycles of the weakly coupled network, and the resulting activity is called *drifting*, *cycle slipping*, or *phase walk-through*. The variable  $\chi$  slowly passes the ghost of the saddle-node point, where  $G(\chi) \approx 0$ , then increases past  $T$ , appears at 0, and approaches the ghost again, thereby slipping a cycle and walking through all the phase values  $[0, T]$ . The frequency of such slipping scales as  $\sqrt{\omega + \min G}$ ; see Sect. 6.1.2.

In Fig. 10.31 we contrast synchronization properties of weakly coupled oscillators of relaxation and non-relaxation type. The function  $G(\chi)$  of the former has a negative

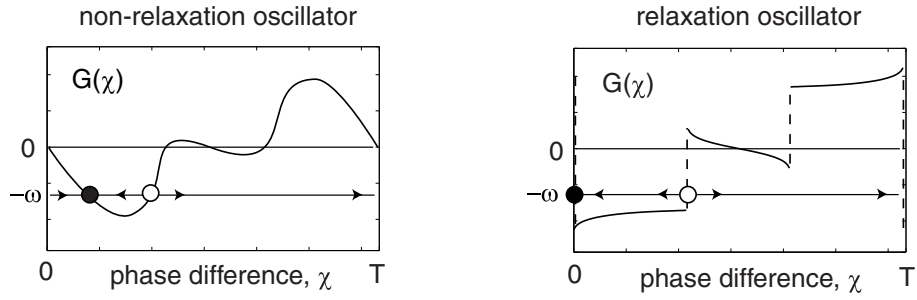


Figure 10.31: Functions  $G(\chi)$  for weakly coupled oscillators of non-relaxation (smooth) and relaxation type. The frequency mismatch  $\omega$  creates a phase difference in the smooth case, but not in the relaxation case.

discontinuity at  $\chi = 0$ ; see Sect. 10.4.4 below. An immediate consequence is that the in-phase synchronization is rapid and persistent in the presence of the frequency mismatch  $\omega$ . Indeed, if  $G$  is smooth, then  $\chi$  slows down while it approaches the equilibrium  $\chi = 0$ . As a result, complete synchronization is an asymptotic process that requires an infinite period of time to attain. In contrast, when  $G$  is discontinuous at 0, the variable  $\chi$  does not slow down and it takes a finite period of time to lock. Changing the frequency mismatch  $\omega$  shifts the root of  $-\omega = G(\chi)$  in the continuous case, but not in the discontinuous case. Hence, the in-phase synchronized state  $\chi = 0$  of coupled relaxation oscillators exists and it is stable in a wide range of  $\omega$ .

### 10.3.2 Chains

Understanding synchronization properties of two coupled oscillators helps one in studying the dynamics of chains of  $n > 2$  oscillators

$$\varphi'_i = \omega_i + H^+(\varphi_{i+1} - \varphi_i) + H^-(\varphi_{i-1} - \varphi_i), \quad (10.18)$$

where the functions  $H^+$  and  $H^-$  describe the coupling in the ascending and descending directions of the chain, as in Fig. 10.32. Any phase-locked solution of (10.18) has the form  $\varphi_i(\tau) = \omega_0\tau + \phi_i$ , where  $\omega_0$  is the common frequency of oscillation and  $\phi_i$  are constants. These satisfy  $n$  conditions

$$\begin{aligned} \omega_0 &= \omega_1 + H^+(\phi_2 - \phi_1), \\ \omega_0 &= \omega_i + H^+(\phi_{i+1} - \phi_i) + H^-(\phi_{i-1} - \phi_i), \quad i = 2, \dots, n-1, \\ \omega_0 &= \omega_n + H^-(\phi_{n-1} - \phi_n). \end{aligned}$$

A solution with  $\phi_1 < \phi_2 < \dots < \phi_n$  or with  $\phi_1 > \phi_2 > \dots > \phi_n$  (as in Fig. 10.32) is called a *traveling wave*. Indeed, the oscillators oscillate with a common frequency  $\omega_0$  but with different phases that increase or decrease monotonically along the chain. Such a behavior is believed to correspond to central pattern generation (CPG) in crayfish, undulatory locomotion in lamprey and dogfish, and peristalsis in vascular and intestinal smooth muscles. Below we consider two fundamentally different mechanisms of generation of traveling waves.

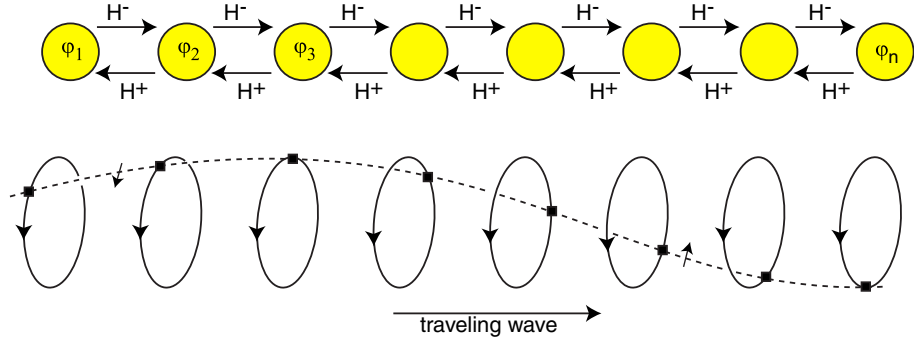


Figure 10.32: Traveling wave solutions in chains of oscillators (10.18) describe undulatory locomotion and central pattern generation.

### Frequency differences

Suppose the connections in (10.18) look qualitatively similar to those in Fig. 10.26, in particular,  $H^+(0) = H^-(0) = 0$ . If the frequencies are all equal, then the in-phase synchronized solution  $\varphi_1 = \dots = \varphi_n$  exists and is stable. A traveling wave exists when the frequencies are not all equal.

Let us seek the conditions for the existence of a traveling wave with a constant phase shift, say  $\chi = \phi_{i+1} - \phi_i$ , along the chain. Subtracting each equation from the second one, we find that

$$0 = \omega_2 - \omega_1 + H^-(-\chi), \quad 0 = \omega_2 - \omega_i, \quad 0 = \omega_2 - \omega_n + H^+(\chi),$$

and  $\omega_0 = \omega_1 + \omega_n - 2\omega_2$ . In particular, if  $\omega_1 \leq \omega_2 = \dots = \omega_{n-1} \leq \omega_n$ , which corresponds to the first oscillator being tuned up and the last oscillator being tuned down, then  $\chi < 0$  and the traveling wave moves up, as in Fig. 10.32, i.e., from the fastest to the slowest oscillator. Interestingly, such an ascending wave exists even when  $H^- = 0$ , i.e., even when the coupling is only in the opposite, descending direction.

When there is a linear gradient of frequencies ( $\omega_1 > \omega_2 > \dots > \omega_n$  or vice versa), as in the cases of the smooth muscle of intestines or leech CPG for swimming, one may still observe a traveling wave but with a non-constant phase difference along the chain. When the gradient is large enough, the synchronized solution corresponding to a single traveling wave disappears, and frequency plateaus may appear (Ermentrout and Kopell 1984). That is, solutions occur in which the first  $k < n$  oscillators are phase locked and the last  $n - k$  oscillators are phase locked as well, but the two pools oscillate with different frequencies. There may be many frequency plateaus.

### Coupling functions

A traveling wave solution may exist even when all the frequencies are equal, if either  $H^+(0) \neq 0$  or  $H^-(0) \neq 0$ . As an example, consider the case of descending coupling ( $H^- = 0$ )

$$\varphi'_i = \omega + H^+(\varphi_{i+1} - \varphi_i), \quad i = 1, \dots, n-1.$$

From  $\varphi'_n = \omega$  we find that  $\omega_0 = \omega$ , i.e., the common frequency is the frequency of the free oscillation of the last, uncoupled oscillator. The phase lag along the chain,  $\chi = \varphi_{i+1} - \varphi_i$ , satisfies  $n - 1$  identical conditions  $0 = H^+(\chi)$ . Thus, the traveling wave with a constant phase shift exists when  $H^+$  has a zero crossing with positive slope, in contrast to Fig. 10.26. The sign of  $\chi$ , and not the direction of coupling, determines the direction of wave propagation.

### 10.3.3 Networks

Now let us consider weakly connected networks (10.11) with arbitrary, possibly all to all coupling. To study synchronized states of the network, we need to determine whether the corresponding phase model (10.15) has equilibria and examine their stability properties. A vector  $\phi = (\phi_1, \dots, \phi_n)$  is an equilibrium of (10.15) when

$$0 = \omega_i + \sum_{j \neq i}^n H_{ij}(\phi_j - \phi_i) \quad \text{for all } i . \quad (10.19)$$

It is stable when all eigenvalues of the linearization matrix (Jacobian) at  $\phi$  have negative real parts, except one zero eigenvalue corresponding to the eigenvector along the circular family of equilibria ( $\phi$  plus a phase shift is a solution of (10.19) too since the phase differences  $\phi_j - \phi_i$  are not affected).

In general, determining the stability of equilibria is a difficult problem. Ermentrout (1992) found a simple sufficient condition. Namely, if

- $a_{ij} = H'_{ij}(\phi_j - \phi_i) \geq 0$ , and
- the directed graph defined by the matrix  $a = (a_{ij})$  is connected, (i.e., each oscillator is influenced, possibly indirectly, by every other oscillator),

then the equilibrium  $\phi$  is neutrally stable, and the corresponding limit cycle  $x(t + \phi)$  of (10.11) is asymptotically stable.

Another sufficient condition was found by Hoppensteadt and Izhikevich (1997). It states that if system (10.15) satisfies

- $\omega_1 = \dots = \omega_n = \omega$  (identical frequencies), and
- $H_{ij}(-\chi) = -H_{ji}(\chi)$  (pair-wise odd coupling)

for all  $i$  and  $j$ , then the network dynamics converge to a limit cycle. On the cycle, all oscillators have equal frequencies  $1 + \varepsilon\omega$  and constant phase deviations.

The proof follows from the observation that (10.15) is a gradient system in the rotating coordinates  $\varphi = \omega\tau + \phi$ , with the energy function

$$E(\phi) = \frac{1}{2} \sum_{i=1}^n \sum_{j=1}^n R_{ij}(\phi_j - \phi_i) , \quad \text{where} \quad R_{ij}(\chi) = \int_0^\chi H_{ij}(s) ds .$$

One can check that  $dE(\phi)/d\tau = -\sum(\phi'_i)^2 \leq 0$  along the trajectories of (10.15), with equality only at equilibria.

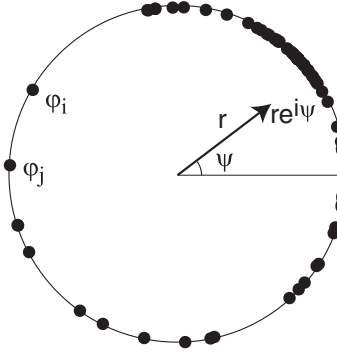


Figure 10.33: The Kuramoto synchronization index (10.21) describes the degree of coherence in the network (10.20).

#### 10.3.4 Mean-field approximations

Synchronization of the phase model (10.15) with randomly distributed frequency deviations  $\omega_i$  can be analyzed in the limit  $n \rightarrow \infty$ , often called thermodynamic limit by physicists. We illustrate the theory using the special case,  $H(\chi) = \sin \chi$  (Kuramoto 1975)

$$\varphi'_i = \omega_i + \frac{K}{n} \sum_{j=1}^n \sin(\varphi_j - \varphi_i), \quad \varphi_i \in [0, 2\pi], \quad (10.20)$$

where  $K > 0$  is the coupling strength and the factor  $1/n$  ensures that the model behaves well as  $n \rightarrow \infty$ . The complex-valued sum of all phases,

$$r e^{i\psi} = \frac{1}{n} \sum_{j=1}^n e^{i\varphi_j} \quad (\text{Kuramoto synchronization index}), \quad (10.21)$$

describes the degree of synchronization in the network. The parameter  $r$  is often called *order parameter* by physicists. Apparently, the in-phase synchronized state  $\varphi_1 = \dots = \varphi_n$  corresponds to  $r = 1$ , with  $\psi$  being the population phase. In contrast, the *incoherent* state with all  $\varphi_i$  having different values randomly distributed on the unit circle, corresponds to  $r \approx 0$ . (The case  $r \approx 0$  can also correspond to two or more clusters of synchronized neurons, oscillating anti-phase or out-of-phase and canceling each other). Intermediate values of  $r$  correspond to a *partially synchronized* or *coherent* state, depicted in Fig. 10.33. Some phases are synchronized forming a cluster, while others roam around the circle.

Multiplying both sides of (10.21) by  $e^{-i\varphi_i}$  and considering only the imaginary parts, we can rewrite (10.20) in the equivalent form

$$\varphi'_i = \omega_i + K r \sin(\psi - \varphi_i),$$

which emphasizes the mean-field character of interactions between the oscillators: They are all pulled into the synchronized cluster ( $\varphi_i \rightarrow \psi$ ) with the effective strength proportional to the cluster size  $r$ . This pull is offset by the random frequency deviations  $\omega_i$ , which pull away from the cluster.

Let us assume that the frequencies  $\omega_i$  are distributed randomly around 0 with a symmetric probability density function  $g(\omega)$ , e.g., Gaussian. Kuramoto (1975) has shown that in the limit  $n \rightarrow \infty$ , the cluster size  $r$  obeys the self-consistency equation

$$r = rK \int_{-\pi/2}^{+\pi/2} g(rK \sin \varphi) \cos^2 \varphi d\varphi \quad (10.22)$$

derived in Ex. 21. Notice that  $r = 0$ , corresponding to the incoherent state, is always a solution of this equation. When the coupling strength  $K$  is greater than a certain critical value,

$$K_c = \frac{2}{\pi g(0)},$$

an additional, nontrivial solution  $r > 0$  appears, which corresponds to a partially synchronized state. It scales as  $r = \sqrt{16(K - K_c)/(-g''(0)\pi K_c^4)}$ , as the reader can prove himself by expanding  $g$  in a Taylor series. Thus, the stronger the coupling  $K$  relative to the random distribution of frequencies, the more oscillators synchronize into a coherent cluster. The issue of stability of incoherent and partially synchronized states is discussed by Strogatz (2000).

## 10.4 Examples

Below we consider simple examples of oscillators to illustrate the theory developed in this chapter. Our goal is to understand which details of oscillators are important in shaping the PRC, the form of the function  $H$  in the phase deviation model, and hence the existence and stability of synchronized states.

### 10.4.1 Phase oscillators

Let us consider the simplest possible kind of a non-linear oscillator, known as the *phase oscillator*:

$$\dot{x} = f(x) + \varepsilon p(t), \quad x \in \mathbb{S}^1, \quad (10.23)$$

where  $f(x) > 0$  is a periodic function, for example,  $f(x) = a + \sin x$  with  $a > 1$ . Notice that this kind of oscillator is quite different from the two- or high-dimensional conductance-based models with limit cycle attractors that we considered in the previous chapters. Here, the state variable  $x$  is one-dimensional defined on a circle  $\mathbb{S}^1$ , that is, it may be interpreted as a measure of distance along a limit cycle attractor of a multi-dimensional system.

Consider the unperturbed ( $\varepsilon = 0$ ) phase oscillator  $\dot{x} = f(x)$ , and let  $x(t)$  be its solution with some period  $T > 0$ . Following Kuramoto's idea, we substitute  $x(\vartheta)$  into (10.23) and use the chain rule,

$$f(x(\vartheta)) + \varepsilon p(t) = \{x(\vartheta)\}' = x'(\vartheta) \vartheta' = f(x(\vartheta))\vartheta',$$

to get the new phase equation

$$\dot{\vartheta} = 1 + \varepsilon p(t)/f(x(\vartheta)) , \quad (10.24)$$

which is equivalent to (10.23) for any, not necessarily small,  $\varepsilon$ .

We can also get (10.24) using any of the three methods of reduction of oscillators to phase models:

- *Malkin's* method is the easiest one: We do not even have to solve the one-dimensional adjoint equation (10.10) having the form  $\dot{Q} = -f'(x(t)) Q$ , because we can get the solution  $Q(t) = 1/f(x(t))$  directly from the normalization condition  $Q(t)f(x(t)) = 1$ .
- *Kuramoto's* method relies on the function  $\vartheta(x)$ , which we can find implicitly. Since the phase at a point  $x(t)$  on the limit cycle is just  $t$ ,  $x(\vartheta)$  is the inverse of  $\vartheta(x)$ . Using the rule for differentiating of inverse functions,  $\vartheta'(x) = 1/x'(\vartheta)$ , we find  $\text{grad } \vartheta = 1/f(x(\vartheta))$ .
- *Winfree's* method relies on PRC ( $\vartheta$ ), which we find using the following procedure: A pulsed perturbation at phase  $\vartheta$  moves the solution from  $x(\vartheta)$  to  $x(\vartheta) + A$ , which is  $x(\vartheta + \text{PRC}(\vartheta, A)) \approx x(\vartheta) + x'(\vartheta)\text{PRC}(\vartheta, A)$  when  $A$  is small. Hence,  $\text{PRC}(\vartheta, A) \approx A/x'(\vartheta) = A/f(x(\vartheta))$ , and the linear response is  $Z(\vartheta) = 1/f(x(\vartheta))$  when  $A \rightarrow 0$ .

Two coupled identical oscillators

$$\begin{aligned} \dot{x}_1 &= f(x_1) + \varepsilon g(x_2) \\ \dot{x}_2 &= f(x_2) + \varepsilon g(x_1) \end{aligned}$$

can be reduced to the phase model (10.17) with  $G(\chi) = H(-\chi) - H(\chi)$ , where

$$H(\chi) = \frac{1}{T} \int_0^T Q(t) g(x(t + \chi)) dt = \frac{1}{T} \int_0^T \frac{g(x(t + \chi))}{f(x(t))} dt$$

The condition for exponential stability of the in-phase synchronized state,  $\chi = 0$ , can be expressed in the following three equivalent forms

$$\int_0^T g'(x(t)) dt > 0 \quad \text{or} \quad \int_{\mathbb{S}^1} \frac{g'(x)}{f(x)} dx > 0 \quad \text{or} \quad \int_{\mathbb{S}^1} \frac{f'(x)}{f^2(x)} g(x) dx > 0 , \quad (10.25)$$

as we prove in Ex. 24.

### 10.4.2 SNIC oscillators

Let us go through all the steps of derivation of the phase equation using a neuron model exhibiting low-frequency periodic spiking. Such a model is near the saddle-node

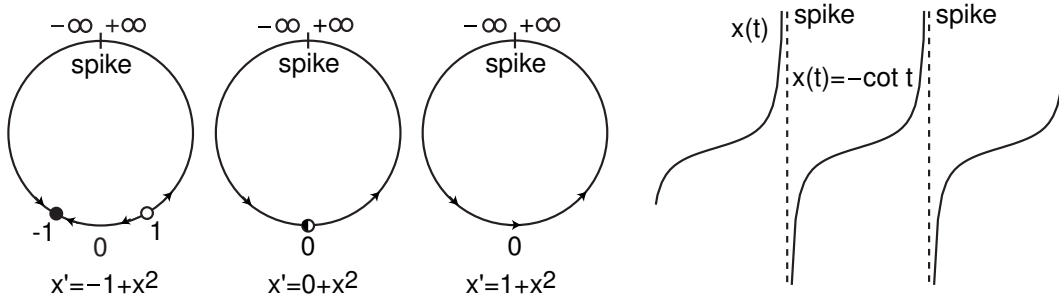


Figure 10.34: Phase portraits and typical oscillations of the quadratic integrate-and-fire neuron  $\dot{x} = I + x^2$  with  $x \in \mathbb{R} \cup \{\pm\infty\}$ . Parameter:  $I = -1, 0, +1$ .

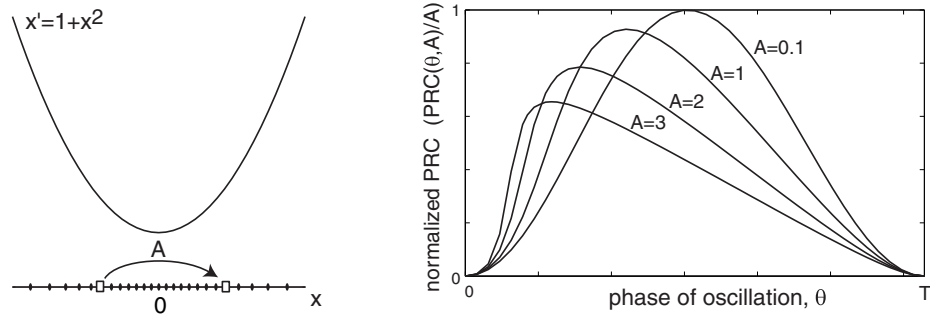


Figure 10.35: The dependence of PRC of the quadratic integrate-and-fire model on the strength of the pulse  $A$ .

on invariant circle (SNIC) bifurcation studied in Sect. 6.1.2. Appropriate rescaling of the membrane potential and time converts the model into the normal form

$$x' = 1 + x^2, \quad x \in \mathbb{R}.$$

Because of the quadratic term,  $x$  escapes to the infinity in a finite time, producing a spike depicted in Fig. 10.34. If we identify  $-\infty$  and  $+\infty$ , then  $x$  exhibits periodic spiking of infinite amplitude. Such a spiking model is called quadratic integrate-and-fire (QIF) neuron; see also Sect. 8.1.3 for some generalizations of the model.

### Strong pulse

The solution of this system starting at the spike, i.e., at  $x(0) = \pm\infty$ , is

$$x(t) = -\cot t,$$

as the reader can check by differentiating. It is a periodic function with  $T = \pi$ , hence, we can introduce the phase of oscillation via the relation  $x = -\cot \vartheta$ . The corresponding PRC can be found explicitly (see Ex. 9) and it has the form

$$\text{PRC}(\vartheta, A) = \pi/2 + \text{atan}(A - \cot \vartheta) - \vartheta,$$

depicted in Fig. 10.35, where  $A$  is the magnitude of the pulse. Notice that PRC tilts to the left as  $A$  increases. Indeed, the density of isochrons, denoted by black points on the  $x$ -axis in the figure, is maximal at the ghost of the saddle-node point  $x = 0$  where the parabola  $1 + x^2$  has the knee. This corresponds to the inflection point of the graph of  $x(t)$  in Fig. 10.34 where the dynamics of  $x(t)$  is the slowest. The effect of a pulse is maximal just before the ghost because  $x$  can jump over the ghost and skip the slow region. The stronger the pulse, the earlier it should arrive, hence the tilt.

## Weak coupling

The PRC behaves as  $A \sin^2 \vartheta$ , with  $\vartheta \in [0, \pi]$ , when  $A$  is small, as the reader can see in Fig. 10.35 or prove himself by differentiating the function  $\text{PRC}(\vartheta, A)$  with respect to  $A$ . Therefore,  $Z(\vartheta) = \sin^2 \vartheta$ , and we can use Winfree's approach to transform the weakly perturbed quadratic integrate-and-fire (QIF) oscillator

$$x' = 1 + x^2 + \varepsilon p(t)$$

into its phase model

$$x' = 1 + \varepsilon(\sin^2 \vartheta)p(t), \quad \vartheta \in [0, \pi].$$

The results of the previous section,  $Q(\vartheta) = 1/f(x(\vartheta)) = 1/(1+\cot^2 \vartheta) = \sin^2 \vartheta$ , confirm the phase model. In fact, any neuronal model  $CV = I - I_\infty(V)$  near saddle-node on invariant circle bifurcation point  $(I_{\text{sn}}, V_{\text{sn}})$  has infinitesimal PRC

$$\text{PRC}(\vartheta) = \frac{C}{I - I_{\text{sn}}} \sin^2 \vartheta, \quad \vartheta \in [0, \pi],$$

as the reader can prove as an exercise. The function  $\sin^2 \vartheta$  coincides with the familiar  $1 - \cos \theta$  when  $\theta = 2\vartheta$  has period  $2\pi$  (notice the font difference).

In Fig. 10.36a we compare the function with numerically obtained PRCs for the  $I_{\text{Na}} + I_K$ -model in Class 1 regime. Since the ghost of the saddle-node point, revealing itself as an inflection of the voltage trace in Fig. 10.36b, moves to the right as  $I$  increases away from the bifurcation value  $I = 4.51$ , so does the peak of the PRC.

Figure 10.36a emphasizes the common features of all systems undergoing saddle-node on invariant circle bifurcation: They are insensitive to the inputs arriving during the spike, since  $\text{PRC} \approx 0$  when  $\vartheta \approx 0, T$ . The oscillators are most sensitive to the input when they are just entering the ghost of the resting state, where PRC is maximal. The location of the maximum tilts to the left as the strength of the input increases, and may tilt to the right as the distance to the bifurcation increases. Finally, PRCs are non-negative, so positive (negative) inputs can only advance (delay) the phase of oscillation.

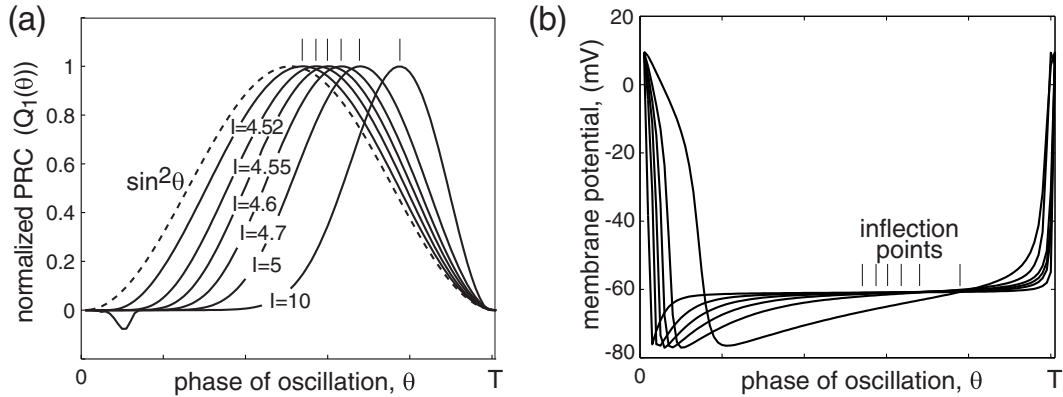


Figure 10.36: (a) Numerically found PRCs of the  $I_{\text{Na}} + I_{\text{K}}$ -oscillator in Class 1 regime (parameters as in Fig. 4.1a) and various  $I$  using the MATLAB program in Ex. 12. (b) Corresponding voltage traces show that the inflection point (slowest increase) of  $V$  moves right as  $I$  increases.

### Gap junctions

Now consider two oscillators coupled via gap junctions, discussed in Sect. 2.3.4,

$$\begin{aligned} x'_1 &= 1 + x_1^2 + \varepsilon(x_2 - x_1) , \\ x'_2 &= 1 + x_2^2 + \varepsilon(x_1 - x_2) . \end{aligned}$$

Let us determine the stability of the in-phase synchronized state  $x_1 = x_2$ . The corresponding phase model (10.12) has the form

$$\begin{aligned} \vartheta'_1 &= 1 + \varepsilon(\sin^2 \vartheta_1)(\cot \vartheta_1 - \cot \vartheta_2) , \\ \vartheta'_2 &= 1 + \varepsilon(\sin^2 \vartheta_2)(\cot \vartheta_2 - \cot \vartheta_1) . \end{aligned}$$

The function (10.16) can be found analytically:

$$H(\chi) = \frac{1}{\pi} \int_0^\pi \sin^2 t (\cot t - \cot(t + \chi)) dt = \frac{1}{2} \sin 2\chi ,$$

so that the model in the phase deviation coordinates,  $\vartheta(t) = t + \varphi$ , has the form

$$\begin{aligned} \varphi'_1 &= (\varepsilon/2) \sin\{2(\varphi_2 - \varphi_1)\} , \\ \varphi'_2 &= (\varepsilon/2) \sin\{2(\varphi_1 - \varphi_2)\} . \end{aligned}$$

The phase difference,  $\chi = \varphi_2 - \varphi_1$ , satisfies the equation (compare with Fig. 10.26)

$$\chi' = -\varepsilon \sin 2\chi ,$$

and, apparently, the in-phase synchronized state,  $\chi = 0$ , is always stable while the anti-phase state  $\chi = \pi/2$  is not.

### Weak pulses

Now consider two weakly pulse-coupled oscillators

$$\begin{aligned} x'_1 &= 1 + x_1^2 + \varepsilon_1 \delta(t - t_2) , \\ x'_2 &= 1 + x_2^2 + \varepsilon_2 \delta(t - t_1) , \end{aligned}$$

where  $t_1$  and  $t_2$  are the moments of firing ( $x(t) = \infty$ ) of the first and the second oscillator, respectively, and  $\varepsilon_1$  and  $\varepsilon_2$  are the strengths of synaptic connections. The corresponding phase model (10.12) has the form

$$\begin{aligned} \vartheta'_1 &= 1 + \varepsilon_1 (\sin^2 \vartheta_1) \delta(t - t_2) \\ \vartheta'_2 &= 1 + \varepsilon_2 (\sin^2 \vartheta_2) \delta(t - t_1) . \end{aligned}$$

Since

$$H(\chi) = \frac{1}{\pi} \int_0^\pi \sin^2 t \delta(t + \chi) dt = \frac{1}{\pi} \sin^2 \chi ,$$

the corresponding phase deviation model (10.15) is

$$\begin{aligned} \varphi'_1 &= \frac{\varepsilon_1}{\pi} \sin^2(\varphi_2 - \varphi_1) , \\ \varphi'_2 &= \frac{\varepsilon_2}{\pi} \sin^2(\varphi_1 - \varphi_2) . \end{aligned}$$

The phase difference  $\chi = \varphi_2 - \varphi_1$  satisfies the equation

$$\chi' = \frac{\varepsilon_2 - \varepsilon_1}{\pi} \sin^2 \chi ,$$

which becomes  $\chi' = 0$  when the coupling is symmetric. In this case, the oscillators preserve (on average) the initial phase difference. When  $\varepsilon_1 \neq \varepsilon_2$ , the in-phase synchronized state  $\chi = 0$  is only neutrally stable. Interestingly, it becomes exponentially unstable in a network of three or more pulse-coupled Class 1 oscillators; see Ex. 23.

### Weak pulses with delays

The synchronization properties of weakly pulse-coupled oscillators could change significantly when explicit axonal conduction delays are introduced. As an example, consider the system

$$\begin{aligned} x'_1 &= 1 + x_1^2 + \varepsilon \delta(t - t_2 - d) , \\ x'_2 &= 1 + x_2^2 + \varepsilon \delta(t - t_1 - d) , \end{aligned}$$

where  $d \geq 0$  is the delay. Ex. 18 shows that delays introduce simple phase shifts, so that the phase model has the form

$$\begin{aligned} \varphi'_1 &= \frac{\varepsilon}{\pi} \sin^2(\varphi_2 - \varphi_1 - d) , \\ \varphi'_2 &= \frac{\varepsilon}{\pi} \sin^2(\varphi_1 - \varphi_2 - d) , \end{aligned}$$

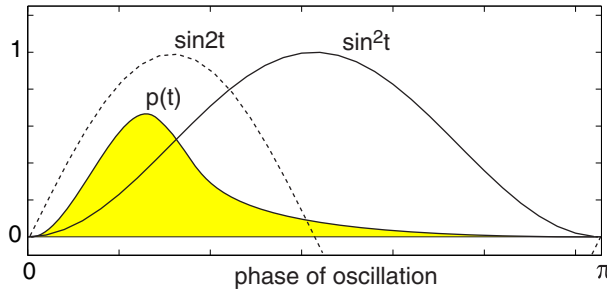


Figure 10.37: Synaptic transmission function  $p(t)$  typically has an asymmetric shape with fast rise and slow decay.

The phase difference  $\chi = \varphi_2 - \varphi_1$  satisfies

$$\chi' = \frac{\varepsilon}{\pi} (\sin^2(\chi + d) - \sin^2(\chi - d)) . = \frac{\varepsilon \sin 2d}{\pi} \sin 2\chi .$$

The stability of synchronized states is determined by the sign of the function  $\sin 2d$ . The in-phase state  $\chi = 0$  is unstable when  $\sin 2d > 0$ , i.e., when the delay is shorter than the half-period  $\pi/2$ , stable when the delay is longer than half-period but shorter than one period  $\pi$ , unstable for even longer delays, etc. The stability of the anti-phase state  $\chi = \pi/2$  is reversed, i.e., it is stable for short delays, unstable for longer delays, then stable again for even longer delays, etc. Finally, when the pulses are inhibitory ( $\varepsilon < 0$ ), the (in)stability character is flipped so that the in-phase state becomes stable for short delays.

### Weak synapses

Now suppose that each pulse is not a delta function, but it is smeared in time, i.e., it has a time course  $p(t - t_i)$  with  $p(0) = p(\pi) = 0$ . That is, the synaptic transmission starts right after the spike of the pre-synaptic neuron and ends before the onset of the next spike. The function  $p$  has a typical unimodal shape with fast rise and slow decay depicted in Fig. 10.37. The discussion below is equally applicable to the case of  $p(t, x) = g(t)(E - x)$  with  $g > 0$  being the synaptic conductance with the shape in the figure and  $E$  being the synaptic reverse potential, positive (negative) for excitatory (inhibitory) synapses.

Two weakly synaptically coupled SNIC (Class 1) oscillators

$$\begin{aligned} x'_1 &= 1 + x_1^2 + \varepsilon p(t - t_2) , \\ x'_2 &= 1 + x_2^2 + \varepsilon p(t - t_1) \end{aligned}$$

can be converted into a general phase model with the connection function (10.16) in the form

$$H(\chi) = \frac{1}{\pi} \int_0^\pi \sin^2 t p(t + \chi) dt ,$$

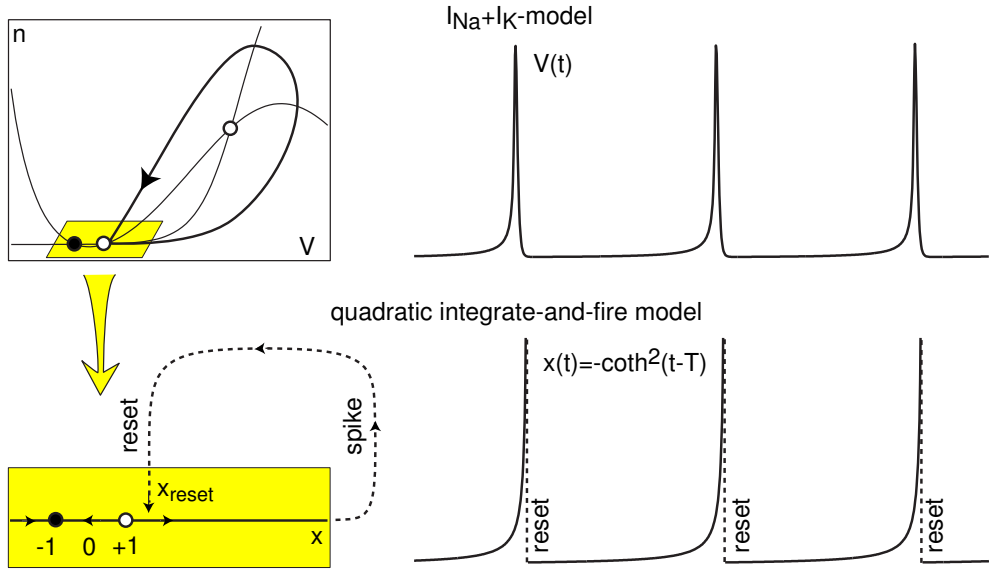


Figure 10.38: *Top:* Periodic spiking of the  $I_{Na} + I_K$ -neuron near saddle-node homoclinic orbit bifurcation (parameters as in Fig. 4.1a with  $\tau(V) = 0.167$  and  $I = 4.49$ ). *Bottom:* Spiking in the corresponding quadratic integrate-and-fire model.

and it can be computed explicitly for some simple  $p(t)$ .

The in-phase synchronized solution,  $\chi = 0$ , is stable when

$$H'(0) = \frac{1}{\pi} \int_0^\pi \sin^2 t p'(t) dt > 0 .$$

Since the function  $\sin^2 t$  depicted in Fig. 10.37 is small at the ends of the interval and large in the middle, the integral is dominated by the sign of  $p'$  in the middle. Fast rising and slowly decaying excitatory ( $p > 0$ ) synaptic transmission has  $p' < 0$  in the middle, as in the figure, so the integral is negative and the in-phase solution is unstable. In contrast, fast rising slowly decaying inhibitory ( $p < 0$ ) synaptic transmission has  $p' > 0$  in the middle, so the integral is positive and the in-phase solution is stable. Another way to see this is to integrate the equation by parts, reduce it to  $-\int p(t) \sin 2t dt$ , and notice that  $p(t)$  is concentrated in the first (left) half of the period where  $\sin 2t$  is positive. Hence, positive (excitatory)  $p$  results in  $H'(0) < 0$ , and vice versa. Both approaches confirm the theoretical results independently obtained by van Vreeswijk et al. (1994) and Hansel et al. (1995) that *inhibition, not excitation synchronizes Class 1 (SNIC) oscillators*. The relationship is inverted for the anti-phase solution  $\chi = \pi/2$  (prove it), and no relationships is known for other types of oscillators.

### 10.4.3 Homoclinic oscillators

Besides the SNIC bifurcation considered above, low frequency oscillations may also be indicative of the proximity of the system to a saddle homoclinic orbit bifurcation, as in

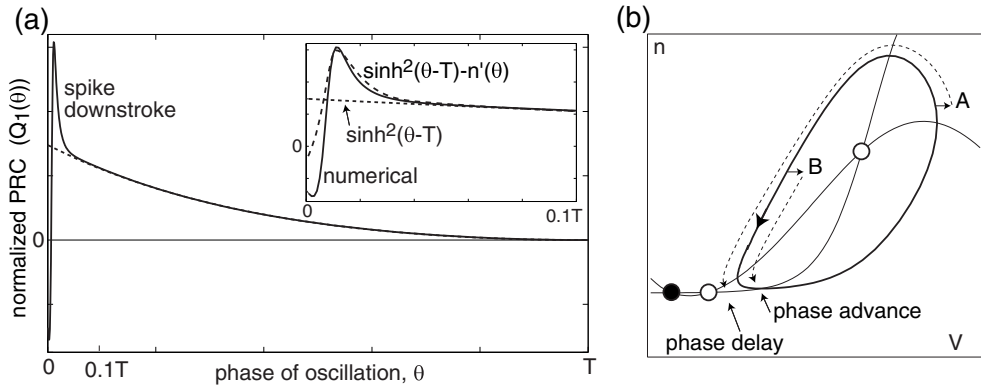


Figure 10.39: (a) Numerically found PRCs of the  $I_{\text{Na}} + I_K$ -oscillator near saddle-node homoclinic orbit bifurcation (as in Fig. 10.38) using the MATLAB program in Ex. 12. Magnification shows the divergence from the theoretical curve  $\sinh^2(\vartheta - T)$  during the spike. (b) A pulsed input during the downstroke of the spike can produce a significant phase delay (pulse A) or advance (pulse B) not captured by the quadratic integrate-and-fire model.

Fig. 10.38, top. The spiking trajectory in the figure quickly approaches a small shaded neighborhood of the saddle along the stable direction, and then slowly diverges from the saddle along the unstable direction, thereby resulting in a large period oscillation. As it is often the case in neuronal models, the saddle equilibrium is near a stable node equilibrium corresponding to the resting state, and the system is near the co-dimension 2 saddle-node homoclinic orbit bifurcation studied in Sect. 6.3.6. As a result, there is a drastic difference between the attraction and divergence rates to the saddle, so that the dynamics in the shaded neighborhood of the saddle-node in the figure can be reduced to the one-dimensional  $V$ -equation, which in return can be transformed into the “quadratic integrate-and-fire” form

$$x' = -1 + x^2, \quad \text{if } x = +\infty, \text{ then } x \leftarrow x_{\text{reset}},$$

with solutions depicted in Fig. 10.38, bottom. The saddle and the node correspond to  $x = \pm 1$ , respectively. One can check by differentiating that the solution of the model with  $x(0) = x_{\text{reset}} > 1$ , is  $x(t) = -\coth(t - T)$ , where  $\coth(s) = (e^s + e^{-s})/(e^s - e^{-s})$  is the hyperbolic cotangent, and  $T = \text{acoth}(x_{\text{reset}})$  is the period of oscillation, which becomes infinite as  $x_{\text{reset}} \rightarrow 1$ .

Using the results of Sect. 10.4.1, we find the function

$$Q(\vartheta) = 1/(-1 + \coth^2(\vartheta - T)) = \sinh^2(\vartheta - T)$$

whose graph is shown in Fig. 10.39a. For comparison, we plotted the numerically found PRC for the  $I_{\text{Na}} + I_K$ -oscillator to illustrate the disagreement between the theoretical and numerical curves in the region  $\vartheta < 0.1T$  corresponding to the downstroke of the spike. Such a disagreement is somewhat expected, since the quadratic integrate-and-fire model ignores spike downstroke. If a pulse arriving during the downstroke

displaces the trajectory to the exterior of the limit cycle, as in Fig. 10.39b, pulse A, then the trajectory becomes closer to the saddle equilibrium when it reenters a small neighborhood of the saddle, thereby leading to a significant phase delay. Displacements to the interior of the cycle, as in Fig. 10.39b, pulse B, push away from the saddle and lead to phase advances. The direction and the magnitude of displacements is determined by the derivative of the slow variable  $n'$  along the limit cycle.

The region of disagreement between theoretical and numerical PRCs becomes infinitesimal relative to  $T \rightarrow \infty$  near the bifurcation. Theoretical PRC can be used to study anti-phase and out-of-phase synchronization of pulse-coupled oscillators, but not in-phase synchronization, because the region of breakdown is the only important region in this case. Finally notice that as  $T \rightarrow \infty$ , the spiking limit cycle fails to be exponentially stable, and the theory of weakly coupled oscillators is no longer applicable to it.

Though the PRC in Fig. 10.39 is quite different from the one corresponding to SNIC oscillators in Fig. 10.36, there is an interesting similarity between these two cases: Both can be reduced to quadratic integrate-and-fire neurons, both have cotangent-shaped periodic spiking solutions and sine-squared-shape PRCs, except they are “regular” in the SNIC case and hyperbolic in the homoclinic case; see also Ex. 26.

#### 10.4.4 Relaxation oscillators and FTM

Consider two relaxation oscillators having weak fast  $\rightarrow$  fast connections

$$\begin{aligned} \mu \dot{x}_i &= f(x_i, y_i) + \varepsilon p_i(x_i, x_k), \\ \dot{y}_i &= g(x_i, y_i), \end{aligned} \quad (10.26)$$

where  $i = 1, 2$  and  $k = 2, 1$ . This system can be converted to a phase model in the relaxation limit  $\varepsilon \ll \mu \rightarrow 0$  (Izhikevich 2000). The connection functions  $H_i(\chi)$  have a positive discontinuity at  $\chi = 0$ , which occurs because the  $x$ -coordinate of the relaxation limit cycle is discontinuous at the jump points. Hence, the phase difference function  $G(\chi) = H_2(-\chi) - H_1(\chi)$  has a negative discontinuity at  $\chi = 0$  depicted in Fig. 10.31. This reflects the profound difference between behaviors of weakly coupled oscillators of relaxation and non-relaxation type, discussed in Sect. 10.3.1: The in-phase synchronized solution,  $\chi = 0$ , in the relaxation limit  $\mu \rightarrow 0$  is stable, persistent in the presence of frequency mismatch  $\omega$ , and it has a rapid rate of convergence. The reduction to a phase model breaks down when  $\varepsilon \gg \mu \rightarrow 0$ , that is, when the connections are relatively strong. One can still analyze such oscillators in the special case considered below.

##### Fast threshold modulation

Consider (10.26) and suppose that  $p_1 = p_2 = p$  is a piece-wise constant function:  $p = 1$  when the pre-synaptic oscillator,  $x_k$ , is on the right branch of the cubic  $x$ -nullcline corresponding to an active state, and  $p = 0$  otherwise; see Fig. 10.40a. Somers and

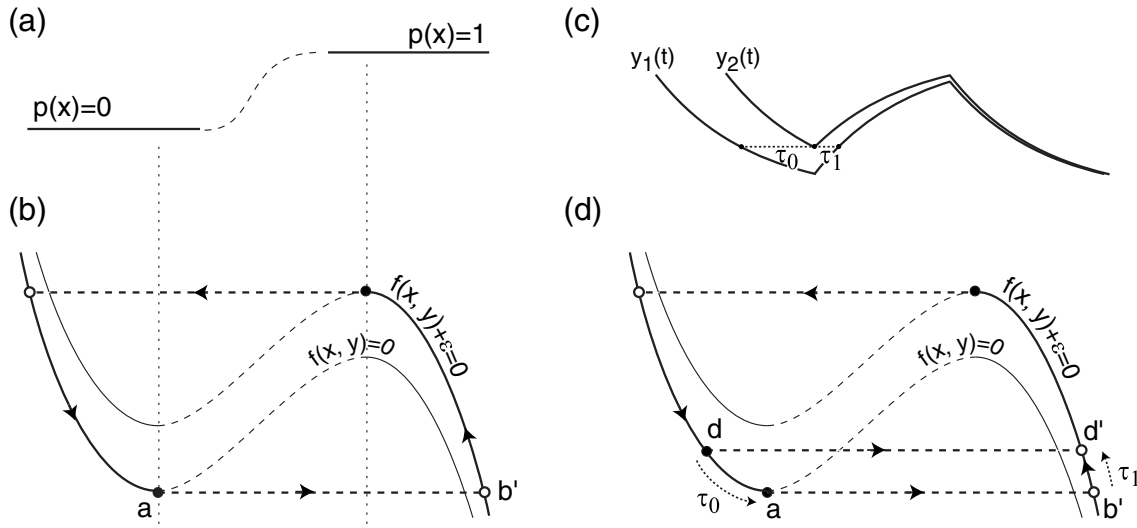


Figure 10.40: Fast threshold modulation of relaxation oscillation. (a) The Heaviside or sigmoidal coupling function  $p(x)$  is constant while  $x$  is on the left or right branch of the  $x$ -nullcline. (b) In the relaxation limit  $\mu = 0$ , the synchronized limit cycle consists of the left branch of the nullcline  $f(x, y) = 0$  and the right branch of the nullcline  $f(x, y) + \varepsilon = 0$ . When oscillator 1 is ahead of oscillator 2 (c), the phase difference between them decreases after the jump (d).

Kopell (1993, 1995) referred to such a coupling in the relaxation limit  $\mu \rightarrow 0$  as fast threshold modulation (FTM), and found a simple criterion of stability of synchronized state that works even for strong coupling.

Since the oscillators are identical, the in-phase synchronized state exists, during which the variables  $x_1$  and  $x_2$  follow the left branch of the  $x$ -nullcline defined by  $f(x, y) = 0$ , see Fig. 10.40b, until they reach the jumping point  $a$ . During the instantaneous jump, they turn on the mutual coupling  $\varepsilon$ , and land at some point  $b'$  on the perturbed  $x$ -nullcline defined by  $f(x, y) + \varepsilon = 0$ . They follow the new nullcline until the right (upper) knee, and then jump back to the left branch.

To determine the stability of the in-phase synchronization, we consider the case when oscillator 1 is slightly ahead of oscillator 2, as in Fig. 10.40c. We assume that the phase difference between the oscillators is so small, or alternatively, the strength of coupling is so large, that when oscillator 1 jumps and turns on its input to oscillator 2, the latter, being at point  $d$  in Fig. 10.40d, is below the left knee of the perturbed  $x$ -nullcline  $f(x, y) + \varepsilon = 0$  and therefore jumps too. As a result, both oscillators jump to the perturbed  $x$ -nullcline and reverse their order. Although the apparent distance between the oscillators, measured by the difference of their  $y$ -coordinates, is preserved during such a jump, the phase difference between them is usually not.

The phase difference between two points on a limit cycle is the time needed to travel from one point to the other. Let  $\tau_0(d)$  be the time needed to slide from point  $d$  to point  $a$  along the  $x$ -nullcline in Fig. 10.40d, i.e., the phase difference just before

the jump. Let  $\tau_1(d)$  be the time needed to slide from point  $b'$  to point  $d'$ , i.e., the phase difference after the jump. The phase difference between the oscillators during the jump changes by the factor  $C(d) = \tau_1(d)/\tau_0(d)$  called the *compression function*. The difference decreases when the compression function  $C(d) < 1$  uniformly for all  $d$  near the left knee  $a$ . This condition has a simple geometrical meaning: The rate of change of  $y(t)$  is slower before the jump than after it, so that  $y(t)$  has a “scalloped” shape, as in Fig. 10.40c. As an exercise, prove that  $C(d) \rightarrow |g(a)|/|g(b')|$  as  $d \rightarrow a$ .

If the compression function at the right (upper) knee is also less than 1, then the in-phase synchronization is stable. Indeed, the phase difference does not change while the oscillators slide along the nullclines, and it decreases geometrically with each jump. In fact, it suffices to require that the product of compression factors at the two knees be less than 1, so that any expansion at one knee is compensated by even stronger compression at the other knee.

### 10.4.5 Bursting oscillators

Let us consider bursting neurons coupled weakly through their fast variables:

$$\dot{x}_i = f(x_i, y_i) + \varepsilon p(x_i, x_j), \quad (10.27)$$

$$\dot{y}_i = \mu g(x_i, y_i), \quad (10.28)$$

$i = 1, 2$  and  $j = 2, 1$ . Since bursting involves two time scales, fast spiking and slow transition between spiking and resting, there are two synchronization regimes: spike synchronization and burst synchronization, illustrated in Fig. 9.51 and discussed in Sect. 9.4. Below we outline some useful ideas and methods of studying both regimes. Our exposition is not complete, but it rather lays the foundation for a more detailed research program.

#### Spike synchronization

To study synchronization of individual spikes within the burst, we let  $\mu = 0$  to freeze the slow subsystem (10.28) and consider the fast subsystem (10.27) describing weakly coupled oscillators. When  $y_i \approx y_j$ , the fast variables oscillate with approximately equal periods, so (10.27) can be reduced to the phase model

$$\dot{\varphi}_i = \varepsilon H(\varphi_j - \varphi_i, y_i),$$

where  $y_i = \text{const}$  parameterize the form of the connection function. For example, during the “circle/Hopf” burst, the function is transformed from  $H(\chi) = \sin^2 \chi$  or  $1 - \cos \chi$  at the beginning of the burst (saddle-node on invariant circle bifurcation) to  $H(\chi) = \sin \chi$  at the end of the burst (supercritical Andronov-Hopf bifurcation). Changing  $y_i$  slowly, one can study when spike synchronization appears and when it disappears during the burst. When the slow variables  $y_i$  have different values, fast variables typically oscillate with different frequencies, so one needs to look at low-order resonances (see next section) to study the possibility of spike synchronization.

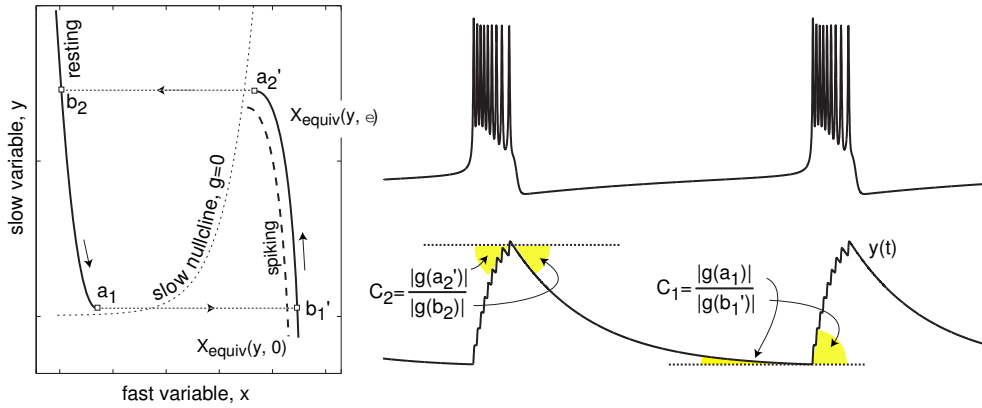


Figure 10.41: Reduction of the  $I_{Na,p} + I_K + I_{K(M)}$ -burster to a relaxation oscillator. The slow variable exhibits “scalloped” oscillations needed for stability of in-phase burst synchronization.  $C_1$  and  $C_2$  are compression functions at the two jumps.

### Burst synchronization

In Chap. 9 we presented two methods, averaging and equivalent voltage, that remove fast oscillations and reduce bursters to slow relaxation oscillators. Burst synchronization is then reduced to synchronization of such oscillators, and it can be studied using phase reduction or fast threshold modulation (FTM) approaches.

To apply FTM, we assume that the coupling in (10.27) is piece-wise constant, that is,  $p(x_i, x_j) = 0$  when the presynaptic burster  $x_j$  is resting, and  $p(x_i, x_j) = 1$  (or any function of  $x_i$ ) when the presynaptic burster is spiking. We also assume that the slow subsystem (10.28) is one-dimensional so that we can use the equivalent voltage method (Sect. 9.2.4) and reduce the coupled system to

$$\begin{aligned} 0 &= X_{\text{equiv}}(y_i, \epsilon p) - x_i, \\ y'_i &= g(x_i, y_i). \end{aligned}$$

When the burster is of the hysteresis loop type, i.e., the resting and spiking states coexist, the function  $x = X_{\text{equiv}}(y, \epsilon p)$  often, but not always, has a Z-shape on the slow/fast plane, as in Fig. 9.16, so that the system corresponds to a relaxation oscillator with nullclines as in Fig. 10.41. Fast threshold modulation occurs via the constant  $\epsilon p$ , which shifts the fast nullcline up or down. The compression criterion for stability of the in-phase burst synchronization, presented in the previous section, has a simple geometrical illustration in the figure. The slow nullcline has to be sufficiently close to the jumping points so that  $y(t)$  slows down before each jump and produces the “scalloped” shape curve. Many hysteresis loop fast/slow bursters do generate such shape. In particular, “fold/\*” bursters exhibit robust in-phase burst synchronization when they are near the bifurcation from quiescence to bursting, since the slow nullcline is so close to the left knee that the compression during the resting  $\rightarrow$  spiking jump ( $C_1$  in Fig. 10.41) dominates the expansion, if any, during the spiking  $\rightarrow$  resting jump.

## Review of Important Concepts

- Oscillations are described by their phase variables  $\vartheta$  rotating on a circle  $\mathbb{S}^1$ . We define  $\vartheta$  as the time since the last spike.
- The phase response curve,  $PRC(\vartheta)$ , describes the magnitude of the phase shift of an oscillator caused by a strong pulsed input arriving at phase  $\vartheta$ .
- PRC depends on the bifurcations of spiking limit cycle, and it defines synchronization properties of an oscillator.
- Two oscillators are synchronized in-phase, anti-phase, or out-of-phase, when their phase difference,  $\vartheta_2 - \vartheta_1$ , equals 0, half-period, or some other value, respectively; see Fig. 10.42.
- Synchronized states of pulse-coupled oscillators are fixed points of the corresponding Poincare phase map.
- Weakly coupled oscillators

$$\dot{x}_i = f(x_i) + \varepsilon \sum g_{ij}(x_j)$$

can be reduced to phase models

$$\dot{\vartheta}_i = 1 + \varepsilon Q(\vartheta_i) \sum g_{ij}(x_j(\vartheta_j)) ,$$

where  $Q(\vartheta)$  is the infinitesimal PRC defined by (10.10).

- Weak coupling induces a slow phase deviation of the natural oscillation,  $\vartheta_i(t) = t + \varphi_i$ , described by the averaged model

$$\dot{\varphi}_i = \varepsilon \left( \omega_i + \sum H_{ij}(\varphi_j - \varphi_i) \right) ,$$

where the  $\omega_i$  denote the frequency deviations, and

$$H_{ij}(\varphi_j - \varphi_i) = \frac{1}{T} \int_0^T Q(t) g_{ij}(x_j(t + \varphi_j - \varphi_i)) dt$$

describe the interactions between the phases.

- Synchronization of two coupled oscillators correspond to equilibria of the one-dimensional system

$$\dot{\chi} = \varepsilon(\omega + G(\chi)) , \quad \chi = \varphi_2 - \varphi_1 ,$$

where  $G(\chi) = H_{21}(-\chi) - H_{12}(\chi)$  describes how the phase difference  $\chi$  compensates for the frequency mismatch  $\omega = \omega_2 - \omega_1$ .

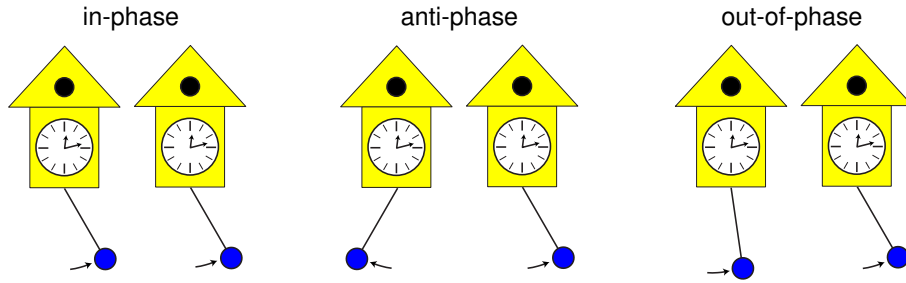


Figure 10.42: Different types of synchronization.

## Bibliographical Notes

Surprisingly, this chapter turned out to be quite different from Chap. 9 (Weakly Connected Oscillators) of the book *Weakly Connected Neural Networks* by Hoppensteadt and Izhikevich (1997) or from the book *Synchronization: A universal concept in nonlinear sciences* by Pikovsky, Rosenblum and Kurths. All three texts, though devoted to the same subject, do not repeat, but rather complement each other. The latter provides an excellent historical overview of synchronization, starting with the work of the famous Dutch mathematician, astronomer, and physicist Christiaan Huygens (1629–1695), who was the first one to describe synchronization of a couple of pendulum clocks hanging from a common support, which was incidentally anti-phase. While providing many examples of synchronization of biological, chemical, and physical systems, the book by Pikovsky et al. also discusses the definition of a phase and synchronization of non-periodic, e.g., chaotic, oscillators, a topic not covered here. A major part of *Spiking Neuron Models* by Gerstner and Kistler (2002) is devoted to synchronization of spiking neurons, with the emphasis on the integrate-and-fire model and spike-response method.

The formalism of phase response curve (PRC) was introduced by Hastings and Sweeney (1958), and it has been used extensively in the context of resetting the circadian rhythms. *Forty Years of PRC — What Have We Learned?* by Johnson (1999) gives an historical overview of this idea and some recent developments. John Guckenheimer (1975) used the theory of normally hyperbolic invariant manifolds to provide a mathematical foundation for the existence of isochrons, and their geometrical properties. An encyclopedic exposition of isochrons and phase resettings in nature, as well as numerous anecdotes, can be found in Arthur Winfree's remarkable book *The Geometry of Biological Time* (first edition 1980, second edition 2001). In particular, Winfree describes the work of George R. Mines (1914) who was doing phase resetting experiments by shocking rabbits at various phases of their heartbeat. He found the phase and shock that could stop a rabbit's heart (black hole in Fig. 10.8), and then applied it to himself. He died.

Glass and MacKey (1988) provide a detailed exposition of circle phase maps. Although the structure of phase-locking regions in Fig. 10.15 was discovered by Cartwright and Littlewood (1945), it is better known at present as Arnold tongues (Arnold 1965).

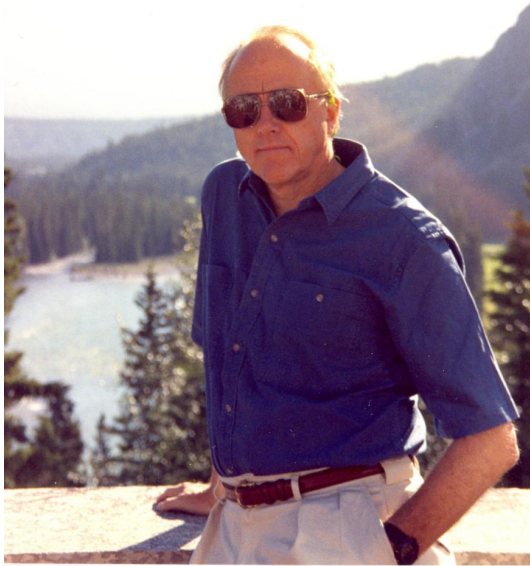


Figure 10.43: Frank Hoppensteadt, the author's adviser and mentor, circa 1989.

Guevara and Glass (1982) found this structure analytically for the Andronov-Hopf oscillator in Fig. 10.3 (radial isochron clock). Hoppensteadt (1997, 2000) provides many examples of oscillatory systems arising in biology and neuroscience; see also Hoppensteadt and Peskin (2002).

Malkin's method of reduction of coupled oscillators to phase equations has been known, at least to Russian scientists, since the early 1950s (Malkin 1949, 1956, Blechman 1971). For example, Melnikov (1963) applied Malkin's theorem to a homoclinic orbit of infinite period to obtain the transversality condition for the saddle homoclinic orbit bifurcation (Kuznetsov 1995).

Malkin's method was rediscovered in the West by J. Neu (1979), and hoorayed by Winfree (1980) who finally saw a mathematical justification for his usage of phase variables. Since then, the field of phase equations was largely dominated by Bard Ermentrout and Nancy Kopell (Ermentrout 1981, 1985, 1992, Ermentrout and Kopell 1986a,b, 1990, 1991, 1994, Kopell and Ermentrout 1990, Kopell 1986, Kopell et al. 1991). In particular, they developed the theory of traveling wave solutions in chains of oscillators, building on the seminal paper by Cohen et al. (1982). Incidentally, the one-page proof of Malkin's theorem provided by Hoppensteadt and Izhikevich (1997, Sect. 9.6) is based on Ermentrout and Kopell idea of using the Fredholm alternative; Malkin's and Neu's proofs are quite long, mostly because they re-prove the alternative.

There are only a handful of examples where the Malkin adjoint problem can be solved analytically, i.e., without resort to simulations. The SNIC, homoclinic and Andronov-Hopf cases are the most important and were considered in detail in this chapter. Brown et al. (2004) also derive PRCs for oscillators with homoclinic orbits to pure saddles (see Ex. 25) and for Bautin oscillators.

Throughout this chapter we define the phase  $\vartheta$  or  $\varphi$  on the interval  $[0, T]$ , where  $T$  is the period of free oscillation, and do not normalize it to be on the interval  $[0, 2\pi]$ .



Figure 10.44: Nancy Kopell in her Boston University office in 1990 (photograph provided by Dr. Kopell).

As a result, we avoided the annoying terms  $2\pi/T$  and  $2\pi/\Omega$  in the formulae. The only drawback is that some of the results may have an “unfamiliar look”, such as  $\sin^2 \vartheta$  with  $\vartheta \in [0, \pi]$  for the PRC of Class 1 neurons, as opposed to  $1 - \cos \vartheta$  with  $\vartheta \in [0, 2\pi]$  used by many authors before.

Hansel, Mato, and Meunier (1995) were the first to notice that the shape of PRC determines the synchronization properties of synaptically coupled oscillators. Ermentrout (1996) related this result to the classification of oscillators and proved that PRCs of all Class 1 oscillators have the form of  $1 - \cos \vartheta$ , though the proof can be found in his earlier papers with Kopell (Ermentrout and Kopell 1986a,b). Reyes and Fetz (1993) measured PRC of a cat neocortical neuron and largely confirmed the theoretical predictions. The experimental method in Sect. 10.2.4 is related to that of Rosenblum and Pikovsky (2001). It needs to be developed further, e.g., by incorporating the measurement uncertainty (error bars). In fact, most experimentally obtained PRCs, including the one in Fig. 10.24, are so noisy that nothing useful could be derived from them. This issue is the subject of active research.

Our treatment of the FTM theory follows closely that of Somers and Kopell (1993, 1995). Anti-phase synchronization of relaxation oscillators is analyzed using phase models by Izhikevich (2000) and FTM theory by Kopell and Somers (1995). Ermentrout (1994) and Izhikevich (1998) considered weakly coupled oscillators with axonal conduction delays and showed that delays result in mere phase shifts (see Ex. 18). Frankel and Kiemel (1993) observed that slow coupling can be reduced to weak coupling. Izhikevich and Hoppensteadt (2003) used Malkin’s theorem to extend the results to slowly coupled networks, and to derive useful formulae for the coupling functions and coefficients. Ermentrout (2003) showed that the result could be generalized to synapses having fast-rising and slow-decaying conductances. Goel and Ermentrout (2002) and

Katriel (2005) obtained many interesting results on in-phase synchronization of identical phase oscillators.

Interactions between resonant oscillators were considered by Ermentrout (1981), Hoppensteadt and Izhikevich (1997) and Izhikevich (1999) in the context of quasi-periodic (multi-frequency) oscillations. Baesens et al. (1991) undertook heroic task of studying resonances and toroidal chaos in a system of three coupled phase oscillators. Mean-field approaches to the Kuramoto model are reviewed by Strogatz (2000) and Acebron et al. (2005). Daido (1996) extended the theory to the general coupling function  $H(\chi)$ . van Hemmen and Wreszinski (1993) were the first to find the Lyapunov function for the Kuramoto model, which was generalized (independently) by Hoppensteadt and Izhikevich (1997) to arbitrary coupling function  $H(\chi)$ .

Ermentrout (1985), Aronson et al. (1990) and Hoppensteadt and Izhikevich (1996, 1997) studied weakly coupled Andronov-Hopf oscillators, and discussed the phenomena of self-ignition (coupling-induced oscillations) and oscillator death (coupling-induced cessation of oscillation). Collins and Stewart (1993, 1994) and Golubitsky and Stewart (2002) applied group theory to study synchronization of coupled oscillators in networks with symmetries.

In this chapter we consider either strong *pulsed* coupling or *weak* continuous coupling. These limitations are severe, but they allow us to derive model-independent results. Studying synchronization in networks of strongly coupled neurons is an active area of research, however, most of such studies fall into two categories: (1) simulations and (2) integrate-and-fire networks. In both cases, the results are model-depended. If the reader wants to pursue this line of research, he or she will definitely need to read the following papers: Miroollo and Strogatz (1990), van Vreeswijk et al. (1994), Chow and Kopell (2000), Rubin and Terman (2000, 2002), Bressloff and Coombes (2000), van Vreeswijk (2000), van Vreeswijk and Hansel (2001), Pfeuty et al. (2003), Hansel and Mato (2003).

## Exercises

- Find the isochrons of the Andronov-Hopf oscillator

$$\dot{z} = (1 + i)z - z|z|^2, \quad z \in \mathbb{C},$$

in Fig. 10.3.

- Prove that the isochrons of the Andronov-Hopf oscillator in the form

$$\dot{z} = (1 + i)z + (-1 + di)z|z|^2, \quad z \in \mathbb{C},$$

are the curves

$$z(s) = s^{(-1+di)} e^{\chi i}, \quad s > 0,$$

where  $\chi$  is the phase of the isochron; see Fig. 10.45.

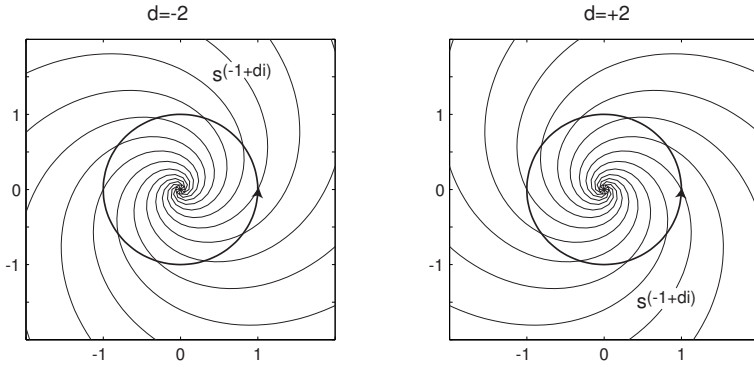


Figure 10.45: Isochrons of the Andronov-Hopf oscillator; see Ex. 2.

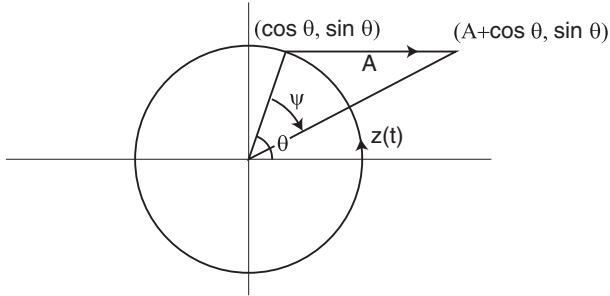


Figure 10.46: Pulsed stimulation of the Andronov-Hopf oscillator in Fig. 10.3; see Ex. 4.

3. [MATLAB] To determine isochrons of an oscillator  $\dot{x} = F(x)$ , one can start with many initial points near the limit cycle and integrate the system backwards, i.e.  $\dot{x} = -F(x)$ . The images of the points at any time  $t$  lie on the same isochron. Write a MATLAB program that implements this algorithm.
4. Prove that the phase response curve of the Andronov-Hopf oscillator in Fig. 10.3 is

$$\text{PRC}(\vartheta, A) = \begin{cases} -\psi & \text{when } 0 \leq \vartheta \leq \pi, \\ +\psi & \text{when } \pi \leq \vartheta \leq 2\pi, \end{cases} \quad (10.29)$$

where

$$\psi = \arccos \frac{1 + A \cos \vartheta}{\sqrt{1 + 2A \cos \vartheta + A^2}}$$

and  $A$  is the magnitude of the horizontal displacement of  $z(t)$ ; see Fig. 10.46.

5. [MATLAB] Write a program that stimulates an oscillator at different phases and determines its phase response curve (PRC).
6. Show that  $Z(\vartheta) = \text{grad } \vartheta$ , so that Winfree's phase model (10.6) is equivalent to Kuramoto's phase model (10.8).
7. Show that  $Z(\vartheta) = Q(\vartheta)$ , so that Winfree's phase model (10.6) is equivalent to Malkin's phase model (10.9).

8. Show that the PRC of the leaky integrate-and-fire neuron (Sect. 8.1.1)

$$\dot{v} = b - v , \quad \text{if } v \geq 1 \text{ (threshold), then } v \leftarrow 0 \text{ (reset)}$$

with  $b > 1$  has the form

$$\text{PRC}(\vartheta) = \min \{ \ln(b/(b \exp(-\vartheta) - A)), T \} - \vartheta ,$$

where  $T = \ln(b/(b - 1))$  is the period of free oscillations and  $A$  is the amplitude of the pulse.

9. Prove that the quadratic integrate-and-fire neuron

$$\dot{v} = 1 + v^2 , \quad \text{if } v = +\infty \text{ (peak of spike), then } v \leftarrow -\infty \text{ (reset)}$$

has  $\text{PTC}(\vartheta) = \pi/2 + \text{atan}(A - \cot \vartheta)$ .

10. Find PRC of the quadratic integrate-and-fire neuron (Sect. 8.1.3)

$$\dot{v} = b + v^2 , \quad \text{if } v \geq 1 \text{ (peak of spike), then } v \leftarrow v_{\text{reset}} \text{ (reset)}$$

with  $b > 0$ .

11. Consider two mutually pulsed-coupled oscillators with periods  $T_1 \approx T_2$  and type 1 phase transition curves  $\text{PTC}_1$  and  $\text{PTC}_2$ , respectively. Show that the locking behavior of the system can be described by the Poincare phase map

$$\chi_{n+1} = T_1 - \text{PTC}_1(T_2 - \text{PTC}_2(\chi_n)) ,$$

where  $\chi_n$  is the phase difference between the oscillators, i.e., the phase of oscillator 2 when oscillator 1 fires a spike.

12. [MATLAB] Write a program that solves the adjoint equation (10.10) numerically (hint: integrate the equation backwards to achieve stability).

13. [MATLAB] Write a program that finds the infinitesimal PRC using the relationship

$$\dot{\vartheta} = 1 + \text{PRC}(\vartheta) \varepsilon p(t) ,$$

the moments of firings of a neuron (zero crossings of  $\vartheta(t)$ ), and the injected current  $\varepsilon p(t)$ ; see Sect. 10.2.4 and Fig. 10.24.

14. Use the approaches of Winfree, Kuramoto, and Malkin to transform the integrate-and-fire neuron  $\dot{v} = b - v + \varepsilon p(t)$  in Ex. 8 to its phase model

$$\dot{\vartheta} = 1 + \varepsilon (e^\vartheta / b) p(t) ,$$

with  $T = \ln(b/(b - 1))$ .

15. Use the approaches of Winfree, Kuramoto, and Malkin to transform the quadratic integrate-and-fire neuron  $\dot{v} = 1 + v^2 + \varepsilon p(t)$  in Ex. 9 to its phase model

$$\dot{\vartheta} = 1 + \varepsilon (\sin^2 \vartheta) p(t) ,$$

with  $T = \pi$ .

16. Use the approaches of Winfree, Kuramoto, and Malkin to transform the Andronov-Hopf oscillator  $\dot{z} = (1 + i)z - z|z|^2 + \varepsilon p(t)$  with real  $p(t)$  to its phase model

$$\dot{\vartheta} = 1 + \varepsilon (-\sin \vartheta) p(t) ,$$

with  $T = 2\pi$ .

17. (PRC for Andronov-Hopf) Consider a weakly perturbed system near supercritical Andronov-Hopf bifurcation (see Sect. 6.1.3)

$$\dot{z} = (b + i)z + (-1 + di)z|z|^2 + \varepsilon p(t) , \quad z \in \mathbb{C} .$$

with  $b > 0$ . Let  $\varepsilon = b\sqrt{b}/\epsilon$  be small. Prove that the corresponding phase model is

$$\dot{\theta} = 1 + d + \varepsilon \operatorname{Im} \{(1 + di)p(t)e^{-i\theta}\} .$$

When the forcing  $p(t)$  is one-dimensional, i.e.,  $p(t) = cq(t)$  with  $c \in \mathbb{C}$  and scalar function  $q(t)$ , the phase model has sinusoidal form

$$\dot{\theta} = 1 + d + \varepsilon s \sin(\theta - \psi) q(t) ,$$

with the strength  $s$  and the phase shift  $\psi$  depending only on  $d$  and  $c$ .

18. (Delayed coupling) Show that weakly coupled oscillators

$$\dot{x}_i = f(x_i) + \varepsilon \sum_{j=1}^n g_{ij}(x_i(t), x_j(t - d_{ij}))$$

with explicit axonal conduction delays  $d_{ij} \geq 0$  have the phase model

$$\dot{\varphi}'_i = \omega_i + \sum_{j \neq i}^n H_{ij}(\varphi_j - d_{ij} - \varphi_i)$$

where  $' = d/d\tau$ ,  $\tau = \varepsilon t$  is the slow time, and  $H(\chi)$  is defined by (10.16). Thus, explicit delays result in explicit phase shifts.

19. Determine the existence and stability of synchronized states in the system

$$\begin{aligned} \dot{\varphi}_1 &= \omega_1 + c_1 \sin(\varphi_2 - \varphi_1) \\ \dot{\varphi}_2 &= \omega_2 + c_2 \sin(\varphi_1 - \varphi_2) \end{aligned}$$

as a function of the parameters  $\omega = \omega_2 - \omega_1$  and  $c = c_2 - c_1$ .

20. Consider the Kuramoto model

$$\varphi_i = \omega + \sum_{j=1}^n c_{ij} \sin(\varphi_j + \psi_{ij} - \varphi_i),$$

where  $c_{ij}$  and  $\psi_{ij}$  are parameters. What can you say about its synchronization properties?

21. Derive the self-consistency equation (10.22) for the Kuramoto model (10.20).

22. Consider the phase deviation model

$$\begin{aligned}\varphi'_1 &= \omega + c_1 H(\varphi_2 - \varphi_1) \\ \varphi'_2 &= \omega + c_2 H(\varphi_1 - \varphi_2)\end{aligned}$$

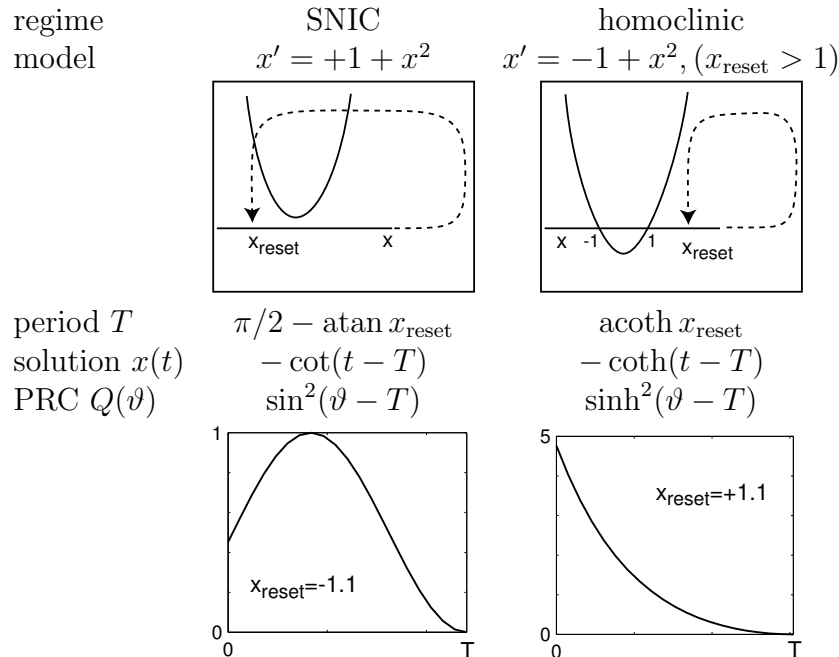
with an even function  $H(-\chi) = H(\chi)$ . Prove that the in-phase synchronized state,  $\varphi_1 = \varphi_2$ , if it exists, cannot be exponentially stable. What can you say about the anti-phase state  $\varphi_1 = \varphi_2 + T/2$ ?

23. Prove that the in-phase synchronized state in a network of three or more pulse-coupled quadratic integrate-and-fire neurons is unstable.

24. Prove (10.25).

25. (Brown et al. 2004) Show that PRC for an oscillator near saddle homoclinic orbit bifurcation scales as  $\text{PRC}(\vartheta) \sim e^{\lambda(T-\vartheta)}$ , where  $\lambda$  is the positive eigenvalue of the saddle and  $T$  is the period of oscillation.

26. Consider the quadratic integrate-and-fire neuron  $\dot{x} = \pm 1 + x^2$  with the resetting “if  $x = +\infty$ , then  $x \leftarrow x_{\text{reset}}$ ”. Prove that



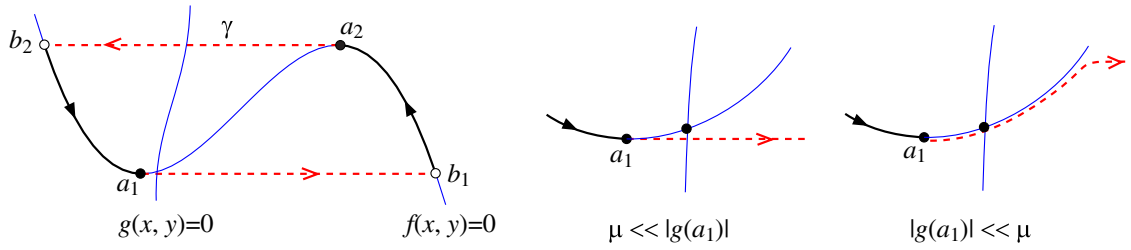


Figure 10.47: *Left:* Relaxation oscillator in the limit  $\mu = 0$  near the onset of oscillation. *Middle and right:* A magnification of a neighborhood of the jump point  $a_1$  for various  $g(a_1)$  and  $\mu$ . Canard (French duck) solutions can appear when  $|g(a_1)| \ll \mu$ .

where  $\coth$ ,  $\operatorname{acoth}$ , and  $\sinh$  are hyperbolic cotangent, hyperbolic inverse cotangent and hyperbolic sine, respectively.

27. [M.S.] Derive the PRC for an oscillator near saddle homoclinic orbit bifurcation that is valid during the spike downstroke. Take advantage of the observation in Fig. 10.39 that the homoclinic orbit consists of two qualitatively different parts.
28. [M.S.] Derive PRC for a generic oscillator near fold limit cycle bifurcation.
29. [M.S.] Simplify the connection function  $H$  for coupled relaxation oscillators (Izhikevich 2000) when the slow nullcline approaches the left knee, as in Fig. 10.47. Explore the range of parameters  $\varepsilon$ ,  $\mu$ , and  $|g(a_1)|$  where the analysis is valid.
30. [Ph.D.] Use ideas outlined in Sect. 10.4.5 to develop the theory of reduction of weakly coupled bursters to phase models. Do not assume that bursting trajectory is periodic.

## Solutions to Chapter 10

1. In polar coordinates,  $z = re^{i\vartheta}$ , the system has the form

$$\dot{\vartheta} = 1, \quad \dot{r} = r - r^3.$$

Since the phase of oscillation does not depend on the amplitude, the isochrons have the radial structure depicted in Fig. 10.3.

2. In polar coordinates, the oscillator has the form

$$\dot{\vartheta} = 1 + dr^2, \quad \dot{r} = r - r^3.$$

The second equation has an explicit solution  $r(t)$ , such that

$$r(t)^2 = \frac{1}{1 - (1 - 1/r(0)^2)e^{-2t}}.$$

The phase difference between  $\dot{\vartheta}_{lc} = 1 + d(1)^2$  and  $\dot{\vartheta} = 1 + dr(t)^2$  grows as  $\dot{\chi} = d(r(t)^2 - 1)$ , and its asymptotic value is

$$\chi(\infty) = \int_0^\infty d(r(t)^2 - 1) = d \log r(0).$$

Thus, on the  $\chi$ -isochron, we have  $\vartheta + d \log r = \chi$ .

### 3. An example is the file `isochrons.m`

```

function isochrons(F,phases,x0)
% plot isochrons of a planar dynamical system x'=F(t,x)
% at points given by the vector 'phases'.
% 'x0' is a point on the limit cycle (2x1-vector)
T= phases(end); % is the period of the cycle
tau = T/600;      % time step of integration
m=200;            % spatial grid
k=5;               % the number of skipped cycles

[t,lc] = ode23s(F,0:tau:T,x0);      % forward integration
dx=(max(lc)-min(lc))/m;             % spatial resolution
center = (max(lc)+min(lc))/2;        % center of the limit cycle
iso=[x0-m^0.5*dx, x0+m^0.5*dx];   % isochron's initial segment

for t=0:-tau:-(k+1)*T              % backward integration
    for i=1:size(iso,2)
        iso(:,i)=iso(:,i)-tau*feval(F,t,iso(:,i)); % move one step
    end;
    i=1;
    while i<=size(iso,2)           % remove infinite solutions
        if any(abs(iso(:,i)-center)>1.5*m*dx)    % check boundaries
            iso = [iso(:,1:i-1), iso(:,i+1:end)]; % remove
        else
            i=i+1;
        end;
    end;
    i=1;
    while i<=size(iso,2)-1
        d=sqrt(sum(((iso(:,i)-iso(:,i+1))./dx).^2)); % normalized distance
        if d > 2                                % add a point in the middle
            iso = [iso(:,1:i), (iso(:,i)+iso(:,i+1))/2 ,iso(:,i+1:end)];
        end;
        if d < 0.5                               % remove the point
            iso = [iso(:,1:i), iso(:,i+2:end)];
        else
            i=i+1;
        end;
    end;
    if (mod(-t,T)<=tau/2) & (-t<k*T+tau)      % refresh the screen
        cla;plot(lc(:,1),lc(:,2),'r'); hold on; % plot the limit cycle
    end;
    if min(abs(mod(-t,T)-phases))<tau/2    % plot the isochrons
        plot(iso(1,:),iso(2,:),'k-'); drawnow;
    end;
end;
```

```
hold off;
```

The call of the function is `isochrons('F',0:0.1:2*pi,[1;0])`; with

```
function dx = F(t,x);
z=x(1)+1i*x(2);
dz=(1+1i)*z-z*z*conj(z);
dx=[real(dz); imag(dz)];
```

4. (Hoppensteadt and Keener 1982) From calculus,  $B \cdot C = |B| |C| \cos(\psi)$ . Since  $|B| = 1$  and  $C = (A + \cos \vartheta, \sin \vartheta)$ , see Fig. 10.46, we have  $B \cdot C = A \cos \vartheta + \cos^2 \vartheta + \sin^2 \vartheta$ . Hence,  $\cos \psi = (1 + A \cos \vartheta) / \sqrt{1 + 2A \cos \vartheta + A^2}$ . When  $\vartheta$  is in the upper (lower) half-plane, the phase is delayed (advanced).
5. An example is the file `prc.m`

```
function PRC=prc(F,phases,x0,A)
% plot phase-resetting curve (PRC) of system x'=F(t,x) + A delta(t)
% at points given by the vector 'phases'.
% 'x0' is a point on the limit cycle with zero phase
% A is the strength of stimulation (row-vector)
% use peaks of spikes to find the phase differences
T= phases(end); % is the period of the cycle
tau = T/6000; % time step of integration
k=3; % the number of cycles needed to determine the new phase
PRC=[];
[tc,lc] = ode23s(F,0:tau:k*T,x0); % find limit cycle
peak=1+find(lc(2:end-1,1)>lc(1:end-2,1)&lc(2:end-1,1)>=lc(3:end,1));
peak0 = tc(peak(end)); % the last peak is used for reference
for i=1:length(phases)
    [m,j]=min(abs(phases(i)-tc));
    [t,x] = ode23s(F,phases(i):tau:k*T,lc(j,:)+A); % stimulate
    peaks=1+find(x(2:end-1,1)>x(1:end-2,1)&x(2:end-1,1)>=x(3:end,1));
    PRC=[PRC, mod(T/2+peak0-t(peaks(end)),T)-T/2];
    subplot(2,1,2);drawnow;
    plot(phases(1:length(PRC)),PRC);
    xlabel('phase of stimulation');ylabel('induced phase difference');
    subplot(2,1,1);
    plot(tc,lc(:,1),'r',t,x(:,1),t(peaks(end)),x(peaks(end),1),'ro');
    xlabel('time');ylabel('membrane potential');
end;
```

An example of a call of the function is `PRC=prc('F',0:0.1:2*pi,[-1 0],[0.1 0])`; with

```
function dx = F(t,x);
z=x(1)+1i*x(2);
dz=(1+1i)*z-z*z*conj(z);
dx=[real(dz); imag(dz)];
```

- 6.

$$\begin{aligned} \text{grad } \vartheta(x) &= \left( \frac{\vartheta(x+h_1) - \vartheta(x)}{h_1}, \dots, \frac{\vartheta(x+h_m) - \vartheta(x)}{h_m} \right) \\ &= \left( \frac{\text{PRC}_1(\vartheta(x), h_1)}{h_1}, \dots, \frac{\text{PRC}_m(\vartheta(x), h_m)}{h_m} \right) \end{aligned}$$

$$\begin{aligned}
& \quad (\text{in the limit } h \rightarrow 0) \\
= & \left( \frac{Z_1(\vartheta(x))h_1}{h_1}, \dots, \frac{Z_m(\vartheta(x))h_m}{h_m} \right) \\
= & (Z_1(\vartheta(x)), \dots, Z_m(\vartheta(x))) = Z(\vartheta(x)) .
\end{aligned}$$

7. (Brown et al. 2004, Appendix A) Let  $x$  be a point on the limit cycle and  $z$  be an arbitrary nearby point. Let  $x(t)$  and  $z(t)$  be the trajectories starting from the two points, and  $y(t) = z(t) - x(t)$  be the difference. All equations below are valid up to  $\mathcal{O}(y^2)$ . The phase shift  $\Delta\vartheta = \vartheta(z(t)) - \vartheta(x(t)) = \text{grad } \vartheta(x(t)) \cdot y(t)$  does not depend on time. Differentiating with respect to time and taking  $\text{grad } \vartheta(x(t)) = Z(\vartheta(t))$  (see previous exercise), results in

$$\begin{aligned}
0 &= (d/dt)(Z(\vartheta(t)) \cdot y(t)) = Z'(\vartheta(t)) \cdot y(t) + Z(\vartheta(t)) \cdot Df(x(t))y(t) \\
&= Z'(\vartheta(t)) \cdot y(t) + Df(x(t))^T Z(\vartheta(t)) \cdot y(t) \\
&= (Z'(\vartheta(t)) + Df(x(t))^T Z(\vartheta(t))) \cdot y(t) .
\end{aligned}$$

Since  $y$  is arbitrary,  $Z$  satisfies  $Z'(\vartheta) + Df(x(\vartheta))^T Z(\vartheta) = 0$ , i.e., the adjoint equation (10.10). The normalization follows from (10.7).

8. The solution to  $\dot{v} = b - v$  with  $v(0) = 0$  is  $v(t) = b(1 - e^{-t})$  with the period  $T = \ln(b/(b-1))$  determined from the threshold crossing  $v(T) = 1$ . From  $v = b(1 - e^{-\vartheta})$  we find  $\vartheta = \ln(b/(b-v))$ , hence

$$\text{PRC}(\vartheta) = \vartheta_{\text{new}} - \vartheta = \min \{ \ln(b/(b \exp(-\vartheta) - A), T) \} - \vartheta .$$

9. The system  $\dot{v} = 1 + v^2$  with  $v(0) = -\infty$  has the solution (check by differentiating)  $v(t) = \tan(t - \pi/2)$  with the period  $T = \pi$ . Since  $t = \pi/2 + \text{atan } v$ , we find

$$\text{PTC}(\vartheta) = \pi/2 + \text{atan}[A + \tan(\vartheta - \pi/2)]$$

and

$$\text{PRC}(\vartheta) = \text{PTC}(\vartheta) - \vartheta = \text{atan}[A + \tan(\vartheta - \pi/2)] - (\vartheta - \pi/2) .$$

10. The system  $\dot{v} = b + v^2$  with  $b > 0$  and the initial condition  $v(0) = v_{\text{reset}}$  has the solution (check by differentiating)

$$v(t) = \sqrt{b} \tan(\sqrt{b}(t + t_0))$$

where

$$t_0 = \frac{1}{\sqrt{b}} \text{atan} \frac{v_{\text{reset}}}{\sqrt{b}} .$$

Equivalently,

$$t = \frac{1}{\sqrt{b}} \text{atan} \frac{v}{\sqrt{b}} - t_0 .$$

From the condition  $v = 1$  (peak of the spike), we find

$$T = \frac{1}{\sqrt{b}} \text{atan} \frac{1}{\sqrt{b}} - t_0 = \frac{1}{\sqrt{b}} \left( \text{atan} \frac{1}{\sqrt{b}} - \text{atan} \frac{v_{\text{reset}}}{\sqrt{b}} \right) ,$$

Hence

$$\text{PRC}(\vartheta) = \vartheta_{\text{new}} - \vartheta = \min \left\{ \frac{1}{\sqrt{b}} \text{atan} \left[ \frac{A}{\sqrt{b}} + \tan(\sqrt{b}(\vartheta + t_0)) \right] - t_0, T \right\} - \vartheta .$$

11. Let  $\vartheta$  denotes the phase of oscillator 1. Let  $\chi_n$  denote the phase of oscillator 2 just before oscillator 1 fires a spike, i.e., when  $\vartheta = 0$ . This spike resets  $\chi_n$  to  $\text{PTC}_2(\chi_n)$ . Oscillator 2 fires a spike when  $\vartheta = T_2 - \text{PTC}_2(\chi_n)$ , and it resets  $\vartheta$  to  $\text{PTC}_1(T_2 - \text{PTC}_2(\chi_n))$ . Finally, oscillator 1 fires its spike when oscillator 2 has the phase  $\chi_{n+1} = T_1 - \text{PTC}_1(T_2 - \text{PTC}_2(\chi_n))$ .

12. [MATLAB] An example is the file `adjoint.m`

```

function Q=adjoint(F,t,x0)
% finds solution to the Malkin's adjoint equation  $Q' = -DF^t Q$ 
% at time-points t with t(end) being the period
% 'x0' is a point on the limit cycle with zero phase
tran=3;           % the number of skipped cycles
dx = 0.000001; dy = 0.000001;   % for evaluation of Jacobian

Q(1,:)=feval(F,0,x0)';          % initial point;
[t,x] = ode23s(F,t,x0);         % find limit cycle

for k=1:tran
    Q(length(t),:)=Q(1,:);      % initial point;
    for i=length(t):-1:2          % backward integration
        L = [(feval(F,t(i),x(i,:)+[dx 0])-feval(F,t(i),x(i,:)))/dx, ...
                (feval(F,t(i),x(i,:)+[0 dy])-feval(F,t(i),x(i,:)))/dy];
        Q(i-1,:) = Q(i,:)+ (t(i)-t(i-1))*(Q(i,:)*L);
    end;
end;
Q = Q/(Q(1,:)*feval(F,0,x0));  % normalization

```

An example of a call of the function is `Q=adjoint('F',0:0.01:2*pi,[1 0])`; with

```

function dx = F(t,x);
z=x(1)+1i*x(2);
dz=(1+1i)*z-z*z*conj(z);
dx=[real(dz); imag(dz)];

```

13. [MATLAB] We assume that  $\text{PRC}(\vartheta)$  is given by its truncated Fourier series with unknown Fourier coefficients. Then, we find the coefficients that minimize the difference between predicted and actual interspike intervals. MATLAB file `findprc.m` takes the row vector of spike moments, not counting the spike at time zero, and the input function  $p(t)$ , determines the sampling frequency, the averaged period of oscillation and then calls file `prcerror.m` to find PRC.

```

function PRC=findprc(sp,pp)
global spikes p tau n
% finds PRC of an oscillator theta'= 1 + PRC(theta)pp(t)
% using the row-vector of spikes 'sp' (when theta(t)=0)
spikes = [0 sp];
p=pp;
tau = spikes(end)/length(p) % time step (sampling period)
n=8;    % The number of Fourier terms approximating PRC
coeff=zeros(1,2*n+1); % initial approximation
coeff(2*n+2) = spikes(end)/length(spikes); % initial period

coeff=fminsearch('prcerror',coeff);
a = coeff(1:n)    % Fourier coefficients for sin
b = coeff(n+1:2*n) % Fourier coefficients for cos
b0= coeff(2*n+1)  % dc term
T = coeff(2*n+2)  % period of oscillation
PRC=b0+sum((ones(floor(T/tau),1)*a).*sin((tau:tau:T)'*(1:n)*2*pi/T),2)+...
sum((ones(floor(T/tau),1)*b).*cos((tau:tau:T)'*(1:n)*2*pi/T),2);

```

The following program must be in the file `prcerror.m`.

```

function err=prcerror(coeff)
global spikes p tau n
a = coeff(1:n);      % Fourier coefficients for sin
b = coeff(n+1:2*n); % Fourier coefficients for cos
b0= coeff(2*n+1);   % dc term
T = coeff(2*n+2);   % period of oscillation
err=0;
i=1;
clf;
for s=2:length(spikes)
    theta=0;
    while i*tau<=spikes(s)
        PRC=b0+sum(a.*sin((1:n)*2*pi*theta/T))+...
            sum(b.*cos((1:n)*2*pi*theta/T));
        theta = theta + tau*(1+PRC*p(i));
        i=i+1;
    end;
    err = err + (theta-T)^2;
    subplot(2,1,1);
    plot(spikes(s),T,'r.',spikes(s),theta,'b.');
    hold on;
end;
axis([0 spikes(end) 0.75*T 1.25*T])
subplot(2,1,2);
PRC=b0+sum((ones(floor(T/tau),1)*a).*sin((tau:tau:T)'*(1:n)*2*pi/T),2)+...
    sum((ones(floor(T/tau),1)*b).*cos((tau:tau:T)'*(1:n)*2*pi/T),2);
plot(PRC);
err = (err/(length(spikes)-1))^0.5; % normalization
text(0,mean(PRC),['err=' num2str(err)]);
drawnow;

```

14. *Winfree approach:* Using results of Ex. 8,

$$\frac{\partial}{\partial A} \ln \frac{b}{be^{-\vartheta} - A} = \frac{1}{be^{-\vartheta} - A}$$

and setting  $A = 0$ , we get  $Z(\vartheta) = e^\vartheta/b$ .

*Kuramoto approach:* The solution is  $v(\vartheta) = b(1 - e^{-\vartheta})$  with  $T = \ln(b/(b-1))$  and  $f(v(\vartheta)) = be^{-\vartheta}$ . From the condition (10.7),  $\text{grad}(\vartheta) = 1/f(v(\vartheta)) = e^\vartheta/b$ .

*Malkin approach:*  $Df = -1$ , hence  $\dot{Q} = 1 \cdot Q$  has the solution  $Q(t) = Ce^t$ . The free constant  $C = 1/b$  is found from the normalization condition  $Q(0) \cdot (b-0) = 1$ .

15. *Winfree approach:* Using results of Ex. 10 and the relation  $\text{PRC} = \text{PTC} - \vartheta$ , we get,

$$\frac{\partial}{\partial A} (\pi/2 + \text{atan}(A - \cot \vartheta) - \vartheta) = \frac{1}{1 + (A - \cot \vartheta)^2}$$

and setting  $A = 0$ , we obtain  $Z(\vartheta) = \sin^2 \vartheta$ .

*Kuramoto approach:* The solution is  $v(\vartheta) = -\cot \vartheta$  with  $T = \pi$  and  $f(v(\vartheta)) = 1/\sin^2 \vartheta$ . From the normalization condition (10.7),  $\text{grad}(\vartheta) = 1/f(v(\vartheta)) = \sin^2 \vartheta$ .

*Malkin approach:*  $Df = 2v$ , hence  $\dot{Q} = 2 \cot(t) \cdot Q$  has the solution  $Q(t) = C \sin^2 t$ . The free constant  $C = 1$  is found from the normalization condition  $Q(\pi/2) \cdot (1 + 0^2) = 1$ .

16. *Winfree approach:* Using results of Ex. 4,

$$Z(\vartheta) = \frac{\partial}{\partial A} \text{acos} \frac{1 + A \cos \vartheta}{\sqrt{1 + 2A \cos \vartheta + A^2}} = -\sin \vartheta$$

at  $A = 0$ .

*Kuramoto approach:* Since  $\text{grad } \vartheta(x)$  is orthogonal to the contour line of the function  $\vartheta(x)$  at  $x$ , i.e., the isochron of  $x$ , and the results of Ex. 1 that isochrons are radial, we get  $\text{grad } (\vartheta) = (-\sin \vartheta, \cos \vartheta)$  using purely geometrical considerations. Since  $p(t)$  is real, we need to keep only the first component.

*Malkin approach:* Let us work in the complex domain. On the circle  $z(t) = e^{it}$  we get  $Df = i$ . Since  $Df^\top$  is equivalent to complex-conjugation in the complex domain, we get  $\dot{Q} = i \cdot Q$ , which has the solution  $Q(t) = Ce^{it}$ . The free constant  $C = i$  is found from the normalization condition  $Q(0)^*i = 1$ , where  $*$  means complex-conjugate.

Alternatively, on the circle  $z(t) = e^{it}$ , we have  $f(z(t)) = f(e^{it}) = ie^{it}$ . From the normalization condition  $Q(t)^*f(z(t)) = 1$  we find  $Q(t) = ie^{it} = -\sin \vartheta + i \cos \vartheta$ .

17. Rescaling the state variable  $z = \sqrt{b}u$  and the time,  $\tau = \epsilon t$ , we obtain the reduced system

$$u' = (1 + i)u + (-1 + di)u|u|^2 + \varepsilon p(t).$$

We can apply the theory only when  $\varepsilon$  is small. That is, the theory is guaranteed to work in a very weak limit  $\epsilon \ll b\sqrt{b} \ll 1$ . As it is often the case, numerical simulations suggest that the theory works well outside the guaranteed interval. Substituting  $u = re^{i\theta}$  into this equation,

$$r'e^{i\theta} + re^{i\theta}i\theta' = (1 + i)re^{i\theta} + (-1 + di)r^3e^{i\theta} + \varepsilon p(t),$$

dividing by  $e^{i\theta}$  and separating real and imaginary terms, we represent the oscillator in polar coordinates

$$\begin{aligned} r' &= r - r^3 + \varepsilon \text{Re } p(t)e^{-i\theta} \\ \theta' &= 1 + dr^2 + \varepsilon \text{Im } r^{-1}p(t)e^{-i\theta}. \end{aligned}$$

When  $\varepsilon = 0$ , this system has a limit cycle attractor  $r(t) = 1$  and  $\theta(t) = (1 + d)t$ , provided that  $d \neq -1$ . On the attractor, the solution to Malkin's adjoint equation (10.10),

$$Q' = - \begin{pmatrix} -2 & 0 \\ 2d & 0 \end{pmatrix}^\top Q \quad \text{with} \quad Q(t) \cdot \begin{pmatrix} 0 \\ 1 + d \end{pmatrix} = 1,$$

is  $Q(t) = (d, 1)/(1+d)$ . Indeed, the normalization condition results in  $Q_2(t) = 1/(1+d)$ . Hence, unique periodic solution of the first equation,  $Q'_1 = 2Q_1 - 2d/(1+d)$ , is  $Q_1(t) = d/(1+d)$ . One can also use Kuramoto's approach and the results of Ex. 2. The corresponding phase model,

$$\vartheta' = 1 + \varepsilon \{d \text{Re } p(t)e^{-i(1+d)\vartheta} + \text{Im } p(t)e^{-i(1+d)\vartheta}\}/(d+1),$$

can be simplified via  $\theta = (1 + d)\vartheta$  (notice the font difference) to get the result.

18. (Delayed coupling) Let  $\vartheta(t) = t + \varphi(\tau)$ , where  $\tau = \varepsilon t$  is the slow time. Since  $\vartheta(t-d) = t-d+\varphi(\tau-\varepsilon d) = t-d+\varphi(\tau)+\mathcal{O}(\varepsilon)$ , we have  $x_j(\vartheta_i(t-d_{ij})) = x_j(t-d_{ij}+\varphi(\tau))$  so that we can proceed as in Sect. 10.2.5 except that there is an extra term,  $-d_{ij}$ , in (10.16). See also Izhikevich (1998).

19. Let  $\chi = \varphi_2 - \varphi_1$ ; then we have

$$\dot{\chi} = \omega - c \sin \chi .$$

If  $|\omega/c| \leq 1$ , then there are two synchronized states,  $\chi = \arcsin(\omega/c)$  and  $\chi = \pi - \arcsin(\omega/c)$ , one stable and the other unstable.

20. From the theorem by Hoppensteadt and Izhikevich (1997) presented in Sect. 10.3.3 it follows that Kuramoto's model is a gradient system when  $c_{ij} = c_{ji}$  and  $\psi_{ij} = -\psi_{ji}$ . From Ermentrout's theorem presented in the same section, it follows that the synchronized state  $\varphi_i = \varphi_j$  is stable if, e.g., all  $\psi_{ij} = 0$  and  $c_{ij} > 0$ .
21. Since the probability density function  $g(\omega)$  is symmetric, the averaged frequency deviation of the network is zero, and rotating the coordinate system, we can make the cluster phase  $\psi = 0$ . The network is split into two populations: One oscillating with the cluster ( $|\omega| < Kr$ ), thereby forming the cluster, and one drifting in and out of the cluster. The latter does not contribute to the Kuramoto synchronization index, because contributions from different oscillators cancel each other on average. In the limit  $n \rightarrow \infty$ , the sum (10.21) becomes the integral

$$r = \int e^{i\varphi(\omega)} g(\omega) d\omega \approx \int_{|\omega| < Kr} e^{i\varphi(\omega)} g(\omega) d\omega .$$

Next, since there are as many oscillators with positive  $\varphi$  as with negative, the imaginary parts of  $e^{i\varphi(\omega)}$  cancel each other, so that

$$r = \int_{|\omega| < Kr} \cos \varphi(\omega) g(\omega) d\omega .$$

Using the condition for locking with the cluster,  $\omega = Kr \sin \varphi$ , we change the variables in the integral and get (10.22).

22. Let  $\chi = \varphi_2 - \varphi_1$ ; then  $\chi' = (c_2 - c_1)H(\chi)$ . The in-phase state  $\chi = 0$  exists when either  $c_1 = c_2$  or  $H(0) = 0$ . Since  $H(\chi)$  is even,  $H'(0) = 0$ , hence it is neutrally stable in either case. The anti-phase state  $\chi = T/2$  exists when  $H(T/2) = 0$ , and it can be exponentially stable or unstable depending on the sign of  $H'(T/2)$ .
23. See Izhikevich (1999), Sect IVB.
24. The exponential stability requirement is  $G'(0) = -2H'(0) < 0$ . Since  $x'(t) = f(x(t))$ , we have

$$TH'(0) = \int_0^T \frac{g'(x(t))f(x(t))}{f(x(t))} dt = \int_0^T g'(x(t)) dt = \int_{\mathbb{S}^1} \frac{g'(x)}{f(x)} dx > 0$$

Integrating the latter equation by parts, or differentiating

$$H(\chi) = \frac{1}{T} \int_0^T \frac{g(x(t))}{f(x(t-\chi))} dt \quad \text{at } \chi = 0, \text{ we obtain} \quad \int_{\mathbb{S}^1} \frac{f'(x)}{f^2(x)} g(x) dx > 0 .$$

25. (Brown et al. 2004) The solution of  $x' = \lambda x$  with  $x(0) = x_0$  is  $x(t) = x_0 e^{\lambda t}$ . The period  $T = \log(\Delta/x_0)/\lambda$  is found from the condition  $x(T) = \Delta$ . Hence,  $Q(\vartheta) = 1/(\lambda x(\vartheta)) = 1/(\lambda x_0 e^{\lambda \vartheta}) = e^{\lambda(T-\vartheta)}/(\Delta \lambda)$ .
26. Let us first consider the SNIC case  $\dot{x} = 1 + x^2$ . The solution starting with  $x(0) = x_{\text{reset}}$  has the form (check by differentiating)  $x(t) = \tan(t + t_0)$ , where  $t_0 = \text{atan } x_{\text{reset}}$ . The period should be found from the condition  $\tan(T + t_0) = +\infty$ , and it is  $T = \pi/2 - t_0$ . Hence,  $x(t) = \tan(t + \pi/2 - T) = -\cot(t - T)$ . Now,  $Q(\vartheta) = 1/(1+x(\vartheta)^2) = 1/(1+\cot^2(\vartheta-T)) = \sin^2(\vartheta-T)$ . The homoclinic case  $\dot{x} = -1 + x^2$  is quite similar. The solution starting with  $x(0) = x_{\text{reset}} > 1$  has the form (check by differentiating)  $x(t) = -\coth(t + t_0)$ , where  $t_0 = \text{acoth}(-x_{\text{reset}}) = -\text{acoth}(x_{\text{reset}})$ . The period is found from the condition  $-\coth(T+t_0) = +\infty$  resulting in  $T = -t_0$ . Hence,  $x(t) = -\coth(t - T)$ . Finally,  $Q(\vartheta) = 1/(-1+x(\vartheta)^2) = 1/(1+\coth^2(\vartheta-T)) = \sinh^2(\vartheta-T)$ .